



Helmholtz-Zentrum  
**hereon**



Christian-Albrechts-Universität zu Kiel

---

# Corrosion inhibitors for bare and PEO-coated Mg alloys

---

## Dissertation

zur Erlangung des akademischen  
Grades Doktor der Ingenieurwissenschaften  
(Dr.-Ing.)  
der Technischen Fakultät  
Der Christian-Albrechts-Universität zu Kiel

**Bahram Vaghefinazari**

aus  
dem Iran

Kiel, 2025



**Gutachtern der Dissertation:**

1. Gutachter: Prof. Dr. Mikhail L. Zheludkevich
2. Gutachter: Prof. Dr. Ingrid Milošev
3. Gutachter: Prof. Dr. rer. Nat. Rainer Adelung

**Vorsitzender des Promotionsausschusses:**

Prof. Dr. Zeynep Altintas

**Datum der Disputation:**

25<sup>th</sup> April 2025




### **Eidesstattliche Erklärung**

Hiermit erkläre ich, dass die beigefügte Dissertation, abgesehen von der Beratung durch die Betreuerin, nach Inhalt und Form meine eigene Arbeit ist.

Die Arbeit, ganz oder zum Teil, wurde nie schon einer anderen Stelle im Rahmen eines Prüfungsverfahrens vorgelegt und ist abgesehen, von den im Anhang angegebenen Veröffentlichungen, nicht anderweitig zur Veröffentlichung vorgelegt worden.

Außerdem ist die Arbeit unter Einhaltung der Regeln guter wissenschaftlicher Praxis der Deutschen Forschungsgemeinschaft entstanden.

Bahram Vaghefinazari

13.11.2024 



## Content

Abstract .....	2
Zusammenfassung.....	3
1 Introduction.....	4
2 Literature review and state of the art .....	6
3 Motivation and objectives.....	74
4 Experimental .....	75
5 Results .....	85
5.1 Overview .....	85
5.2 Screening of corrosion inhibitors .....	86
5.3 Adverse effect of 2,5-PDC corrosion inhibitor on PEO coated magnesium.....	95
5.4 Exploring the corrosion inhibition mechanism of 8-hydroxyquinoline for a PEO-coated magnesium alloy.....	112
5.5 Corrosion inhibition of decylphosphonate on bare and PEO-coated Mg alloy .....	133
6 Discussion .....	156
Comparison between 8HQ and DP .....	160
7 Conclusion and Outlook .....	161
8 References .....	162
Publications during candidacy.....	173
Acknowledgement.....	175

## Abstract

The increasing demand for sustainable and energy-efficient materials in industries such as automotive, aerospace, and biomedical engineering has brought magnesium (Mg) alloys to the forefront due to their exceptional strength-to-weight ratio, low density, and biocompatibility. However, the application of Mg alloys is significantly hindered by their high susceptibility to corrosion, particularly in aqueous environments. Plasma Electrolytic Oxidation (PEO) coatings have been proposed as a promising solution, offering a protective barrier and the potential for "active protection" through the incorporation of corrosion inhibitors within their porous structure. Despite the potential of this approach, the field remains underexplored, with limited research on effective corrosion inhibitors for PEO-coated Mg alloys.

This thesis addresses this gap by systematically investigating a range of corrosion inhibitors to enhance the corrosion resistance of PEO-coated Mg alloys. An initial evaluation of more than twenty potential inhibitors revealed that their effectiveness on bare Mg alloys does not necessarily translate to improved corrosion resistance in PEO-coated systems. For example, while the sodium salt of 2,5-pyridinedicarboxylate (2,5PDC-Na) was effective on bare Mg, it was found to accelerate the degradation of PEO coatings, highlighting the complexity of inhibitor interactions within PEO-coated magnesium systems. Consequently, an in-depth investigation was conducted to understand these unexpected adverse effects, ultimately providing insights into the selection of effective inhibitors for PEO-coated Mg alloys.

Among the tested inhibitors, sodium salts of 8-hydroxyquinoline (8HQ) and decylphosphonic acid (DP) were found to significantly improve the corrosion resistance of PEO-coated AZ21 Mg alloy. DP, in particular, demonstrated superior inhibition performance by delaying the failure of the PEO coating by over 50 days, compared to the 4-day failure time of the reference PEO coating without an inhibitor. The formation of insoluble compounds between these inhibitors and  $Mg^{2+}$  ions contributed to the enhanced protection through several mechanisms. Given DP's outstanding inhibition performance, a protective PEO system was further developed by loading the PEO layer with a high concentration of DP, which significantly reduced corrosion creep from defect in a salt spray test.

Based on the findings from the in-depth investigation of the inhibition effects of these three chemicals (2,5PDC-Na, 8HQ, and DP), a set of criteria was established for selecting effective corrosion inhibitors to be incorporated into PEO coatings on magnesium. A key parameter in these criteria is the formation of highly insoluble compounds resulting from the interaction between the inhibitor and  $Mg^{2+}$  ions. These criteria were evaluated for the initially screened compounds to assess their validity across different types of inhibitors.

The findings of this thesis contribute to a deeper understanding of the interactions between corrosion inhibitors and PEO-coated Mg alloys, providing a framework for the selection and application of inhibitors for PEO-coated magnesium. The insights gained from this research are expected to inform future studies and industrial practices, ultimately supporting the development of more durable and corrosion-resistant Mg alloy-based components for various critical applications.

## Zusammenfassung

Die steigende Nachfrage nach nachhaltigen und energieeffizienten Materialien in Branchen wie der Automobil-, Luft- und Raumfahrt- sowie der biomedizinischen Technik hat Magnesium (Mg)-Legierungen aufgrund ihres außergewöhnlichen Stärke-Gewichts-Verhältnisses, ihrer niedrigen Dichte und Biokompatibilität in den Vordergrund gerückt. Die Anwendung von Mg-Legierungen wird jedoch erheblich durch ihre hohe Korrosionsanfälligkeit, insbesondere in wässrigen Umgebungen, eingeschränkt. Plasmaelektrolytische Oxidationsbeschichtungen (PEO) werden als vielversprechende Lösung vorgeschlagen, da sie eine schützende Barriere bilden und ein "aktiven Schutz" durch die Einbindung von Korrosionsinhibitoren in ihre poröse Struktur ermöglichen. Trotz des Potenzials dieses Ansatzes ist das Feld wenig erforscht, und es gibt nur begrenzte Forschung zu wirksamen Korrosionsinhibitoren für PEO-beschichtete Mg-Legierungen.

Diese Arbeit widmet sich dieser Lücke, indem eine systematische Untersuchung verschiedener Korrosionsinhibitoren durchgeführt wird, um die Korrosionsbeständigkeit von PEO-beschichteten Mg-Legierungen zu verbessern. Eine anfängliche Bewertung von mehr als zwanzig potenziellen Inhibitoren zeigte, dass deren Wirksamkeit auf unbeschichteten Mg-Legierungen nicht zwangsläufig zu einer verbesserten Korrosionsbeständigkeit in PEO-beschichteten Systemen führt. Zum Beispiel beschleunigte das Natriumsalz von 2,5-Pyridindicarboxylat (2,5PDC-Na), obwohl es auf unbeschichtetem Mg wirksam war, den Abbau der PEO-Beschichtung, was die Komplexität der Inhibitor-Interaktionen in PEO-beschichteten Magnesiumsystemen verdeutlicht. Infolgedessen wurde eine eingehende Untersuchung durchgeführt, um diese unerwarteten nachteiligen Effekte zu verstehen und letztlich Einblicke in die Auswahl effektiver Inhibitoren für PEO-beschichtete Mg-Legierungen zu gewinnen.

Unter den getesteten Inhibitoren verbesserten Natriumsalze von 8-Hydroxychinolin (8HQ) und Decylphosphonsäure (DP) signifikant die Korrosionsbeständigkeit von PEO-beschichteten AZ21-Mg-Legierungen. Insbesondere DP zeigte eine überlegene Inhibitorleistung, indem es das Versagen der PEO-Beschichtung um über 50 Tage verzögerte, verglichen mit einer Versagenszeit von 4 Tagen bei der Referenz-PEO-Beschichtung ohne Inhibitor. Die Bildung unlöslicher Verbindungen zwischen diesen Inhibitoren und  $Mg^{2+}$ -Ionen trug durch verschiedene Mechanismen zum verbesserten Schutz bei. Angesichts der hervorragenden Inhibitorleistung von DP wurde ein schützendes PEO-System weiterentwickelt, indem die PEO-Schicht mit einer hohen Konzentration an DP beladen wurde, was die Korrosionsausbreitung bei einem Salzsprühtest erheblich reduzierte.

Basierend auf den Erkenntnissen aus der eingehenden Untersuchung der Hemmeffekte dieser drei Chemikalien (2,5PDC-Na, 8HQ und DP) wurde ein Satz von Kriterien zur Auswahl wirksamer Korrosionsinhibitoren entwickelt, die in PEO-Beschichtungen auf Magnesium eingebunden werden sollen. Ein entscheidender Parameter in diesen Kriterien ist die Bildung hochgradig unlöslicher Verbindungen, die aus der Interaktion zwischen dem Inhibitor und  $Mg^{2+}$ -Ionen resultieren. Diese Kriterien wurden für die anfangs untersuchten Verbindungen bewertet, um ihre Gültigkeit über verschiedene Inhibitortypen hinweg zu prüfen.

Die Ergebnisse dieser Arbeit tragen zu einem tieferen Verständnis der Wechselwirkungen zwischen Korrosionsinhibitoren und PEO-beschichteten Mg-Legierungen bei und bieten einen Rahmen für die Auswahl und Anwendung von Inhibitoren für PEO-beschichtetes Magnesium. Die gewonnenen Erkenntnisse sollen künftige Studien und industrielle Anwendungen informieren und letztlich die Entwicklung langlebigerer und korrosionsbeständigerer Mg-Legierungskomponenten für verschiedene kritische Anwendungen unterstützen.

# 1 Introduction

The growing concern for environmental impact and energy efficiency has led industries such as automobile manufacturing, aerospace, and aeronautics to prioritize the use of lightweight and eco-friendly materials. In this regard, Mg alloys, known for being the lightest of all structural metals, are of significant interest as alternatives to traditional aluminum alloys and steel. Magnesium has high strength-to-weight ratio of 158, which is approximately 3.4 times greater than that of steel and 1.4 times higher than aluminum. With a low density of 1.74 g/cm<sup>3</sup>, Mg is about 60% lighter than steel and 33% lighter than aluminum. It also offers good machinability, favorable casting properties, and excellent dimensional stability.

Moreover, magnesium-based materials are especially promising for use in the biomedical industry, including tissue engineering, orthopedic, and cardiovascular applications [1, 2] primarily due to their biodegradability, biocompatibility, and mechanical properties similar to natural bone [3, 4].

Despite the advantageous properties of magnesium alloys in several applications, their primary limitation in achieving widespread commercial applications is their high susceptibility to corrosion in aqueous environments, which leads to the rapid loss in their mechanical strength. Therefore, extensive research is being undertaken on understanding and controlling the degradation of Mg alloys.

One of the primary methods to control Mg alloy corrosion involves applying protective coatings to shield the metal from corrosive media. Several categories of coatings on Mg include metal-based coatings [5] conversion coatings [6, 7], silane sol-gel [6, 8, 9], and natural and synthetic polymeric coating [10]. Plasma Electrolytic Oxidation (PEO) is also an advanced electrochemical technique that produces ceramic-like coating on light metals, including Mg alloys. The PEO process involves polarizing the Mg substrate immersed in an electrolyte to a voltage above the anodic barrier breakdown, which accompanies with microdischarges on the surface of the substrate. The formed layer acts as a barrier against the penetration of corrosive substances, effectively preventing corrosion of Mg substrate. Additionally, this layer exhibits high tribological properties, enhancing the Mg substrate resistance to wear and friction.

The PEO layer features a porous microstructure, with pores that reach diameters of several microns. On one hand, these pores do not offer barrier properties against the penetration of corrosive medium towards the substrate. However, on the other hand, these pores can serve as reservoirs for various substances, allowing for functionalization of the PEO coating based on the desired application. For instance, in biomedical applications, the PEO surface and pores can be loaded with bioactive materials or drugs [11-13]. When the aim is to improve tribological properties, lubricants can be loaded [14, 15]. Most commonly, the PEO pores are suitable location to accommodate corrosion inhibitors. This not only enhances the corrosion resistance of the coating system but also provides active corrosion protection on demand.

Although the effectiveness of loading PEO coatings with corrosion inhibitors was demonstrated nearly 15 years ago [16], only a handful of studies have since reported on this approach for different metallic substrates. The majority of these studies are limited to just two inhibitors, namely 8-hydroxyquinoline and Ce salts. However, a significantly larger number of potential inhibitors, particularly for Mg alloys, have been discovered [17], the inhibition efficiency of some of them is already confirmed by other researchers on different Mg substrate and conditions [8]. These can be considered as potential candidates for incorporation into the PEO coating to enhance its anti-corrosion and active inhibition performance.

Therefore, the primary objectives of this dissertation are to discover effective corrosion inhibitors for a PEO-coated Mg system, to uncover the underlying mechanisms through which they inhibit the corrosion, and ultimately to establish criteria for determining the suitability of potential inhibitors.

The structure of this dissertation is divided into seven separate sections. The literature review and state of the art in [section 2](#) provides an overview and advances of PEO coatings and includes a published review paper on corrosion inhibitors for Mg, as well as strategies for incorporating them with other protection systems including PEO. [Section 3](#) outlines the motivation behind this research and the objectives we aim to achieve. [Section 4](#) details all the materials used and experimental methods employed in this study. [Section 5](#) presents the results obtained from this research, which includes three published papers and supplementary unpublished findings. In [section 6](#), a comprehensive discussion on all the experimental results is provided. [Section 7](#) summarizes the key findings of this work and presents

the conclusions drawn from all the results. This section also offers insights into potential applications and future research directions for inhibitor-loaded PEO coatings.

## 2 Literature review and state of the art

### 2.1 Overview

This section provides a review of the fundamental and state-of-the-art knowledge related to the two primary components of this thesis:

1. PEO coatings
2. Corrosion inhibitors

In the first section, PEO is introduced as a surface modification technique for metals. The current understanding of its formation mechanisms is discussed, followed by an analysis of the process parameters that influence its performance. Additionally, contemporary strategies for enhancing the properties and performance of PEO coatings are reviewed. The topics covered in this section are outlined below:

- PEO Formation Mechanism
- Composition of PEO Coatings
  - Core Chemistry
  - Particle Addition
  - Non-Aqueous Electrolytes
- Applied Electrical Parameters
- Energy Consumption
- Pre-treatment
- Post-treatment
- Applications and Commercialization

The second section, focusing on "corrosion inhibitors", is provided from a published review paper:

**B. Vaghefinazari**, E. Wierzbicka, P. Visser, R. Posner, R. Arrabal, E. Matykina, M. Mohedano, C. Blawert, M.L. Zheludkevich, S.V. Lamaka, Chromate-Free Corrosion Protection Strategies for Magnesium Alloys—A Review: Part III—Corrosion Inhibitors and Combining Them with Other Protection Strategies, *Materials*, 15 (2022) 8489. <https://doi.org/10.3390/ma15238489>.

#### **CRedit authorship contribution statement:**

**Bahram Vaghefinazari:** Conceptualization, Investigation, Validation, Writing – original draft, Writing – review & editing. **Ewa Wierzbicka:** Investigation, Writing – review & editing. **Peter Visser:** Investigation, Writing – review & editing. **Ralf Posner:** Investigation, Writing – review & editing. **Raúl Arrabal:** Investigation, Writing – review & editing. **Endzhe Matykina:** Investigation, Writing – review & editing. **Marta Mohedano:** Investigation, Writing – review & editing. **Carsten Blawert:** Investigation, Writing – review & editing. **Mikhail L. Zheludkevich:** Conceptualization, Supervision, Writing – review & editing. **Sviatlana V. Lamaka:** Conceptualization, Supervision, Writing – review & editing.

This review specifically covers corrosion inhibitors for magnesium and explores various approaches for incorporating them into different coating systems, including PEO coatings loaded with inhibitors. The content of the review is organized as follows:

- Foreword

- Inorganic Inhibitors
- Organic Inhibitors
- Inhibitor Mixtures: Synergistic Inhibiting Effects
- Integration of Inhibitors with Other Corrosion Protection Strategies
  - Sol-Gel Coatings
  - Layered Double Hydroxides (LDH)
  - PEO Coatings
- Summary and Perspectives

## 2.2 Plasma Electrolytic Oxidation (PEO)

### 2.2.1 Introduction

Plasma Electrolytic Oxidation (PEO), also called micro-arc oxidation (MAO), is surface modification technique to form ceramic-like layers on magnesium, aluminum, zinc, titanium and other metals, mainly aiming for enhancement in wear and corrosion resistance. More than 3000 scientific papers registered after 2010 with keywords of “Plasma Electrolytic Oxidation” in Scopus database shows its popularity among scientist which indeed is supported by the interest of the industry.

Similar to traditional anodizing process of metals, PEO process involves polarization of metal surfaces exposed to electrolyte. However, in contrast to anodizing that operates below a so-called breakdown voltage of original oxide films on the substrate, PEO requires polarizations of typically several hundreds of volts that is above the breakdown voltage. The coating process is featured with the formation of short-lived microdischarges on the surface of the metal, resulting in extremely high local temperature and pressure, which leads to compositional and morphological alteration of the metal surface and finally formation of ceramic-like PEO coating.

PEO coatings have a unique layered structure, consisting of a thin inner barrier layer, well adhered to the substrate and an outer porous layer. In some cases, a third layer known as the “pore band” or sometimes called as just “inner layer”, characterized by micron-sized pores, also exists between the two layers [18]. The inner layer is compact and offers superior adhesion and resistance to corrosion, while the outer porous layer and the pore band do not provide considerable barrier properties against the penetration of corrosive media. **Figure 2.1** presents an example of PEO microstructure.

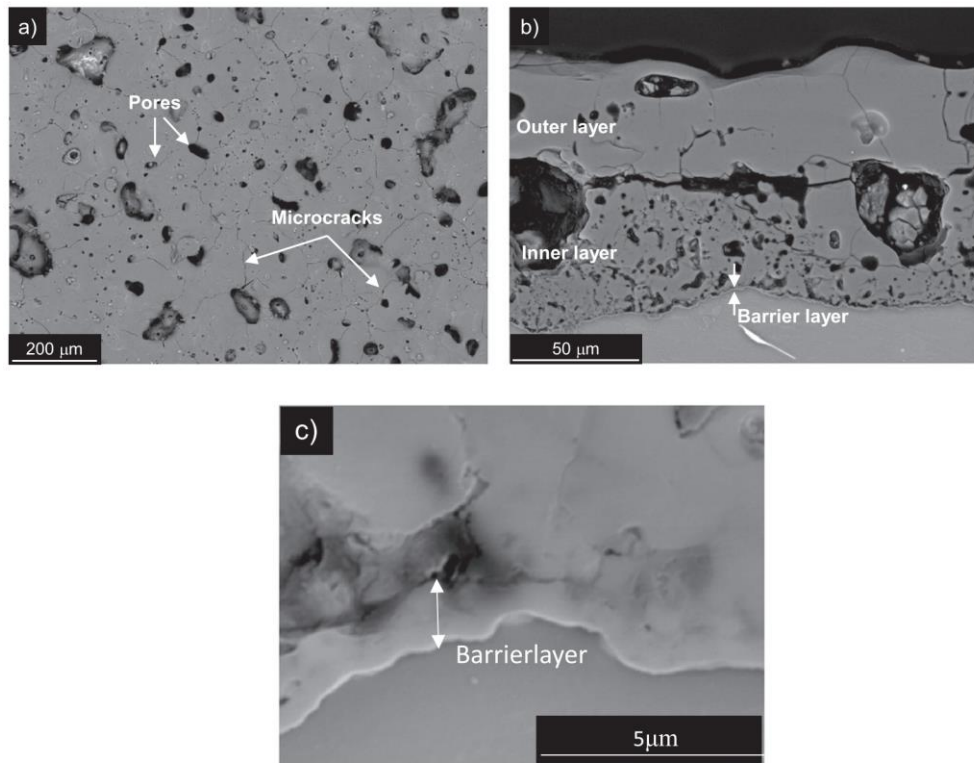


Figure 2.1 an example of PEO coating microstructure on a Mg alloy. (a) top view, cross section, (c) higher magnification of PEO/substrate interface. Adapted from [19] with permission from Elsevier.

The composition of the electrolyte plays a crucial role in determining the properties and composition of the coating. Typical PEO electrolytes consist of aqueous solutions of alkali metal silicates, aluminates, and phosphates. Additionally, adjusting the applied electrical regime—such as voltage, current, mode and polarity, duty cycle, pulse

shape, and frequency—is a common strategy to achieve coatings with the desired properties and performance. **Figure 2.2** summarizes the key parameters that influence the morphology and properties of PEO coatings. The figure also includes other strategies for modifying the functionality of PEO coatings and enhancing their performance.

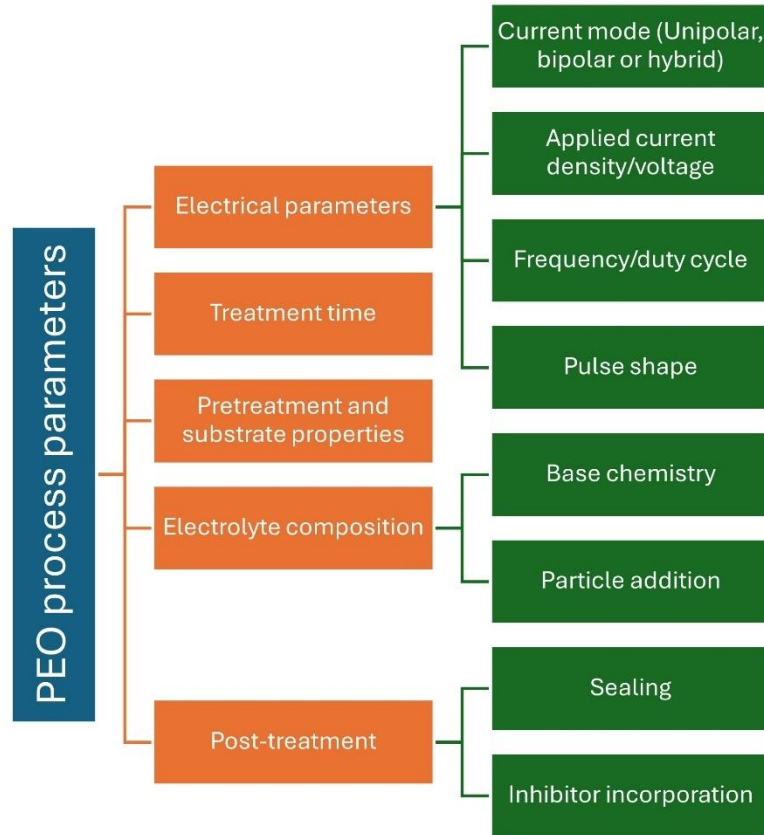


Figure 2.2 Effective parameters of PEO coatings and strategies to modify their properties. Adapted from [20].

In the following sections, the current models for the formation mechanisms of PEO are reviewed. Then, an overview of the most important parameters of PEO, as highlighted in **Figure 2.2**, is provided.

### 2.2.2 Mechanism of formation

The mechanisms behind the formation of the PEO layer are complex, as they involve electrochemical, thermal, and plasma-chemical reactions within the electrolyte [21]. As mentioned above, PEO formation involves the application of a voltage high enough that a dielectric breakdown of the anodic barrier layer occurs which is accompanied with microdischarges that appear as sudden and local spark formation on the surface. The breakdown voltage ( $V_b$ ) (aka sparking voltage) depends on many parameters including the nature of the metallic substrate, electrolyte components and concentrations. On the other hand, other parameters, including the applied current density, surface topography of the substrate, and the history of the film formation, are believed to have negligible effect on the breakdown voltage [22].

There are many studies to model the discharges and explain their contribution to the PEO coating formation, among which the most commonly accepted explanations can be summarized in the followings:

The occurrence of a discharge locally damages the oxide films, forming a discharge channel, due to high current caused by electron avalanche [22, 23]. The presence of high electrical field and discharge channel result in the high ionic transport towards the substrate [23], which contributes to the coating formation at coating/substrate interface[24]. At the same time high local temperature caused by the formed plasma (several thousands of degrees of Celsius [21, 25]), melts the high melting point oxides and substrate, as well as vaporizes the electrolyte. The resultant high pressure (can reach 100MPa [25]) cause the ejection of the molten oxide material from the discharge channel onto the coating surface. The molten oxide is then quenched and solidified on the coating surface, which

result in pancake-form features [26] on the coating surface with a discharge channel in its center. The thermal stress, volume change, and extensive gas formation [27] lead to the microstructural microcracks and voids within the coating.

Based on the location and intensity of the occurrence of discharges within the PEO layer, several types of discharges have been proposed to explain the mechanism formation of PEO coating, as depicted in **Figure 2.3** [21, 27-29]. **Figure 2.3** (a) depicts the initial model proposed by Hussein et al. [21], who only considers three types of discharges that appear on the top surface of the PEO coating. While, **Figure 2.3** (b) is the modified version by Cheng et al. [30], which also consider the existence of sparks within the PEO layer, based on the cross-sectional characterization evidence .

- Type A: at the coating top layer. Mostly results in nodular features on the coating surface
- Type B: at metal-oxide interface. Mostly results in pancake-shape features on the coating surface
- Type C: at the oxide-electrolyte interface within the upper coating. Mostly results in nodular features on the coating surface
- Type D: near the large pores near the interface between the inner and outer layer; in other words, in the pore band. It contributes more to the growth of inner layer.
- Type E: within the outer layer. The discharge does not reach the substrate.

Each of these discharges results in different coating growth and composition. Type A and C involve more concentration of electrolyte components, while type B and D yields compounds rich from the substrate. In the case of the schematic presented in **Figure 2.3** (b), the electrolyte was silicate-based, which resulted in silicon-rich particles forming at the location of occurrence of discharge type-A. These types of discharge also contributes to inward or outward growth differently [31]. The PEO coating on Mg grows inwards to the substrate as well as outwards to the coating surface simultaneously [21, 31], although the inward/outward ratio is believed to be different at different stage of PEO formation [32]. The growth direction and kinetics of the coating formation are mainly controlled by the intensity, type and distribution of discharges [31].

Note that, although the models in **Figure 2.3** might be initially proposed for the PEO coating on Al substrate, the evident similarities between the morphologies of the PEO layer as well as the spectroscopical characterization of the formed discharges of several metallic substrates, e.g. Al, Mg, Zr, Ti, can be speculated as the validity of these models for them as well.

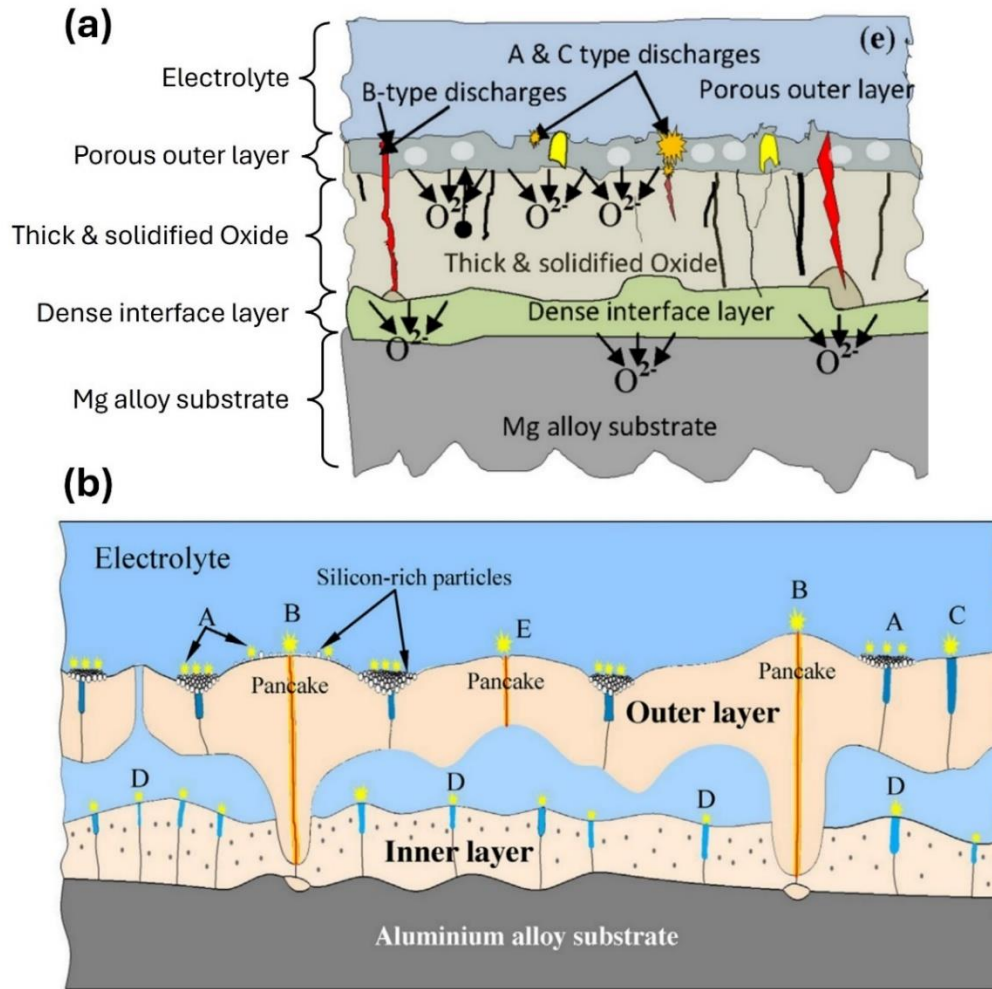


Figure 2.3 (a) schematic diagram of the discharge models for the PEO process [21] (b) Schematic of the modified discharge model in (a), considering the discharges within a PEO layer with large pores between inner and outer layer [30]. With permission from Elsevier.

### 2.2.3 PEO coating composition

The composition of PEO coatings is primarily determined by the electrolyte used during the process. For magnesium alloys, PEO electrolytes are typically highly alkaline. When using a simple alkaline electrolyte, such as one based on KOH, the PEO coating predominantly consists of a MgO layer. It is believed that MgO forms either through the dehydration of  $\text{Mg}(\text{OH})_2$ , driven by the high temperatures generated by the discharges, or through the direct oxidation of molten Mg produced during these discharges. Additionally, the diffusion of oxygen anions towards the magnesium substrate is significantly enhanced by the strong electric field within the discharge channel, which facilitates the movement of anions towards the Mg surface [33].

This MgO layer generally provides only limited corrosion protection. However, incorporating additional elements into the electrolyte allows for their integration into the PEO coating, offering new opportunities for customizing the coating's design and achieving specific desired properties. **Figure 2.4** provides a more detailed overview of various PEO electrolyte compositions along with the corresponding phases formed in the PEO layer.

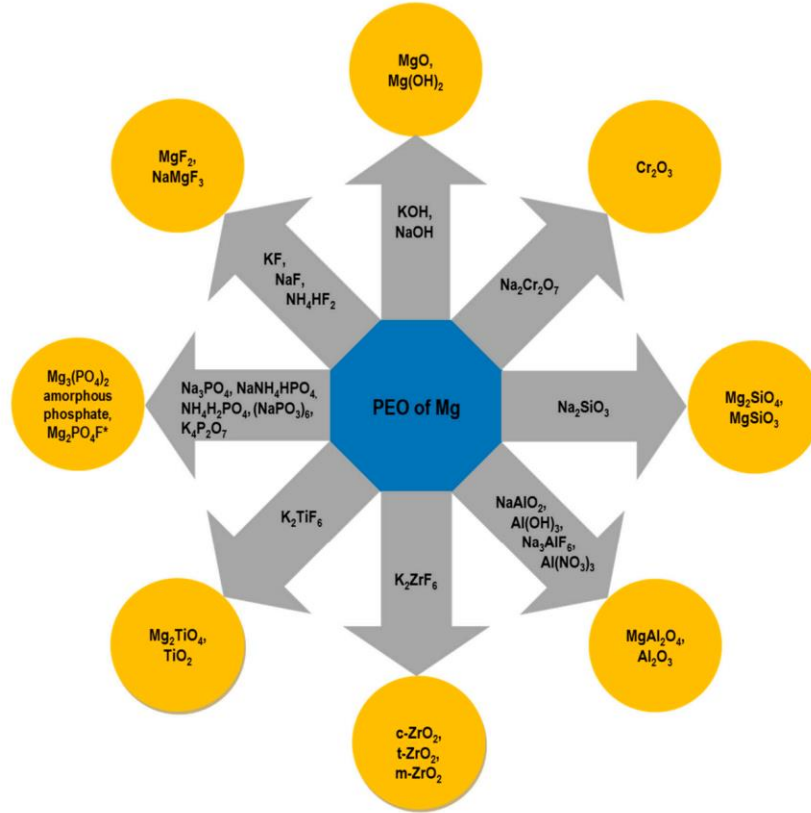


Figure 2.4 An overview of the most frequently used electrolyte components and phases formed in the PEO process on Mg alloys [34].

Among the various PEO electrolyte chemistries, those based on silicate, phosphate, and aluminate are the most frequently employed. In addition to the common MgO phase, they lead to the formation of  $\text{Mg}_2\text{SiO}_4$ ,  $\text{Mg}_3(\text{PO}_4)_2$ , and  $\text{MgAl}_2\text{O}_4$ , respectively. **Figure 2.5** presents the XRD patterns of a PEO-coated magnesium alloy substrate treated in electrolytes containing  $\text{NaAlO}_2$ ,  $\text{Na}_3\text{PO}_4$ , and  $\text{Na}_2\text{SiO}_3$ . NaF, or other fluoride salts, is commonly added to the PEO electrolyte, leading to the formation of the  $\text{MgF}_2$  phase. This phase not only enhances the corrosion protection properties of the final PEO coating but is also reported to be beneficial in promoting the growth of the PEO layer [35].

Several studies have compared the stability of the phases formed during PEO and the corresponding corrosion resistance of these coatings. For example, the following order of corrosion resistance to  $\text{Cl}^-$  attack has been identified for different phases: amorphous material <  $\text{MgO}$  <  $\text{Mg}_3(\text{PO}_4)_2$  <  $\text{Mg}_2\text{SiO}_4$  [37]. However, it is important to note that this sequence does not necessarily correspond to improved corrosion resistance of the PEO coating when prepared from their respective precursors.

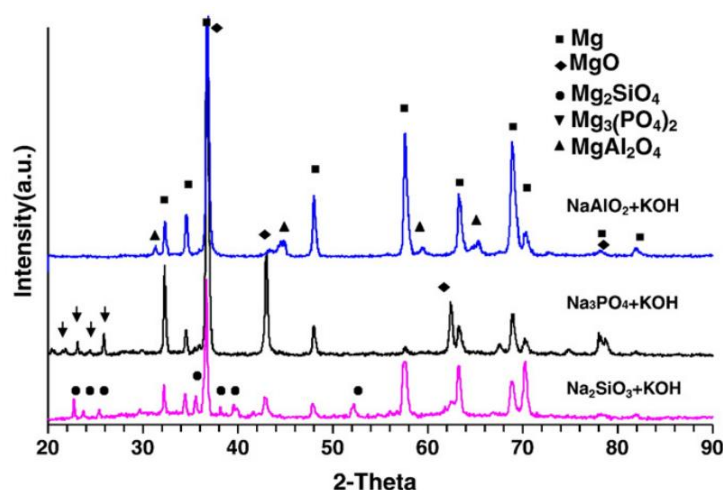


Figure 2.5 XRD patterns to determine the chemical composition of the PEO coatings. Adapted from [36] with permission from Elsevier.

Mixtures of the individual precursors outlined in **Figure 2.4** often outperform simple electrolyte compositions. For example, Wierzbicka et al. [38-40] developed an electrolyte combining silicate, aluminate, phosphate, and fluoride-based compounds. They utilized a "flash-PEO" concept, characterized by a very short process time (less than 2 minutes) to minimize energy consumption (see more in Section **Energy consumption**). The protective performance of the PEO layer applied to an AZ31 alloy was notably high, comparable to that of a chromate conversion coating (CCC) reference sample.

Organic and inorganic additives are also commonly added to the PEO electrolytes outlined in **Figure 2.4**, focusing on improving coating properties. Inorganic additives, such as Mo(VI) and rare-earth elements (Ce(III), La(III)), can enhance the passivity and self-healing capabilities of coatings [34, 41, 42], while titanium/zirconium-based compounds are noted for their stability and pore-sealing effects [41, 43-45]. Organic additives typically do not alter coating composition but can influence the coating process, reducing surface porosity and improving corrosion resistance. Despite the potential for enhanced protection, the effectiveness of additives depends on careful control of their concentration and interaction with the electrolyte composition. Summary of effects of organic and inorganic additives on PEO coating and the corresponding formed phases are presented in **Figure 2.6**.

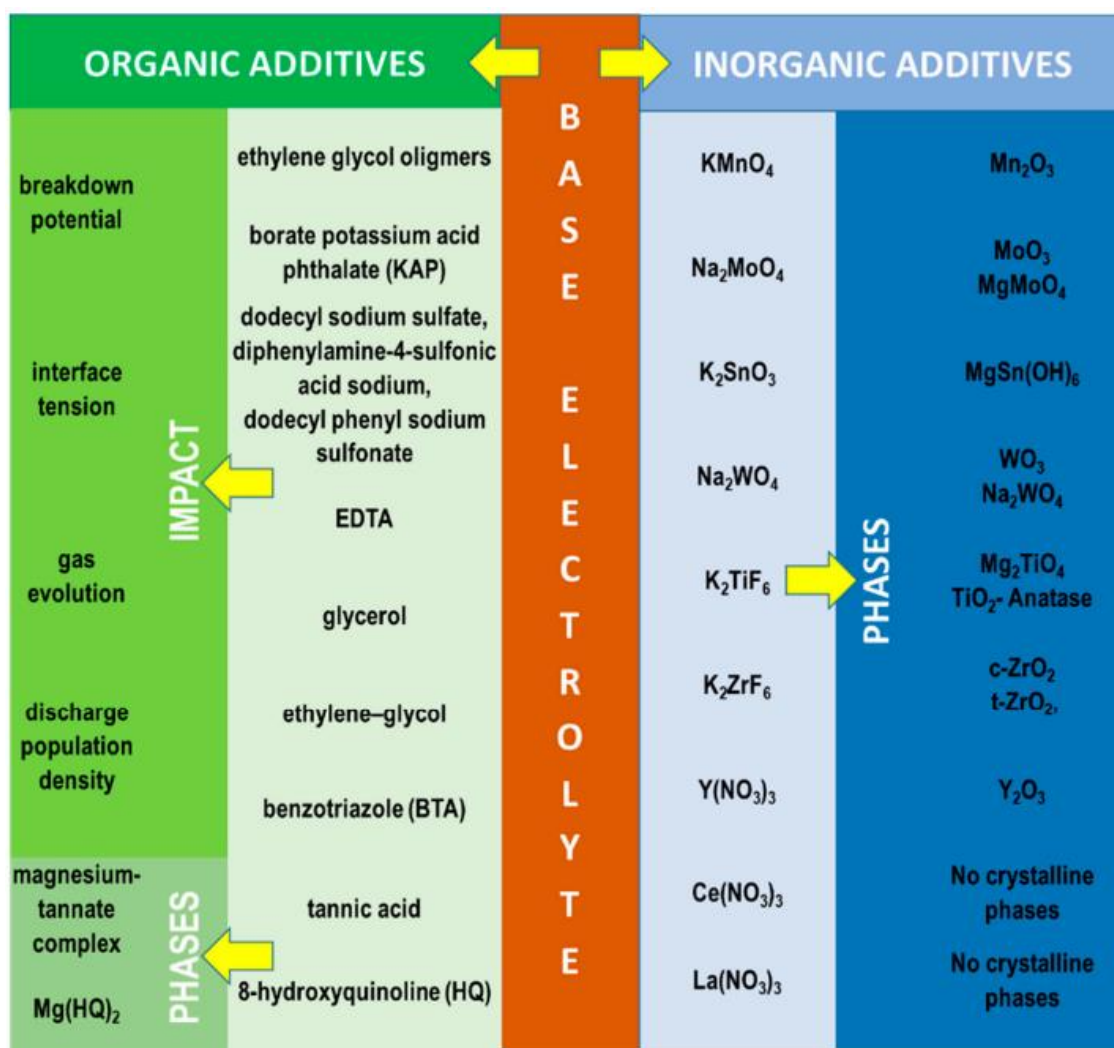


Figure 2.6 Schematic of soluble organic and inorganic substances added to PEO electrolytes and their effect on the resulting coatings [34].

### 2.2.3.1 Particle addition

Recent research trends have been focused on modification of PEO coating composition by addition of particles into the PEO electrolyte, thereby achieving in-situ incorporation of particles, which provides desired features or seal the pores of PEO [46]. Particles with various properties have been used to produce multifunctional PEO coatings with anti-corrosion [19, 47-49], self-lubrication [50-52], anti-wear [53], bioactive [46, 54-57] and photocatalytic properties [58].

The particles can be inert to the PEO process so that their size, shape and composition does not change during the PEO process [59]. For instance, Ag particles have been added to a silicate-based PEO coating on a commercially pure Mg, mainly aiming to achieve an antibacterial functionality. The Ag particles were inertly imbedded into the PEO coating, mostly in the large-sized pores of PEO coating. In another study by Lu et al. [58] were able to incorporate TiO<sub>2</sub> particles into a PEO coating on an AM50 Mg alloy. Although most of the TiO<sub>2</sub> particles were incorporated inertly into the PEO coating, a small amount of Mg<sub>2</sub>TiO<sub>4</sub> also was reported that formed within the coating. Due to the presence of TiO<sub>2</sub> particles, a higher photocatalytic activity of the PEO coating was registered.

Another possibility is that the high-energy discharges in the PEO melt the particles or activate them to react with other present species in the electrolyte and PEO coating. For instance, Blawert et al. [49] used clay particles with low melting temperature of <1200 °C as a “sintering additive” to the PEO electrolyte. They showed that the melting of the clay particles during the PEO process contributes to facilitation of the coating formation and sealing of the coating

channels and micropores. **Figure 2.7** presents an overview of the insoluble particles added to the PEO electrolyte to be applied on Mg alloys.

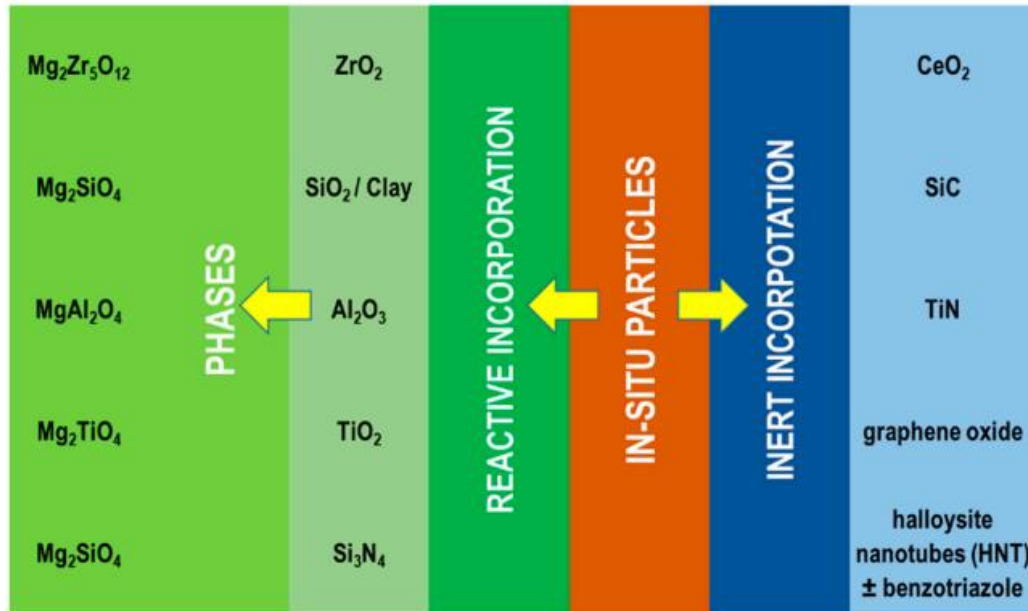


Figure 2.7 Overview of the insoluble particle types added into the PEO electrolyte and their effect on the formed phases [34].

The incorporation of particles into the PEO coating, whether inert or reactive, depends on various parameters, including the substrate, applied electrical conditions, electrolyte composition, and the properties of the particles (such as size, melting temperature, and chemical stability) [46]. For instance, the incorporation of  $ZrO_2$  particles into the coating has been observed both inertly and reactively under identical electrical conditions but with different electrolytes [60].

Particles are more frequently observed around and within the PEO pores than in other areas of the coating [61]. The incorporation of particles into the PEO layer occurs through different mechanisms. The local vigorous fluctuations and mechanical mixing of the electrolyte, caused by the discharges, play a role in moving particles closer to the substrate [62]. Electrophoresis forces are also believed to drag charged particles towards the anodically polarized substrate under the imposed electrical field during the PEO process. However, some argue [63] against the significant contribution of this mechanism, noting the very slow movement of fine particles ( $<1 \mu\text{m}$  diameter) due to electrophoresis forces—typically just a fraction of a micron for a supply frequency of 50 Hz. This movement is especially insignificant compared to other phenomena occurring during PEO formation, such as gas bubbling, which induces a convective motion of approximately  $10 \text{ m}\cdot\text{s}^{-1}$  [64].

In another proposed mechanism, the particles are swept into the PEO pores during a discharge cycle that involves plasma gas bubble. **Figure 2.8** shows a schematic depiction of a single cycle discharge with explanation of each step, for an electrolyte containing particles in a suspension form.

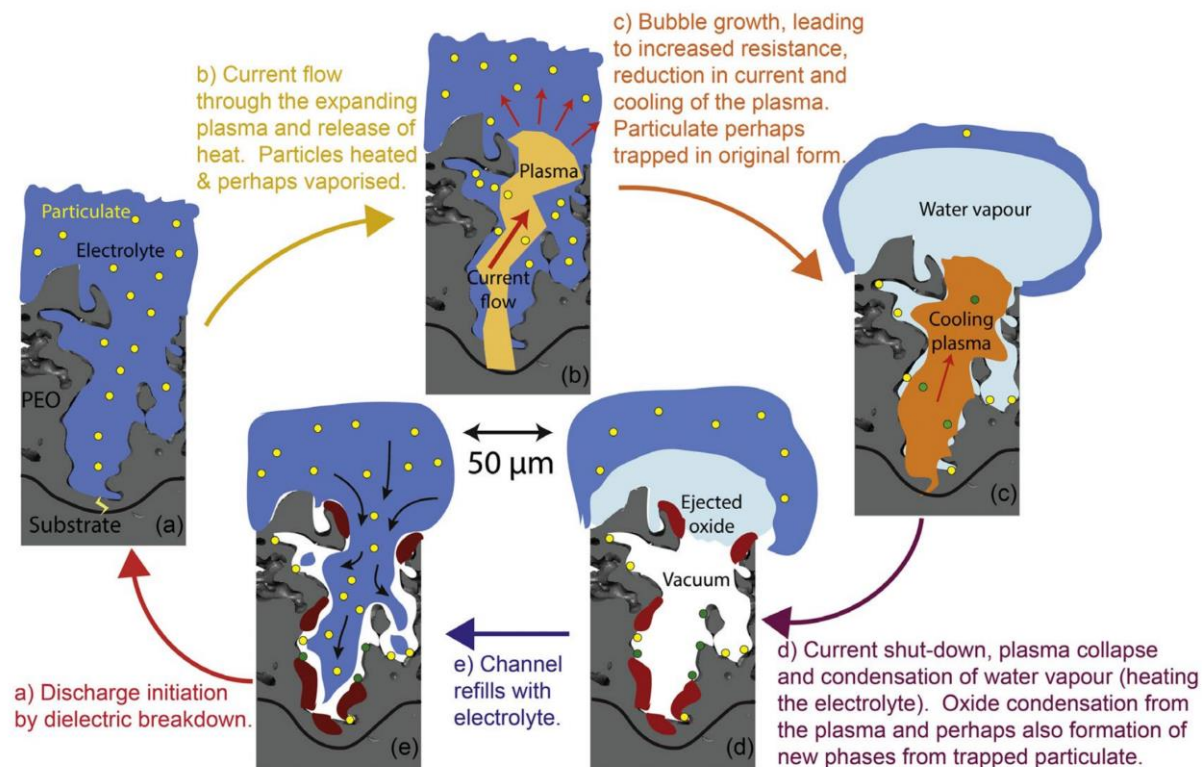


Figure 2.8 Schematic of a single PEO discharge cycle, with the electrolyte containing particles in suspension form that leads to the sweeping of the particles into the PEO pores. Adapted from [63] with permission from Elsevier.

### 2.2.3.2 Non-aqueous electrolyte

Most studies on the PEO coating process have been conducted in aqueous media. However, recent efforts have also explored the application of PEO in non-aqueous media, such as molten salts [65–68]. The use of molten salts aims to circumvent the drawbacks of the aqueous-based PEO process, which include the formation of undesired compounds in the resulting coatings and the need for electrolyte cooling.

A molten salt of  $\text{NaNO}_3$ - $\text{KNO}_3$  has been investigated as an electrolyte for several substrates, including Al alloys [67, 69, 70], Ti alloys [71, 72] and Zr alloys [66]. The electrolyte temperature is around 280 °C. In a recent study by Yuferov et al. [68], an electrolyte based on a ternary eutectic system of  $\text{Ca}(\text{NO}_3)_2$ + $\text{NaNO}_3$ + $\text{KNO}_3$  was used. The electrolyte has a significantly lower melting temperature of 129 °C, which not only improves the economic viability of the process but also facilitates the introduction of desired components into the PEO coating. In their work, they introduced ammonium dihydrogen phosphate (ADP) into the electrolyte.

PEO coatings formed in molten salts, similar to those formed in aqueous-based electrolytes, exhibit high adhesion, high hardness, and improved wear and corrosion resistance compared to the uncoated substrate. However, the challenges associated with PEO in molten salts include the high operating temperature, which can lead to substrate degradation, and the corrosive nature of some molten salts, requiring specialized equipment and safety measures.

The voltage at which the discharge sparks begin to form in molten salts is usually significantly lower than in the traditional PEO process using aqueous electrolyte. For instance, electric sparks were detected in the PEO process in a  $\text{KNO}_3$ + $\text{NaNO}_3$  mixture on a Ti-6Al-4V alloy at voltages as low as 16V [65, 71]. The minimum voltage, at which discharges were observed for a Zr alloy is reported to be 10V [66]. Although the applied voltage is considerably lower than in the case of an aqueous electrolyte, a systematic comparison is necessary, taking into account the energy consumption and the heat required to raise the electrolyte temperature to melt the salt mixture.

To the best of our knowledge, as of the time of writing this thesis, there are no reports on the use of molten salts as the PEO process medium for Mg alloys.

## 2.2.4 Applied electrical parameters

The influence of electrical parameters on the properties of PEO coatings is a central topic in its development research. Fine-tuning these parameters is essential for customizing coatings to meet specific application requirements. Despite extensive research and the development of general conclusions, the intricate and multifaceted interplay between electrical parameters and PEO coating properties make this a highly active and evolving field of study.

The PEO process was initially developed by increasing the applied voltage in the anodizing process higher than the breakdown voltage, leading to the observation of microdischarging on the surfaces of magnesium and aluminum alloys [73, 74]. However, the early stages of PEO coating development using this approach resulted in highly porous and defective layers. Subsequent advancements involved the adoption of alternative electrical regimes, including pulsed DC, alternating polarization, and bipolar electrical configurations [73, 75, 76]. These modifications significantly mitigated the adverse effects associated with discharges under DC conditions, leading to notable improvements in both coating performance and process efficiency.

For example, Hussein et al. [77] demonstrated that using a specific bipolar mode with cathodic periods produces a denser, less porous layer of aluminate-based PEO coating on AJ62 magnesium alloy compared to coatings formed under unipolar conditions with the same parameters (see **Figure 2.9**). Notably, the inclusion of cathodic periods in bipolar regimes was found to substantially reduce microdischarge activity and its detrimental effects on the PEO layer during formation [77], while maintaining a satisfactory coating growth rate even over extended processing times. The term "soft-sparking" is commonly used to describe this type of mild discharging, which has been a focus of extensive investigation in recent years [78].

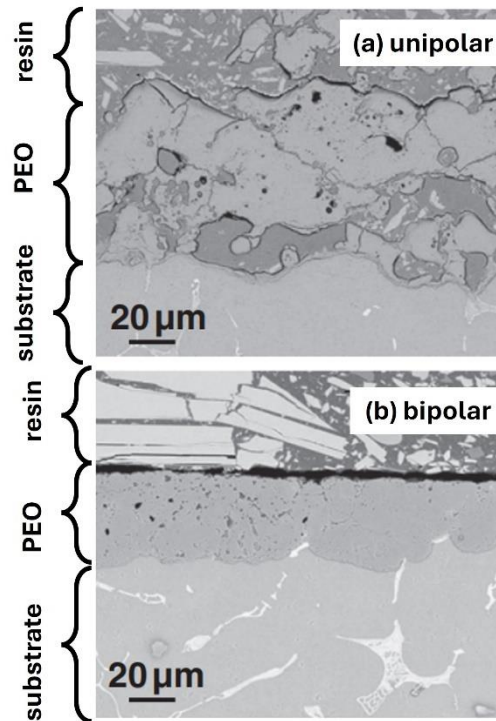


Figure 2.9 EM micrographs of cross-section view of PEO coatings on an Mg AJ62 alloy by means of unipolar (a) and bipolar (b) current modes. Adapted from [77] with permission from Elsevier.

Several parameters govern the electrical regime in a bipolar AC mode during the PEO process, including applied current/voltage, duty cycle, frequency, and the ratio cathodic/anodic currents. The modification of these parameters may affect the PEO microstructure and composition. For instance, as illustrated in **Figure 2.10**, the surface morphology of PEO coatings varies significantly with applied frequencies ranging from 60 to 2000 Hz. Increasing the frequency results in smaller surface pore sizes. Generally, an improvement in the corrosion resistance of PEO-coated

magnesium alloys with increasing frequency has been reported [79-81]. This enhancement in PEO coating quality is thought to be due to the lower intensity of micro-sparks occurring during each cycle of the PEO process, which is attributed to the reduced power and shorter duration available for electrical discharge [81].

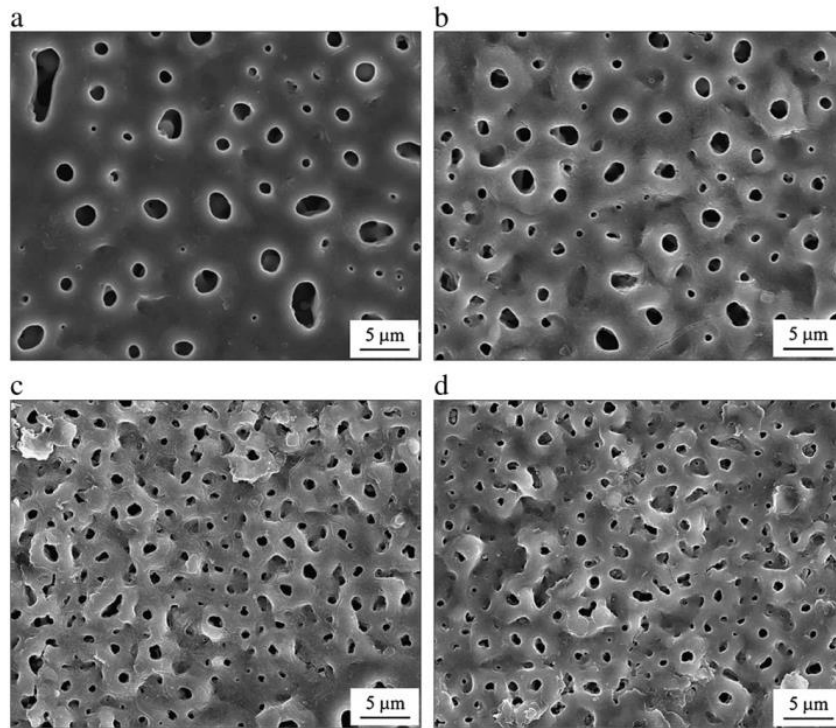


Figure 2.10 SEM images showing the surface structures of a PEO coating on a Mg alloy at different frequencies of (a) 60, (b) 500, (c) 1000, and (d) 2000 Hz. Adapted from [81] with permission from Elsevier.

The majority of the pulses applied in PEO processes are rectangular in shape. However, there have been a few reports exploring alternative pulse shapes, such as trapezoidal waveforms using Ceratronic® hardware [82-84], sine waveforms [85], and asymmetric bipolar pulse [86]. The use of non-square waveforms is generally reported to positively influence the density and corrosion resistance properties of the PEO layer. This improvement is primarily attributed to the reduction in the formation of sharp, high-intensity discharges that can be destructive.

Recently, Rogov [87] introduced a novel power supply system capable of delivering desired waveforms at the high voltages and currents required for the PEO process. This system offers high precision and flexibility in controlling pulse shapes. Moreover, the applied pulses can be dynamically adjusted based on real-time analysis of the instantaneous current/voltage output. Utilizing this highly controllable power supply, Guo et al. [88] applied a PEO coating with a primary composition of  $\text{Mg}_2\text{SiO}_4$  on CP-Mg using an electrical regime based on sawtooth-shaped anodic current pulses with extended ascending or descending segments (ramps). The use of sawtooth pulses was shown to enable precise control over microdischarge characteristics and coating morphology in both pulsed unipolar and reversed current regimes. Notably, they observed that applying anodic sawtooth pulses with a negative ramp could facilitate the healing of defects in the PEO layer, leading to reduced porosity and enhanced corrosion protection properties.

The shape of the electrical regime impacts several aspects of the PEO formation process [88, 89], including:

- The kinetics of electrode reactions (e.g., metal oxidation and gas evolution).
- Local conditions at the electrode/electrolyte interface (e.g., breakdown power, heating and cooling rates).
- Transport processes (e.g., migration, diffusion, and convection due to bubble collapse).

### 2.2.5 Energy consumption

One of the primary challenges in the commercialization of the Plasma Electrolytic Oxidation (PEO) process is its relatively high energy consumption, as it typically requires the application of high voltages (in the hundreds of volts) and high current densities (generally 10–60 A/dm<sup>2</sup>). To put this in perspective, the energy consumption for PEO on aluminum alloys can be 20 to 50 times higher than that of conventional anodizing methods [90].

Given this, numerous studies have aimed to enhance the energy efficiency of the PEO process by optimizing various processing parameters, such as treatment time, temperature, applied current density, and electrolyte composition [90–92]. For example, research has shown that increasing the concentration of electrolytes containing phosphate, silicate, and aluminate within the range of 0.0625–0.5M can reduce both the breakdown and operating voltages during the coating process on AZ31 magnesium alloy, thereby lowering energy consumption [93].

In another study by Tian et al. [94], the addition of organic and inorganic compounds—Borax ( $\text{Na}_2\text{B}_4\text{O}_7 \cdot 10\text{H}_2\text{O}$ ), trisodium citrate dihydrate ( $\text{Na}_3\text{C}_6\text{H}_5\text{O}_7 \cdot 2\text{H}_2\text{O}$ ), and EDTA—to a reference  $\text{Na}_2\text{SiO}_3 + \text{NaOH}$  electrolyte resulted in a PEO coating that maintained similar morphology, thickness, and elemental distribution as the reference sample but with significantly improved corrosion resistance and a reduced maximum voltage (~100V compared to ~250V for the reference sample).

A significant area of focus in reducing the energy consumption of the PEO process is the "soft-sparking" regime. This regime refers to a transition in the micro-arc state during PEO, marked by a notable drop in anodic voltage and decreased light and acoustic emissions. The "soft-sparking" transition typically occurs after the coating has reached a certain thickness [75, 95–97]. In this regime, the micro-discharges become more uniform and less intense compared to the conventional arcing regime, which is more chaotic and can damage the surface [98]. Besides reducing energy consumption, the "soft-sparking" regime also enhances the overall quality of the PEO layer, resulting in a denser layer with fewer microstructural defects, such as pores and cracks.

By adjusting waveform parameters—specifically by incorporating cathodic polarization into the pulsing sequence—the "soft-sparking" regime can be initiated earlier (see section 2.2.4). Although the mechanism behind "soft-sparking" and its relationship with the applied waveform is complex and currently a highly active area of research, most studies have focused on aluminum alloy substrates. There is significantly less research on other metals, including magnesium alloys [76, 89, 99, 100]. So far, the positive effects of "soft-sparking" in forming a thick, dense layer on aluminum alloys have not been replicated on magnesium. Notably, Tsai et al. [101] reviewed the literature on the soft-sparking of magnesium alloys and suggested that even if a dense and thick inner layer could be achieved on magnesium through soft-sparking, it might still be due to the formation of  $\text{Al}_2\text{O}_3$  from aluminate-containing electrolytes.

Beyond waveform modifications, another strategy to induce the "soft-sparking" regime is the application of a "precursor" film prior to the PEO process [90, 102–104]. Mohedano et al. [105] reported energy savings of up to ~66% by applying a precursor anodic film compared to conventional direct PEO treatment on AA6082 aluminum samples, while still achieving comparable corrosion protection. In a follow-up study by the same group [102], a combination of high-frequency (400 Hz) and high current (500 mA/cm<sup>2</sup>) on anodized AA6082 samples led to a 76% reduction in energy consumption, with the optimized coating also exhibiting improved corrosion and wear resistance. However, this approach, like others focused on easing the transition to the "soft-sparking" regime, has been predominantly applied to aluminum alloys. While there have been investigations into pre-treatments on magnesium alloys to improve their properties, as detailed in section 2.2.6, these studies have not aimed at achieving the "soft-sparking" regime.

The concept of "flash" plasma electrolytic oxidation (F-PEO) has also gained attention as a means to reduce the energy consumption of the PEO process. This approach emphasizes optimizing the electrolyte composition to produce a thin but adequately protective coating, typically ranging from 1 to 5  $\mu\text{m}$  in thickness, within a very short treatment time, usually under 2 minutes. For instance, Wierzbicka et al. [38–40] demonstrated a successful F-PEO strategy by systematically screening electrolytes containing varying concentrations of silicate, aluminate, phosphate, and fluoride-based compounds.

### 2.2.6 Pre-treatment

Compared to pre-breakdown anodizing, the properties of PEO coatings are less influenced by the substrate surface condition or pre-treatment [90, 106]. This suggests a simplification of the PEO process, which can shorten processing time and reduce associated costs, making it advantageous for industrial applications.

However, several studies [107-110] have reported a significant impact of pre-treatment on the properties of the subsequent PEO coating, particularly on the overall corrosion resistance of the coated sample. In most of these cases, the employed pre-treatment method significantly alters the composition and microstructure of the substrate. For instance, laser surface melting (LSM) was employed on an AZ91D magnesium substrate as a pre-treatment step before applying the PEO coating [110]. LSM substantially modified the microstructure by reducing grain size and altering the distribution of the second phase. Consequently, even without the PEO coating, the corrosion resistance of the substrate was affected [111-113].

Other examples include the formation of an additional layer or the introduction of new elements onto the surface before PEO application, which ultimately contribute to the chemical composition of the PEO coating itself. For example, Wei et al. [109] dipped a Mg AZ91 alloy in an HF solution while simultaneously applying ultrasonic waves as the pre-treatment process. Fluorine element was found in the inner layer of the PEO coating after HF pre-treatment, which contributed to the stabilization of the barrier layer on the Mg surface and formation of thin protective  $\text{MgF}_2$  film [6, 114]. Similarly, Cai et al. [107] formed a Ce-based conversion layer on an AZ91D alloy by immersion in a  $\text{Ce}(\text{NO}_3)_3 + \text{H}_2\text{O}_2$  solution prior to PEO application. As a result, the  $\text{CeO}_2$  phase was incorporated into the PEO layer, effectively blocking PEO pores, thereby improving its corrosion resistance.

### 2.2.7 Post-treatment

Modifying the PEO layer with post-treatment techniques is a powerful approach to optimize its performance and achieve specific functionalities based on the application. To improve anti-corrosion capabilities and ensure long-term protection, it is crucial to seal the pores in the PEO layer and incorporate active protection mechanisms. This can be achieved through various techniques, including the application of sol-gel coatings [115-121], electrophoretic deposition [122-126], and the use of barrier topcoats. Another effective method involves immersion in solutions that promote the formation or precipitation of materials to block the PEO pores [127-130]. These post-treatment strategies can also be customized to achieve or improve the desired functionalities, such as increasing hydrophobicity, activating bioactivity, and enhancing the aesthetic qualities of the surface.

For instance, natural biodegradable polymers, such as collagen [131] and chitosan (CS) [132, 133], along with synthetic biodegradable polymers like polycaprolactone (PCL) [134, 135] and poly-L-lactide (PLLA) [136], can be used as post-treatments for PEO (plasma electrolytic oxidation) coatings. These polymers enhance the PEO-coated properties by not only improving corrosion resistance—providing an additional barrier against the penetration of corrosive media—but also by imparting biocompatibility. For instance, a  $\text{Cu}(\text{II})$ -chitosan/PVA nanofiber layer was applied to an AZ31 alloy with a PEO coating through electrospinning [137]. The resulting coatings demonstrated effective antibacterial activity against both gram-positive and gram-negative bacteria, attributed to the presence of copper ions, which are known for their antimicrobial effects, such as disrupting bacterial cell membranes and inhibiting growth. Additionally, in vitro tests indicated higher cell viability rates on these treated surfaces compared to untreated ones, suggesting favorable interactions with biological tissues. In another study, integrin-active organic components, such as the RGD peptide, were incorporated into a PEO coating on a titanium substrate via a simple immersion procedure. The functionalized PEO coating resulted in a 37% increase in the proliferation of human osteosarcoma (MG-63) cells [138].

To impart "active inhibition" or "self-healing" properties to PEO coatings, corrosion inhibitors can be incorporated into the PEO pores. In this context, the pores, typically considered a vulnerability in PEO coatings due to their impact on corrosion resistance, become an asset by serving as reservoirs for corrosion inhibitors. Designing a system that combines PEO with inhibitors and sealing treatments has demonstrated superior corrosion protection, being able to surpass the performance of traditional chromium (VI)-based coatings. A comprehensive review of the techniques for incorporating corrosion inhibitors into PEO coatings to achieve self-healing properties is discussed in detail in Section of [corrosion inhibitors](#).

### 2.2.8 Applications and commercialization

Despite the many advantages of PEO coatings across various applications, their use is still not as widespread as traditional anodizing, particularly for aluminum and its alloys. The primary barrier to their commercialization, as discussed earlier, is the relatively high energy consumption [85, 105, 139, 140], which is typically 20 to 50 times greater than that of conventional anodic oxidation [94]. Additionally, the PEO process is still a relatively young technology with numerous controlling parameters that require further investigation [73]. However, the need for extensive trial-and-error studies can be significantly reduced through a deeper understanding of the fundamental mechanisms that govern PEO coating formation.

For magnesium, several commercial PEO processes have been developed to enhance corrosion resistance and wear properties. These include MAGOXID-COAT [141] (Aalberts Surface Technologies), Keronite [142] (Keronite International Ltd), Tagnite [143], and CERANOD [144] (Eloxalwerk Ludwigsburg Helmut Zerrer GmbH). Emerging trends in PEO processing are increasingly focused on applications involving magnesium as degradable implants and stents [145-147], which require a controlled degradation rate characterized by an initial slow phase followed by accelerated degradation towards the end of their lifecycle. An example of this is the Kermasorb® PEO coating (Meotec GmbH, Germany), which has been patented for mitigating corrosion in bioabsorbable magnesium-based implants [148].

The potential applications of PEO coatings can be further expanded by incorporating specific species into the electrolyte or through post-processing techniques that promote the formation of new compounds and phases within or on the surface of the PEO layer. For instance, a PEO coating with photoluminescent and photocatalytic properties was developed on AZ31 magnesium alloy by adding  $\text{Eu}_2\text{O}_3$  particles to the PEO electrolyte [149], resulting in  $\text{MgO}/\text{MgAl}_2\text{O}_4$  phases doped with  $\text{Eu}^{3+}$  [150, 151]. In another study, a PEO coating on an aluminum substrate was functionalized with magnetic properties by introducing  $\text{Fe}_2(\text{C}_2\text{O}_4)_3 \cdot 5\text{H}_2\text{O}$  into the PEO electrolyte, which led to the formation of a PEO coating containing  $\text{Fe}^0$  [152, 153].

## Review

# Chromate-Free Corrosion Protection Strategies for Magnesium Alloys—A Review: Part III—Corrosion Inhibitors and Combining Them with Other Protection Strategies

Bahram Vaghefinazari <sup>1</sup>, Ewa Wierzbicka <sup>2,3</sup>, Peter Visser <sup>4</sup>, Ralf Posner <sup>5</sup>, Raúl Arrabal <sup>2</sup>,  
Endzhe Matykina <sup>2</sup>, Marta Mohedano <sup>2</sup>, Carsten Blawert <sup>1</sup>, Mikhail L. Zheludkevich <sup>1</sup>  
and Sviatlana V. Lamaka <sup>1,\*</sup>

<sup>1</sup> Institute of Surface Science, Helmholtz-Zentrum Hereon, 21502 Geesthacht, Germany

<sup>2</sup> Departamento de Ingeniería Química y de Materiales, Facultad de Ciencias Químicas, Universidad Complutense de Madrid, 28040 Madrid, Spain

<sup>3</sup> Department of Functional Materials and Hydrogen Technology, Faculty of Advanced Technologies and Chemistry, Military University of Technology, 2 Kaliskiego Street, 00-908 Warsaw, Poland

<sup>4</sup> AkzoNobel, 2171 AJ Sassenheim, The Netherlands

<sup>5</sup> Henkel AG & Co. KGaA, 40589 Düsseldorf, Germany

\* Correspondence: sviatlana.lamaka@hereon.de



**Citation:** Vaghefinazari, B.; Wierzbicka, E.; Visser, P.; Posner, R.; Arrabal, R.; Matykina, E.; Mohedano, M.; Blawert, C.; Zheludkevich, M.L.; Lamaka, S.V. Chromate-Free Corrosion Protection Strategies for Magnesium Alloys—A Review: Part III—Corrosion Inhibitors and Combining Them with Other Protection Strategies. *Materials* **2022**, *15*, 8489. <https://doi.org/10.3390/ma15238489>

Academic Editor: Hongxiang Li

Received: 9 September 2022

Accepted: 20 November 2022

Published: 28 November 2022

**Publisher's Note:** MDPI stays neutral with regard to jurisdictional claims in published maps and institutional affiliations.



**Copyright:** © 2022 by the authors. Licensee MDPI, Basel, Switzerland. This article is an open access article distributed under the terms and conditions of the Creative Commons Attribution (CC BY) license (<https://creativecommons.org/licenses/by/4.0/>).

**Abstract:** Owing to the unique active corrosion protection characteristic of hexavalent chromium-based systems, they have been projected to be highly effective solutions against the corrosion of many engineering metals. However, hexavalent chromium, rendered a highly toxic and carcinogenic substance, is being phased out of industrial applications. Thus, over the past few years, extensive and concerted efforts have been made to develop environmentally friendly alternative technologies with comparable or better corrosion protection performance to that of hexavalent chromium-based technologies. The introduction of corrosion inhibitors to a coating system on magnesium surface is a cost-effective approach not only for improving the overall corrosion protection performance, but also for imparting active inhibition during the service life of the magnesium part. Therefore, in an attempt to resemble the unique active corrosion protection characteristic of the hexavalent chromium-based systems, the incorporation of inhibitors to barrier coatings on magnesium alloys has been extensively investigated. In Part III of the Review, several types of corrosion inhibitors for magnesium and its alloys are reviewed. A discussion of the state-of-the-art inhibitor systems, such as iron-binding inhibitors and inhibitor mixtures, is presented, and perspective directions of research are outlined, including *in silico* or computational screening of corrosion inhibitors. Finally, the combination of corrosion inhibitors with other corrosion protection strategies is reviewed. Several reported highly protective coatings with active inhibition capabilities stemming from the on-demand activation of incorporated inhibitors can be considered a promising replacement for hexavalent chromium-based technologies, as long as their deployment is adequately addressed.

**Keywords:** corrosion; inhibitor; magnesium; hexavalent chromium; self-healing

## 1. Foreword

Magnesium (Mg) and its alloys are characterized by their low density and high specific strength, which make them competitive alternatives to traditional structural materials in aerospace and automotive industries. However, Mg alloys are prone to corrosion, particularly when in contact with aqueous solutions. While this property of magnesium alloys is taken as an advantage in the field of biodegradable metallic implants and primary Mg–air batteries, it stifles magnesium utilization for structural applications in aerospace and automotive. The traditional approach to suppress the corrosion of magnesium and other metals is to apply a coating system, which acts as a barrier against the penetration of corrosive

species toward the metal surface. In a complementary approach, corrosion inhibitors are added to a corrosive medium or a protective coating to further retard the corrosion of the exposed metallic part [1]. Inhibitors are widely used for various industrial applications, including the protection of engineering parts, pipelines, and petroleum-handling facilities [2]. Application of inhibitors is considered a cost-effective, easy-to-operate, and practical method for corrosion control. The best-known chemical with inhibitive features is hexavalent chromium, which functions as a panacea to the corrosion susceptibility of many engineering metals. However, due to the strict rules and regulations imposed by environmental agencies, the utilization of hexavalent chromate has been limited [3]. In particular, in Europe, the use of Cr(VI) substances is regulated by the European Chemical Agency, an agency of the European Union that composed an authorization list, also known as the list of substances included in Annex XIV of REACH [4]. Three leading chromate-containing substances have been banned since 21 May 2015. The majority of the other Cr(VI) compounds have been banned since 21 September 2017, while strontium chromate and three more Cr(VI) compounds were banned starting from 22 January 2019 [5]. Since no adequate substitutes for chromates have been adapted in a timely manner by concerned industries, a number of key players in the European space industry have initiated the Space Chromate Task Force, aiming to postpone the ban to use Cr(VI) compounds in aerospace industry [6]. As a result, the sunset date for the use of Cr(VI) compounds for surface treatment for a number of companies related to aeronautics and aerospace industries has been postponed until the year 2024 [7]. Nevertheless, the use of Cr(VI) is expected to be prohibited for all industries in the future. In light of these factors, the search for new corrosion inhibitors suitable for industrial applications is urgent and extremely pertinent. Thus, numerous recent scientific works have been dedicated to the discovery of adequate substitutes for chromates.

This review is the third part of a trilogy on Cr(VI)-free corrosion protection strategies for magnesium alloys. In **PART I** of the review [8], conversion coating technologies are reviewed as one of the most widely used methods of protecting metal surfaces. As a controlling step for the performance of a conversion coating, pre-treatment of magnesium surface is also discussed in **PART I**. **PART II** of the review [9] focuses on Plasma Electrolytic Oxidation (PEO) coating as one of the highly developed methods to protect magnesium surface in the recent years. This part of the review (**PART III**) focuses on corrosion inhibitors for magnesium and approaches to incorporate them into coating systems. An overview of the review trilogy is illustrated in the graphical abstract of all three review parts. Figure 1 high-lights the outline of **PART III** with the most promising corrosion inhibitors and inhibitor classes.

In contrast with coatings, which aim to isolate the whole surface of an engineering part from corrosive media, inhibitors are able to target specific regions of the metal surface (the cathodic region and the anodic region). In this context, inhibitors can be classified as **cathodic**, **anodic**, or **mixed** types. Another way to categorize inhibitors is based on their interaction with a metal surface in corrosive media. Inhibitors can precipitate in the form of an insoluble compound or can be adsorbed on the surface of metal: **precipitation**, **passivation**, or **adsorption** inhibitors. The distinction between these three groups is subtle, especially with the passivation and precipitation types. The latter is deposited as a partially protective layer (e.g., cerium and lanthanum hydroxides), while the former is similar to conversion coating, forming a layer of sparingly soluble magnesium products (phosphates and fluorides). Many of the inhibitors that form precipitation layers on the surface can also be considered as conversion coating precursors (see **PART I** of this review [8]). For instance, chromate has been frequently addressed in the literature as either an inhibitor or a chemical used to form conversion coatings. Although they follow a similar protection mechanism, technical features can distinguish them as belonging to distinct categories. The main difference is that inhibitors are present in the corrosive medium throughout the service life of an engineering component. In contrast, precursors for conversion coatings are removed from the media when the coating formation is finished. Moreover, conversion

coating solution baths are usually at low pH levels and contain oxidizing agents in order to accelerate the dissolution of the magnesium substrate. On the contrary, inhibitors are typically incorporated into coating systems under conditions that are the least corrosive to the coating system.

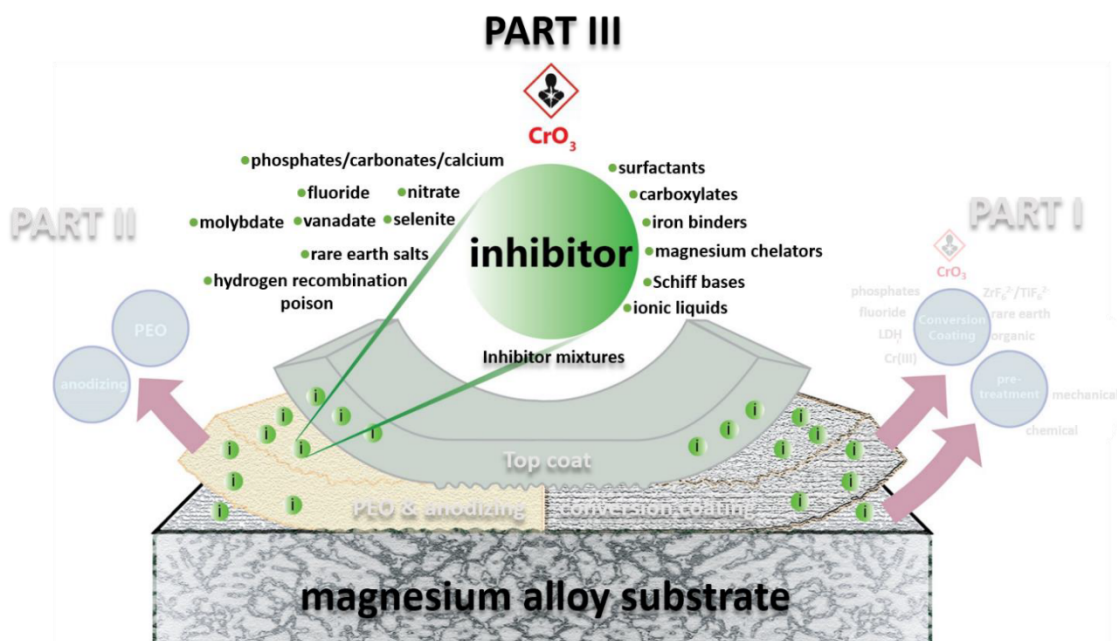


**Figure 1.** Schematic of review trilogy. This work, as **PART III** of the review, has been highlighted with more vivid colors, in contrast to the dimmed color of **PART I** and **PART II**.

There are numerous factors affecting the chemistry of the interaction between inhibitor and metal. Small variations in each factor may result in very different inhibition behaviors. This must always be kept in mind when different scientific work results are being compared; for instance, in the case of magnesium alloys, a minor variation in Al and Zn content in alloy composition can activate or deactivate the inhibitive properties of many inhibitors [10].

This review focuses neither on magnesium corrosion mechanisms nor on the methods used to measure corrosion rates. These aspects were extensively reviewed by Esmaily et al. [11]. The experimental methods for calculating the inhibiting efficiency (IE) are typically thoroughly discussed in the original papers and refer to the well-known relation,  $IE(\%) = 100\% \times (\text{ExpPar}_{\text{blank}} - \text{ExpPar}_{\text{inh}}) / \text{ExpPar}_{\text{blank}}$ . ExpPar refers to measured experimental parameter; *blank* and *inh* refer to a blank testing medium, e.g., NaCl solution and that with added corrosion inhibitor, respectively. Most typical measured experimental parameters include weight loss, volume of evolved hydrogen, polarization resistance, or low-frequency impedance accessed from EIS measurements (Electrochemical Impedance Spectroscopy), and corrosion current density calculated from potentiodynamic polarization curves.

In this review, the substances used as inhibitors for magnesium alloys are first categorized as organic and inorganic inhibitors, since this leads to a comparable interaction between inhibitors and metal surface in each category. The corrosion inhibition mechanisms stand at the center of this review when placing inhibitors in a particular group. In each category, in addition to reviewing the important inhibitors that have been studied at length, the most promising and most recent inhibitors are discussed. Emerging approaches of inhibitor discovery using *in silico*, or computational, screening are briefly described.

## 2. Inorganic Inhibitors

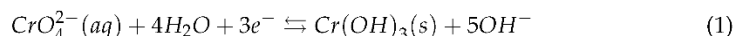
As mentioned in the introduction, corrosion inhibitors with the ability to form precipitating compounds can also be classified as conversion coating precursors. This overlap between two categories mostly happens for inorganic substances such as chromate, vanadate, phosphate, and rare earth elements salts. Therefore, here, we briefly provide a review of some inorganic inhibitors studied for magnesium alloys, while the complementary information about conversion coatings formed based on these inhibitors has been provided in **PART I** of the review [8].

### 2.1. Chromate Based Inhibition

Hexavalent chromium is a panacea for corrosion of engineering metals. Compounds containing hexavalent chromium remain among the most effective inhibitors, with superior protective properties for steel, aluminum alloys, and magnesium alloys [12].

Chromate or hexavalent chromium (Cr(VI)) is a strong oxidizing agent that is reduced to trivalent chromium by oxidizing the magnesium on the surface. Then, the hydroxide Cr(OH)<sub>3</sub> and oxide Cr<sub>2</sub>O<sub>3</sub> of chromium co-precipitate on the Mg surface to form a mixed hydroxide compound [13,14]. Apart from Cr(III), this complex film contains trapped residual hexavalent chromium that acts as the active inhibitor and provides the ability of film “regeneration” [15,16]. Trapped hexavalent chromium is enriched more in the outermost layer of the film, since reducing Cr(VI) by magnesium is less probable due to coverage of the surface [17]. However, the chromates trapped in the formed film have relatively high mobility, and are thus capable of reaching the defects and locally re-passivating the exposed area [18].

Although the excellent corrosion inhibition effect of chromate-based inhibitors has been known for decades, the exact mechanism of inhibition is still not fully understood, especially for Mg alloys. Williams et al. [19] reported a mechanism for cathodic site depolarization by chromate ions based on SVET measurement over AZ31 magnesium alloy from the initial stages of immersion in an aerated 5% *w/v* aqueous NaCl solution containing Na<sub>2</sub>CrO<sub>4</sub> salt. They observed very intense cathodic “hotspots” over the exposed surface, which decreased in number per unit area over time of immersion. Moreover, these cathodic hotspots have a limited lifetime (less than 15 min), emerging and disappearing at different locations over the scan area. Based on the SVET observations, they concluded that this transient intense local cathodic current is due to the reduction of Cr(VI) oxyanions to Cr(III) and hydrolysis of the Cr(III) species according to the following reaction, rather than typical cathodic hydrogen evolution reaction:



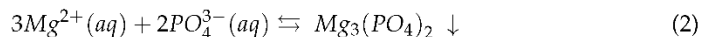
The abovementioned reaction occurs mostly on cathodic sites where the elevated local pH imposes more precipitation of chromium hydroxide, which prevents further cathodic activity.

### 2.2. Phosphates

Phosphates have been extensively researched as an alternative to chromate-based inhibitors due to their environmentally friendly properties and comparatively high protective properties for magnesium alloys. Numerous phosphate solutions modified with different organic and inorganic additives have been reported, mainly with the aim of achieving a conversion coating on magnesium alloys with higher protective behavior (see **PART I** of this review [8]). However, only a few studies have addressed the mechanism of corrosion inhibition caused by phosphate ions in corrosive media.

Depending on the pH of the solution, phosphate ions can be protonated to different degrees. Tribasic phosphate anions PO<sub>4</sub><sup>3−</sup>, which predominantly exist at elevated pH, can bond with Mg<sup>2+</sup> ions and form sparingly soluble Mg<sub>3</sub>(PO<sub>4</sub>)<sub>2</sub> (see Reaction (2)) that is believed to play the main role in the inhibition of magnesium alloys [16]. Other compounds

of magnesium with phosphates such as  $\text{Mg}(\text{H}_2\text{PO}_4)_2$  and  $\text{MgHPO}_4$  are relatively soluble in aqueous environments and do not contribute to magnesium surface passivation [20].



pH increase in the vicinity of cathodic sites such as iron-rich impurities and second phases results in the deprotonation of  $\text{HPO}_4^{2-}$  species to  $\text{PO}_4^{3-}$ . Free magnesium ions produced by oxidation of magnesium surface migrate to the regions with a high concentration of  $\text{PO}_4^{3-}$  and form solid  $\text{Mg}_3(\text{PO}_4)_2$  [21]. Figure 2 depicts a schematic representation of corrosion inhibition by phosphate anions at neutral or slightly acidic pH (between 4–7), with  $\text{HPO}_4^{2-}$  as the dominant species. At higher pH values, the inhibition efficiency is reduced due to the precipitation of  $\text{Mg}_3(\text{PO}_4)_2$  away from the Mg surface.

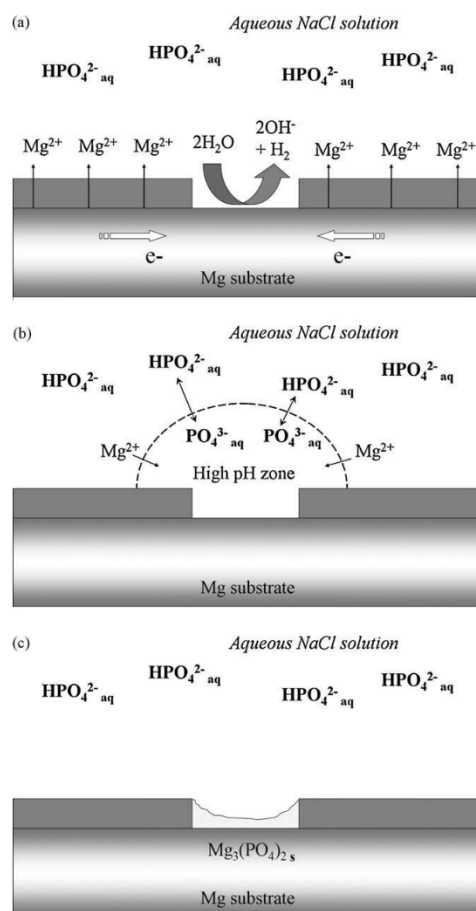


**Figure 2.** Schematic representation of the mechanism of magnesium corrosion inhibition by aqueous phosphate ions at neutral pH, showing (a) localization of the early stages of corrosion, (b) phosphate speciation in the vicinity of the local cathode, and (c) deposition of an insoluble film [21]. Adapted from [21] with permission from Elsevier.

Therefore,  $\text{Mg}_3(\text{PO}_4)_2$  is more likely to precipitate on cathodic sites, on which local alkalization occurs due to the cathodic reactions. Consequently, phosphates are usually considered cathodic inhibitors and shift  $E_{\text{corr}}$  to more negative values [19]. Preferential precipitation of  $\text{Mg}_3(\text{PO}_4)_2$  on the beta phase in Mg–Li alloy [22] and AZ91D alloy [23] is also in agreement with the abovementioned mechanism. On the other hand, it has been shown that local pH on Mg surface reaches a value of above 10 within the first minute of

exposure to the electrolyte [24]. Hence, phosphate precipitation should normally occur homogeneously on the entire surface.

Diammonium phosphate  $(\text{NH}_4)_2\text{HPO}_4$  is also reported to provide a high inhibiting effect on magnesium alloys with co-precipitation of  $\text{Mg}_3(\text{PO}_4)_2$  and  $\text{MgNH}_4\text{PO}_4$  [25,26]. Relatively high dissolution of AM60 alloy has been observed instantaneously in  $(\text{NH}_4)_2\text{HPO}_4$  solution that is substantially reduced within a few h due to the formation of a denser protective film.

### 2.3. Rare Earth Salts

Rare earth salts, especially cerium salts, have also been intensively used as a possible candidate for the replacement of chromate-base inhibitors to protect non-ferrous alloys. Their exact inhibition mechanism on magnesium alloys is still under critical scrutiny. Sparingly soluble cerium hydroxides are believed to be the main components of the protective layer on the magnesium substrate when it is immersed in a cerium-containing solution.

Montemor et al. [27] observed that the film formed on AZ31 Mg alloy at the very early stage of immersion (less than 1 min) in  $1.0 \times 10^{-3}$  M  $\text{Ce}(\text{NO}_3)_3$  is mainly composed of Mg oxide/hydroxide. The cerium content in the formed film is enriched after 1 min of immersion, and for a longer immersion time, the concentration of Ce becomes approximately constant, mainly reflecting film thickening.

Williams et al. [19] observed a poor corrosion inhibition on AZ31 alloy by addition of  $10^{-2}$  M  $\text{Ce}(\text{NO}_3)_3$  into the 5% *v/w* NaCl solution. The critical pH value for precipitation of cerium (III) hydroxide was obtained as pH 8.5, which is a near-neutral pH value. Therefore, they suggested that cerium (III) hydroxide precipitation occurs in the bulk electrolyte above the corroding surface, leading to inefficient protection properties. Similar results were observed, and the same conclusions were drawn by Lamaka et al. [10] with regard to  $\text{Ce}^{3+}$  and  $\text{La}^{3+}$  salts. It is crucial that when inhibitors are added to the aqueous solution as salts, the effect of both anions and cations must be taken into consideration. For instance, in the case of Ce-base inhibitors,  $\text{Ce}(\text{NO}_3)_3$  salt exhibits good corrosion resistance for Mg alloys, whereas  $\text{CeCl}_3$  may even accelerate the corrosion rate [10,19]. This can be related to the increase in corrosiveness of the electrolyte when additional chlorides are introduced. More importantly, there is clear evidence [10,28] of the strong inhibition effect of  $\text{NO}_3^-$  on magnesium alloys that can synergistically boost the overall inhibition effect when it is present along with  $\text{Ce}^{3+}$  ions in the electrolyte.

It is worth mentioning here that, despite a few reports on the remarkable inhibition effects of  $\text{NO}_3^-$  on the corrosion of magnesium and its alloys [10,28–30], the inhibition mechanism has not been addressed in detail.

### 2.4. Inhibition Preventing Hydrogen Re-Combination

Another class of corrosion inhibitors has been introduced by Williams, McMurray, and Birbilis [31–33]. Arsenic species, either soluble arsenates added to corrosive medium [31] or metallic arsenic alloyed with magnesium [32,34], exhibited marked cathodic inhibition owing to the ability of arsenate to inhibit hydrogen atom recombination, and thus the cathodic  $\text{H}_2$  evolution, Figure 3a–c. The poisoning mechanism is based on the reduction of arsenates in the electrolyte to metallic arsenic on Fe-rich impurities in the Mg matrix. At elevated pH values, analogous to phosphates, the precipitation of  $\text{Mg}_3(\text{AsO}_4)_2$  in the electrolyte away from the Mg surface leads to the depletion of arsenates close to the substrate. Thus, the poisoning of the HER is reported to be more effective in the acidic condition below four. Furthermore, the precipitation of insoluble  $\text{Mg}_3(\text{AsO}_4)_2$  ( $K_{\text{sp}} = 2 \times 10^{-20}$  at 25 °C) itself plays a role in the corrosion inhibition of magnesium alloys. Considering the toxicity of arsenic, there is a small likelihood that any water-soluble arsenic species can find an unrestricted commercial application as a corrosion inhibitor.

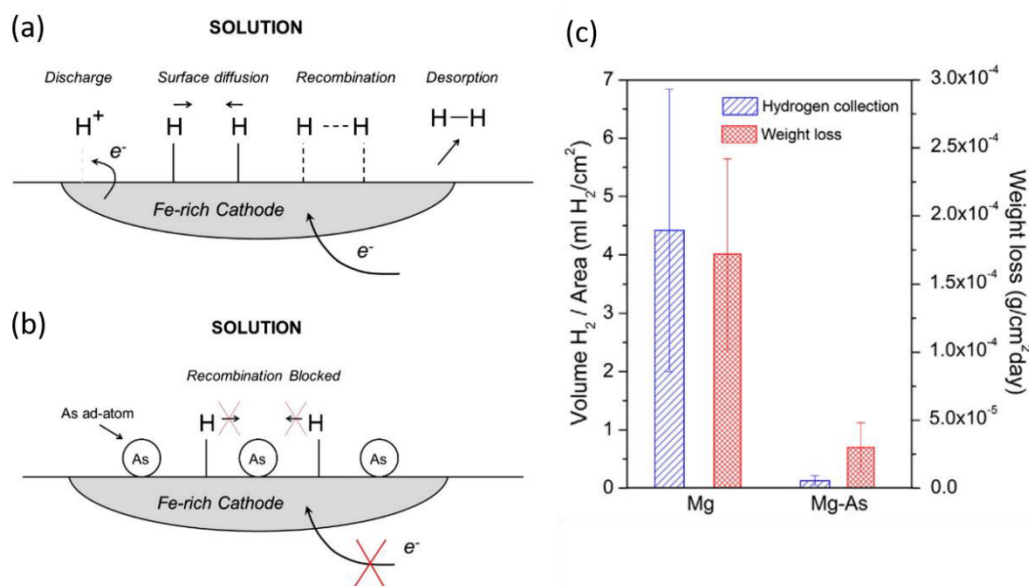


**Figure 3.** (a,b) Schematic representation of the mechanism of hydrogen recombination poisoning and (c) decreased corrosion rate in presence of arsenic alloyed with Mg [32]. Adapted from [32] with permission from Elsevier.

A similar advantageous poisoning effect has also been reported via alloying of magnesium with germanium [33,35], antimony [36], and indium [37,38]. Thus, a similar effect is expected from the addition of their soluble salts to the electrolyte, rendering them potential corrosion inhibitors. In addition to the advantageous poisoning effect of indium on the water reduction cathodic reaction, precipitation of  $In(OH)_2$  on the surface can contribute to the corrosion inhibition of Mg substrate [39]. However, in common with the adverse effect of  $Ce^{3+}$  and  $La^{3+}$  ions in the electrolyte, the formation of  $In(OH)_2$  can hinder the increase in the local pH close to the Mg substrate, which may lead to a higher corrosion rate [37,39].

In addition to the reduction of metals and their salts on Fe-rich impurities, a recent report by Mercier et al. [40] have reported adsorption of sulfur on Fe-rich impurities from  $H_2S_{aq}$  in the electrolyte. As a result, a significant reduction in HER at OCP and anodic polarization (OCP + 0.25 V and OCP + 0.5 V) was observed.

### 2.5. Other Inorganic Inhibitors

There are several inorganic inhibitor systems reported to effectively reduce the corrosion rate of Mg alloys, but limited studies have been conducted on them. Many of the related studies are promising in terms of performance and environmental impact and are worthy of more investigation. Below, some of them are briefly reviewed:

#### Fluorides

Hydrofluoric acid (HF) has been intensively investigated and used as a component of pretreatment and conversion coatings on Mg, establishing a uniform passive thin layer made of partially hydrated magnesium fluoride  $MgF_{2-x}OH_x \cdot yH_2O$  or a mixture of  $Mg(OH)_2$  and  $MgF_2$  (see PART I of the review [8]). As an inhibitor in neutral or alkaline conditions,  $F^-$  has been shown to exhibit some degrees of inhibition effect on different Mg alloys [10,25,41–43]. Similar to the conversion coating based on HF, the formation of  $MgF_2$  film along with  $Mg(OH)_2$  on the Mg surface has been mentioned as the main inhibition mechanism. However, perovskite crystals ( $NaMgF_3$ ) are also frequently observed in such cases, which is promoted by the increase in  $F^-$  concentration [44,45]. Hydrofluoric acid also passivates Mg surface and was used to dissolve Ti phase from Mg-Ti

micro-composite [46] or Ti-Ta-Cu phase from bicontinuous nanocomposite [47], leaving micro-porous or nanoporous magnesium, correspondingly.

### Bi/Carbonate

Dissolved carbonate anions ( $\text{HCO}_3^{2-}$  and  $\text{CO}_3^{--}$ ) are able to reduce the corrosion rate of magnesium alloys through the formation of insoluble magnesium carbonate [48]. Their effect on the atmospheric corrosion of magnesium alloys has drawn more attention due to the higher supply of dissolved  $\text{CO}_2$  in the thin electrolyte film. Magnesium carbonate, formed during atmospheric exposure, is a primary corrosion product and has better protectiveness than the magnesium hydroxide [49]. Similarly, in the physiological environment, due to the presence of a variety of carbonates, their influence on the corrosion rate of Mg alloys has been demonstrated to be profound [50]. The inhibition performance of dissolved bi/carbonate is highly dependent on the electrolyte pH, being more effective at alkaline pH [51], since the concentration of bi/carbonate rapidly decreases in favor of carbonic acid as the pH becomes more acidic. The inhibition effect of individual carbonates seems to be unsatisfactory for severe corrosive conditions, while the synergistic effects with other inhibitors, including  $\text{Li}^+$  ions [51,52] and phosphates ( $\text{H}_2\text{PO}_4^-/\text{HPO}_4^{2-}/\text{PO}_4^{3-}$ ) [50], can boost the overall reduction in corrosion rate. The environmental benignity of the carbonates also renders them suitable and unrestricted components to improve corrosion inhibition.

### Calcium

Calcium is a well-known component of phosphate conversion coatings for magnesium alloys (see PART I of this review [8,53,54]). Although standalone calcium cation,  $\text{Ca}^{2+}$ , does not look like a typical corrosion inhibitor for magnesium alloys, even a very low concentration of carbonate, characteristic for tap water or carbonate and phosphate found in freshwater lakes, is sufficient for triggering precipitation of calcium-carbonate (and phosphate) species. Multiple reports refer to a strong corrosion inhibition effect when  $\text{Ca}^{2+}$  is combined with anions that form sparingly soluble precipitates in an alkaline environment, which is immediately (within the first minute of immersion) generated on Mg interface upon contact with aqueous electrolytes. These ions include phosphates ( $\text{H}_2\text{PO}_4^-/\text{HPO}_4^{2-}/\text{PO}_4^{3-}$ ), carbonates ( $\text{HCO}_3^-$  and  $\text{CO}_3^{2-}$ ), and fluorides,  $\text{F}^-$  [24,25,50,55,56]. Under the presence of  $\text{Ca}^{2+}$  cations, the precipitation of several Ca-containing phases such as hydroxyapatite ( $\text{Ca}_5(\text{PO}_4)_3\text{OH}$ ),  $\text{CaMg}(\text{CO}_3)_2$ , and  $\text{CaCO}_3$  occurs on magnesium surface, prompted by the alkalization front due to cathodic HER and ORR. The formation of these products buffers the interface pH in a range of 7.8–8.5 at room temperature. Figure 4 illustrates the formation of the additional layer of  $\text{CaCO}_3$  on top of  $\text{Mg}(\text{OH})_2$  upon immersing binary Mg0.5Zn or ternary Mg0.5ZnX (0.5Ca or 0.2Ge) alloys in 0.9 wt.% NaCl when tap water was used for solution preparation. In the presence of 59 mg/L calcium at pH 7.48 in tap water, the corrosion resistance of the alloys was improved by almost one order of magnitude, according to the electrochemical test results [55]. Besides, EIS clearly shows the formation of an additional time constant at high frequencies ascribed to an outer layer containing calcium-carbonate (and often phosphate) species [50,55]. Similar to calcium ions,  $\text{Sr}^{2+}$ ,  $\text{Zn}^{2+}$ , and  $\text{Mn}^{2+}$  ions promote precipitation of phosphates on alkaline Mg surface and are used for chemical conversion treatments; see PART I of this review [8].

### Vanadates

Vanadate salts, well known for their corrosion suppressing properties when applied to aluminum [57] and zinc [58] alloys, have also been tested as corrosion inhibitors for magnesium alloys [59]. Feng et al. [59] found that the inhibition mechanism of vanadates applied on AZ31 magnesium alloy differs from that observed for aluminum alloys. Due to the considerable reduction power of magnesium, vanadate oxyanions containing  $\text{V}^{5+}$  under neutral and alkaline conditions are reduced to  $\text{V}^{3+}$  and  $\text{V}^{2+}$  in the short term. Reductive adsorption of vanadium oxoions under acidic conditions results in a film containing  $\text{V}^{4+}$ , also in the short term. However, independent of pH, all the reduced vanadium species are reoxidized back to  $\text{V}^{5+}$  upon exposure to air. Corrosion inhibition by vanadate is

attributed to the formation of a reductively adsorbed layer comprised of vanadium oxides and magnesium hydroxides. Only dense and continuous layers of tetrahedral vanadate speciation, formed under neutral and alkaline conditions, provide reasonable protection. Given the specific chemistry of vanadate oxyanions, they are quite efficient at forming corresponding conversion layers or combined with other protective approaches, such as incorporation in Layer Double Hydroxide (LDH) [8] or Plasma Electrolytic Oxidation (PEO) surface layers [60]; see below in this review.

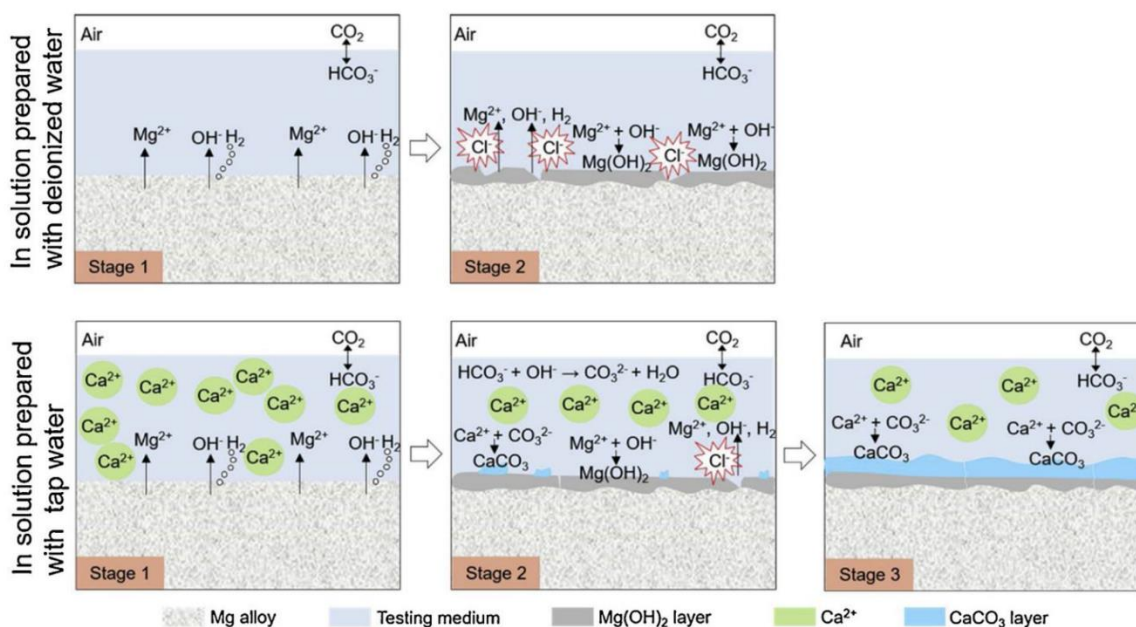


**Figure 4.** Schematic presentation of the corrosion processes and formation of corrosion products of binary  $Mg_{0.5}Zn$  or ternary  $Mg_{0.5}ZnX$  ( $X = 0.5Ca$  or  $0.2Ge$ ) alloys in 0.9 wt.% NaCl solutions prepared with deionized water and tap water (as source of  $Ca^{2+}$  and  $HCO_3^-$ ). Adapted from [55] with permission from Elsevier.

### Molybdates

Molybdate protective systems have been investigated for Mg alloys, either as conversion coatings (see PART I of this review [8]), or as inhibitors incorporated into other coating systems (see Section 5). However, the inhibition effect and mechanism of individual molybdates on bare Mg substrate have not been investigated in depth until recently. Kharitonov et al. [61] investigated the effect of  $Na_2MoO_4$  with concentrations of 5–150 mM in 0.05 M NaCl solution on WE43. A significant corrosion inhibition was observed after 24 h for 100 mM concentration of sodium molybdate Figure 5a,b. The formation of a mixed-valence Mo(VI)–Mo(V) polymerized layer was proposed as the inhibition mechanism of molybdate ions [61]. Additionally, the precipitation of brownish hydroxide  $MoO(OH)_3$  could block the Mg surface. The formation of insoluble magnesium molybdate  $MgMoO_4$  has also been hypothesized [62].

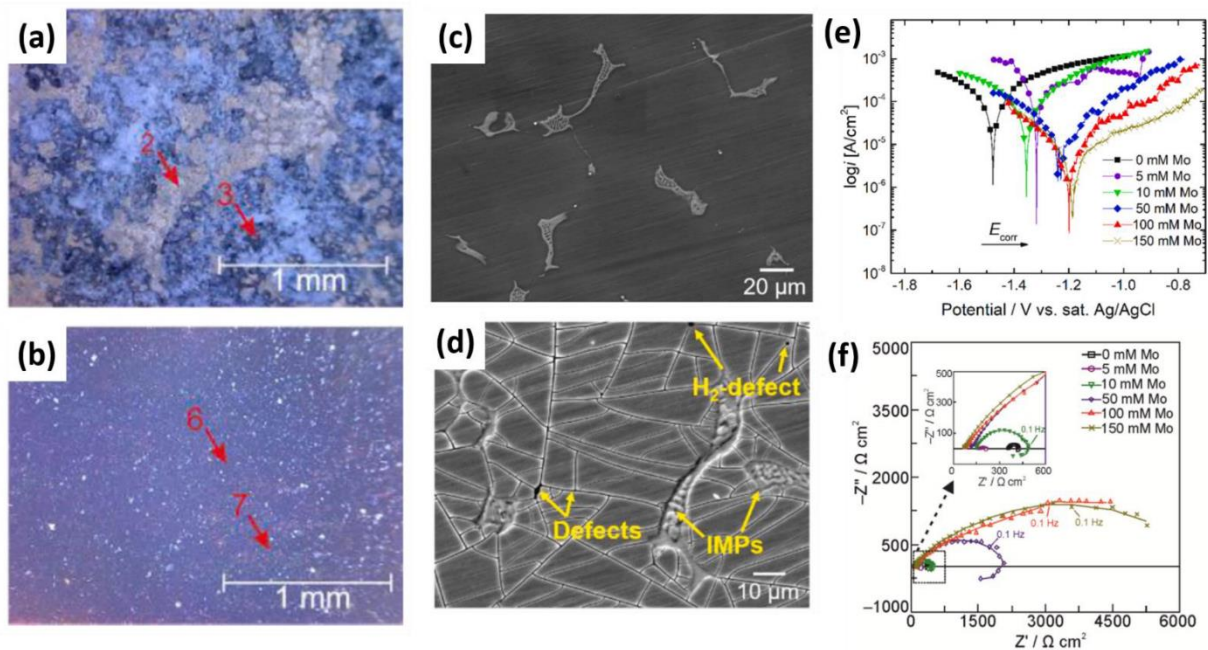


**Figure 5.** (a,b) light microscopy images of the WE43 alloy surface after 24 h exposure to 0.05 M NaCl solution without (a) and with (b) 100 mM of  $\text{Na}_2\text{MoO}_4$  inhibitor. Numbers and arrows indicate the areas of Raman spectroscopy carried out in the corresponding paper [61] (c) SEM image of as-polished WE43 surface. (d) Surface morphology of the WE43 alloy after 24 h exposure to 0.05 M NaCl solution with 100 mM  $\text{Na}_2\text{MoO}_4$ . (e) Potentiodynamic polarization curves obtained after 24 h exposure to 0.05 M NaCl without and with molybdate inhibitor. (f) Nyquist EIS plots in 0.05 M NaCl solution without and with varying amounts of  $\text{Na}_2\text{MoO}_4$  inhibitor after 24 h of exposure. Adapted from [61] with permission from Elsevier.

The Mo-containing precipitates exhibited a high tendency to form on the Mg matrix rather than the second phases Figure 5c,d, which resulted in a significant positive shift of OCP and a reduction in anodic activity of the Mg substrate Figure 5e. Reaching a critical concentration is essential to achieve a high inhibition efficiency, below which the corrosion rate of the Mg substrate is accelerated (Figure 5f). The acceleration occurs due to the partial surface coverage, which in turn may intensify the local corrosion. A very similar high corrosion inhibition performance of  $\text{Na}_2\text{MoO}_4$  was also reported for AZ31 magnesium substrate [63], which may be reflective of its universal effect. Molybdates have low harmfulness to the environment and can be considered a promising substitute for chrome(VI)-based inhibitors.

### Selenite

Similar to arsenate, selenite ( $\text{SeO}_3^{2-}$ ) can be reduced in the form of crystalline and amorphous  $\text{Se}^0$  on an AZ31 magnesium alloy [64,65]. The reduction reaction to  $\text{Se}^0$  was shown to be not limited only to low pH values, as in the case of arsenate. A strong reduction in cathodic activity was recorded independent of selenite concentration in the range of 1–50 mM. A mixed layer containing  $\text{MgSeO}_3$  hydrate and Mg–Se oxyhydroxide film containing  $\text{Se}^0$  and  $\text{Se}^{4+}$  was formed on the Mg surface, which led to a significant reduction in the corrosion rate. Similar to arsenate, selenite poses some risks from a human health perspective, and the concentration in use must be kept at low levels for industrial uses [66–68].

## Nitrates

Nitrates are commonly used as corrosion inhibitors for steel. A few reports also showed their significant positive effect on magnesium alloys [10,28–30,69]. A universal high inhibition effect of  $\text{KNO}_3$  has been observed by Lamaka et al. [10]. In spite of several auspicious results, the inhibition mechanism is quite untouched. Additionally, as with the RE-based inhibitors, cations in the form of salts of nitrates are frequently studied as corrosion inhibitors, overlooking the effect of nitrate anion itself. It has been suggested that the inhibition mechanism of  $\text{NO}_3^-$  is not related to the competitive adsorption between  $\text{NO}_3^-$  and  $\text{Cl}^-$  [29]. Rather, the inhibiting effect of  $\text{NO}_3^-$  and its reduced form  $\text{NO}_2^-$  might be related to the interference in  $\text{Fe}^{2+}/\text{Fe}^{3+}/\text{Fe}$  oxidation–reduction–redemption cycle as one of the main cathodic impurities in most Mg alloys [10].

There are still many untouched inorganic systems to be explored as corrosion inhibitors for magnesium and its alloys. Many of them are potentially expected to provide corrosion inhibition effect based on their performance either as corrosion inhibitors for aluminum and its alloys, or as precursors for effective conversion coatings, or as alloying elements in Mg with a low corrosion rate.

For instance, the corrosion inhibition mechanism of some alloying elements, such as germanium, indium, and arsenic, is partially attributable to the re-deposition of zero-valent forms of the same elements following their dissolution in the corrosive medium during corrosion. The same mechanism has also been proposed for salts of the same elements that act as corrosion inhibitors in solution. However, there are still scanty (if any) reports on the effect of salts of indium and germanium as corrosion inhibitors.

## 3. Organic Inhibitors

Numerous environmentally benign organic inhibitors have been tested in search of chromate-free inhibitors. Many organic substances with a relatively high ability to reduce the corrosion rate of magnesium alloys have already been reported, while their inhibition efficiency has rarely been compared with that of chromate. The reported effective organic substances range from very simple organic molecules such as salts of formic acid, the simplest carboxylic acid, to very complex molecules such as tannic acid or high-molecular-weight surfactants.

What makes the understanding of the inhibition mechanism of organic substances difficult is that even small variations in the molecular structure and composition of either inhibitor or substrate can significantly change the mechanism of inhibition. The inhibition mechanisms prompted by organic substances are mostly based on forming a complex with either magnesium ions already dissolved into the corrosive solution or atoms located on the magnesium alloy surface. Complex formation occurs by donating one or more electron pairs by organic ligands to a magnesium atom. The atoms in an organic molecule with the ability to donate electron pairs are O, N, S. When the complexation occurs on the surface of magnesium, it results in an adsorptive layer, isolating the magnesium surface from the corrosive medium. On the other hand, when the complexing occurs in the solution with magnesium ions, it must form an insoluble compound that precipitates on the magnesium surface to function as an effective precipitation inhibitor. In the following, the most important and effective groups of organic inhibitors are studied, and current progress in the understanding of their inhibition mechanisms is reviewed.

### 3.1. Adsorption and Precipitation Inhibitors

The inhibition mechanism of several effective corrosion inhibitors for Mg alloys has been ascribed to their ability to be adsorbed on the Mg surface. The adsorption of molecules on the surface can be viewed as forming a barrier layer, preventing corrosive species from reaching the Mg surface. This adsorption mechanism is usually postulated from the inhibitor molecule chemistry, which has electron donor atoms, which can interact with Mg atoms on the surface. However, the direct evidence of such adsorption has been barely reported for Mg alloys. The other effect of such adsorption is changing the morphology of

Mg(OH)<sub>2</sub> as the main corrosion product of Mg corrosion. For instance, the adsorption of organic molecules such as BTA has been claimed to serve as a nucleating agent on the Mg surface, stimulating the precipitation of denser crystalline Mg(OH)<sub>2</sub> film [70].

**Triazole** and its derivatives, such as 3-amino-, 4-amino-, 3-mercapto-, and 3-hydroxy-, have also been tested as corrosion inhibitors for Mg alloys [10,71–76]. Benzotriazole also exists in commercial inhibiting compounds such as Ardrex 3961 [77]. Reported results are controversial, ranging from high corrosion inhibition to dramatically accelerated degradation of Mg alloy. Similarly, it has been shown that the effect of benzotriazole (BTA) and its 5-chloro- derivative differs depending on experimental conditions and tested alloy [10,70,71,75,78–80]. Considering the high condition dependency of BTA and its harmfulness to aquatic life, it is not likely to find any industrial application.

**Schiff base (SB) compounds** are a group of organic substances with at least one double bond between carbon and nitrogen atom -C=N-R (imine; R is either Alkyl or Aryl group). The imine group offers a strong bond with the metallic ions. SBs with polar substituents at suitable molecular positions can form chelates with metal ions, which boosts their bonding strength. The effective inhibitive properties of many Schiff base compounds have been frequently reported for corrosion protection of aluminum [81–83], steel [84–86], and copper [87,88]. Their inhibition effect is mainly attributed to their adsorption on the metallic surface to form a protective film that isolates the metals from the aggressive environment. The same mechanism of corrosion inhibition is also claimed for Mg and its alloys, although direct evidence for such adsorption has been barely reported. The relatively simple route for synthesizing a countless number of SBs via condensation reactions of aromatic or aliphatic amine and carbonyl compounds [89] renders them a highly potential territory for looking for an effective corrosion inhibitor for Mg alloys. SBs are widely used in bio-applications such as antimicrobial, anti-inflammatory, antiviral, and anticancer agents, which implies their low environmental toxicity [89]. Nevertheless, there are only a few reports of SBs for magnesium; many of them have been tested in acidic conditions or in ethylene glycol aqueous solutions, which are not common conditions for the industrial application of magnesium [90–92].

Recently, Ma et al. [93] synthesized three different SBs molecules via a condensation reaction of paeonol with amino acids tyrosine (PCTyr), phenylalanine (PCPhe), and cysteine (PCCys). All the SBs in the concentration range of 10<sup>−3</sup>–10<sup>−2</sup> M could inhibit the corrosion of a Mg–Zn–Y–Nd alloy in 0.9 wt.% NaCl solution, among which PCCys (see the molecular structure in Figure 6a) at a concentration of 10<sup>−2</sup> yield the highest inhibition efficiency of 92%. A strong reduction in the anodic activity of the Mg alloys was observed for all the SBs (Figure 6b), reflecting their anodic-type inhibition. The morphology of the corrosion products has been changed in the presence of the SBs in the electrolyte, Figure 6c–f, which was postulated as the precipitation of insoluble complexes between Mg<sup>2+</sup> and the SBs. The possibility of a precipitation mechanism has also been postulated in other works; however, direct evidence of this was not provided.

In addition to the adsorption of inhibitors, they can form insoluble complexes with magnesium ions that precipitate and block the magnesium surface. Of course, their tendency to form a bond with magnesium atoms can still occur on the surface of magnesium; however, experimental results show that a precipitation mechanism is more likely to happen than direct adsorption of this group of organic substances on the magnesium substrate.

**8-Hydroxyquinoline (8HQ)** is a strong complexing agent that has the ability to chelate with Mg<sup>2+</sup> and form an insoluble complex, which is highly stable in the pH range of 9.4 to 12.7 [94]. It is actually used in classical analytical analysis as a low-selectivity group reagent due to its ability to form insoluble chelates with a number of cations. At pH > 8, apart from Mg<sup>2+</sup>, the following cations precipitate with 8HQ: Ca<sup>2+</sup>, Al<sup>3+</sup>, Fe<sup>3+</sup>, Cr<sup>3+</sup>, Co<sup>2+</sup>, Ni<sup>2+</sup>, Zn<sup>2+</sup>, Cd<sup>2+</sup>, Cu<sup>2+</sup>, and Ag<sup>+</sup>. Several reports of strong corrosion inhibition by 8HQ on different magnesium alloys confirm that 8HQ is a plausible candidate for commercial use on Mg parts [25,95–98]. On the other hand, some reports [10,80,99,100] suggest that 8HQ and its derivatives have a minimal or negligible inhibition effect on magnesium alloys,

notwithstanding critical factors related to testing conditions, such as the substrate elemental composition and microstructure, the composition and concentration of testing electrolyte, concentration of inhibitors, initial solution pH, the ratio between electrolyte volume and exposed magnesium surface area, and eventually the testing time. Generally, the corrosion inhibition effect of 8HQ is attributed to the formation of an insoluble complex with  $Mg^{2+}$  ions (8HQ(Mg)), which precipitates and blocks the surface of magnesium substrate [25,95]. Although the flower-like morphology of 8HQ(Mg) complex (Figure 7a) may provide some degree of hydrophobicity [101], a continuous blocking layer seems to be achieved with delay. This is evident in the slow increase in Mg AZ21 impedance exposed to a 8HQ-containing corrosive NaCl electrolyte (compare Figure 7b,c) as well as rather dispersed 8HQ(Mg) flakes present on the already formed corrosion product layer after 1 day of immersion (Figure 7d).

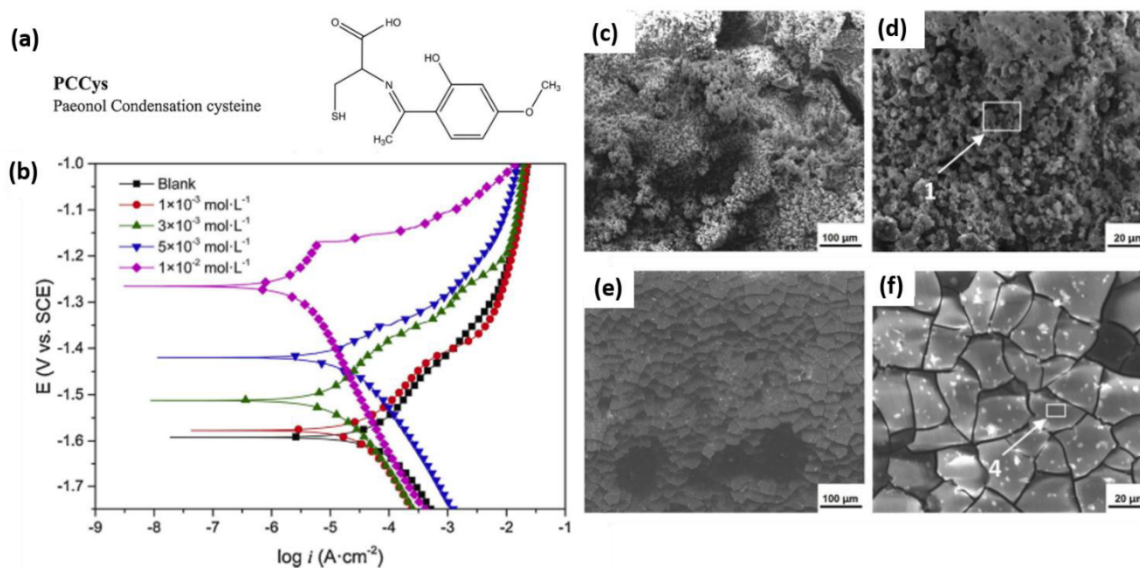


**Figure 6.** (a) Chemical structure of PCCys Schiff-based molecule. (b) Potentiodynamic polarization curves for Mg-Zn-Y-Nd alloy in 0.9 wt.% NaCl solution with and without different concentration of PCCys. (c–f) Corrosion morphologies of Mg-Zn-Y-Nd alloy after 7 days immersion in 0.9 wt.% NaCl solution: (c,d) without PCCys, (e,f) with  $10^{-2}$  M PCCys. Numbers and arrows in (d,f) indicate the areas of EDS analysis carried out in the corresponding paper Adapted from [93] with permission from Elsevier.

A layer of 8HQ(Mg) precipitating on a Mg substrate is believed to provide self-healing properties [96]. The corrosion of a Mg substrate at a defect leads to a locally high concentration of  $Mg^{2+}$  and  $OH^{-}$ . The latter causes the partial dissolution of 8HQ(Mg) flakes, which re-precipitates in the local enriched  $Mg^{2+}$  region on the coating defect (see Figure 8 for the schematic mechanism of self-healing by 8HQ(Mg)).

Although the effectiveness of 8HQ as a corrosion inhibitor for Mg has resulted in numerous previous and recent related research activities [103–105], the risk of mutagenicity and chemical instability in light hinders the wide use of 8HQ in commercial applications.

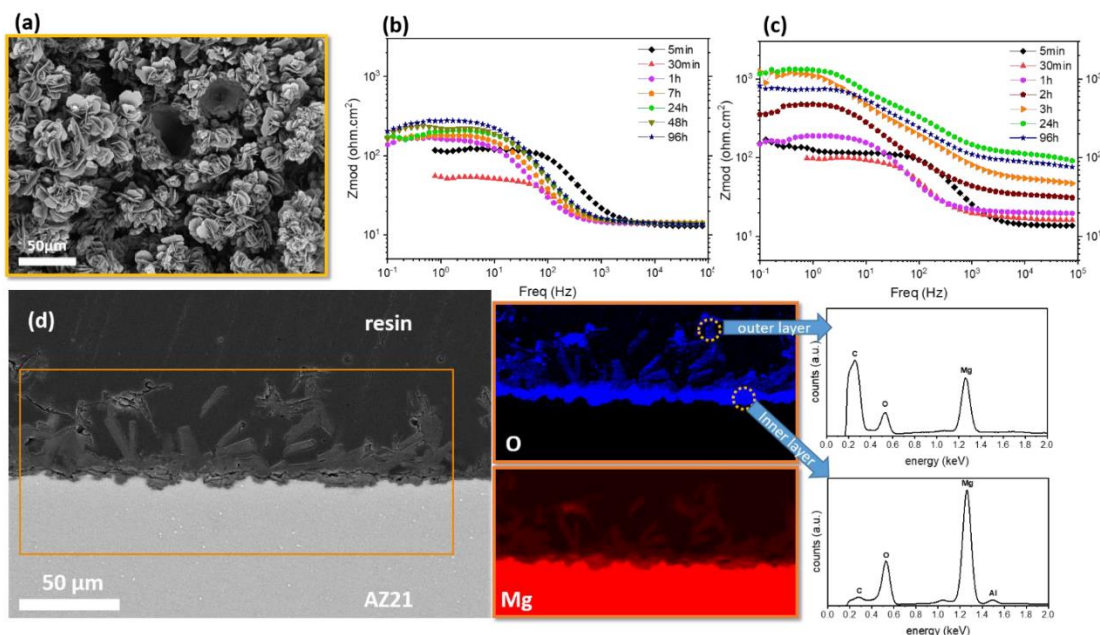


**Figure 7.** (a) Surface morphology of bare AZ31 exposed to 3.5 wt.% NaCl electrolyte containing 8HQ. (b,c) Bode plots of the EIS spectra obtained for the AZ31 Mg during 4 days of immersion in NaCl 3.5 wt.% solution with and without 8HQ, respectively. (d) Cross section view of (a) along with the elemental mappings of the marked area. Adapted from [102] with permission from Elsevier.

### 3.2. Surfactants

Surfactant (the short form of surface active agent) is a general term used for a group of organic molecules that are conventionally described as a single hydrocarbon tail connected to an ionic or polar head group [106]. Many surfactants are already used in various industries to control the corrosion rate of steel and Al engineering parts [2]. Similar to other organic inhibitors, surfactants interact with magnesium atoms, mostly by forming bonds through their electron donor atoms, N, O, and S. For surfactants, electron donation occurs mostly on the metal surface, resulting in their predominant adsorptive characteristic. Therefore, surfactants are able to cover the metal surface and act as a barrier to corrosive media. The barrier effect is intensified when the complex of surfactants with Mg cation is highly insoluble and precipitates along with surfactant adsorption. Moreover, a surfactant molecule consists of one (or more) long organic chain (also called a “tail”) that brings two main enhancements to the inhibitive characteristics of this group of chemicals:

1. Due to the hydrophobic properties of the tail of surfactants in aqueous environments, they can effectively keep corrosive media from coming into contact with the magnesium surface.
2. Due to the bulky tail of surfactants, they are highly effective at covering surfaces, even in small concentrations.

It has been shown that as the length of the surfactant chain increases (when other factors are equal), higher inhibition efficiency is achieved [107,108], mainly due to the fact that the abovementioned inhibitive characteristics become more effective [109]. However, the inhibition efficiency reduces when the chain length exceeds a certain value [110,111]. Steric hindrance prevents the bulky molecules from staying close to each other and covering the entire surface. Moreover, the chain length affects the electronegativity of the head group in the surfactant, which influences the adsorption ability of the surfactant molecule on the surface. Furthermore, the long surfactant tail limits its solubility in aqueous media.

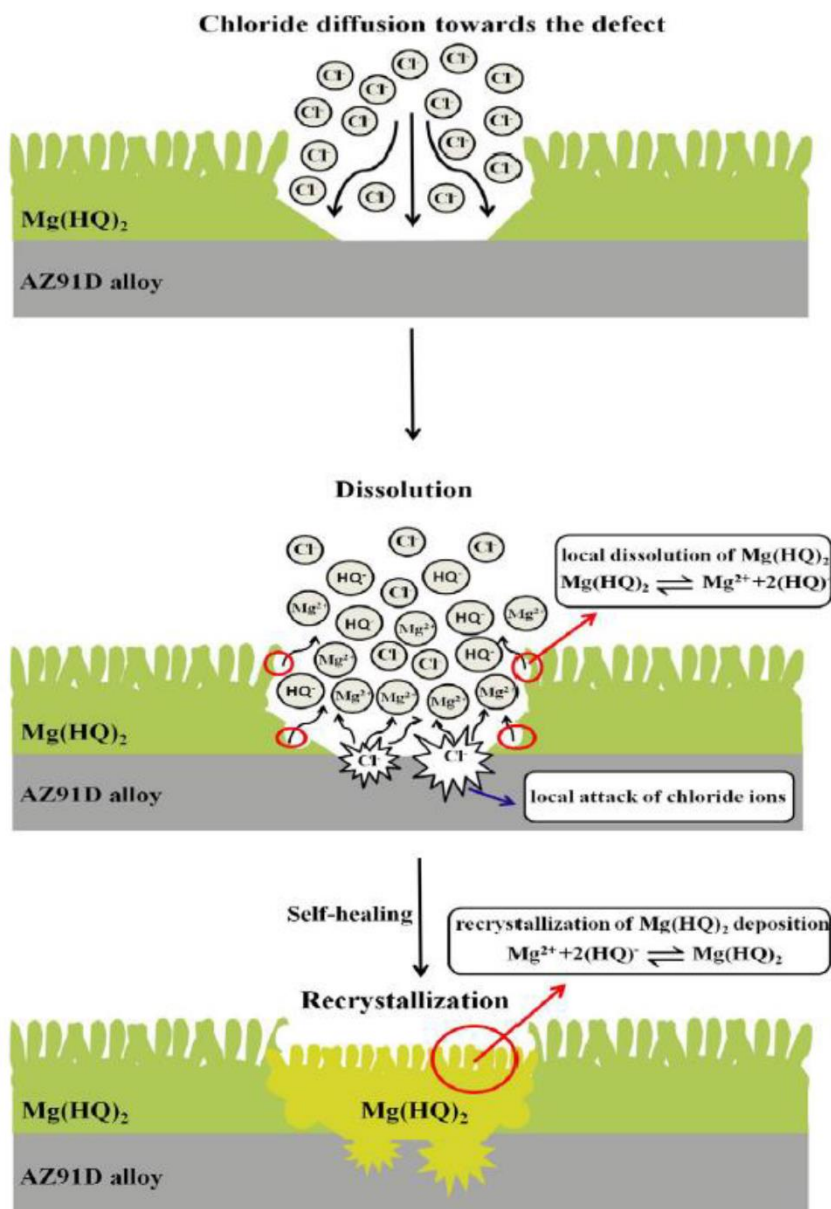


**Figure 8.** Schematic illustration of inhibition mechanism of 8HQ(Mg) layer on a Mg substrate. Note:  $\text{Mg}(\text{HQ})_2$  in the figure and 8HQ(Mg) in the text refer to the same complex. Adapted from [96] with permission from Elsevier.

Changes in the head of surfactants, which function as the adsorptive part of the surfactant, can significantly change the inhibition efficiency. Various surfactants with the molecular structure of carboxylic head linked to alkyl chains of different lengths have been studied as corrosion inhibitors for Mg alloys [10,75,80,109,112–115]. They are environment-friendly organics that are mostly derived from natural sources. For instance, lauric acid (C12) and myristic acid (C14) are mainly found in human breast milk and coconut milk. Stearic acid (C18) and palmitic acid (C16) are widely used in the production of soaps and detergents. Most of the alkyl carboxylates were reported as mixed-type inhibitors with a small shift in the corrosion potential to noble values. However, chemisorption of the

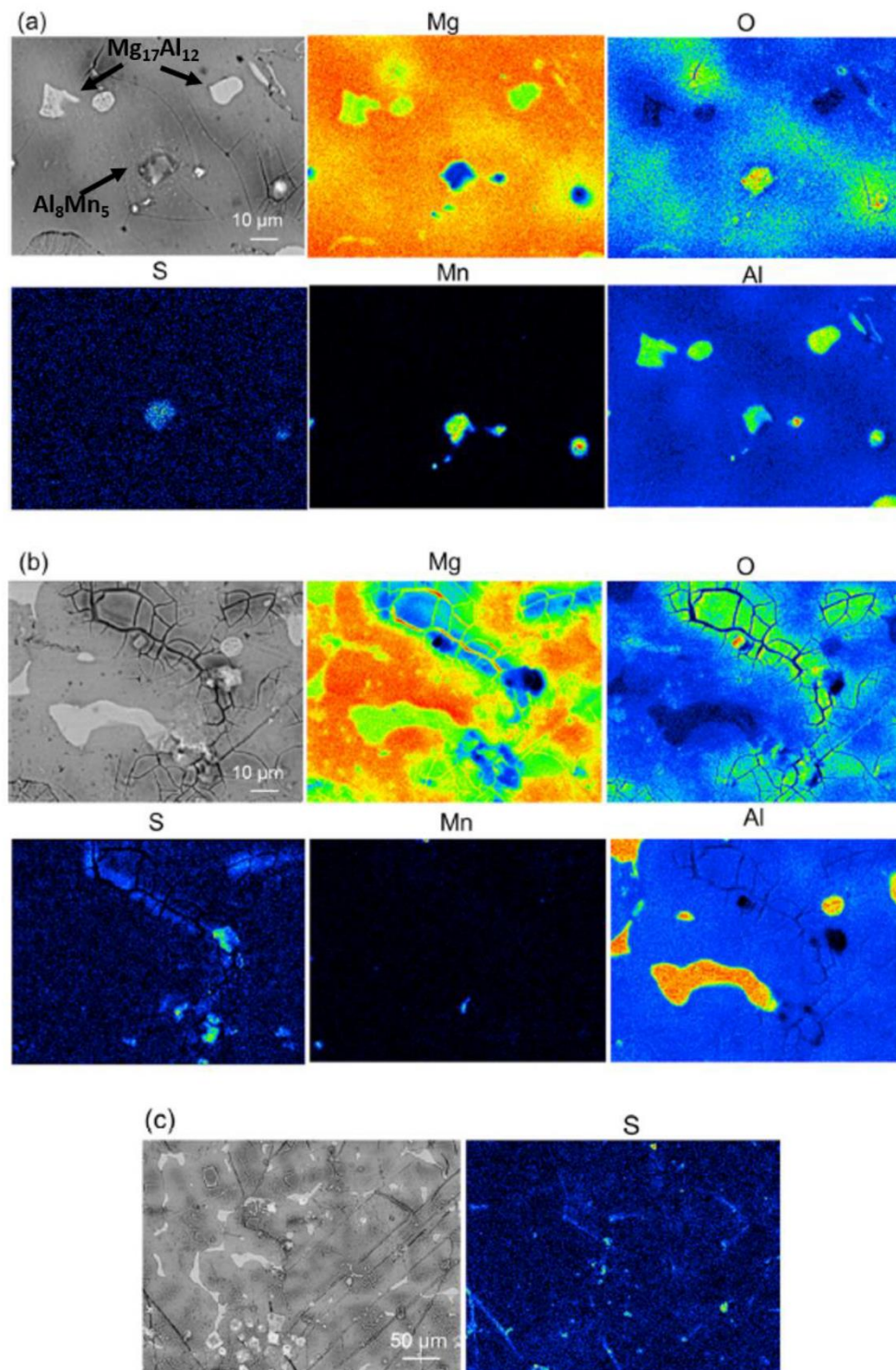
surfactant's head on regions that are characterized by cathodic behavior can effectively improve the protective performance of inhibitors on magnesium alloys. Adsorption of surfactants on phases with cathodic characteristics is particularly effective when low d-orbital energy elements such as Zr and RE are present in the chemical composition of the magnesium alloy [80,112]. Analogously, the preferential adsorption of sodium dodecylsulfate (SDS) on the Mn-containing second phase  $\text{Al}_8\text{Mn}_5$  rather than on  $\text{Mg}_{17}\text{Al}_{12}$  in AZ91 Mg alloy has been detected by [116], as shown in Figure 9. However, possible preferential adsorption of SDS on  $\text{Mg}(\text{OH})_2$ , which forms more on the Mn-containing secondary phase with a higher galvanic potential difference to the Mg matrix [117,118], should also be taken into consideration.

Figure 10 is a schematic representation of the surface film formation on ZE41 alloy immersed in an aqueous solution containing alkyl carboxylates. The formed surface film consists of a complex of alkyl carboxylate with magnesium ion,  $\text{Mg}(\text{OH})_2$ , and chemisorbed surfactant, dominantly on the second phases with higher cathodic characteristics with respect to  $\alpha$ -Mg phase [112]. It is believed that anodic inhibition of magnesium alloys is achieved mainly through densification of the porous surface  $\text{Mg}(\text{OH})_2$  film by physical adsorption of Mg carboxylates [115] rather than the direct adsorption of alkyl carboxylate anions on magnesium surface.

Sulfates and sulfonates are other functional groups as the head-group of surfactants. Sodium lauryl sulfate [119], N-lauroyl-N-methyltaurine [119], sodium N-lauroylsarcosine [10,119], sodium dodecylsulfate (SDS) [116,120–123], and sodium dodecylbenzenesulfonate (SDBS) [10,25,80,95,119,124–128] have been studied as inhibitors for magnesium alloys, among which SDS and SDBS have drawn more attention. In addition to oxygen and sulfur atoms with lone-pair electrons, the benzene ring is also able to share its lone-pair electrons with magnesium atoms on the surface. Due to its chemical composition and molecular structure, SDBS is considered a good adsorptive organic chemical. Adsorption of SDBS molecules on the surface is combined and reinforced by precipitation of SDBS-Mg complex that further blocks corrosion active sites [119,128,129]. Chen et al. [128] proposed an inhibition mechanism model based on the competition between  $\text{DBS}^-$  and the aggressive  $\text{Cl}^-$  ions to be adsorbed on the Mg surface. They suggested that the inhibition efficiency of the SDBS increases with the concentration until it exceeds the concentration required to form a bi-layer (hemi-micelle adsorption) of  $\text{DBS}^-$  molecules covering the  $\text{Mg}(\text{OH})_2$  nano-sheets on the Mg surface (Figure 11a–d). This trend was also confirmed by the inhibition efficiency extracted from the dynamic polarization test (Figure 11e,f).

Recently, Li et al. [121,122] have claimed that the presence of SDS in a NaCl electrolyte exposed to AZ91 and AM50 Mg alloy can facilitate the oxidation reaction of the Mg matrix with the dissolved  $\text{O}_2$  in the electrolyte. As a result, a relatively thick passivating  $\text{MgO}$  layer can form on the Mg matrix, significantly reducing the anodic activity of the substrate. This claim was confirmed by the nine-fold increase in the corrosion rate in the same electrolyte after deaeration by purging with  $\text{N}_2$  gas. However, the chemical mechanism of such enhancement in the  $\text{MgO}$  formation has remained unanswered.

In general, the high corrosion inhibition ability of surfactants at reasonable cost effectiveness can be reflected in their common use in commercial inhibition products, which are also effective for Mg alloys [77,130].



**Figure 9.** Main elemental distribution (Mg, O, S, Mn, and Al) on Mg surface after immersion for 6 h (a) and 48 h (b,c) in 3.5 wt.% NaCl solution with addition of 0.05M SDS. Adapted from [116] with permission from Elsevier.

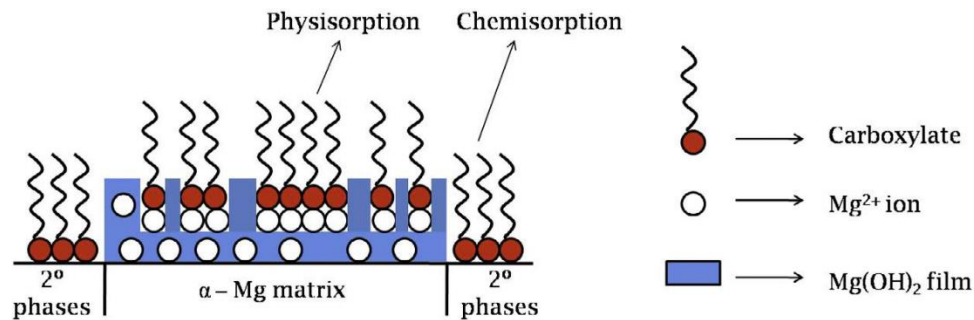


Figure 10. The schematic representation for the surface adsorption of alkyl carboxylates over different phases of ZE41. Adapted from [112] with permission from Elsevier.

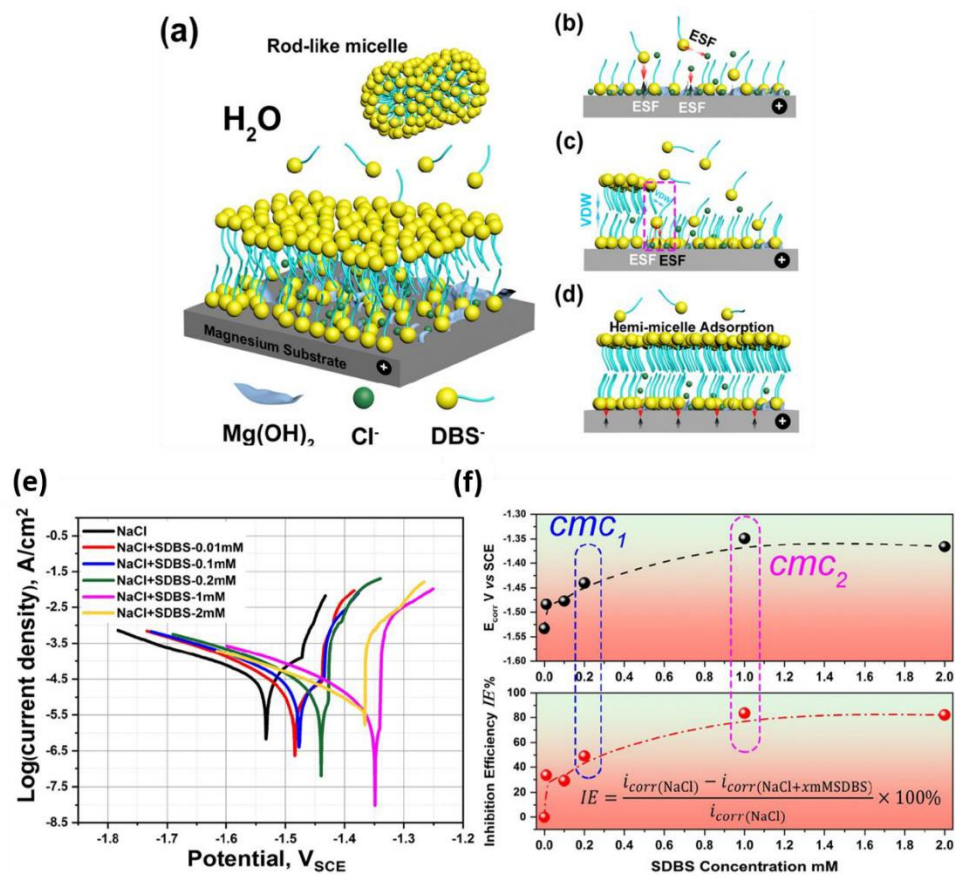


Figure 11. (a–d) Adsorption model of Mg surface in NaCl+SDBS solution with high SDBS concentration. (a) Bilayer structure formed by DBS<sup>-</sup> surfactant. (b) Negatively charged DBS<sup>-</sup> and Cl<sup>-</sup> adsorb on positively charged Mg substrate via electrostatic force (the black and white marked “ESF”, respectively, represent electrostatic repulsion and attraction). (c) Competitive adsorption between DBS<sup>-</sup> and Cl<sup>-</sup> (VDW illustrates “van der Waals” force) (d) Formation of hemi-micelle adsorption film. (e,f) Tafel potentiodynamic polarization measurements. (e) Tafel curves recorded in different solutions. (f) Corrosion potential and inhibition efficiency. The labeled cmc<sub>1</sub> and cmc<sub>2</sub> represent the concentrations of SDBS reaching spherical and rod-like micelles, respectively. Adapted from [128] with permission from Elsevier.

### 3.3. Ionic Liquids

**Ionic liquid (IL)** is a type of salt with a low melting point below 100 °C [131], which is mostly composed of organic cation–anion pairs [132,133]. High conductivity (0.1–14 mS/cm), broad electrochemical stability windows, high thermal stability, and low vapor pressure [134] are some of the unique physicochemical properties of ILs. In addition, the organic nature of the cation–anion pair allows innumerable formulations of the ILs, which can also be “designed” according to their desired properties. Several reports have investigated the use of ILs to form a conversion coating on Mg alloys (PART I of the review). However, only recent studies (mainly published after 2020) by a few scientific groups have investigated the application of ILs as corrosion inhibitors for Mg alloys [135–142].

So far, only bis(trifluoromethanesulfonyl)imide (NTf<sub>2</sub>, also abbreviated as TFSA in the literature) has been the most used anion for ILs as Mg corrosion inhibitors; while the effect of different cations, including pyrazolium [135,136,138], imidazolium [137], and phosphonium [139–142] have been investigated. The role of NTf<sub>2</sub> anion in IL inhibitors plays an important role in forming a protective layer on the Mg substrate. The decomposition of NTf<sub>2</sub> into smaller fragments, including F<sup>−</sup> ion, leads to the formation of a thin protective MgF<sub>2</sub> film. The presence of MgS and MgSO<sub>4</sub>, as the result of the reaction of Mg ions with fragmented NTf<sub>2</sub>, has also been concluded from XPS analysis [137,138]. Although the decisive role of cations in ILs can be clearly reflected in their different corrosion protection performances, the mechanistic view of their inhibition roles is not clear and is usually explained by the different degrees of adsorption of their fragments on the Mg surface.

The concentration of investigated ILs is usually below 1 mM, with an increasing inhibition efficiency with their concentration. A relatively high (~87%) inhibition efficiency (calculated based on a potentiodynamic test) has been reported for 1 mM 1-decyl-3-methylimidazolium bis(trifluoromethylsulfonyl)amide ([DMIm][NTf<sub>2</sub>]) in rigorous 3.5 wt.% NaCl solution on an AZ31 alloy [137].

In a recent work by Kurchavov et al. [143], the surface activity of a CP-Mg and AZ61 alloy was investigated in two IL-water mixture solutions, in which the ILs were composed of acetate (OAc<sup>−</sup>) anion and two different 1-methyl-pyrrolidinium-based cations, denoted as BMPyr<sup>+</sup> (1-butyl-) and mPEG<sub>n</sub>MPyr<sup>+</sup> (1-methoxy-polyethyleneglycol-). Their difference is that the former contains an aliphatic chain, while the latter contains an etheric chain of polyethylene glycol. Interestingly, although Mg alloys dissolved in these electrolytes at relatively high anodic potential and current, the HER rate on both magnesium substrates was significantly reduced at anodic polarization (up to +1 V vs. E<sub>oc</sub>) only when mPEG<sub>n</sub>MPyr<sup>+</sup>OAc-H<sub>2</sub>O (rather than BMPyr<sup>+</sup>OAc-H<sub>2</sub>O) was employed. This was explained by formation of low adherent acetate-containing passivating film.

The limited recent reports of the remarkable effects of ILs as “green” corrosion inhibitors for Mg alloys can be taken as a promising approach to finding an effective substitute for chromate-based inhibitors. Nevertheless, it is at its nascent stage and deserves further investigation.

### 3.4. Iron Binding Inhibitors

Most of the organic inhibitors described above target the anodic dissolution of magnesium. Inhibition of cathodic activity is another possibility for suppressing corrosion. The detrimental effect of iron impurities on the acceleration of magnesium corrosion via cathodic activation has been known for decades [144] and keeps attracting the attention of many scientific groups [145–147]. In a recent explanation of this phenomenon proposed by Höche et al. [147], the cathodic activity of the corroding front can be increased over time (which means a higher galvanic corrosion rate) by re-deposition of iron ions that originated from already detached iron-rich impurity particles from the surface and dissolved into the electrolyte. The negative difference effect (NDE), which is the acceleration of cathodic hydrogen evolution reaction at anodic polarization, has also been explained by such re-deposition of iron. Michailidou et al. [148] and Mercier et al. [149] supported this mechanism by providing new experimental evidence. Based on this explanation, Lamaka

et al. [150] showed that the prevention of iron re-deposition by strong iron complexing agents can effectively reduce the corrosion rate of commercially pure magnesium. Moreover, Vaghefinazari et al. [151] have clearly shown that the NDE can be suppressed by the presence of the strong complexing agent EDTA on a CP-Mg. Following this concept, numerous organic inhibitors have been found with inhibition efficiencies comparable to or exceeding that of chromium (VI) [10].

In particular, derivatives of salicylic and pyridinedicarboxylic acids were found to have the highest inhibiting efficiency for a number of commercially important alloys (AZ31, AZ91, AM50, WE43, ZE41, and Elektron 21) and three grades of pure magnesium.

Corrosion of most of the tested magnesium materials were strongly inhibited by amino-, methyl-, thio-, nitro-, and dinitro-derivatives of salicylate. The suppression of iron re-deposition was accounted for the observed high inhibition effects. In contrast with the aforementioned derivatives of salicylate, sodium salts of salicylic itself and sulfosalicylic had weak or even adverse inhibition effects for on the tested alloys, which is due to the formation of stable and soluble complexes with  $Mg^{2+}$  ( $\log K_{Mg^{2+}}^{st} = 5.1$  for sulfosalicylic acid) [152]. In this instance, the positive effect of iron complexation is counteracted by the accelerated dissolution of magnesium. Amino-, methyl-, nitro-, and dinitro-derivatives of salicylic acid also form stable complexes with  $Fe^{3+}$  ( $\log K_{Fe^{3+}}^{st} = 18.13$  for 3-methyl-,  $\log K_{Fe^{3+}}^{st} = 14.57$  for 5-methyl-,  $\log K_{Fe^{3+}}^{st} = 14.19$  for 3-nitrosalicylic acid [152–154]). The highest inhibiting effect of salicylic acid derivatives was found for highly corroding pure Mg with active iron impurity particles and aluminum-containing alloys AZ31, AZ91, and AM50. The formation of stable and soluble complexes between  $Mg^{2+}$  and two derivatives of benzoic acids, namely 4-hydroxybenzoate and 3,4-dihydroxybenzoate ( $\log K_{Mg^{2+}}^{st} = 9.84$  for 3,4-dihydroxybenzoic acid), also resulted in a high dissolution rate of tested Mg materials, in spite of their chelating effect with  $Fe^{3+}$  [153]. Salicylaldehyde demonstrated high inhibiting efficiency for RE-containing alloys but should not be considered for industrial use due to its toxicity to aquatic life [10,155,156].

Sodium salts of several derivatives of pyridinedicarboxylic acids, (2,6-, 2,5-, 2,3- and 3,4-PDCA) showed high inhibition efficiency (more than 70% on average) for all tested magnesium materials. PDCAs are also able to form strong chelates with  $Fe^{2+/3+}$  (e.g., for 2,6-PDCA  $\log K_{Fe^{3+}}^{st} = 17.13$  [157]); thus, their observed high corrosion inhibition effect was partially attributed to the suppression of iron re-deposition. Sodium salts of derivatives of pyridine with only one carboxylic acid group, namely picolinic and nicotinic acids, could also weakly inhibit most of the test Mg materials.

Figure 12 provides an overview of the most efficient corrosion inhibitors as derived from hydrogen evolution measurements in pH neutral 0.5 wt.% NaCl electrolyte with or without corrosion inhibitor. A corrosion inhibitor that is found to be effective for RE-containing Mg alloys is not always effective for Al-containing Mg alloys, though it is more likely to be effective if it is applied within the same group of Mg alloys.

One of the valuable outcomes of the comprehensive screening of corrosion inhibitors for different magnesium alloys by Lamaka et al. [10] was the discovery of chemical substances that are able to effectively inhibit six tested alloys and three grades of pure magnesium, which can be considered “universal” inhibitors. Among them, PDCs, fumarate, and derivatives of salicylates were further investigated in several reports at different experimental conditions and using different characterization methods to gain more insights into their inhibition mechanisms [158–162]. Apart from their role in suppressing the iron re-deposition of these inhibitors, it was found that the complex formation between 2,5PDC and  $Mg^{2+}$  precipitates as a coordination polymer, further protecting the Mg substrate. The corrosion inhibition of 2,5PDC requires an initial dissolution of Mg substrate, which was evident from the induction period in rate of  $Mg(OH)_2$  growth measured by in situ Raman characterization of the Mg surface (Figure 13a,b). Salicylate is also able to stabilize the  $Mg(OH)_2$  nano-crystals via a chemisorption mechanism. Similar to 2,5PDC, salicylate requires an initial dissolution of Mg in order for its inhibition to become activated. Adsorption of fumarate on the metallic Mg or MgO leads to an immediate inhibition effect.

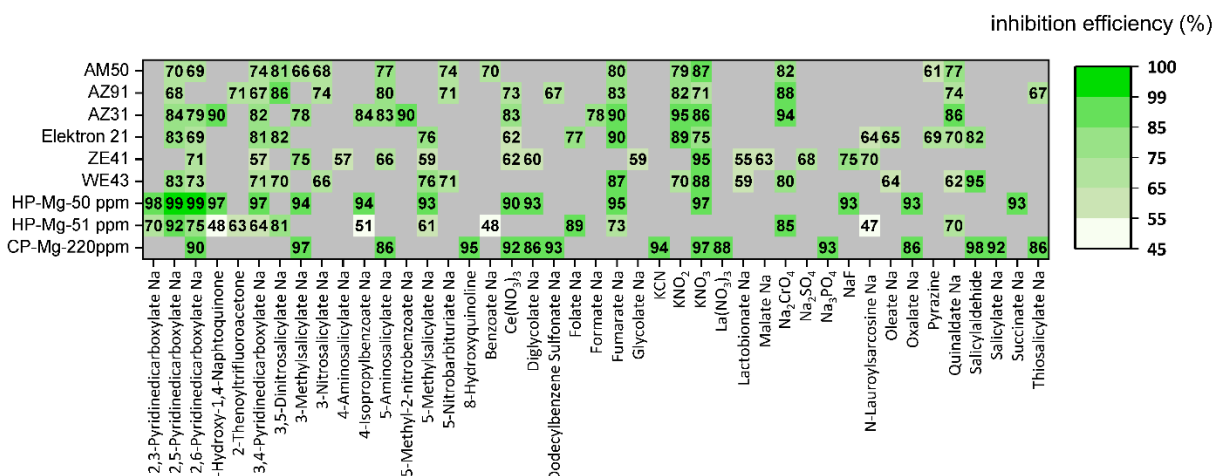


**Figure 12.** Inhibiting efficiency of top 15 corrosion inhibitors for pure Mg, RE, and Al containing Mg alloys. Based on the data presented in Table 5 of reference [10].

Moreover, all of the abovementioned universal inhibitors affect the morphology of  $\text{Mg}(\text{OH})_2$  as the main corrosion product, resulting in a more compact and less porous microstructure (Figure 13c), which in turn hinders the penetration of corrosive species. A recent work by Cui et al. also emphasizes the effect of organic molecules on the nucleation and growth of  $\text{Mg}(\text{OH})_2$ , which can determine their corrosion inhibition efficiency [163].

### 3.5. In Silico Screening of Corrosion Inhibitors

Another valuable outcome of the comprehensive screening of 150 organic corrosion inhibitors for different magnesium alloys by Lamaka et al. [10] is that it created a relatively large database of inhibiting efficiency values, acquired under the same conditions. These coherent data allowed extension of the data-driven computational methods, such as machine learning [164–167], to the field of magnesium corrosion inhibition [168–171]. The successful predictions of several new corrosion inhibitors for Mg alloys via *in silico* methods have already been reported in several recent papers [168,170]. There are technically a limitless number of organic compounds potentially effective at inhibiting the corrosion of metals. Experimental approaches are capable of evaluating only an insignificant percentage of such infinite chemistry space. Thus, *in silico* methods have recently come into play to expand the explored chemical space and predict the effective corrosion inhibitors for Mg alloys [168–173].

Although time consuming (months scale) at the stage of methodological development of robust and reliable models, data-driven computational methods can explore large chemical spaces much more quickly, thus saving resources and labor while not generating any waste. In a recent paper by Würger et al. [168], the accuracy of the developed model was tested by screening a commercial database containing 7094 organic compounds (provided by Thermo Fisher Scientific). Experimental testing of such scale is unrealistic, as it would require years of continuous experimenting, even employing high-throughput methods and associated costs of millions of euros. This *in silico* screening resulted in the prediction of a number of molecular structures, which were proven to be rather strong corrosion inhibitors. 1,2,4-benzenetricarboxylate and two nitro-phthalates were shown to possess inhibiting efficiency above 70% through experimental testing. The similarity-based discovery workflow is available online at [www.exchem.de](http://www.exchem.de); accessed on 2 December 2020. Other examples of predicted (and experimentally validated) inhibitors for a commercial purity magnesium are sodium salts of 0.05 M of trimesic acid and n-Octyl-gallate with inhibition efficiencies of more than 80% in 0.5 wt.% NaCl solution [170].

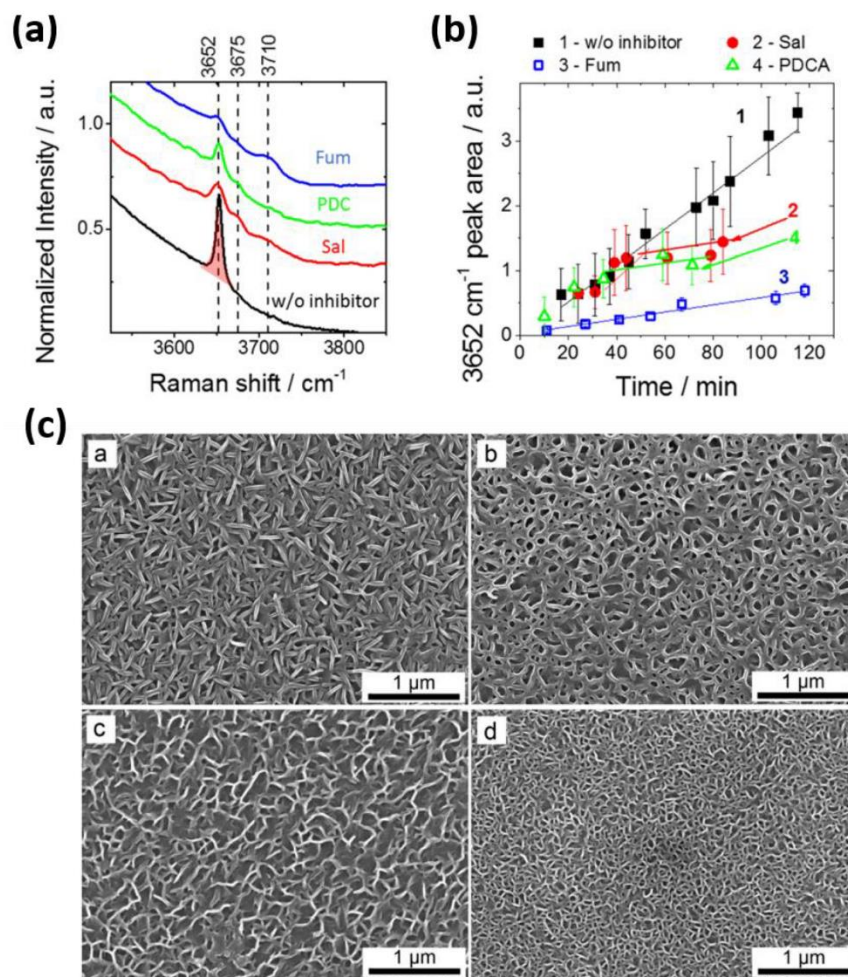


**Figure 13.** (a) Fragments of in situ Raman spectra recorded on CP-Mg342 in 0.1 M NaCl in absence and in presence of corrosion inhibitors; (b) growth kinetics of  $\text{Mg}(\text{OH})_2$  recorded on CP-Mg342 in 0.1 M NaCl with or without the corrosion inhibitors; (c) SEM micrographs of CP-Mg342 surface after 30 min contact with flowing 0.1 M NaCl solution with and without 0.05 M inhibitors (a: without inhibitors; b: sodium salicylate (Sal); c: 2,5-pyridin-dicarboxylate (PDCA); d: fumarate (Fum)). Adapted from [158] with permission from Elsevier.

With the fast development of computational methods, software, and computational power, computational algorithms are able to rapidly process the experimental databases to train machine learning models. The lack of coherent and reliable experimental databases, covering large chemical spaces, for data-hungry artificial intelligence approaches remains a problem.

The most valuable datasets are those acquired under the same experimental conditions so that the data in the set are directly comparable. This, however, limits the further extension of such models to other magnesium alloys, inhibitor concentrations, etc. Additionally, the quickly growing amount of corrosion inhibition efficiency values, acquired by a large variety of methods, for different substrates (Al-, Zn-, Cu-alloys and steels along with Mg), with different experimental conditions and testing times, calls for efficient ways to organize them and possibly find the most efficient “universal” corrosion inhibitors with a broad window of conditions where such inhibitors remain highly efficient. Galvão et al. [174] have established an online database of corrosion inhibitors, which are freely available

for contributors [datacor.shinyapps.io/cordata/](https://datacor.shinyapps.io/cordata/); accessed on 8 May 2021. It enables a better overview, centralized access, and simultaneous yet independent methods of data processing, possibly yielding valuable general trends.

An overview of different organic and inorganic categories of corrosion inhibitors for Mg and its alloys is presented in Figure 14. The following sections focus on the strategies to boost the inhibition effect via mixing individual inhibitors from different categories and incorporating individual and mixtures of inhibitors into various coating systems.

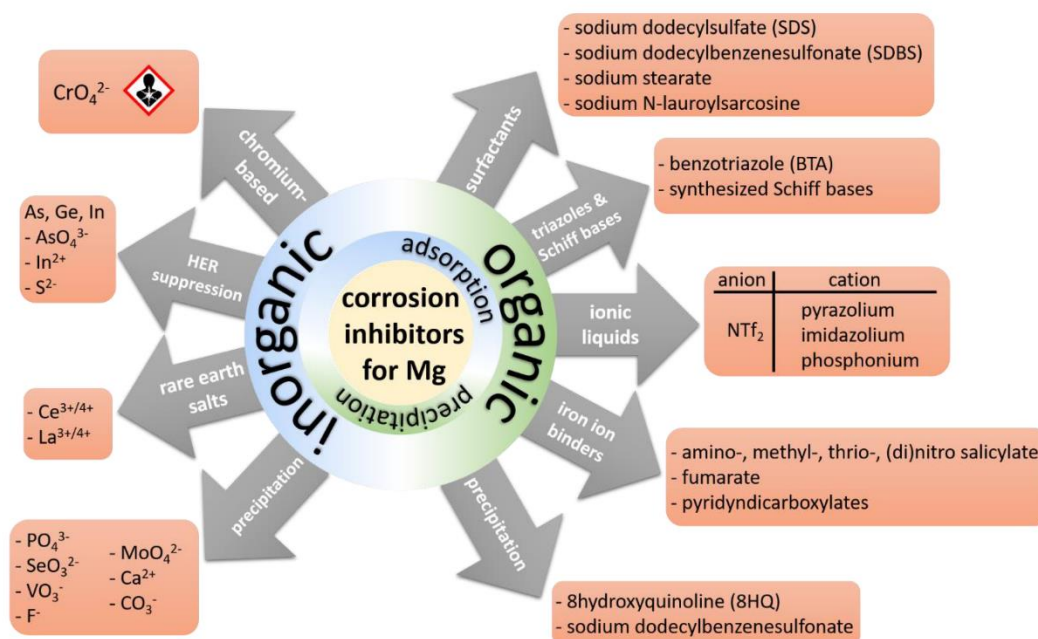


**Figure 14.** General overview of different categories of corrosion inhibitors for Mg and its alloys with their most effective examples.

#### 4. Inhibitor Mixtures: Synergistic Inhibiting Effect

The combination of individual inhibitors in order to boost the overall inhibition performance by a synergistic effect is a simple and promising approach. Synergy occurs when the inhibitive property of the combination exceeds the sum of the individual components' performance. The synergistic combinations of inhibitors cannot be predicted a priori because the behavior of synergies is usually non-linear. In spite of requiring extensive testing and combinatorial optimization [175], inhibitor mixtures are a promising research direction.

It should be noted that many already developed inhibitors are actually a combination of two components, yielding a synergistic inhibition effect, however, the impact of one component is usually overlooked. For instance, when nitrates of organic and inorganic cations are studied, the effect of nitrate on the corrosion of Mg is usually neglected, and the observed inhibition is fully attributed to the cation.

Synergic effect of two well-known inhibitors, SDBS and 8HQ, on AZ91D was investigated by Gao et al. [95]. Although the stand-alone 8HQ could achieve a 95% inhibition efficiency (calculated by data extracted from EIS) after 72 h of immersion in ASTM D1384-87 corrosive solution, with the addition of SDBS, the highest inhibition efficiency of 98% could be achieved after a shorter time of 48 h. Note that the presence of sodium bicarbonate in the ASTM D1384-87 has been neglected in this work, in spite of its reported inhibition impact (see Section 2.5).

Hu et al. [176] investigated the inhibition effect of organo-silicate aminopropyltriethoxysilicate (ATPS-Na) accompanied by inorganic zinc nitrate on Mg-10Gd-3Y (GW103). Although each of these inhibitors shows a weak inhibition effect, their combination boosts the corrosion protection. The improvement is attributed to the remarkable reduction in the size of the cracks in the formed film on the substrate. This is the result of the co-deposition of zinc and magnesium organo-silicate. Figure 15 presents SEM micrographs of the surface of GW103 alloy after immersion in a solution containing both inhibitors individually and in combination. Nevertheless, the effect of  $\text{NO}_3^-$  in zinc nitrate and bicarbonate in the blank corrosive solution has been overlooked again.

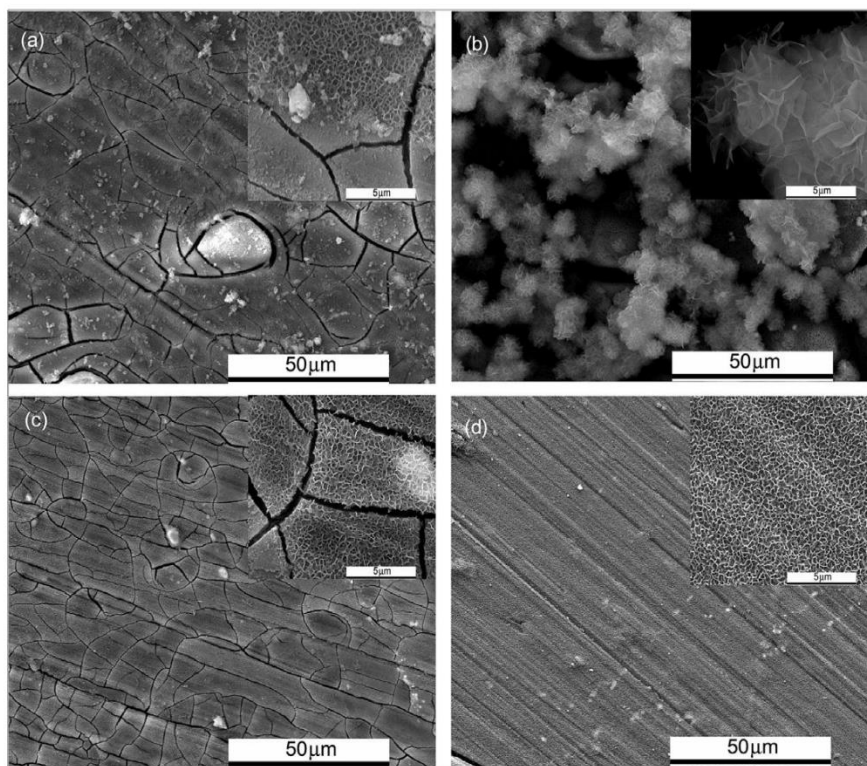


**Figure 15.** SEM micrograph of the surface of GW103 alloy after 24 h of immersion in (a) blank solution; (b) blank solution + 0.1 mM zinc nitrate; (c) blank solution + 0.5 mM ATPS-Na and (d) blank solution + 0.5 mM ATPS-Na + 0.1 mM zinc nitrate [176]. “Blank solution” is a corrosion testing solution from ASTM D1384, which consists of corrosion test solution: 184 mg/L  $\text{Na}_2\text{SO}_4$  + 138 mg/L  $\text{NaHCO}_3$  + 165 mg/L  $\text{NaCl}$ . Adapted from [176] with permission from Elsevier.

Alginic acid and its derivatives have been widely used as environmentally friendly corrosion inhibitors for some engineering metals such as steel [177–179] and aluminum [180–182]. Few works also have reported the limited effectiveness of sodium alginate (SA) additives in corrosive inhibition of magnesium alloys [183]. The main issue of using SA as corrosion inhibitor is its inherent massive molecule, which is likely to face steric hindrance when it is adsorbed on the surface, preventing the formation of a compact film on magnesium alloy [184]. Li et al. [185] added sodium alginate to a 3.5 wt.% NaCl at concentrations between 0 and 0.05 M, while two other inhibitive substances, sodium tungstate, and sodium silicate, were already present at fixed concentrations. The EIS results revealed that the presence of SA could significantly improve the inhibition efficiency up to 94% for 0.03 M SA. At the same time, excessive SA addition can almost completely negate this positive effect. They suggested that at SA concentrations lower than 0.03 M, SA is adsorbed on the defects of the

already formed passivation composite film of  $\text{MgWO}_4$  and  $\text{MgSiO}_3$ . However, at higher concentrations, the preferential adsorption of SA on the surface hinders the deposition of silicate and tungstate, causing deterioration of their corrosion inhibition characteristics. These results emphasize the fact that achieving the highest synergistic inhibition effect from individual inhibitors may depend on finding a sweet spot of mixture concentration; any deviation from this composition may have an adverse effect.

In another recent work, Hou et al. [184] investigated the combined inhibitive effect of SA at a fixed concentration of 0.05 wt.% and sodium phosphate at a concentration range of 0.05–0.2 wt.% on AZ31. Thermodynamic studies on the formation of insoluble  $\text{Mg}_3(\text{PO}_4)_2$ , and SA-Mg complexes showed that SA-Mg complex is the dominant component of the film covering the AZ31 surface under the initial stage of immersion. Then, deposition of insoluble  $\text{Mg}_3(\text{PO}_4)_2$  modifies this film as the immersion time is extended, and corrosion of Mg substrate results in the formation of a more protective complex film consisting of  $\text{Mg}(\text{OH})_2$ , SA-Mg complex and  $\text{Mg}_3(\text{PO}_4)_2$ . Sodium phosphate has also been coupled with other organic inhibitors, including sodium dodecylsulfate (SDS) [186], sodium dodecylbenzene sulfonate (SDBS) [80], and 2-mercaptobenzothiazole (MBT) [187], with the aim of achieving a synergistic inhibition effect. The synergistic effect of these combinations has been attributed to the formation of an adsorption layer on the  $\text{Mg}_3(\text{PO}_4)_2/\text{Mg}(\text{OH})_2$  film and Mg substrate. The highest synergistic effect strongly depends on the sweet spot in the ratio of two components to assure the sufficient precipitation of  $\text{Mg}_3(\text{PO}_4)_2$  and adsorption of the organic component.

Recently, Qui et al. [45] investigated the synergistic corrosion inhibition of NaF and DL-malate (DMA) on a Mg-Al-Mn magnesium alloy. The DL-malate molecules chemisorb on  $\text{Mg}(\text{OH})_2/\text{MgO}$  film through binding of the carboxylate groups with Mg sites, which itself, to some degree, hinders the penetration of corrosive  $\text{Cl}^-$  ions towards the substrate. On the other hand, precipitation of  $\text{MgF}_2$  and  $\text{NaMgF}_3$  as the result of the interaction of  $\text{Mg}^{2+}$  ions with  $\text{F}^-$  ions is a well-known inhibition mechanism of fluoride-based inhibitors. Indeed, the concurrency of these two inhibition mechanisms may boost Mg corrosion mitigation. However, the synergistic corrosion inhibition was rationalized based on an additional factor, which is the modification of the morphology of  $\text{NaMgF}_3$  precipitates with DMA molecules. Figure 16I shows the morphology of  $\text{NaMgF}_3$  particles synthesized with different ratios of  $\text{NaF}:\text{MgCl}_2$ . Decreasing the  $\text{F}^-:\text{Mg}^{2+}$  ratio leads to the modification of  $\text{NaMgF}_3$  particles from cubic to spherical form. The same variation in the morphology of the precipitated particles on the Mg alloy was observed when the concentration of DMA in the corrosion electrolyte increased (Figure 16II). Thus, it was postulated that DMA could regulate the  $\text{F}^-:\text{Mg}^{2+}$  ratio by forming a complex with  $\text{Mg}^{2+}$ , hindering them from interacting with  $\text{F}^-$  ions. As a result of the precipitation of spherical  $\text{NaMgF}_3$  particles with higher efficacy to cover the surface, a significantly enhanced passivation of the Mg surface could be achieved (Figure 16III). The schematic illustration of the synergistic corrosion inhibition mechanism of NaF and DMA can be seen in Figure 16IV.

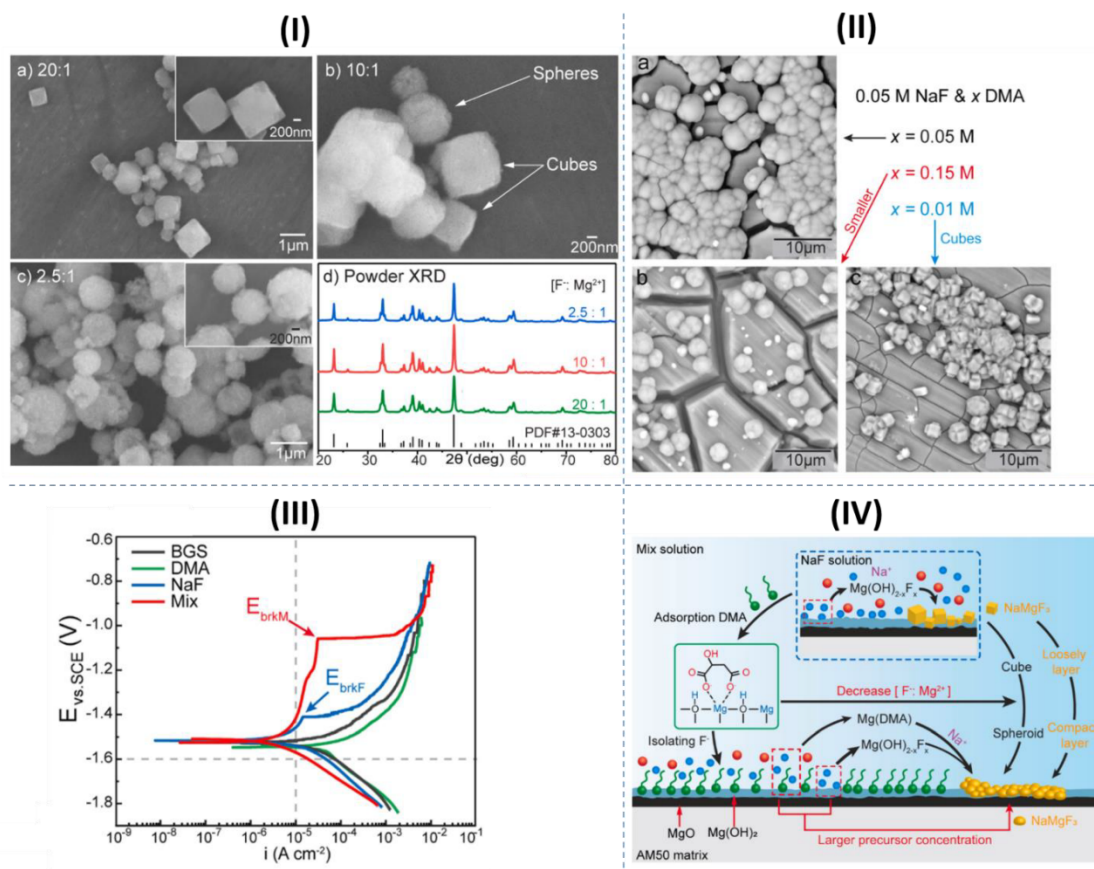


**Figure 16.** (I) The morphology of NaMgF<sub>3</sub> particles synthesized at varied reactants (NaF: MgCl<sub>2</sub>) molar ratios of (a) 20:1, (b) 10:1, (c) 2.5:1, and (d) the XRD patterns of the synthesized particles. (II) Morphology of NaMgF<sub>3</sub> particles obtained from Mix solutions containing 0.05 M NaF and different molar concentrations of DMA (a) 0.05 M, (b) 0.15 M, and (c) 0.01 M. (III) Potentiodynamic polarization curves of the AM50 specimen immersed in the NaCl background solution (BGS) with and without 0.05 M DMA, 0.05 M NaF, and Mix after 24 h of stabilization. (IV) Schematic illustration of the synergistic corrosion inhibition mechanism of NaF and DMA hybrid inhibitor. Adapted from [45] with permission from Elsevier.

## 5. Combining Inhibitors with Other Corrosion Protection Strategies

The application of corrosion inhibitors onto metallic surfaces can be accomplished in a number of ways. If the metallic part is used in continuous contact with an aqueous electrolyte, the simplest way to deliver the inhibiting substances to the corroding region is to load the corrosive medium with the inhibitor. For example, in an engine cooling system, the coolant contains inhibitors to protect the part from premature failure due to corrosion. However, in most applications, the metallic parts are not fully submerged in a liquid medium and experience only periodic contact with a corrosive electrolyte or thin condensation electrolyte films. In such a case, the corrosion inhibitors can be incorporated into the coatings applied onto the metallic substrate.

The addition of corrosion inhibitors to the coating system can impart active inhibition properties and improve overall protective performance, provided that the coating's barrier properties are not adversely affected by the inhibitors. Furthermore, the interaction between the inhibitors and the coating's components may lead to a (partial) loss of the active capacity of the inhibitor. One of the promising ways to incorporate inhibitors into coatings is to

encapsulate the corrosion inhibitor in a container that is ideally fully compatible with the inhibitor, coating matrix, and substrate. Several types of repository systems for inhibitor substances have been described in the literature over the last decade [188]. Repository systems can be classified by their composition (e.g., nano-containers with polyelectrolyte shells, polymer shells, layered double hydroxides, mesoporous inorganic materials, etc., reviewed in [189]) or by the release mechanism (e.g., mechanical rupture, desorption, ion exchange, pH, or  $\Delta E$ -controlled release, etc., reviewed in [190]). The following section reviews several technologies relevant to magnesium alloys, enabling loading protective coatings with corrosion inhibitors.

**Sol-gel** is an effective and economical coating technique that is environmentally friendly, can be applied onto complex shapes, and has a low process temperature [191]. Additionally, sol-gel-based systems provide good adhesion to metallic surfaces and top coats, which are subsequently applied to the cured sol-gel [192]. Loading sol-gel matrix with corrosion inhibitors has been reported as a highly effective strategy to enhance the corrosion protection properties of the coated magnesium alloys.

Galio et al. [193] added 8HQ inhibitor into a sol-gel coating formulation deposited on an AZ31 magnesium alloy at different stages of sol-gel synthesis: after and before hydrolysis of the sol-gel precursors. Higher corrosion protection was observed when 8HQ was incorporated after the hydrolysis. They postulated that the addition of the inhibitor in the sol-gel formulation before the hydrolysis step can partly deactivate the 8HQ, while the already formed silane-based network after hydrolysis is more inert to 8HQ molecules. The improvement in the corrosion protection properties of the sol-gel coating was attributed to the formation of a complex between the 8HQ and the  $Mg^{2+}$  during the corrosion of the Mg substrate. The insoluble 8HQ(Mg) blocks the micropores and cracks of the sol-gel coating, which results in enhanced barrier properties of the coating.

Toorani et al. [194] incorporated 5 ppm of four different organic inhibitors, namely 8HQ, indole-3-carbaldehyde (I3C), 2-mercaptobenzoxazole (MBO), and sodium diethyldithiocarbamate (DDTC), into a sol-gel with the mixture of  $\gamma$ -amino propyltriethoxysilane (APS) and  $\gamma$ -glycidoxypolytrimethoxysilane ( $\gamma$ -GPS). The modified sol-gel mixture was applied on a PEO-coated AZ31 substrate. All the inhibitors showed adverse or negligible effects on the barrier properties of the sol-gel coating except for 8HQ. The initial corrosion resistance of the system modified by 8HQ (evaluated by low-frequency impedance values) was comparable to the unmodified system. However, a sharp increase in the charge transfer resistance value after 6 h of immersion indicated an active inhibition characteristic. As a result, the incorporation of 8HQ into the sol-gel coating significantly improved the overall corrosion resistance of the system.

The modification of silane-based sol-gel coatings with cerium ions has been extensively studied with the aim of improving the corrosion protection of different metallic substrates. The barrier properties of a silane coating are improved by the addition of cerium in the sol formulation owing to several proposed mechanisms. The incorporation of  $Ce^{4+}$  ions into the silane network as a substitution for Si atoms leads to a more packed and interconnected silane network [195]. Moreover, the higher rate of sol bath acidification due to the presence of Ce accelerates the hydrolysis process [196,197]. Furthermore, cerium ion remnants inside the sol-gel micropores can form insoluble hydroxides and block the pathways for the penetration of the corrosive medium towards the substrate. This improvement in the barrier properties of the sol-gel coating may further intensify during the corrosion of Mg due to the generation of more  $OH^-$  as a result of cathodic reaction on the Mg substrate [195,197]. In one of the early studies on the incorporation of Ce in sol-gel coatings, Montemor and Ferreira [195] observed considerably weaker anodic and cathodic current densities using SVET over an artificial defect made on a silane coating doped with cerium ions. The active corrosion inhibition was claimed to be caused by the release of cerium ions and their precipitations in the form of hydroxides on the bare Mg. It should be noted that the incorporation of  $Ce^{3+}$  ions into the sol-gel coating is often conducted using the nitrate salt

of cerium. However, as previously mentioned, the inhibition effect of nitrate ion itself on the corrosion of the Mg substrate [10] is often ignored.

One drawback of cerium-based corrosion inhibitors is their high solubility in neutral aqueous environments, which may result in their high release rate and early leaching from a coating [198]. The application of organic anions, such as phosphates, to bind to cerium cations can control their solubility in the aqueous solution [199]. Recently, inspired by the same approach, Calado et al. [200,201] synthesized a cerium Tri(bis(2-ethylhexyl)phosphate) ( $\text{Ce}(\text{DEHP})_3$ ) inhibitor. Then, an epoxy-silane coating modified by 325 ppm  $\text{Ce}(\text{DEHP})_3$  was applied on AZ31 and WE43 magnesium alloys. The barrier properties of the coating on AZ31 alloy were significantly improved, resulting in three orders of magnitude higher impedance value (modulus of impedance at 0.01 Hz) after 600 days of immersion in 0.05 M NaCl compared to the non-modified coating after just 70 days of immersion, Figure 17I. The local pH increase due to the cathodic reactions on the magnesium substrate leads to the hydrolysis of  $\text{Ce}(\text{DEHP})_3$ , resulting in the release of  $\text{Ce}^{3+}$  cations and organophosphate anions. The  $\text{Ce}^{3+}$  precipitates on the cathodically active area as cerium hydroxides. On the other hand, the organophosphates can form a hydrophobic layer at the anodic area or make stable complexes with  $\text{Mg}^{2+}$ . The combined effect of released  $\text{Ce}^{3+}$  and organophosphate ions leads to “self-healing” properties, as observed on an artificially defected area on the coated Mg substrate via SVET and SIET measurements (Figure 17II). The schematic mechanism of corrosion inhibition and self-healing is illustrated in Figure 17III.

Incorporated cerium does not always show good compatibility with the sol-gel matrix [197,202,203]. For instance, the incorporation of cerium nitrate into a sol-gel network at a concentration higher than 0.6 wt.% resulted in the formation of network defects in the sol-gel matrix. The formed micro-holes retained water, facilitating the penetration of corrosive substances through the sol-gel coating [204]. The formation of structural defects in the sol-gel matrix by increasing the concentration of doped  $\text{Ce}^{3+}$  has also been observed elsewhere [205].

The inefficacy of the barrier properties of sol-gel coatings due to the incompatibility of the sol-gel matrix with the incorporated inhibitors can be overcome by loading nano/micro containers with good compatibility with the sol-gel coating, and then incorporating them into the coating [206–212]. Thus, the detrimental interaction of the inhibitors with the sol-gel is minimized. For instance, in a recent work, Adsul et al. [206] loaded the  $\text{Ce}^{3+}/\text{Zr}^{4+}$  ions into halloysite nanotubes, which were capped with polymeric microcapsules. Then, the loaded nanotubes were dispersed into a silica sol-gel and deposited on AZ91 magnesium alloy. A significant increase in the sol-gel coating resistance over 24 h of immersion in 3.5 wt.% NaCl was reported.

It is of essential importance that the terms “active protection” and “self-healing” be properly used when the effect of an inhibitor incorporated into a coating system is under investigation. Initial stronger barrier properties of a coating with incorporated inhibitors do not necessarily mean that it is able to be actively involved in the suppression of the corrosion process on the substrate. Attempts to incorporate several amino acid inhibitors into different sol-gel coatings have resulted in significant improvement in the barrier properties of the coating on Mg alloys [202,213–215], yet the active inhibition effect of the incorporated inhibitors is not evidenced. Note that the “intrinsic self-healing” ability of sol-gel coatings, which does not require the addition of corrosion inhibiting agents, is another well-known approach to achieving “self-healing” properties in sol-gel coatings [216]. In this case, the “healing” properties involve reversible chemical reactions in the sol-gel network that lead to the closure or sealing of damage in the coating.

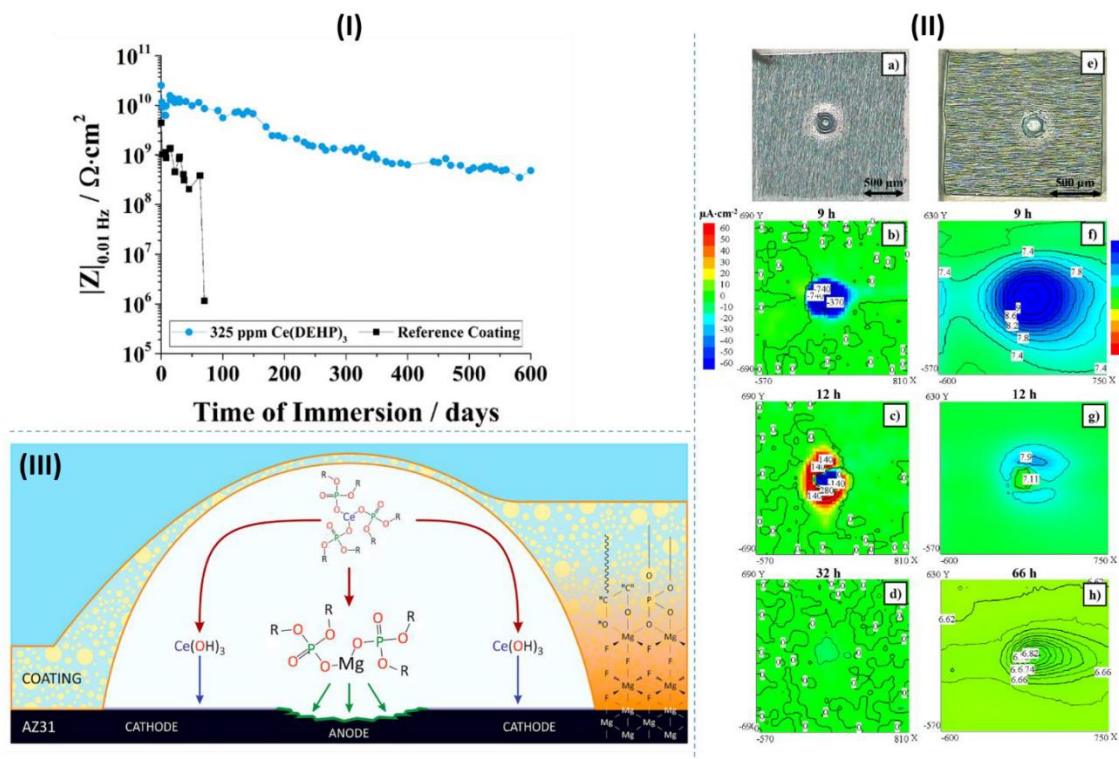


**Figure 17.** (I) Evolution of low-frequency impedance modulus (0.01 Hz, obtained through EIS) for reference and Ce(DEHP)<sub>3</sub>-modified coatings during immersion in 0.05M NaCl. (II) Optical micrographs, and SVET (b–d) and SIET (f–h) maps obtained for different immersion times of the Ce(DEHP)<sub>3</sub>-modified coating in 0.05M NaCl. Optical micrographs correspond to the beginning of immersion for SVET (a) and SIET (e) measurements. (III) Schematic mechanism of action of Ce(DEHP)<sub>3</sub> corrosion inhibitor added to the hybrid epoxy-silane coating for protection of magnesium alloy substrate. R represents the hydrocarbon chain. Adapted from [200] with permission from Elsevier.

### LDH

The application of Layered Double Hydroxides (LDH) in corrosion protection systems has been one of the most active topics under scrutiny due to their unique anion-exchange properties (see PART I of the review [8]). LDHs are generally composed of stacking of positively charged mixed metals M<sup>I</sup>/M<sup>II</sup>-M<sup>III</sup> hydroxide layers, balanced by the presence of anions [217]. Organic and inorganic inhibitors in their anion form can be intercalated within the LDH inter-galleries and can be released into the corrosive medium in exchange for the corrosive Cl<sup>−</sup> ions. Therefore, there is a higher control on the inhibitor release rate, which results in long-term active corrosion protection rather than fast leaching of the inhibitor. Furthermore, the trapping of the corrosive Cl<sup>−</sup> ions mitigates the severity of corrosion at local conditions. It is of importance to identify whether the inhibitors are successfully intercalated into the LDH inter-galleries to benefit from the controlled release functionality or physically trapped within its porous morphology. This can be checked by observing a shift in the diffraction angle of characteristic peaks (003 and 006) [218], as a result of the change in the LDH layer's distance, accommodating anions with different ionic sizes.

LDHs in a powder/slurry form can be incorporated into a coating system to act as nano-containers for desired inhibitors; or they can be grown directly on the metal surface as a conversion coating (see PART I of this review [8]). Inhibitors can be intercalated

into LDH inter-galleries during the formation process or post-treatment via an anion-exchange process.

Different inorganic inhibitors such as molybdate [62,219], vanadate [219–222], phosphate [219], and nitrate [220] have been successfully intercalated into LDH conversion coatings on Mg alloys. The corrosion inhibition of  $\text{CO}_3^{2-}$  on Mg alloys has been reviewed in Section 2.5, can also be intercalated into LDH structure. However, the higher stability of intercalated  $\text{CO}_3^{2-}$  compared to  $\text{Cl}^-$  ions [223,224] leads to an inefficient release of  $\text{CO}_3^{2-}$  during the immersion in  $\text{Cl}^-$ -containing electrolyte.  $\text{Ce}^{3+}$  ion can be inserted into the LDH structure as a trivalent cation, rather than being intercalated. In such a case, self-healing properties have been postulated when the LDH coating is degraded, and Ce ions precipitate as cerium hydroxide [221,225].

Phytic acid, aspartic acid (ASP) [226,227], lauric acid (LA) [226], 8HQ [228,229], sodium dodecyl benzene sulfonate (SDBS) [230], sodium alginate [230], and 2-mercaptobenzothiazole (MBT) [230] are examples of organic inhibitors that are successfully intercalated in LDH conversion coating on Mg alloys. Deprotonation of mentioned organic molecules, which is usually carried out with NaOH solution, is required to obtain their anion form, so that they can be intercalated within the LDH layers [217]. The increased  $d_{(003)}$ -spacing between the LDH layers by hosting large anions of organic inhibitors facilitates the anion exchange process with aggressive  $\text{Cl}^-$  [226].

Numerous remarkable enhancements in the anti-corrosion performance of LDH coatings on Mg alloys by hosting inhibitors have been reported during the recent decades. The enhancement of the corrosion resistance is frequently attributed to the sole active inhibition by the inhibitors. However, it should be taken into account that the intercalation of inhibitors into the LDH structure, either via a post anion exchange method or directly during the LDH formation, can affect the LDH morphology, thickness, and porosity, which in turn influence the corrosion protection properties of the LDH layer. For instance, Figure 18 illustrates how the intercalation of sodium dodecyl sulfate (SDS),  $\text{NO}_3^-$ , and  $\text{MoO}_4^{2-}$  yield different morphologies of MgAl-LDH flakes on Mg alloy.

Moreover, the adsorption of surfactants on LDH flakes during the intercalation step endows the specimen surface with a high hydrophobicity, which in turn, enhances the overall corrosion protection performance [232,233] and does not necessarily yield active corrosion properties. Furthermore, the hosted inhibitors may react or form a complex with the LDH precursors during the intercalation process. For example, Anjum et al. [228] intercalated 8HQ inhibitor molecules into a Mg-Al-LDH during the hydrothermal growth of LDH on a AZ31 alloy. The shift of the diffraction peak of (003) plane at the lower  $2\theta$  angles indicates the intercalation of anions of 8HQ molecules into the LDH structure, Figure 19. However, the relatively strong peak at  $2\theta$  of  $6.8^\circ$  reveals a considerable amount of 8HQ(Mg) complex precipitation [102], which can already fill the pores of LDH and improves its corrosion resistance.

Although the application of LDH in the corrosion field is labeled with “active” and “self-healing”, such functionalities have rarely been evaluated, and presuming an effective inhibition of the intercalated inhibitors is commonly postulated as a necessary “active” corrosion inhibition. Nevertheless, the anion-exchange rate between the intercalated inhibitor and  $\text{Cl}^-$  ion determines the local concentration of anions, and thus the inhibition efficiency of the inhibitor.

## PEO

Plasma electrolytic oxidation (PEO) coatings can be used as containers for inhibitors owing to their porous structure that provides a potentially high-capacity reservoir for corrosion inhibitors. Incorporation of inhibitors into the PEO pores is usually carried out after the coating process. This is due to the fact that process parameters such as high local heat generation and high-energy arc discharge formation are likely to alter the molecular structure or oxidize the inhibitor, especially in the case of organic inhibitors.

In situ addition of organic/inorganic substances into the PEO bath has been carried out in many scientific works, but their impact on corrosion behavior can be primarily due

to their influence on PEO coatings morphology rather than their inhibitive characteristics themselves [234–238]. For instance, the addition of 2 g/L of 8HQ in a PEO bath, containing NaOH and Na<sub>2</sub>SO<sub>4</sub>, results in better uniformity of pores, with a lower number of pores per area in the PEO coating on AZ91 (Figure 20a,b). Some leaf-like particles also appears (indicated with arrows in Figure 20b) with the addition of 8HQ. However, a further increase in 8HQ concentration results in more heterogeneous morphology, with some regions porous and others compact (Figure 20c,d) [234]. A comprehensive review of the effects of organic/inorganic additives to the PEO electrolytes for Mg alloys has been provided in **PART II** of this review [9]. One of the very first attempts to incorporate inhibitors into a PEO layer during the coating formation on a magnesium alloy in a PEO bath was carried out by Blawert et al. [239]. They reported that the addition of chromate to the PEO bath, apart from its undesirable environmental issues, does not exhibit any improvement in the corrosion resistance of the substrate.

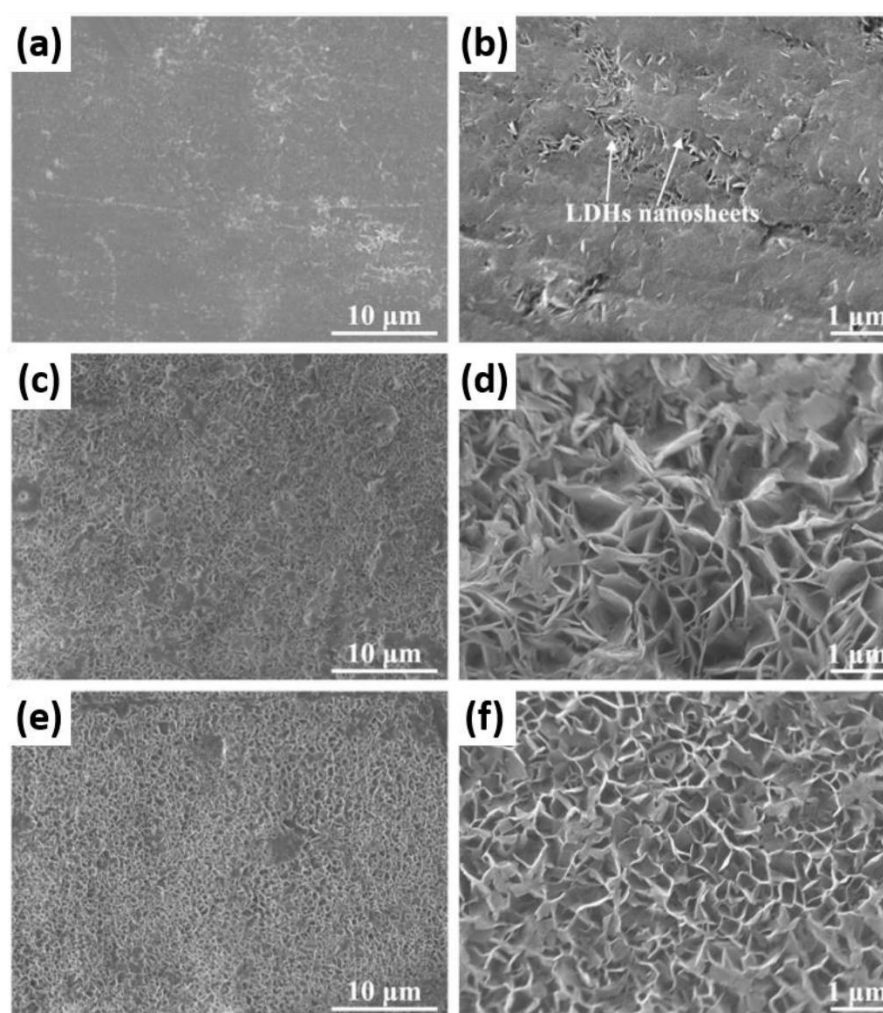


**Figure 18.** SEM surface micrographs of (a,b) MgAl-NO<sub>3</sub><sup>−</sup>-LDHs, (c,d) MgAl-MoO<sub>4</sub><sup>2−</sup>-LDHs, and (e,f) MgAl-SDS-LDHs. Adapted from [231] with permission from Elsevier.

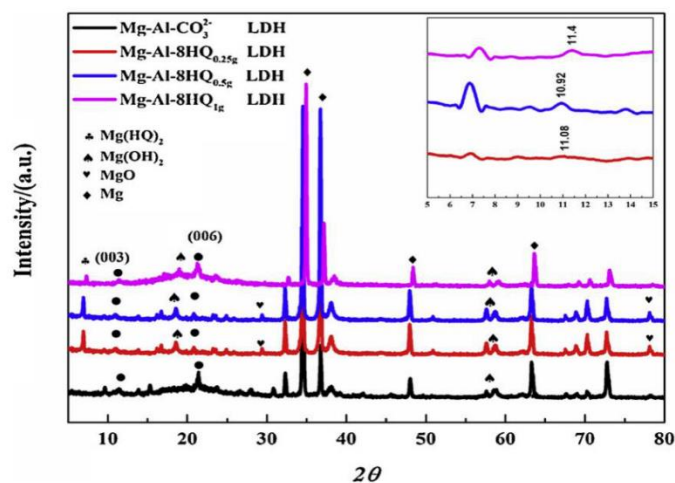


**Figure 19.** XRD patterns of AZ31 with  $\text{Mg-Al-CO}_3^{2-}$  and  $\text{Mg-Al-8HQ}_x\text{g}$  ( $x = 0.25, 0.5$  and  $1$ ) LDH coatings. Adapted from [228] with permission from Elsevier.

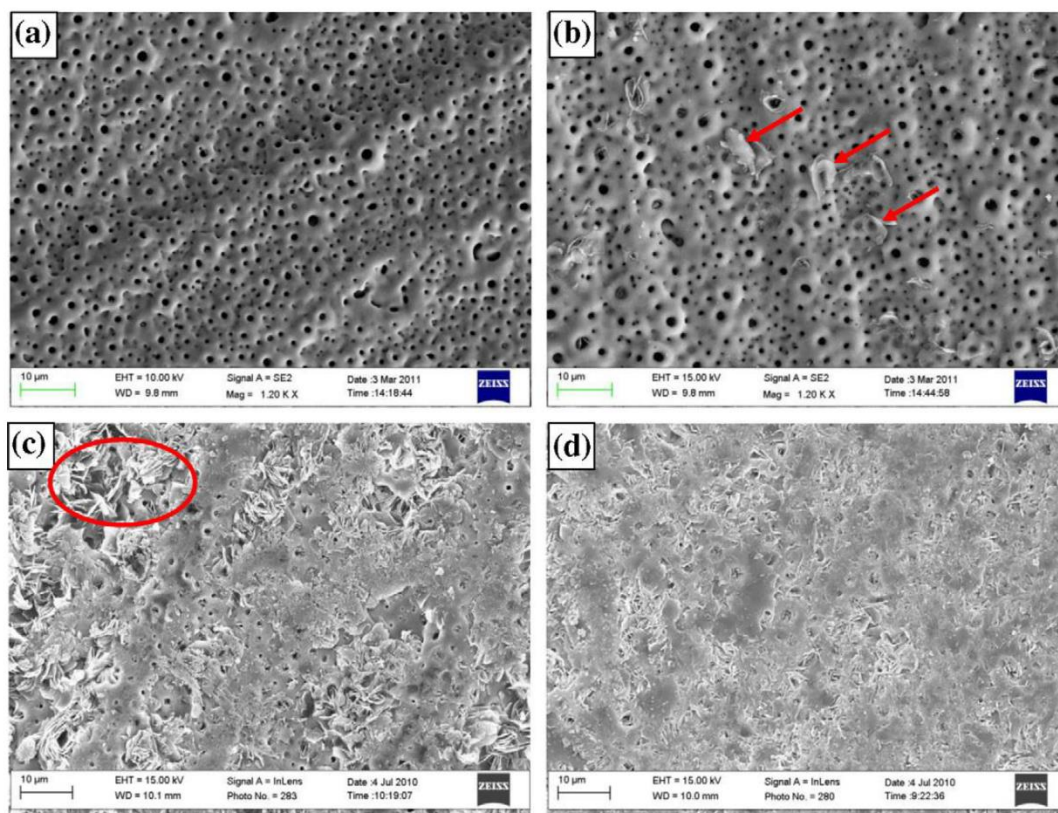


**Figure 20.** Surface morphologies of anodic films formed in the solutions of 10 g/L NaOH and 18 g/L  $\text{Na}_2\text{SiO}_3$  (a) without 8-HQ, with addition of (b) 2 g/L 8-HQ, (c) 5 g/L 8-HQ and (d) 8 g/L 8-HQ under current density 40 mA/cm<sup>2</sup>, frequency 2000 Hz, duty cycle 20% and anodizing time 3 min. Adapted from [234] with permission from Elsevier.

Incorporation of the inhibitors into the formed PEO layer has two main positive contributions to the corrosion protection properties of the coated substrate: 1—corrosion inhibition functionality on the Mg substrate when the PEO coating is damaged or corroded. 2—Blocking the pores of the PEO coating triggered by the substrate corrosion to provide a more compact barrier between Mg substrate and corrosive medium via either adsorption of the organic molecules themselves or via the formation of secondary compounds such as insoluble hydroxides or metal complexes. A schematic illustration of the corrosion protection mechanisms provided by PEO coating with incorporated inhibitors is shown in Figure 21.

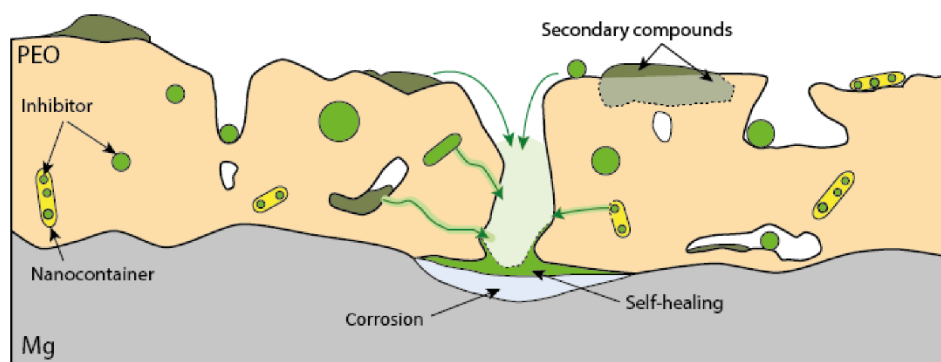


**Figure 21.** Schematic illustration of the corrosion protection mechanisms provided by PEO coating with inhibitors.

Sealing of the PEO pores after the inhibitor loading is essential to prevent the wasteful release of the inhibitors into the corrosive medium. Sealing of the pores can be achieved via different surface post-treatments that are described in detail in **PART II** of this review [9]. Some chemicals known for their inhibition effect on Mg alloys, such as rare earth element salts [240–249], phosphates [242,250], stannate [240], and surfactants [240], can be used primarily for the sealing post-treatment. In such a case, their inhibition effect on the Mg substrate also contributes to a reduction in the corrosion rate and provides active inhibition.

One of the very first attempts to incorporate inhibitors in PEO coating on Mg alloy, followed by sealing of the PEO pores with an organic top layer, was made by Lamaka et al. in 2009 [100]. Cerium nitrate and 8HQ were incorporated in the porous PEO layer by simple post-immersion in inhibitor-containing solutions, then dried and sealed with a thin sol–gel coating (3–4  $\mu\text{m}$ ) synthesized from (3glycidoxypropyl)-trimethoxysilane and titanium(IV) iso-propoxide. Figure 22 illustrates the composite corrosion protection coating based on a PEO coating, loaded with corrosion inhibitors, and sealed with a thin sol–gel layer. Results showed that the incorporated cerium nitrate has good compatibility with the silane-based sol–gel coating that improves its barrier effect, which was reflected in the resistance of the sol–gel layer measured via EIS. Stable and insoluble cerium hydroxides are formed due to the consumption of  $\text{OH}^-$  produced by the cathodic reactions on magnesium. These cerium hydroxides can further improve the barrier properties of the coating complex by sealing the pores of the PEO layer. Moreover, an active corrosion inhibition was observed via SVET on an artificial defect on the coating loaded with cerium. On the other hand, incompatibility of 8HQ with a silane-based sol–gel as the sealing topcoat caused its impairment. Since this pioneering study, the incorporation of 8HQ and Ce-based chemicals into the PEO coating on magnesium alloys with different approaches has been frequently investigated [251–254].

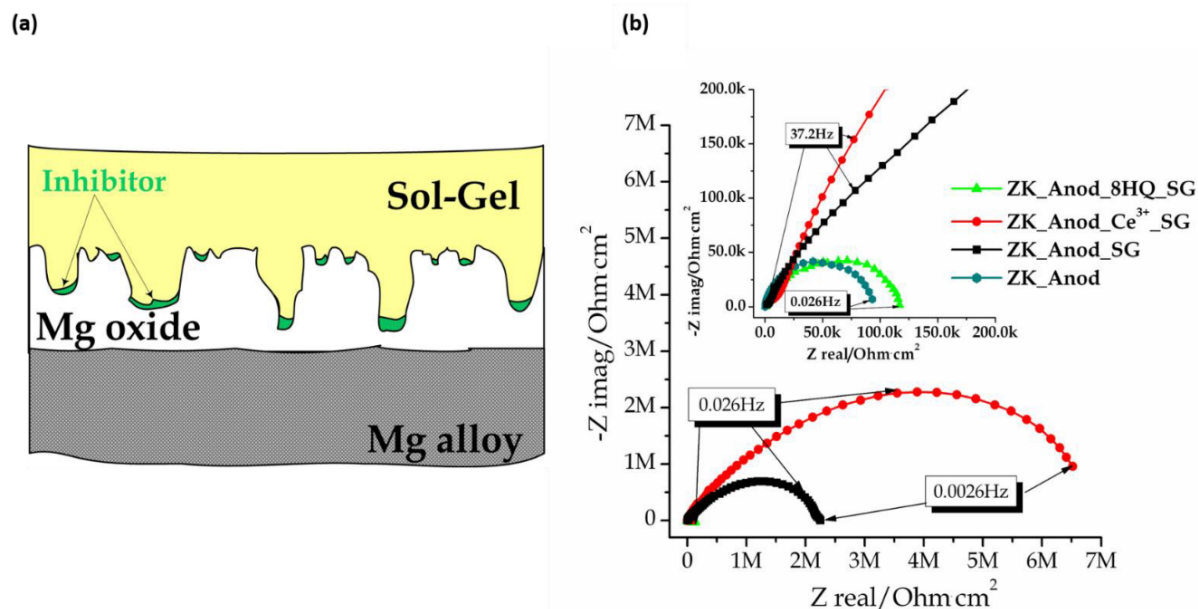


**Figure 22.** (a) Schematic representation of the composite protective coating comprising the highly porous anodized or PEO layer enriched with corrosion inhibitors and sealed with the organic coating; (b) Nyquist plots of corresponding ZK30 Mg alloy samples enriched with  $\text{Ce}^{3+}$  or 8HQ after 2 weeks in 0.05 M NaCl solution. Adapted from [100] with permission from Elsevier.

For instance, Gnedenkov et al. [252] loaded 8HQ into a PEO coating on MA8 alloy via simple immersion in a saturated 8HQ bath. Local current density was measured via SVET over an artificial defect in the PEO coating immersed in 0.05 M NaCl. Loaded 8HQ can be activated by pH increase on cathodic sites due to its higher solubility at elevated pH, and then precipitated again in the form of 8HQ(Mg) complex on anodic sites. As a result, the measured anodic local current density on the defected zone was considerably reduced. The increase in the concentration of the 8HQ solution and the duration of the incorporation period enhances the overall corrosion resistance of the system [255]. However, 8HQ is known to form insoluble complexes with  $\text{Mg}^{2+}$ , which can be supplied not only from the Mg substrate, but also from the dissolution of the Mg-containing phases in a PEO coating [102]. As a result, the incorporation step can lead to the sealing of the PEO pores, which improves the barrier properties of the PEO even before 8HQ comes to play as an inhibitor.

A similar concept of multilayer coating was applied on ZE41 magnesium alloy, loaded with 1,2,4-triazole inhibitor and covered by a sol-gel layer [76]. The self-healing properties of this multilayer coating were evaluated using SVET, measuring the local current density over two artificial defects on the coating (with diameter of 200  $\mu\text{m}$  each), Figure 23. An intensive corrosion attack was observed at the beginning of immersion in 0.05 M NaCl solution for the sample loaded with the inhibitor. However, after 30 min, the measured current density reduced to a negligible value, showing active corrosion protection of the coating. No corrosion activity was observed for the next 10 h of immersion. However, after 16 h of immersion, filiform corrosion was observed next to the artificial defects, which was gradually suppressed within the next 6 h [76], indicating active corrosion inhibition. On the other hand, when the coating was not loaded by the inhibitor, considerable ionic currents were firstly detected after 3 h of immersion in the NaCl solution. Then, the detected currents were gradually intensified during the immersion measured.

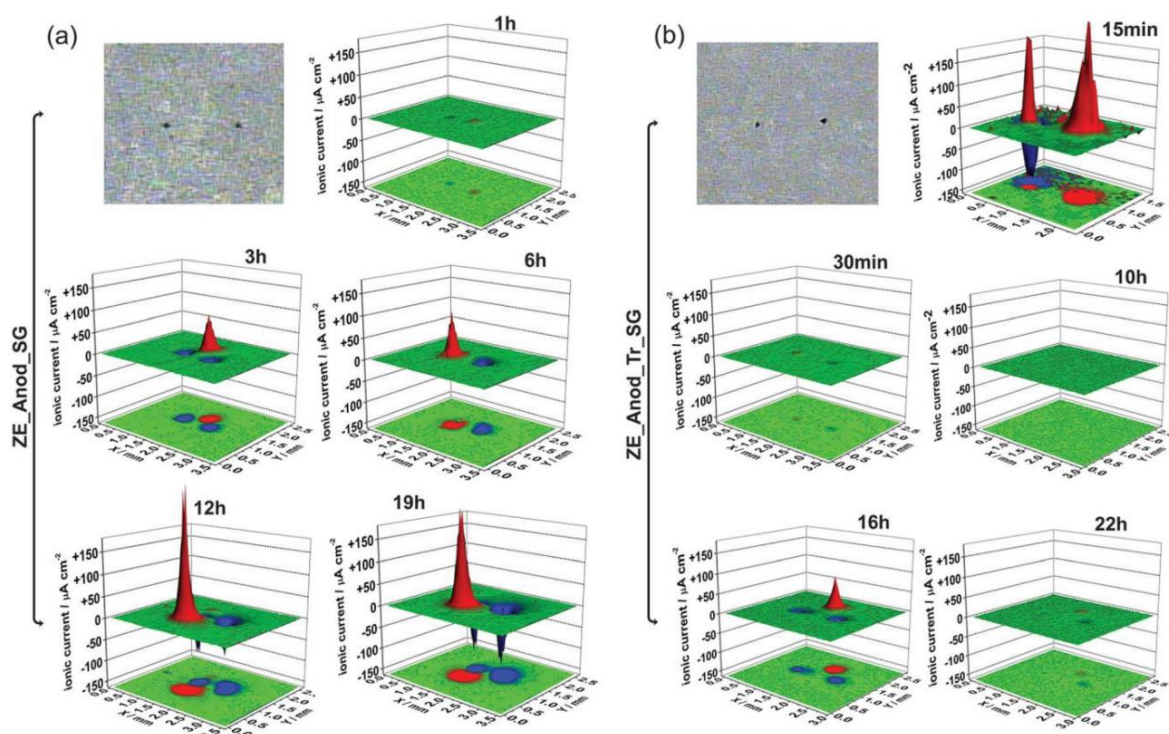


**Figure 23.** Microphotograph of scanned area and distribution of ionic currents (measured by SVET) for the ZE41 magnesium alloy coated with composite film after different immersion time in 0.05 M NaCl solution (a) without loaded 1,2,4 triazole and (b) with loaded 1,2,4 triazole. Adapted and reprinted from [76].

Liu et al. [256] compared the self-healing properties of a PEO coating on AM60 alloy loaded with  $\text{Ce}(\text{NO}_3)_3$ ,  $\text{Na}_3\text{PO}_4$ , and  $\text{NaVO}_3$  by observing the surface of an artificial scratch made on the coating during the immersion in 3.5 wt.% NaCl solution, Figure 24. The scratched area of the specimen without any loaded inhibitor was severely corroded after 24 h immersion. The release of  $\text{Ce}(\text{NO}_3)_3$  was able to mitigate the corrosion on the scratched area, resulting in a reduced amount of observed corrosion products. Both specimens with loaded  $\text{NaVO}_3$  and  $\text{Na}_3\text{PO}_4$  could significantly suppress the corrosion, although localized corrosion sites could be observed at high magnification for the  $\text{NaVO}_3$ -loaded specimen, as shown in Figure 24d–g. The considerably higher impedance of the scratched specimen loaded with  $\text{Na}_3\text{PO}_4$  also confirm its superior self-healing properties (Figure 24h).

The capillary effect can help the inhibitor solution to enter the micro/nano-size pores in PEO coatings. However, since the pores are semi-closed, the air trapped inside them often hinders the solution uptake [257,258]. Therefore, the effective way to load the pores with more inhibitor solution is to force out the air from the pores by applying low pressure during the loading [256]. Prolonging immersion time and increasing the number of successive immersions can increase the amount of inhibitor loaded inside the pores. However, excessive exposure of PEO film to the aqueous solution has been reported to have an adverse effect on the corrosion protection of the PEO coating [159,256,259,260]. The quantification of incorporated inhibitors in the PEO pores and their release rate in a corrosive medium is a determining factor for evaluating the ability and time of self-healing functionality. As an example, Liu et al. [256] incorporated  $\text{Na}_3\text{PO}_4$  in a PEO coating through immersion in 0.5 M  $\text{Na}_3\text{PO}_4$  for 10 min in a low-pressure vacuum condition. The PEO pores were then sealed with top paint. The concentration of the released phosphate from a scratched specimen exposed to 3.5 wt.% NaCl solution was quantified according to national

standard of GB/T 9727-2007 (for details, see [256]). They reported that the concentration of released phosphate reaches a stable value after 7 days, meaning the phosphate is almost fully released within 7 days. Similar investigations on the release rate of the inhibitors from any type of coatings, which is a piece of valuable information to evaluate the self-healing ability of the coating, are unfortunately scanty in the literature [208,261,262].

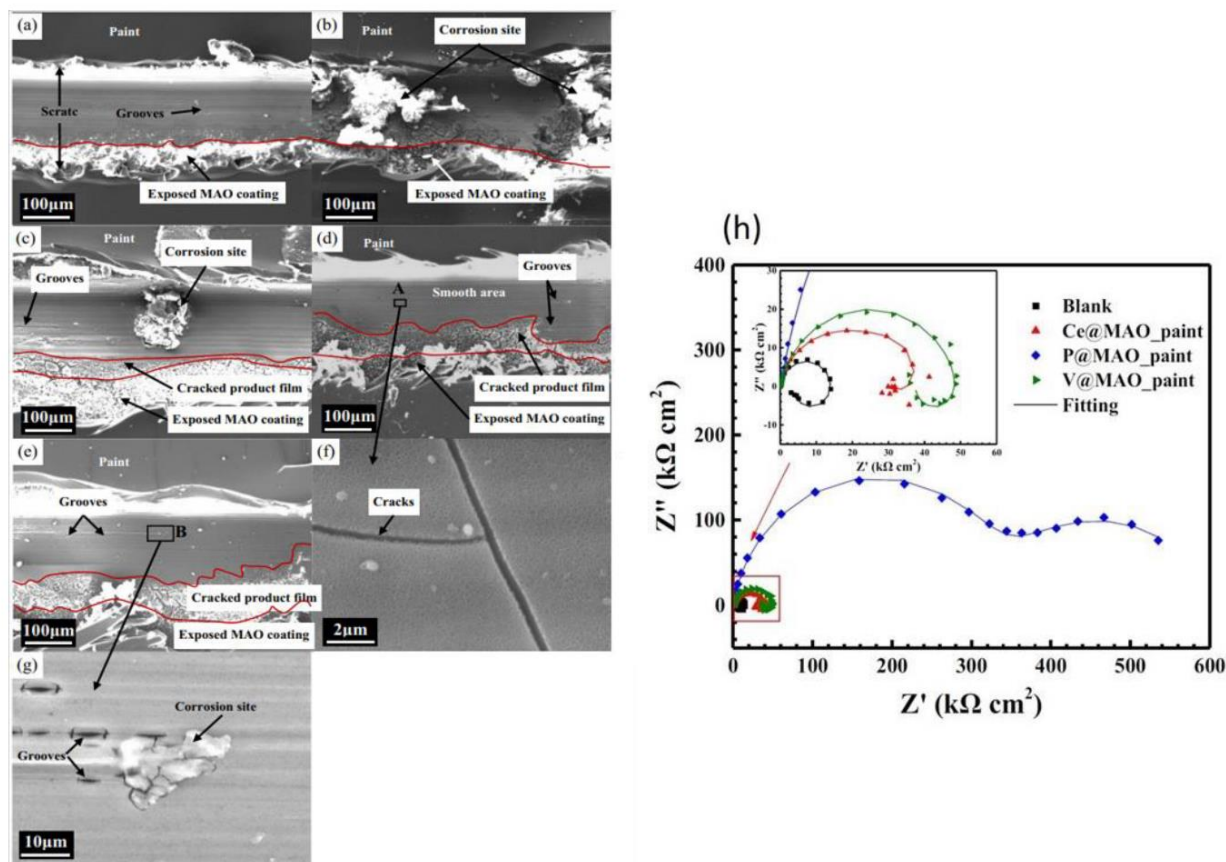


**Figure 24.** (a) SEM micrographs of the scratched areas of a PEO coating on AM60 alloy sealed with a water-based paint; (b) after immersion in 3.5 wt.% NaCl for 24 h (c) with  $\text{Ce}(\text{NO}_3)_3$ , (d,f) with  $\text{Na}_3\text{PO}_4$ , (e,g) with  $\text{NaVO}_3$ . (h) EIS spectra of the scratched composite coatings after immersion in 3.5 wt.% NaCl for 24 h. Adapted from [256] with permission from ECS.

The concentration of incorporated organic inhibitors on the PEO layer can be enhanced using a secondary substance loaded into the PEO and facilitate the adsorption of the organic substances. In a recent work by Al Zoubi et al. [263],  $\text{TiO}_2$  nano particles were incorporated into a PEO layer on a Mg alloy during the PEO formation process. Diethyl-5-hydroxyisophthalate (DEIP) was loaded into a PEO inorganic coating by immersion in 1 M ethanolic solution of DEIP. The presence of  $\text{TiO}_2$  particles resulted in a significantly higher amount of DEIP-contained layer on the PEO layer. As a result, the corrosion rate of the coated Mg was considerably improved, although the active corrosion inhibition was not discussed.

In a recent work by Wierzbicka et al. [264], a PEO coating was formed on an AZ31 alloy in a solution containing silicate  $\text{Na}_2\text{SiO}_3$ ,  $\text{Na}_3\text{PO}_4$ , and KF. Sodium salt of 4-Methylsalicylate (4MSA) was incorporated into the PEO pores via immersion in low-pressure condition. SVET maps over the sample surface (shown in Figure 25) revealed a rather unique corrosion suppression behavior. Filiform corrosion appeared on the samples with and without the

inhibitor after approximately 60 h of immersion in 0.05 M NaCl solution, which was also reflected in the local cathodic and anodic activity in their SVET maps. The filiform corrosion on the sample with inhibitor was temporary and largely suppressed over time. Further immersion time revealed similar activation/suppression behavior at another location, demonstrating the endowed active corrosion protection with the incorporated 4MSA inhibitor. In contrast, the inhibitor-free sample exhibited a much higher local anodic current. Interestingly, in comparison to a commercial chromate conversion coating (CCC), the 4MSA-loaded PEO exhibited a lower corrosion activity within 96 h of immersion. Another isomer of the same inhibitor (3-Methylsalicylate) has also shown a strong active inhibition characteristic when it is loaded into a PEO coating on CP-Mg [262]. Some other recently discovered organic corrosion inhibitors, including sodium salts of glycolic, 4-aminosalicylic, and 2,6-pyridinedicarboxylic acids have been loaded into a PEO coating on AZ91 alloy and sealed with a thin sol-gel to prevent uncontrolled leaching [265]. The active corrosion protection of such composite coating was proven by continuous SVET measurements for 48 h.

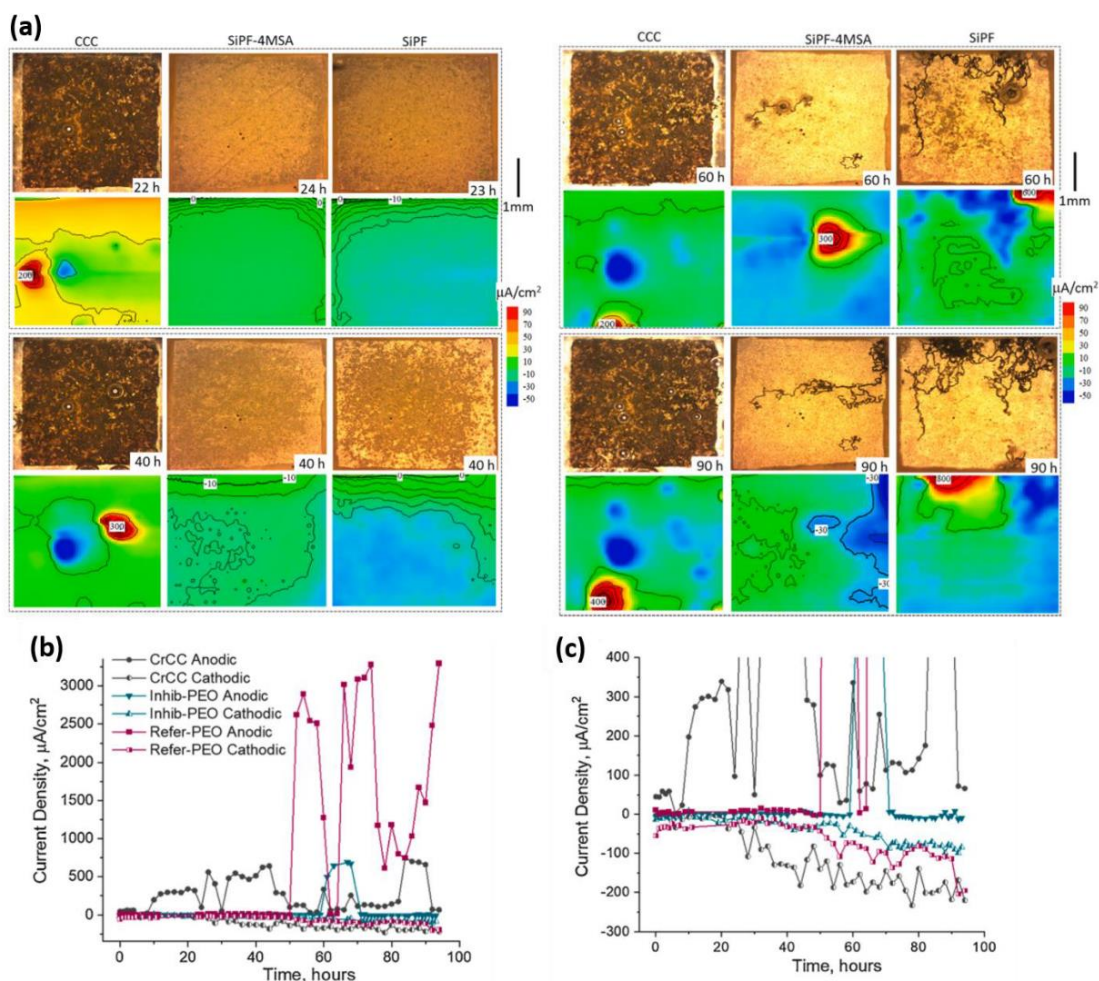


**Figure 25.** (a) Optical micrographs and SVET current density maps of reference CCC and PEO coatings with and without 4MSA inhibitor, acquired during immersion in 0.05 M NaCl. The immersion time is specified in each section of this Figure. (b,c) Evolution of the peak current density, anodic and cathodic, for three types of tested samples during 96 h of immersion in 0.05 M NaCl. “SiPF” refers to the reference PEO sample. Adapted [264] with permission from Elsevier.

Inhibitors can also be loaded into nanocontainers, such as halloysite nanotubes [60,266–268] and LDH, and subsequently applied onto PEO coating via immersion post-treatment. Such an approach yields more control on the release of inhibitors, which is triggered by the effect of corrosion reaction byproducts (e.g., increase in  $\text{OH}^-$  or  $\text{Mg}^{2+}$ ) or corrosive ions (e.g.,  $\text{Cl}^-$  or  $\text{SO}_4^{2-}$ ). Thus, active and long-term corrosion protection can be achieved [60]. Recent research has highlighted LDH's potential to serve as nanocontainers in the PEO layer [30,254,260,261,269–272]. A LDH layer can be directly grown on the PEO layer, which also blocks the PEO pores and improves its barrier properties.

Recently, Zhang et al. [273] showed that the application of a thin  $\text{MnOOH}$  layer on a PEO coating via a simple immersion in  $\text{MnCl}_2$  solution can promote the formation of LDH flakes, which are supplied by the corrosion products of Mg dissolution ( $\text{Mg}^{2+}$  and  $\text{OH}^-$  ions). Active corrosion protection was confirmed in different ways, including the increase in the impedance value of the specimen during the immersion in a NaCl solution (Figure 26a,b), observing the LDH growth on an artificially defected zone (Figure 26c), and detecting the  $\text{Cl}^-$  on the defected zone (Figure 26c). A similar concept of promoting the formation of LDH film by inhibitors (in this case, Li) and as the response to corrosion of aluminum alloy was firstly proposed by Visser et al. [274–279].

PEO coating is a ceramic film that usually features inertness toward many chemicals, including neutral inhibitor-containing aqueous solution. However, in a recent study, Vaghefinazari et al. [159] demonstrated that although the significant corrosion inhibition effect of 2,5PDC has been reported for several Mg alloys [10], it can deteriorate the protective properties of a PEO coating on Mg, which in turn, leads to overall faster degradation of PEO-coated Mg substrate. Figure 27a illustrates the reduction in the  $\text{H}_2$  evolution rate of bare AZ21 Mg with the increase in the concentration of 2,5PDCA in corrosive 3.5 wt.% NaCl solution. Meanwhile, in Figure 27b, the severe degradation of the same Mg substrate coated with PEO immersed in solutions with an increasing concentration of 2,5PDCA is shown. The adverse effect of 2,5PDC on the PEO coating is attributed to the formation of soluble complexes between 2,5PDC and Mg, which destabilize the PEO components. Moreover, the inhibition mechanism of 2,5PDC on bare Mg alloys has been shown to be tied to the formation of a relatively thick  $\text{Mg}(\text{OH})_2$  film on the substrate [159]. The formation of such  $\text{Mg}(\text{OH})_2$  layer in the PEO/Mg interface exerts mechanical force on the PEO layer atop, which in turn facilitates its detachment. Therefore, it is crucial to preliminarily investigate the interaction of an effective corrosion inhibitor with both a bare and PEO layer to foresee its potential adverse effects on the overall corrosion protection performance of the system. Such adverse effects of 2,5PDC have also been reflected in another recent report [260].

Zhang et al. [260] loaded a PEO layer on AZ31 with 0.1 M concentration of 2,5PDC and two other inhibitors, namely metavanadate and 5-aminosalicylate. The adverse effect of inhibitor impregnation on the initial (within 20 min) impedance of the samples immersed in 3.5 wt.% was observed. However, further immersion led to a slightly higher impedance value for the corresponding samples with metavanadate and 5-aminosalicylate inhibitors. To prevent the wasteful release of inhibitors into the electrolyte during immersion, the PEO pores were sealed via immersion in  $\text{Ce}(\text{NO}_3)_3$  and oxidative  $\text{H}_2\text{O}_2$  solution, which resulted in a  $\text{CeO}_2$  sealing layer. Eventually,  $\text{MgAl-LDH}$  was grown on PEO in an autoclave at  $398^\circ\text{K}$ . The composite coatings loaded with 5-aminosalicylate and sealed with  $\text{CeO}_2$  and LDH layers excelled in high protective properties, demonstrating  $0.1\text{--}0.5\text{ Gohm.cm}^2$  low-frequency impedance during the first day of immersion in 3.5% NaCl. The results showed that the incorporated inhibitors can promote the formation of the LDH layer via modification of the Mg ion supply through complexation with Mg ions, possibly from both the PEO layer and Mg substrate. Nevertheless, a very complex active corrosion mechanism could be hypothesized from the loaded inhibitors, the cerium-containing layer, and the LDH layer.

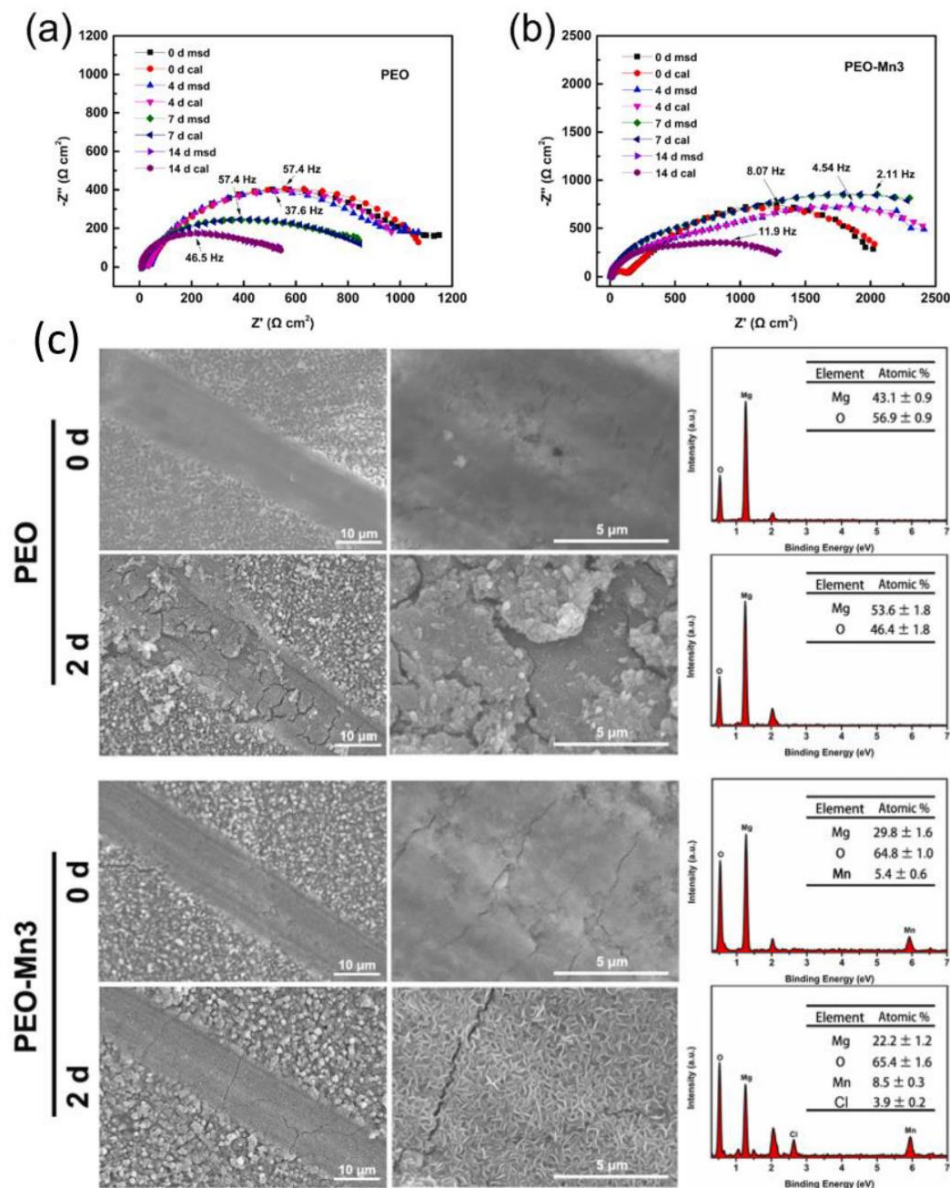


**Figure 26.** (a) Nyquist plots of the PEO sample without (a) and with (b) deposited MnOOH layer immersed in 0.9 wt.% NaCl solution for various times. (c) SEM surface views and EDS spectra of scratches area on the PEO sample without and with deposited MnOOH layer immersed in 0.9 wt.% NaCl solution for various times. PEO-Mn3 denotes the PEO-coated sample immersed in 12 g/L  $\text{MnCl}_2$  for 9 h. Adapted [273] with permission from Elsevier.

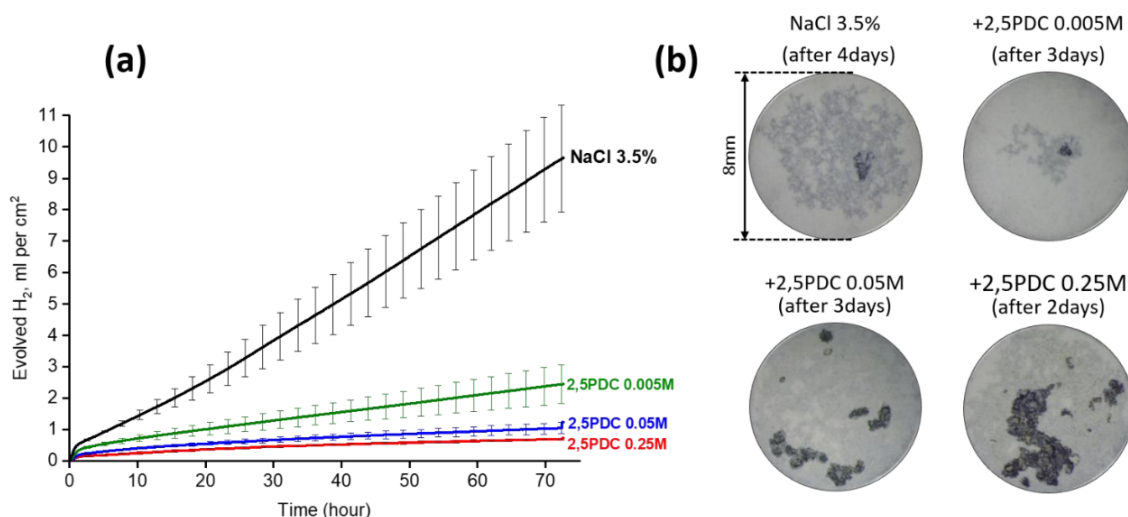


**Figure 27.** (a)  $H_2$  evolved during immersion of the AZ21 sample in 3.5 wt.% NaCl solution containing different concentrations of 2,5PDC. (b) The surface appearance of PEO-coated AZ21 after the failure (duration is specified in each case) in 3.5 wt.% NaCl solution containing different concentration of 2,5PDC. Adapted [159] with permission from Elsevier.

The growing number of studies on PEO coating with incorporated corrosion inhibitors indicates the highly promising properties of PEO layer in storing the inhibitors. Combined use of protective strategies, i.e., loading of porous PEO layers with corrosion inhibitors alone or in nanocontainers, followed by sealing with hybrid or organic coatings loaded with inhibitor, provides enhanced long-term corrosion protection for magnesium alloys possessing strong barrier and active corrosion protection in case the coating is damaged.

## 6. Summary and Perspectives

The acute needs of Mg corrosion protection research have been discussed, emphasizing the development of durable barrier corrosion protection, the continuing quest for replacement of carcinogenic chromates, and especially the ways of merging barrier and active protection by developing new corrosion-inhibiting coating technologies. Despite recent achievements uncovering new effective corrosion protection systems on Mg alloy, the quest continues to replace carcinogenic Cr(VI) from everyday corrosion protection practice. Durable barrier corrosion protection can be endowed with active corrosion inhibition by accommodating corrosion inhibitors, achieving the benchmark “self-healing” properties of Cr(VI)-based protection technologies.

Despite the remarkable corrosion inhibition of several inorganic inhibitors, including vanadate, arsenate, and selenite, they are not likely to become industrially acceptable candidates for the replacement of Cr(VI) due to their environmental and toxicity issues. Nitrates and molybdates, given their seemingly universal and significant inhibition effects, have not received the dedicated attention they deserve.

Given the vast number of organic molecules with potentially corrosion-inhibiting properties, computational (*in silico*) screening of the most effective corrosion inhibitors is the only way to find optimized solutions within a relatively short time. Machine learning, successfully applied to solve other chemical problems, allows rational design of bespoke inhibitors for each specific magnesium alloy. This will be much more time and cost efficient compared to a purely experimental approach. Representative and reliable experimental databases are needed for setting up the initial training space. A systematic approach to comparing the inhibiting efficiency of multiple corrosion inhibitors to specific alloys is needed, given the significant influence of individual alloy impurities and surface treatment.

This calls for application of existing and development of new, reliable high-throughput testing techniques, potentially involving robotic testing. Collection of big datasets, however, does not substitute the in-depth study of inhibiting mechanisms of selected most effective or representative inhibitors.

Development of new experimental techniques and data processing methods is needed to alleviate the influence or benefit from critical factors related to testing conditions (elemental composition and microstructure of alloy, the composition and concentration of testing electrolyte, inhibitor concentration, initial pH, the ratio of exposed surface area to electrolyte volume, and eventually the testing time).

Loading coating systems with inhibitors is an effective approach to improve the overall corrosion protection performance and achieve active corrosion inhibition. PEO coatings feature porous microstructure to accommodate a high concentration of inhibitors, LDH coatings possess a more controlled release of the inhibitor and trap the aggressive chloride in exchange, and sol-gel coatings with potentially highly achievable barrier properties also can benefit from the loaded inhibitors, as long as their barrier properties are not impaired by the inhibitors. Unfortunately, despite the numerous combinations of coatings and inhibitor with remarkable corrosion protection performance, the “active” inhibition properties are commonly taken for granted and left without putting into examination, presuming a successful corrosion inhibition of bare Mg by the inhibitor. Thorough experimental validation of self-healing or active protection effect needs to be acquired, including that by (local) electrochemical methods and industrially relevant salt-spray tests or long atmospheric exposure.

In addition to the high corrosion protective performance of the reviewed inhibitor-loaded systems, their environmentally friendliness renders them as a suitable replacement technology to Cr(VI)-based coatings. Indeed, cost effectiveness and feasibility of developed inhibitor-loaded systems for engineering parts in industrial scale must be justified by the industry.

**Funding:** This research was funded by H2020 Clean Sky 2 project AIMAGIC (Grant Agreement Number 755515) and the support of the ADITIMAT-CM (S2018/NMT-4411, Regional Government of Madrid and EU Structural and Social Funds), PID2021-124341OB-C22 and RYC-2017-21843 (MICINN/AEI/FEDER, UE) projects.

**Data Availability Statement:** Not applicable.

**Acknowledgments:** The authors acknowledge the financial support of H2020 Clean Sky 2 project AIMAGIC (Grant Agreement Number 755515) and the support of the ADITIMAT-CM (S2018/NMT-4411, Regional Government of Madrid and EU Structural and Social Funds), PID2021-124341OB-C22 and RYC-2017-21843 (MICINN/AEI/FEDER, UE) projects. Authors would like to sincerely acknowledge Gerald Jordens for his contribution to the preparation of this manuscript. Sadly, he passed away before the final version of this review was completed.

**Conflicts of Interest:** The authors declare no conflict of interest.

## References

1. Handbook, A. *Corrosion—Fundamentals, Testing and Protection*; ASM International, The Materials Information Society: Materials Park, OH, USA, 2003; Volume 13A.
2. Flick, E.W. *Corrosion Inhibitors: An Industrial Guide*; Noyes Publications: Park Ridge, NJ, USA, 1987.
3. Sastri, V.S. *Green Corrosion Inhibitors: Theory and Practice*; Wiley: Hoboken, NJ, USA, 2012.
4. ECHA. Authorisation List. 2017. Available online: <https://echa.europa.eu/authorisation-list> (accessed on 1 September 2017).
5. ECHA. Authorisation List with Sunset Dates. 2017. Available online: [https://echa.europa.eu/authorisation-list?p\\_p\\_id=disslists\\_WAR\\_disslistsportlet&p\\_p\\_lifecycle=1&p\\_p\\_state=normal&p\\_p\\_mode=view&p\\_p\\_col\\_id=column-1&p\\_p\\_col\\_pos=1&p\\_p\\_col\\_count=2&disslists\\_WAR\\_disslistsportlet.javax.portlet.action=searchDissLists](https://echa.europa.eu/authorisation-list?p_p_id=disslists_WAR_disslistsportlet&p_p_lifecycle=1&p_p_state=normal&p_p_mode=view&p_p_col_id=column-1&p_p_col_pos=1&p_p_col_count=2&disslists_WAR_disslistsportlet.javax.portlet.action=searchDissLists) (accessed on 1 September 2017).
6. ASD-Eurospace. Space Chromate Task Force Concludes REACH Authorisation Dossier Development for Chromium Trioxide. 2016. Available online: [https://chemycal.com/news/7049d07a-149c-4759-a159-685a5aee3224/Space\\_Chromate\\_Task\\_Force\\_concludes\\_REACH\\_authorisation\\_dossier\\_development\\_for\\_chromium\\_trioxide](https://chemycal.com/news/7049d07a-149c-4759-a159-685a5aee3224/Space_Chromate_Task_Force_concludes_REACH_authorisation_dossier_development_for_chromium_trioxide) (accessed on 1 May 2016).

7. ECHA Recommends Authorising Critical Continued Uses of Chromium Trioxide under Strict Conditions. 2016. Available online: [https://echa.europa.eu/view-article/-/journal\\_content/title/echa-recommends-authorising-critical-continued-uses-of-chromium-trioxide-under-strict-conditions](https://echa.europa.eu/view-article/-/journal_content/title/echa-recommends-authorising-critical-continued-uses-of-chromium-trioxide-under-strict-conditions) (accessed on 1 May 2016).
8. Vaghefinazari, B.; Wierzbicka, E.; Visser, P.; Posner, R.; Jordens, G.; Arrabal, R.; Matykina, E.; Mohedano, M.; Blawert, C.; Zheludkevich, M.L.; et al. Chromate-Free Corrosion Protection Strategies for Magnesium Alloys—A Review: PART I. Pre-treatment and Conversion Coatings. *Materials*, 2022; *accepted*.
9. Wierzbicka, E.; Vaghefinazari, B.; Mohedano, M.; Visser, P.; Posner, R.; Jordens, G.; Blawert, C.; Zheludkevich, M.L.; Lamaka, S.V.; Matykina, E.; et al. Chromate-Free Corrosion Protection Strategies for Magnesium Alloys—A Review: Part II. PEO and anodizing. *Materials*, 2022; *accepted*.
10. Lamaka, S.V.; Vaghefinazari, B.; Mei, D.; Petrauskas, R.P.; Hoche, D.; Zheludkevich, M.L. Comprehensive screening of Mg corrosion inhibitors. *Corros. Sci.* **2017**, *128*, 224–240. [CrossRef]
11. Esmaily, M.; Svensson, J.E.; Fajardo, S.; Biribilis, N.; Frankel, G.S.; Virtanen, S.; Arrabal, R.; Thomas, S.; Johansson, L.G. Fundamentals and advances in magnesium alloy corrosion. *Prog. Mater. Sci.* **2017**, *89*, 92–193. [CrossRef]
12. Twite, R.L.; Bierwagen, G.P. Review of alternatives to chromate for corrosion protection of aluminum aerospace alloys. *Prog. Org. Coat.* **1998**, *33*, 91–100. [CrossRef]
13. Kendig, M.; Davenport, A.J.; Isaacs, H. The mechanism of corrosion inhibition by chromate conversion coatings from X-ray absorption near edge spectroscopy (XANES). *Corros. Sci.* **1993**, *34*, 41–49. [CrossRef]
14. Schmutz, P.; Guillaumin, V.; Lillard, R.; Lillard, J.; Frankel, G. Influence of dichromate ions on corrosion processes on pure magnesium. *J. Electrochem. Soc.* **2003**, *150*, B99. [CrossRef]
15. Kendig, M.; Jeanjaquet, S.; Addison, R.; Waldrop, J. Role of hexavalent chromium in the inhibition of corrosion of aluminum alloys. *Surf. Coat. Technol.* **2001**, *140*, 58–66. [CrossRef]
16. Pommiers, S.; Frayret, J.; Castetbon, A.; Potin-Gautier, M. Alternative conversion coatings to chromate for the protection of magnesium alloys. *Corros. Sci.* **2014**, *84*, 135–146. [CrossRef]
17. Zhang, X.; van den Bos, C.; Sloof, W.G.; Hovestad, A.; Terryn, H.; de Wit, J.H.W. Comparison of the morphology and corrosion performance of Cr(VI)- and Cr(III)-based conversion coatings on zinc. *Surf. Coat. Technol.* **2005**, *199*, 92–104. [CrossRef]
18. Zhao, J.; Xia, L.; Sehgal, A.; Lu, D.; McCreery, R.L.; Frankel, G.S. Effects of chromate and chromate conversion coatings on corrosion of aluminum alloy 2024-T3. *Surf. Coat. Technol.* **2001**, *140*, 51–57. [CrossRef]
19. Williams, G.; Grace, R.; Woods, R.M. Inhibition of the localized corrosion of mg alloy AZ31 in chloride containing electrolyte. *Corrosion* **2015**, *71*, 184–198. [CrossRef]
20. Chen, X.; Biribilis, N.; Abbott, T. Review of corrosion-resistant conversion coatings for magnesium and its alloys. *Corrosion* **2011**, *67*, 035005-1. [CrossRef]
21. Williams, G.; McMurray, H.N.; Grace, R. Inhibition of magnesium localised corrosion in chloride containing electrolyte. *Electrochim. Acta* **2010**, *55*, 7824–7833. [CrossRef]
22. Song, Y.; Shan, D.; Chen, R.; Zhang, F.; Han, E.H. Formation mechanism of phosphate conversion film on Mg-8.8Li alloy. *Corros. Sci.* **2009**, *51*, 62–69. [CrossRef]
23. Zhou, W.; Shan, D.; Han, E.-H.; Ke, W. Structure and formation mechanism of phosphate conversion coating on die-cast AZ91D magnesium alloy. *Corros. Sci.* **2008**, *50*, 329–337. [CrossRef]
24. Lamaka, S.V.; Gonzalez, J.; Mei, D.; Feyerabend, F.; Willumeit-Römer, R.; Zheludkevich, M.L. Local pH and Its Evolution Near Mg Alloy Surfaces Exposed to Simulated Body Fluids. *Adv. Mater. Interfaces* **2018**, *5*, 1800169. [CrossRef]
25. Kartsonakis, I.A.; Stanciu, S.G.; Matei, A.A.; Karaxi, E.K.; Hristu, R.; Karantonis, A.; Charitidis, C.A. Evaluation of the protective ability of typical corrosion inhibitors for magnesium alloys towards the Mg ZK30 variant. *Corros. Sci.* **2015**, *100*, 194–208. [CrossRef]
26. Liu, D.; Song, Y.W.; Shan, D.Y.; Han, E.H. Comparison of the Inhibition Effect of Four Inhibitors on the Corrosion Behaviour of AM60 Magnesium Alloy. *Int. J. Electrochem. Sci.* **2018**, *13*, 2219–2235. [CrossRef]
27. Montemor, M.F.; Simoes, A.M.; Carmezim, M.J. Characterization of rare-earth conversion films formed on the AZ31 magnesium alloy and its relation with corrosion protection. *Appl. Surf. Sci.* **2007**, *253*, 6922–6931. [CrossRef]
28. Richey, F.W.; McCloskey, B.D.; Luntz, A.C. Mg anode corrosion in aqueous electrolytes and implications for Mg-air batteries. *J. Electrochem. Soc.* **2016**, *163*, A958–A963. [CrossRef]
29. Wang, S.; Li, Q.; Zhong, X.; Li, L.; Chen, F.; Luo, F.; Dai, Y.; Gao, H.; Liu, F.; Zhang, H. Effects of NO<sub>3</sub><sup>−</sup> in NaCl solution on corrosion protection of AZ91D magnesium alloy coated with silane films. *Trans. IMF* **2012**, *90*, 78–85. [CrossRef]
30. Snihirova, D.; Wang, L.; Lamaka, S.V.; Wang, C.; Deng, M.; Vaghefinazari, B.; Hoche, D.; Zheludkevich, M.L. Synergistic Mixture of Electrolyte Additives: A Route to a High-Efficiency Mg-Air Battery. *J. Phys. Chem. Lett.* **2020**, *11*, 8790–8798. [CrossRef]
31. Eaves, D.; Williams, G.; McMurray, H.N. Inhibition of self-corrosion in magnesium by poisoning hydrogen recombination on iron impurities. *Electrochim. Acta* **2012**, *79*, 1–7. [CrossRef]
32. Biribilis, N.; Williams, G.; Gusieva, K.; Samaniego, A.; Gibson, M.A.; McMurray, H.N. Poisoning the corrosion of magnesium. *Electrochem. Commun.* **2013**, *34*, 295–298. [CrossRef]
33. Liu, R.L.; Hurley, M.F.; Kvryan, A.; Williams, G.; Scully, J.R.; Biribilis, N. Controlling the corrosion and cathodic activation of magnesium via microalloying additions of Ge. *Sci. Rep.* **2016**, *6*, 28747. [CrossRef]

34. Williams, G.; Dafydd, H.A.-L.; McMurray, H.N.; Birbilis, N. The influence of arsenic alloying on the localised corrosion behaviour of magnesium. *Electrochim. Acta* **2016**, *219*, 401–411. [\[CrossRef\]](#)
35. Glover, C.; Liu, R.; McNally, E.; Mahboubi, S.; McDermid, J.; Kish, J.; Birbilis, N.; McMurray, H.; Williams, G. Toward a Physical Description of the Role of Germanium in Moderating Cathodic Activation of Magnesium. *Corrosion* **2021**, *77*, 134–147. [\[CrossRef\]](#)
36. Yuwono, J.A.; Birbilis, N.; Liu, R.; Ou, Q.; Bao, Q.; Medhekar, N.V. Aqueous Electrochemical Activity of the Mg Surface: The Role of Group 14 and 15 Microalloying Elements. *J. Electrochem. Soc.* **2017**, *164*, C918–C929. [\[CrossRef\]](#)
37. Gore, P.; Fajardo, S.; Birbilis, N.; Frankel, G.S.; Raja, V.S. Anodic activation of Mg in the presence of  $\text{In}^{3+}$  ions in dilute sodium chloride solution. *Electrochim. Acta* **2019**, *293*, 199–210. [\[CrossRef\]](#)
38. Bao, T.; Hou, L.; Sun, J.; Liu, X.; Du, H.; Wei, H.; Wei, Y. Effect of Indium on the Negative Difference Effect for Magnesium Alloy. *J. Electrochem. Soc.* **2021**, *168*, 031515. [\[CrossRef\]](#)
39. Wang, L.Q.; Snihirova, D.; Deng, M.; Wang, C.; Hoche, D.; Lamaka, S.V.; Zheludkevich, M.L. Indium chloride as an electrolyte additive for primary aqueous Mg batteries. *Electrochim. Acta* **2021**, *373*, 137916. [\[CrossRef\]](#)
40. Mercier, D.; Świątowska, J.; Protopopoff, E.; Zanna, S.; Seyeux, A.; Marcus, P. Inhibition of Mg Corrosion by Sulfur Blocking of the Hydrogen Evolution Reaction on Iron Impurities. *J. Electrochem. Soc.* **2020**, *167*, 121504. [\[CrossRef\]](#)
41. Xu, J.; Yang, Q.; Javed, M.S.; Gong, Y.; Aslam, M.K.; Chen, C. The effects of NaF concentration on electrochemical and corrosion behavior of AZ31B magnesium alloy in a composite electrolyte. *RSC Adv.* **2017**, *7*, 5880–5887. [\[CrossRef\]](#)
42. El-Taib Heikal, F.; Tantawy, N.S.; Shehata, O.S. Impact of chloride and fluoride additions on surface reactivity and passivity of AM60 magnesium alloy in buffer solution. *Corros. Sci.* **2012**, *64*, 153–163. [\[CrossRef\]](#)
43. Heikal, F.E.-T.; Fekry, A.; Fatayerji, M. Influence of halides on the dissolution and passivation behavior of AZ91D magnesium alloy in aqueous solutions. *Electrochim. Acta* **2009**, *54*, 1545–1557. [\[CrossRef\]](#)
44. Barros, C.; Muzeau, B.; L'hostis, V.; François, R. Impact of fluoride concentration on general corrosion of Mg-Zr alloy in a Na-geopolymer and alkaline solutions. *Corros. Sci.* **2020**, *176*, 109009. [\[CrossRef\]](#)
45. Qiu, Y.; Tu, X.; Lu, X.; Yang, J. A novel insight into synergistic corrosion inhibition of fluoride and DL-malate as a green hybrid inhibitor for magnesium alloy. *Corros. Sci.* **2022**, *199*, 110177. [\[CrossRef\]](#)
46. Cheng, M.-Q.; Wahafu, T.; Jiang, G.-F.; Liu, W.; Qiao, Y.-Q.; Peng, X.-C.; Cheng, T.; Zhang, X.-L.; He, G.; Liu, X.-Y. A novel open-porous magnesium scaffold with controllable microstructures and properties for bone regeneration. *Sci. Rep.* **2016**, *6*, 1–14. [\[CrossRef\]](#) [\[PubMed\]](#)
47. Okulov, I.V.; Lamaka, S.V.; Wada, T.; Yubuta, K.; Zheludkevich, M.L.; Weissmüller, J.; Markmann, J.; Kato, H. Nanoporous magnesium. *Nano Res.* **2018**, *11*, 6428–6435. [\[CrossRef\]](#)
48. Prince, L.; Rousseau, M.A.; Noifalisse, X.; Dangreau, L.; Coelho, L.B.; Olivier, M.G. Inhibitive effect of sodium carbonate on corrosion of AZ31 magnesium alloy in NaCl solution. *Corros. Sci.* **2021**, *179*, 109131. [\[CrossRef\]](#)
49. Liu, H.; Cao, F.; Song, G.-L.; Zheng, D.; Shi, Z.; Dargusch, M.S.; Atrons, A. Review of the atmospheric corrosion of magnesium alloys. *J. Mater. Sci. Technol.* **2019**, *35*, 2003–2016. [\[CrossRef\]](#)
50. Mei, D.; Lamaka, S.V.; Gonzalez, J.; Feyerabend, F.; Willumeit-Römer, R.; Zheludkevich, M.L. The role of individual components of simulated body fluid on the corrosion behavior of commercially pure Mg. *Corros. Sci.* **2019**, *147*, 81–93. [\[CrossRef\]](#)
51. Zaghoul, B.; Glover, C.; Scully, J.; Kish, J. Inhibiting Corrosion of Mg Alloy AZ31B-H24 Sheet Metal with Lithium Carbonate. *Corrosion* **2021**, *77*, 192–203. [\[CrossRef\]](#) [\[PubMed\]](#)
52. Zaghoul, B.; Kish, J. Corrosion Inhibition of Mg Alloy ZEK100 Sheet Metal by Dissolved Lithium Carbonate. *J. Electrochem. Soc.* **2021**, *168*, 081507. [\[CrossRef\]](#)
53. Chen, X.B.; Birbilis, N.; Abbott, T.B. Effect of  $[\text{Ca}^{2+}]$  and  $[\text{PO}_4^{3-}]$  levels on the formation of calcium phosphate conversion coatings on die-cast magnesium alloy AZ91D. *Corros. Sci.* **2012**, *55*, 226–232. [\[CrossRef\]](#)
54. Su, Y.; Guo, Y.; Huang, Z.; Zhang, Z.; Li, G.; Lian, J.; Ren, L. Preparation and corrosion behaviors of calcium phosphate conversion coating on magnesium alloy. *Surf. Coat. Technol.* **2016**, *307*, 99–108. [\[CrossRef\]](#)
55. Jiang, P.; Blawert, C.; Scharnagl, N.; Zheludkevich, M.L. Influence of water purity on the corrosion behavior of Mg0.5ZnX (X= Ca, Ge) alloys. *Corros. Sci.* **2019**, *153*, 62–73. [\[CrossRef\]](#)
56. Gonzalez, J.; Lamaka, S.V.; Mei, D.; Scharnagl, N.; Feyerabend, F.; Zheludkevich, M.L.; Willumeit-Römer, R. Mg Biodegradation Mechanism Deduced from the Local Surface Environment under Simulated Physiological Conditions. *Adv. Healthc. Mater.* **2021**, *10*, 2100053. [\[CrossRef\]](#)
57. Iannuzzi, M.; Frankel, G.S. Mechanisms of corrosion inhibition of AA2024-T3 by vanadates. *Corros. Sci.* **2007**, *49*, 2371–2391. [\[CrossRef\]](#)
58. Hurley, B.L.; Ralston, K.D.; Buchheit, R.G. Corrosion inhibition of zinc by aqueous vanadate species. *J. Electrochem. Soc.* **2014**, *161*, C471. [\[CrossRef\]](#)
59. Feng, Z.; Hurley, B.; Li, J.; Buchheit, R. Corrosion inhibition study of aqueous vanadate on Mg alloy AZ31. *J. Electrochem. Soc.* **2018**, *165*, C94. [\[CrossRef\]](#)
60. Mingo, B.; Guo, Y.; Leiva-Garcia, R.; Connolly, B.J.; Matthews, A.; Yerokhin, A. Smart Functionalization of Ceramic-Coated AZ31 Magnesium Alloy. *ACS Appl. Mater. Interfaces* **2020**, *12*, 30833–30846. [\[CrossRef\]](#) [\[PubMed\]](#)
61. Kharitonov, D.S.; Zimowska, M.; Ryl, J.; Zieliński, A.; Osipenko, M.A.; Adamiec, J.; Wrzesińska, A.; Claesson, P.M.; Kurilo, I.I. Aqueous molybdate provides effective corrosion inhibition of WE43 magnesium alloy in sodium chloride solutions. *Corros. Sci.* **2021**, *190*, 109664. [\[CrossRef\]](#)

62. Zeng, R.-C.; Liu, Z.-G.; Zhang, F.; Li, S.-Q.; Cui, H.-Z.; Han, E.-H. Corrosion of molybdate intercalated hydrotalcite coating on AZ31 Mg alloy. *J. Mater. Chem. A* **2014**, *2*, 13049–13057. [\[CrossRef\]](#)
63. Osipenko, M.A.; Kharytonau, D.S.; Kasach, A.A.; Ryl, J.; Adamiec, J.; Kurilo, I.I. Inhibitive Effect of Sodium Molybdate on Corrosion of AZ31 Magnesium Alloy in Chloride Solutions. *Electrochim. Acta* **2022**, *414*, 140175. [\[CrossRef\]](#)
64. Feng, Z.; Hurley, B.; Zhu, M.; Yang, Z.; Hwang, J.; Buchheit, R. Corrosion Inhibition of AZ31 Mg Alloy by Aqueous Selenite ( $\text{SeO}_3^{2-}$ ). *J. Electrochem. Soc.* **2019**, *166*, C520. [\[CrossRef\]](#)
65. Feng, Z.; Xu, C.C.; Zhang, D.; Buchheit, R. Corrosion Protective Film Formation on Mg Alloy AZ31 by Exposure to Dilute Selenite Solutions. *Materials* **2021**, *14*, 286. [\[CrossRef\]](#)
66. Whanger, P.; Vendeland, S.; Park, Y.-C.; Xia, Y. Metabolism of subtoxic levels of selenium in animals and humans. *Ann. Clin. Lab. Sci.* **1996**, *26*, 99–113.
67. Spallholz, J.E. On the nature of selenium toxicity and carcinostatic activity. *Free Radic. Biol. Med.* **1994**, *17*, 45–64. [\[CrossRef\]](#)
68. Navarro-Alarcon, M.; López-Martínez, M. Essentiality of selenium in the human body: Relationship with different diseases. *Sci. Total Environ.* **2000**, *249*, 347–371. [\[CrossRef\]](#)
69. Cui, Z.; Ge, F.; Lin, Y.; Wang, L.; Lei, L.; Tian, H.; Yu, M.; Wang, X. Corrosion behavior of AZ31 magnesium alloy in the chloride solution containing ammonium nitrate. *Electrochim. Acta* **2018**, *278*, 421–437. [\[CrossRef\]](#)
70. Wang, J.L.; Ke, C.; Pohl, K.; Birbilis, N.; Chen, X.B. The Unexpected Role of Benzotriazole in Mitigating Magnesium Alloy Corrosion: A Nucleating Agent for Crystalline Nanostructured Magnesium Hydroxide Film. *J. Electrochem. Soc.* **2015**, *162*, C403–C411. [\[CrossRef\]](#)
71. Fukumura, K.; Shiraishi, T. Surface-Treating Agent for Magnesium-Based Part and Method of Surface Treatment. U.S.6569264B1, 27 May 2003.
72. Fukumura, K.; Yu, Y.; Kajimoto, M.; Hama, H.; Hamauzu, T.; Yagi, H. Rust Preventive for Magnesium and/or Magnesium Alloy. U.S.20070080319A1, 12 April 2007.
73. Supplitt, R.; Koch, T.; Schubert, U. Evaluation of the anti-corrosive effect of acid pickling and sol-gel coating on magnesium AZ31 alloy. *Corros. Sci.* **2007**, *49*, 3015–3023. [\[CrossRef\]](#)
74. Karavai, O.V.; Bastos, A.C.; Zheludkevich, M.L.; Taryba, M.G.; Lamaka, S.V.; Ferreira, M.G.S. Localized electrochemical study of corrosion inhibition in microdefects on coated AZ31 magnesium alloy. *Electrochim. Acta* **2010**, *55*, 5401–5406. [\[CrossRef\]](#)
75. Semiletov, A.M. Metals Passivation by Aqueous Solutions of Organic Acids and Trialkoxysilanes. Ph.D. Thesis, Moscow State University, Moscow, Russia, 2016.
76. Ivanou, D.K.; Yasakau, K.A.; Kallip, S.; Lisenkov, A.D.; Sarykevich, M.; Lamaka, S.V.; Ferreira, M.G.S.; Zheludkevich, M.L. Active corrosion protection coating for a ZE41 magnesium alloy created by combining PEO and sol-gel techniques. *Rsc Adv.* **2016**, *6*, 12553–12560. [\[CrossRef\]](#)
77. Soltan, A.; Dargusch, M.S.; Shi, Z.; Gerrard, D.; Atrens, A. Influence of commercial corrosion-inhibiting compounds on the atmospheric corrosion of the magnesium alloys EV31A, WE43B, ZE41A and pure magnesium. *Mater. Corros.* **2021**, *72*, 672–693. [\[CrossRef\]](#)
78. Guo, X.; An, M.; Yang, P.; Li, H.; Su, C. Effects of benzotriazole on anodized film formed on AZ31B magnesium alloy in environmental-friendly electrolyte. *J. Alloys Compd.* **2009**, *482*, 487–497. [\[CrossRef\]](#)
79. Ostanina, T.N.; Rudoi, V.M.; Ovsyannikova, A.N.; Malkov, V.B. Magnesium alloys spontaneous dissolution features under external anodic polarization in presence of inhibitors. *Russ. J. Electrochem.* **2010**, *46*, 707–713. [\[CrossRef\]](#)
80. Huang, D.; Hu, J.; Song, G.-L.; Guo, X. Inhibition effect of inorganic and organic inhibitors on the corrosion of Mg–10Gd–3Y–0.5Zr alloy in an ethylene glycol solution at ambient and elevated temperatures. *Electrochim. Acta* **2011**, *56*, 10166–10178. [\[CrossRef\]](#)
81. Ashassi-Sorkhabi, H.; Shabani, B.; Aligholipour, B.; Seifzadeh, D. The effect of some Schiff bases on the corrosion of aluminum in hydrochloric acid solution. *Appl. Surf. Sci.* **2006**, *252*, 4039–4047. [\[CrossRef\]](#)
82. Gomma, G.K.; Wahdan, M.H. Schiff bases as corrosion inhibitors for aluminium in hydrochloric acid solution. *Mater. Chem. Phys.* **1995**, *39*, 209–213. [\[CrossRef\]](#)
83. Yurt, A.; Ulutas, S.; Dal, H. Electrochemical and theoretical investigation on the corrosion of aluminium in acidic solution containing some Schiff bases. *Appl. Surf. Sci.* **2006**, *253*, 919–925. [\[CrossRef\]](#)
84. Yurt, A.; Balaban, A.; Kandemir, S.U.; Bereket, G.; Erk, B. Investigation on some Schiff bases as HCl corrosion inhibitors for carbon steel. *Mater. Chem. Phys.* **2004**, *85*, 420–426. [\[CrossRef\]](#)
85. Hosseini, M.; Mertens, S.F.L.; Ghorbani, M.; Arshadi, M.R. Asymmetrical Schiff bases as inhibitors of mild steel corrosion in sulphuric acid media. *Mater. Chem. Phys.* **2003**, *78*, 800–808. [\[CrossRef\]](#)
86. Ashassi-Sorkhabi, H.; Shaabani, B.; Seifzadeh, D. Corrosion inhibition of mild steel by some schiff base compounds in hydrochloric acid. *Appl. Surf. Sci.* **2005**, *239*, 154–164. [\[CrossRef\]](#)
87. Behpour, M.; Ghoreishi, S.M.; Salavati-Niasari, M.; Ebrahimi, B. Evaluating two new synthesized S-N Schiff bases on the corrosion of copper in 15% hydrochloric acid. *Mater. Chem. Phys.* **2008**, *107*, 153–157. [\[CrossRef\]](#)
88. Ma, H.; Chen, S.; Niu, L.; Zhao, S.; Li, S.; Li, D. Inhibition of copper corrosion by several Schiff bases in aerated halide solutions. *J. Appl. Electrochem.* **2002**, *32*, 65–72. [\[CrossRef\]](#)
89. Verma, C.; Quraishi, M. Recent progresses in Schiff bases as aqueous phase corrosion inhibitors: Design and applications. *Coord. Chem. Rev.* **2021**, *446*, 214105. [\[CrossRef\]](#)

90. Seifzadeh, D.; Bezaatpour, A.; Joghani, R.A. Corrosion inhibition effect of N, N'-bis (2-pyridylmethylidene)-1,2-diiminoethane on AZ91D magnesium alloy in acidic media. *Trans. Nonferrous Met. Soc. China (Engl. Ed.)* **2014**, *24*, 3441–3451. [\[CrossRef\]](#)
91. Thirugnanaselvi, S.; Kuttirani, S.; Emelda, A.R. Effect of Schiff base as corrosion inhibitor on AZ31 magnesium alloy in hydrochloric acid solution. *Trans. Nonferrous Met. Soc. China (Engl. Ed.)* **2014**, *24*, 1969–1977. [\[CrossRef\]](#)
92. Guo, Y.; Yang, S.; Feng, W.; Li, Y.; Cheng, Y. Electrochemical study of inhibition effect of a schiff base towards magnesium alloy corrosion. *Int. J. Electrochem. Sci.* **2016**, *11*, 6043–6051. [\[CrossRef\]](#)
93. Ma, L.; Li, W.; Zhu, S.; Wang, L.; Guan, S. Corrosion inhibition of Schiff bases for Mg-Zn-Y-Nd alloy in normal saline: Experimental and theoretical investigations. *Corros. Sci.* **2021**, *184*, 109268. [\[CrossRef\]](#)
94. Lamaka, S.V.; Zheludkevich, M.L.; Yasakau, K.A.; Montemor, M.F.; Ferreira, M.G.S. High effective organic corrosion inhibitors for 2024 aluminium alloy. *Electrochim. Acta* **2007**, *52*, 7231–7247. [\[CrossRef\]](#)
95. Gao, H.; Li, Q.; Dai, Y.; Luo, F.; Zhang, H.X. High efficiency corrosion inhibitor 8-hydroxyquinoline and its synergistic effect with sodium dodecylbenzenesulphonate on AZ91D magnesium alloy. *Corros. Sci.* **2010**, *52*, 1603–1609. [\[CrossRef\]](#)
96. Zong, Q.; Wang, L.; Sun, W.; Liu, G. Active deposition of bis (8-hydroxyquinoline) magnesium coating for enhanced corrosion resistance of AZ91D alloy. *Corros. Sci.* **2014**, *89*, 127–136. [\[CrossRef\]](#)
97. Argade, G.R.; Sanders, S.; Mohandass, G.; Alsaleh, A.; D'Souza, F.; Golden, T.D.; Mishra, R.S. Corrosion Inhibition Study of Mg-Nd-Y High Strength Magnesium Alloy Using Organic Inhibitor. *J. Mater. Eng. Perform.* **2019**, *28*, 852–862. [\[CrossRef\]](#)
98. Seifzadeh, D.; Hamzedoust-Hasankiadeh, S.; Shamkhali, A. Electrochemical and DFT studies of 8-hydroxyquinoline as corrosion inhibitor for AZ61 magnesium alloy in acidic media. *Prot. Met. Phys. Chem. Surf.* **2013**, *49*, 229–239. [\[CrossRef\]](#)
99. Slavcheva, E.; Schmitt, G. Screening of new corrosion inhibitors via electrochemical noise analysis. *Mater. Corros.* **2002**, *53*, 647–655. [\[CrossRef\]](#)
100. Lamaka, S.V.; Knörrschild, G.; Snihirova, D.V.; Taryba, M.G.; Zheludkevich, M.L.; Ferreira, M.G.S. Complex anticorrosion coating for ZK30 magnesium alloy. *Electrochim. Acta* **2009**, *55*, 131–141. [\[CrossRef\]](#)
101. Al Zoubi, W.; Kim, M.J.; Kim, Y.G.; Ko, Y.G. Fabrication of graphene oxide/8-hydroxyquinolin/inorganic coating on the magnesium surface for extraordinary corrosion protection. *Prog. Org. Coat.* **2019**, *137*, 105314. [\[CrossRef\]](#)
102. Vaghefinazari, B.; Lamaka, S.V.; Blawert, C.; Serdechnova, M.; Scharnagl, N.; Karlova, P.; Wieland, D.C.F.; Zheludkevich, M.L. Exploring the corrosion inhibition mechanism of 8-hydroxyquinoline for a PEO-coated magnesium alloy. *Corros. Sci.* **2022**, *203*, 110344. [\[CrossRef\]](#)
103. Verma, C.; Quraishi, M.A.; Ebenso, E.E. Quinoline and its derivatives as corrosion inhibitors: A review. *Surf. Interfaces* **2020**, *21*, 100634. [\[CrossRef\]](#)
104. Verma, C.; Rhee, K.Y.; Quraishi, M.A.; Ebenso, E.E. Pyridine based N-heterocyclic compounds as aqueous phase corrosion inhibitors: A review. *J. Taiwan Inst. Chem. Eng.* **2020**, *117*, 265–277. [\[CrossRef\]](#)
105. Lavanya, K.; Saranya, J.; Chitra, S. Recent reviews on quinoline derivatives as corrosion inhibitors. *Corros. Rev.* **2018**, *36*, 365–371. [\[CrossRef\]](#)
106. Menger, F.M.; Keiper, J.S. Gemini surfactants. *Angew. Chem. Int. Ed.* **2000**, *39*, 1906–1920. [\[CrossRef\]](#)
107. Rocca, E.; Steinmetz, J. Inhibition of lead corrosion with saturated linear aliphatic chain monocarboxylates of sodium. *Corros. Sci.* **2001**, *43*, 891–902. [\[CrossRef\]](#)
108. McCafferty, E. *Introduction to Corrosion Science*; Springer: New York, NY, USA, 2010.
109. Frignani, A.; Grassi, V.; Zucchi, F.; Zanotto, F. Mono-carboxylate conversion coatings for AZ31 Mg alloy protection. *Mater. Corros.* **2011**, *62*, 995–1002. [\[CrossRef\]](#)
110. Daloz, D.; Rapin, C.; Steinmetz, P.; Michot, G. Corrosion Inhibition of Rapidly Solidified Mg-3% Zn-15% Al Magnesium Alloy with Sodium Carboxylates. *Corrosion* **1998**, *54*, 444–450. [\[CrossRef\]](#)
111. Zucchi, F.; Grassi, V.; Zanotto, F. Sodium monocarboxylates as inhibitors of AZ31 alloy corrosion in a synthetic cooling water. *Mater. Corros.* **2009**, *60*, 199–205. [\[CrossRef\]](#)
112. Dinodi, N.; Shetty, A.N. Alkyl carboxylates as efficient and green inhibitors of magnesium alloy ZE41 corrosion in aqueous salt solution. *Corros. Sci.* **2014**, *85*, 411–427. [\[CrossRef\]](#)
113. Szillies, S.; Thissen, P.; Tabatabai, D.; Feil, F.; Fürbeth, W.; Fink, N.; Grundmeier, G. Formation and stability of organic acid monolayers on magnesium alloy AZ31: The role of alkyl chain length and head group chemistry. *Appl. Surf. Sci.* **2013**, *283*, 339–347. [\[CrossRef\]](#)
114. Mesbah, A.; Juers, C.; Lacouture, F.; Mathieu, S.; Rocca, E.; François, M.; Steinmetz, J. Inhibitors for magnesium corrosion: Metal organic frameworks. *Solid State Sci.* **2007**, *9*, 322–328. [\[CrossRef\]](#)
115. Kuznetsov, Y.I. Organic corrosion inhibitors: Where are we now? A review. Part II. Passivation and the role of chemical structure of carboxylates. *Int. J. Corros. Scale Inhib.* **2016**, *5*, 282–375. [\[CrossRef\]](#)
116. Lu, X.; Li, Y.; Ju, P.; Chen, Y.; Qian, K.; Zhang, T.; Wang, F. Unveiling the inhibition mechanism of an effective inhibitor for AZ91 Mg alloy. *Corros. Sci.* **2019**, *148*, 264–271. [\[CrossRef\]](#)
117. Pardo, A.; Merino, M.C.; Coy, A.E.; Arrabal, R.; Viejo, F.; Matykina, E. Corrosion behaviour of magnesium/aluminium alloys in 3.5wt.% NaCl. *Corros. Sci.* **2008**, *50*, 823–834. [\[CrossRef\]](#)
118. Bland, L.G.; Scully, L.C.; Scully, J.R. Assessing the corrosion of multi-phase Mg-Al alloys with high Al content by electrochemical impedance, mass loss, hydrogen collection, and inductively coupled plasma optical emission spectrometry solution analysis. *Corrosion* **2017**, *73*, 526–543. [\[CrossRef\]](#) [\[PubMed\]](#)

119. Frignani, A.; Grassi, V.; Zanutto, F.; Zucchi, F. Inhibition of AZ31 Mg alloy corrosion by anionic surfactants. *Corros. Sci.* **2012**, *63*, 29–39. [\[CrossRef\]](#)
120. Yang, X.; Pan, F.; Zhang, D. A study on corrosion inhibitor for magnesium alloy. In *Materials Science Forum*; Trans Tech Publications Ltd.: Wollerau, Switzerland, 2009; Volume 610–613, pp. 920–926.
121. Li, Y.; Lu, X.; Wu, K.; Yang, L.; Zhang, T.; Wang, F. Exploration the inhibition mechanism of sodium dodecyl sulfate on Mg alloy. *Corros. Sci.* **2020**, *168*, 108559. [\[CrossRef\]](#)
122. Li, Y.; Lu, X.; Mei, D.; Zhang, T.; Wang, F. Passivation of corrosion product layer on AM50 Mg by corrosion inhibitor. *J. Magnes. Alloy.* **2022**, *10*, 2563–2573. [\[CrossRef\]](#)
123. Song, H.; Xu, Z.; Benabou, L.; Yin, Z.; Guan, H.; Yan, H.; Chao, L.; Hu, Z.; Wang, X. Sodium dodecyl sulfate (SDS) as an effective corrosion inhibitor for Mg-8Li-3Al alloy in aqueous NaCl: A combined experimental and theoretical investigation. *J. Magnes. Alloy.* **2021**. [\[CrossRef\]](#)
124. Abd El Rehim, S.S.; Amin, M.A.; Moussa, S.O.; Ellithy, A.S. The corrosion inhibition of aluminum and its copper alloys in 1.0 M H<sub>2</sub>SO<sub>4</sub> solution using linear-sodium dodecyl benzene sulfonate as inhibitor. *Mater. Chem. Phys.* **2008**, *112*, 898–906. [\[CrossRef\]](#)
125. Kellou-Kerkouche, F.; Benchettara, A.; Amara, S. Effect of sodium dodecyl benzene sulfonate on the corrosion inhibition of Fe-1Ti-20C alloy in 0.5M H<sub>2</sub>SO<sub>4</sub>. *Mater. Chem. Phys.* **2008**, *110*, 26–33. [\[CrossRef\]](#)
126. Li, L.; Pan, F.; Lei, J. Environmental Friendly Corrosion Inhibitors for Mg Alloys. In *Magnesium Alloys-Corrosion and Surface Treatments*; Czerwinski, F., Ed.; InTech: London, UK, 2011.
127. Lin, J.; Battocchi, D.; Bierwagen, G.P. Inhibitors for prolonging corrosion protection of Mg-rich primer on Al alloy 2024-T3. *J. Coat. Technol. Res.* **2017**, *14*, 497–504. [\[CrossRef\]](#)
128. Chen, J.; He, J.; Li, L. Spectroscopic insight into the role of SDBS on the interface evolution of Mg in NaCl corrosive medium. *Corros. Sci.* **2021**, *182*, 109215. [\[CrossRef\]](#)
129. Tezak, D.; Strajnar, F.; Sarcevic, D.; Milat, O.; Stubicar, M. Solid/liquid equilibria in aqueous system of dodecyl benzene sulphonate and alkaline earth ions. *Croat. Chem. Acta* **1984**, *57*, 93–107.
130. Soltan, A.; Dargusch, M.S.; Shi, Z.; Jones, F.; Wood, B.; Gerrard, D.; Atrens, A. Effect of corrosion inhibiting compounds on the corrosion behaviour of pure magnesium and the magnesium alloys EV31A, WE43B and ZE41A. *J. Magnes. Alloy.* **2021**, *9*, 432–455. [\[CrossRef\]](#)
131. Sun, J.; Howlett, P.C.; MacFarlane, D.R.; Lin, J.; Forsyth, M. Synthesis and physical property characterisation of phosphonium ionic liquids based on P(O)2(OR)2– and P(O)2(R)2– anions with potential application for corrosion mitigation of magnesium alloys. *Electrochim. Acta* **2008**, *54*, 254–260. [\[CrossRef\]](#)
132. Armand, M.; Endres, F.; MacFarlane, D.R.; Ohno, H.; Scrosati, B. Ionic-liquid materials for the electrochemical challenges of the future. *Nat. Mater.* **2009**, *8*, 621–629. [\[CrossRef\]](#) [\[PubMed\]](#)
133. Huang, P.; Latham, J.-A.; MacFarlane, D.R.; Howlett, P.C.; Forsyth, M. A review of ionic liquid surface film formation on Mg and its alloys for improved corrosion performance. *Electrochim. Acta* **2013**, *110*, 501–510. [\[CrossRef\]](#)
134. Galiński, M.; Lewandowski, A.; Stepniak, I. Ionic liquids as electrolytes. *Electrochim. Acta* **2006**, *51*, 5567–5580. [\[CrossRef\]](#)
135. Gao, X.; Ma, D.; Huang, Q.; Ren, T.; Li, G.; Guo, L. Pyrazole ionic liquid corrosion inhibitor for magnesium alloy: Synthesis, performances and theoretical explore. *J. Mol. Liq.* **2022**, *353*, 118769. [\[CrossRef\]](#)
136. Gao, X.; Huang, Q.; Ma, D.; Jiang, Y.; Ren, T.; Guo, X.; Zhang, J.; Guo, L. Improving environmental adaptability and long-term corrosion resistance of Mg alloys by pyrazole ionic liquids: Experimental and theoretical studies. *J. Mol. Liq.* **2021**, *333*, 115964. [\[CrossRef\]](#)
137. Jiang, Y.; Liu, Y.; Gao, S.; Guo, X.; Zhang, J. Experimental and theoretical studies on corrosion inhibition behavior of three imidazolium-based ionic liquids for magnesium alloys in sodium chloride solution. *J. Mol. Liq.* **2021**, *345*, 116998. [\[CrossRef\]](#)
138. Gao, X.; Wu, Y.; Huang, Q.; Jiang, Y.; Ma, D.; Ren, T. The inhibition behavior of novel ionic liquids for magnesium alloy in NaCl solution: Experimental and theoretical investigation. *J. Mol. Liq.* **2021**, *324*, 114732. [\[CrossRef\]](#)
139. Su, H.; Wu, Y.; Zhang, Y.; Jiang, Y.; Ding, Y.; Wang, L.; Zhang, J. Enhancing the long-term anti-corrosion property of Mg alloy by quaternary phosphonium salt: Integrated experimental and theoretical approaches. *Corros. Sci.* **2021**, *178*, 109010. [\[CrossRef\]](#)
140. Zhang, Y.; Yaxu, W.; Jiang, Y.; Wang, L.; Zhang, J. Adsorbed film and synergistic effect of Benzyltriphenylphosphonium chloride and L-Histidine for magnesium alloys corrosion in NaCl. *J. Alloys Compd.* **2020**, *849*, 156230. [\[CrossRef\]](#)
141. Su, H.; Wang, L.; Wu, Y.; Zhang, Y.; Zhang, J. Insight into inhibition behavior of novel ionic liquids for magnesium alloy in NaCl solution: Experimental and theoretical investigation. *Corros. Sci.* **2020**, *165*, 108410. [\[CrossRef\]](#)
142. Su, H.; Liu, Y.; Gao, X.; Qian, Y.; Li, W.; Ren, T.; Wang, L.; Zhang, J. Corrosion inhibition of magnesium alloy in NaCl solution by ionic liquid: Synthesis, electrochemical and theoretical studies. *J. Alloys Compd.* **2019**, *791*, 681–689. [\[CrossRef\]](#)
143. Kurchavov, D.; Haddad, M.; Lair, V.; Volovitch, P. Mg-alloys in water-hydrophilic ionic liquid mixtures: Is there a negative difference effect? *Corros. Sci.* **2022**, *200*, 110178. [\[CrossRef\]](#)
144. McNulty, R.E.; Hanawalt, J.D. Some Corrosion Characteristics of High Purity Magnesium Alloys. *Trans. Electrochem. Soc.* **1942**, *81*, 423–433. [\[CrossRef\]](#)
145. Cain, T.; Madden, S.B.; Birbilis, N.; Scully, J.R. Evidence of the enrichment of transition metal elements on corroding magnesium surfaces using rutherford backscattering spectrometry. *J. Electrochem. Soc.* **2015**, *162*, C228–C237. [\[CrossRef\]](#)
146. Lysne, D.; Thomas, S.; Hurley, M.F.; Birbilis, N. On the Fe enrichment During anodic polarization of Mg and its impact on hydrogen evolution. *J. Electrochem. Soc.* **2015**, *162*, C396–C402. [\[CrossRef\]](#)

147. Höche, D.; Blawert, C.; Lamaka, S.V.; Scharnagl, N.; Mendis, C.; Zheludkevich, M.L. The effect of iron re-deposition on the corrosion of impurity-containing magnesium. *Phys. Chem. Chem. Phys.* **2015**, *18*, 1279–1291. [\[CrossRef\]](#)
148. Michailidou, E.; McMurray, H.N.; Williams, G. Quantifying the Role of Transition Metal Electrodeposition in the Cathodic Activation of Corroding Magnesium. *J. Electrochem. Soc.* **2018**, *165*, C195–C205. [\[CrossRef\]](#)
149. Mercier, D.; Światowska, J.; Zanna, S.; Seyeux, A.; Marcus, P. Role of Segregated Iron at Grain Boundaries on Mg Corrosion. *J. Electrochem. Soc.* **2018**, *165*, C42–C49. [\[CrossRef\]](#)
150. Lamaka, S.V.; Höche, D.; Petrauskas, R.P.; Blawert, C.; Zheludkevich, M.L. A new concept for corrosion inhibition of magnesium: Suppression of iron re-deposition. *Electrochem. Commun.* **2016**, *62*, 5–8. [\[CrossRef\]](#)
151. Vaghefinazari, B.; Snihirova, D.; Wang, C.; Wang, L.; Deng, M.; Höche, D.; Lamaka, S.V.; Zheludkevich, M.L. Exploring the effect of sodium salt of Ethylenediaminetetraacetic acid as an electrolyte additive on electrochemical behavior of a commercially pure Mg in primary Mg-air batteries. *J. Power Sources* **2022**, *527*, 231176. [\[CrossRef\]](#)
152. Martell, A.E.; Smith, R.M. *Critical Stability Constants: Second Supplement, V. 6*; Springer Science & Business Media: Berlin/Heidelberg, Germany, 1989; Volume 6.
153. Martell, A.E.; Smith, R.M. *Critical Stability Constants, Other Organic Ligands, V. 3*; Springer: New York, NY, USA, 1977; Volume 3.
154. Martell, A.E.; Smith, R.M. *Critical Stability Constants: First Supplement, V. 5*; Springer Science & Business Media: Berlin/Heidelberg, Germany, 1982; Volume 5.
155. Lamaka, S.; Höche, D.; Blawert, C.; Zheludkevich, M. Corrosion Inhibitor Composition for Magnesium or Magnesium Alloys. WO/2017/064185, 20 April 2017.
156. Lamaka, S.V.; Höche, D.; Blawert, C.; Zheludkevich, M.L. Corrosion Inhibitor Composition for Magnesium or Magnesium Alloys. EP15189674.3, 14 October 2015.
157. Dean, J.A. *Lange's Chemistry Handbook*, 15th ed.; McGraw-Hill: New York, NY, USA, 1999.
158. Maltseva, A.; Lamaka, S.V.; Yasakau, K.A.; Mei, D.; Kurchavov, D.; Zheludkevich, M.L.; Lefèvre, G.; Volovitch, P. In situ surface film evolution during Mg aqueous corrosion in presence of selected carboxylates. *Corros. Sci.* **2020**, *171*, 108484. [\[CrossRef\]](#)
159. Vaghefinazari, B.; Wang, C.; Mercier, D.; Mei, D.; Seyeux, A.; Marcus, P.; Blawert, C.; Lamaka, S.V.; Zheludkevich, M.L. Adverse effect of 2,5PDC corrosion inhibitor on PEO coated magnesium. *Corros. Sci.* **2021**, *192*, 109830. [\[CrossRef\]](#)
160. Fockaert, L.I.; Würger, T.; Unbehau, R.; Boelen, B.; Meißner, R.H.; Lamaka, S.V.; Zheludkevich, M.L.; Terryn, H.; Mol, J.M.C. ATR-FTIR in Kretschmann configuration integrated with electrochemical cell as in situ interfacial sensitive tool to study corrosion inhibitors for magnesium substrates. *Electrochim. Acta* **2020**, *345*, 136166. [\[CrossRef\]](#)
161. Yang, J.; Jiang, P.; Qiu, Y.; Jao, C.-Y.; Blawert, C.; Lamaka, S.; Bouali, A.; Lu, X.; Zheludkevich, M.L.; Li, W. Experimental and quantum chemical studies of carboxylates as corrosion inhibitors for AM50 alloy in pH neutral NaCl solution. *J. Magnes. Alloy.* **2021**, *10*, 555–568. [\[CrossRef\]](#)
162. Yasakau, K.A.; Maltseva, A.; Lamaka, S.V.; Mei, D.; Orvi, H.; Volovitch, P.; Ferreira, M.G.S.; Zheludkevich, M.L. The effect of carboxylate compounds on Volta potential and corrosion inhibition of Mg containing different levels of iron. *Corros. Sci.* **2022**, *194*, 109937. [\[CrossRef\]](#)
163. Cui, Y.; Zhang, T.; Wang, F. New understanding on the mechanism of organic inhibitors for magnesium alloy. *Corros. Sci.* **2022**, *192*, 110118. [\[CrossRef\]](#)
164. Winkler, D.A.; Breedon, M.; White, P.; Hughes, A.; Sapper, E.; Cole, I. Using high throughput experimental data and in silico models to discover alternatives to toxic chromate corrosion inhibitors. *Corros. Sci.* **2016**, *106*, 229–235. [\[CrossRef\]](#)
165. Winkler, D.A.; Breedon, M.; Hughes, A.E.; Burden, F.R.; Barnard, A.S.; Harvey, T.G.; Cole, I. Towards chromate-free corrosion inhibitors: Structure–property models for organic alternatives. *Green Chem.* **2014**, *16*, 3349–3357. [\[CrossRef\]](#)
166. Galvão, T.L.; Novell-Leruth, G.; Kuznetsova, A.; Tedim, J.o.; Gomes, J.R. Elucidating structure–property relationships in aluminum alloy corrosion inhibitors by machine learning. *J. Phys. Chem. C* **2020**, *124*, 5624–5635. [\[CrossRef\]](#)
167. Fernandez, M.; Breedon, M.; Cole, I.S.; Barnard, A.S. Modeling corrosion inhibition efficacy of small organic molecules as non-toxic chromate alternatives using comparative molecular surface analysis (CoMSA). *Chemosphere* **2016**, *160*, 80–88. [\[CrossRef\]](#)
168. Würger, T.; Mei, D.; Vaghefinazari, B.; Winkler, D.A.; Lamaka, S.V.; Zheludkevich, M.L.; Meißner, R.H.; Feiler, C. Exploring structure-property relationships in magnesium dissolution modulators. *npj Mater. Degrad.* **2021**, *5*, 2. [\[CrossRef\]](#)
169. Schiessler, E.J.; Würger, T.; Lamaka, S.V.; Meißner, R.H.; Cyron, C.J.; Zheludkevich, M.L.; Feiler, C.; Aydin, R.C. Predicting the inhibition efficiencies of magnesium dissolution modulators using sparse machine learning models. *npj Comput. Mater.* **2021**, *7*, 1–9. [\[CrossRef\]](#)
170. Feiler, C.; Mei, D.; Vaghefinazari, B.; Würger, T.; Meißner, R.H.; Luthringer-Feyerabend, B.J.C.; Winkler, D.A.; Zheludkevich, M.L.; Lamaka, S.V. In silico screening of modulators of magnesium dissolution. *Corros. Sci.* **2020**, *163*, 108245. [\[CrossRef\]](#)
171. Würger, T.; Feiler, C.; Musil, F.; Feldbauer, G.B.V.; Höche, D.; Lamaka, S.V.; Zheludkevich, M.L.; Meißner, R.H. Data Science Based Mg Corrosion Engineering. *Front. Mater.* **2019**, *6*, 53. [\[CrossRef\]](#)
172. Zeller-Plumhoff, B.; Gile, M.; Priebe, M.; Slominska, H.; Boll, B.; Wiese, B.; Würger, T.; Willumeit-Römer, R.; Meißner, R.H. Exploring key ionic interactions for magnesium degradation in simulated body fluid—A data-driven approach. *Corros. Sci.* **2021**, *182*, 109272. [\[CrossRef\]](#)
173. Feiler, C.; Mei, D.; Luthringer-Feyerabend, B.; Lamaka, S.; Zheludkevich, M. Rational design of effective Mg degradation modulators. *Corrosion* **2021**, *77*, 204–208. [\[CrossRef\]](#)

174. Galvão, T.L.P.; Ferreira, I.; Kuznetsova, A.; Novell-Leruth, G.; Song, C.; Feiler, C.; Lamaka, S.V.; Rocha, C.; Maia, F.; Zheludkevich, M.L.; et al. CORDATA: An open data management web application to select corrosion inhibitors. *NPJ Mater. Degrad.* **2022**, *6*, 48. [\[CrossRef\]](#)
175. Muster, T.; Sullivan, H.; Lau, D.; Alexander, D.; Sherman, N.; Garcia, S.; Harvey, T.; Markley, T.; Hughes, A.; Corrigan, P. A combinatorial matrix of rare earth chloride mixtures as corrosion inhibitors of AA2024-T3: Optimisation using potentiodynamic polarisation and EIS. *Electrochim. Acta* **2012**, *67*, 95–103. [\[CrossRef\]](#)
176. Hu, J.; Huang, D.; Song, G.L.; Guo, X. The synergistic inhibition effect of organic silicate and inorganic Zn salt on corrosion of Mg-10Gd-3Y magnesium alloy. *Corros. Sci.* **2011**, *53*, 4093–4101. [\[CrossRef\]](#)
177. Tawfik, S.M. Alginate surfactant derivatives as an ecofriendly corrosion inhibitor for carbon steel in acidic environments. *RSC Adv.* **2015**, *5*, 104535–104550. [\[CrossRef\]](#)
178. Sangeetha, Y.; Meenakshi, S.; Sundaram, C.S. Investigation of corrosion inhibitory effect of hydroxyl propyl alginate on mild steel in acidic media. *J. Appl. Polym. Sci.* **2016**, *133*, 43004. [\[CrossRef\]](#)
179. Obot, I.B.; Onyeachu, I.B.; Kumar, A.M. Sodium alginate: A promising biopolymer for corrosion protection of API X60 high strength carbon steel in saline medium. *Carbohydr. Polym.* **2017**, *178*, 200–208. [\[CrossRef\]](#)
180. Hassan, R.; Zaafarani, I.; Gobouri, A.; Takagi, H. A revisit to the corrosion inhibition of aluminum in aqueous alkaline solutions by water-soluble alginates and pectates as anionic polyelectrolyte inhibitors. *Int. J. Corros.* **2013**, *2013*, 508596. [\[CrossRef\]](#)
181. Zaafarani, I. Corrosion inhibition of aluminum in aqueous alkaline solutions by alginate and pectate water-soluble natural polymer anionic polyelectrolytes. *Port. Electrochim. Acta* **2012**, *30*, 419–426. [\[CrossRef\]](#)
182. Umoren, S.A.; Eduok, U.M. Application of carboxylate polymers as corrosion inhibitors for metal substrates in different media: A review. *Carbohydr. Polym.* **2016**, *140*, 314–341. [\[CrossRef\]](#) [\[PubMed\]](#)
183. Dang, N.; Wei, Y.H.; Hou, L.F.; Li, Y.G.; Guo, C.L. Investigation of the inhibition effect of the environmentally friendly inhibitor sodium alginate on magnesium alloy in sodium chloride solution. *Mater. Corros.* **2015**, *66*, 1354–1362. [\[CrossRef\]](#)
184. Hou, L.; Dang, N.; Yang, H.; Liu, B.; Li, Y.; Wei, Y.; Chen, X.B. A combined inhibiting effect of sodium alginate and sodium phosphate on the corrosion of magnesium alloy AZ31 in NaCl solution. *J. Electrochem. Soc.* **2016**, *163*, C486–C494. [\[CrossRef\]](#)
185. Li, Y.; Ba, Z.X.; Li, Y.L.; Ge, Y.; Zhu, X.C. Influence of sodium alginate inhibitor addition on the corrosion protection performance of AZ91D magnesium alloy in NaCl solution. *Anti-Corros. Methods Mater.* **2017**, *64*, 486–491. [\[CrossRef\]](#)
186. Zhao, T.; Wang, Z.; Feng, Y.; Li, Q. Synergistic corrosion inhibition of sodium phosphate and sodium dodecyl sulphate on magnesium alloy AZ91 in 3.5 wt% NaCl solution. *Mater. Today Commun.* **2022**, *31*, 103568. [\[CrossRef\]](#)
187. Liu, D.; Han, E.H.; Song, Y.; Shan, D. Enhancing the self-healing property by adding the synergetic corrosion inhibitors of Na<sub>3</sub>PO<sub>4</sub> and 2-mercaptobenzothiazole into the coating of Mg alloy. *Electrochim. Acta* **2019**, *323*, 134796. [\[CrossRef\]](#)
188. Lamaka, S.V.; Lourenço, M.M.; Ivanov, D.K.; Zheludkevich, M.L.; Ferreira, M.G.S.; Hack, T. Fault-tolerant composite protective coating for WE43 magnesium alloy. In Proceedings of the IMA 2014 World Annual Magnesium Conference, München, Germany, 1–3 June 2014; pp. 116–122.
189. Shchukin, D.G. Container-based multi-functional self-healing polymer coatings. *Polym. Chem.* **2013**, *4*, 4871–4877.
190. Zheludkevich, M.L.; Tedim, J.; Ferreira, M.G.S. “Smart” coatings for active corrosion protection based on multi-functional micro and nanocontainers. *Electrochim. Acta* **2012**, *82*, 314–323. [\[CrossRef\]](#)
191. Wang, D.; Bierwagen, G.P. Sol-gel coatings on metals for corrosion protection. *Prog. Org. Coat.* **2009**, *64*, 327–338. [\[CrossRef\]](#)
192. Zhong, X.; Li, Q.; Hu, J.; Zhang, S.; Chen, B.; Xu, S.; Luo, F. A novel approach to heal the sol-gel coating system on magnesium alloy for corrosion protection. *Electrochim. Acta* **2010**, *55*, 2424–2429. [\[CrossRef\]](#)
193. Galio, A.F.; Lamaka, S.V.; Zheludkevich, M.L.; Dick, L.F.P.; Müller, I.L.; Ferreira, M.G.S. Inhibitor-doped sol-gel coatings for corrosion protection of magnesium alloy AZ31. *Surf. Coat. Technol.* **2010**, *204*, 1479–1486. [\[CrossRef\]](#)
194. Toorani, M.; Aliofkhaezai, M.; Mahdavian, M.; Naderi, R. Superior corrosion protection and adhesion strength of epoxy coating applied on AZ31 magnesium alloy pre-treated by PEO/Silane with inorganic and organic corrosion inhibitors. *Corros. Sci.* **2021**, *178*, 109065. [\[CrossRef\]](#)
195. Montemor, M.F.; Ferreira, M.G.S. Electrochemical study of modified bis-[triethoxysilylpropyl] tetrasulfide silane films applied on the AZ31 Mg alloy. *Electrochim. Acta* **2007**, *52*, 7486–7495. [\[CrossRef\]](#)
196. Zanotto, F.; Grassi, V.; Frignani, A.; Zucchi, F. Protection of the AZ31 magnesium alloy with cerium modified silane coatings. *Mater. Chem. Phys.* **2011**, *129*, 1–8. [\[CrossRef\]](#)
197. Hernández-Barrios, C.A.; Saavedra, J.A.; Higuera, S.L.; Coy, A.E.; Viejo, F. Effect of cerium on the physicochemical and anticorrosive features of TEOS-GPTMS sol-gel coatings deposited on the AZ31 magnesium alloy. *Surf. Interfaces* **2020**, *21*, 100671. [\[CrossRef\]](#)
198. Van Soestbergen, M.; Baukh, V.; Erich, S.; Huinink, H.; Adan, O. Release of cerium dibutylphosphate corrosion inhibitors from highly filled epoxy coating systems. *Prog. Org. Coat.* **2014**, *77*, 1562–1568. [\[CrossRef\]](#)
199. Birbilis, N.; Buchheit, R.G.; Ho, D.L.; Forsyth, M. Inhibition of AA2024-T3 on a phase-by-phase basis using an environmentally benign inhibitor, cerium dibutyl phosphate. *Electrochem. Solid State Lett.* **2005**, *8*, C180–C183. [\[CrossRef\]](#)
200. Calado, L.M.; Taryba, M.G.; Morozov, Y.; Carmezim, M.J.; Montemor, M.F. Novel smart and self-healing cerium phosphate-based corrosion inhibitor for AZ31 magnesium alloy. *Corros. Sci.* **2020**, *170*, 108648. [\[CrossRef\]](#)
201. Calado, L.M.; Taryba, M.G.; Morozov, Y.; Carmezim, M.J.; Montemor, M. Cerium phosphate-based inhibitor for smart corrosion protection of WE43 magnesium alloy. *Electrochim. Acta* **2021**, *365*, 137368. [\[CrossRef\]](#)

202. Ashassi-Sorkhabi, H.; Moradi-Alavian, S.; Esrafil, M.D.; Kazempour, A. Hybrid sol-gel coatings based on silanes-amino acids for corrosion protection of AZ91 magnesium alloy: Electrochemical and DFT insights. *Prog. Org. Coat.* **2019**, *131*, 191–202. [\[CrossRef\]](#)
203. Shchukin, D.G.; Zheludkevich, M.; Yasakau, K.; Lamaka, S.; Ferreira, M.G.S.; Möhwald, H. Layer-by-layer assembled nanocontainers for self-healing corrosion protection. *Adv. Mater.* **2006**, *18*, 1672–1678. [\[CrossRef\]](#)
204. Garcia-Heras, M.; Jimenez-Morales, A.; Casal, B.; Galvan, J.C.; Radzki, S.; Villegas, M.A. Preparation and electrochemical study of cerium–silica sol–gel thin films. *J. Alloys Compd.* **2004**, *380*, 219–224. [\[CrossRef\]](#)
205. Zhong, X.; Li, Q.; Hu, J.; Yang, X.; Luo, F.; Dai, Y. Effect of cerium concentration on microstructure, morphology and corrosion resistance of cerium-silica hybrid coatings on magnesium alloy AZ91D. *Prog. Org. Coat.* **2010**, *69*, 52–56. [\[CrossRef\]](#)
206. Adsul, S.H.; Siva, T.; Sathiyarayanan, S.; Sonawane, S.H.; Subasri, R. Self-healing ability of nanoclay-based hybrid sol-gel coatings on magnesium alloy AZ91D. *Surf. Coat. Technol.* **2017**, *309*, 609–620. [\[CrossRef\]](#)
207. Ashassi-Sorkhabi, H.; Moradi-Alavian, S.; Kazempour, A. Salt-nanoparticle systems incorporated into sol-gel coatings for corrosion protection of AZ91 magnesium alloy. *Prog. Org. Coat.* **2019**, *135*, 475–482. [\[CrossRef\]](#)
208. Adsul, S.H.; Bagale, U.D.; Sonawane, S.H.; Subasri, R. Release rate kinetics of corrosion inhibitor loaded halloysite nanotube-based anticorrosion coatings on magnesium alloy AZ91D. *J. Magnes. Alloy.* **2021**, *9*, 202–215. [\[CrossRef\]](#)
209. Ding, C.; Xu, J.; Tong, L.; Gong, G.; Jiang, W.; Fu, J. Design and Fabrication of a Novel Stimulus-Feedback Anticorrosion Coating Featured by Rapid Self-Healing Functionality for the Protection of Magnesium Alloy. *ACS Appl. Mater. Interfaces* **2017**, *9*, 21034–21047. [\[CrossRef\]](#) [\[PubMed\]](#)
210. Samadianfard, R.; Seifzadeh, D.; Habibi-Yangjeh, A. Sol-gel coating filled with SDS-stabilized fullerene nanoparticles for active corrosion protection of the magnesium alloy. *Surf. Coat. Technol.* **2021**, *419*, 127292. [\[CrossRef\]](#)
211. Mahmoudi, R.; Kardar, P.; Arabi, A.M.; Amini, R.; Pashbakhsh, P. The active corrosion performance of silane coating treated by praseodymium encapsulated with halloysite nanotubes. *Prog. Org. Coat.* **2020**, *138*, 105404. [\[CrossRef\]](#)
212. Shchukin, D.G.; Lamaka, S.V.; Yasakau, K.A.; Zheludkevich, M.L.; Ferreira, M.G.S.; Möhwald, H. Active Anticorrosion Coatings with Halloysite Nanocontainers. *J. Phys. Chem. C* **2008**, *112*, 958–964. [\[CrossRef\]](#)
213. Mei, D.; Lamaka, S.V.; Feiler, C.; Zheludkevich, M.L. The effect of small-molecule bio-relevant organic components at low concentration on the corrosion of commercially pure Mg and Mg-0.8Ca alloy: An overall perspective. *Corros. Sci.* **2019**, *153*, 258–271. [\[CrossRef\]](#)
214. Ashraf, M.A.; Liu, Z.; Peng, W.-X.; Yoysefi, N. Amino acid and TiO<sub>2</sub> nanoparticles mixture inserted into sol-gel coatings: An efficient corrosion protection system for AZ91 magnesium alloy. *Prog. Org. Coat.* **2019**, *136*, 105296. [\[CrossRef\]](#)
215. Upadhyay, V.; Bergseth, Z.; Kelly, B.; Battocchi, D. Silica-Based Sol-Gel Coating on Magnesium Alloy with Green Inhibitors. *Coatings* **2017**, *7*, 86. [\[CrossRef\]](#)
216. Abdollah Zadeh, M.; van der Zwaag, S.; Garcia, S.J. Self-healing corrosion-protective sol-gel coatings based on extrinsic and intrinsic healing approaches. In *Advances in Polymer Science*; Springer: Berlin/Heidelberg, Germany, 2016; Volume 273, pp. 185–218.
217. Bouali, A.C.; Serdechnova, M.; Blawert, C.; Tedim, J.; Ferreira, M.G.S.; Zheludkevich, M.L. Layered double hydroxides (LDHs) as functional materials for the corrosion protection of aluminum alloys: A review. *Appl. Mater. Today* **2020**, *21*, 100857. [\[CrossRef\]](#)
218. Yun, S.K.; Pinnavaia, T.J. Water content and particle texture of synthetic hydrotalcite-like layered double hydroxides. *Chem. Mater.* **1995**, *7*, 348–354. [\[CrossRef\]](#)
219. Tang, Y.; Wu, F.; Fang, L.; Guan, T.; Hu, J.; Zhang, S. A comparative study and optimization of corrosion resistance of ZnAl layered double hydroxides films intercalated with different anions on AZ31 Mg alloys. *Surf. Coat. Technol.* **2019**, *358*, 594–603. [\[CrossRef\]](#)
220. Guo, L.; Zhang, F.; Lu, J.-C.; Zeng, R.-C.; Li, S.-Q.; Song, L.; Zeng, J.-M. A comparison of corrosion inhibition of magnesium aluminum and zinc aluminum vanadate intercalated layered double hydroxides on magnesium alloys. *Front. Mater. Sci.* **2018**, *12*, 198–206. [\[CrossRef\]](#)
221. Wu, L.; Ding, X.; Zheng, Z.; Tang, A.; Zhang, G.; Atrens, A.; Pan, F. Doublely-doped Mg-Al-Ce-V2O7-LDH composite film on magnesium alloy AZ31 for anticorrosion. *J. Mater. Sci. Technol.* **2021**, *64*, 66–72. [\[CrossRef\]](#)
222. Wu, Y.; Wu, L.; Zheludkevich, M.L.; Chen, Y.; Serdechnova, M.; Yao, W.; Blawert, C.; Atrens, A.; Pan, F. MgAl-V2O7 4-LDHs/(PEI/MXene) 10 composite film for magnesium alloy corrosion protection. *J. Mater. Sci. Technol.* **2021**, *91*, 28–39. [\[CrossRef\]](#)
223. Wang, X.; Li, L.; Xie, Z.-H.; Yu, G. Duplex coating combining layered double hydroxide and 8-quinolinol layers on Mg alloy for corrosion protection. *Electrochim. Acta* **2018**, *283*, 1845–1857. [\[CrossRef\]](#)
224. Miyata, S. Anion-exchange properties of hydrotalcite-like compounds. *Clays Clay Miner.* **1983**, *31*, 305–311. [\[CrossRef\]](#)
225. Asl, V.Z.; Zhao, J.; Anjum, M.J.; Wei, S.; Wang, W.; Zhao, Z. The effect of cerium cation on the microstructure and anti-corrosion performance of LDH conversion coatings on AZ31 magnesium alloy. *J. Alloys Compd.* **2020**, *821*, 153248.
226. Song, Y.; Tang, Y.; Fang, L.; Wu, F.; Zeng, X.; Hu, J.; Zhang, S.F.; Jiang, B.; Luo, H. Enhancement of corrosion resistance of AZ31 Mg alloys by one-step in situ synthesis of ZnAl-LDH films intercalated with organic anions (ASP, La). *J. Magnes. Alloy.* **2021**, *9*, 658–667. [\[CrossRef\]](#)
227. Chen, J.; Fang, L.; Wu, F.; Xie, J.; Hu, J.; Jiang, B.; Luo, H. Corrosion resistance of a self-healing rose-like MgAl-LDH coating intercalated with aspartic acid on AZ31 Mg alloy. *Prog. Org. Coat.* **2019**, *136*, 105234. [\[CrossRef\]](#)

228. Anjum, M.J.; Zhao, J.; Asl, V.Z.; Yasin, G.; Wang, W.; Wei, S.; Zhao, Z.; Khan, W.Q. In-situ intercalation of 8-hydroxyquinoline in Mg-Al LDH coating to improve the corrosion resistance of AZ31. *Corros. Sci.* **2019**, *157*, 1–10. [\[CrossRef\]](#)
229. Anjum, M.J.; Zhao, J.-M.; Asl, V.Z.; Malik, M.U.; Yasin, G.; Khan, W.Q. Green corrosion inhibitors intercalated Mg:Al layered double hydroxide coatings to protect Mg alloy. *Rare Met.* **2021**, *40*, 2254–2265. [\[CrossRef\]](#)
230. Li, L.-X.; Xie, Z.-H.; Fernandez, C.; Wu, L.; Cheng, D.; Jiang, X.-H.; Zhong, C.-J. Development of a thiophene derivative modified LDH coating for Mg alloy corrosion protection. *Electrochim. Acta* **2020**, *330*, 135186. [\[CrossRef\]](#)
231. Song, Y.; Wang, H.; Liu, Q.; Li, G.; Wang, S.; Zhu, X. Sodium dodecyl sulfate (SDS) intercalated MgAl layered double hydroxides film to enhance the corrosion resistance of AZ31 magnesium alloy. *Surf. Coat. Technol.* **2021**, *422*, 127524. [\[CrossRef\]](#)
232. Yang, Q.; Tabish, M.; Wang, J.; Zhao, J. Enhanced Corrosion Resistance of Layered Double Hydroxide Films on Mg Alloy: The Key Role of Cationic Surfactant. *Materials* **2022**, *15*, 2028. [\[CrossRef\]](#)
233. Huang, M.; Lu, G.; Pu, J.; Qiang, Y. Superhydrophobic and smart MgAl-LDH anti-corrosion coating on AZ31 Mg surface. *J. Ind. Eng. Chem.* **2021**, *103*, 154–164. [\[CrossRef\]](#)
234. Zhang, R.F.; Zhang, S.F.; Yang, N.; Yao, L.J.; He, F.X.; Zhou, Y.P.; Xu, X.; Chang, L.; Bai, S.J. Influence of 8-hydroxyquinoline on properties of anodic coatings obtained by micro arc oxidation on AZ91 magnesium alloys. *J. Alloys Compd.* **2012**, *539*, 249–255. [\[CrossRef\]](#)
235. Cao, F.h.; Cao, J.l.; Zhang, Z.; Zhang, J.q.; Cao, C.n. Plasma electrolytic oxidation of AZ91D magnesium alloy with different additives and its corrosion behavior. *Mater. Corros.* **2007**, *58*, 696–703. [\[CrossRef\]](#)
236. Liu, Y.; Wei, Z.; Yang, F.; Zhang, Z. Environmental friendly anodizing of AZ91D magnesium alloy in alkaline borate-benzoate electrolyte. *J. Alloys Compd.* **2011**, *509*, 6440–6446. [\[CrossRef\]](#)
237. Darband, G.B.; Aliofkhaezai, M.; Hamghalam, P.; Valizade, N. Plasma electrolytic oxidation of magnesium and its alloys: Mechanism, properties and applications. *J. Magnes. Alloy.* **2017**, *5*, 74–132. [\[CrossRef\]](#)
238. Toorani, M.; Aliofkhaezai, M.; Golabadi, M.; Rouhaghdam, A.S. Effect of lanthanum nitrate on the microstructure and electrochemical behavior of PEO coatings on AZ31 Mg alloy. *J. Alloys Compd.* **2017**, *719*, 242–255. [\[CrossRef\]](#)
239. Blawert, C.; Heitmann, V.; Dietzel, W.; Nykyforchyn, H.M.; Klappkiv, M.D. Influence of electrolyte on corrosion properties of plasma electrolytic conversion coated magnesium alloys. *Surf. Coat. Technol.* **2007**, *201*, 8709–8714. [\[CrossRef\]](#)
240. Mingo, B.; Arrabal, R.; Mohedano, M.; Llamazares, Y.; Matykina, E.; Yerokhin, A.; Pardo, A. Influence of sealing post-treatments on the corrosion resistance of PEO coated AZ91 magnesium alloy. *Appl. Surf. Sci.* **2018**, *433*, 653–667. [\[CrossRef\]](#)
241. Mohedano, M.; Blawert, C.; Zheludkevich, M.L. Cerium-based sealing of PEO coated AM50 magnesium alloy. *Surf. Coat. Technol.* **2015**, *269*, 145–154. [\[CrossRef\]](#)
242. Van Phuong, N.; Fazal, B.R.; Moon, S. Cerium-and phosphate-based sealing treatments of PEO coated AZ31 Mg alloy. *Surf. Coat. Technol.* **2017**, *309*, 86–95. [\[CrossRef\]](#)
243. Laleh, M.; Kargar, F.; Rouhaghdam, A.S. Investigation of rare earth sealing of porous micro-arc oxidation coating formed on AZ91D magnesium alloy. *J. Rare Earths* **2012**, *30*, 1293–1297. [\[CrossRef\]](#)
244. Mohedano, M.; Pérez, P.; Matykina, E.; Pillado, B.; Garcés, G.; Arrabal, R. PEO coating with Ce-sealing for corrosion protection of LPSO Mg–Y–Zn alloy. *Surf. Coat. Technol.* **2020**, *383*, 125253. [\[CrossRef\]](#)
245. Pezzato, L.; Babbolin, R.; Cerchier, P.; Marigo, M.; Dolcet, P.; Dabalà, M.; Brunelli, K. Sealing of PEO coated AZ91magnesium alloy using solutions containing neodymium. *Corros. Sci.* **2020**, *173*, 108741. [\[CrossRef\]](#)
246. Pezzato, L.; Brunelli, K.; Babbolin, R.; Dolcet, P.; Dabalà, M. Sealing of PEO coated AZ91 magnesium alloy using La-based solutions. *Int. J. Corros.* **2017**, *2017*, 5305218. [\[CrossRef\]](#)
247. Sun, M.; Matthews, A.; Yerokhin, A. Plasma electrolytic oxidation coatings on cp-Mg with cerium nitrate and benzotriazole immersion post-treatments. *Surf. Coat. Technol.* **2018**, *344*, 330–341. [\[CrossRef\]](#)
248. Mohedano, M.; Blawert, C.; Zheludkevich, M. Silicate-based plasma electrolytic oxidation (PEO) coatings with incorporated CeO<sub>2</sub> particles on AM50 magnesium alloy. *Mater. Des.* **2015**, *86*, 735–744. [\[CrossRef\]](#)
249. Toorani, M.; Aliofkhaezai, M.; Sabour Rouhaghdam, A. Microstructural, protective, inhibitory and semiconducting properties of PEO coatings containing CeO<sub>2</sub> nanoparticles formed on AZ31 Mg alloy. *Surf. Coat. Technol.* **2018**, *352*, 561–580. [\[CrossRef\]](#)
250. Malayoglu, U.; Tekin, K.C.; Shrestha, S. Influence of post-treatment on the corrosion resistance of PEO coated AM50B and AM60B Mg alloys. *Surf. Coat. Technol.* **2010**, *205*, 1793–1798. [\[CrossRef\]](#)
251. Gnedenkov, A.S.; Sinebryukhov, S.L.; Mashtalyar, D.V.; Gnedenkov, S.V. Protective properties of inhibitor-containing composite coatings on a Mg alloy. *Corros. Sci.* **2016**, *102*, 348–354. [\[CrossRef\]](#)
252. Gnedenkov, A.S.; Sinebryukhov, S.L.; Mashtalyar, D.V.; Gnedenkov, S.V. Localized corrosion of the Mg alloys with inhibitor-containing coatings: SVET and SIET studies. *Corros. Sci.* **2016**, *102*, 269–278. [\[CrossRef\]](#)
253. Kaseem, M.; Ko, Y.G. Formation of flower-like structures for optimizing the corrosion resistance of Mg alloy. *Mater. Lett.* **2018**, *221*, 196–200. [\[CrossRef\]](#)
254. Zhang, G.; Wu, L.; Tang, A.; Ma, Y.; Song, G.-L.; Zheng, D.; Jiang, B.; Atrens, A.; Pan, F. Active corrosion protection by a smart coating based on a MgAl-layered double hydroxide on a cerium-modified plasma electrolytic oxidation coating on Mg alloy AZ31. *Corros. Sci.* **2018**, *139*, 370–382. [\[CrossRef\]](#)
255. Al Zoubi, W.; Ko, Y.G. Self-assembly of hierarchical N-heterocycles-inorganic materials into three-dimensional structure for superior corrosion protection. *Chem. Eng. J.* **2019**, *356*, 850–856. [\[CrossRef\]](#)

256. Liu, D.; Song, Y.; Shan, D.; Han, E.H. Self-Healing Coatings Prepared by Loading Interphase Inhibitors into MAO Coating of AM60 Mg Alloy. *J. Electrochem. Soc.* **2018**, *165*, C412–C421. [\[CrossRef\]](#)
257. Lu, X.P.; Blawert, C.; Tolnai, D.; Subroto, T.; Kainer, K.U.; Zhang, T.; Wang, F.H.; Zheludkevich, M.L. 3D reconstruction of plasma electrolytic oxidation coatings on Mg alloy via synchrotron radiation tomography. *Corros. Sci.* **2018**, *139*, 395–402. [\[CrossRef\]](#)
258. Curran, J.A.; Clyne, T.W. Porosity in plasma electrolytic oxide coatings. *Acta Mater.* **2006**, *54*, 1985–1993. [\[CrossRef\]](#)
259. Dong, K.; Song, Y.; Shan, D.; Han, E.-H. Corrosion behavior of a self-sealing pore micro-arc oxidation film on AM60 magnesium alloy. *Corros. Sci.* **2015**, *100*, 275–283. [\[CrossRef\]](#)
260. Zhang, G.; Jiang, E.; Wu, L.; Ma, W.; Yang, H.; Tang, A.; Pan, F. Corrosion protection properties of different inhibitors containing PEO/LDHs composite coating on magnesium alloy AZ31. *Sci. Rep.* **2021**, *11*, 2774. [\[CrossRef\]](#)
261. Peng, F.; Wang, D.; Tian, Y.; Cao, H.; Qiao, Y.; Liu, X. Sealing the pores of PEO coating with Mg-Al layered double hydroxide: Enhanced corrosion resistance, cytocompatibility and drug delivery ability. *Sci. Rep.* **2017**, *7*, 1–12. [\[CrossRef\]](#) [\[PubMed\]](#)
262. Yang, J.; Blawert, C.; Lamaka, S.V.; Snihrova, D.; Lu, X.; Di, S.; Zheludkevich, M.L. Corrosion protection properties of inhibitor containing hybrid PEO-epoxy coating on magnesium. *Corros. Sci.* **2018**, *140*, 99–110. [\[CrossRef\]](#)
263. Zoubi, W.A.; Min, J.H.; Ko, Y.G. Hybrid organic-inorganic coatings via electron transfer behaviour. *Sci. Rep.* **2017**, *7*, 7063. [\[CrossRef\]](#) [\[PubMed\]](#)
264. Wierzbicka, E.; Vaghefinazari, B.; Lamaka, S.V.; Zheludkevich, M.L.; Mohedano, M.; Moreno, L.; Visser, P.; Rodriguez, A.; Velasco, J.; Arrabal, R.; et al. Flash-PEO as an alternative to chromate conversion coatings for corrosion protection of Mg alloy. *Corros. Sci.* **2021**, *180*, 109189. [\[CrossRef\]](#)
265. Chen, Y.; Lu, X.; Lamaka, S.V.; Ju, P.; Blawert, C.; Zhang, T.; Wang, F.; Zheludkevich, M.L. Active protection of Mg alloy by composite PEO coating loaded with corrosion inhibitors. *Appl. Surf. Sci.* **2020**, *504*, 144462. [\[CrossRef\]](#)
266. Wu, W.X.; Wang, W.P.; Lin, H.C. A study on corrosion behavior of micro-arc oxidation coatings doped with 2-aminobenzimidazole loaded halloysite nanotubes on AZ31 magnesium alloys. *Surf. Coat. Technol.* **2021**, *416*, 127116. [\[CrossRef\]](#)
267. Sun, M.; Yerokhin, A.; Bychkova, M.Y.; Shtansky, D.V.; Levashov, E.A.; Matthews, A. Self-healing plasma electrolytic oxidation coatings doped with benzotriazole loaded halloysite nanotubes on AM50 magnesium alloy. *Corros. Sci.* **2016**, *111*, 753–769. [\[CrossRef\]](#)
268. Mingo, B.; Guo, Y.; Němcová, A.; Gholinia, A.; Mohedano, M.; Sun, M.; Matthews, A.; Yerokhin, A. Incorporation of halloysite nanotubes into forsterite surface layer during plasma electrolytic oxidation of AM50 Mg alloy. *Electrochim. Acta* **2019**, *299*, 772–788. [\[CrossRef\]](#)
269. Li, Y.; Lu, X.; Serdechnova, M.; Blawert, C.; Zheludkevich, M.L.; Qian, K.; Zhang, T.; Wang, F. Incorporation of LDH nanocontainers into plasma electrolytic oxidation coatings on Mg alloy. *J. Magnes. Alloy.* **2021**, in press. [\[CrossRef\]](#)
270. Zhang, G.; Wu, L.; Serdechnova, M.; Tang, A.; Wang, C.; Blawert, C.; Pan, F.; Zheludkevich, M.L. In-situ LDHs growth on PEO coatings on AZ31 magnesium alloy for active protection: Roles of PEO composition and conversion solution. *J. Magnes. Alloy.* **2021**, in press. [\[CrossRef\]](#)
271. Chen, J.; Lin, W.; Liang, S.; Zou, L.; Wang, C.; Wang, B.; Yan, M.; Cui, X. Effect of alloy cations on corrosion resistance of LDH/MAO coating on magnesium alloy. *Appl. Surf. Sci.* **2019**, *463*, 535–544. [\[CrossRef\]](#)
272. Song, Z.; Xie, Z.; Ding, L.; Zhang, Y.; Hu, X. Preparation of corrosion-resistant MgAl-LDH/Ni composite coating on Mg alloy AZ31B. *Colloids Surf. A: Physicochem. Eng. Asp.* **2022**, *632*, 127699. [\[CrossRef\]](#)
273. Zhang, D.; Peng, F.; Qiu, J.; Tan, J.; Zhang, X.; Chen, S.; Qian, S.; Liu, X. Regulating corrosion reactions to enhance the anti-corrosion and self-healing abilities of PEO coating on magnesium. *Corros. Sci.* **2021**, *192*, 109840. [\[CrossRef\]](#)
274. Visser, P.; Gonzalez-Garcia, Y.; Mol, J.M.C.; Terryn, H. Mechanism of Passive Layer Formation on AA2024-T3 from Alkaline Lithium Carbonate Solutions in the Presence of Sodium Chloride. *J. Electrochem. Soc.* **2018**, *165*, C60–C70. [\[CrossRef\]](#)
275. Visser, P.; Liu, Y.; Zhou, X.; Hashimoto, T.; Thompson, G.E.; Lyon, S.B.; Van Der Ven, L.G.J.; Mol, A.J.M.C.; Terryn, H.A. The corrosion protection of AA2024-T3 aluminium alloy by leaching of lithium-containing salts from organic coatings. *Faraday Discuss.* **2015**, *180*, 511–526. [\[CrossRef\]](#) [\[PubMed\]](#)
276. Visser, P.; Marcoen, K.; Trindade, G.F.; Abel, M.L.; Watts, J.F.; Hauffman, T.; Mol, J.M.C.; Terryn, H. The chemical throwing power of lithium-based inhibitors from organic coatings on AA2024-T3. *Corros. Sci.* **2019**, *150*, 194–206. [\[CrossRef\]](#)
277. Marcoen, K.; Visser, P.; Trindade, G.F.; Abel, M.L.; Watts, J.F.; Mol, J.M.C.; Terryn, H.; Hauffman, T. Compositional study of a corrosion protective layer formed by leachable lithium salts in a coating defect on AA2024-T3 aluminium alloys. *Prog. Org. Coat.* **2018**, *119*, 65–75. [\[CrossRef\]](#)
278. Visser, P.; Terryn, H.; Mol, J.M.C. Active corrosion protection of various aluminium alloys by lithium-leaching coatings. *Surf. Interface Anal.* **2019**, *51*, 1276–1287. [\[CrossRef\]](#)
279. Visser, P.; Lutz, A.; Mol, J.M.C.; Terryn, H. Study of the formation of a protective layer in a defect from lithium-leaching organic coatings. *Prog. Org. Coat.* **2016**, *99*, 80–90. [\[CrossRef\]](#)



### 3 Motivation and objectives

The global push for sustainable development and energy efficiency is driving industries like automotive, aerospace, and biomedical engineering to seek materials that reduce environmental impact while maintaining high performance. Magnesium alloys are at the forefront of this movement due to their remarkable strength-to-weight ratio, low density, and other advantageous properties, making them ideal for a wide range of applications. However, the potential of Mg alloys is significantly hindered by their high susceptibility to corrosion, particularly in aqueous environments. Overcoming this limitation is essential for the broader adoption of Mg alloys in critical industrial applications.

The use of PEO coatings has emerged as a promising solution to this challenge by providing a protective barrier against corrosive media. An especially valuable feature of PEO coatings is their ability to offer “active protection” by accommodating corrosion inhibitors within their porous structure. This active protection capability is highly desirable and has often been benchmarked against the traditional chromate(VI)-based protective systems, which are now banned in many industries due to environmental concerns, unless they are authorized under strict conditions.

Despite more than a decade of research, the field of incorporating corrosion inhibitors into PEO coatings on Mg alloys remains underexplored, with a limited number of inhibitors successfully integrated into PEO coatings. The need to identify and understand effective corrosion inhibitors for PEO-coated Mg alloys presents a significant scientific challenge and an industrial necessity, motivating the research presented in this thesis.

This thesis aims to identify and evaluate effective corrosion inhibitors specifically for PEO-coated Mg alloys. A critical aspect of this research is to uncover the mechanisms by which these inhibitors interact with both the PEO coating and the Mg substrate, addressing the challenges observed when inhibitors effective on bare Mg fail to perform in PEO-coated systems. The research also seeks to establish criteria for selecting the most effective corrosion inhibitors, providing a framework that can guide future investigations. Ultimately, the findings from this research are intended to offer valuable insights for future studies and practical applications in the development of durable, corrosion-resistant Mg alloys.

## 4 Experimental

### 4.1 Materials

AZ21 magnesium alloy cast and rolled in house (at Helmholtz Zentrum Hereon), was used as the main substrate. The thickness of the rolled plate was 2mm. The chemical composition of the AZ21 sheet, obtained via spark discharge-optical emission spectroscopy (SD-OES), Ametek-Spectro, is presented in **Table 1**. The concentrations of other trace elements were measured as below 5 ppm.

*Table 1 Elemental composition of AZ21 Mg substrate*

element	Al	Zn	Mn	Fe	Cu	Ni	Si	Mg
Concentration (unit)	1.59 ± 0.07 (wt.%)	1.05 ± 0.07 (wt.%)	0.29 (wt.%)	28 ± 1 (ppm)	22 ± 3 (ppm)	23 ± 1 (ppm)	650 (ppm)	balanced

In addition to the AZ21 magnesium alloy, a commercial pure (CP) magnesium was used in a part of investigations. The detail of material characterizations and sample preparation of the CP magnesium can be found in [154].

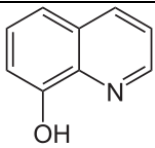
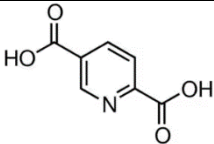
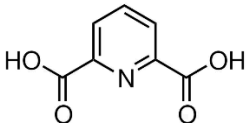
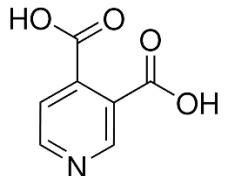
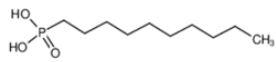
The surface of the specimens was ground under a stream of water, using SiC emery paper with progressively increasing grit sizes of 800, 1200, and 2500. Then, the samples were flushed with ethanol and dried with pressurized air.

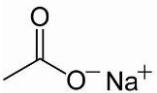
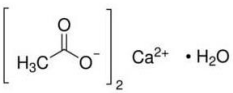
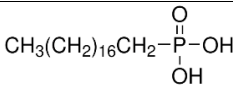
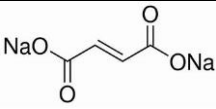
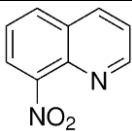
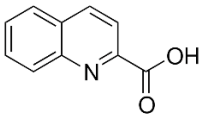
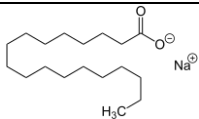
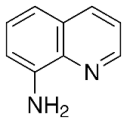
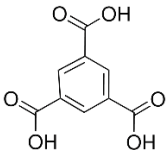
The main chemicals used in this work are listed in **Table 2**, along with their molecular structure, purity, and supplier.

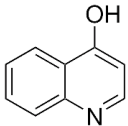
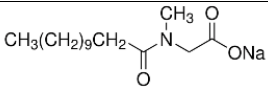
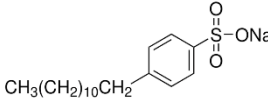
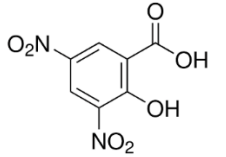
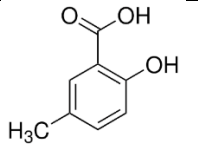
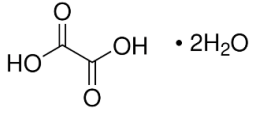
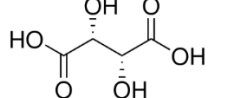
The concentration of inhibitors was 0.05 M, unless otherwise mentioned. In particular, the concentrations of 8HQ and DP in NaCl 3.5 wt.% were ~5mM and ~2mM, both at saturation condition, respectively.

The initial pH of solution containing inhibitors were always adjusted to  $7.0 \pm 0.1$  using NaOH solution. The pH values deviating from  $7.0 \pm 0.1$  are mentioned individually. The pH of the solutions was measured with Metrohm 713 pH meter equipped with InLab® Expert Pt1000 pH electrode from Mettler Toledo.

Table 2 information of chemicals used in this research.

	chemical	chemical formula (linear or empirical)	Molecular structure	purity	CAS number	application	supplier
1	8-Hydroxyquinoline (8HQ)	C <sub>9</sub> H <sub>7</sub> NO		99%	148-24-3	inhibitor	Alfa Aesar
2	2,5-Pyridinedicarboxylic acid (2,5-PDCA)	C <sub>7</sub> H <sub>5</sub> NO <sub>4</sub>		98%	100-26-5	inhibitor	Sigma-Aldrich
3	2,6-Pyridinedicarboxylic acid (2,6PDCA)	C <sub>7</sub> H <sub>5</sub> NO <sub>4</sub>		99%	499-83-2	inhibitor	Sigma-Aldrich
4	3,4-Pyridinedicarboxylic acid (3,4-PDCA)	C <sub>7</sub> H <sub>5</sub> NO <sub>4</sub>		97%	490-11-9	inhibitor	Sigma-Aldrich
5	Decylphosphonic acid	C <sub>10</sub> H <sub>23</sub> O <sub>3</sub> P		97%	6874-60-8	inhibitor	Sigma-Aldrich
6	Magnesium Oxide	MgO	MgO	97%	1309-48-4	Investigate the effect in the presence of 2,5PDC	Sigma-Aldrich
7	Sodium fluoride	NaF	NaF	>99%	7681-49-4	inhibitor	Carl Roth

8	Sodium acetate trihydrate	$\text{CH}_3\text{COONa} \cdot 3\text{H}_2\text{O}$		>99%	64-19-7	inhibitor	Carl Roth
9	Calcium acetate hydrate	$\text{C}_4\text{H}_8\text{CaO}_5$		>99%	5743-26-0	inhibitor	Fuka
10	Octadecylphosphonic acid	$\text{C}_{18}\text{H}_{39}\text{O}_3\text{P}$		97%	4724-47-4	inhibitor	Sigma-Aldrich
11	Sodium fumarate dibasic	$\text{NaOOCCH=CHCOONa}$		>99%	17013-01-3	inhibitor	Sigma-Aldrich
12	8-Nitroquinoline	$\text{C}_9\text{H}_6\text{N}_2\text{O}_2$		98%	607-35-2	inhibitor	Sigma-Aldrich
13	Quinaldic acid	$\text{C}_{10}\text{H}_7\text{NO}_2$		98%	93-10-7	inhibitor	Alfa Aesar
14	Stearic acid sodium salt	$\text{C}_{18}\text{H}_{35}\text{NaO}_2$		>88%	822-16-2	inhibitor	Carl Roth
15	8-Aminoquinoline	$\text{C}_9\text{H}_8\text{N}_2$		98%	578-66-5	inhibitor	Sigma-Aldrich
16	Trimesic acid	$\text{C}_6\text{H}_3(\text{CO}_2\text{H})_3$		95%	554-95-0	inhibitor	Sigma-Aldrich

17	4-Quinolinol	$C_9H_7NO$		98%	611-36-9	inhibitor	Sigma-Aldrich
18	N-Lauroylsarcosine sodium salt	$CH_3(CH_2)_{10}CON(CH_3)CH_2COONa$		>94%	137-16-6	inhibitor	Sigma-Aldrich
19	Sodium dodecylbenzenesulfonate	$CH_3(CH_2)_{11}C_6H_4SO_3Na$		Technical grade	25155-30-0	inhibitor	Sigma-Aldrich
20	Calcium Chloride	$CaCl_2$	$CaCl_2$	>98%	10043-52-4	inhibitor	Merck
21	3,5-Dinitrosalicylic acid	$(O_2N)_2C_6H_2-2-(OH)CO_2H$		>98%	609-99-4	inhibitor	Sigma-Aldrich
22	5-Methylsalicylic acid	$CH_3C_6H_3(OH)CO_2H$		98%	89-56-5	inhibitor	Alfa Aesar
23	Oxalic acid dihydrate	$HO_2CCO_2H \cdot 2H_2O$		99%	6153-56-6	inhibitor	Chempure
24	L(+)-Tartaric acid	$HO_2CCH(OH)CH(OH)CO_2H$		99.5%	87-69-4	inhibitor	Merck

## 4.2 PEO preparation

PEO coating was applied on AZ21 specimens with dimensions of  $20 \times 20 \times 2 \text{ mm}^3$  using a pulsed DC power source (Electro Automatik, Germany) and polarizing the sample at constant current regime.

A preliminary investigation was carried out to identify appropriate parameters for the application of PEO with two different electrolyte compositions based on phosphate and silicate. The primary acceptance criterion for the coatings was the uniformity of the coating, with no signs of partial detachment. This was assessed through visual observation and SEM characterization of the PEO cross-sections. The main PEO process parameters are provided in **Table 3**.

The electrolyte temperature is controlled at  $20 \pm 1 \text{ }^\circ\text{C}$  by a cooling system that utilizes a stainless-steel tube cathode. The PEO electrolyte was mixed during the PEO process via purging bubble air in the electrolyte.

After the PEO process, the specimens were first rinsed with a flush of DI-W and then immersed in DI-W for 20 min at a low-pressure condition ( $\sim 0.1 \text{ atm}$  pressure). This step was necessarily taken to diminish the influence of the remained PEO electrolytes on the evaluation of the results. Subsequently, the specimens were immersed in acetone (EMSURE<sup>®</sup> supplied by Sigma-Aldrich) for 20 min and finally dried in an oven at  $80 \text{ }^\circ\text{C}$  for 30 min.

To incorporate inhibitors into the PEO pores, the PEO-coated samples were immersed in the inhibitor solution under low-pressure conditions ( $\sim 0.9 \text{ atm}$ ) to increase the amount of solution entering the semi-closed pores of the PEO layer.

*Table 3 Process parameters of two PEO coatings*

	chemistry	electrolyte composition	applied current density	duration (minute)	duty cycle	final voltage (V)
1	phosphate	20g/L $\text{Na}_3\text{PO}_4$ + 2g/L KOH	$40 \text{ mA.cm}^{-2}$	10	1ms on, 9ms off	$400 \pm 4$
2	silicate	20g/L $\text{Na}_2\text{SiO}_3$ + 250mL/L Glycerol + 5 g/L KF + 2g/L KOH	$40 \text{ mA.cm}^{-2}$	10	1ms on, 9ms off	$471 \pm 8$

## 4.3 Localized measurement

The electrochemical corrosion processes typically lead to change of pH, and concentrations of  $\text{O}_2$  and  $\text{H}_2$  in the electrolyte. Therefore, monitoring these values provides valuable insights into the corrosion mechanisms and rate.

However, the conventional methods of measuring these values often fail to capture the highly localized nature of corrosion phenomena at the interface between metal surface and the electrolyte. Therefore, monitoring the local conditions near the substrate surface during exposure to a corrosive provides valuable insights into the corrosion mechanisms and rate.

Local concentration of dissolved  $\text{O}_2$  was measured using a fiber-optic OXR50-UHS  $\text{O}_2$  micro-optode coupled with a FireStringO2 fiber-optics oxygen meter (Pyroscience, Germany). Local concentration of dissolved  $\text{H}_2$  was measured using a  $\text{H}_2$  microsensor (10  $\mu\text{m}$  tip diameter, H2-10) connected to a fx-6 UniAmp (both from Unisense, Denmark). Both  $\text{O}_2$  optode and  $\text{H}_2$  probes were calibrated considering the salinity and temperature of the solution. Local pH was measured using a glass-type pH microelectrode (Unisense, pH-10).  $\text{H}_2$  and  $\text{O}_2$  local concentrations were measured simultaneously, using custom made dual-head stage, while the local pH was measured in a separate experiment with the same experimental setup. All three types of micro-sensors were integrated in commercial SVET-SIET system from Applicable Electronics for probe positioning and movement.

**Figure 4.1** presents an example of the localized measurement setup with two probes of  $\text{O}_2$  micro-optode and pH microelectrodes, simultaneously measuring the local ( $\sim 50\mu\text{m}$  above the surface) concentration of  $\text{O}_2$  and pH of the solution. The sample is exposed to a NaCl electrolyte.

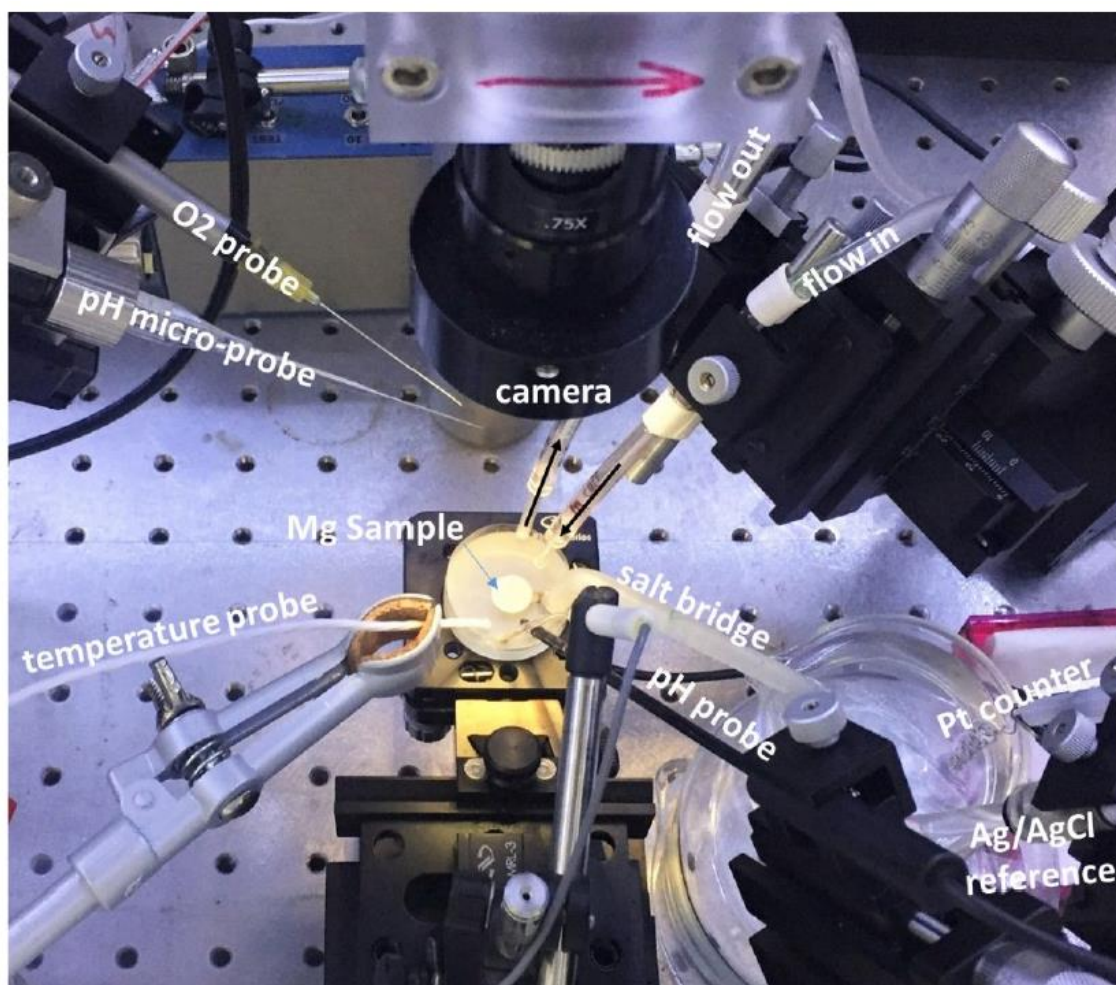


Figure 4.1 an example of the localized measurement setup adapted from [155] with permission from ACS Publications.

#### 4.4 Crystallographic characterization

Crystallographic characterization was carried out using an X-ray diffractometer (Bruker D8 Advance, Karlsruhe, Germany) with Cu K $\alpha$  radiation source generated with a voltage and current of 40 kV and 40 mA, respectively. The incident angle was between 3-4°. The dwell time was 1 s and 5 s for bare and PEO-coated magnesium specimens, respectively. The higher dwell time for PEO-coated specimens was chosen to reduce the strong noise in the acquired spectra. The diffraction angle ( $2\theta$ ) ranged between 5° and 70° with 0.02° step size.

High-resolution two dimensional XRD maps were acquired at the nanofocused end-station of beamline P03 at PETRAIII storage ring, Deutsches Elektronen-Synchrotron (DESY, Hamburg, Germany) [156]. The beam cross-section was 1.5  $\mu\text{m}$   $\times$  1.5  $\mu\text{m}$ . The beam energy was in the range of 15-19.8 keV employing an Eiger9m detector. Calibration of the detector with respect to beam center and sample to detector distance was done with lanthanum hexaboride. The acquisition time of each diffraction pattern was set to 0.5 s. Regions of 80  $\mu\text{m}$   $\times$  80  $\mu\text{m}$  were scanned with the step sizes of 2  $\mu\text{m}$  for both vertical and horizontal directions, respectively. Data reduction was performed using the software package pyFAI [157]. The analysis of the two-dimensional diffraction maps was conducted by inhouse developed Matlab scripts. The horizontal direction is parallel to the substrate surface. The details of the experimental set-up can be found in [158]. The  $2\theta$  values from the synchrotron beam wavelength were converted to Cu K $\alpha$  for easier comparison to the results obtained from lab XRD measurements.

## 4.5 Microscopy

The surface and cross-sectional morphology of the specimens were characterized using a scanning electron microscope (SEM, TESCAN Vega3 SB), equipped with an energy dispersive spectrometer system (EDS, eumeX IXRD systems). The acceleration voltage was 15 kV.

For selected cases, higher magnification microscope, a TESCAN LYRA3 equipped with a focused ion beam (FIB) system was used. For the preparation of the specimen cross-section, the samples were embedded in epoxy resin (EpoxiCure 2, Beuhler). The surface of the specimens was ground with SiC emery papers up to 4000 grit size. The subsequent polishing of the surface was carried out using a water-free silicon oxide polishing suspension (OPS™, Cloeren Technology GmbH). The surface of the samples was gold sputtered prior to SEM observation using a Cressington Sputter Coater 108auto.

## 4.6 Electrochemical tests

All the electrochemical characterizations were performed using Gamry interface 1000/1010 or reference 600 potentiostats. Platinum coil and Ag/AgCl electrode in saturated KCl were used as counter and reference electrodes, respectively. A surface area of 0.5 cm<sup>2</sup> from the working electrode was exposed to 400 ml of the testing solutions. **Figure 4.2** illustrates the general electrochemical test setup and connections between the potentiostat and electrodes.

The reference corrosion test electrolyte was NaCl 3.5 wt.%. The tests were carried out at  $22 \pm 2$  °C. Electrochemical impedance spectroscopy (EIS) tests were carried out under potentiostatic mode at open circuit potential (OCP) with a perturbation voltage of 10 mV<sub>rms</sub>. The scanned frequency ranged from 100 kHz to 0.01 Hz with 9 points per frequency decade acquisition.

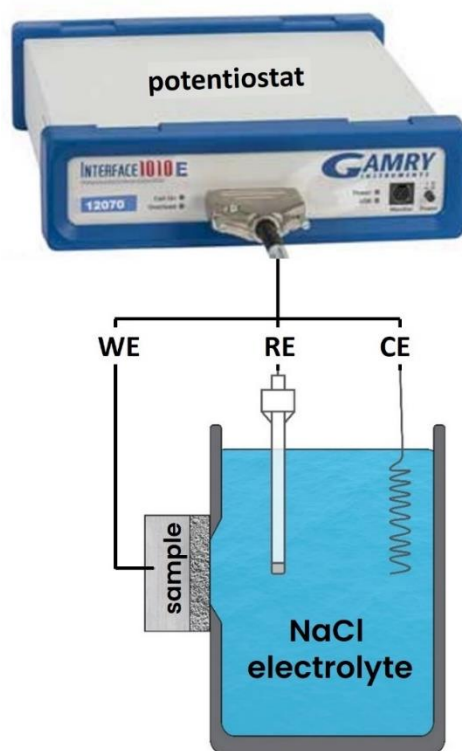


Figure 4.2 schematic electrode connections to potentiostat. RE : reference electrode. WE : working electrode. CE: counter electrode.

The stationarity of the system, as the requirement for the EIS tests, was assured by carefully observing the Lissajous curves during the test, especially at the low frequency range. Drift of Lissajous curve indicates deviation from the OCP condition, which means the non-stationarity of the system. In such cases, the EIS test was aborted and only the

acquired data points in the spectra were reported. In the case of testing bare AZ substrate, the solution was continuously stirred during the EIS test.

#### 4.7 Preparation of 8HQ(Mg) powder

8HQ(Mg) powder was used for comparison reasons and synthesized according to the following procedure: saturated solution of 8HQ was prepared in deionized water. 5 mM  $\text{MgCl}_2 \cdot 6\text{H}_2\text{O}$  (supplied from Sigma Aldrich) was added to the saturated 8HQ solution. Then, the solution pH was slowly adjusted to 9.5 using 0.1 M NaOH solution, at which the full yield of 8HQ(Mg) precipitation can be achieved [159]. During the entire process, the solution was vigorously stirred using a stirring magnet. The 8HQ(Mg) precipitations were collected from the solution using a centrifuge. The obtained powder was rinsed thoroughly with deionized water to remove the  $\text{Cl}^-$  ions. Finally, the powder was dried in oven at 80 °C.

#### 4.8 Weight loss measurement

The samples weight loss after exposure to the corrosive medium was measured by subtracting the initial and final weight of the samples. The corrosion products were removed using a solution of 180-200  $\text{g.l}^{-1}$   $\text{CrO}_3$  in deionized water.

The corrosion rate of the specimen was calculated from the weight loss based on **equation 4.1** according to standard ASTM-G1-03:

$$\text{corrosion rate (mm/year)} = \left( \frac{8.76 \times 10^4 \times \Delta W}{A \times t \times D} \right) \quad \text{equation 4.1,}$$

where  $\Delta W$  denotes mass loss in grams, A is the exposed area of the sample in  $\text{cm}^2$ , t is time of exposure in second, and D is the density of substrate in  $\text{g.cm}^{-3}$ .

The inhibition efficiency (IE) was calculated using the equation below:

$$IE (\%) = \frac{W_{ref} - W_{inh}}{W_{ref}} \times 100 \quad \text{equation 4.2}$$

$W_{ref}$  and  $W_{inh}$  denote the weight loss of bare AZ21 after exposure to the NaCl electrolyte without and with inhibitor, respectively.

#### 4.9 $\text{H}_2$ evolution test

A setup using eudiometers was adopted to measure the corrosion rate of bare AZ21 in different electrolytes by monitoring  $\text{H}_2$  evolution. The schematic of the  $\text{H}_2$  evolution test using the eudiometers is presented in **Figure 4.3**. The eudiometer cylinder was initially filled with water by pumping air into the cylinder from a valve on top. The evolved  $\text{H}_2$  from the cathodic hydrogen evolution reaction (HER) on the magnesium substrate displaced the water in the cylinder, pushing it back to the main water source bottle.

The volume of the collected  $\text{H}_2$  was recorded by weighing the displaced water returned to the main water bottle using an electronic balance (OHAUS, SKX2202). These values were automatically recorded using a USB data logger (OHAUS, 30268984) and a custom-developed Python script. AZ21 pieces with dimensions of  $2 \text{ mm} \times 100 \pm 1 \text{ mm} \times 14 \pm 1 \text{ mm}$  ( $32.2 \pm 2.9 \text{ cm}^2$  total surface area) were fully immersed in the testing electrolyte inside a container, which was connected and sealed to the eudiometer cylinder. The length of the samples allowed them to lean on the wall of the bottle, resulting in negligible contact points between the sample and the bottle. During the test, the 500 ml electrolyte was constantly stirred using magnetic stirrers. The effects of ambient temperature ( $22 \pm 1^\circ\text{C}$ ) and pressure on the volume of collected  $\text{H}_2$  were offset by simultaneously recording variations for an additional reference electrolyte without any immersed sample.

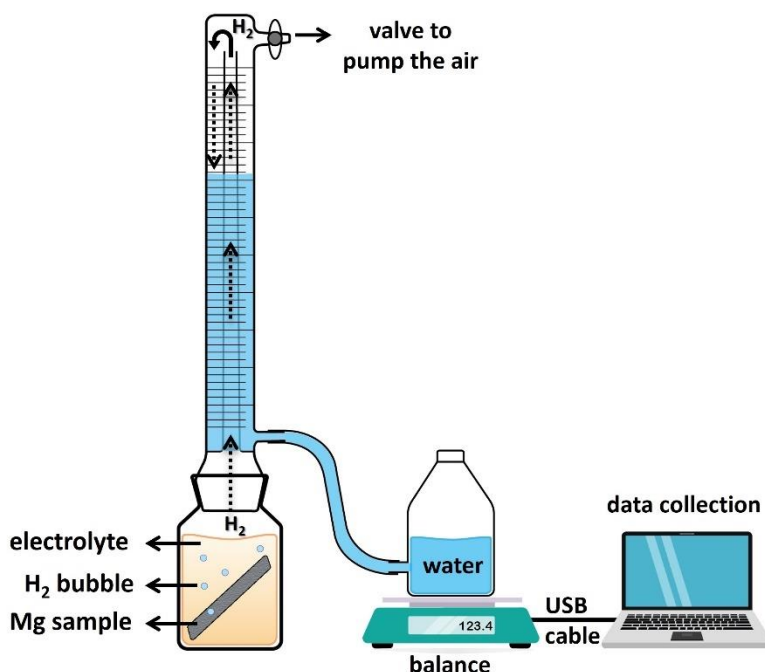


Figure 4.3 schematic of  $H_2$  evolution test. The generated  $H_2$  displaces the water inside the eudiometers, pushing it back into the water bottle on the balance. The change in the bottle's weight is continuously recorded by a data logger and a custom-developed Python script..

#### 4.10 Atomic Force Microscopy (AFM)

Atomic force microscopy (AFM, Nanowizard 4, JPK Instruments AG) in AC mode coupled with scanning Kelvin probe force microscopy (SKPFM) was conducted to analyze the surface morphology and measure the Volta potential difference (VPD) of the bare AZ21 Mg substrate. VPD measurements were carried out in HoverMode. In a first pass (trace) over the sample the topography is measured, and on the return pass (retrace) this topography information is used to maintain the cantilever at a constant offset height above the surface while running the Kelvin probe measurements procedure. The following parameters for the measurements were used: height offset 100 nm, modulation amplitude 1 V, scan size  $40\ \mu\text{m} \times 40\ \mu\text{m}$ , number of lines 512 and scan rate 0.3 Hz. Pt covered probes purchased from BudgetSensors (Multi75E-G; resonance frequency 75 kHz, force constant 3 N/m) were used. Prior to the measurements the VPD of the probes was recorded on a clean Ni surface and the results reported in this work display VPD (V) values measured on Mg samples vs. Ni. The output values were negative to be able to compare VPD with the electrochemical potentials of metals [160-162], where more negative values represent more active metals, while more positive represent more noble metals and/or presence of surface films [163]. The AFM measurement was carried out in open air condition and at room temperature about 22 °C and relative humidity of about 50%. The surface of the specimens was polished using a water-free silicon oxide polishing suspension (OPS™, Cloeren Technology GmbH). Then, the samples were flushed with ethanol and subsequently polished on a clean polishing cloth soaked in ethanol absolute (>99.9%, Chemsolute). Then, the surface of the samples was dried with pressurized  $N_2$ . Drop tests were carried out on the polished sample before the AFM measurement as follows: 50  $\mu\text{l}$  of different electrolytes were dispensed on the surface of the polished sample, dwelling for 60 s. Then, the drops were removed from the surface using pressurized  $N_2$ . All the drops from different electrolytes left similar circular marks with diameter between 7 and 8.5 mm.

#### 4.11 Time of Flight Secondary Ion Mass Spectroscopy (ToF-SIMS)

Time of Flight Secondary Ion Mass Spectrometry (ToF-SIMS) analyses were performed using a ToF-SIMS V spectrometer (ION TOF GmbH, Munster, Germany) operating at a pressure of approximately  $10^{-9}$  mbar. Data acquisition and post processing analysis were performed using the SurfaceLab software (version 6.5). The spectrometer was run in the HC-BUNCHED mode in order to get a high mass resolution ( $M/DM$  around 8000).

Negative ions depth profiles were recorded by sequential analysis ( $\text{Bi}^+$ , 25 keV, 1 pA,  $100 \times 100 \mu\text{m}^2$ ) and sputtering of the sample surface. The analysis beam was a pulsed 25 keV  $\text{Bi}^+$  ion source delivering 1.2 pA of target current over a  $100 \times 100 \mu\text{m}^2$  area, interlaced with a 1 keV  $\text{Cs}^+$  sputter beam delivering 30 nA target current over a  $300 \times 300 \mu\text{m}^2$  area. Both guns have a  $45^\circ$  incidence angle with respect to the specimen surface.  $\text{Bi}^+$  ion flux was set below  $10^{12} \text{ ions.cm}^{-2}$  to ensure quasi-static conditions. Analysis was centered inside the sputtered crater to avoid edge effects. In the depth profiles, the intensity of the characteristic species is reported using a logarithmic scale, which gave equal emphasis to signals of all intensities. The variation of the intensity with sputtering time reflects the variation of the in-depth concentration but is also dependent on the matrix from which the ions are emitted.

Specific ions were chosen to describe the corrosion layer, the inhibitor, and the elements constituting the electrolyte. Thus,  $\text{MgO}_2^-$  (55.975 amu),  $\text{MgOH}^-$  (40.988 amu),  $\text{MgH}^-$  (24.993 amu),  $25\text{MgH}^-$  (25.994 amu) are selected since these ions are characteristic of the Mg oxide, Mg hydroxide and Mg hydride species respectively [164].  $\text{Cl}^-$  (34.969 amu),  $\text{Na}^-$  (22.990 amu) and  $\text{CO}_3^-$  (59.985 amu) represent chloride, sodium and carbonate species, respectively, while  $\text{C}_7\text{H}_4\text{NO}_4\text{Mg}^-$  (157.022 amu) is a marker of the PDCA (as identified on the ToF-SIMS mass spectrum, not shown here).

#### 4.12 Raman spectroscopy

Confocal Raman spectroscopy was performed by a Senterra Raman microscope (Bruker). All spectra were collected with an excitation wavelength of 785 nm, a laser power of 50 mW, an aperture of  $25 \mu\text{m}$  and 256 scans for the PEO layers and 64 scans for the raw materials, which were used for an appropriate signal-to-noise ratio. The integration time was 3 s in all cases. Validation and evaluation of the data were carried out with the Bruker OPUS software version 7.5.

## 5 Results

### 5.1 Overview

The results of this thesis are presented in four separate sections, as outlined below:

- **Section 5.2:** Screening of Corrosion Inhibitors
- **Section 5.3:** Adverse Effect of 2,5-PDC Corrosion Inhibitors (Peer-Reviewed Paper)
- **Section 5.4:** Exploring the Corrosion Inhibition Mechanism of 8-Hydroxyquinoline for a PEO-Coated Magnesium Alloy (Peer-Reviewed Paper)
- **Section 5.5:** Corrosion Inhibition of Decylphosphonate on Bare and PEO-Coated Mg Alloy (Peer-Reviewed Paper)

The initial phase of this research involved screening various compounds for their corrosion inhibition effects on bare and PEO-coated magnesium. In the first section of this chapter (**Section 5.2**), the screened inhibitors are listed, and their effects on both bare and PEO-coated AZ21 alloy are discussed. Based on the screening results, three inhibitors were selected for more detailed investigation. First, an unexpected adverse effect of the corrosion inhibitor 2,5-pyridinedicarboxylate on the PEO-coated AZ21 alloy was examined (**Section 5.3**). Subsequently, two outperforming inhibitors, 8-Hydroxyquinoline (**Section 5.4**) and decylphosphonate (**Section 5.5**), were investigated to explore their inhibition mechanisms. The findings from these studies have been published in peer-reviewed scientific journals and are incorporated into this thesis in the corresponding chapters.

## 5.2 Screening of corrosion inhibitors

The initial stage of this research focused on the screening of several potentially effective corrosion inhibitors. A list of corrosion inhibitor candidates was compiled mainly based on a literature review. Notably, a comprehensive screening by Lamaka et al. [17] provided a list of more than 150 chemicals and their corrosion inhibition effect for several magnesium alloys in their bare condition. As a result of this study several inhibitors with universal inhibition effect for different Mg alloys have been discovered, including Na-fumarate and derivatives of pyridinedicarboxylates. Later their effect was confirmed and their inhibition mechanisms were investigated by several studies [154, 163, 165-168]. The list of candidate inhibitors, however, was not limited to chemicals with high level of consistency from the literature in their positive effects. Several chemicals based on internal, unpublished results on corrosion inhibitors were also included in the screening campaign. The corrosion screening process was adaptive and iterative, with the list being updated based on the result of each test.

The inhibitor screening was conducted on two types of samples: 1) bare AZ21 substrate and 2) PEO-coated AZ21. For the bare AZ21 substrate, the assessment parameter was the weight loss of the samples after 4 days of exposure to a 3.5% NaCl solution, both with and without the inhibitor candidates. The electrolyte was in stagnant condition.

The evaluation of the effect of the inhibitor candidates on the PEO-coated AZ21 samples was conducted via EIS tests on the samples exposed to the NaCl medium with and without inhibitors. The exposure tests were stopped as soon as a failure in the PEO coating was observed. Failure of the PEO coating is defined as the detachment of a chunk of the PEO layer, which usually appears as a black, pitting-like region on the sample surface. **Figure 5.1 (a)** shows an example of failure marks on the PEO coating exposed to NaCl 3.5 wt.% after 4 days. This failure is also reflected as a drastic drop in impedance values at low-frequency range due to the complete deterioration of the PEO layer in the locally affected area. **Figure 5.1 (b)** illustrates such a drop in the EIS spectra at low frequency range.

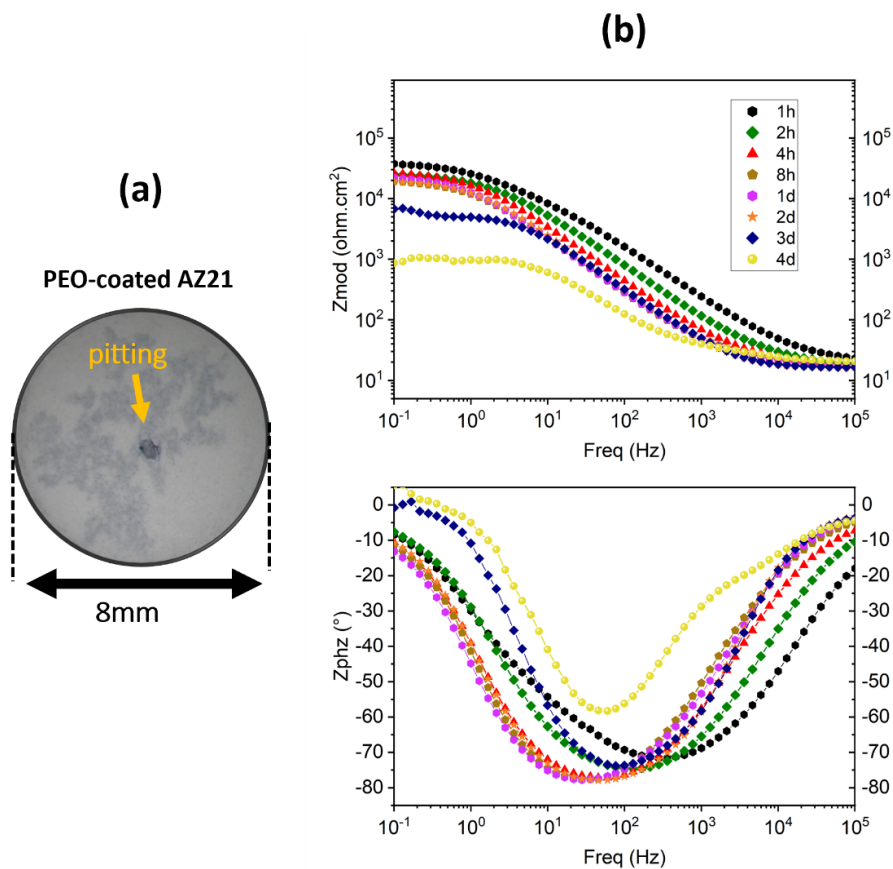


Figure 5.1 (a) The surface appearance of the reference PEO-coated AZ21 after the failure. (b) Bode plot of PEO-coated AZ21 exposed to 3.5 wt.% NaCl over time.

It is worth mentioning that the sign of corrosion process on this type of PEO coating (based on phosphate electrolyte) usually emerges by surface discoloration (see around the pitting **Figure 5.1 (a)**) with a shape and progression resembling typical filiform corrosion on magnesium. However, detecting this discoloration on PEO-coated samples is often challenging to the naked eye, especially when submerged in the testing electrolyte. Additionally, the precipitation of products resulting from the interaction between the inhibitor and the PEO coating, and/or  $Mg^{2+}$  ions from the substrate, can further obscure the appearance of the PEO coating underneath.

More details on the mechanism of PEO degradation and failure will be provided in **sections 5.2-5.3**.

**Figure 5.2** displays the tested chemicals, sorted by their effect on the weight loss of the AZ21 bare samples, which directly correlates with the inhibition efficiency of each chemical. Chemicals highlighted in green exhibit a corrosion inhibition effect, while those in red indicate an adverse effect on the corrosion rate of the bare AZ21. The impact of these inhibitor candidates on the PEO-coated samples is also shown, with positive and negative signs above each chemical. As explained in the figure legend, a positive sign denotes that the chemical extends the PEO coating failure time. The number above the positive sign represents the additional days the PEO coating lasts compared to the reference sample (4 days). Conversely, a negative sign indicates that the PEO coating fails in less than 4 days or has clearly lower absolute values of impedance at low frequency range as compared to those of the reference sample tested without any inhibitor.

The EIS spectra and visual appearance of the PEO-coated samples after the test, corresponding to each chemical, are provided in **Figure 5.3**. The chemicals in **Figure 5.3** are sorted based on their effectiveness in postponing PEO failure, where differentiation is possible.

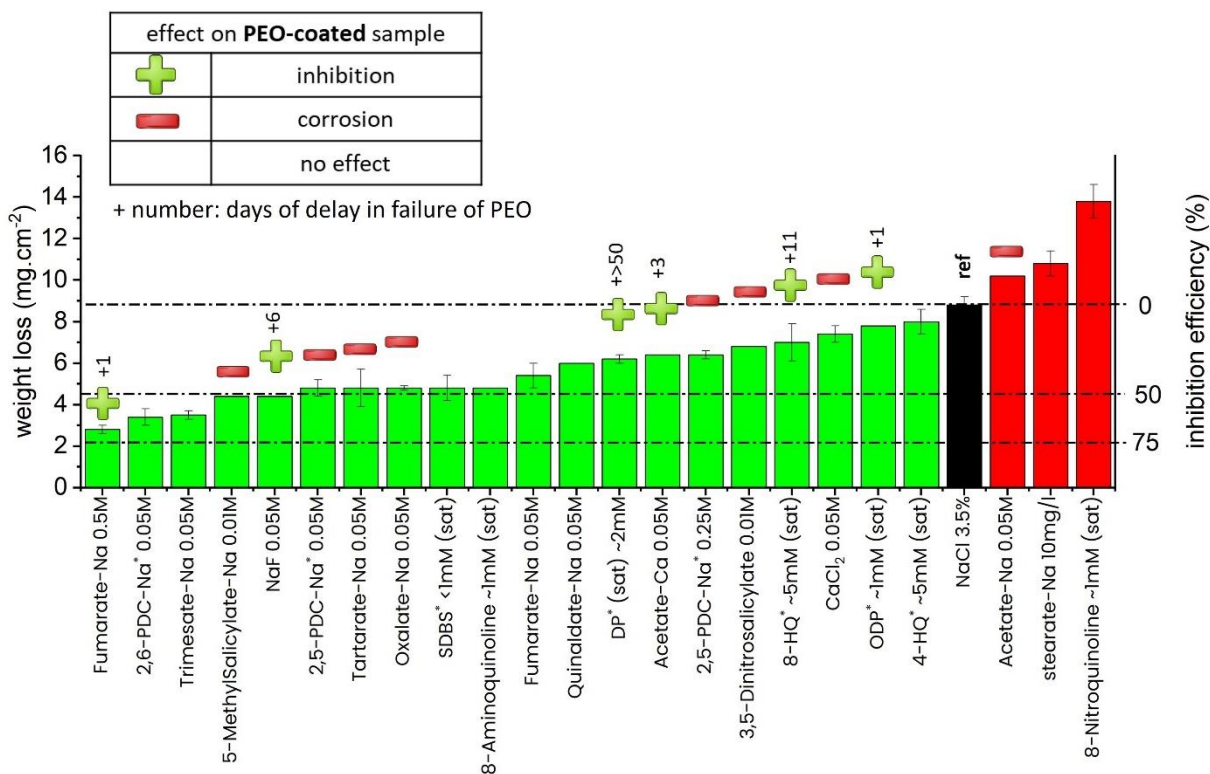


Figure 5.2 inhibition efficiency and the corresponding weight loss of the bare AZ21 sample exposed to the NaCl 3.5% with and without inhibitor candidates in stagnant condition. Additionally, the effect of the inhibitor candidates on the PEO-coated sample has been indicated on top of each bar with positive and negative signs, and numbers, as described in the figure legend. The names of chemicals marked with an asterisk (\*) are the abbreviated version of the names as follows: 2,6PDC = 2,6-pyridinedicarboxylate; 2,5PDC = 2,5-pyridinedicarboxylate; SDBS = sodium dodecylbenzenesulfonate; DP = decylphosphonate; 8-HQ = 8-hydroxyquinoline; 4-HQ = 4-hydroxyquinoline; ODP = octadecylphosphonate.

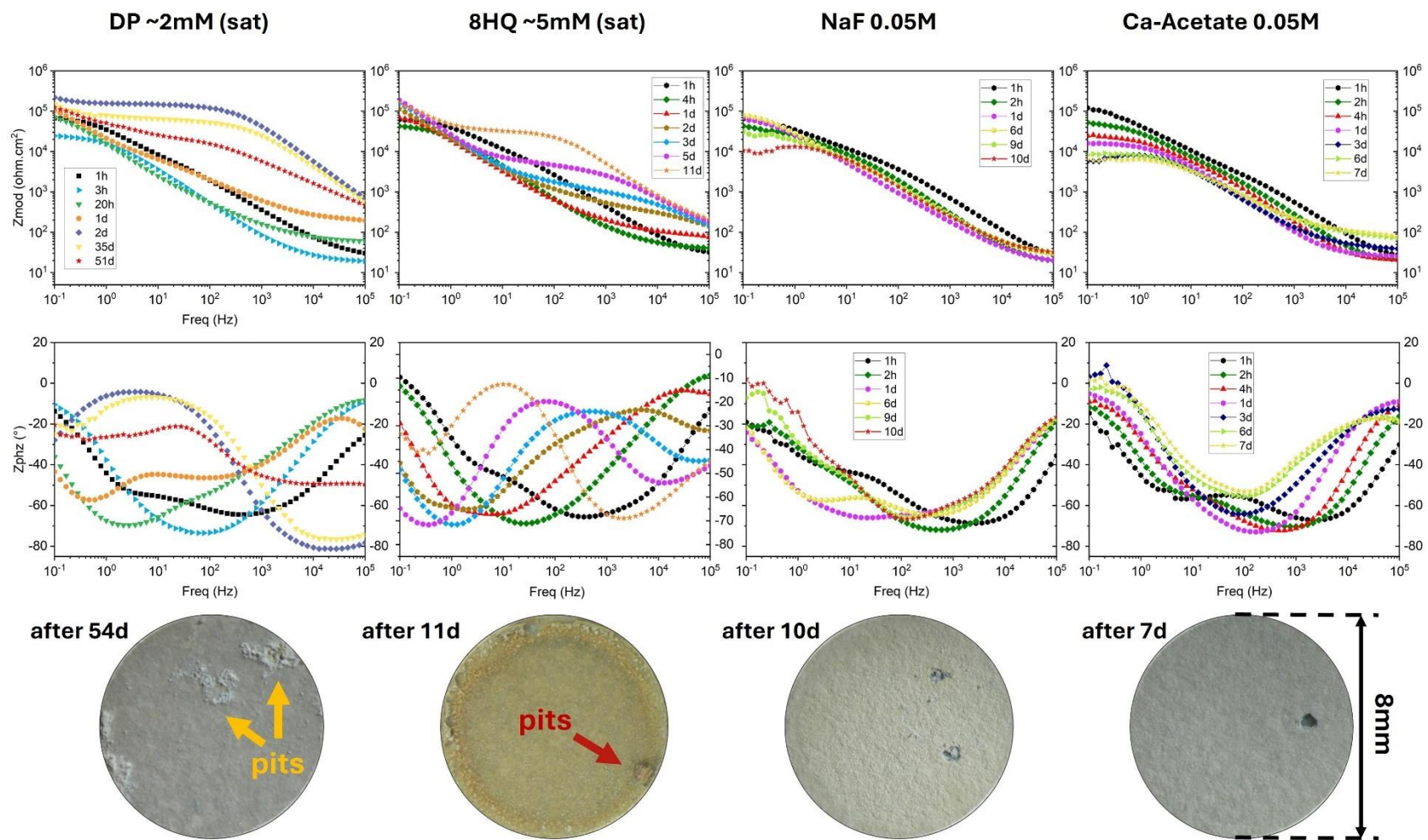


Figure 5.3 Bode plots of PEO-coated AZ21 immersed in 3.5 wt.% NaCl containing until the failure of PEO coating. The surface appearance of PEO-coated AZ21 after the failure is shown in the bottom of each case.

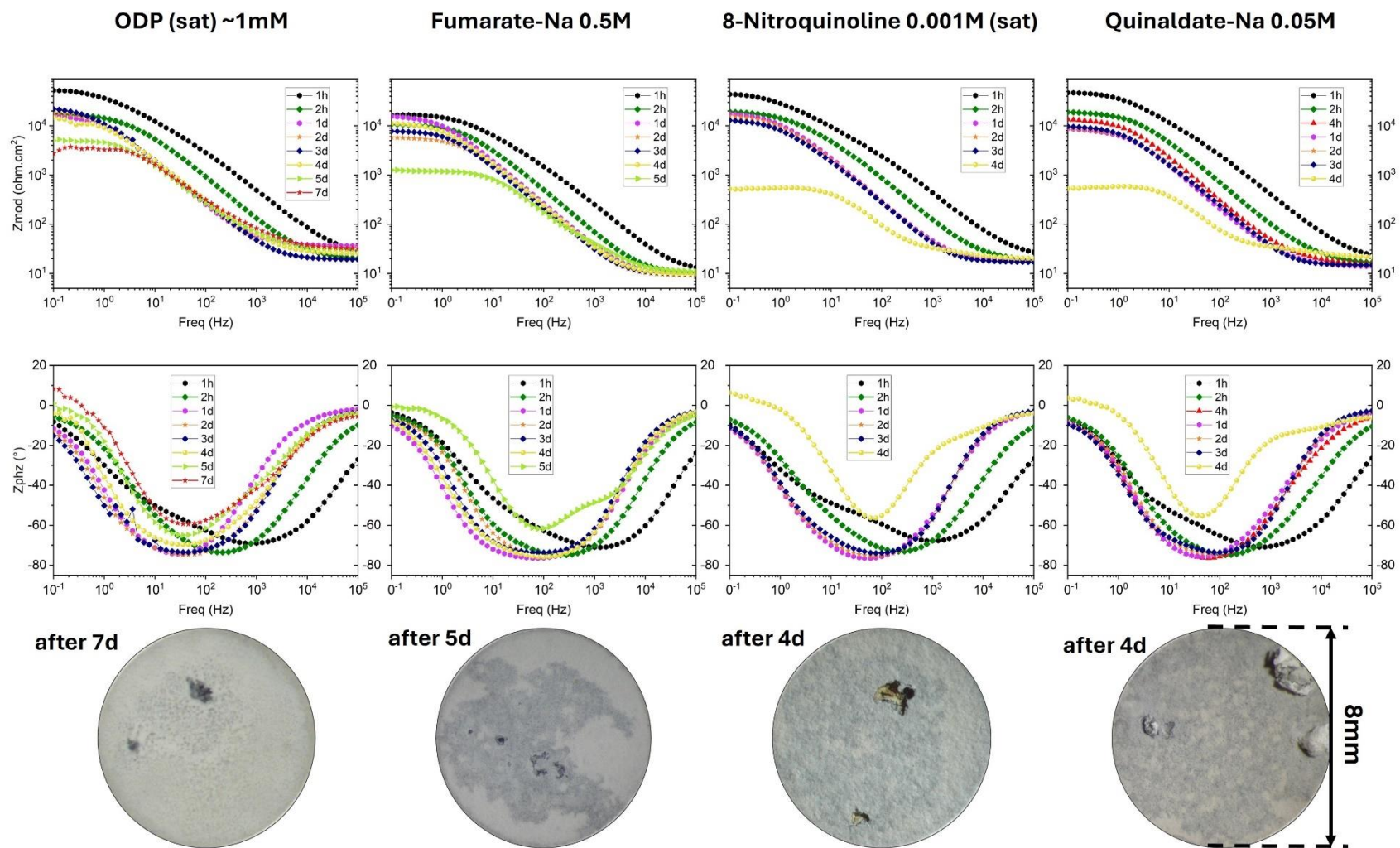


Figure 5.3 (continue).

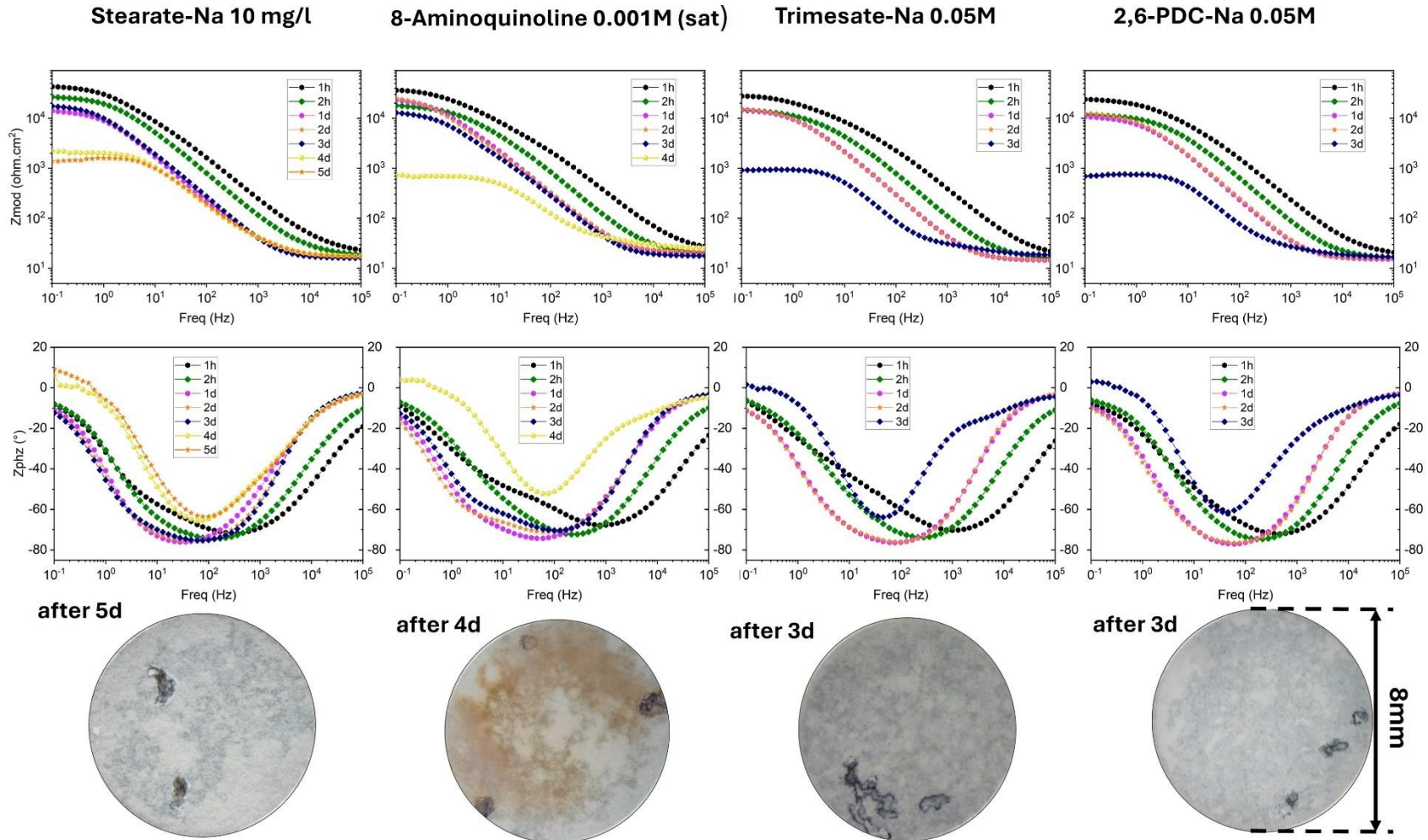


Figure 5.3 (continue).

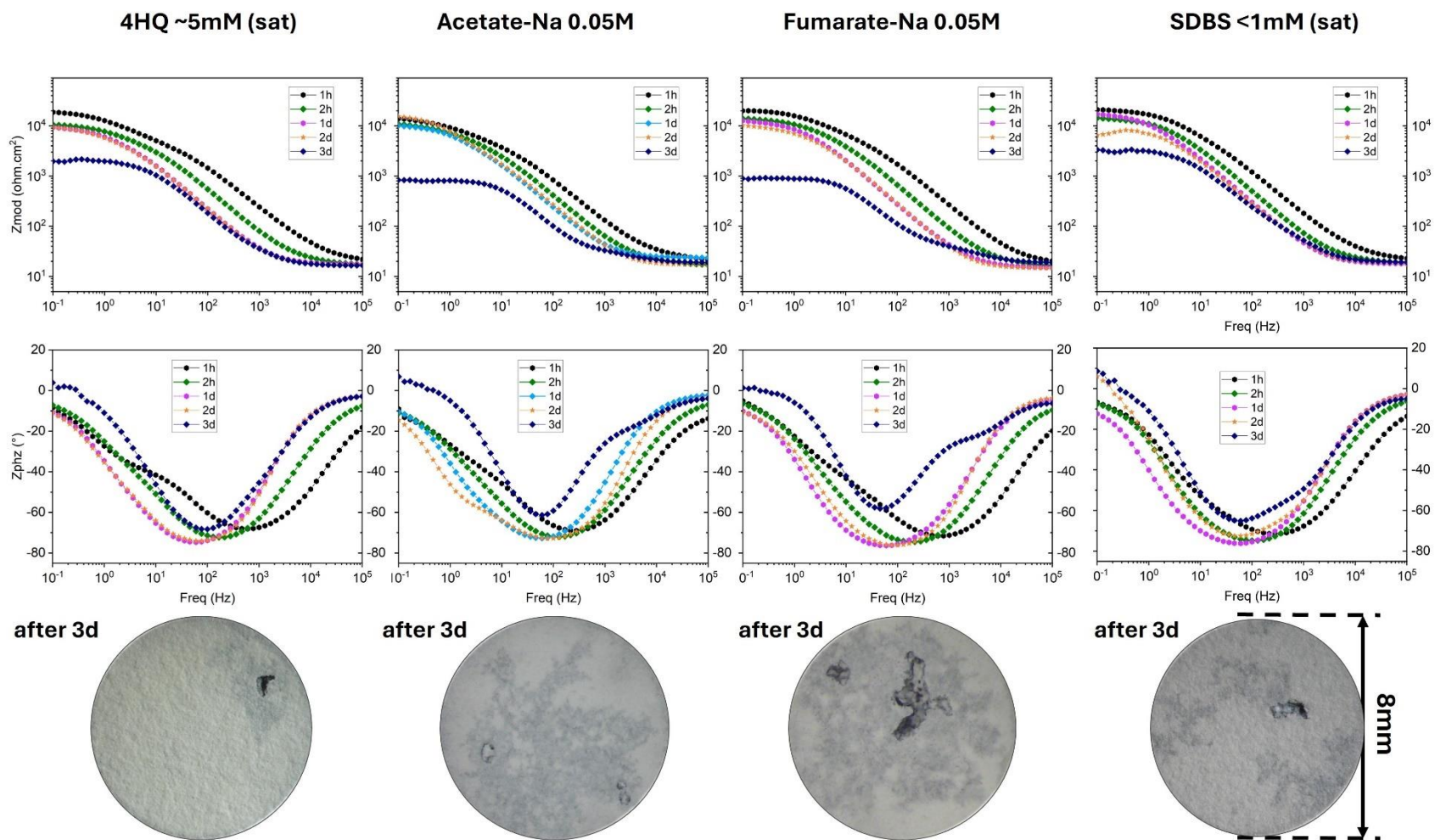


Figure 5.3 (continue).

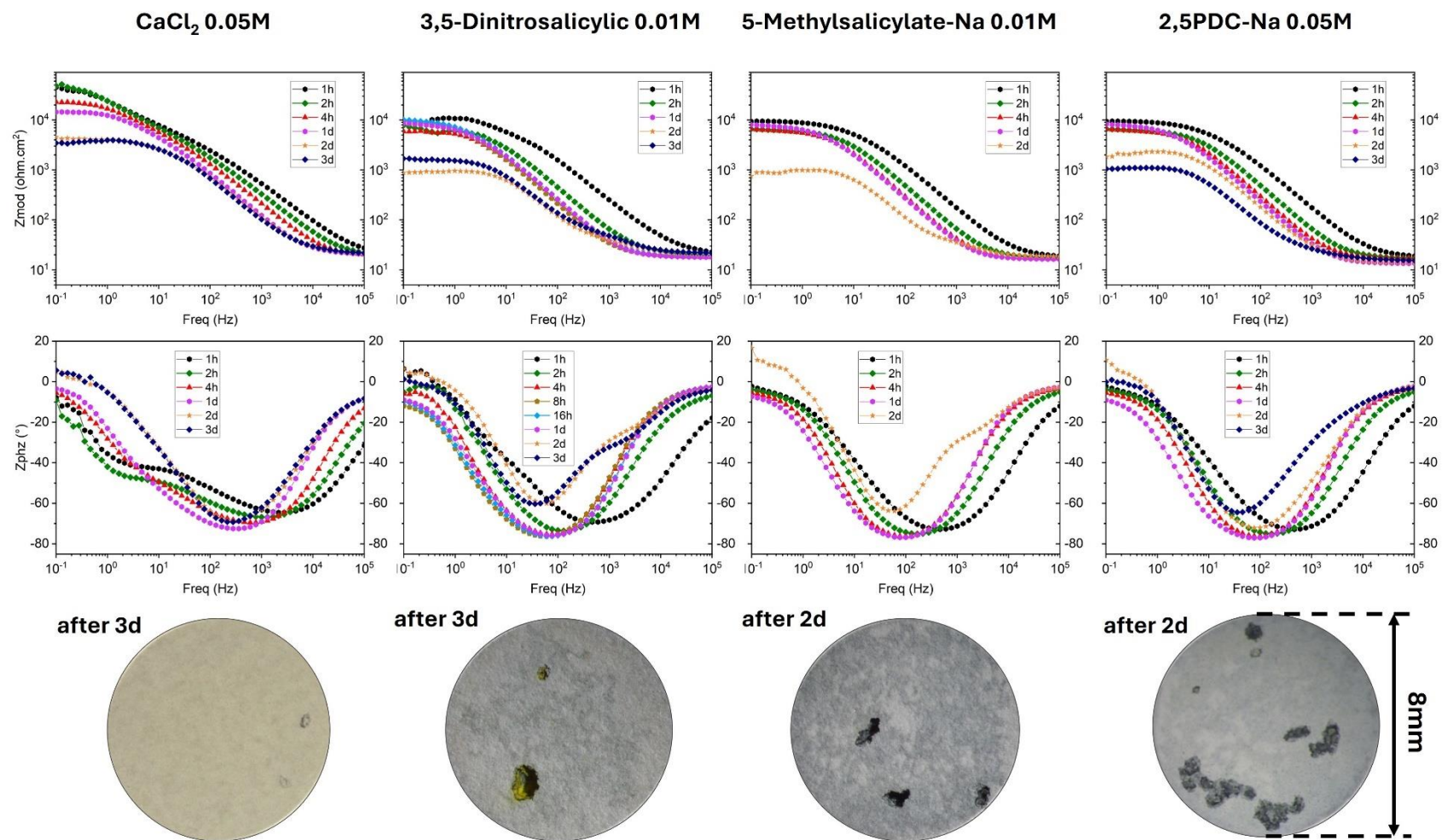


Figure 5.3 (continue).

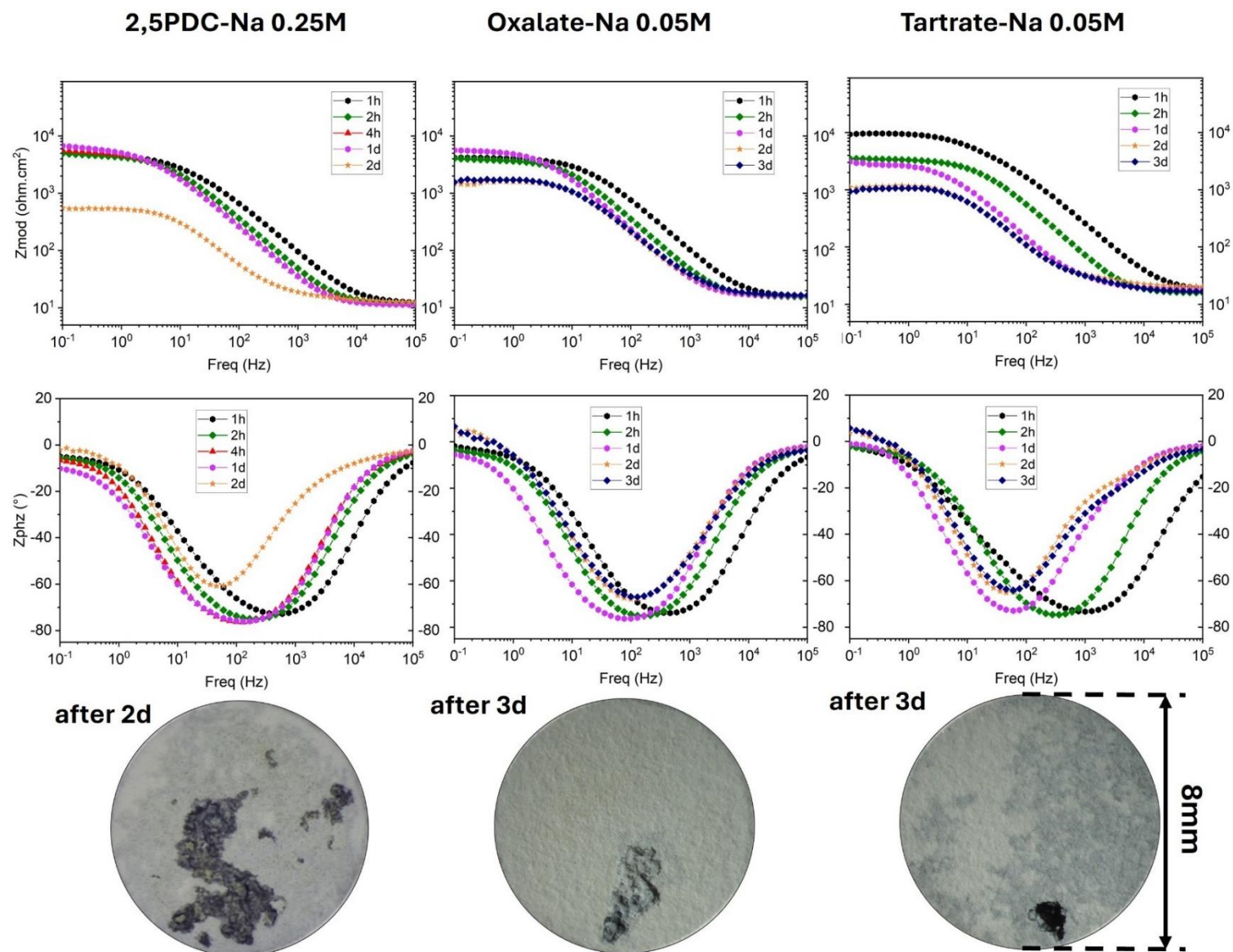


Figure 5.3 (continue).

The first observation that stands out in **Figure 5.2**, which is quite counterintuitive, is that the majority of the chemicals with positive corrosion inhibition on the bare AZ21 sample have either no effect or even an accelerating effect on the degradation of the PEO-coated samples. On the other hand, the chemicals that accelerate the corrosion of bare AZ21 seem to have no substantial adverse effect on the corrosion of PEO-coated samples. This observation reveals that the corrosion inhibition of a chemical on a bare AZ21 substrate should not be taken for granted and does not automatically apply to PEO-coated AZ21 magnesium.

The data presented in **Figure 5.2** and **Figure 5.3** for all chemicals can be analyzed and interpreted individually. However, below, we focus on analyzing only some of the chemicals, as this is required for further discussion in the subsequent chapters.

Among the tested inhibitors, a high concentration of 0.5M sodium fumarate (fumarate-Na) yields the highest inhibition effect on the corrosion of the bare AZ21 substrate. It can also delay the failure of the PEO-coated sample by one day. However, a lower concentration of 0.05M has a negligible effect on the degradation rate of the PEO coating. The inhibition effect of fumarate-Na on bare magnesium has been demonstrated for several Mg alloys [17, 165-169], making fumarate-Na a highly applicable and universal inhibitor. To the best of our knowledge, there is only one report on the incorporation of sodium fumarate into a PEO coating on the AZ91D alloy, which claims an inhibition effect [169]. However, this report lacks information about the concentration of sodium fumarate used. Additionally, since sodium fumarate was not used as a standalone inhibitor but rather in a mixture with  $\text{NaH}_2\text{PO}_4$ , primarily to seal the PEO pores, the specific inhibition effect attributed to sodium fumarate based on the provided results is unclear.

Trimesate-Na is the second most effective inhibitor of corrosion for the bare AZ21 substrate. Our group has recently reported the significant inhibition effect of trimesate-Na on Mg alloys [170], indicating it is worthy of further investigation. Similar to fumarate-Na, although trimesate-Na demonstrates a remarkable corrosion inhibition effect on bare AZ21, it does not impact the degradation of the PEO-coated sample.

The positive corrosion inhibition of 2,6PDC-Na was also expected since different derivatives of pyridinedicarboxylates have already proved to show a universal corrosion inhibition effect for several magnesium alloys [17]. However, neither of the tested 2,6PDC-Na nor 2,5PDC-Na were able to improve the corrosion resistance of the PEO-coated sample. In fact, a substantially higher deterioration of the PEO coating was observed with the addition of 2,5PDC-Na to the electrolyte.

Other effective inhibitors for bare AZ21, including tartrate-Na [17], oxalate-Na [17], 5-Methylsalicylate-Na [17, 171], and SDBS [17, 172, 173], which have also been reported as effective corrosion inhibitors in the literature, were found to accelerate the corrosion of PEO-coated AZ21.

Regarding the corrosion behavior of the PEO-coated samples, DP outperformed all other chemicals, delaying PEO degradation by more than 50 days. Local corrosion signs, indicated by accumulated products marked with arrows in the corresponding pictograph of the sample, were observed. Although the PEO layer might be degraded in these spots, no significant decline in the EIS spectrum was noted, unlike the reference sample, which showed about an order of magnitude decline in  $|Z|_{0.1\text{Hz}}$ . The formation and accumulation of corrosion products were challenging to spot due to their similar color to the rest of the PEO coating. The test was stopped upon noticing a slight drop in  $|Z|$  at low frequencies.

8HQ ranked second, extending the PEO coating life by 11 days compared to the reference sample. The most effective chemicals in delaying PEO degradation exhibited higher impedance values across the entire frequency range than the reference sample. Notably, an additional time constant at high frequencies was observed over time for the top five performing chemicals, likely due to the formation of an additional layer on the sample surface, possibly from the formation of an insoluble  $\text{Mg}^{2+}$  complex with the inhibitor. Precipitation on the PEO layer was also noted, particularly in the sample treated with 8HQ, which resulted in a yellowish/orange precipitate covering the surface.

As one of the study's aims is to identify effective corrosion inhibitors for incorporation into PEO coatings, 8HQ and DP, as the best performing inhibitors in the screening phase, were selected for further detailed investigation in separate **sections 5.4** and **5.5**, respectively. However, understanding why effective corrosion inhibitors for bare AZ21 have adverse effects on PEO-coated AZ21 samples is also crucial. Therefore, the detailed investigation on the interaction of 2,5PDC-Na with both bare and PEO coating is provided in **section 5.3**.

Understanding the mechanisms of both corrosion inhibition and acceleration by the selected inhibitors will help establish criteria for effective corrosion inhibitors to be incorporated into PEO coatings.

### 5.3 Adverse effect of 2,5-PDC corrosion inhibitor on PEO coated magnesium

Based on the inhibitor screening results presented in the previous chapter, we observed that the corrosion inhibition effectiveness of several molecules on bare AZ21 is not consistently replicated when the AZ21 substrate is coated with a PEO layer. A notable example of this unexpected behavior is the sodium salt of 2,5-pyridinedicarboxylate (2,5PDC).

It is crucial to investigate the mechanisms behind this negative interaction to understand why a corrosion inhibitor effective for bare magnesium can become detrimental when used on a PEO-coated substrate.

The following published paper, incorporated as **section 5.3** of this thesis, aiming to address why the highly effective corrosion inhibitor 2,5PDC, which has been established as a universal corrosion inhibitor, not only loses its inhibitory effect but also has a detrimental impact on PEO-coated magnesium substrates.

**B. Vaghefinazari**, C. Wang, D. Mercier, D. Mei, A. Seyeux, P. Marcus, C. Blawert, S.V. Lamaka, M.L. Zheludkevich, Adverse effect of 2,5PDC corrosion inhibitor on PEO coated magnesium, Corrosion Science, 192 (2021) 109830. <https://doi.org/10.1016/j.corsci.2021.109830>

#### CRediT authorship contribution statement:

**Bahram Vaghefinazari**: Conceptualization, Investigation, Validation, Writing – original draft, Writing – review & editing. **Cheng Wang**: Investigation, Writing – review & editing. **Dimitri Mercier**: Investigation, Writing – review & editing. **Di Mei**: Investigation, Writing – review & editing. **Antoine Seyeux**: Investigation, Writing – review & editing. **Philippe Marcus**: Supervision, Writing – review & editing. **Carsten Blawert**: Conceptualization, Supervision, Writing – review & editing. **Sviatlana V. Lamaka**: Conceptualization, Supervision, Writing – review & editing. **Mikhail L. Zheludkevich**: Conceptualization, Supervision, Writing – review & editing.



# Adverse effect of 2,5PDC corrosion inhibitor on PEO coated magnesium

Bahram Vaghefinazari<sup>a,\*</sup>, Cheng Wang<sup>a</sup>, Dimitri Mercier<sup>b</sup>, Di Mei<sup>a,c</sup>, Antoine Seyeux<sup>b</sup>, Philippe Marcus<sup>b</sup>, Carsten Blawert<sup>a</sup>, Sviatlana V. Lamaka<sup>a</sup>, Mikhail L. Zheludkevich<sup>a,d</sup>

<sup>a</sup> Institute of Surface Science, Helmholtz-Zentrum Hereon, 21502 Geesthacht, Germany

<sup>b</sup> Chimie ParisTech-CNRS, PSL Research University, Institut de Recherche de Chimie Paris (IRCP), Physical Chemistry of Surfaces Group, 75005 Paris, France

<sup>c</sup> School of Materials Science and Engineering & Henan Key Laboratory of Advanced Magnesium Alloy, Zhengzhou University, Zhengzhou 450001, PR China

<sup>d</sup> Institute of Materials Science, Faculty of Engineering, Kiel University, 24143 Kiel, Germany

## ARTICLE INFO

### Keywords:

Magnesium  
Corrosion inhibitor  
Plasma electrolytic oxidation  
Corrosion

## ABSTRACT

Besides their noteworthy tribological and corrosion protection properties, Plasma Electrolytic Oxidation (PEO) coatings feature a porous microstructure that is able to host corrosion inhibitors. This study reveals that although 2,5pyridindicarboxylate (2,5PDC) shows a remarkable corrosion inhibition effect for bare AZ21 Mg alloy, it can extensively deteriorate a PEO coating on the same Mg substrate, resulting in an overall accelerated failure of the PEO-coated AZ21 alloy. The deteriorative behavior of 2,5PDC towards PEO-coated AZ21 is explained based on the characterization of the bare and PEO-coated AZ21 exposed to the NaCl electrolyte with and without inhibitor using EIS, SEM, STEM and ToF-SIMS.

## 1. Introduction

Plasma Electrolytic Oxidation (PEO) is a well-known surface treatment technology that forms a ceramic layer with good tribological and protective properties via the formation of high voltage discharges on a metallic substrate submerged in aqueous electrolytes [1]. The formed layer provides a barrier against the penetration of a corrosive medium, rendering this technology effective in the prevention of corrosion on metallic surfaces [2]. However, the relatively high porosity of the PEO layer limits its long-term use in offering protection against corrosion [3]. Therefore, intensive research work aiming at improving the corrosion protection abilities of PEO is actively being carried out. Modification of the chemistry of PEO electrolyte and power supply parameters are the main approaches meant to enhance the corrosion protection properties of PEO layers [4].

Incorporation of corrosion inhibitors into coating systems is a typical cost-effective approach to further enhance the overall corrosion resistance and provide active corrosion protection properties to coatings [5]. In fact, the high porosity of PEO layer has been promisingly studied as an appropriate reservoir for corrosion inhibitors. The impregnation of an inhibitor into a PEO coating is typically achieved via simple immersion of the PEO-coated sample into a solution containing the inhibitor. In this case, a subsequent sealing layer is applied onto the PEO coating to prevent the fast leaching of the incorporated inhibitors into the

corrosive environment [6].

Several organic and inorganic corrosion inhibitors have been incorporated in PEO coatings on magnesium alloys [3,6–11] and their positive effect on corrosion protection has been reported. For instance, Yang et al. [7] impregnated a phosphate-based PEO on a commercially pure (CP) magnesium with inhibitor 3-Methylsalicylate (3-MS) followed by sealing of the pores with an epoxy layer. In addition to a significant barrier effect offered by the combination of PEO and epoxy coatings, active corrosion protection of the coating system, granted by the local release of 3-MS, was concluded via observation of local current density using Scanning Vibrating Electrode Technique (SVET) over artificially-formed defects in the coating. Apart from simple immersion, other approaches have been utilized to introduce inhibitors into the PEO coating system. For instance, inhibitors can be put directly in the sealing top layer [12] or incorporated into nano/micro containers such as layered double hydroxide (LDH) film developed on or within PEO coating. The latter is a recent approach providing promising benefits due to the on-demand release of inhibitors by LDH in exchange for corrosive Cl<sup>-</sup> ions in the medium [13–16]. Jiang et al. [13] investigated a multi-layer coating system on AZ91 stratified as PEO/LDH/lubricant. Through a hydrothermal process, the LDH, intercalated with molybdate as an inhibitor, was formed on the PEO layer. During the immersion in NaCl solution, the suppressed local electrochemical activity on a defected area of the coated sample was observed via SVET technique.

\* Corresponding author.

E-mail address: [bahram.vaghefinazari@hzg.de](mailto:bahram.vaghefinazari@hzg.de) (B. Vaghefinazari).

<https://doi.org/10.1016/j.corsci.2021.109830>

Received 21 June 2021; Received in revised form 3 September 2021; Accepted 6 September 2021

Available online 10 September 2021

0010-938X/© 2021 Elsevier Ltd. All rights reserved.

The observed self-healing behavior was partly attributed to the active release of inhibitive molybdate ions in exchange for detrimental  $\text{Cl}^-$  ions in the solution.

The positive corrosion inhibition effect of a chemical for a magnesium alloy in a relevant environment is usually considered as the primary criterion for the selection of inhibitors to be incorporated into a PEO coating system on a Mg alloy. This is confirmed by the fact that most of the reported related studies have utilized inhibitors that had already been investigated [17]; or the performance of the incorporated inhibitors was initially established in the same work [11,18,19]. As a rational approach, the mechanism of enhancement to the coating system by incorporation of the inhibitors is mainly justified by examining an artificially defected coating, causing the local but direct exposure of the bare substrate to the corrosive medium [20,21]. However, the chemical interaction that takes place between the PEO layer itself and the incorporated corrosion inhibitor is usually overlooked, probably owing to the presumption that the ceramic-like PEO layer possesses rather high chemical stability and can withstand a neutral aqueous environment.

This study, however, seeks to demonstrate how 2,5PDCA, as an effective and universal corrosion inhibitor for magnesium alloys (shown to be effective for a wide range of Mg alloys [22]), can be detrimental to the overall corrosion protection properties when it is introduced to a magnesium substrate coated with PEO. This will mount the significance of taking into consideration the interaction between the desired inhibitor and the PEO layer as a criterion for choosing an effective inhibitor for a PEO-coated magnesium substrate.

## 2. Experimental procedure

### 2.1. Materials

AZ21 magnesium alloy cast and rolled in house (at Helmholtz Zentrum Hereon), was used as the substrate. The chemical composition of the alloy is  $1.59 \pm 0.07$  wt% Al,  $1.05 \pm 0.07$  wt% Zn, 0.29 wt% Mn, measured by spark discharge-optical emission spectroscopy (SD-OES), Ametek-Spectro. All AZ21 substrates were ground with emery paper up to 2500 grit size, followed by rinsing with ethanol and drying with cold pressurized air. KOH (CHEMSOLUTE®, > 85%) and  $\text{Na}_3\text{PO}_4$  (Alfa Aesar), were used for preparation of the PEO electrolyte.

Different derivatives of pyridinedicarboxylic acid (PDCA), including 2,5PDCA, 2,6PDCA and 3,4PDCA, all were supplied by Sigma-Aldrich. The molecular structure of studied PDCAs are given in Table 1. All the solutions for different corrosion tests were prepared by dissolving different concentrations of PDCA and NaCl in deionized water (DI-W) and the pH of the solutions were adjusted to  $7.0 \pm 0.2$  using NaOH. The pH of the solutions was measured with Metrohm 713 pH meter equipped with InLab® Expert Pt1000 pH electrode from Mettler Toledo. At pH 7, all the carboxyl groups of PDCA are deprotonated, and thus, exist in the form of soluble salt in the solution, which hereafter are denoted as PDC.

### 2.2. PEO preparation

PEO coating on AZ21 samples with the dimensions of  $40 \text{ mm} \times 40 \text{ mm} \times 2 \text{ mm}$  was conducted using a standard power supply (Electro Automatik, Germany) with a self-designed pulsing unit in the electrolyte of 20 g/L  $\text{Na}_3\text{PO}_4$  and 2 g/L KOH. A constant current density of  $40 \text{ mA cm}^{-2}$  with pulse ratio ( $t_{\text{on}}:t_{\text{off}}$ ) of 1 ms:9 ms was applied to the bare AZ21 samples for 10 min, which resulted in the final voltage of  $400 \pm 4 \text{ V}$ . The electrolyte temperature was kept constant at  $20 \pm 0.2^\circ\text{C}$  using a stainless steel hollow tube coil, which was functioning as the cathode as well. Afterwards, the specimens were immersed in DI-W for 20 min at low-pressure condition ( $\sim 0.9 \text{ atm}$  pressure), which was applied using a water jet pump. During this careful rinsing step, the DI-W is able to penetrate into the pores of the PEO layer and dilute the PEO electrolyte remnant. In addition, release of entrapped air in the pores due to the applied low pressure helps the convection of the DI-W into the pores. This step is necessary to reduce the effect of the remained phosphate for any unambiguous interpretation of the results. Following the rinsing step, the specimens were immersed in acetone (EMSURE® supplied by Sigma-Aldrich) for 20 min and finally dried in oven at  $80^\circ\text{C}$  for 30 min.

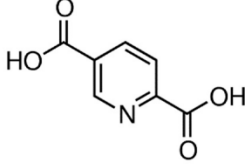
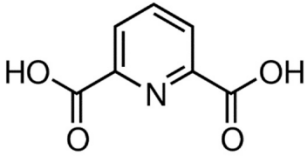
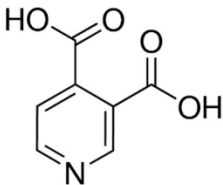
### 2.3. Electrochemical measurements

Gamry reference 600 potentiostat with conventional 3-electrode arrangement was used for Electrochemical Impedance Spectroscopy (EIS) measurements. Pt wire and Ag/AgCl electrode served as the counter and the reference electrode, respectively. An area limited to  $0.5 \text{ cm}^2$  of the samples were exposed to the 400 ml of corrosive electrolyte. EIS measurements were carried out under potentiostatic mode after at least 10 min of open circuit condition to ensure a relatively stable OCP condition. The scanned frequency was ranged from 100 kHz to 0.1 Hz with 9 points per decade and the applied perturbation voltage was  $10 \text{ mV}_{\text{rms}}$ .

### 2.4. Localized measurement

Local concentration of dissolved  $\text{O}_2$  was measured using a fiber-optic OXR50-UHS  $\text{O}_2$  micro-optode coupled with a FireString $\text{O}_2$  fiber-optics oxygen meter (Pyroscience, Germany). Local concentration of dissolved  $\text{H}_2$  was measured using a  $\text{H}_2$  microsensor ( $10 \mu\text{m}$  tip diameter,  $\text{H}_2$ -10) connected to a fx-6 UniAmp (both from Unisense, Denmark). Both  $\text{O}_2$  optode and  $\text{H}_2$  probes were calibrated considering the salinity and temperature of the solution. Local pH was measured using a glass-type pH microelectrode (Unisense, pH-10).  $\text{H}_2$  and  $\text{O}_2$  local concentrations were measured simultaneously, using custom made dual-head stage, while the local pH was measured in a separate experiment with the same experimental setup. All three types of micro-sensors were integrated in commercial SVET-SIET system from Applicable Electronics for probe positioning and movement.

**Table 1**  
Molecular structure of different derivatives of PDCA studied in this work.

2,5PDCA	2,6PDCA	3,4PDCA
		

## 2.5. Characterization methods

Bruker D8 Advance diffractometer (Karlsruhe, Germany) with Cu K $\alpha$  radiation (40 kV and 40 mA) was adopted for X-ray diffraction analysis (XRD) and investigation of phase composition of the PEO layer. The incident angle was 3° with 5 s dwell time and 0.02° step size. The surface morphology of bare and PEO layer as well as their cross-section were investigated by a scanning electron microscope (SEM) (TESCAN Vega3 SB). Higher magnification microscopy was carried out using a scanning tunneling electron microscopy (STEM) mode of TESCAN LYRA3. STEM was used on the lamellar obtained from the PEO/substrate interface. For detailed procedure of lamellar formation, see the [Supplementary Material](#) (section S.1).

## 2.6. ToF-SIMS

Time of Flight Secondary Ion Mass Spectrometry (ToF-SIMS) analyses were performed using a ToF-SIMS V spectrometer (ION TOF GmbH, Munster, Germany) operating at a pressure of approximately  $10^{-9}$  mbar. Data acquisition and post processing analysis were performed using the SurfaceLab software (version 6.5). The spectrometer was run in the HC-BUNCHED mode in order to get a high mass resolution (M/DM around 8000). Negative ions depth profiles were recorded by sequential analysis ( $\text{Bi}^+$ , 25 keV, 1 pA,  $100 \times 100 \mu\text{m}^2$ ) and sputtering of the sample surface. The analysis beam was a pulsed 25 keV  $\text{Bi}^+$  ion source delivering 1.2 pA of target current over a  $100 \times 100 \mu\text{m}^2$  area, interlaced with a 1 keV  $\text{Cs}^+$  sputter beam delivering 30 nA target current over a  $300 \times 300 \mu\text{m}^2$  area. Both guns have a 45° incidence angle with respect to the specimen surface.  $\text{Bi}^+$  ion flux was set below  $1012 \text{ ions cm}^{-2}$  to ensure quasi-static conditions. Analysis was centered inside the sputtered crater to avoid edge effects. In the depth profiles, the intensity of the characteristic species are reported using a logarithmic scale, which gave equal emphasis to signals of all intensities. The variation of the intensity with sputtering time reflects the variation of the in-depth concentration but is also dependent on the matrix from which the ions are emitted.

Specific ions were chosen to describe the corrosion layer, the inhibitor, and the elements constituting the electrolyte. Thus,  $\text{MgO}_2^-$  (55.975 amu),  $\text{MgOH}^-$  (40.988 amu),  $\text{MgH}^-$  (24.993 amu),  $25\text{MgH}^-$  (25.994 amu) are selected since these ions are characteristic of the Mg oxide, Mg hydroxide and Mg hydride species respectively [23].  $\text{Cl}^-$  (34.969 amu),  $\text{Na}^+$  (22.990 amu) and  $\text{CO}_3^-$  (59.985 amu) represent chloride, sodium and carbonate species, respectively, while  $\text{C}_7\text{H}_4\text{NO}_4\text{Mg}^-$  (157.022 amu) is a marker of the PDCA (as identified on the ToF-SIMS mass spectrum, not shown here).

## 2.7. $\text{H}_2$ evolution test

$\text{H}_2$  evolution setup using eudiometers, described in details in our previous work [24], was adopted to measure the corrosion rate of the bare AZ21 in the different electrolytes. The eudiometer cylinder was initially filled with water and the evolved  $\text{H}_2$  due to the cathodic reaction of hydrogen evolution reaction (HER) on the magnesium substrate displaces the water in the cylinder. The volume of the collected  $\text{H}_2$  was recorded by weighing the displaced water using an electronic balance (OHAUS, SKX2202). The values were automatically recorded using a USB data logger (OHAUS, 30268984) and an in-house developed Python script. The AZ21 pieces with the dimensions of  $2 \text{ mm} \times 100 \pm 1 \text{ mm} \times 14 \pm 1 \text{ mm}$  ( $32.2 \pm 2.9 \text{ cm}^2$  total surface area) were fully immersed in either 0.5 wt% or 3.5 wt% NaCl electrolyte inside a container, which was connected and sealed to the eudiometer cylinder. The exact concentration for each specific experiment is noted below in the text. During the test, the 500 ml electrolyte was constantly stirred using magnetic stirrers. The effects of ambient temperature ( $23 \pm 1^\circ\text{C}$ ) and pressure on the volume of collected  $\text{H}_2$  were offset by the variations simultaneously recorded for an extra reference electrolyte

without any immersed sample. The samples weight loss after the  $\text{H}_2$  evolution test was measured by subtracting the initial and final weight of the samples. The corrosion products were removed using 180 g/l chromic acid solution. The equivalent weight loss according to the evolved  $\text{H}_2$  was also calculated in the testing condition (ambient temperature and the pressure during the test were considered) and compared with the actual sample weight loss.

## 3. Results

### 3.1. Validating the effectiveness of PDC inhibitor

The PDCs have been recently identified as universal magnesium corrosion inhibitors [22]. To validate the effectiveness of PDCs as corrosion inhibitors for the AZ21 substrate,  $\text{H}_2$  evolution tests were carried out for three different PDCs - namely 2,5-PDC, 3,4-PDC and 2,6-PDC in 0.5 wt% NaCl. The concentration of all the tested PDCs was 0.05 M. Fig. 1 shows the evolved  $\text{H}_2$  for each PDC along with the appearance of magnesium samples after the test. Generally, it can be seen that all the tested PDCs were able to inhibit the corrosion of magnesium substrate because of the lower rate of evolved  $\text{H}_2$  throughout the immersion. The magnesium sample immersed in the NaCl electrolyte without any inhibitor experienced a filiform corrosion propagating all over the surface, which intermittently ended up in pitting sites observable as the black regions on the sample in Fig. 1. Upon adding any of the three different PDCs, the filiform corrosion was still observed, but at significantly lower rates of propagation. Moreover, a lower number of active pitting sites were observed at the end of the immersion test compared to the sample immersed in NaCl solution without any inhibitor. Having outperformed the other PDCs, 2,5PDC was chosen for further investigations. Note that the low concentration of NaCl (0.5 wt %) was used so that the validation experiment is consistent with all the studies published regarding the corrosion inhibition effect of PDCs on magnesium alloys, where the same concentration of NaCl was used [3, 22,25–27]. However, to induce a harsher corrosive medium, a higher concentration of NaCl (3.5 wt%) was used as the background solution for the rest of the study. This leads to a faster assessment of corrosion protection properties of PEO-coated AZ21 [28].

### 3.2. Concentration effect of 2,5PDC on bare AZ21

When a corrosion inhibitor is incorporated into a system, it will gradually take part in the inhibition process, triggered by different corrosion reaction responses. Therefore, reduction in the amount of remaining inhibitors will reduce the real-time efficiency of the corrosion inhibitors over time. Furthermore, it is impractical to determine the actual concentration of the incorporated inhibitor on the locally active region on the magnesium surface. Therefore, a prudent approach to assure a positive inhibition performance of inhibitor on a magnesium alloy is to evaluate a range of concentrations of the inhibitor in immersion methods such as  $\text{H}_2$  evolution test. Fig. 2 illustrates that all concentrations of 2,5PDC, ranging from 5 mM to 0.25 M, are able to reduce the corrosion rate of AZ21 immersed in the 3.5 wt% NaCl electrolyte. The rate of corrosion (i.e.  $\text{H}_2$  evolution rate) declines as the concentration of 2,5PDC in the electrolyte increases, which sustains for the whole immersion period. The highest inhibition efficiency of  $92.4 \pm 1.7\%$  was obtained for the electrolyte containing 0.25 M of 2,5PDC after 72 h of immersion. Observation of surfaces of the samples after the immersion revealed that the corresponding sample without any inhibitor in the electrolyte was fully covered with corrosion products, with some areas where the underneath filiform corrosion is still visible. The surface of the corresponding sample with low concentration (0.005 M) of 2,5PDC is similar to that of the sample without inhibitor, but with different color and more visible filiform corrosion beneath the formed corrosion products, suggesting a thinner layer of  $\text{Mg}(\text{OH})_2$  on the surface. When higher concentrations of 2,5PDC are present in the

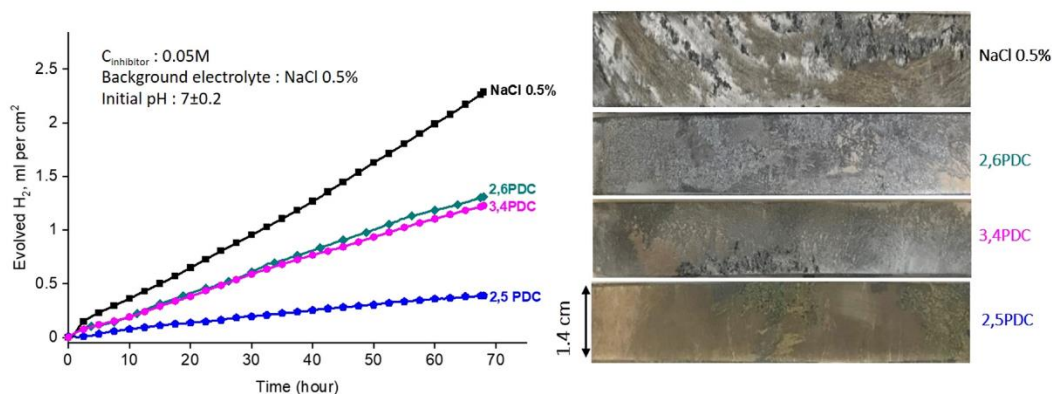


**Fig. 1.** (left)  $H_2$  evolved during immersion of AZ21 samples in 0.5 wt% NaCl solution containing different isomer of pyridinedicarboxylates (right) macrographs of the magnesium samples after 68 h of immersion in the corresponding solutions.

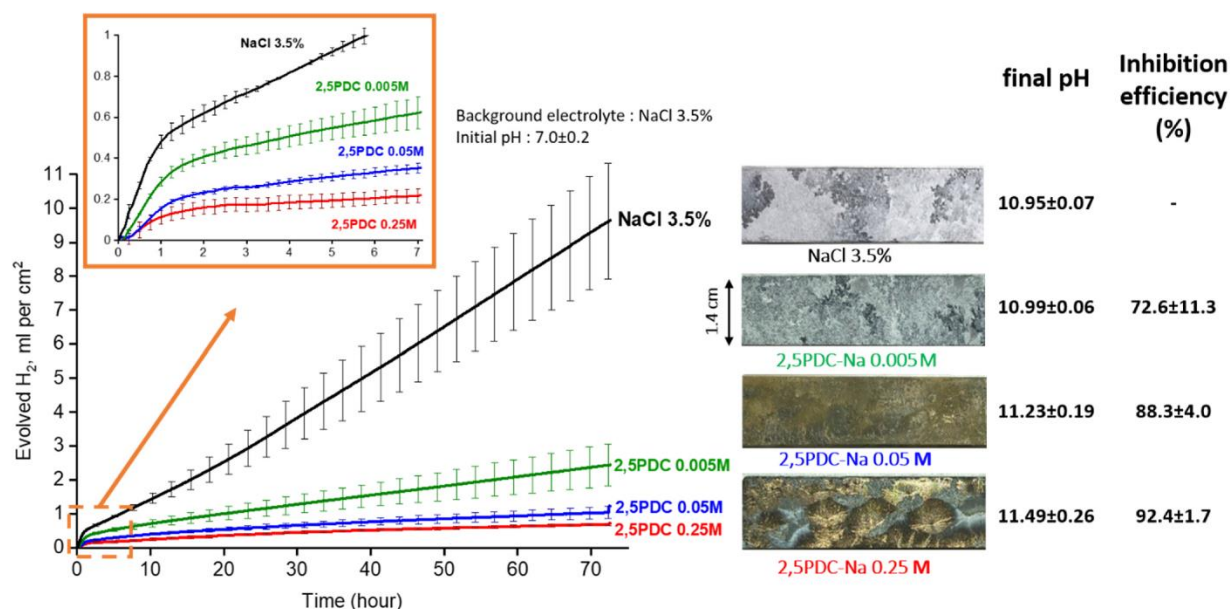


**Fig. 2.** (left)  $H_2$  evolved during immersion of the AZ21 sample in 3.5 wt% NaCl solution containing different concentrations of 2,5PDC (middle) optical macrographs of the AZ21 samples after 72 h of immersion in the corresponding solutions. (right) final pH of solution and inhibition efficiency after 72 h of immersion. The error bars present the standard deviation of the three measurements away from the mean value.

electrolyte, some regions on the surface of AZ21 have a smooth and yellowish appearance free of filiform corrosion. These regions are significantly larger when the highest concentration of 2,5PDC (0.25 M) is present in the electrolyte. Two different rates of  $H_2$  evolution during the course of immersion can be noticed for all the cases (see insert in Fig. 2). The initial high rate of  $H_2$  evolution occurs within the first hour of immersion, followed by a lower rate of evolved  $H_2$ , which remains stable for the rest of the immersion period. This transition between two different rates of  $H_2$  evolution can be linked to the stabilization of  $Mg(OH)_2$  formation at alkaline pH [29], which is mainly due to the cathodic  $H_2$  evolution reaction. Against expectations, the final pH of the electrolyte has higher values when the sample was corroded with lower rates that is when the electrolyte contains higher concentrations of 2,5PDC. Fig. 3 shows the weight loss of the samples after removal of the corrosion products as well as the equivalent weight loss calculated based on the amount of evolved hydrogen. A slightly lower value can be observed in each of the calculated equivalent weight loss based on  $H_2$  volume as

compared to the actual weight loss of the sample after 72 h of immersion. This variance between the actual and calculated weight loss is more pronounced in lower corrosion rate conditions. Similar inconsistency between the actual weight loss and the equivalent weight loss obtained from evolved  $H_2$  has been previously documented for magnesium alloys with low corrosion rates [30]. This disparity can be due to the secondary cathodic oxygen reduction reaction (ORR) that occurs on the magnesium alloy surface, which is often overlooked in corrosion immersion tests for magnesium alloys [31–34].

### 3.3. Effect of 2,5PDC on PEO-coated AZ21

Fig. 4(a) illustrates the voltage and current density registered during the formation of PEO coating on AZ21 substrate. The diagram marks three main consecutive stages during the PEO formation. The initial rapid rise of voltage to  $\sim 200$  V within the stage(I) is attributed to the development of a barrier film assimilating the conventional anodizing

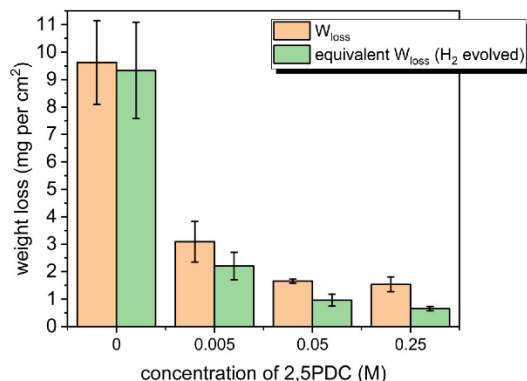


**Fig. 3.** Actual weight loss and equivalent weight loss based on the  $H_2$  volume evolved after 72 h immersion of AZ21 samples in NaCl solution containing different concentrations of 2,5PDC. The error bars present the standard deviation of the three measurements away from the mean value.

process [35]. Stage (II) is characterized by the formation of homogeneously distributed microdischarges on the surface, accompanied by the declining rate of voltage increase. In stage (III), the voltage increases with a relatively low and constant rate and the micro discharges grow bigger in size and smaller in number. Moreover, the microdischarges stay longer at one position. The steadily increasing voltage is correlated with the thickening of the PEO layer [36]. XRD analysis presented in Fig. 4(b) reveals the phase composition of the PEO coating formed on AZ21 substrate. The incident angle of  $3^\circ$  was chosen to ensure that the X-ray is diffracted from the entire thickness of the coating, which is confirmed by the presence of Mg peaks in the obtained spectra. The XRD spectra indicated the presence of MgO and  $Mg_3(PO_4)_2$  as the main phases of the PEO layer. A few small peaks can be observed in the  $2\theta$  range of  $10$ – $20^\circ$ , which remained unidentified and possibly associated with the minor phases that contain aluminum and zinc from the substrate. The hump observed in the  $2\theta$  range of  $20$ – $40^\circ$ , which is situated where the majority of  $Mg_3(PO_4)_2$  diffraction peaks are populated, can be attributed to nano-crystalline or amorphous  $Mg_3(PO_4)_2$  phase [37,38].

The incorporation of an inhibitor in a coating system inherently runs into the problem of inefficient release of the inhibitor that is consumed during the exposure to corrosive medium. Moreover, it is challenging to determine the local concentration of inhibitors in the coating. Therefore, to overcome the hurdle of the abovementioned obscurities, here we directly immerse a circular area of the PEO-coated magnesium substrate with diameter of 8 mm into a NaCl solution containing 2,5PDC. This approach allows for better control of the corrosion inhibitor concentration that is exposed to the PEO-coated sample. Besides, in this

method, the inhibitor is being supplied to the sample from an ample source of electrolyte that helps to solve the problem of insufficiency of inhibitors during the immersion test.

Fig. 5 illustrates the Bode plots of the PEO-coated AZ21 exposed to 3.5 wt% NaCl containing different concentrations of 2,5PDC. The surface macrographs of the PEO-coated AZ21 after the immersion in each solution are presented at the bottom of each case. The immersion tests were stopped when a failure in the PEO coating was observable. Failure of PEO coating occurs when a chunk of the PEO layer is detached from the coating which appears as a black pitting-like region, marked with an arrow in Fig. 5. This failure appears as a relatively drastic drop of impedance value (at low frequencies) due to the complete deterioration of PEO layer in the local area. Fig. 6 displays the modulus of the impedance at low-frequency 0.1 Hz for the spectra shown in Fig. 5, which can be considered as the corrosion resistance of the samples. For the sake of clarity, only a selection of the recorded EIS spectra during the immersion is presented in Fig. 5 for each case, while all the data points are provided in Fig. 6. Fig. 6 and Fig. 5, clearly show that the addition of 2,5PDC in the solution, in all the tested concentrations, did not have any positive effect on the corrosion protection properties of PEO-coated AZ21, but rather reduced the corrosion resistance and accelerated the failure. The increase in the concentration of 2,5PDC in the solution results in faster deterioration of PEO protective properties in different manners: decrease in  $Z_{mod}$  values at low frequencies, faster observable failure, and faster extension of failure region. Similar slightly negative effect of 2,5PDC (along with 5-aminosalicylate and metavanadate) on protective properties of PEO treated AZ31 alloy was recently reported by Zhang et al. [39].

This discrepancy between the corrosion inhibition effect of 2,5PDC on bare AZ21 and PEO-coated AZ21 is, as of now, the focus of this work in the search for possible criteria to choose an effective inhibitor for PEO-coated magnesium alloys. Since the higher concentrations of 2,5PDC led to a more adverse effect on the PEO-coated AZ21, 0.25 M was chosen as the 2,5-PDC concentration to be used for the rest of the investigation.

To have a better understanding of the variation in PEO barrier properties during the immersion, the impedance of PEO-coated AZ21 immersed in 3.5 wt% NaCl with and without 0.25 M 2,5PDC was recorded in more frequent time intervals within 24 h of immersion, as shown in Fig. 7. The Nyquist curves between 10 and 90 min of immersion in 3.5 wt% NaCl reveal two distinguishable capacitive semicircles at the high and low-frequency range. The corresponding time constant at high-frequency range is attributed to the oxide layer on the Mg substrate that comprises the inner layer of PEO at the beginning of the immersion. The low-frequency range time constant is attributed to the double layer capacitance coupled with the charge transfer resistance on the surface of the corroding magnesium substrate. Bear in mind that the relatively high thickness ( $\sim 43 \mu m$ ) of the PEO outer layer with large pores does not

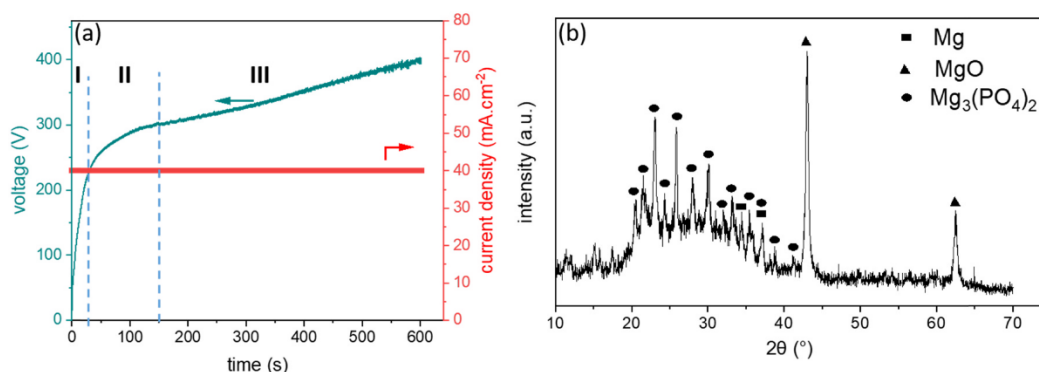


**Fig. 4.** (a) Current density/voltage – time characteristics of the PEO formed on the AZ21 substrate (b) XRD spectrum of PEO-coated AZ21.

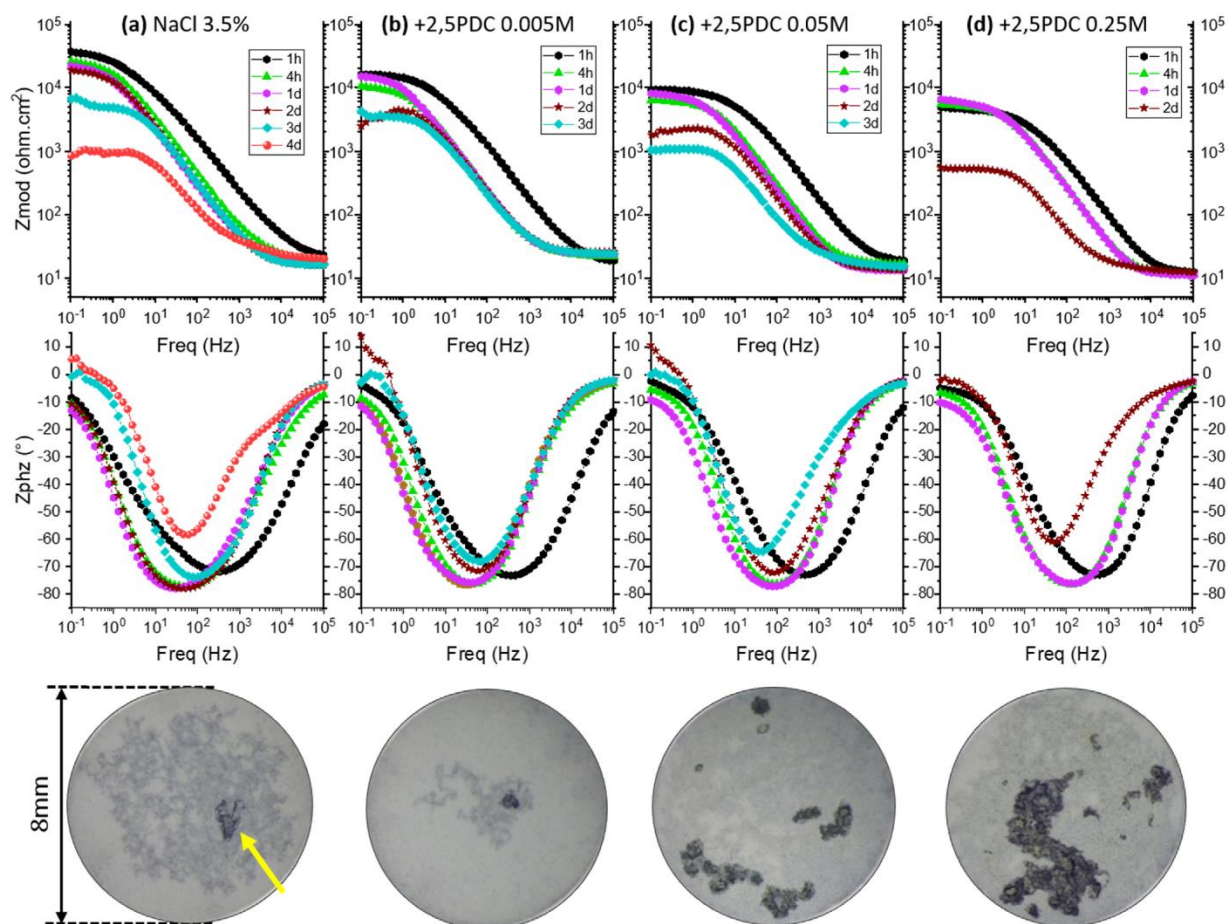


Fig. 5. Bode plots of PEO-coated AZ21 immersed in 3.5 wt% NaCl containing (a) 0, (b) 0.005 M, (c) 0.05 M, and (d) 0.25 M 2,5PDC until the failure of PEO coating. The surface appearance of PEO-coated AZ21 after the failure is shown in the bottom of each case.

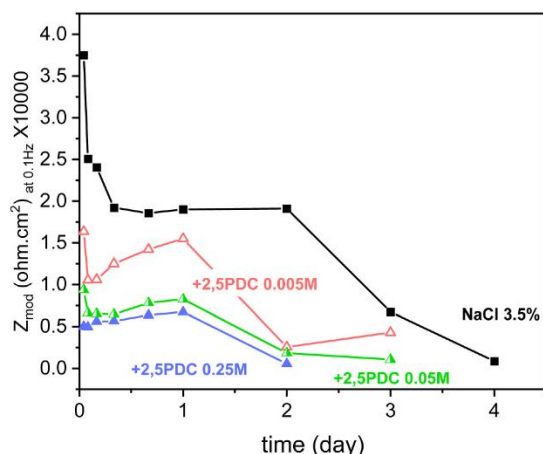


Fig. 6. Impedance modulus at 0.1 Hz for the EIS spectra presented in Fig. 5.

impose any impedance response visible in the EIS spectra, and the applied potential perturbation during the EIS measurement perceives the electrolyte inside the outer layer pores as similar to the electrolyte in the bulk electrolyte away from the PEO layer. The two time constants

extensively overlap during the immersion, seemingly appearing as one semi-circle within the measured frequency range after 150 min of immersion. Further immersion in the electrolyte leads to a gradual shrinkage of the overall impedance, which reaches its minimum at 13 h of immersion. Only a negligible variation can be observed from the 13th to the 24th hour.

When 2,5PDC is introduced to the solution, a similar two-time constant curve can be seen at the beginning of immersion, followed by the extensive overlapping of the two time constants and shrinkage of the overall impedance amid the immersion. The minimum overall impedance is achieved only after 60 min of immersion, which is significantly lower than that of NaCl solution without 2,5PDC. Interestingly, unlike the electrolyte without 2,5PDC, the continued immersion in the solution leads to a considerable increase in the impedance for the remainder of the immersion period. Such a remarkable enhancement of impedance after its initial rapid drop can also be seen in Fig. 6 for the electrolyte containing all tested concentrations of 2,5PDC. This increase reflects a relatively fast formation of a protective layer on the substrate, yet weaker as compared to the barrier properties of the film at any time of immersion for the case of electrolyte without 2,5PDC.

The EIS spectra in Fig. 7 are modeled with the equivalent circuit in Fig. 8(d) and the extracted values of the resistant elements are illustrated in Fig. 8(a–c). In the equivalent circuit,  $R_s$  represents for the solution resistance.  $R_{ox}$  and  $CPE_{ox}$  denote the resistance and the constant phase element of the oxide layer on the Mg substrate, respectively.  $R_{ct}$  and

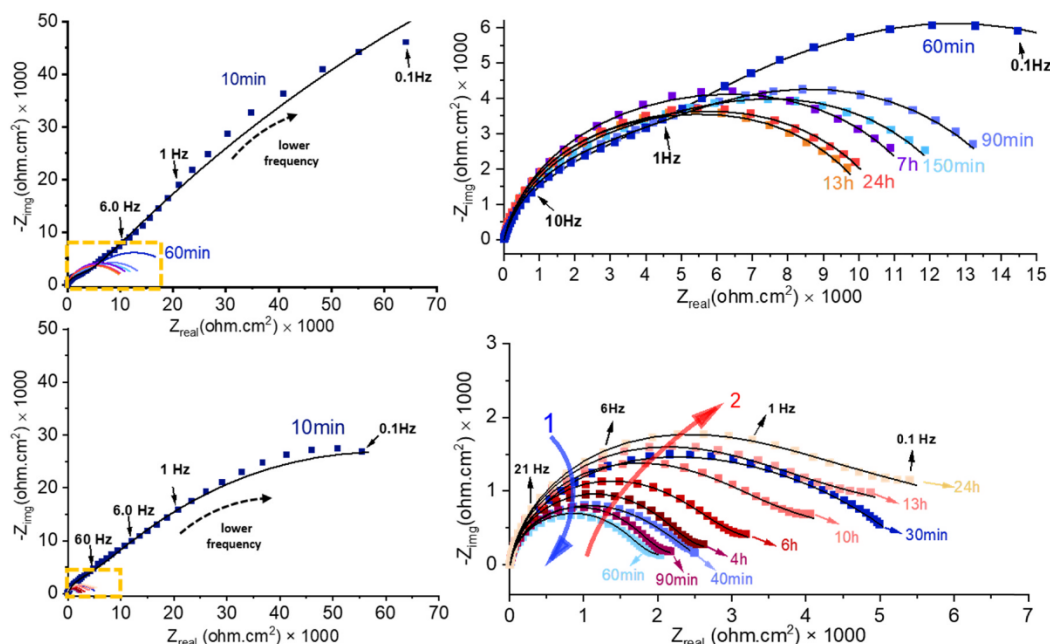


**Fig. 7.** Nyquist plots of PEO-coated magnesium immersed in 3.5 wt% NaCl without (a) and with (b) 0.25 M 2,5PDC. The frequency of the data points range between  $10^5$ –0.1 Hz. Higher magnification of marked area in each case is depicted on its right side. Colors blue and red reflect the shrinking and growing periods of impedance, respectively. The solid black lines are illustrating the fitting curves based on the equivalent circuit shown in Fig. 8. (For interpretation of the references to color in this figure legend, the reader is referred to the web version of this article.)

$CPE_{dl}$  signify for the charge transfer resistance and the double layer constant phase element corresponding to the corrosion occurring on the surface of magnesium. During the first hour of immersion in the electrolyte with and without 2,5PDC the  $R_{ox}$  rapidly declines to a minimum value due to the fast degradation of the inner layer of PEO. Subsequently, the resistance of the oxide layer on the magnesium substrate increases, which can be ascribed to the local alkalization during the corrosion of the magnesium substrate [40]. In the case of the electrolyte without 2,5PDC,  $R_{ox}$  shows a diminishing trend again after 6 h for the rest of the immersion. However, the presence of 2,5PDC in the electrolyte leads to a continuous enhancement of the  $R_{ox}$  till the end of 24 h. Within the first hours of immersion,  $R_{ct}$ , corresponding to the electrolyte with 2,5PDC, experiences a sharp decline to its minimum value. This is followed by a continuous growth for the rest of the immersion. On the other hand, in the case of the blank NaCl electrolyte,  $R_{ct}$  continuously decreases until it reaches a plateau after about 13 h. Thus, the  $R_{ct}$  value for of 2,5PDC-containing electrolyte surpasses that of blank NaCl electrolyte at the end 24 h of immersion.  $R_{total}$  was calculated from the sum of  $R_{ox}$  and  $R_{ct}$ , which roughly reflects the corrosion resistance of the sample. From Fig. 8(c), the corrosion resistance of the PEO-coated AZ21 immersed in the 2,5PDC-containing electrolyte initially steeply reduces to a lower value than that of blank NaCl electrolyte. However, the immediate and continuous increase of corrosion resistance amid the immersion stems from the formation of a protective layer on the magnesium substrate, as explained from the visual interpretation of the Nyquist plots in Fig. 7.

Fig. 9 represents the surface and cross-sectional morphology of PEO-coated AZ21 before and after 1 day of immersion in 3.5 wt% NaCl solution in presence or absence of 2,5PDC. The as-received PEO layer has average thickness of  $43.7 \pm 10.8 \mu\text{m}$  and features large pores in the outer layer, capacious for storing inhibitor. Moreover, several cracks can be observed in the PEO outer layer, which are formed due to the thermal stresses generated during the PEO process [41].

Immersion in 3.5 wt% NaCl with and without 2,5PDC for 1 day causes deterioration of the PEO layer which is evident by more open and

frequent cracks observable on both top and cross-sectional view of the PEO layer. Corrosion products are also formed uniformly at the PEO/substrate interface after 1 day of immersion, which is typical of the initial degradation stage of stand-alone phosphate-based PEO coatings on magnesium alloys [42,43]. Evidently, the presence of 2,5PDC in the electrolyte exacerbates the deterioration of PEO-coated AZ21 immersed in the 3.5 wt% NaCl solution, which is evident from larger pores and wider cracks in the PEO layer. Furthermore, a significantly thicker corrosion product is formed at the PEO/substrate interface.

Higher magnification images taken in STEM mode from a lamella taken at the interface between the PEO and the substrate are presented in Fig. 10. The PEO layer features nano-size pores at some regions marked in Fig. 10(a). Comparing the interface of the samples immersed in 3.5 wt% NaCl with and without 2,5PDC reveals that the corrosion product formed on AZ21 substrate is considerably more porous when 2,5PDC is present in the solution. Moreover, the corrosion products in the case of NaCl solution without 2,5PDC are limited to the substrate/PEO interface, while the corrosion products in the case of 2,5PDC-containing solution have extended even to the pores of the PEO outer layer.

Fig. 11 presents the variation of dissolved  $O_2$  and  $H_2$  concentrations at about 50  $\mu\text{m}$  above the PEO-coated specimen during the first 4 h of immersion in 3.5 wt% NaCl solution in the presence and absence of 2,5PDC. The concentration of dissolved  $O_2$  and  $H_2$  in the solution can be affected by different chemical/electrochemical reactions occurring during immersion.

Coupled with the anodic magnesium oxidation reaction in Eq. (1),  $H_2$  evolution reaction (HER) is commonly considered as the main cathodic reaction occurring on Mg alloys surface according to the Eq. (2).



Based on the same concept of  $H_2$  evolution test, concentration of dissolved  $H_2$  in the solution can be used as an indication of the cathodic reaction rate in Eq. (2). The local measurement of the  $H_2$  concentration

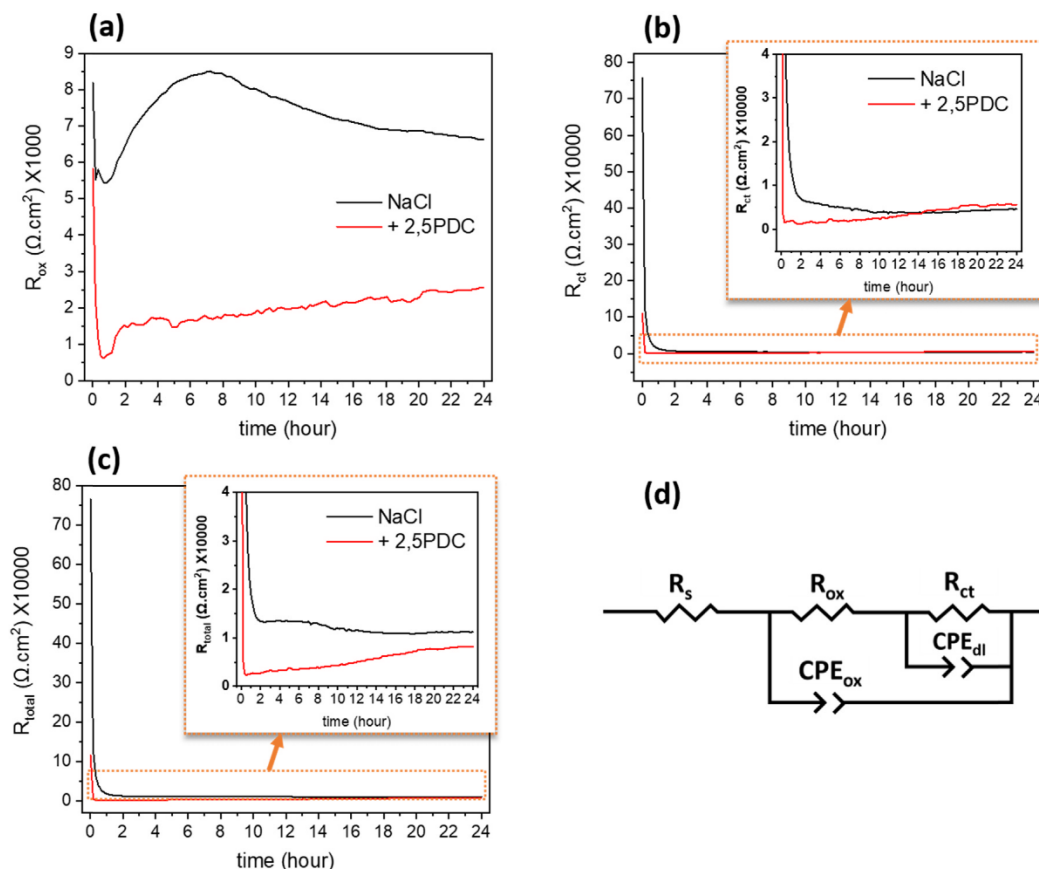


Fig. 8. Evolution of parameter obtained from the fitting of EIS spectra in Fig. 7 with the corresponding equivalent circuit depicted in (d).

provides valuable information on the magnesium substrate corrosion rate that is out of the detection limit of a typical integral  $H_2$  evolution test. In fact, the dissolved  $H_2$  in the electrolyte solution is considered as the source of error for typical  $H_2$  evolution measurements [44], especially for specimens with substantially low corrosion rates [30,45], which include magnesium substrates protected by a PEO layer. The solubility of  $H_2$  in the 3.5 wt% NaCl solution with and without 2,5PDC 0.25 M is 679.24 and 508.47  $\mu\text{mol L}^{-1}$ , which was calculated based on the salinity of the solution at 22 °C [46]. As can be seen in Fig. 11(a),  $H_2$  concentration increases progressively from the onset of immersion in 3.5 wt% NaCl solution until it reaches the maximum value of about 40  $\mu\text{mol L}^{-1}$  after about 4 h. However, immersion of the sample in the solution containing 2,5PDC leads to a higher initial rate of evolved  $H_2$ , which reaches its maximum value at about 85  $\mu\text{mol L}^{-1}$  after 3 h of immersion. A slight decline in the dissolved  $H_2$  content can be observed for the rest of the immersion period. Therefore, it can be claimed that the corrosion rate of PEO-coated AZ21 due to the cathodic reaction of Eq. (2) is much higher when 2,5PDC is present in the solution. The same is observed from the bigger bubbles appeared on the surface of 2,5PDC sample. The slight drop of  $H_2$  concentration after 3 h of immersion is consistent with the increased barrier effect observed from the EIS result (Fig. 7(b)), explaining the reduction of the corrosion rate based on the  $H_2$  evolution.

The oxygen reduction reaction (ORR) is the second possible cathodic reaction that occurs on magnesium surface according to Eq. (3):



The oxygen concentration value above the PEO layer immersed in

3.5 wt% NaCl (Fig. 11(b)) remains at 7 ppm for the whole course of immersion, with only a negligible decrease.

Addition of 2,5PDC to the NaCl solution causes an overall decrease in the solubility of the  $O_2$  in the solution due to its higher ionic strength. Thus, the initial dissolved oxygen concentration has a lower value (around 6 ppm) as compared to the solution containing 2,5PDC. Note that, to the best of our knowledge, 2,5PDC and its isomers do not react with oxygen in aqueous environment. The oxygen concentration in the solution containing 2,5PDC is not subjected to any significant change within the first 30 min of immersion. Then, a drastic decrease to almost full local depletion of oxygen after 90 min can be observed, suggesting that the ORR is highly activated on the substrate. Finally, the oxygen concentration gradually increases to about 2 ppm after 4 h of immersion. Akin to the  $H_2$  concentration trend, the last slight rise of oxygen content is attributed to the mild protective film forming on the substrate. Moreover, the formation of a thicker corrosion product layer (see Fig. 9) in the case of immersion in the electrolyte containing 2,5PDC can impede the penetration of dissolved  $O_2$  towards the substrate.

Fig. 11(c) represents the pH values measured above the PEO layer during the immersion. pH in both solutions abruptly surges from neutral pH to a plateau in less than a minute of immersion. The rapid increase of pH in the proximity of the PEO layer mainly stems from the cathodic reactions in Eqs. (3) and (2). In addition to the HER and ORR, the hydrolysis of MgO [47–49] and dissolution of  $Mg_3(PO_4)_2$  as the main components of the PEO layer can cause a pH increase at the proximity of the PEO layer (see Eqs. (4–7)). Note that hydrolysis of  $Mg^{2+}$  (Eq. (8)), released due to the dissolution of  $Mg_3(PO_4)_2$  (Eq. (5)) and the anodic reaction on the bare magnesium in (Eq. (1)), generates low amount of

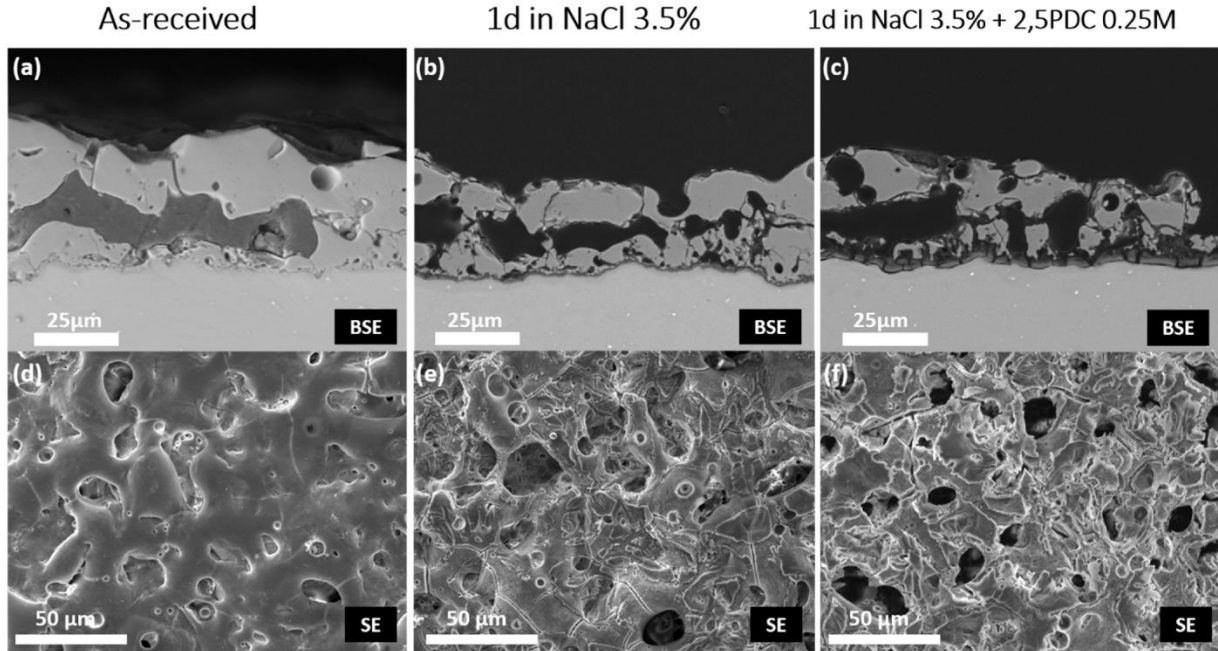


**Fig. 9.** Cross-sectional and surface morphologies of PEO-coated AZ21 (a) and (d) as-received; (b) and (e) after 1 day immersion in 3.5 wt% NaCl; (c) and (f) after 1 day immersion in 3.5 wt% NaCl + 0.25 M 2,5PDC.

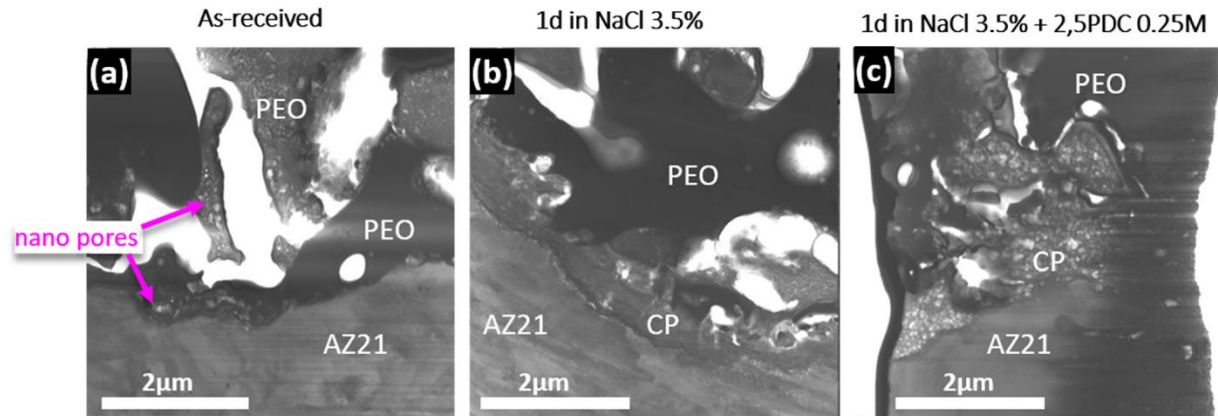
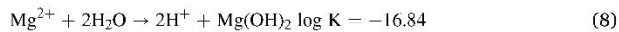
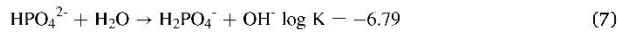
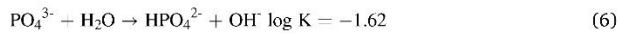
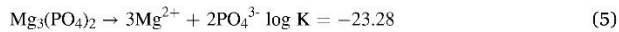
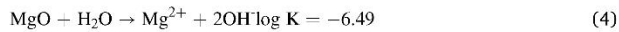


**Fig. 10.** Bright field STEM image of lamella from the PEO/substrate interface of (a) as received sample (b) after 1 day immersion in 3.5 wt% NaCl (c) after 1 day immersion in 3.5 wt% NaCl + 0.25 M 2,5PDC. (CP here stands for corrosion products).

$H^+$ , negligible as compared to all the alkalinizing reactions from HER and ORR (Eq. (7)) [50].



The plateau pH value is slightly higher (about 0.5 pH unit) when the solution contains 2,5PDC, which is in line with the bulk pH observed in Fig. 2.

Formation of  $Mg(OH)_2$  after the elevation of pH substantially hinders

further pH increase in the solution [51] which is reflected by a plateau in Fig. 11(c). This can be seen in the equilibrium chemical composition obtained using Hydra-Medusa software [52] for the aqueous system containing PEO components with and without the presence of 2,5PDC, as depicted in Fig. 12. The input concentrations for  $Mg^{2+}$  and  $PO_4^{3-}$  ions are approximately given, although, the main interpretation of solution pH variation and the effect of the addition of 2,5PDC into the system remains consistent for different rational range of concentrations (two orders of magnitude variation in the given concentration of  $Mg^{2+}$  or  $PO_4^{3-}$ ). It is observed that the presence of 2,5PDC leads to a shrinkage of stability region for  $Mg_3(PO_4)_2$ , which in turn means higher dissolution of this phase into the solution. Furthermore, the  $Mg(OH)_2$  formation pH is slightly shifted to a higher value with the presence of 2,5PDC in the electrolyte, which is in line with the observed higher plateau pH in Fig. 11(c) and higher pH bulk in Fig. 2.

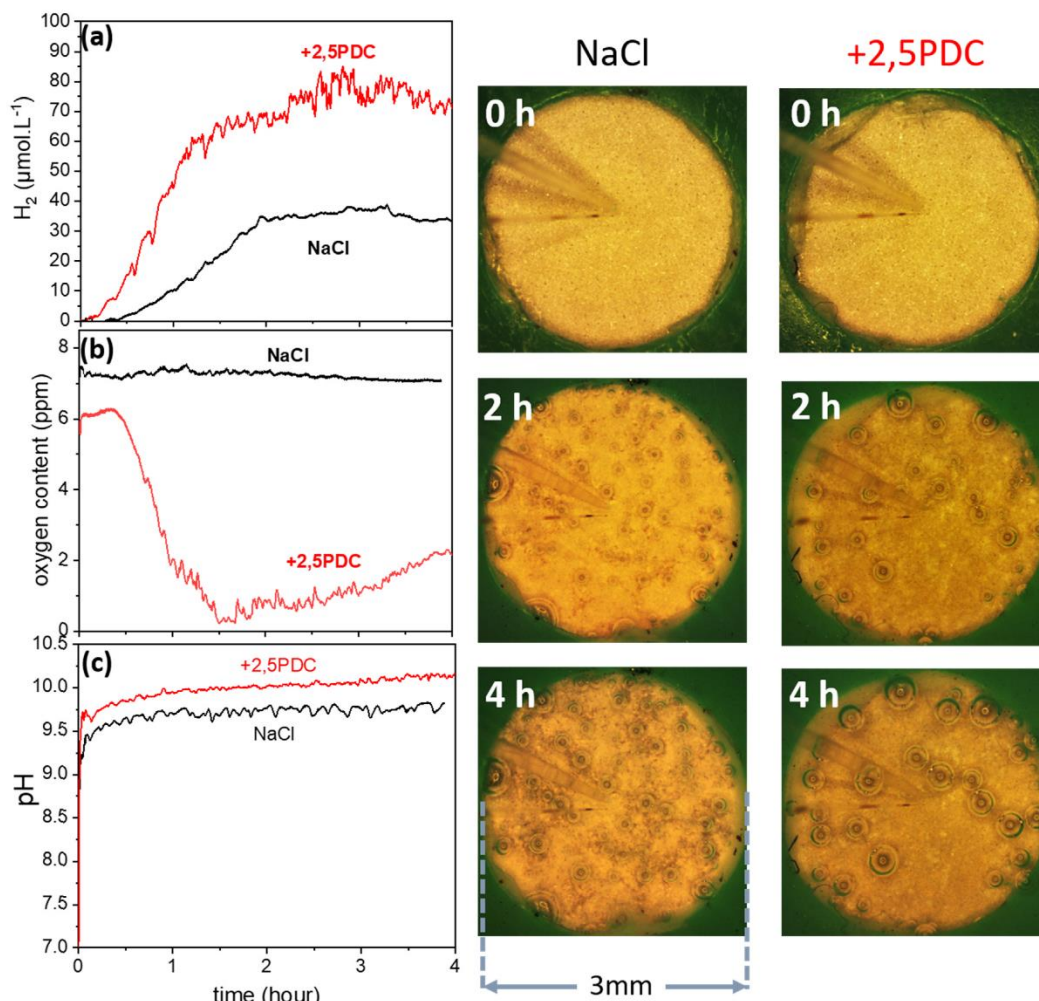


**Fig. 11.** (a) H<sub>2</sub> and (b) O<sub>2</sub> concentration, and (c) pH locally measured above the PEO-coated magnesium during 4-h immersion in 3.5 wt% NaCl with and without the presence of 2,5PDC 0.25 M. Macrographs on the bottom: visual appearance of PEO-coated magnesium after 0, 2, and 4 h of immersion.

#### 4. Discussion

##### 4.1. Inhibition mechanism of 2,5PDC on bare AZ21 magnesium alloy

The corrosion inhibition effect of 2,5PDC on the AZ21 magnesium substrate was validated via the H<sub>2</sub> evolution test; however, when the AZ21 magnesium is coated with the PEO, it failed earlier in the presence of 2,5PDC in corrosive NaCl solution. To better understand the observed contradictory effect of 2,5PDC towards bare and PEO-coated AZ21, the available knowledge of the inhibition mechanism of PDCs on bare magnesium alloys is meticulously reviewed and provided in this section. Moreover, an additional characterization of surface of a bare pure magnesium in the interaction with one PDC is discussed.

The universal corrosion inhibitive properties of PDCs on Mg alloys were introduced and initially investigated by Lamaka et al. [22]. Four different isomers of PDCs were found to have effective corrosion inhibition on six different magnesium alloys (WE43, ZE41, E21, AZ31, AZ91, and AM50) and three different grades of pure magnesium (two high purity (HP) magnesium and one commercially pure (CP) magnesium). One deduced mechanism of inhibition was established based on PDCs' affinity to form complexes with Fe<sup>2+/3+</sup> that suppresses the re-deposition of Fe impurities onto a corroding Mg substrate [53,54].

Yang et al. [25] substantiated the dominating anodic inhibition mechanism of 2,5-PDC on a CP-Mg (342 ppm Fe) using electrochemical characterization methods. In particular, when the PDC was introduced to the NaCl solution, the OCP was shifted towards more positive values, a lower anodic current density was detected using potentiodynamic polarization method, and the magnesium surface experienced higher barrier properties detected by EIS. An in-situ characterization using Confocal Raman Microscopy (CRM) on the same CP Mg (342 ppm Fe) immersed in NaCl solution containing 2,5PDC detected a delayed strong fluorescent response on the same CP magnesium (342 ppm Fe), suggesting a coordination polymer formed by the complexation between Mg ions and 2,5PDC [26]. Employing GD-OES depth profiling, the detected polymer layer was stratified in between two Mg(OH)<sub>2</sub> layers. Moreover, using the same technique, it was found that the Cl<sup>-</sup> concentration in the formed corrosion layer was significantly limited when 2,5PDC was present in the NaCl solution. Fockaert et al. [27] investigated the in-situ interaction of a 2,5PDC solution with pure magnesium surface using the ATR-FTIR measurement in Kretschmann configuration. The formation of a hydroxylated Mg(OH)<sub>2</sub>/MgO was observed, which rapidly increased at the beginning of the exposure to the electrolyte, followed by a sharp decrease in the detected quantity of Mg(OH)<sub>2</sub> after 2 min of immersion.

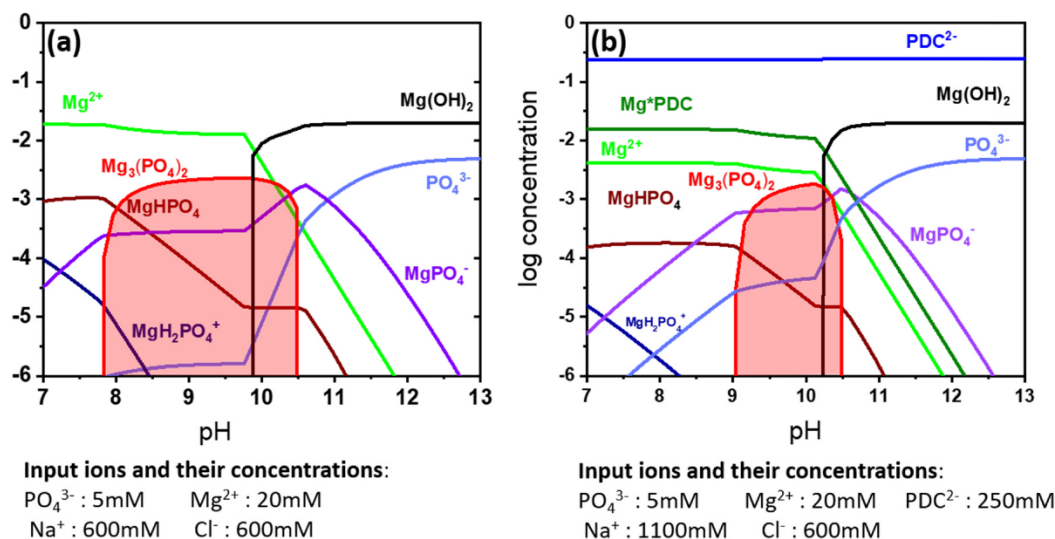


**Fig. 12.** Thermodynamic calculation of the equilibrium composition of the aqueous electrolyte containing  $\text{PO}_4^{3-}$ ,  $\text{Mg}^{2+}$  ions (a) without and (b) with 2,5PDC $^{2-}$ . Note 1: Presence of  $\text{Na}^+$ ,  $\text{Cl}^-$  and other protonated forms of phosphates and its compounds with Mg have been taken into account for the calculations, but only a selection of important ions is illustrated here. Note 2: The plotted result is based on the stability constant of 2,6PDCA, which is expected to be similar to 2,5PDCA.

In brief, based on the review of available literature on PDCs' interaction with bare magnesium alloys, it can be deduced that the inhibition mechanism on bare magnesium is inextricably tied to the formation of  $\text{Mg}(\text{OH})_2$  on the surface. This points out the major effect of magnesium matrix and fits well with the observed universal effect of PDCs on a wide range of alloys with different second phases. Additionally, in the reviewed studies, a sort of initial incubation time for the inhibition response from PDCs has been recorded that can be inferred as the required time to stabilize the formation of  $\text{Mg}(\text{OH})_2$ /PDC combination.

Following the same experimentation as the reviewed scientific studies above, an additional characterization using ToF-SIMS was carried out on a CP magnesium (342 ppm Fe). Chemical in-depth profiles have been measured on the surface of freshly polished samples before and after 15 min immersion in 0.5 wt% NaCl solution with or without 2,6PDC. They are presented in Fig. 13.

Before immersion, the CP-Mg substrate is covered by a corrosion product layer, whose thickness is determined from the decrease of the  $\text{MgO}_2^-$  ion signal. The thickness of the corrosion layer corresponds to 25 s of sputtering, which means, after calibration of the sputtering rate from XPS data (not presented here), around 5 nm. The oxide scale is characterized by intense  $\text{MgO}_2^-$  and  $\text{MgOH}^-$  ions, meaning that it comprises Mg oxide and Mg hydroxide. The position of the maxima of intensity of these ions ( $\text{MgO}_2^-$  and  $\text{MgOH}^-$ ) clearly shows that the oxide is stratified with a MgO inner layer and a  $\text{Mg}(\text{OH})_2$  outer layer. This reflects the widely accepted  $\text{Mg}(\text{OH})_2$ /MgO bilayer model of the corrosion products on magnesium substrates [40,55–58]. A more detailed examination of the depth profile shows that the maximum of the  $\text{CO}_3^-$  signal is located above the  $\text{MgOH}^-$  signal. This is assigned to the formation of a carbonate layer, likely  $\text{MgCO}_3$ , covering the surface. Finally,  $\text{MgH}^-$  and  $^{25}\text{MgH}^-$  signals, indicating the presence of  $\text{MgH}_2$  [49], were also identified, which are more pronounced close to the oxide/substrate. The presence of magnesium hydride in the corrosion products formed on magnesium alloys has been reported before [23,55,59]. However, further discussion about the role of this compound in magnesium corrosion is out of the scope of this work and will not be addressed in the rest of this paper.

The depth profile of the magnesium surface after immersion in NaCl solution with and without the presence of 2,6PDC shows the same ions as for the polished sample before immersion. Except for the very low amount found at the extreme surface, the  $\text{C}_7\text{H}_4\text{NO}_4\text{Mg}^-$  fragment related

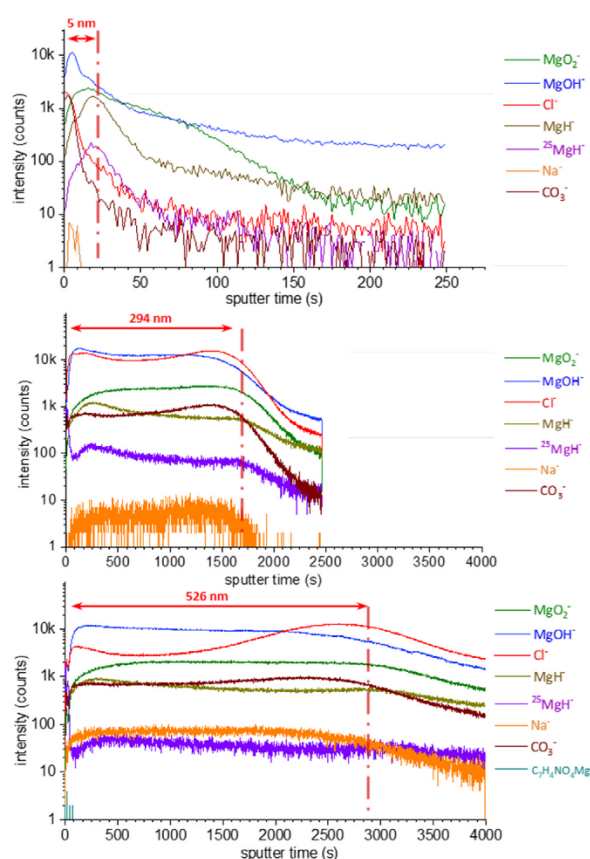


**Fig. 13.** ToF-SIMS (negative polarity) depth profiles recorded on the polished CP-Mg (a) before immersion (b) after immersion in 0.5 wt% NaCl (c) after immersion in 0.5 wt% NaCl + 2,6PDC.

to the presence of 2,6PDC was not detected after the immersion in the solution containing this inhibitor. A high  $\text{Cl}^-$  signal, especially close to the substrate, indicates that the  $\text{Cl}^-$  are mainly located at the  $\text{MgO}/\text{Mg}$  interface and at the extreme surface. This observation suggests that chloride are entrapped within the formed film and the rinsing step could not remove them.  $\text{MgO}^-$  and  $\text{MgOH}^-$  intensities remain at the same level in the whole thickness of the corrosion product layer. After immersion, the stratification of the corrosion layer is no longer clearly marked. Nevertheless, a slight gradual decrease in intensity of the  $\text{MgOH}^-$  signal towards the substrate interface and a progressive increase of the  $\text{MgO}_2^-$  signal close to the surface are observed, indicating a more pronounced  $\text{Mg}(\text{OH})_2$  and  $\text{MgO}$  concentration at the outer interface and oxide-substrate interface, respectively. The total estimated thicknesses (based on the sputtering rate determined from XPS for the reference sample before immersion) of the formed films are 294 nm and 526 nm when the sample is immersed in NaCl without and with 2,6PDC, respectively. From this result, it can be concluded that 2,6PDC has initially promoted the corrosion product formation on the magnesium substrate that resulted in a thicker corrosion product layer. This conclusion is again in line with all the reviewed results that a rapid establishment of an initial corrosion product layer, mainly made of  $\text{Mg}(\text{OH})_2$ , is crucial to activate the corrosion inhibition effect of PDCs on magnesium alloys.

#### 4.2. Adverse effect of 2,5PDC on AZ21 magnesium alloy coated with PEO

Fig. 14 shows the schematic of the failure mechanism for PEO-coated AZ21 immersed in NaCl solution containing 2,5PDC. At the beginning of the immersion, the water penetrates through the PEO pores and transfers  $\text{Cl}^-$  and 2,5PDC towards the Mg substrate Fig. 14(a). The aqueous medium reaches the AZ21 substrate within the first few minutes of immersion, which leads to the immediate cathodic HER occurring on the Mg substrate, as was evident in the increasing local concentration of dissolved  $\text{H}_2$  in Fig. 11(a).

Despite being often disregarded as the contributing cathodic reaction on magnesium surface, recent studies have strongly substantiated the potentially high contribution of ORR to the magnesium corrosion rate, especially if the overall corrosion rate of magnesium is relatively low [31,33,45,60]. A recent study conducted by Wang et al. [33] has reported that a considerably high rate of ORR can occur on ultra-high-purity magnesium, while comparatively low oxygen is consumed on commercially pure magnesium (CP-Mg) during the immersion in 0.05 M NaCl solution. This observation was explained by the barrier effect of intensively formed  $\text{Mg}(\text{OH})_2$  on CP-Mg against the

diffusion of dissolved oxygen towards the substrate. Analogously, the thin barrier layer of the PEO on the AZ21 substrate can restrict the diffusion of dissolved oxygen molecules towards the substrate. Thus, ORR could not occur on the PEO-coated AZ21 immersed in NaCl solution amid 4 h of measurement (Fig. 11(b)). The stable oxygen content at the first 30 min of immersion in the solution containing 2,5PDC can be similarly explained by the barrier effect of the PEO layer against the penetration of  $\text{O}_2$  molecules towards the AZ21 substrate. However, the rapid deterioration of the PEO layer by 2,5PDC, which was evident in the cross-sectional images in Fig. 9(c), opens up cracks and pores in the PEO coating, facilitating the diffusion of oxygen molecules, as illustrated in Fig. 14(b). Therefore, the ORR on the substrate becomes activated, which appears in the rapid drop of oxygen concentration after 30 min of immersion. Furthermore, the widened pathways within the PEO layer can deliver higher concentrations of  $\text{Cl}^-$  towards the AZ21 substrate that intensifies its corrosion rate [61–63].

The deteriorating effect of the 2,5PDC against the PEO layer stems from its capability to form soluble complexes with  $\text{Mg}^{2+}$ . Thus, the presence of 2,5PDC in the NaCl solution facilitates the dissolution of  $\text{Mg}_3(\text{PO}_4)_2$ , as one of the main phases in the PEO layer (Fig. 4(b)), which was confirmed by the thermodynamic calculation of equilibrium compositions presented in Fig. 12. Note that, the amorphous form of  $\text{Mg}_3(\text{PO}_4)_2$ , which was confirmed by the apparent hump in the XRD spectrum in Fig. 4(b), undergoes a relatively faster dissolution as compared to the crystalline  $\text{Mg}_3(\text{PO}_4)_2$ .  $\text{MgO}$  is thermodynamically unstable in an aqueous environment. Therefore, there is no stability region for  $\text{MgO}$  in the equilibrium condition illustrated in Fig. 12. However, as compared to the amorphous  $\text{Mg}_3(\text{PO}_4)_2$ ,  $\text{MgO}$  has a higher stability in a  $\text{Cl}^-$  containing aqueous electrolyte [42]. On the other hand, it has been reported that  $\text{MgO}$  hydration kinetics can be affected by the presence of carboxylic acids [64] in the solution, which in turn leads to different morphology of the formed  $\text{Mg}(\text{OH})_2$  [26]. Such effect is attributed to the decrease of the energetic barrier for the interaction between  $\text{MgO}$  and  $\text{H}_2\text{O}$  at the sites where the carboxylate group has bonded (or adsorbed) to the  $\text{MgO}$  surface [65]. The inner barrier layer of PEO, which primarily endows the corrosion protection properties of this coating technique, is reported to be mainly made of  $\text{MgO}$  [66,67]. During the exposure of this layer to an aqueous solution,  $\text{MgO}$  undergoes hydrolysis, which is intensified by the presence of  $\text{Cl}^-$  in the solution [28]. This degradation process of the PEO inner barrier layer occurs within the first 13 h of immersion in the NaCl solution as the impedance response of the sample surface reached its minimum value (Figs. 7 and 8). 2,5PDC accelerates the degradation of PEO inner barrier layer, which is shown by the considerably faster decline of the impedance response.

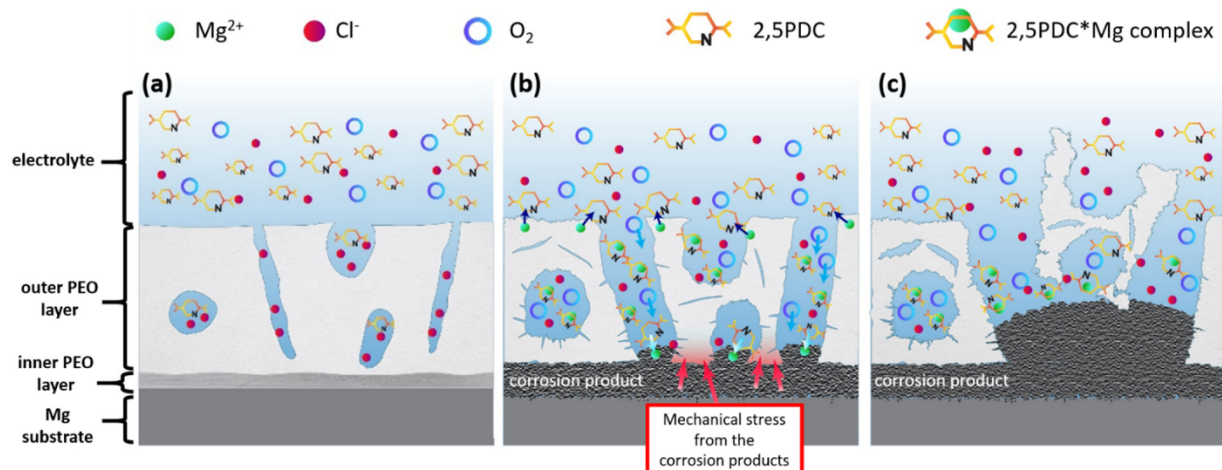


Fig. 14. Schematic of failure mechanism for PEO-coated magnesium immersed in NaCl solution containing 2,5PDC.

After only 1 h of immersion in the solution containing 2,5PDC, when the PEO inner barrier layer is already eradicated, the corrosion prevention response of the inhibitor on the bare Mg starts to develop. This was reflected in the gradual reduction in HER and ORR rates and the rapid increase of impedance during the same immersion time window attributed to the formation of a thick modified  $\text{MgO}/\text{Mg}(\text{OH})_2$  film. However, the barrier properties of this film are considerably lower than that of the inner barrier layer of the PEO, resulting in a much lower impedance value.

The formation of corrosion product in the interface of PEO/substrate exerts stress on the PEO layer atop during the immersion in a corrosive medium. The accumulated stress can cause a local breakdown of the PEO layer (Fig. 14(c)), which is considered as the failure for the PEO and reflects in a considerable drop of impedance value. The establishment of a thick protective  $\text{MgO}/\text{Mg}(\text{OH})_2$  layer on the AZ21 substrate due to the presence of 2,5PDC intensifies the applied stress on the PEO layer atop, which in turn causes its earlier breakdown. The destructive accumulation of  $\text{MgO}/\text{Mg}(\text{OH})_2$  in the PEO/substrate interface is not only due to the corrosion process of the substrate. The soluble complex formed between the 2,5PDC and Mg ions taken from the PEO outer layer can transport more Mg ions towards the proximity of the PEO/substrate interface, which features high alkalinity owing to the cathodic reactions on the substrate. Consequently,  $\text{Mg}(\text{OH})_2$  precipitates and piles up on the interface or between the PEO pores, applying more destructive force to the PEO layer.

Furthermore, the interaction of 2,5PDC with the PEO layer itself causes consumption of free 2,5PDC during its pathway towards the substrate. Thus, lower concentrations of 2,5PDC reach the substrate, which degrades the inhibitive properties of 2,5PDC on AZ21 substrate (shown in Fig. 2).

## 5. Conclusion

In this study, the universal corrosion inhibition effect of 2,5PDC was validated on AZ21 magnesium alloy via the common  $\text{H}_2$  evolution test. However, it was observed that when AZ21 substrate was coated with the PEO, the presence of 2,5PDC in the corrosive NaCl solution caused an earlier failure of the coated sample. The positive inhibition effect on the bare AZ21 and the adverse effect on the PEO layer are both intensified with the increase of 2,5PDC concentration in the electrolyte.

The main mechanisms of such discrepancy of 2,5PDC effect are summarized as follows:

1. 2,5PDC forms soluble complexes with Mg ion. 2,5PDC expedites the decomposition of the PEO coating in the aqueous medium, which occurs by destabilization of  $\text{Mg}_3(\text{PO}_4)_2$  and facilitation of  $\text{MgO}$  hydration. This results in hastened obliteration of the protective inner barrier layer of PEO, as well as opening up the pathways for diffusion of the corrosive medium containing  $\text{Cl}^-$  and  $\text{O}_2$ .
2. The inhibitory mechanism of 2,5PDC on magnesium alloys entails the initial formation of a thick  $\text{Mg}(\text{OH})_2/\text{MgO}$  layer which further limits the magnesium corrosion. The formed protective layer provides considerably lower corrosion protection properties as compared to that of the already degraded inner barrier layer of PEO. Moreover, the additional mechanical stress exerted by the formation of this film on the PEO layer atop leads to its local breakdown.

The findings of this study suggest that the positive effect of an inhibitor towards the corrosion of a bare magnesium alloy must not be taken for granted when it is aimed to be incorporated in a PEO layer. The interaction between the PEO layer and the effective inhibitor must be investigated prior to its incorporation into the PEO layer.

## CRediT authorship contribution statement

**Bahram Vaghefinazari:** Conceptualization, Investigation,

Validation, Writing – original draft, Writing – review & editing. **Cheng Wang:** Investigation, Writing – review & editing. **Dimitri Mercier:** Investigation, Writing – review & editing. **Di Mei:** Investigation, Writing – review & editing. **Antoine Seyeux:** Investigation, Writing – review & editing. **Philippe Marcus:** Supervision, Writing – review & editing. **Carsten Blawert:** Conceptualization, Supervision, Writing – review & editing. **Sviatana V. Lamaka:** Conceptualization, Supervision, Writing – review & editing. **Mikhail L. Zheludkevich:** Conceptualization, Supervision, Writing – review & editing.

## Declaration of Competing Interest

The authors declare that they have no known competing financial interests or personal relationships that could have appeared to influence the work reported in this paper.

## Data

The raw/processed data required to reproduce these findings cannot be shared at this time as the data also forms part of an ongoing study.

## Acknowledgements

The authors would like to acknowledge the technical support from Mr. Ulrich Burmester, Mr. Volker Heitmann and Mr. Gert Wiese. Cheng Wang thanks China Scholarship Council for the award of fellowship and funding (No. 201806310128).

## Declaration of Competing Interest

The authors report no declarations of interest.

## Appendix A. Supporting information

Supplementary data associated with this article can be found in the online version at doi:10.1016/j.corsci.2021.109830.

## References

- [1] X. Lu, M. Moledano, C. Blawert, E. Matykina, R. Arrabal, K.U. Kainer, M. L. Zheludkevich, Plasma electrolytic oxidation coatings with particle additions – a review, *Surf. Coat. Technol.* 307 (2016) 1165–1182, <https://doi.org/10.1016/j.surfcoat.2016.08.055>.
- [2] G. Barati Darband, M. Aliofkhaei, P. Hamghalam, N. Valizade, Plasma electrolytic oxidation of magnesium and its alloys: mechanism, properties and applications, *J. Magnes. Alloy.* 5 (2017) 74–132, <https://doi.org/10.1016/j.jma.2017.02.004>.
- [3] Y. Chen, X. Lu, S.V. Lamaka, P. Ju, C. Blawert, T. Zhang, F. Wang, M. L. Zheludkevich, Active protection of Mg alloy by composite PEO coating loaded with corrosion inhibitors, *Appl. Surf. Sci.* 504 (2020), 144462, <https://doi.org/10.1016/j.apsusc.2019.144462>.
- [4] Y.H. Gao, A. Yerokhin, A. Matthews, Effect of current mode on PEO treatment of magnesium in Ca- and P-containing electrolyte and resulting coatings, *Appl. Surf. Sci.* 316 (2014) 558–567, <https://doi.org/10.1016/j.apsusc.2014.08.035>.
- [5] X.P. Lu, C. Blawert, D. Tolnai, T. Subroto, K.U. Kainer, T. Zhang, F.H. Wang, M. L. Zheludkevich, 3D reconstruction of plasma electrolytic oxidation coatings on Mg alloy via synchrotron radiation tomography, *Corros. Sci.* 139 (2018) 395–402, <https://doi.org/10.1016/j.corsci.2018.05.019>.
- [6] S.V. Lamaka, G. Krönschild, D.V. Snihirova, M.G. Taryba, M.L. Zheludkevich, M. G.S. Ferreira, Complex anticorrosion coating for ZK30 magnesium alloy, *Electrochim. Acta* 55 (2009) 131–141, <https://doi.org/10.1016/j.electacta.2009.08.018>.
- [7] J. Yang, C. Blawert, S.V. Lamaka, D. Snihirova, X. Lu, S. Di, M.L. Zheludkevich, Corrosion protection properties of inhibitor containing hybrid PEO-epoxy coating on magnesium, *Corros. Sci.* 140 (2018) 99–110, <https://doi.org/10.1016/j.corsci.2018.06.014>.
- [8] D.K. Ivanou, K.A. Yasakau, S. Kallip, A.D. Lisenkov, M. Starykevich, S.V. Lamaka, M.G.S. Ferreira, M.L. Zheludkevich, Active corrosion protection coating for a ZE41 magnesium alloy created by combining PEO and sol-gel techniques, *RSC Adv.* 6 (2016) 12553–12560, <https://doi.org/10.1039/c5ra22639b>.
- [9] E. Wierzbicka, B. Vaghefinazari, S.V. Lamaka, M.L. Zheludkevich, M. Moledano, L. Moreno, P. Visser, A. Rodriguez, J. Velasco, R. Arrabal, E. Matykina, Flash-PEO as an alternative to chromate conversion coatings for corrosion protection of Mg

- alloy, *Corros. Sci.* 180 (2021), 109189, <https://doi.org/10.1016/j.corsci.2020.109189>.
- [10] A.S. Gnedenkov, S.L. Sinebryukhov, D.V. Mashtalyar, S.V. Gnedenkov, Localized corrosion of the Mg alloys with inhibitor-containing coatings: SVET and SIET studies, *Corros. Sci.* 102 (2016) 269–278, <https://doi.org/10.1016/j.corsci.2015.10.015>.
  - [11] B. Mingo, Y. Guo, R. Leiva-Garcia, B.J. Connolly, A. Matthews, A. Yerokhin, Smart functionalization of ceramic-coated AZ31 magnesium alloy, *ACS Appl. Mater. Interfaces* 12 (2020) 30833–30846, <https://doi.org/10.1021/acsami.0c07726>.
  - [12] M. Toorani, M. Aliofkhaezari, M. Mahdavian, R. Naderi, Superior corrosion protection and adhesion strength of epoxy coating applied on AZ31 magnesium alloy pre-treated by PEO/Silane with inorganic and organic corrosion inhibitors, *Corros. Sci.* 178 (2021), 109065, <https://doi.org/10.1016/j.corsci.2020.109065>.
  - [13] D. Jiang, X. Xia, J. Hou, G. Cai, X. Zhang, Z. Dong, A novel coating system with self-repairable slippery surface and active corrosion inhibition for reliable protection of Mg alloy, *Chem. Eng. J.* 373 (2019) 285–297, <https://doi.org/10.1016/j.cej.2019.05.046>.
  - [14] A.C. Bouali, E.A. Straumal, M. Serdechnova, D.C.F. Wielan, M. Starykevich, C. Blawert, J.U. Hammel, S.A. Lermontov, M.G.S. Ferreira, M.L. Zheludkevich, Layered double hydroxide based active corrosion protective sealing of plasma electrolytic oxidation/sol-gel composite coating on AA2024, *Appl. Surf. Sci.* 494 (2019) 829–840, <https://doi.org/10.1016/j.apsusc.2019.07.117>.
  - [15] A.C. Bouali, M. Serdechnova, C. Blawert, J. Tedim, M.G.S. Ferreira, M. L. Zheludkevich, Layered double hydroxides (LDHs) as functional materials for the corrosion protection of aluminum alloys: a review (ARTN), *Appl. Mater. Today* 21 (2020), 100857, <https://doi.org/10.1016/j.apmt.2020.100857>.
  - [16] M. Serdechnova, M. Mohehdano, B. Kuznetsov, C.L. Mendis, M. Starykevich, S. Karpushenkov, J. Tedim, M.G.S. Ferreira, C. Blawert, M.L. Zheludkevich, PEO coatings with active protection based on in-situ formed LDH-nanocomposites, *J. Electrochem. Soc.* 164 (2016) C36–C45, <https://doi.org/10.1149/2.0301702jes>.
  - [17] A.S. Gnedenkov, S.L. Sinebryukhov, D.V. Mashtalyar, S.V. Gnedenkov, Inhibitor-containing composite coatings on Mg alloys: corrosion mechanism and self-healing protection, *Solid State Phenom.* 245 (2015) 89–96, <https://doi.org/10.4028/www.scientific.net/SSP.245.89>.
  - [18] D. Liu, E.H. Han, Y. Song, D. Shan, Enhancing the self-healing property by adding the synergetic corrosion inhibitors of Na<sub>3</sub>PO<sub>4</sub> and 2-mercaptobenzothiazole into the coating of Mg alloy, *Electrochim. Acta* 323 (2019), 134796, <https://doi.org/10.1016/j.electacta.2019.134796>.
  - [19] W. Al Zoubi, Y.G. Ko, Self-assembly of hierarchical N-heterocycles-inorganic materials into three-dimensional structure for superior corrosion protection, *Chem. Eng. J.* 356 (2019) 850–856, <https://doi.org/10.1016/j.cej.2018.09.089>.
  - [20] M. Sun, A. Yerokhin, M.Y. Bychkova, D.V. Shtansky, E.A. Levashov, A. Matthews, Self-healing plasma electrolytic oxidation coatings doped with benzotriazole loaded halloysite nanotubes on AM50 magnesium alloy, *Corros. Sci.* 111 (2016) 753–769, <https://doi.org/10.1016/j.corsci.2016.06.016>.
  - [21] D. Liu, Y.W. Song, D.Y. Shan, E.H. Han, Self-healing coatings prepared by loading interphase inhibitors into MAO coating of AM60 Mg alloy, *J. Electrochem. Soc.* 165 (2018) C412–C421, <https://doi.org/10.1149/2.0011809jes>.
  - [22] S.V. Lamaka, B. Vaghefinazari, D. Mei, R.P. Petrasauskas, D. Höche, M. L. Zheludkevich, Comprehensive screening of Mg corrosion inhibitors, *Corros. Sci.* 128 (2017) 224–240, <https://doi.org/10.1016/j.corsci.2017.07.011>.
  - [23] A. Seyeux, M. Liu, P. Schmutz, G. Song, A. Atrens, P. Marcus, ToF-SIMS depth profile of the surface film on pure magnesium formed by immersion in pure water and the identification of magnesium hydride, *Corros. Sci.* 51 (2009) 1883–1886, <https://doi.org/10.1016/j.corsci.2009.06.002>.
  - [24] D. Mei, S.V. Lamaka, C. Feiler, M.L. Zheludkevich, The effect of small-molecule bio-relevant organic components at low concentration on the corrosion of commercially pure Mg and Mg-0.8Ca alloy: an overall perspective, *Corros. Sci.* 153 (2019) 258–271, <https://doi.org/10.1016/j.corsci.2019.03.039>.
  - [25] J. Yang, C. Blawert, S.V. Lamaka, K.A. Yasakau, L. Wang, D. Laipple, M. Schieda, S. Di, M.L. Zheludkevich, Corrosion inhibition of pure Mg containing a high level of iron impurity in pH neutral NaCl solution, *Corros. Sci.* 142 (2018) 222–237, <https://doi.org/10.1016/j.corsci.2018.07.027>.
  - [26] A. Maltseva, S.V. Lamaka, K.A. Yasakau, D. Mei, D. Kurachov, M.L. Zheludkevich, G. Lefevre, P. Volovitch, In situ surface film evolution during Mg aqueous corrosion in presence of selected carboxylates, *Corros. Sci.* 171 (2020), 108484, <https://doi.org/10.1016/j.corsci.2020.108484>.
  - [27] L.I. Fockaert, T. Würger, R. Unbehau, B. Boelen, R.H. Meißner, S.V. Lamaka, M. L. Zheludkevich, H. Terryn, J.M.C. Mol, ATR-FTIR in Kretschmann configuration integrated with electrochemical cell as in situ interfacial sensitive tool to study corrosion inhibitors for magnesium substrates, *Electrochim. Acta* 345 (2020), 136166, <https://doi.org/10.1016/j.electacta.2020.136166>.
  - [28] J. Liang, P.B. Srinivasan, C. Blawert, W. Dietzel, Influence of chloride ion concentration on the electrochemical corrosion behaviour of plasma electrolytic oxidation coated AM50 magnesium alloy, *Electrochim. Acta* 55 (2010) 6802–6811, <https://doi.org/10.1016/j.electacta.2010.05.087>.
  - [29] A. Maltseva, V. Shkirskiy, G. Lefevre, P. Volovitch, Effect of pH on Mg(OH)<sub>2</sub> film evolution on corroding Mg by in situ kinetic Raman mapping (KRM), *Corros. Sci.* 153 (2019) 272–282, <https://doi.org/10.1016/j.corsci.2019.03.024>.
  - [30] A. Atrens, G.L. Song, Z. Shi, A. Soltan, S. Johnston, M.S. Dargusch, Understanding the corrosion of mg and mg alloys, in: *Encyclopedia of Interfacial Chemistry: Surface Science and Electrochemistry*, 2018, pp. 515–534.
  - [31] E.L. Silva, S.V. Lamaka, D. Mei, M.L. Zheludkevich, The reduction of dissolved oxygen during magnesium corrosion, *ChemistryOpen* 7 (2018) 664–668, <https://doi.org/10.1002/open.201800076>.
  - [32] M. Strebl, M. Bruns, S. Virtanen, Editors' choice—respirometric in situ methods for real-time monitoring of corrosion rates: part I. Atmospheric corrosion, *J. Electrochem. Soc.* 167 (2020), 021510, <https://doi.org/10.1149/1945-7111/ab6c61>.
  - [33] C. Wang, D. Mei, G. Wiese, L.Q. Wang, M. Deng, S.V. Lamaka, M.L. Zheludkevich, High rate oxygen reduction reaction during corrosion of ultra-high-purity magnesium, *ARTN 42*, *Npj Mater. Degrad.* 4 (2020) 42, <https://doi.org/10.1038/s41529-020-00146-1>.
  - [34] M.G. Strebl, M.P. Bruns, G. Schulze, S. Virtanen, Respirometric in situ methods for real-time monitoring of corrosion rates: part II. Immersion, *J. Electrochem. Soc.* 168 (2021), 011502, <https://doi.org/10.1149/1945-7111/abdb4a>.
  - [35] S. Stojadinović, R. Vasilčić, M. Petković, I. Belča, B. Kasalica, M. Perić, L. Zeković, Luminescence during anodization of magnesium alloy AZ31, *Electrochim. Acta* 59 (2012) 354–359.
  - [36] R. Arrabal, E. Matytkina, T. Hashimoto, P. Skeldon, G.E. Thompson, Characterization of AC PEO coatings on magnesium alloys, *Surf. Coat. Technol.* 203 (2009) 2207–2220, <https://doi.org/10.1016/j.surfcoat.2009.02.011>.
  - [37] S. Yagi, K. Kuwabara, Y. Fukuta, K. Kubota, E. Matsubara, Formation of self-repairing anodized film on ACM522 magnesium alloy by plasma electrolytic oxidation, *Corros. Sci.* 73 (2013) 188–195, <https://doi.org/10.1016/j.corsci.2013.03.035>.
  - [38] A. Jangde, S. Kumar, C. Blawert, Evolution of PEO coatings on AM50 magnesium alloy using phosphate-based electrolyte with and without glycerol and its electrochemical characterization, *J. Magnes. Alloy.* 8 (2020) 692–715, <https://doi.org/10.1016/j.jma.2020.05.002>.
  - [39] G. Zhang, E. Jiang, L. Wu, W. Ma, H. Yang, A. Tang, F. Pan, Corrosion protection properties of different inhibitors containing PEO/LDHs composite coating on magnesium alloy AZ31, *Sci. Rep.* 11 (2021) 2774, <https://doi.org/10.1038/s41598-021-81029-6>.
  - [40] L. Wang, D. Snihirova, M. Deng, C. Wang, B. Vaghefinazari, G. Wiese, M. Langridge, D. Höche, S.V. Lamaka, M.L. Zheludkevich, Insight into physical interpretation of high frequency time constant in electrochemical impedance spectra of Mg, *Corros. Sci.* 187 (2021), 109501, <https://doi.org/10.1016/j.corsci.2021.109501>.
  - [41] G. Rapheal, S. Kumar, N. Scharnagl, C. Blawert, Effect of current density on the microstructure and corrosion properties of plasma electrolytic oxidation (PEO) coatings on AM50 Mg alloy produced in an electrolyte containing clay additives, *Surf. Coat. Technol.* 289 (2016) 150–164, <https://doi.org/10.1016/j.surfcoat.2016.01.033>.
  - [42] X. Lu, S.P. Sah, N. Scharnagl, M. Störmer, M. Starykevich, M. Mohehdano, C. Blawert, M.L. Zheludkevich, K.U. Kainer, Degradation behavior of PEO coating on AM50 magnesium alloy produced from electrolytes with clay particle addition, *Surf. Coat. Technol.* 269 (2015) 155–169, <https://doi.org/10.1016/j.surfcoat.2014.11.027>.
  - [43] J. Liang, P.B. Srinivasan, C. Blawert, M. Störmer, W. Dietzel, Electrochemical corrosion behaviour of plasma electrolytic oxidation coatings on AM50 magnesium alloy formed in silicate and phosphate based electrolytes, *Electrochim. Acta* 54 (2009) 3842–3850, <https://doi.org/10.1016/j.electacta.2009.02.004>.
  - [44] M. Esmaily, J.E. Svensson, S. Fajardo, N. Birbilis, G.S. Frankel, S. Virtanen, R. Arrabal, S. Thomas, L.G. Johansson, Fundamentals and advances in magnesium alloy corrosion, *Prog. Mater. Sci.* 89 (2017) 92–193, <https://doi.org/10.1016/j.pmatsci.2017.04.011>.
  - [45] M. Deng, L. Wang, D. Höche, S.V. Lamaka, C. Wang, D. Snihirova, Y. Jin, Y. Zhang, M.L. Zheludkevich, Approaching “stainless magnesium” by Ca micro-alloying, *Mater. Horiz.* 8 (2021) 589–596, <https://doi.org/10.1039/D0MH01380C>.
  - [46] D.A. Wiesenburger, N.L. Guinasso, Equilibrium solubilities of methane, carbon monoxide, and hydrogen in water and sea water, *J. Chem. Eng. Data* 24 (1979) 356–360, <https://doi.org/10.1021/je60083a006>.
  - [47] J.J. Thomas, S. Musso, I. Prestini, Kinetics and activation energy of magnesium oxide hydration, *J. Am. Ceram. Soc.* 97 (2014) 275–282, <https://doi.org/10.1111/jace.12661>.
  - [48] S.D.F. Rocha, M.B. Mansur, V.S.T. Ciminella, Kinetics and mechanistic analysis of caustic magnesia hydration, *J. Chem. Technol. Biotechnol.* 79 (2004) 816–821, <https://doi.org/10.1002/jctb.1038>.
  - [49] S. Liu, Y. Qi, Z. Peng, J. Liang, A chemical-free sealing method for micro-arc oxidation coatings on AZ31 Mg alloy, *Surf. Coat. Technol.* 406 (2021), 126655, <https://doi.org/10.1016/j.surfcoat.2020.126655>.
  - [50] S.V. Lamaka, R.M. Souto, M.G.S. Ferreira, In-situ visualization of local corrosion by Scanning Ion-selective Electrode Technique (SIET), in: *Microscopy: Science, Technology, Applications and Education*, vol. 3, 2010, pp. 2162–2173.
  - [51] S. Gnedenkov, D. Mei, S.V. Lamaka, S. Sinebryukhov, D. Mashtalyar, I.E. Vyalyi, M. L. Zheludkevich, S. Gnedenkov, Localized currents and pH distribution studied during corrosion of MA8 Mg alloy in the cell culture medium, *Corros. Sci.* 170 (2020), 108689, <https://doi.org/10.1016/j.corsci.2020.108689>.
  - [52] I. Puigdomenech, Hydra-Medusa software, Chemical Equilibrium Diagrams. (<https://sites.google.com/site/chemdiagr/home/>).
  - [53] D. Höche, C. Blawert, S.V. Lamaka, N. Scharnagl, C. Mendis, M.L. Zheludkevich, The effect of iron re-deposition on the corrosion of impurity-containing magnesium, *Phys. Chem. Chem. Phys.* 18 (2015) 1279–1291, <https://doi.org/10.1039/c5cp05577f>.
  - [54] D. Höche, S.V. Lamaka, B. Vaghefinazari, T. Braun, R.P. Petrasauskas, M. Fichtner, M.L. Zheludkevich, Performance boost for primary magnesium cells using iron complexing agents as electrolyte additives, *Sci. Rep.* 8 (2018) 7578, <https://doi.org/10.1038/s41598-018-25789-8>.

- [55] H. Ardelean, A. Seyeux, S. Zanna, F. Prima, I. Frateur, P. Marcus, Corrosion processes of Mg–Y–Nd–Zr alloys in Na<sub>2</sub>SO<sub>4</sub> electrolyte, *Corros. Sci.* 73 (2013) 196–207, <https://doi.org/10.1016/j.corsci.2013.03.036>.
- [56] M. Liu, S. Zanna, H. Ardelean, I. Frateur, P. Schmutz, G. Song, A. Atrous, P. Marcus, A first quantitative XPS study of the surface films formed, by exposure to water, on Mg and on the Mg–Al intermetallics: Al<sub>3</sub>Mg<sub>2</sub> and Mg<sub>17</sub>Al<sub>12</sub>, *Corros. Sci.* 51 (2009) 1115–1127, <https://doi.org/10.1016/j.corsci.2009.02.017>.
- [57] M. Santamaria, F. Di Quarto, S. Zanna, P. Marcus, Initial surface film on magnesium metal: a characterization by X-ray photoelectron spectroscopy (XPS) and photocurrent spectroscopy (PCS), *Electrochim. Acta* 53 (2007) 1314–1324, <https://doi.org/10.1016/j.electacta.2007.03.019>.
- [58] D. Mercier, J. Świątowska, E. Protopopoff, S. Zanna, A. Seyeux, P. Marcus, Inhibition of Mg corrosion by sulfur blocking of the hydrogen evolution reaction on iron impurities, *J. Electrochem. Soc.* 167 (2020), 121504, <https://doi.org/10.1149/1945-7111/abaf79>.
- [59] W. Jeffrey Binns, F. Zargazad, V. Dehnavi, J. Chen, J.J. Noël, D.W. Shoesmith, Physical and electrochemical evidence for the role of a Mg hydride species in Mg alloy corrosion, *Corrosion* 75 (2019) 58–68, <https://doi.org/10.5006/2918>.
- [60] M. Strebl, S. Virtanen, Real-time monitoring of atmospheric magnesium alloy corrosion, *J. Electrochem. Soc.* 166 (2019) C3001–C3009, <https://doi.org/10.1149/2.001191jes>.
- [61] M.P. Brady, G. Rother, L.M. Anovitz, K.C. Littrell, K.A. Unocic, H.H. Elsentriecy, G. L. Song, J.K. Thomson, N.C. Gallego, B. Davis, Film breakdown and nano-porous Mg(OH)<sub>2</sub> formation from corrosion of magnesium alloys in salt solutions, *J. Electrochem. Soc.* 162 (2015) C140–C149, <https://doi.org/10.1149/2.0171504jes>.
- [62] L. Wang, T. Shinohara, B.-P. Zhang, Influence of chloride, sulfate and bicarbonate anions on the corrosion behavior of AZ31 magnesium alloy, *J. Alloy. Compd.* 496 (2010) 500–507, <https://doi.org/10.1016/j.jallcom.2010.02.088>.
- [63] G. Williams, H. Ap Llwyd Dafydd, R. Subramanian, H.N. McMurray, The influence of chloride ion concentration on passivity breakdown in magnesium, *Corrosion* 73 (2017) 471–481, <https://doi.org/10.5006/2328>.
- [64] T. dos Santos, J. dos Santos, A.P. Luz, C. Pagliosa, V.C. Pandolfelli, Kinetic control of MgO hydration in refractory castables by using carboxylic acids, *J. Eur. Ceram. Soc.* 38 (2018) 2152–2163, <https://doi.org/10.1016/j.jeurceramsoc.2017.11.046>.
- [65] M. Lintuluoto, H. Nakatsuji, M. Hada, H. Kanai, Theoretical study of the decomposition of HCOOH on an MgO(100) surface, *Surf. Sci.* 429 (1999) 133–142, [https://doi.org/10.1016/S0039-6028\(99\)00357-X](https://doi.org/10.1016/S0039-6028(99)00357-X).
- [66] M.P. Kamil, M. Kaseem, Y.H. Lee, Y.G. Ko, Microstructural characteristics of oxide layer formed by plasma electrolytic oxidation: nanocrystalline and amorphous structures, *J. Alloy. Compd.* 707 (2017) 167–171, <https://doi.org/10.1016/j.jallcom.2017.01.051>.
- [67] Y.G. Ko, S. Namgung, D.H. Shin, Correlation between KOH concentration and surface properties of AZ91 magnesium alloy coated by plasma electrolytic oxidation, *Surf. Coat. Technol.* 205 (2010) 2525–2531, <https://doi.org/10.1016/j.surfcoat.2010.09.055>.

### 5.3.1 Supplementary material

#### S.1 forming lamellar from the AZ21 substrate/PEO interface for STEM mode of SEM characterization

PEO-coated samples (either as-received or after immersion in the electrolytes) were embedded in resin and ground up to 2500# grit size emery paper to obtain the desired cross-section. Then, samples were polished using  $\text{Al}_2\text{O}_3$  slurry (average  $1\mu\text{m}$  particle size) to obtain a smooth surface at the microscale. The samples' surface was gold-sputtered to avoid the charging effect due to the insulating PEO layer and corrosion products. Lamellae were carved out using FIB in-situ lift-out technique (TESCAN LYRA3) from the PEO/substrate interface. See marked area in **Figure S1** (a) and (b) as an example of the lamellar region on the as-received PEO-coated AZ21. The final thickness of the lamellae was approximately  $100 \pm 10\text{ nm}$ . **Figure S1** (c) shows the final prepared lamellar welded on a copper grid. **Figure S1** shows lamellar production steps only for the as-received PEO-coated sample; however, lamellar formation for the rest of the samples follows the same procedure.

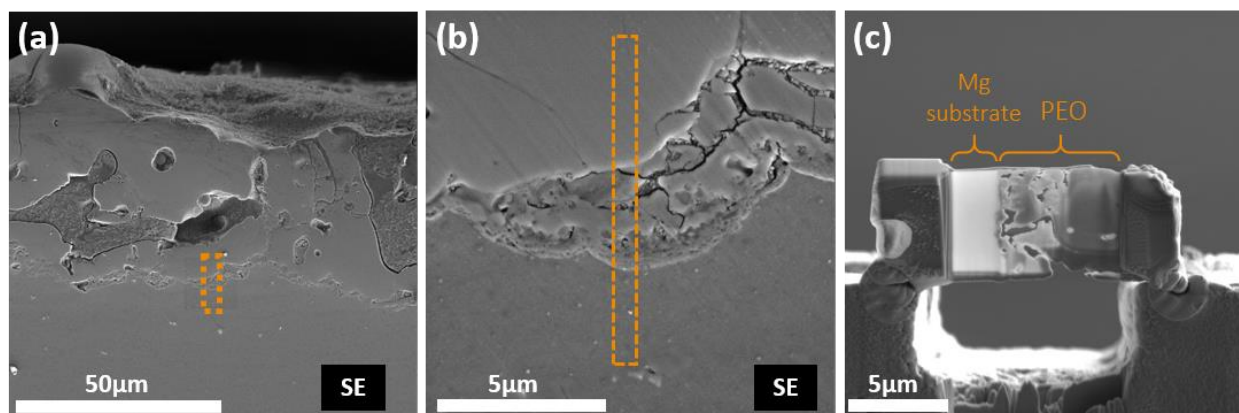


Figure S1 (a) and (b) secondary electron image from the PEO-coated AZ21 cross-section at different magnification. The marked area shows the place and geometry of taken lamellar. (c) image of obtained lamellar welded on a copper grid

## 5.4 Exploring the corrosion inhibition mechanism of 8-hydroxyquinoline for a PEO-coated magnesium alloy

8-Hydroxyquinoline (8HQ) was one of the best-performing inhibitors from the screening stage (**Figure 5.3**). 8HQ has already been used and investigated as effective corrosion inhibitor for different metallic substrates including steel, copper, aluminum, and magnesium for decades [174, 175]. The promising effectiveness of 8HQ has made researchers to also investigate it as incorporated inhibitor into different coating systems including sol-gel, halloysite nanotubes (HNT), and PEO. However, the specific effects of 8HQ on the PEO layer and the detailed mechanisms behind this enhancement remain rather unexplored.

The following published paper is incorporated as **section 5.4**, with the emphasis on how 8HQ interacts with both bare magnesium AZ21 substrate and PEO layer to facilitate an in-depth understanding of the overall inhibition effect of 8HQ in contact with a PEO-coated AZ21 substrate.

**B. Vaghefinazari**, Lamaka, S.V., Blawert, C., Serdechnova, M., Scharnagl, N., Karlova, P., Wieland, D.C.F., Zheludkevich, M.L., Exploring the corrosion inhibition mechanism of 8-hydroxyquinoline for a PEO-coated magnesium alloy, Corrosion Science, (2022) 110344. <https://doi.org/10.1016/j.corsci.2022.110344>.

### CRedit authorship contribution statement:

**Bahram Vaghefinazari**: Conceptualization, Investigation, Validation, Writing – original draft, Writing – review & editing. **Sviatlana V. Lamaka**: Conceptualization, Supervision, Writing – review & editing. **Carsten Blawert**: Conceptualization, Supervision, Writing – review & editing. **Maria Serdechnova**: Investigation, Writing – review & editing. **Nico Scharnagl**: Investigation, Writing – review & editing. **Polina Karlova**: Investigation, Writing – review & editing. **D.C.Florian Wieland**: Investigation, Writing – review & editing. **Mikhail L. Zheludkevich**: Conceptualization, Supervision, Writing – review & editing.



## Exploring the corrosion inhibition mechanism of 8-hydroxyquinoline for a PEO-coated magnesium alloy

Bahram Vaghefinazari<sup>a,\*</sup>, Sviatlana V. Lamaka<sup>a</sup>, Carsten Blawert<sup>a</sup>, Maria Serdechnova<sup>a</sup>, Nico Scharnagl<sup>a</sup>, Polina Karlova<sup>a</sup>, D.C. Florian Wieland<sup>b</sup>, Mikhail L. Zheludkevich<sup>a,c</sup>

<sup>a</sup> Institute of Surface Science, Helmholtz-Zentrum Hereon, 21502 Geesthacht, Germany

<sup>b</sup> Institute of Metallic Biomaterials, Helmholtz-Zentrum Hereon, 21502 Geesthacht, Germany

<sup>c</sup> Institute for Material Science, Faculty of Engineering, Kiel University, 24143 Kiel, Germany

### ARTICLE INFO

#### Keywords:

Magnesium  
Corrosion inhibitor  
Plasma electrolytic oxidation  
8-hydroxyquinoline

### ABSTRACT

In this study, the corrosion inhibition effect of 8-hydroxyquinoline (8HQ) on a PEO-coated AZ21 magnesium alloy is explored. The interaction of 8HQ molecules with both bare AZ21 and PEO layer was thoroughly scrutinized during the exposure to a corrosive NaCl electrolyte using different characterization methods, including EIS, SEM, Raman spectroscopy, and XRD. The corrosion inhibition mechanism stems from the extensive precipitation of the insoluble complex between 8HQ molecules and  $Mg^{2+}$  on top of the PEO layer, which leads to subsequently inhibition-enhancing phenomena, including modification of the corrosion products and re-precipitation of the PEO amorphous phase.

### 1. Introduction

PEO (Plasma Electrolytic Oxidation) is a surface treatment process on metallic substrates based on the formation of a ceramic-like coating with remarkable tribological properties and promising corrosion protection performance [1,2]. PEO coatings have already found applications in a wide range of consumer industries, including biomedical, aerospace, transportation and electronic [3]. The coating is formed by applying a high voltage to the substrate while immersed in an aqueous electrolyte [4], thereby generating short-living micro-discharges on the substrate surface. The high-energy plasma formed in the micro-discharges causes local melting of the substrate surface and fast re-solidification of the oxides and other compounds depending on the electrolyte chemistry [2,5]. The formed coating comprises an outer porous layer and a compact inner layer. PEO coatings provide a relatively good corrosion resistance thanks to the barrier effect of the inner layer, while the corrosive medium can easily penetrate through the relatively large pores of the outer layer. However, the porous feature of the outer layer can be utilized as spacious containers to store chemicals with desired functionalities. Loading of the pores of the layer, which is formed on Mg alloys during high-voltage treatment, with corrosion inhibitors has been first proposed in 2009 [6]. Since then, this became an established procedure to improve the overall corrosion protection

properties of the PEO-coated metals [7–11]. The PEO pores are usually loaded by simply immersing the sample into the inhibitor-containing solution. For instance, the impregnation of a flash-PEO coating on an AZ31 magnesium alloy with inhibitor 4-Methylsalicylic acid significantly reduced the corrosion rate of the Mg substrate as compared to the stand-alone flash-PEO without any inhibitor [11]. Moreover, the inhibitor-loaded sample outperformed a commercially treated Mg substrate with chromate conversion coating in a salt spray test. A subsequent sealing step is usually carried out by applying a top layer on the PEO coating to minimize the unnecessary leaching of the inhibitors from the open pores of PEO. Several reports of the enhancement of corrosion protection properties of PEO on Mg alloys by the incorporation of corrosion inhibitors into the PEO coating have already been published [6–8,12–16].

8-Hydroxyquinoline (8HQ) is a well-known chemical for its remarkable corrosion inhibition effects on different metallic substrates, including steel, aluminum, and copper. The scientific content pertaining to the corrosion inhibition of 8HQ available in the Scopus database dates back to 1929 [17] that reported a strong inhibition effect on steel in sulfuric acid. As a result of a significant body of research on the application of 8HQ and its derivatives, several review papers have recently been published on this matter [18–20]. Several reports of the strong corrosion inhibition effect of 8HQ on different magnesium alloys also

\* Corresponding author.

E-mail address: [bahram.vaghefinazari@hereon.de](mailto:bahram.vaghefinazari@hereon.de) (B. Vaghefinazari).

<https://doi.org/10.1016/j.corsci.2022.110344>

Received 16 February 2022; Received in revised form 11 April 2022; Accepted 24 April 2022

Available online 29 April 2022

0010-938X/© 2022 Elsevier Ltd. All rights reserved.

render 8HQ a propitious candidate for commercial applications of industrial magnesium parts [21–25]. However, it is notable that some reports [6,26–28] on the adverse or minimal inhibition effect of 8HQ and its derivatives on magnesium alloys reveal the highly crucial roles of testing conditions, such as tested magnesium substrate, corrosive background electrolyte, and the ratio between electrolyte volume and exposed Mg surface area. The corrosion inhibition effect of 8HQ on magnesium alloys is generally ascribed to the formation of an insoluble complex with the  $Mg^{2+}$  ions (hereafter denoted as 8HQ(Mg)) that precipitates on the Mg surface and forms a barrier layer against the corrosive species [21,25].

Being indicated as an auspicious corrosion inhibitor for bare magnesium, 8HQ is also one of the most studied chemicals as an incorporated inhibitor into different coating systems. For example, Galio et al. [29], in one of the early attempts to incorporate 8HQ in a coating on a magnesium alloy, found out that the incorporation of 8HQ in a sol-gel coating can significantly enhance the protective properties of the sol-gel coating. This is attributed to the formation of the insoluble 8HQ (Mg) that blocks the micro-pores of the sol-gel layer. Several attempts have been made to incorporate 8HQ into the PEO porous outer layer formed on magnesium alloys [6,15,30,31]. In order to control the release of 8HQ during the exposure to the corrosive medium, it has also been initially loaded to different micro/nano-containers such as halloysite nanotubes (HNT), before being incorporated into the PEO outer layer [31]. This way, the stimulations generated during the corrosion process of the magnesium substrate, such as the increase in the pH, liberates the 8HQ molecules from the containers.

Although improvement in the overall corrosion resistance of the coating by incorporation of 8HQ into PEO coatings on magnesium alloys has been reported [9,31–34], the individual effect of 8HQ on the PEO layer and the mechanism of enhancement in its corrosion resistance is yet to be addressed in detail. In the majority of these studies, the presence of other components of the coating system, such as the sealing layer, as well as its interaction with 8HQ molecules affect the final corrosion resistance of the coating system, thus rendering the understanding of the 8HQ inhibition mechanism complicated [35]. Furthermore, the mechanism of enhancement in the corrosion protection properties of the PEO coatings on Mg by adding 8HQ in a majority of the research items have been justified by a simple formation of the insoluble 8HQ(Mg) complex, without elaborating any details on the interaction of 8HQ molecules with the PEO layer.

It is worth mentioning that the use of 8HQ in the industry may be restricted concerning its potential toxicity. However, in-depth studies of highly effective inhibitors such as 8HQ help understanding the inhibition mechanism, which will eventually give insight into finding more green inhibitors with superior corrosion inhibition properties.

This work places the emphasis on how 8HQ interacts with both bare magnesium AZ21 substrate and PEO layer to facilitate an in-depth understanding of the overall inhibition effect of 8HQ in contact with a PEO-coated AZ21 substrate.

## 2. Experimental procedure

### 2.1. Materials

Magnesium alloy AZ21 sheet (cast and rolled at Helmholtz Zentrum Hereon) was used as the substrate. The chemical composition of the alloy, determined by spark discharge-optical emission spectroscopy (SD-OES), Ametek-Spectro, is  $1.59 \pm 0.07$  wt% Al,  $1.05 \pm 0.07$  wt% Zn,  $0.29$  wt% Mn,  $28 \pm 1$  ppm Fe, and  $23 \pm 1$  ppm Ni. All the AZ21 specimens were mechanically ground up to 2500 grit SiC abrasive paper.

All the solutions containing 8HQ (Alfa Aesar, 99%) were in saturation condition ( $\sim 5$  mM), which were prepared by 1 h vigorous stirring of the solution containing an excessive amount of 8HQ at room temperature. The remaining undissolved 8HQ was filtered out using filter paper (LLG-filter medium/fast). The pH of the 8HQ-containing electrolyte was

7.1. The pH of the reference NaCl 3.5 wt% electrolyte was 5.6.

### 2.2. Preparation of PEO

PEO coating was applied on AZ21 specimens in an electrolyte containing 20 g/L  $Na_3PO_4$  (Alfa Aesar) and 2 g/L KOH (CHEMSOLUTE®, >85%), using a pulsed DC power source (Electro Automatik, Germany). The samples were subjected to constant current density of  $40 \text{ mA}\cdot\text{cm}^{-2}$  and a duty cycle of 1 ms:9 ms for a period of 10 min, resulting in a final voltage of  $400 \pm 4$  V. The electrolyte temperature is controlled at  $20^\circ\text{C}$  by a cooling system that utilizes a stainless steel tube cathode. Rinsing after the PEO process was done by immersion in deionized water for 20 min. The rinsing was carried out at low-pressure condition ( $\sim 0.9$  atm pressure) to remove the entrapped air inside the pores and ensure that the deionized water can penetrate through the pores and dilute the remaining PEO electrolyte. This step was necessarily taken to diminish the influence of the remained PEO electrolytes on the evaluation of the results. Subsequently, the specimens were immersed in acetone (EMSURE® supplied by Sigma-Aldrich) for 20 min and finally dried in an oven at  $80^\circ\text{C}$  for 30 min.

### 2.3. Preparation of 8HQ(Mg) powder

8HQ(Mg) powder was used for comparison reasons and synthesized according to the following procedure: saturated solution of 8HQ was prepared in deionized water. 5 mM  $MgCl_2 \cdot 6H_2O$  (supplied by Sigma Aldrich) was added to the saturated 8HQ solution. Then, the solution pH was slowly adjusted to 9.5 using 0.1 M NaOH solution, at which the full yield of 8HQ(Mg) precipitation can be achieved [36]. During the entire process, the solution was vigorously stirred using a stirring magnet. The 8HQ(Mg) precipitations were collected from the solution using a centrifuge. The obtained powder was rinsed thoroughly with deionized water to remove the  $Cl^-$  ions. Finally, the powder was dried in oven at  $80^\circ\text{C}$ .

### 2.4. Crystallographic characterization

The bulk phase composition of the coating was analyzed by a diffractometer (Bruker D8 Advance, Karlsruhe, Germany) with  $Cu K_\alpha$  X-ray beam generated with a voltage and current of 40 kV and 40 mA, respectively. The incident angle was  $4^\circ$  with 5 s acquisition time per point and  $0.02^\circ$  step size in the range of  $5-70^\circ$ .

High resolution two dimensional XRD maps were acquired at the nanofocused endstation of beamline P03 at PETRAIII storage ring, Deutsches Elektronen-Synchrotron (DESY, Hamburg, Germany) [37]. The beam size was  $1.5 \mu\text{m} \times 1.5 \mu\text{m}$ . Beam exposure for each step was set at 15 keV for the dwell time of 0.5 s. Regions of  $80 \mu\text{m} \times 80 \mu\text{m}$  were scanned with the step sizes of  $2 \mu\text{m}$  and  $4 \mu\text{m}$  for vertical and horizontal directions, respectively. The horizontal direction is parallel to the substrate surface. For the sake of clarity, the XRD pattern is presented after the converting the 2 $\theta$  values from the Synchrotron beam wavelength to that of  $Cu K_\alpha$ .

### 2.5. Electrochemical measurements

The electrochemical measurements were carried out using a Gamry interface 1010 potentiostat with a 3-electrode arrangement. The adopted reference electrode was Ag/AgCl electrode in saturated KCl solution. Pt coil was served as the counter electrode. A sample surface of  $0.5 \text{ cm}^2$  was exposed in a vertical position to 400 ml of 3.5 wt% NaCl electrolyte with and without the presence of 8HQ at stagnant condition. Electrochemical Impedance Spectroscopy (EIS) was performed under potentiostatic mode at open circuit potential (OCP), and after an adequate immersion time (5 min for bare AZ21 and 30 min for PEO-coated samples) to ensure stable conditions. The scanned frequency was ranged from 100 kHz to 0.01 Hz for PEO-coated samples and from

100 kHz to 0.1 Hz for bare magnesium samples, with 9 points per decade acquisition. A 10 mV<sub>rms</sub> AC perturbation voltage was applied. During the impedance acquisition for the PEO-coated sample, careful observation of the obtained Lissajous curves was conducted, especially at low frequency range, to avoid any significant deviation from the zero response current, which means a strong deviation from the OCP condition and destructive polarization of the specimen. In such a case, the EIS acquisition was aborted. All the electrochemical measurements were carried out at  $21 \pm 1$  °C, in air-conditioned lab.

To evaluate the corrosion rate of the bare AZ21 by weight loss measurement, chromic acid (prepared by dissolving 200 g/l CrO<sub>3</sub> in deionized water) was used to remove the corrosion products formed after immersion. The inhibition efficiency (IE) was calculated using the equation below:

$$IE (\%) = \frac{W_{ref} - W_{8HQ}}{W_{ref}} \times 100$$

$W_{ref}$  and  $W_{8HQ}$  denote the weight loss of bare AZ21 after exposure to the NaCl electrolyte without and with 8HQ, respectively.

## 2.6. Raman spectroscopy

Confocal Raman spectroscopy was performed by a Senterra Raman microscope (Bruker). All spectra were collected with an excitation wavelength of 785 nm, a laser power of 50 mW, an aperture of 25 μm and 256 scans for the PEO layers and 64 scans for the raw materials, which were used for an appropriate signal-to-noise ratio. The integration time was 3 s in all cases. Validation and evaluation of the data were carried out with the Bruker OPUS software version 7.5.

## 2.7. Microscopy

The surface morphology and cross-section of bare and PEO-coated substrate was characterized using scanning electron microscope (SEM) (TESCAN Vega3 SB) and energy dispersion spectrometer (EDS) (iXRF

system). The acceleration voltage was 15 kV. The SEM images were taken with both secondary electron (SE) and backscattered electron (BSE) modes.

For the cross-sectional observations, the samples were embedded in epoxy resin (EpoxiCure, Buehler). Then the surface of the sample was ground with SiC emery papers up to 2500# grit number and polished with water-free silicon oxide polishing suspension (OPSTM, Cloeren Technology GmbH). Samples' surface was sputter coated with gold using Cressington Sputter Coater 108auto, except for those samples analyzed with Raman spectroscopy.

## 3. Results

### 3.1. Effect of 8HQ on bare AZ21

#### 3.1.1. EIS

In order to understand the effect of 8HQ on the PEO-coated magnesium, it is important to first understand the interaction of 8HQ with the bare AZ21 substrate during the corrosion in the NaCl electrolyte. The AZ21 samples were immersed in the corrosion testing electrolyte of 3.5 wt% NaCl with the presence and the absence of 8HQ at saturated concentration. Meanwhile, EIS was employed to characterize the surface condition of the magnesium substrate. Fig. 1 shows the evolution of Bode plots obtained from the AZ21 substrate during the immersion in the NaCl solution with and without 8HQ.

In the case of the blank NaCl solution without the presence of 8HQ, two time constants are visible at the high (between 10<sup>3</sup> and 10 Hz) and low frequency range (between 10 and 1 Hz) for 5 min and 30 min of immersion times, which can be attributed to the oxide layer [38] and a double layer formed on the Mg surface [39], respectively. The positive phase angle located at the low-frequency range is believed to be originated from the non-stationary condition of the Mg surface during the EIS measurement [40]. For the immersion times that exceed 30 min, the time constant at low frequency (i.e., the double layer response) is no more identifiable in the phase angle spectra. When 8HQ is present in the

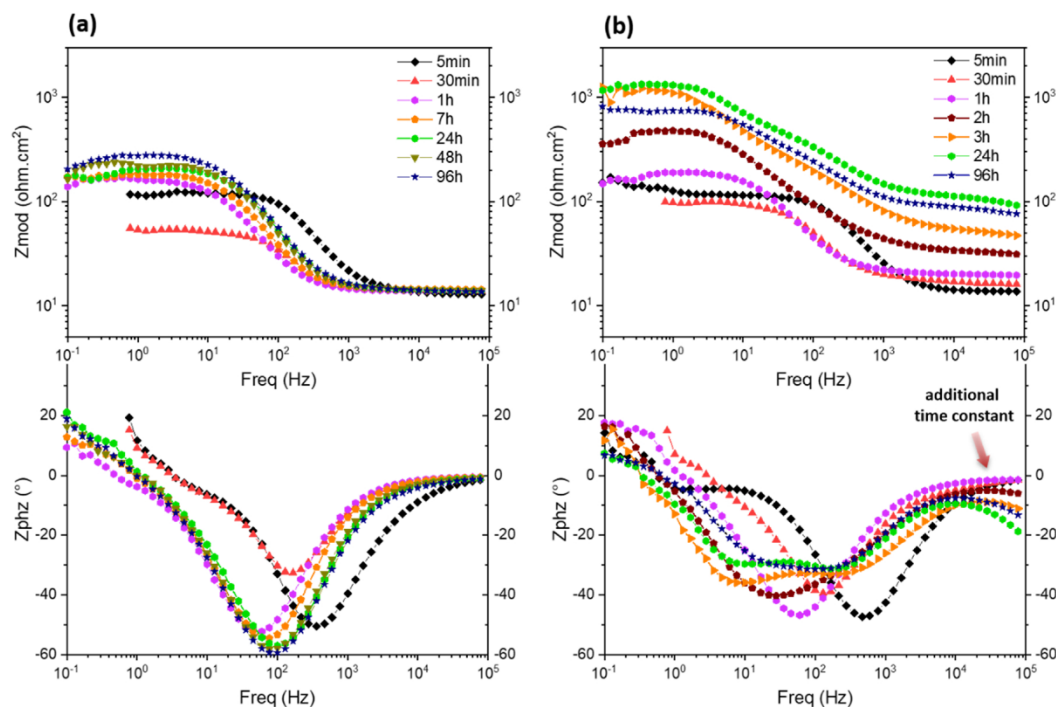
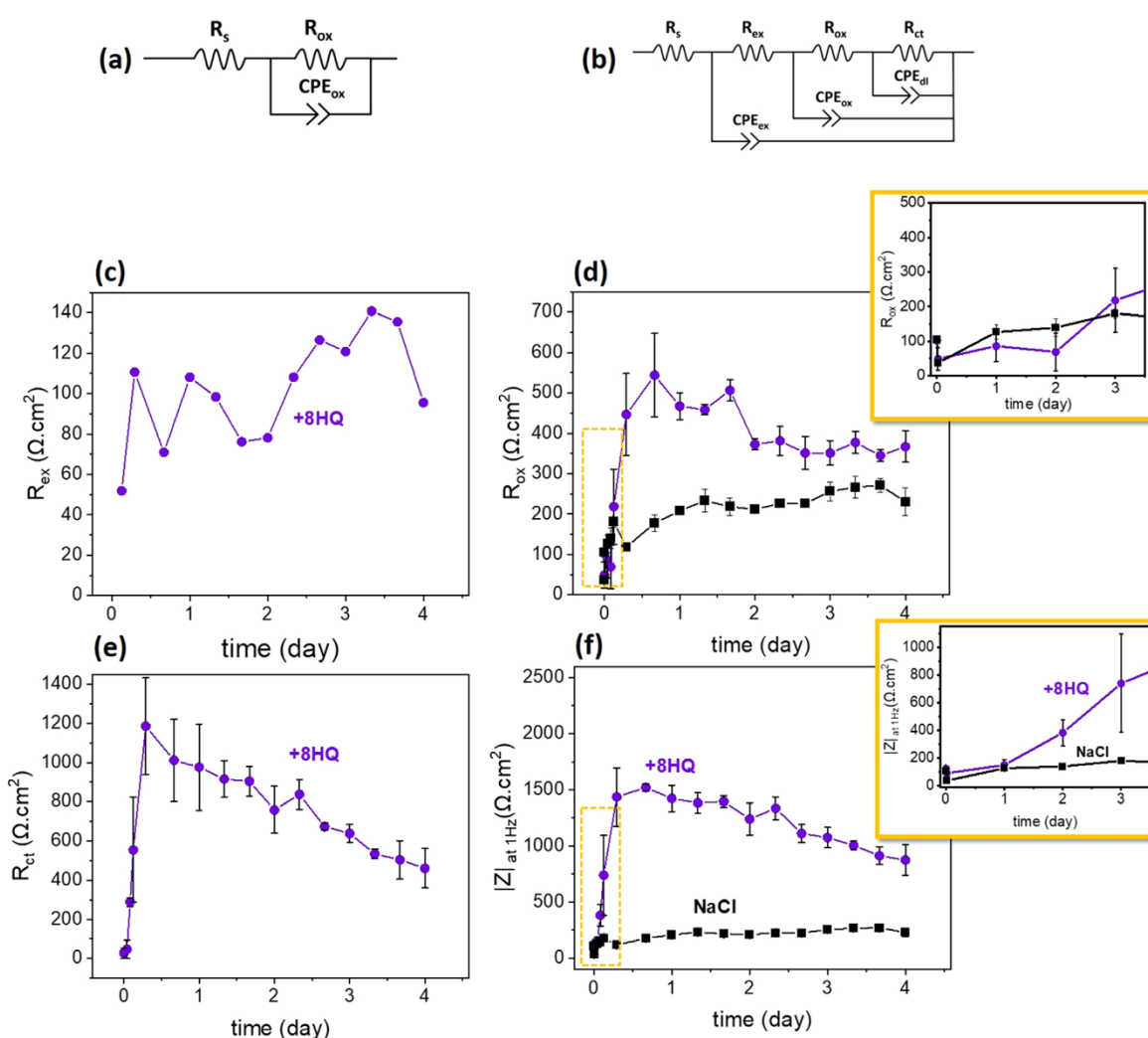


Fig. 1. Bode plots of the EIS spectra obtained for the AZ21 sample during 4 days of immersion in NaCl 3.5 wt% NaCl solution (a) without and (b) with 8HQ.

NaCl electrolyte, the phase angle spectra indicate two capacitive relaxation processes similar to that of blank NaCl electrolyte for the first hour of immersion, with a not so easily identifiable low-frequency capacitive behavior. However, further immersion results in the emergence of a third capacitive time constant at the very high-frequency range (as evidenced at frequencies more than  $10^4$  Hz), marked in Fig. 1. This, in turn, is attributed to the formation of an extra layer on the Mg surface, containing 8HQ(Mg) precipitates, which leads to a remarkable increase in the modulus of impedance at the high-frequency range until the first day of immersion. This increase in the impedance value at the high-frequency range occurs concomitantly with the enhancement in the low-frequency impedance. During this period, the time constants attributed to the oxide layer and the double layer also become more distinct in the phase angle representations.

The equivalent circuits presented in Fig. 2 (a and b) are employed to model the EIS spectra. Moreover, the impedance modulus at the low frequency of 1 Hz (hereafter denoted as  $|Z|_{1\text{ Hz}}$ ) was considered as the corrosion resistance indicator and presented in Fig. 2 (f). As explained above, the frequency range less than 1 Hz is influenced by the non-stationary condition, thereby rendering the comparative evaluation of

the corrosion rate faulty.  $R_s$  represents the electrolyte resistance.  $R_{ox}$  denotes the resistance of the oxide layer on the magnesium surface.  $CPE_{ox}$  is the constant phase element that models the non-ideal capacitive behavior of the oxide layer on the magnesium surface.  $R_{ct}$  is coupled with the  $CPE_{dl}$  to model the charge transfer resistance and the capacitive behavior of the double-layer, respectively. Both  $R_{ex}$  and  $CPE_{ex}$  also denote the electrical properties of the extra layer formed in the case 8HQ is present in the electrolyte. Note that for the blank NaCl electrolyte, the charge transfer resistance and double-layer capacitive behavior are eliminated from the equivalent circuit since their values are negligible and indecisive to the fitting results. Fig. 2 (c-e) illustrates the evaluation of the extracted parameters from the equivalent circuits over the time of immersion.  $R_{ex}$  shows an increasing trend over the time of immersion, albeit very fluctuating, which can imply the instantaneous deterioration and healing of the extra layer's barrier properties over the immersion time. Note that the average values of three measurements for  $R_{ex}$  have been presented in the supplementary materials, while in Fig. 2, only the result of one measurement has been illustrated to show the highly fluctuating values of  $R_{ex}$  over immersion time. When 8HQ is present in the electrolyte,  $R_{ox}$ ,  $R_{ct}$ , and  $|Z|_{1\text{ Hz}}$  tend to develop a rapid enhancement



**Fig. 2.** (a) and (b): the equivalent circuits employed to fit the EIS spectra for the NaCl electrolyte without and with the presence of 8HQ, respectively. (c-e): evolution of parameters obtained from the fitting of EIS spectra of bare AZ21 exposed to the NaCl electrolyte with and without 8HQ. (f)  $|Z|_{1\text{ Hz}}$  value at 1 Hz obtained from the corresponding Bode plots in Fig. 1. The error bars indicate the standard deviation of the three measurements.

within the first 7 h of immersion in comparison to those of blank electrolyte. Subsequently, they are subjected to a gradual inclination until the end of the 4 days of immersion. Nevertheless, the  $|Z|_{1\text{ Hz}}$  value for the 8HQ-containing electrolyte remains significantly higher than that of blank NaCl electrolyte for the entire duration of immersion.

The corrosion rate of the AZ21 samples in the electrolyte with and without 8HQ, calculated based on the weight loss of the samples after 4 days of immersion, is presented in Fig. 3, which confirms the corrosion inhibition effect of 8HQ on AZ21 magnesium, yielding an inhibition efficiency (IE) of 65%. The visual appearances of the AZ21 surface after 4 days of immersion are also presented in the same figure. The surface of the sample exposed to the 8HQ-containing solution was covered with a yellowish precipitation.

### 3.1.2. SEM

Fig. 4 shows the surface of bare AZ21 after different periods of exposure to the blank NaCl solution. After only 5 min of immersion, some filiform corrosion is already formed on the surface. The increased duration of exposure till 1 day leads to the complete coverage of the surface with corrosion products mainly made of  $\text{Mg}(\text{OH})_2$ , which features a cracked morphology all over the surface.

Fig. 5 shows the surface of bare AZ21 after different periods of exposure to the NaCl solution containing 8HQ. The filiform corrosion was also observed within the first 5 min of immersion (Fig. 5 (a)). Flower-like precipitations are formed on random places of the Mg surface. These precipitations, as will be characterized later by XRD and Raman methods, are the insoluble complex between 8HQ and  $\text{Mg}^{2+}$  released by the degradation of the Mg substrate.

After 1 h of immersion, 8HQ(Mg) precipitates covered a larger surface of the AZ21. However, some places can still be found free of 8HQ (Mg) precipitates, evidenced in the higher magnification of Fig. 5(b).

After 1 day of immersion (Fig. 5 (c)), the substrate is fully concealed by the 8HQ(Mg) precipitates. An analysis of higher magnification reveals spherical voids surrounded by flakes of 8HQ(Mg), as marked in Fig. 5 (c).  $\text{H}_2$  bubbles as the product of cathodic water reduction on the magnesium substrate can be trapped in the corrosion products for a short duration, and the 8HQ(Mg) flakes precipitate around the bubble

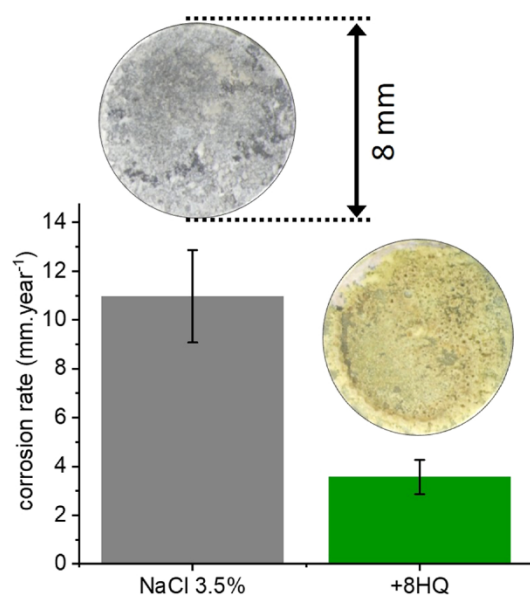


Fig. 3. Corrosion rate of the AZ21 substrate after 4 days of immersion in the NaCl electrolyte with and without 8HQ. The error bars indicate the standard deviation of the three measurements. The visual appearance of the AZ21 surface after 4 days of immersion is shown on the top of each bar.

shaping a spherical void on the surface.

Fig. 6 shows the cross-sectional morphology of the AZ21 substrate after 1 day of immersion in the NaCl electrolyte with and without 8HQ. Wide cracks in the corrosion products in the case of NaCl electrolyte without 8HQ are present in its entire thickness. When 8HQ was present in the electrolyte, a two-layered corrosion product could be observed (Fig. 6 (b)), comprising a top layer of 8HQ(Mg) flakes and an inner layer similar to the corrosion products in the case of the blank NaCl electrolyte, albeit with considerably denser morphology and narrower cracks.

Elemental mapping conducted by EDS also confirms the two-layer structure of the precipitations with different chemical compositions in the case of the presence of 8HQ in the electrolyte. The small amount of detected carbon in the inner layer of corrosion products in Fig. 6 (b) as well as in the corrosion products in Fig. 6 (a) could be due to the contaminations from the embedding resin that occurs during the polishing/grinding step. Furthermore, the trace of carbon can be ascribed to the presence of magnesium hydroxy carbonates [41,42], formed as the result of the reaction of  $\text{Mg}(\text{OH})_2$  with the dissolved  $\text{CO}_2$  from the environment. Notably, the element N could also be selected to identify 8HQ molecules. However, the relatively high quantity of O and C atoms in  $\text{Mg}(\text{OH})_2$  (main corrosion products on Mg alloys) as well as in the surrounding resin lead to a strong overlapping with the characteristic x-ray energy peak of the N atom.

### 3.2. Effect of 8HQ on PEO

The effect of 8HQ as a corrosion inhibitor on the AZ21 substrate coated with PEO was investigated by the direct addition of 8HQ to the corrosive NaCl electrolyte. EIS test was conducted during the exposure to the corrosive electrolyte to evaluate the corrosion protective properties of the PEO-coated sample.

#### 3.2.1. EIS

Fig. 7 illustrates the Bode plots of the AZ21 coated with PEO during the immersion in NaCl electrolyte with and without 8HQ. The impedance at low frequency, which roughly represents the corrosion resistance of the Mg surface, experiences a slight variation during the first 2 days of immersion in the blank NaCl solution, followed by a rapid drop in its value after 3 days. This significant decline in the impedance accompanies the emergence of corrosion pits, as marked in the corresponding macrograph in Fig. 7, which is considered as the failure of PEO coating.

When 8HQ is present in the electrolyte, the impedance value at low-frequency range gradually grows over the immersion time. A visible formation of bubbles at the place marked in the associated macrograph in Fig. 7 after 11 days of immersion is assigned the PEO coating's failure, albeit still considerably higher impedance value in comparison to that of the blank NaCl electrolyte. As can be seen, a yellowish film has covered the PEO layer, resembling the same precipitation on the surface of bare AZ21 after exposure to the 8HQ-containing electrolyte (Fig. 1).

Two time constants can be identified at all immersion periods in the blank NaCl electrolyte. The high-frequency range time constant is associated with the oxide layer on the Mg substrate [35]. The middle frequency time constant is associated with the double-layer capacitive behavior coupled with the resistive charge transfer on the Mg substrate.

In the case of the presence of 8HQ in the electrolyte, an extra time constant gradually develops at the high-frequency range, observable after 1 day of immersion. This is attributed to the formation of an extra layer with barrier properties. The time constant at the low-frequency range is related to the oxide layer on the Mg surface. The time constant related to the corrosion of Mg substrate (charge transfer resistance coupled with the double layer) has been shifted to the frequencies lower than 0.01 Hz, and cannot be clearly observed in the spectra. Only hardly distinguishable evidence of corrosion-related time constant can be observed at the low-frequency range for immersion time before 1 day.

Additionally, a less evident time constant also can be detected

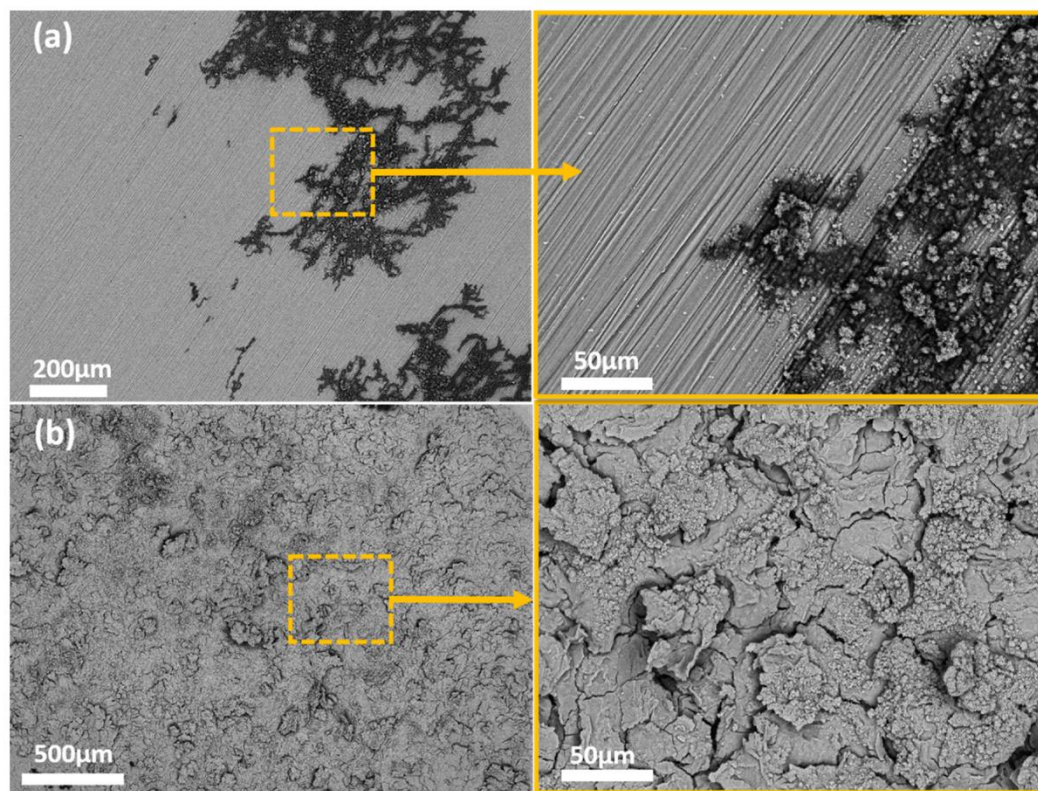


Fig. 4. Surface morphology of AZ21 exposed to NaCl solution after (a) 5 min and (b) 1 day.

between high and low frequency ranges. For instance, this time constant is located in the frequency range of  $10^4$ – $10^2$  Hz for the corresponding EIS spectrum of 2 days of immersion in the 8HQ-containing electrolyte. This time constant can be attributed to an intermediate film between the oxide layer on the Mg substrate and the extra layer evident at high-frequency range. Although this intermediate time constant appears to be inappreciable as compared to the other time constants, it was considered in the equivalent circuit for a better fit, especially at low immersion times.

The equivalent circuits employed to fit the EIS spectra as well the corresponding extracted parameters are presented in Fig. 8.  $R_s$  represents the electrolyte resistance.  $R_{ex}$  and  $CPE_{ex}$  represent the resistance and the capacitive properties of the extra layer attributed to the high-frequency range time constant in the presence of 8HQ in the electrolyte.  $R_{in}$  and  $CPE_{in}$  are implemented to simulate the intermediate protective layer between the oxide layer on the Mg substrate and the extra protective layer.

$R_{ox}$  and  $CPE_{ox}$  were used to simulate the barrier oxide layer on the magnesium surface.  $R_{ct}$  and  $CPE_{dl}$  indicate the charge transfer resistance and the double layer constant phase element corresponding to the corrosion activity on the magnesium surface.

The resistance of the oxide layer on the magnesium surface ( $R_{ox}$ ) experiences an initial slight increase in the case of blank NaCl electrolyte, probably due to the local alkalization, which stems from the cathodic reactions on the magnesium [38]. Note that the initial inner barrier layer of the PEO is subjected to degradation by the corrosive medium within the first hours of immersion, as reported for the same condition and material in our previous work [35].

The addition of 8HQ in the electrolyte leads to higher values of  $R_{ox}$  for the entire duration of immersion, which gradually rises until a drastic decline after 8 days. Further immersion time reveals unstable

values for  $R_{ox}$ , implying a continuous change in the Mg surface condition.

$R_{ex}$  has an increasing trend for the entire duration of the immersion, which implies a continuous enhancement of the formed extra barrier film on the PEO. The  $R_{ex}$  does not change significantly even after the failure of the sample (this also holds in linear scale presentation, which is not shown here).

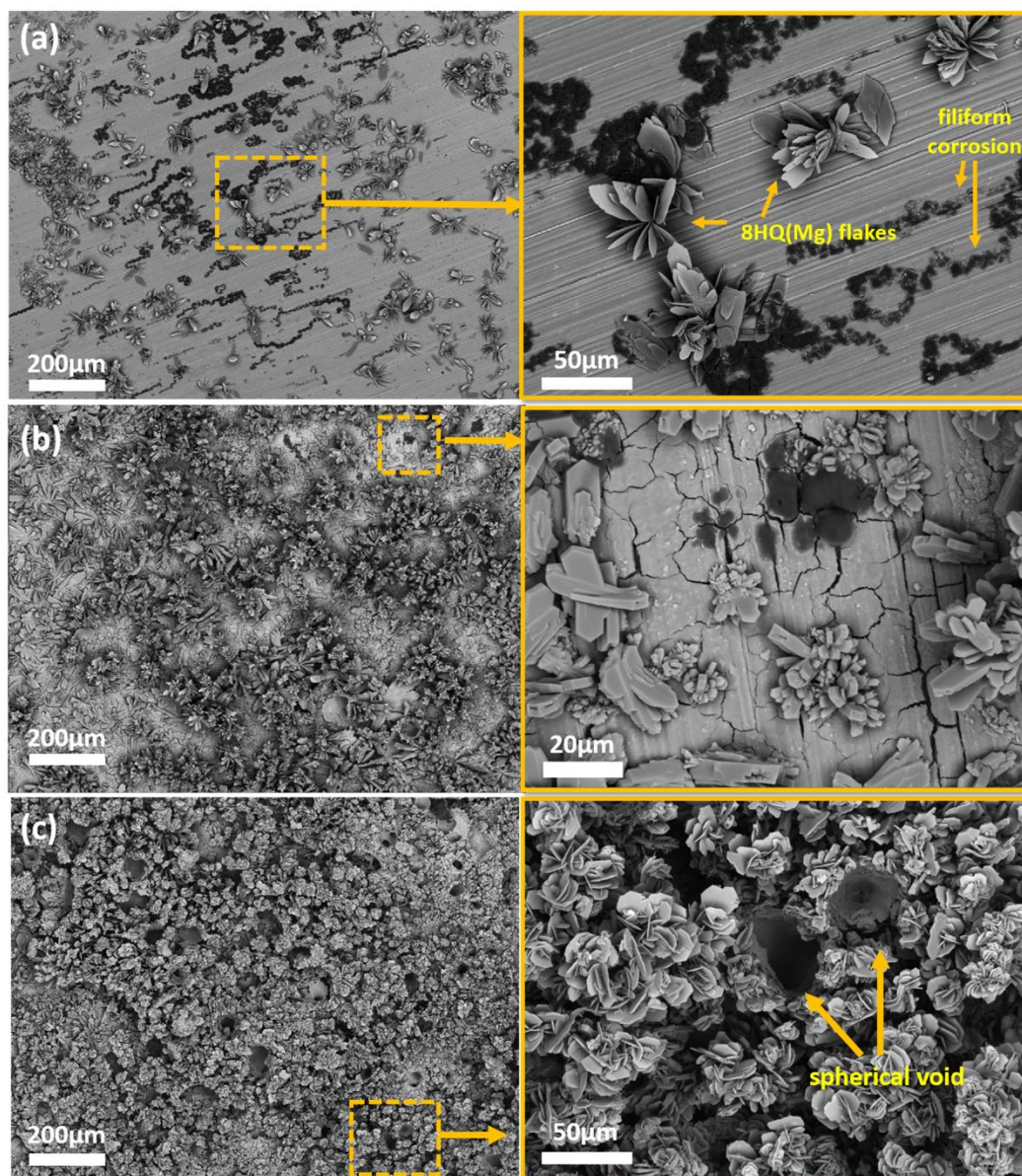
### 3.3. XRD of PEO

Fig. 9 shows the XRD patterns obtained from the PEO-coated magnesium before and after 3 days of exposure to the NaCl electrolyte with and without 8HQ.

The XRD pattern of the reference sample (before immersion) reveals that the PEO coating is mainly composed of MgO (Periclase) and  $Mg_3(PO_4)_2$  (Farringtonite) phases. The appearance of the Mg peak in the pattern ensures that the XRD incident beam passed through the thickness of the coating and reached the Mg substrate. The hump in the  $2\theta$  region between  $20^\circ$  and  $40^\circ$  is explained by the presence of amorphous  $Mg_3(PO_4)_2$  phase. Other peaks with relatively low intensities that are not marked in the spectra cannot be assigned to any phase with certainty.

After 3 days of immersion in the NaCl electrolyte, all phases in the reference PEO (before immersion) can be identified, albeit with much lower intensity as compared to the XRD peaks assigned to the Mg. This could be due to the degradation of the PEO layer that lets the incident X-ray penetrate easier towards the magnesium substrate.

The XRD pattern obtained from the sample after immersion in the 8HQ-containing electrolyte was dominated by the diffraction peak at  $2\theta$  of  $6.8^\circ$ , which is the most intense peak of 8HQ(Mg) complex (Fig. 9 (d)). While the diffraction patterns from the PEO phases, as well as the substrate, remain detectable at higher magnification, the hump associated



**Fig. 5.** Surface morphologies of bare AZ21 exposed to the NaCl electrolyte containing 8HQ after (a) 5 min, (b) 1 h, and (c) 1 day. An enlarged version of each marked area is illustrated on its right hand side. All images are taken in the backscatter electron (BSE) mode of SEM.

with the  $\text{Mg}_3(\text{PO}_4)_2$  cannot be observed, probably due to the considerably low intensity concealed by the background noise spectra. XRD peaks of  $\text{Mg}(\text{OH})_2$  were not found in the spectrum of the samples after corrosion in neither blank nor 8HQ-containing NaCl electrolyte.

### 3.4. SEM

Fig. 10 illustrates the surface and cross-section of PEO coating before and after 1 day of immersion in the NaCl solution. Prior to the immersion, the PEO layer contains large pores in its outer layer. The average total thickness of the PEO layer was measured  $44 \pm 10 \mu\text{m}$ . Cracks are also visible, spreading all over the surface and in the thickness of the PEO outer layer, which could be caused by the thermal stresses during the PEO coating formation [43,44]. Following 1 day of immersion in

NaCl solution, the surface of the PEO layer (Fig. 10 (b)) becomes rougher as compared to that of the reference PEO layer (Fig. 10 (a)), showing its degradation. Magnesium substrate is also subjected to corrosion that is evident from the thin layer of corrosion products at the PEO/substrate interface, as marked in Fig. 10 (e). Higher magnification from the surface of the PEO layer after corrosion is shown in Fig. 10 (c) that reveals two distinctive regions, labeled as “smooth” and “rough”. The smooth region possesses a similar morphology to the surface of reference PEO before immersion, based on which it can be inferred that this region has not been degraded after 1 day of immersion. On the other hand, the rough region, which appears as a deeper level as compared to the surrounding smooth one, has been degraded. The elemental composition of these regions was measured using a statistical (20 data points for each region) EDS analysis, which is shown in Fig. 10 (f). The atomic

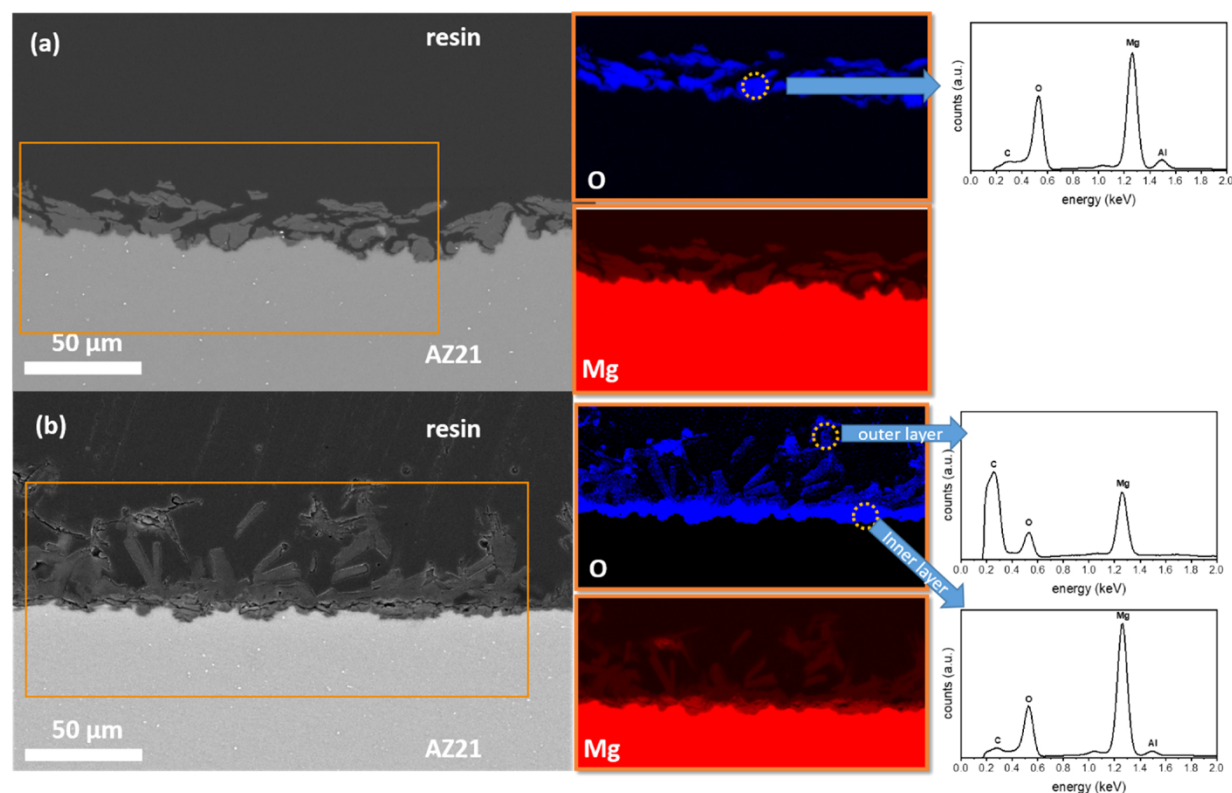


**Fig. 6.** Cross-sectional morphology of the AZ21 after 1 days of exposure to NaCl electrolyte (a) without and (b) with 8HQ. The elemental mappings of the marked area are depicted on the right side of each case.

percentage of element P appears to be slightly lower in the rough degraded region, which suggests that  $\text{Mg}_3(\text{PO}_4)_2$  has been preferentially degraded in comparison to  $\text{MgO}$ . This conclusion can also be drawn from the atomic ratio  $\text{Mg}:\text{O}$  in different phases, as presented in the table in Fig. 10 (f). Assuming the PEO layer is only composed of  $\text{MgO}$  and  $\text{Mg}_3(\text{PO}_4)_2$ , a higher  $\text{Mg}:\text{O}$  atomic ratio means higher ratio of the  $\text{MgO}$  phase in the measured volume of the EDS analysis, which again means more dissolution of  $\text{Mg}_3(\text{PO}_4)_2$ .

Fig. 11 shows the cross-sectional and surface morphology of the PEO layer after 1 h and 1 day immersion span in NaCl solution with 8HQ. After 1 h of immersion, two morphologies/sizes of the 8HQ(Mg) flakes were identified: 1- Small flakes mostly located directly on the very top surface of the PEO layer (Fig. 11 (a1)), 2- Relatively larger flakes mostly grown from/around the PEO pores, which occasionally appeared as the spherical voids similar to the ones observed on the bare AZ21 in Fig. 5. The large flakes were also identified inside the pores in the PEO outer layer, as marked in Fig. 11 (a3). Different morphology of the flakes suggests different supply of its precursors, namely  $\text{Mg}^{2+}$  or 8HQ. The  $\text{Mg}^{2+}$  required for the formation of smaller flakes, which are formed directly on the outer PEO layer surface, are supplied mostly from the dissolution of the PEO layer itself, which takes place during the exposure of PEO to the NaCl solution, as depicted in Fig. 10. On the other hand, the  $\text{Mg}^{2+}$  participating in the formation of the larger flakes are supplied by the corrosion of both PEO and the Mg substrate, which was evident in the corrosion product formed at the PEO/substrate interface (Fig. 11 (a3)).

After 1 day of immersion, the top surface of the PEO outer layer was completely covered with the 8HQ(Mg) flakes, and the frequently observed spherical voids, which are formed on the PEO pores. The white patches appearing in random places on the surface were rich in Na and Cl, which are probably due to the precipitation of the NaCl solution

residue, entrapped in the rough morphology of the flakes.

Note that the resin for the embedding of the substrate was able to penetrate through the PEO outer layer and fill the pores, as is evident from the same shade of gray from the resin in Fig. 11 (a3). After 1 day of immersion, the precipitation of 8HQ(Mg) on the PEO surface seems to block the penetration of the resin through the pores that lead to occasionally observed voids, as shown in Fig. 11 (b3). This suggests the potential hindrance effect of 8HQ(Mg) precipitates on the PEO surface against the penetration of the corrosive solution toward the substrate. Some other pores in the PEO outer layer seem to be partially filled with some compounds with a similar elemental composition to that of the PEO layer (see the EDS results of the points marked Fig. 11 (b3)). Thus, these filling compounds, could contain the dissolved  $\text{Mg}_3(\text{PO}_4)_2$  from the PEO layer that is subsequently re-precipitated in the form of the same phase or its hydrated compounds. All the pores are fully filled with a similar compound after 11 days of immersion, as shown in the supplementary material Fig. S2. However, wide cracks are also frequently observable within these filling compounds. The presence of Si element in the EDS analysis of these filled pores is attributable to the presence of silicon oxide remnant from the sample polishing step using silica polishing suspension.

### 3.5. Localized diffractometry

Local diffractometry was conducted to investigate the local phase distribution in the PEO coating. Fig. 12 shows an example of a series of vertical scans along the thickness of the PEO layer (before exposure to any electrolytes). More examples of PEO-coated samples after exposure to the electrolytes are presented in the supplementary materials (Fig. S4). As compared to the XRD pattern obtained from the bulk of the PEO layer, in Fig. 9, the local diffractometry revealed more peaks that

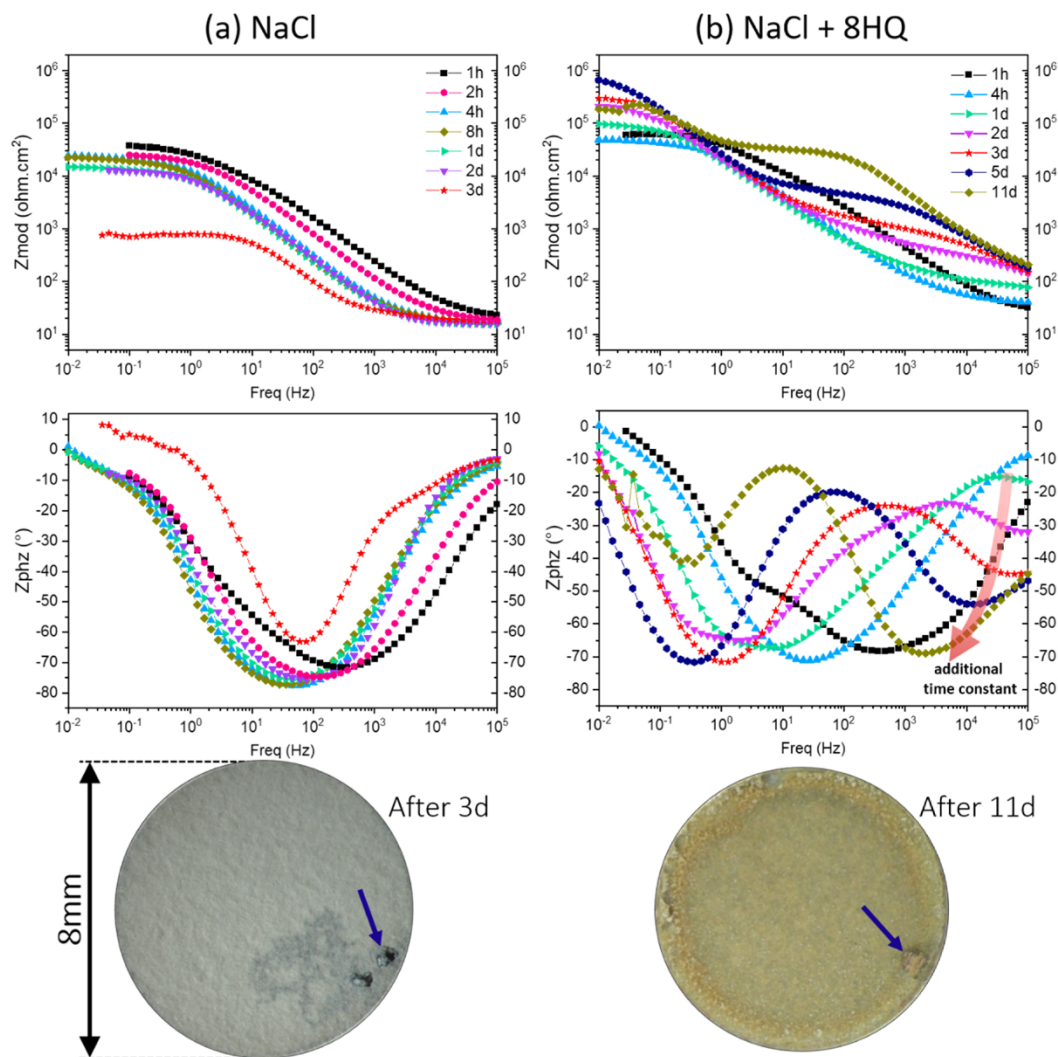


**Fig. 7.** Bode plots of PEO-coated AZ21 immersed in the NaCl solution (a) with and (b) without 8HQ. On the bottom of each case, the surface appearance of the PEO-coated AZ21 at the end of the testing is illustrated.

mostly belonged to the  $\text{Mg}_3(\text{PO}_4)_2$  phase, though they are not marked in Fig. 12 for the sake of visual clarity.

The integrated peak intensity of the strongest diffraction from each phase can be considered as a qualitative evaluation of the presence of each phase. The XRD peaks positioned at  $2\theta$  of  $37^\circ$  and  $6.8^\circ$  are taken as the strongest peaks associated with  $\text{MgO}$  and  $8\text{HQ}(\text{Mg})$  phases, respectively.  $\text{Mg}_3(\text{PO}_4)_2$  phase showed a preferential orientation in different scanned positions of PEO. This can be seen in the noticeable variation of relative intensities of diffracted peaks associated with different crystallographic planes of  $\text{Mg}_3(\text{PO}_4)_2$  phase within the thickness of the PEO layer (Fig. 12). This could be attributed to the fact that the focused X-ray beam volume is too small to be located inside  $\text{Mg}_3(\text{PO}_4)_2$  grains with different crystallographic orientations. Therefore, it is not practical to make even a qualitative evaluation of the  $\text{Mg}_3(\text{PO}_4)_2$  phase based on the integrated intensity of any of its corresponding peaks. Note that a negligible local inhomogeneity was also observed for  $\text{MgO}$  crystal orientations. The 2D maps of the  $\text{MgO}$ ,  $\text{Mg}$  and  $8\text{HQ}(\text{Mg})$  complex within the cross-section of the PEO-coated AZ21 after 3 days of immersion in the 8HQ-containing NaCl electrolyte are presented in Fig. 13.

$\text{MgO}$  seems to be distributed homogeneously along with the

thickness of the PEO coating. While the  $8\text{HQ}(\text{Mg})$  phase is mostly located on the top of the PEO layer and its intensity significantly declines within the PEO outer layer. There was no clear evidence of the presence of  $\text{Mg}(\text{OH})_2$  in all the obtained spectra. This could be due to either its low amount or its low crystallinity.

### 3.6. Raman spectroscopy

Raman spectroscopy of the different regions in the PEO cross-section of the sample after 11 days of immersion in the 8HQ-containing electrolyte was carried out to primarily characterize the different regions of the PEO cross-section. In particular, the filling compounds in the PEO outer pores, which is marked in the SEM micrograph (Fig. 11 (b3) region 2) was the subjected for characterization. For the sake of comparison, the Raman spectrum obtained from the synthesized  $8\text{HQ}(\text{Mg})$  powder is also depicted in the same figure. As can be seen, the Raman spectrum derived from the flakes on the PEO layer are fully coincident with that of synthesized  $8\text{HQ}(\text{Mg})$  powder in the presented spectral range, further confirming the formation of pure  $8\text{HQ}(\text{Mg})$  on the PEO surface. In particular, the most intense band at  $1370 \text{ cm}^{-1}$  corresponds

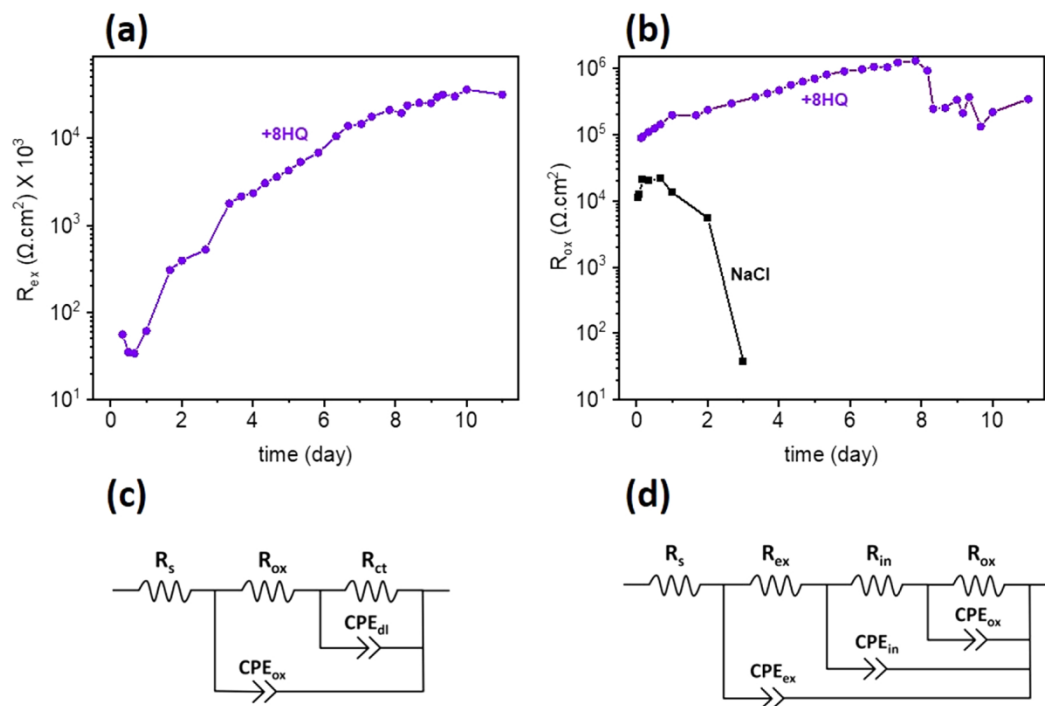


**Fig. 8.** (a) and (b) evolution of  $R_{ex}$  and  $R_{ox}$  extracted from the fitting of EIS spectra with the equivalent circuits presented in (c) and (d). (c) and (d): the equivalent circuit employed to fit the EIS spectra for the NaCl electrolyte without and with 8HQ, respectively.

to the combined mode of C-H bending and stretching of the quinoline ring [45]. Other two intense bands at  $500$  and  $733 \text{ cm}^{-1}$  are due to the in-plane bending of the quinoline ring [46].

The characteristic bands of the 8HQ(Mg) complex also appear in the Raman spectra of the filled PEO pores, indicating the local presence of this complex, albeit with a considerably lower intensity ratio to the other existing bands.

The filled pores of the PEO outer layer are highly prone to be contaminated with the used commercial OPS solution during the polishing step of the sample preparation, as confirmed by the EDS results in Fig. 11, which also shows a considerable presence of Si element in the same region. Therefore, the Raman spectrum of this region shows several bands that may overlap, and thus, it casts doubts on the asserted presence of other possible chemicals, including magnesium phosphate. Nevertheless, the presence of the 8HQ(Mg) complex in the pores is induced.

## 4. Discussion

### 4.1. Inhibition effect of 8HQ on bare AZ21

The inhibition effect of 8HQ on magnesium alloys has been proposed based on the formation of the insoluble complex with  $\text{Mg}^{2+}$  ( $K_{sp, 8\text{HQ}(\text{Mg})} = 4 \times 10^{-16}$  [47]). On AZ21 substrate, the exposure to the 8HQ-containing electrolyte results in immediate precipitation of 8HQ(Mg) flakes, growing like flowers in separate locations, rather than uniform precipitation on the Mg surface, although the effect of concentration gradient close to the magnesium surface was tried to be minimized by the constant stirring of the electrolyte.

Therefore, a full coverage of the magnesium surface by 8HQ(Mg) precipitates is slowly achieved, so that even after 1 h of exposure to the corrosive medium, regions free of 8HQ(Mg) precipitates are still visible, depicted in Fig. 5 (b). This is also evident from the negligible difference between the corresponding EIS spectra of the electrolytes with and

without 8HQ at the earlier stages of the immersion (before 2 h). However, the emergence of an extra capacitive behavior at the very high-frequency range of the EIS suggests that the extra layer fully covers the magnesium surface, as also visible from Figs. 5(c) and 6 (b). Consequently, after 1 day of exposure to the electrolyte containing 8HQ, a two-layer film is formed on the magnesium substrate, consisting of the outer layer of 8HQ(Mg) and the cracked inner layer of  $\text{Mg}(\text{OH})_2$ .

Cracks in the corrosion products and other precipitations on magnesium alloys have been associated with the post-processing of the surface rather than the inherent existence of cracks within their structure. For instance, the shrinkage in the volume of corrosion products due to the dehydration of the present compounds can lead to the formation of cracks [48,49]. The low-pressure condition during the SEM/EDX surface characterization may also intensifies the crack formation in the corrosion/conversion films on the Mg surface [50]. However, assuming the influencing post-processing steps are identical for both cases, Fig. 6 clearly indicates that the presence of 8HQ in the electrolyte led to a stronger resistance of the formed inner layer corrosion products against any crack-inducing post-processing step as compared to the corrosion products formed in the case of electrolyte without 8HQ. Thus, it can be inferred that the inner layer is capable of obstructing the penetration of the corrosive medium towards the substrate more effectively than the corrosion products formed after exposure to the blank NaCl electrolyte. Simultaneously, the  $\text{OH}^-$  generated during the corrosion of the substrate is also confined within the dense corrosion products that escalate the local alkalinity. This not only enhances the barrier properties of the oxide layer [38], which is consistent with the  $R_{ox}$  trend in Fig. 2, but also leads to a denser  $\text{Mg}(\text{OH})_2$  morphology with a smaller flake size [51].

Moreover, the presence of organic molecules is reported to form complexes with  $\text{Mg}^{2+}$  that can modify the morphology of the formed  $\text{Mg}(\text{OH})_2$ . For example, Maltseva et al. [52] pointed out that the presence of some organic corrosion inhibitors with carboxylate functional groups densifies the  $\text{Mg}(\text{OH})_2$  flakes. Thus, 8HQ molecules are also expected to play a role in the denser appearance of  $\text{Mg}(\text{OH})_2$  in the inner layer.

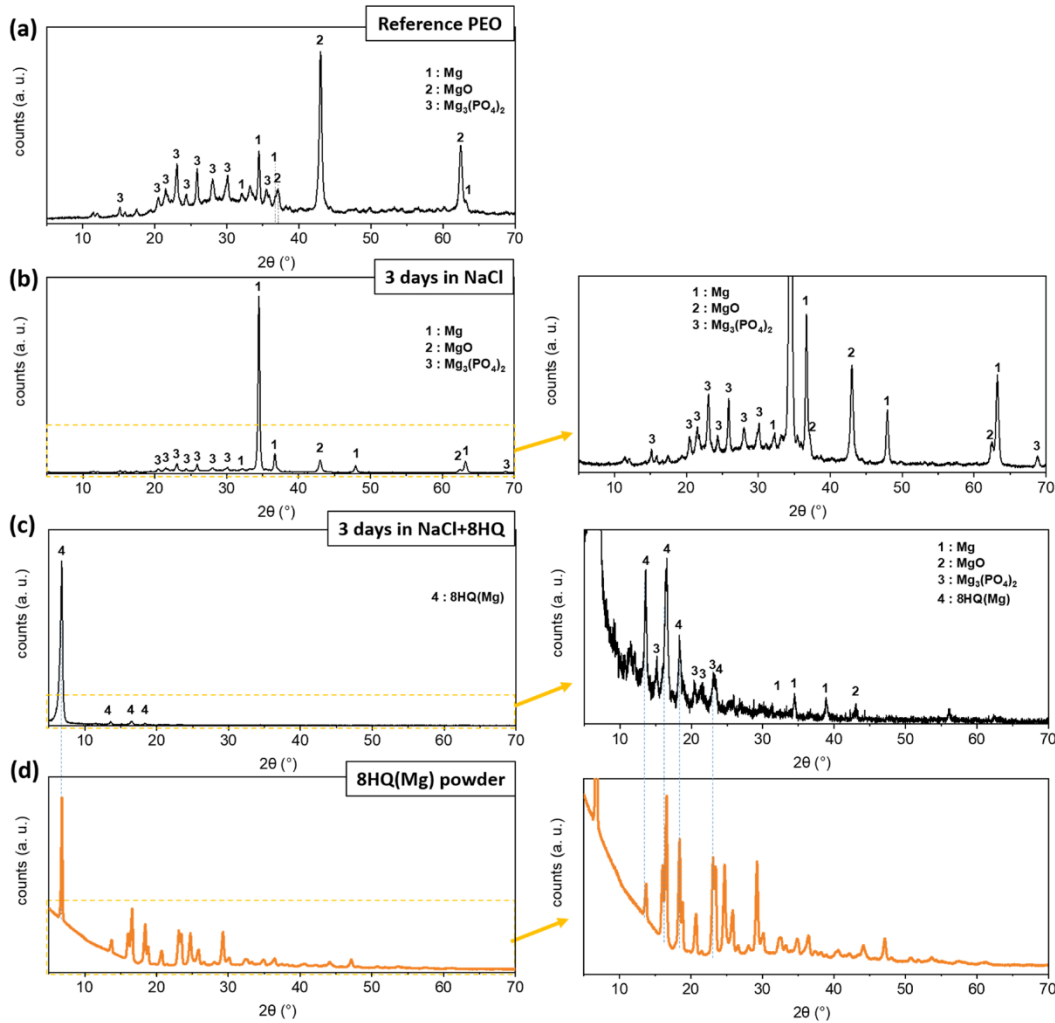


**Fig. 9.** XRD spectra of PEO-coated Mg (a) before and after 3 days of immersion in (b) NaCl (c) NaCl + 8HQ solution. (d) XRD spectra of the synthesized 8HQ (Mg) powder.

**Fig. 14.**

The progressive formation of  $\text{Mg}(\text{OH})_2$ , along with the formation of  $\text{H}_2$  bubbles, exert mechanical forces on the top  $8\text{HQ}(\text{Mg})$  layer, which causes its local breakdown. The reaction of more released  $\text{Mg}^{2+}$  from the substrate and the 8HQ in the electrolyte in the local breakdown heals the outer layer. In Fig. 2, the very fluctuating value of  $R_{\text{ex}}$  implies the active successive breakdown and healing of the outer layer, albeit with a rising trend. Despite the general improvement in the barrier properties of the extra layer over the immersion time, which is supplied by the abundant source of 8HQ molecules in the electrolyte, the inner layer is progressively deprived from the free 8HQ molecules, which in turn, leads to the gradual declination of  $R_{\text{ox}}$ ,  $R_{\text{ct}}$ , and consequently  $|Z|_1$  Hz.

#### 4.2. Inhibitory effect of 8HQ on PEO-coated AZ21

Fig. 15 illustrates the schematic presentation of inhibition mechanism of 8HQ against the corrosion of PEO-coated magnesium substrate.

When AZ21 substrate is coated with the PEO layer, dissolution of  $\text{Mg}_3(\text{PO}_4)_2$  and  $\text{MgO}$  in the electrolyte provides the  $\text{Mg}^{2+}$  to react with 8HQ ( $K_{\text{sp}, 8\text{HQ}(\text{Mg})} = 4 \times 10^{-16}$  [47]), which is evident in the early precipitation of the fine  $8\text{HQ}(\text{Mg})$  flakes on the PEO outer layer. The

interaction of PEO-coated AZ21 at its early stages of exposure to the 8HQ-containing NaCl electrolyte is schematically presented in Fig. 15 (a) and (b).

The EDS results obtained from the different regions on top of the PEO layer suggest that  $\text{Mg}_3(\text{PO}_4)_2$  is prone to dissolution more preferably than the  $\text{MgO}$  phase. However, the dissolving  $\text{Mg}_3(\text{PO}_4)_2$  is probably in the amorphous phase, as its existence was confirmed by the XRD analysis in Fig. 9. Amorphous phases are typically more prone to dissolution than their crystalline counterparts [43,53]. The higher content of amorphous  $\text{Mg}_3(\text{PO}_4)_2$  has also been reported to cause a swifter decomposition of the PEO coating [43,54]. In a mixed phosphate/silicate PEO coating on AM50 alloy, the stability of the PEO phases under the attack of  $\text{Cl}^-$ -containing aqueous electrolyte has been concluded as follows: amorphous materials  $< \text{MgO} < \text{Mg}_3(\text{PO}_4)_2 < \text{Mg}_2\text{SiO}_4$  [55].

However, the dissolved amorphous  $\text{Mg}_3(\text{PO}_4)_2$  could re-precipitate [53,56], the probability of which is higher when the liberated  $\text{Mg}^{2+}$  and  $\text{PO}_4^{3-}$  ions are confined in a region in the electrolyte like the PEO pores, and cannot be diluted to the bulk electrolyte. The precipitation of  $8\text{HQ}(\text{Mg})$  on top of the PEO layer can hinder the dilution of liberated  $\text{Mg}^{2+}$  and  $\text{PO}_4^{3-}$  to the bulk electrolyte. Consequently, the PEO pores are filled with  $\text{Mg}_3(\text{PO}_4)_2$  during the exposure to the 8HQ-containing NaCl

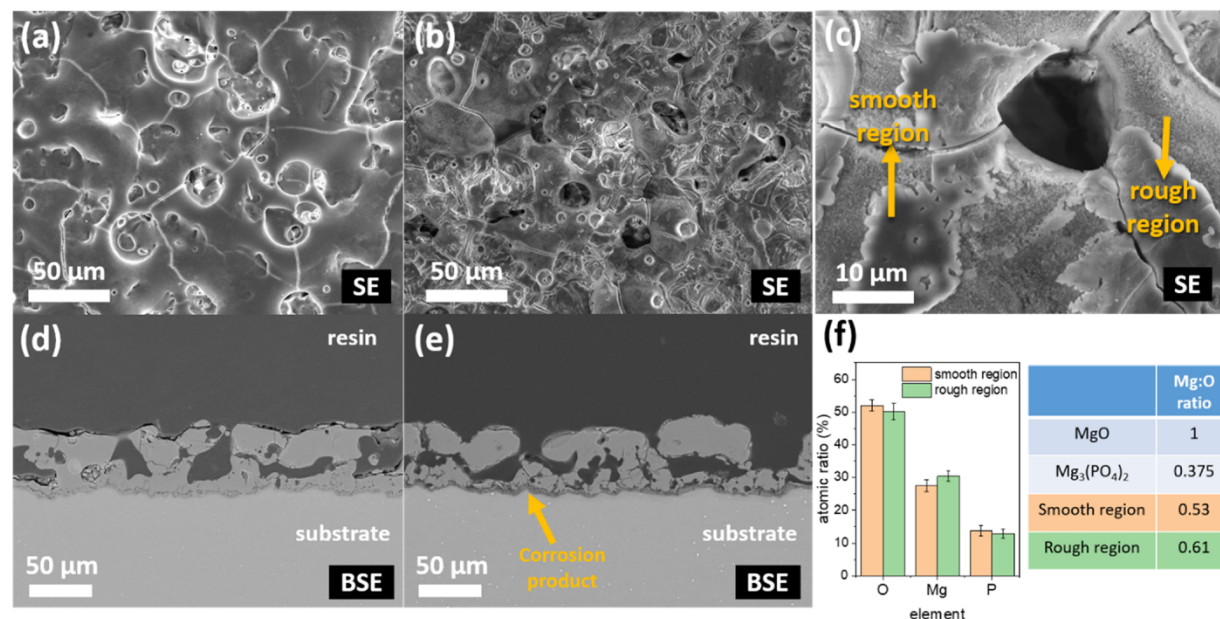


**Fig. 10.** Cross-sectional and surface morphologies of PEO-coated AZ21 (a) & (d) before and (b) & (e) after 1 day of immersion in NaCl solution. (c) higher magnification of (b). (f) average elemental composition of regions marked in (c) from 20 data points. “SE” and “BSE” stand for secondary electron and backscattered electron modes, respectively.

electrolyte, which is evident based on the SEM micrographs in Fig. 11 and Fig. S1. Although the re-deposited form of magnesium phosphate has been hypothesized to be a hydrated form (as Cattite:  $\text{Mg}_3(\text{PO}_4)_2 \cdot 22 \text{H}_2\text{O}$  or Bobierite:  $\text{Mg}_3(\text{PO}_4)_2 \cdot 8 \text{H}_2\text{O}$ ) [43,53], local and bulk XRD analysis in this work cannot conclude a confident detection of such phases.

The precipitation of 8HQ(Mg) occurs extensively on top of the PEO layer, as it is evident from the SEM micrographs (Fig. 11) and phase map (Fig. 13) obtained from the cross-section of PEO. This is because the initial grown layer on top of PEO can, to some degree, impede the further passage of 8HQ molecules into the pores of the PEO layer by its physical barrier properties. Moreover, the higher concentration of 8HQ in the bulk electrolyte tends to participate in the crystal growth of already formed 8HQ(Mg) flakes on the top PEO layer, as schematically presented in Fig. 15 (b) and (c). Similar to the case of bare AZ21, the partial physical barrier properties of the formed 8HQ(Mg) layer leads to the accumulation of the generated  $\text{OH}^-$  within the PEO layer, thereby resulting in the formation of a denser  $\text{Mg}(\text{OH})_2$  as the corrosion product. The high local alkalinity also enhances the oxide film barrier properties [38], which is evident in the higher  $R_{\text{ox}}$  (Fig. 8 (b)).

Furthermore, the re-precipitation of the  $\text{Mg}_3(\text{PO}_4)_2$  along with the formation of the 8HQ(Mg) complex (as confirmed from the Raman spectra) inside the pores of the PEO outer layer help hindering the penetration of the corrosive electrolyte toward the magnesium substrate. It is worth mentioning that the re-deposition of the  $\text{Mg}_3(\text{PO}_4)_2$  from the PEO coating can also occur when the electrolyte does not contain 8HQ, as similar behavior has been observed for PEO coatings containing magnesium phosphate [11,53]. Such re-deposition, indeed, can mitigate the corrosion of the Mg substrate. However, the effect of re-deposition could be more pronounced when 8HQ is present in the electrolyte since the blockage of the 8HQ(Mg) layer on top of the PEO causes the re-depositions to occur within the confines of the PEO pores rather than the dilution of dissolved magnesium phosphate into the bulk electrolyte. This can also be induced by the considerably higher amount of P-rich precipitates in the pores of PEO after 1 day of immersion when 8HQ is present in the electrolyte (compare Fig. 11 (b3) and Fig. 10 (e)). Nevertheless, considerably wide cracks and voids in the filled pores of

the PEO outer layer were observed even after 11 days of exposure to the 8HQ-containing electrolyte (Fig. S2). Thus, the entire PEO outer layer cannot result in the emergence of the additional layer with capacitive characteristics sensed by EIS at high frequencies. The extra layer observable in EIS is probably limited to the region close to the substrate where the PEO pores are considerably smaller as compared to that of the PEO outer layer, which can be filled and form a barrier more efficiently, as schematically shown in Fig. 15 (c).

Such re-precipitation of magnesium phosphate in the pores of the PEO outer layer was not observed in the case of exposure to the blank NaCl electrolyte even after 3 days of immersion, which could be ascribed to the free diffusion of released  $\text{Mg}^{2+}$  and  $\text{PO}_4^{3-}$  ions from the open pores of PEO to the bulk.

As the corrosion of the substrate proceeds, more corrosion products form at the PEO/substrate interface, which exerts more mechanical forces on the top layers. Meanwhile, 8HQ is being depleted locally by precipitating in the form of 8HQ(Mg). At one point, the increasing mechanical forces of the formed corrosion products, as well as the formed  $\text{H}_2$  bubbles, induce cracks to the top protective layer, thus allowing for greater penetration of corrosive  $\text{Cl}^-$  toward the substrates. This is visible in the sudden drop of  $R_{\text{ox}}$  after 8 days of immersion.

## 5. Conclusion

The investigation of the interaction of 8HQ with both bare AZ21 and phosphate-based PEO coating revealed the main corrosion inhibition mechanism of 8HQ as summarized below:

1. The  $\text{Mg}^{2+}$  liberated due to the corrosion of the magnesium substrate and the dissolution of the PEO layer forms an insoluble complex with 8HQ molecules, which is adequately supplied from the saturated electrolyte.
2. Both the accumulated  $\text{OH}^-$  ions within the PEO pores, as well as the presence of 8HQ, modify the formation of the corrosion products on the magnesium substrate, resulting in a denser morphology of the corrosion products.

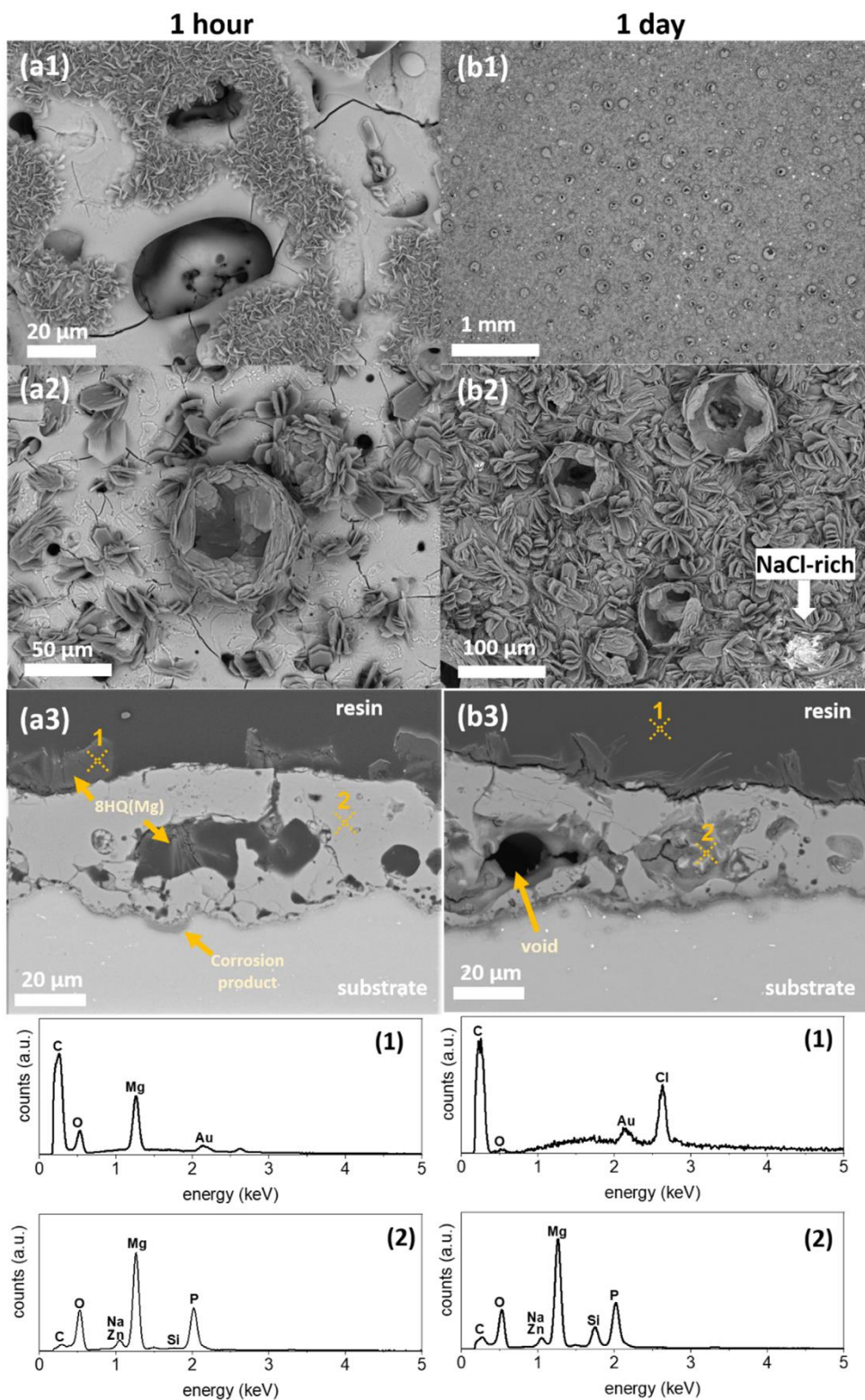


**Fig. 11.** Cross-sectional and surface morphology of the PEO-coated AZ21 after (a) 1 h and (b) 1 day of immersion in NaCl solution containing 8HQ. The EDS spectra obtained from the point measurement marked on (a3) and (b3) are provided below the corresponding image.

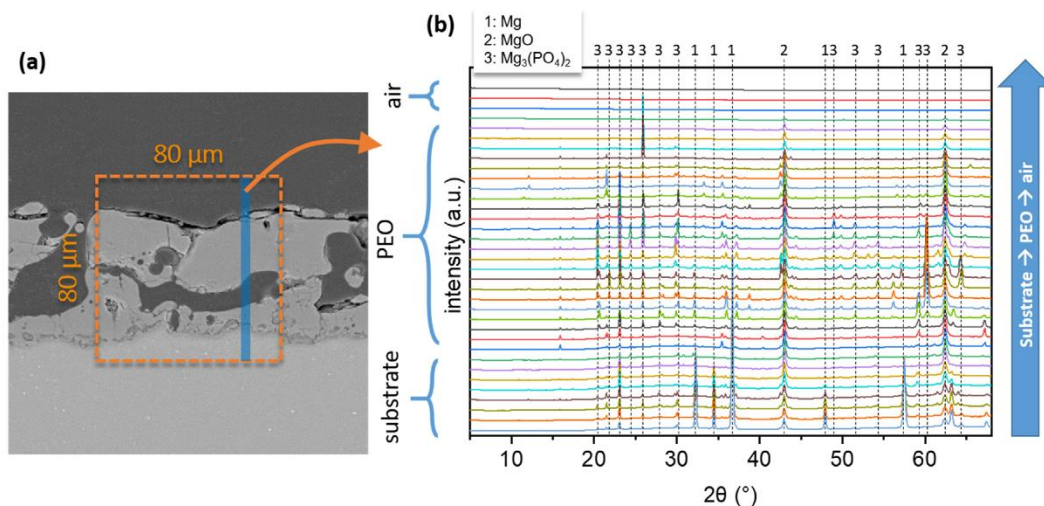


**Fig. 12.** (a) Scheme of diffractometry map on PEO coating. (b) XRD patterns obtained from scanning of one vertical line along the PEO thickness. The results are for reference PEO sample before immersion in any electrolyte.

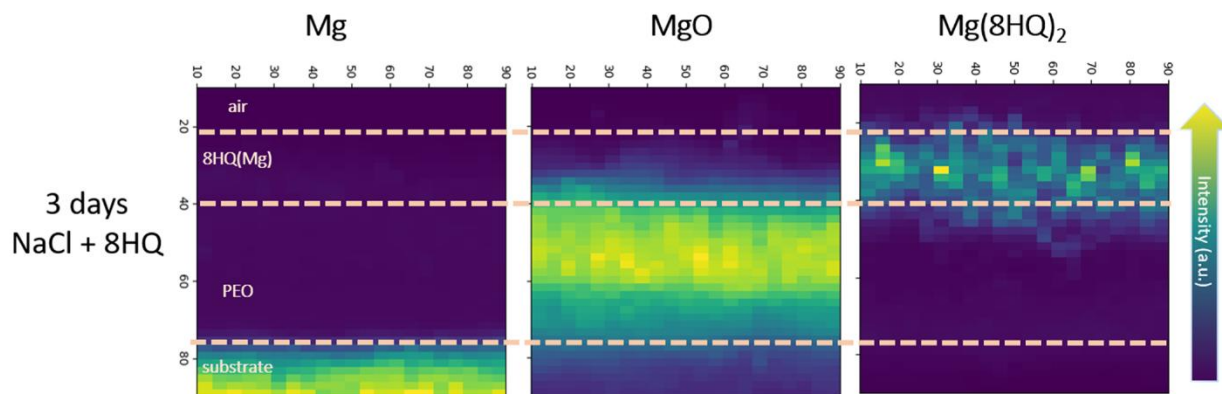


**Fig. 13.** 2D maps of the phases present in the cross-section of the PEO-coated AZ31 after 3 days immersion in the 8HQ-containing NaCl electrolyte. All the positional scales are in micrometer.

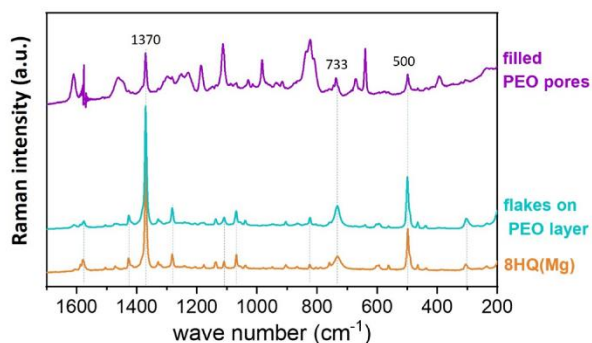


**Fig. 14.** Raman spectra of synthesized 8HQ(Mg) complex, the 8HQ(Mg) flakes on the PEO layer, and the filled PEO pores.

- Co-precipitation of 8HQ(Mg) and re-deposited Mg<sub>3</sub>(PO<sub>4</sub>)<sub>2</sub> inside the PEO pores provides further barrier properties against the penetration of corrosive Cl<sup>-</sup> toward the magnesium substrate.

The findings of this study provide an in-depth and mechanistic understanding of the inhibition effect of 8HQ, upon being incorporated into a PEO layer.

#### CRediT authorship contribution statement

**Bahram Vaghefinazari:** Conceptualization, Investigation, Validation, Writing – original draft, Writing – review & editing. **Sviatlana V. Lamaka:** Conceptualization, Supervision, Writing – review & editing. **Carsten Blawert:** Conceptualization, Supervision, Writing – review & editing. **Maria Serdechnova:** Investigation, Writing – review & editing. **Nico Scharnagl:** Investigation, Writing – review & editing. **Polina Karlova:** Investigation, Writing – review & editing. **D.C. Florian Wieland:** Investigation, Writing – review & editing. **Mikhail L. Zheludkevich:** Conceptualization, Supervision, Writing – review & editing.

#### Declaration of Competing Interest

The authors declare that they have no known competing financial interests or personal relationships that could have appeared to influence the work reported in this paper.

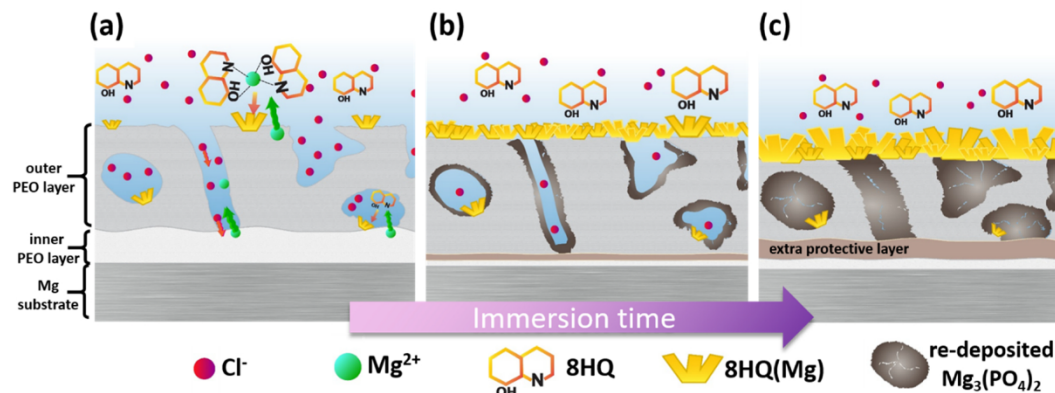


**Fig. 15.** Schematic presentation of inhibition mechanism of 8HQ against the corrosion of PEO-coated Mg in NaCl solution. (a), (b), and (c) illustrate the interaction of 8HQ-containing NaCl electrolyte with the PEO-coated magnesium in the order of immersion time.

### Data Availability

The raw/processed data required to reproduce these findings cannot be shared at this time as the data also forms part of an ongoing study.

### Acknowledgement

The authors would like to acknowledge the technical support from Mr. Ulrich Burmester, Mr. Volker Heitmann and Mr. Gert Wiese. We also thank PETRA III (DESY, Hamburg, Germany) for support of proposal I-20191340 and Dr. Anton Davydok for technical support during the beamtime.

### Appendix A. Supporting information

Supplementary data associated with this article can be found in the online version at [doi:10.1016/j.corsci.2022.110344](https://doi.org/10.1016/j.corsci.2022.110344).

### References

- [1] M. Kaseem, S. Fatimah, N. Nashrah, Y.G. Ko, Recent progress in surface modification of metals coated by plasma electrolytic oxidation: principle, structure, and performance, *Prog. Mater. Sci.* (2020), 100735.
- [2] M. Moledano, X. Lu, E. Matykina, C. Blawert, R. Arrabal, M.L. Zheludkevich, Plasma electrolytic oxidation (PEO) of metals and alloys, in: K. Wandelt (Ed.), *Encyclopedia of Interfacial Chemistry*, Elsevier Oxford, 2018, pp. 423–438.
- [3] S. Sikdar, P.V. Menezes, R. Maccione, T. Jacob, P.L. Menezes, Plasma electrolytic oxidation (PEO) process—processing, properties, and applications, *Nanomaterials* 11 (2021) 1375.
- [4] X. Lu, M. Moledano, C. Blawert, E. Matykina, R. Arrabal, K.U. Kainer, M. L. Zheludkevich, Plasma electrolytic oxidation coatings with particle additions – a review, *Surf. Coat. Technol.* 307 (2016) 1165–1182.
- [5] A. Fattah-alhosseini, R. Chaharmahali, K. Babaei, Effect of particles addition to solution of plasma electrolytic oxidation (PEO) on the properties of PEO coatings formed on magnesium and its alloys: a review, *J. Magnes. Alloy* 8 (2020) 799–818.
- [6] S.V. Lamaka, G. Knörnschild, D.V. Snihirova, M.G. Taryba, M.L. Zheludkevich, M. G.S. Ferreira, Complex anticorrosion coating for ZK30 magnesium alloy, *Electrochim. Acta* 55 (2009) 131–141.
- [7] Y. Chen, X. Lu, S.V. Lamaka, P. Ju, C. Blawert, T. Zhang, F. Wang, M. L. Zheludkevich, Active protection of Mg alloy by composite PEO coating loaded with corrosion inhibitors, *Appl. Surf. Sci.* 504 (2020), 144462.
- [8] G. Zhang, E. Jiang, L. Wu, W. Ma, H. Yang, A. Tang, F. Pan, Corrosion protection properties of different inhibitors containing PEO/LDHs composite coating on magnesium alloy AZ31, *Sci. Rep.* 11 (2021) 2774.
- [9] M. Toorani, M. Aliofkhaizadeh, M. Mahdavian, R. Naderi, Superior corrosion protection and adhesion strength of epoxy coating applied on AZ31 magnesium alloy pre-treated by PEO/Silane with inorganic and organic corrosion inhibitors, *Corros. Sci.* 178 (2021), 109065.
- [10] G. Zhang, L. Wu, A. Tang, X. Ding, B. Jiang, A. Atrous, F. Pan, Smart epoxy coating containing zeolites loaded with Ce on a plasma electrolytic oxidation coating on Mg alloy AZ31 for active corrosion protection, *Prog. Org. Coat.* 132 (2019) 144–147.
- [11] E. Wierzbicka, B. Vaghefiazari, S.V. Lamaka, M.L. Zheludkevich, M. Moledano, L. Moreno, P. Visser, A. Rodriguez, J. Velasco, R. Arrabal, E. Matykina, Flash-PEO as an alternative to chromate conversion coatings for corrosion protection of Mg alloy, *Corros. Sci.* 180 (2021), 109189.
- [12] D.K. Ivanou, K.A. Yasakau, S. Kallip, A.D. Lisenkov, M. Starykevich, S.V. Lamaka, M.G.S. Ferreira, M.L. Zheludkevich, Active corrosion protection coating for a ZE41 magnesium alloy created by combining PEO and sol-gel techniques, *RSC Adv.* 6 (2016) 12553–12560.
- [13] W.A. Zoubi, J.H. Min, Y.G. Ko, Hybrid organic-inorganic coatings via electron transfer behaviour, *Sci. Rep.* 7 (2017).
- [14] J. Yang, C. Blawert, S.V. Lamaka, D. Snihirova, X. Lu, S. Di, M.L. Zheludkevich, Corrosion protection properties of inhibitor containing hybrid PEO-epoxy coating on magnesium, *Corros. Sci.* 140 (2018) 99–110.
- [15] A.S. Gnedenkov, S.L. Sinebryukhov, D.V. Mashtalyar, S.V. Gnedenkov, Localized corrosion of the Mg alloys with inhibitor-containing coatings: SVET and SIET studies, *Corros. Sci.* 102 (2016) 269–278.
- [16] D. Liu, Y.W. Song, D.Y. Shan, E.H. Han, Self-healing coatings prepared by loading interphase inhibitors into MAO coating of AM60 Mg alloy, *J. Electrochem. Soc.* 165 (2018) C412–C421.
- [17] F.H. Rhodes, W.E. Kuhn, Inhibitors in the action of acid on steel, *Ind. Eng. Chem.* 21 (1929) 1066–1070.
- [18] C. Verma, M.A. Quraishi, E.E. Ebenso, Quinoline and its derivatives as corrosion inhibitors: a review, *Surf. Interfaces* 21 (2020), 100634.
- [19] C. Verma, K.Y. Rhee, M.A. Quraishi, E.E. Ebenso, Pyridine based N-heterocyclic compounds as aqueous phase corrosion inhibitors: a review, *J. Taiwan Inst. Chem. Eng.* 117 (2020) 265–277.
- [20] K. Lavanya, J. Saranya, S. Chitra, Recent reviews on quinoline derivatives as corrosion inhibitors, *Corros. Rev.* 36 (2018) 365–371.
- [21] H. Gao, Q. Li, Y. Dai, F. Luo, H.X. Zhang, High efficiency corrosion inhibitor 8-hydroxyquinoline and its synergistic effect with sodium dodecylbenzenesulphonate on AZ91D magnesium alloy, *Corros. Sci.* 52 (2010) 1603–1609.
- [22] Q. Zong, L. Wang, W. Sun, G. Liu, Active deposition of bis (8-hydroxyquinoline) magnesium coating for enhanced corrosion resistance of AZ91D alloy, *Corros. Sci.* 89 (2014) 127–136.
- [23] G.R. Argade, S. Sanders, G. Mohandass, A. Alsaleh, F. D'Souza, T.D. Golden, R. S. Mishra, Corrosion inhibition study of Mg–Nd–Y high strength magnesium alloy using organic inhibitor, *J. Mater. Eng. Perform.* 28 (2019) 852–862.
- [24] D. Seifzadeh, S. Hamzedoust-Hasankiadeh, A. Shamkhali, Electrochemical and DFT studies of 8-hydroxyquinoline as corrosion inhibitor for AZ61 magnesium alloy in acidic media, *Prot. Met. Phys. Chem. Surf.* 49 (2013) 229–239.
- [25] I.A. Kartsonakis, S.G. Stanciu, A.A. Matei, E.K. Karaxi, R. Hristu, A. Karantonis, C. A. Charitidis, Evaluation of the protective ability of typical corrosion inhibitors for magnesium alloys towards the Mg ZK30 variant, *Corros. Sci.* 100 (2015) 194–208.
- [26] E. Slavcheva, G. Schmitt, Screening of new corrosion inhibitors via electrochemical noise analysis, *Mater. Corros.* 53 (2002) 647–655.
- [27] D. Huang, J. Hu, G.-L. Song, X. Guo, Inhibition effect of inorganic and organic inhibitors on the corrosion of Mg–10Gd–3Y–0.5Zr alloy in an ethylene glycol solution at ambient and elevated temperatures, *Electrochim. Acta* 56 (2011) 10166–10178.
- [28] S.V. Lamaka, B. Vaghefiazari, D. Mei, R.P. Petrauskas, D. Hoche, M. L. Zheludkevich, Comprehensive screening of Mg corrosion inhibitors, *Corros. Sci.* 128 (2017) 224–240.
- [29] A.F. Galio, S.V. Lamaka, M.L. Zheludkevich, L.F.P. Dick, L.L. Müller, M.G. S. Ferreira, Inhibitor-doped sol-gel coatings for corrosion protection of magnesium alloy AZ31, *Surf. Coat. Technol.* 204 (2010) 1479–1486.
- [30] W. Al Zoubi, M.J. Kim, Y.G. Kim, Y.G. Ko, Fabrication of graphene oxide/8-hydroxyquinolin/inorganic coating on the magnesium surface for extraordinary corrosion protection, *Prog. Org. Coat.* 137 (2019), 105314.
- [31] B. Mingo, Y. Guo, R. Leiva-Garcia, B.J. Connolly, A. Matthews, A. Yerokhin, Smart functionalization of ceramic-coated AZ31 magnesium alloy, *ACS Appl. Mater. Interfaces* 12 (2020) 30833–30846.

- [32] A.S. Gnedenkov, S.L. Sinebryukhov, D.V. Mashtalyar, S.V. Gnedenkov, Inhibitor-Containing Composite Coatings on Mg Alloys: Corrosion Mechanism and Self-Healing Protection, *Solid State Phenom.* 245 (2015) 89–96.
- [33] M. Kaseem, Y.G. Ko, Formation of flower-like structures for optimizing the corrosion resistance of Mg alloy, *Mater. Lett.* 221 (2018) 196–200.
- [34] X. Shi, Y. Wang, H. Li, S. Zhang, R. Zhao, G. Li, R. Zhang, Y. Sheng, S. Cao, Y. Zhao, L. Xu, Y. Zhao, Corrosion resistance and biocompatibility of calcium-containing coatings developed in near-neutral solutions containing phytic acid and phosphoric acid on AZ31B alloy, *J. Alloy. Compd.* 823 (2020), 153721.
- [35] B. Vaghefinazari, C. Wang, D. Mercier, D. Mei, A. Seyeux, P. Marcus, C. Blawert, S. V. Lamaka, M.L. Zheludkevich, Adverse effect of 2,5PDC corrosion inhibitor on PEO coated magnesium, *Corros. Sci.* (2021), 109830.
- [36] H.R. Fleck, A. Ward, The determination of metals by means of 8-hydroxyquinoline. Part I. The effect of pH on the precipitation of magnesium, zinc, cobalt, nickel, copper and molybdenum from acetate solutions, *Analyst* 58 (1933) 388–395.
- [37] C. Krywka, H. Neubauer, M. Priebe, T. Salditt, J. Keckes, A. Buffet, S.V. Roth, R. Doehrmann, M. Mueller, A two-dimensional waveguide beam for X-ray nanodiffraction, *J. Appl. Crystallogr.* 45 (2012) 85–92.
- [38] L. Wang, D. Snihirova, M. Deng, C. Wang, B. Vaghefinazari, G. Wiese, M. Langridge, D. Höche, S.V. Lamaka, M.L. Zheludkevich, Insight into physical interpretation of high frequency time constant in electrochemical impedance spectra of Mg, *Corros. Sci.* 187 (2021), 109501.
- [39] L. Wang, D. Snihirova, M. Deng, B. Vaghefinazari, D. Höche, S.V. Lamaka, M. L. Zheludkevich, Revealing physical interpretation of time constants in electrochemical impedance spectra of Mg via Tribo-EIS measurements, *Electrochim. Acta* (2021), 139582.
- [40] V. Shkirskiy, A.D. King, O. Gharbi, P. Volovitch, J.R. Scully, K. Ogle, N. Biribilis, Revisiting the electrochemical impedance spectroscopy of magnesium with online inductively coupled plasma atomic emission spectroscopy, *ChemPhysChem* 16 (2015) 536–539.
- [41] L. Wang, B.-P. Zhang, T. Shinohara, Corrosion behavior of AZ91 magnesium alloy in dilute NaCl solutions, *Mater. Des.* 31 (2010) 857–863.
- [42] M. Esmaily, J.E. Svensson, S. Fajardo, N. Biribilis, G.S. Frankel, S. Virtanen, R. Arrabal, S. Thomas, L.G. Johansson, Fundamentals and advances in magnesium alloy corrosion, *Prog. Mater. Sci.* 89 (2017) 92–193.
- [43] G. Rapheal, S. Kumar, N. Scharnagl, C. Blawert, Effect of current density on the microstructure and corrosion properties of plasma electrolytic oxidation (PEO) coatings on AM50 Mg alloy produced in an electrolyte containing clay additives, *Surf. Coat. Technol.* 289 (2016) 150–164.
- [44] G. Barati Darband, M. Aliofkhaeaei, P. Hamghalam, N. Valizade, Plasma electrolytic oxidation of magnesium and its alloys: Mechanism, properties and applications, *J. Magnes. Alloy.* 5 (2017) 74–132.
- [45] N. Muraki, M. Yoshikawa, Characterization of the interface between metal and tris (8-hydroxyquinoline) aluminum using surface-enhanced Raman scattering with glass cap encapsulation, *Chem. Phys. Lett.* 496 (2010) 91–94.
- [46] I.A. Kartsonakis, S.G. Stanciu, A.A. Matei, R. Hristu, A. Karantonis, C.A. Charitidis, A comparative study of corrosion inhibitors on hot-dip galvanized steel, *Corros. Sci.* 112 (2016) 289–307.
- [47] Lange's Handbook of Chemistry AU - Dean, J.A, Mater. Manuf. Process. 5 (1990) 687–688.
- [48] M. Mosialek, G. Mordarski, P. Nowak, W. Simka, G. Nawrat, M. Hanke, R.P. Socha, J. Michalska, Phosphate-permanganate conversion coatings on the AZ81 magnesium alloy: SEM, EIS and XPS studies, *Surf. Coat. Technol.* 206 (2011) 51–62.
- [49] Z.A. Hamid, M.T.A. El-khair, H.B. Hassan, Synthesis and protection of AM50 magnesium alloy and its composites using environmentally pretreatment electrolyte, *Surf. Coat. Technol.* 206 (2011) 1041–1050.
- [50] Y. Song, Z. Xu, K. Dong, D. Shan, E.H. Han, Investigation of microcracks on conversion film of AZ80 Mg alloy, *Surf. Eng.* (2018).
- [51] A. Maltseva, V. Shkirskiy, G. Lefèvre, P. Volovitch, Effect of pH on Mg(OH)<sub>2</sub> film evolution on corroding Mg by in situ kinetic Raman mapping (KRM), *Corros. Sci.* 153 (2019) 272–282.
- [52] A. Maltseva, S.V. Lamaka, K.A. Yasakau, D. Mei, D. Kurchavov, M.L. Zheludkevich, G. Lefèvre, P. Volovitch, In situ surface film evolution during Mg aqueous corrosion in presence of selected carboxylates, *Corros. Sci.* 171 (2020), 108484.
- [53] Y. Mori, A. Koshi, J. Liao, H. Asoh, S. Ono, Characteristics and corrosion resistance of plasma electrolytic oxidation coatings on AZ31B Mg alloy formed in phosphate – Silicate mixture electrolytes, *Corros. Sci.* 88 (2014) 254–262.
- [54] P.B. Srinivasan, J. Liang, R. Balajee, C. Blawert, M. Störmer, W. Dietzel, Effect of pulse frequency on the microstructure, phase composition and corrosion performance of a phosphate-based plasma electrolytic oxidation coated AM50 magnesium alloy, *Appl. Surf. Sci.* 256 (2010) 3928–3935.
- [55] X. Lu, S.P. Sah, N. Scharnagl, M. Störmer, M. Starykevich, M. Mohedano, C. Blawert, M.L. Zheludkevich, K.U. Kainer, Degradation behavior of PEO coating on AM50 magnesium alloy produced from electrolytes with clay particle addition, *Surf. Coat. Technol.* 269 (2015) 155–169.
- [56] S. Fatimah, M.P. Kamil, D.I. Han, W. Al-Zoubi, Y.G. Ko, Development of anti-corrosive coating on AZ31 Mg alloy subjected to plasma electrolytic oxidation at sub-zero temperature, *J. Magnes. Alloy.* (2021) doi.org/10.1016/j.jma.2021.1007.1013.

#### 5.4.1 Supplementary material

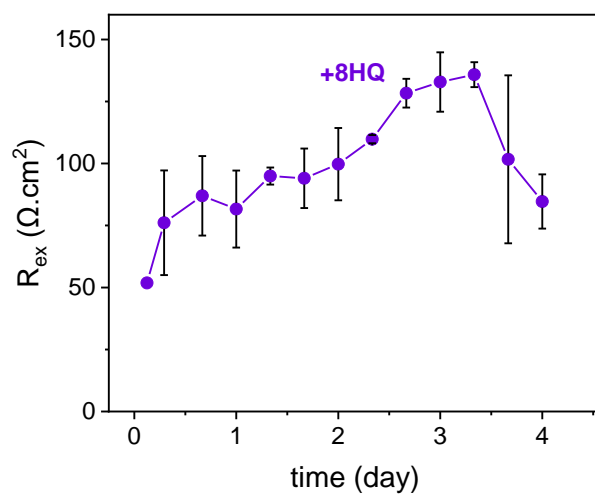


Figure S1 Evolution of parameters obtained from the fitting of EIS spectra of bare AZ21 exposed to the NaCl electrolyte with and without 8HQ. The error bars present the standard deviation of the three measurements from the mean value.

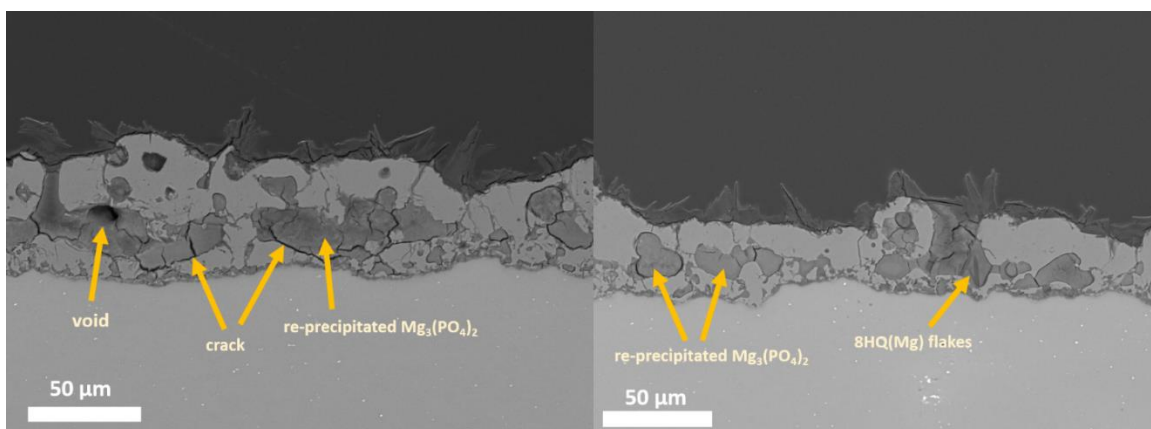


Figure S2 Cross-sectional SEM image in backscattered mode. PEO-coated AZ21 after 11 days immersed in NaCl electrolyte containing 8HQ.

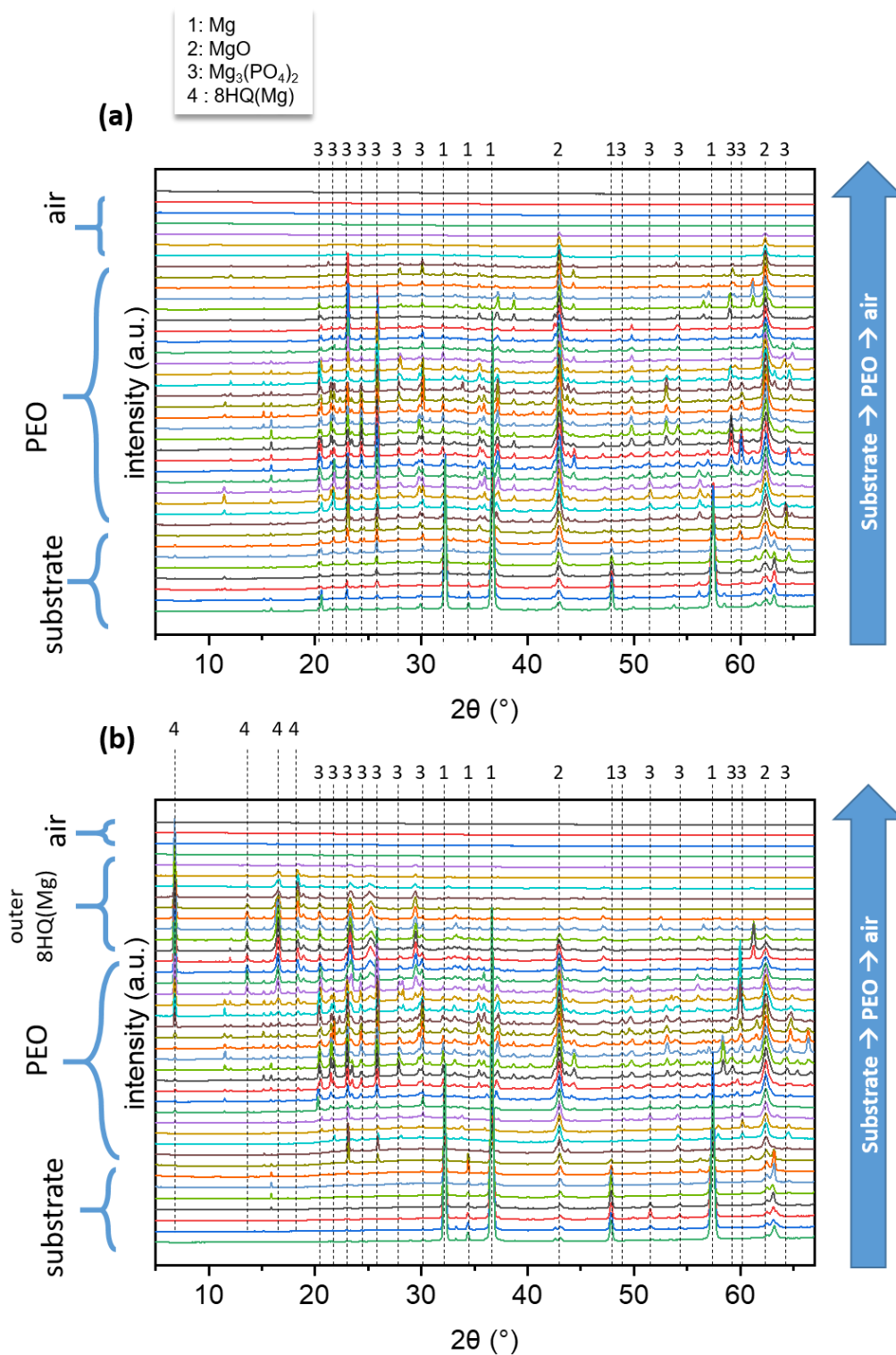


Figure S3 (a) XRD patterns obtained from scanning of one vertical line along the PEO thickness after (a) 1 day immersion in NaCl 3.5% (b) 3 days immersion in NaCl + 8HQ.

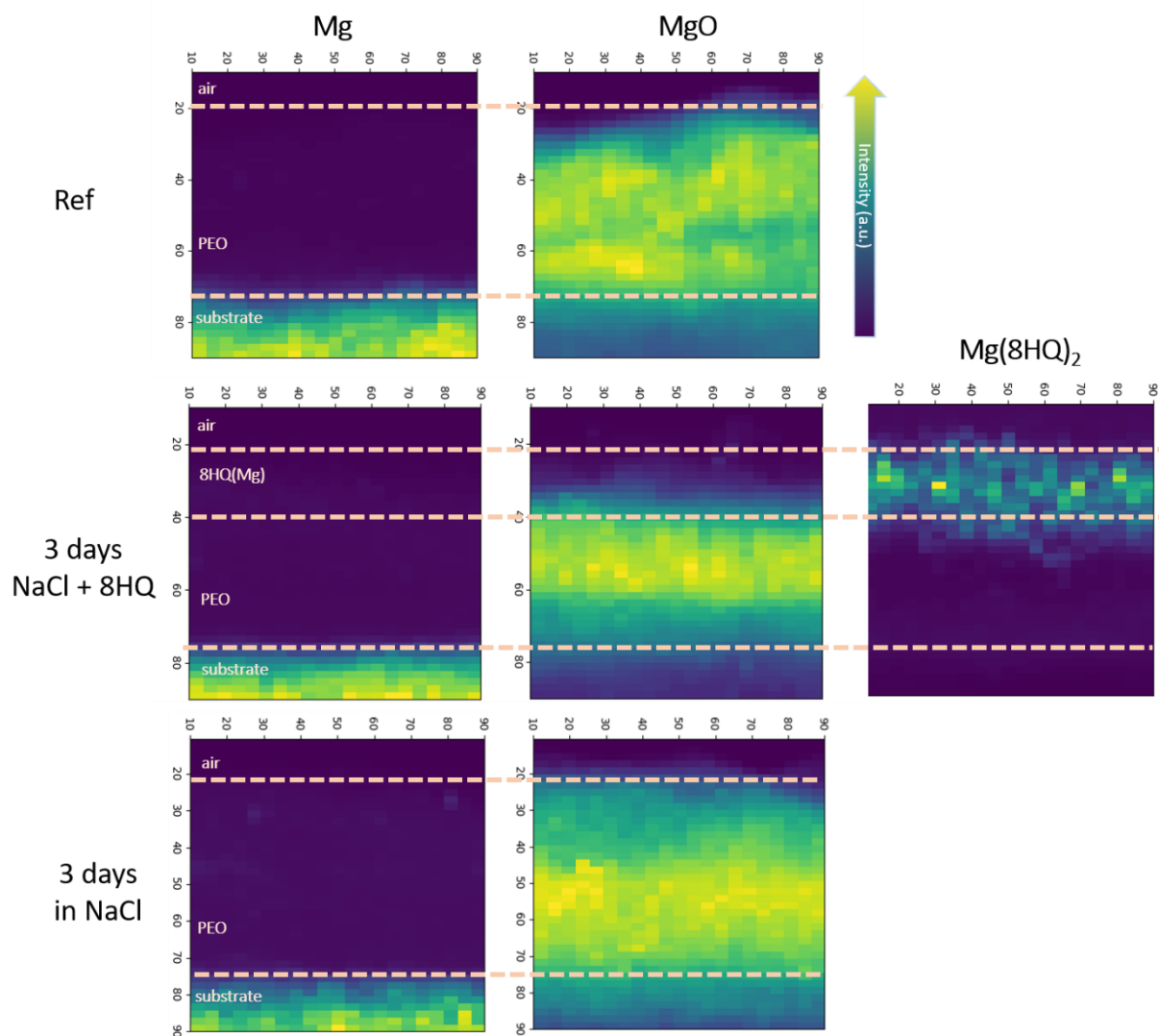


Figure S4 2D maps of the phases present in the cross-section of the PEO-coated AZ21 before and after immersion in the NaCl electrolyte with and without 8HQ.

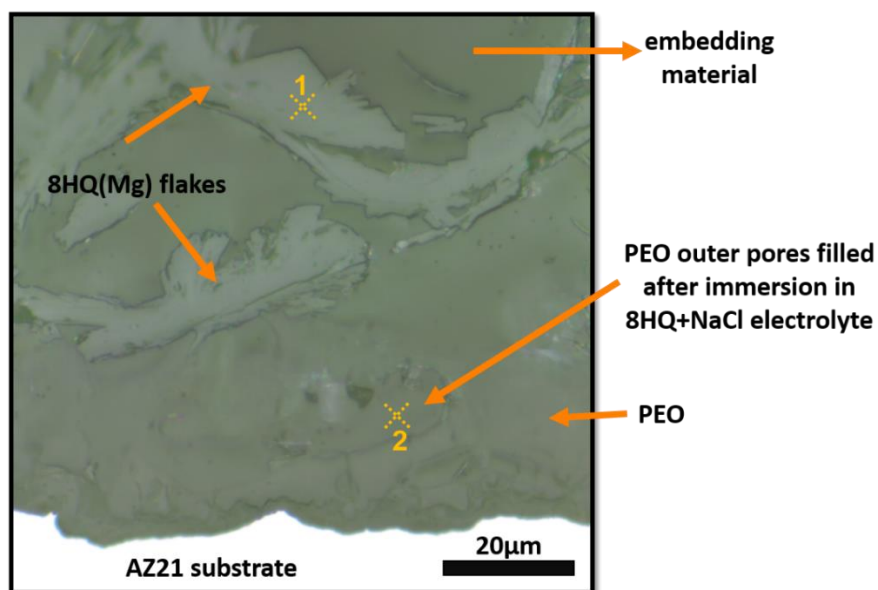


Figure S5 Optical microscopy image of the regions characterized by Raman spectroscopy. Region 1: the center of the spot chosen for characterizing the 8HQ(Mg) flakes on PEO layer. Region 2: the center of the spot chosen for characterizing the material inside the filled PEO outer pores after immersion in 8HQ+NaCl electrolyte.

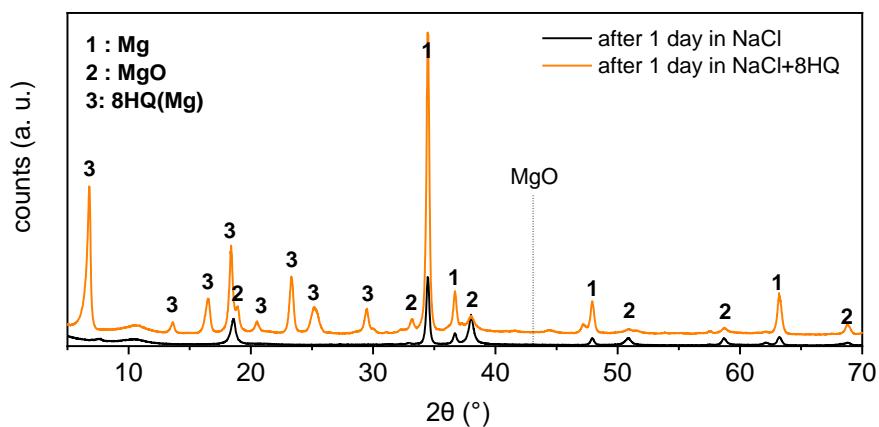


Figure S6 XRD spectra of bare AZ21 after 1 day of immersion in NaCl with and without 8HQ. The position of the strongest characteristic peak of MgO has been marked.

## 5.5 Corrosion inhibition of decylphosphonate on bare and PEO-coated Mg alloy

Sodium salt of decylphosphonic acid (DP) demonstrated superior performance compared to all other tested chemicals during the screening stage (**Figure 5.3**). The inclusion of DP in the NaCl electrolyte extended the lifespan of the PEO coating to over 50 days without a considerable decrease in impedance values at low frequencies. The underlying mechanism of DP's remarkable corrosion inhibition has been explored in detail in a published paper incorporated in the following chapter of this thesis, focusing on its interactions with both the bare AZ21 substrate and the PEO layer.

Considering the promising corrosion inhibition effects of DP, an effective approach to incorporate it into the PEO layer for achieving active corrosion inhibition properties has been proposed and evaluated.

**B. Vaghefinazari**, S.V. Lamaka, E. Gazenbiller, K. Yasakau, C. Blawert, M. Serdechnova, N. Scharnagl, D.C.F. Wieland, M.L. Zheludkevich, Corrosion inhibition of decylphosphonate on bare and PEO-coated Mg alloy, *Corrosion Science*, 226 (2024) 111651. <https://doi.org/10.1016/j.corsci.2023.111651>.

### CRedit authorship contribution statement:

**Bahram Vaghefinazari**: Conceptualization, Investigation, Validation, Writing – original draft, Writing – review & editing. **Sviatlana V. Lamaka**: Conceptualization, Supervision, Writing – review & editing. **Eugen Gazenbiller**: Investigation, Writing – review & editing. **Kiryl Yasakau**: Investigation, Writing – review & editing. **Carsten Blawert**: Conceptualization, Supervision, Writing – review & editing. **Maria Serdechnova**: Investigation, Writing – review & editing. **Nico Scharnagl**: Investigation, Writing – review & editing. **D.C.Florian Wieland**: Investigation, Writing – review & editing. **Mikhail L. Zheludkevich**: Conceptualization, Supervision, Writing – review & editing.



## Corrosion inhibition of decylphosphonate on bare and PEO-coated Mg alloy

Bahram Vaghefinazari<sup>a,\*</sup>, Sviatlana V. Lamaka<sup>a</sup>, Eugen Gazenbiller<sup>a</sup>, Kiryl Yasakau<sup>b</sup>, Carsten Blawert<sup>a</sup>, Maria Serdechnova<sup>a</sup>, Nico Scharnagl<sup>a</sup>, D.C. Florian Wieland<sup>c</sup>, Mikhail L. Zheludkevich<sup>a,d</sup>

<sup>a</sup> Institute of Surface Science, Helmholtz-Zentrum Hereon, 21502 Geesthacht, Germany

<sup>b</sup> CICECO-Aveiro Institute of Materials, Department of Materials and Ceramic Engineering, University of Aveiro, Campus Universitário de Santiago, Aveiro, Portugal

<sup>c</sup> Institute of Metallic Biomaterials, Helmholtz-Zentrum Hereon, 21502 Geesthacht, Germany

<sup>d</sup> Institute for Material Science, Faculty of Engineering, Kiel University, 24143 Kiel, Germany

## ARTICLE INFO

## Keywords:

Corrosion inhibitor

Surfactant

PEO

Alkylphosphonic acid

Magnesium

## ABSTRACT

PEO coatings, aside from their reasonable corrosion protection, also feature a porous microstructure that can serve as a repository for corrosion inhibitors. This study presents and investigates the high corrosion inhibition effect of sodium salt of decylphosphonate (DP) when incorporated into PEO coating on a magnesium substrate. The interaction of DP with both bare and PEO-coated magnesium substrates was studied to understand its corrosion inhibition mechanism. Additionally, a strategy to enhance the active anti-corrosion ability of the DP-containing system was suggested and examined. The findings provide new insights into the potential of surfactants as corrosion inhibitors for magnesium alloys.

## 1. Introduction

Plasma electrolytic oxidation (PEO), also known as micro-arc oxidation (MAO), is a surface treatment process that has been widely applied on Mg, Al, Ti, and their alloys to enhance their corrosion resistance and tribological properties [1–3]. The ceramic-like coating formed via PEO process typically consists of two layers: the inner barrier layer and the outer layer. The inner barrier layer prevents the access of corrosive species to the metallic substrate, while the outer layer has a porous microstructure that readily allows the penetration of corrosive media. Research on PEO coatings has focused on modifying their morphology to achieve more compact layers and to enhance overall corrosion protection [4–9]. On the other hand, the large pores in the outer layer can be exploited as a repository of different substances with various functionalities, including corrosion inhibitors [10].

The highly promising concept of using PEO pores as inhibitor repositories has already resulted in several reports with successful enhancements of the overall corrosion protection performance of the PEO coating on magnesium substrates [5,11–21]. Additionally, active corrosion inhibition is also highly sought through the incorporation of corrosion inhibitors into the PEO layer. This is particularly desirable when a barrier coating is disrupted, exposing the unprotected substrate to the corrosive medium. Thus, the release of corrosion inhibitors from

the coating onto the unprotected substrate inhibits severe corrosion. For instance, Wierzbicka et al. [5] impregnated a thin (~5 µm thickness) PEO coating on an AZ31 magnesium alloy with sodium salt of 4-methyl-salicylic acid via a simple immersion method. A commercial primer coating was then applied on the PEO layer to moderate leaching of the corrosion inhibitors. Compared to the sample without inhibitor, a remarkable reduction in corrosion propagation from an artificially-made defect on the coated sample was observed, indicating successful active corrosion protection. Further analysis of the samples via Scanning Vibrating Electrode Technique (SVET) on the inhibitor-loaded sample revealed a unique recurring activation/suppression of corrosion activity, corresponding to the initiation/suppression of filiform corrosion at different locations of the sample.

In another work, Gnedenkov et al. [19] loaded a PEO coating on a MA8 magnesium alloy with 8-hydroxyquinoline (8HQ) corrosion inhibitor via a simple immersion procedure in a saturated 8HQ solution. The impregnated PEO layer was then sealed with two different polymer coatings to augment the barrier properties of the coating as well as to prevent the rapid dissolution of the inhibitor from the substrate. The significant retardation of corrosion processes observed in the presence of 8HQ inhibitor was attributed to the formation of a thin adsorption film on the surface of the substrate. The local alkalization due to the

\* Corresponding author.

E-mail address: [bahram.vaghefinazari@hereon.de](mailto:bahram.vaghefinazari@hereon.de) (B. Vaghefinazari).

<https://doi.org/10.1016/j.corsci.2023.111651>

Received 31 July 2023; Received in revised form 26 October 2023; Accepted 4 November 2023

Available online 7 November 2023

0010-938X/© 2024 The Authors. Published by Elsevier Ltd. This is an open access article under the CC BY license (<http://creativecommons.org/licenses/by/4.0/>).

cathodic activity during the corrosion of Mg substrate was believed to facilitate the dissolution of impregnated 8HQ, which leads to the formation of an insoluble complex between magnesium and 8HQ on the defected site, which is rich in  $\text{Mg}^{2+}$  ions. As a result, active corrosion protection was achieved.

Typically, the selection of an inhibitor to be incorporated into a PEO coating is based on previously observed corrosion inhibition of a substance on a bare substrate. Consequently, the corrosion inhibition is typically explained based on the inhibition mechanism of the incorporated inhibitor on the bare substrate. Further, the relatively high chemical stability of ceramic-like PEO layers may give the false impression that corrosion inhibitors are harmless to the PEO layer. Therefore, in the research route for taking advantage of the incorporation of inhibitors in the PEO coating, the interaction between the inhibitor and PEO layer itself is often overlooked. However, in our recent studies [20,22], we have demonstrated that such interaction is a highly influential factor for the corrosion protection performance of the PEO layer itself. For instance, 2,5-pyridinedicarboxylate (2,5-PDC), which has been reported as an effective corrosion inhibitor for several different Mg alloys [17,22–25], actually accelerates the corrosion of PEO-coated Mg. The study of the corrosion inhibition mechanism of 2,5-PDC on bare Mg substrate, as well as its interaction with the PEO layer, uncovered the mechanism of this adverse effect. The parallel study of the interaction of corrosion inhibitors with bare and PEO-coated Mg substrate is also beneficial in understanding the inhibition mechanism of corrosion inhibitors incorporated into PEO layers [10].

Despite the auspicious approach of enhancing the corrosion resistance and equipping a coating with active corrosion protection capability, the incorporation of inhibitors into PEO coatings has been investigated only for a limited number of organic and inorganic substances [10]. Surfactants have been frequently investigated as corrosion inhibitors for Mg alloys since they are economical and environmentally friendly [23,26–28]. Their promising corrosion inhibition has been reflected as actively ongoing research on understanding their inhibition mechanism on bare Mg [28–35]. Moreover, their presence in commercial corrosion-inhibiting compounds highlights their cost-effectiveness and environmental friendliness [36,37]. Nevertheless, there is very limited scientific report on the application of surfactants on PEO coatings on Mg [38]. The majority of the available studies have used surfactants with the aim of achieving hydrophobic PEO surface, which improves the overall corrosion resistance of the system. Despite their potential as corrosion inhibitors, surfactants have been barely investigated as substances incorporated into PEO layers.

Alkylphosphonic acids are a group of surfactants that have been widely researched for their corrosion inhibition effects on various metallic substrates, including Al [39–41], Cu [42–44], and steel [45,46]. In this work, we illustrate the significant corrosion inhibition effect of sodium salt of decylphosphonate (DP), as a surfactant substance, on both bare and PEO-coated AZ21 Mg alloy, which, to the best of our knowledge, have not been reported before. Several electrochemical and surface characterizations have been carried out to gain a comprehensive and in-depth understanding of the observed inhibition effects. By investigating the inhibition mechanism of DP on bare AZ21 Mg as well as its interaction with the PEO layer, the study sheds light on the mechanisms of overall and active corrosion protection. In the end, a strategy to augment the active corrosion capability of incorporated DP has been proposed and evaluated.

## 2. Experimental procedure

### 2.1. Material

AZ21 Mg sheets with a thickness of 2 mm were used as the substrate. The chemical composition of the AZ21 sheet, obtained via spark discharge-optical emission spectroscopy (SD-OES), Ametek-Spectro, is presented in Table 1.

The surface of the specimens was ground under a stream of water, using SiC emery paper with progressively increasing grit sizes of 800, 1200, and 2500. The last grinding step was repeated under a stream of ethanol. Then, the samples were flushed with ethanol and dried with pressurized air.

Potassium hydroxide (KOH) pellets (99.99% purity) and sodium phosphate anhydrous ( $\text{Na}_3\text{PO}_4$ ) powder (technical purity, >95 wt%) were supplied from Sigma-Aldrich and Alfa Aesar, respectively. Decylphosphonic acid (DPA) (97% purity) was supplied from Sigma-Aldrich.

A saturated solution of sodium salt of DPA (which will be denoted as DP hereafter), was prepared by addition of excessive DPA powder to a NaCl 3.5 wt% solution, as the reference corrosion test solution. The solution pH was adjusted to  $7.0 \pm 0.1$  using NaOH. The pH of the solutions was controlled by Metrohm 713 pH meter equipped with InLab® Expert Pt1000 pH electrode from Mettler Toledo. The remaining undissolved DPA was filtered out using filter paper (LLG-filter medium/fast). The saturation concentration of DP at the prepared pH was  $\sim 2$  mM.

A micellar solution of DP in deionized water (DI-W) with a total DP concentration of 0.1 M was prepared at an elevated temperature of 60 °C. Krafft temperature ( $T_K$ ) of DP was visually determined in the range of 35–40 °C. The micellar solution of DP was used to incorporate a relatively high concentration of DP into the PEO pores.

### 2.2. Preparation of PEO coating

The PEO process on AZ21 substrate was carried out using a DC power source (Electro Automatik, Germany) and a self-made pulsing unit. A constant current density of  $40 \text{ mA}\cdot\text{cm}^{-2}$  with a duty cycle of 1 ms:9 ms was applied to AZ21 specimens with dimensions of  $20 \times 20 \times 2 \text{ mm}^3$  for 10 min. The specimens were immersed in an electrolyte containing 20 g  $\cdot \text{L}^{-1}$   $\text{Na}_3\text{PO}_4$  and 2 g  $\cdot \text{L}^{-1}$  KOH. A stainless steel hollow tube was used as the cathode for the PEO process. The electrolyte temperature was kept at  $20 \pm 0.1$  °C by running temperature-regulated water through the stainless steel tube. The PEO electrolyte was mixed during the PEO process via purging bubble air in the electrolyte. After the PEO process, the specimens were first rinsed with a flush of DI-W and then immersed in DI-W for 20 min at a low-pressure condition ( $\sim 0.1$  atm pressure). With this, the air entrapped inside the PEO pores escapes, and instead, the DI-W electrolyte can penetrate into the pores, diluting the remained electrolyte from the PEO process. Then, the specimens were immersed in acetone (EMSURE® supplied by Sigma-Aldrich) for 20 min and finally dried in an oven at 80 °C for 30 min.

Incorporation of DP into the PEO coating was carried out via immersion in the micellar solution of DP 0.1 M for 2 h at 60 °C. The 2-hour incorporation process included an initial immersion of 20 min at a low pressure of  $\sim 0.9$  atm to release the entrapped air inside the pores, followed by immersion under atmospheric pressure.

**Table 1**  
Elemental composition of AZ21 Mg substrate.

element	Al	Zn	Mn	Fe	Cu	Ni	Si	Mg
Concentration (unit)	$1.59 \pm 0.07$ (wt%)	$1.05 \pm 0.07$ (wt%)	0.29 (wt%)	$28 \pm 1$ (ppm)	$22 \pm 3$ (ppm)	$23 \pm 1$ (ppm)	650 (ppm)	balanced

### 2.3. Electrochemical measurements

All the electrochemical characterizations were performed using Gamry reference 600 potentiostat. Platinum coil and Ag/AgCl electrode in saturated KCl were used as counter and reference electrodes, respectively. A surface area of  $0.5 \text{ cm}^2$  from the working electrode was exposed to 400 ml of the testing solutions. The reference corrosion test electrolyte was NaCl 3.5 wt%. The tests were carried out at  $22 \pm 2^\circ\text{C}$ .

Electrochemical impedance spectroscopy (EIS) tests were carried out under potentiostatic mode at open circuit potential (OCP) with a perturbation voltage of  $10 \text{ mV}_{\text{rms}}$ . The scanned frequency ranged from 100 kHz to 0.01 Hz with 9 points per frequency decade acquisition. For bare magnesium substrates, the low frequency range was limited to 0.5 Hz. The stationary condition, as the requirement for the EIS tests was assured by carefully observing the Lissajous curves during the test, especially at the low frequency range. Drift of Lissajous curve indicates deviation from the OCP condition, which means the non-stationarity of the system. In such cases, the EIS test was aborted and only the acquired data points in the spectra were reported. In the case of testing bare AZ substrate, the solution was continuously stirred during the EIS test.

### 2.4. Weight loss measurement

Weight loss measurements on bare AZ21 Mg specimens were carried out to evaluate their corrosion rates. A solution of  $200 \text{ g.L}^{-1} \text{ CrO}_3$  in deionized water was used to remove the corrosion products.

### 2.5. Microscopy

The surface and cross-sectional morphology of the specimens were characterized using a scanning electron microscope (SEM, TESCAN Vega3 SB), equipped with an energy dispersive spectrometer system (EDS, eumeX IXR systems). The acceleration voltage was 15 kV. For selected cases, higher magnification microscope, a TESCAN LYRA3 equipped with a focused ion beam (FIB) system was used.

For the preparation of the specimens' cross-section, the samples were embedded in epoxy resin (EpoxiCure 2, Beuhler). The surface of the specimens was ground with SiC emery papers up to 4000 grit size. The subsequent polishing of the surface was carried out using a water-free silicon oxide polishing suspension (OPS<sup>TM</sup>, Cloeren Technology GmbH). The surface of the samples was gold sputtered prior to SEM observation using a Cressington Sputter Coater 108auto. For higher magnification of cross-sectional images, the FIB system on TESCAN LYRA3 was used.

### 2.6. Crystallographic characterization

Crystallographic characterization was carried out using an X-ray diffractometer (Bruker D8 Advance) with Cu K $\alpha$  radiation source generated with a voltage and current of 40 kV and 40 mA, respectively. The incident angle was  $3^\circ$ . The dwell time was 1 s and 5 s for bare and PEO-coated magnesium specimens, respectively. The higher dwell time for PEO-coated specimens was chosen to reduce the strong noise in the acquired spectra. The diffraction angle ( $2\theta$ ) ranged between  $5^\circ$  and  $70^\circ$  with  $0.02^\circ$  step size.

High-resolution two dimensional XRD maps were acquired at the nanofocused end-station of beamline P03 at PETRAIII storage ring, Deutsches Elektronen-Synchrotron (DESY, Hamburg, Germany) [47]. The beam cross-section was  $1.5 \mu\text{m} \times 1.5 \mu\text{m}$ . The beam energy was 19.8 keV employing an Eiger9m detector. Calibration of the detector with respect to beam center and sample to detector distance was done lanthanum hexaboride. The acquisition time of each diffraction pattern was set to 0.5 s. Regions of  $80 \mu\text{m} \times 80 \mu\text{m}$  were scanned with the step sizes of  $2 \mu\text{m}$  for both vertical and horizontal directions, respectively. Data reduction was performed using the software package pyFAI [48]. The analysis of the two dimensional diffraction maps was conducted by

inhouse developed Matlab scripts. The horizontal direction is parallel to the substrate surface. The details of the experimental set-up can be found in [49]. The  $2\theta$  values from the synchrotron beam wavelength were converted to Cu K $\alpha$  for easier comparison to the results obtained from lab XRD measurements.

### 2.7. Atomic Force Microscopy (AFM)

Atomic force microscopy (AFM, Nanowizard 4, JPK Instruments AG) in AC mode coupled with scanning Kelvin probe force microscopy (SKPFM) was conducted to analyze the surface morphology and measure the Volta potential difference (VPD) of the bare AZ21 Mg substrate. VPD measurements were carried out in HoverMode. In a first pass (trace) over the sample the topography is measured, and on the return pass (retrace) this topography information is used to maintain the cantilever at a constant offset height above the surface while running the Kelvin probe measurements procedure. The following parameters for the measurements were used: height offset 100 nm, modulation amplitude 1 V, scan size  $40 \mu\text{m} \times 40 \mu\text{m}$ , number of lines 512 and scan rate 0.3 Hz. Pt covered probes purchased from BudgetSensors (Multi75E-G; resonance frequency 75 kHz, force constant 3 N/m) were used. Prior to the measurements the VPD of the probes was recorded on a clean Ni surface and the results reported in this work display VPD (V) values measured on Mg samples vs. Ni. The output values were negative to be able to compare VPD with the electrochemical potentials of metals [50–52], where more negative values represent more active metals, while more positive represent more noble metals and/or presence of surface films [53].

The AFM measurement was carried out in open air condition and at room temperature about  $22^\circ\text{C}$  and relative humidity of about 50%. The surface of the specimens was polished using a water-free silicon oxide polishing suspension (OPS<sup>TM</sup>, Cloeren Technology GmbH). Then, the samples were flushed with ethanol and subsequently polished on a clean polishing cloth soaked in ethanol absolute (>99.9%, Chemsolute). Then, the surface of the samples was dried with pressurized  $\text{N}_2$ .

Drop tests were carried out on the polished sample before the AFM measurement as follows: 50  $\mu\text{l}$  of different electrolytes were dispensed on the surface of the polished sample, dwelling for 60 s. Then, the drops were removed from the surface using pressurized  $\text{N}_2$ . All the drops from different electrolytes left similar circular marks with diameter between 7 and 8.5 mm.

### 2.8. Salt spray test

Specimens with dimensions of  $40 \text{ mm} \times 20 \text{ mm} \times 2 \text{ mm}$  were prepared for salt spray test. To prevent corrosion on the edges and corners, they were insulated with a mixture of beeswax and gum rosin at a weight ratio of 9:7, both were supplied by Sigma-Aldrich. The salt spray test was carried out in accordance with the ASTM B117 standard in NaCl 5 wt% fog and at  $35^\circ\text{C}$  for 30 days. The scratch on the defected samples was made using a tool made of tungsten carbide with  $90^\circ$  tip included angle. The scratch was  $150 \mu\text{m}$  deep which corresponds to  $\sim 215 \mu\text{m}$  width on the surface. The samples' surface appearance was periodically documented during the salt spray test. The process of taking pictures of the samples were shortened as much as possible to avoid drying of the samples, and only the remaining NaCl droplets were gently removed from the surface. However, the thoroughly dried samples after 30 days of SST are also provided for the better visual perception of the extent of corrosion products.

### 2.9. Contact angle measurement

Static contact angle measurements were carried out using contact angle meter (Krüss Drop Shape Analyzer DSA100, Germany), with the sessile droplet method. Air was used as a medium for the measurement, with milli-Q  $\text{H}_2\text{O}$  and the droplet volume was 2  $\mu\text{l}$ . Contact angle

measurements were performed randomly on the whole sample surface after 5 s and reported as the average of six.

### 3. Result

#### 3.1. Effect of DP on bare AZ21

The electrochemical properties of the bare AZ21 surface were investigated during exposure to the NaCl test solution with and without DP using EIS measurements. The Bode plots acquired during 4 days of immersion are selectively presented in Fig. 1.

In the case of blank NaCl electrolyte, the phase angle spectra are dominated by one time constant in the middle-frequency range (between  $10^4 - 10^1$  Hz) that is attributed to the oxide film on the magnesium surface [54]. A secondary time constant usually appears at the low-frequency range, which is attributed to the capacitive characteristics of the double layer coupled with the charge transfer phenomena on the magnesium surface [54,55]. However, the low-frequency time constant is difficult to discern from the corresponding Bode plots of the blank NaCl solution, probably due to its relatively low value.

As it was mentioned in the experimental procedure in Section 3.3, the low frequency range for the EIS measurements of bare Mg substrate was limited to 0.5 Hz. This is because of known non-stationarity of Mg substrate during the exposure to NaCl solution and during the EIS test [56], which leads to not only the misinterpretation of the EIS spectra but also to undesirable polarization of the Mg surface. The response to this non-stationarity potentially is reflected as inductive behavior at low frequency range. Such deviation from the stationarity can also be observed from the corresponding Lissajous curves during the EIS measurement [56]. Therefore, by the real-time observation of the phase angle and Lissajous curve, the EIS test was aborted in case of entering to the non-stationarity condition. This is reflected in the missing data

points for 5 and 30 min of exposure. Albeit such precaution, as can be seen in the EIS spectra of AZ21 after 5 and 30 min of exposure, the phase angle is shifting to positive values, indicating the inductive behavior.

When DP is present in the electrolyte, a similar dominant middle-frequency range time constant, which is attributed to the oxide layer on the magnesium surface, appears in the Bode plots. The second time constant at low-frequency range is better identifiable as compared to the reference electrolyte. In addition, a gradual increase of the magnitude of impedance ( $Z_{mod}$ ) at high-frequency range ( $>10^4$  Hz), which is accompanied with the gradual shift of the corresponding phase angle to more negative values, suggests a formation of an extra layer on the magnesium surface. Similar phenomena was described earlier for  $Ca^{2+}$ ,  $HPO_4^{2-}$ ,  $HCO_3^-$  containing electrolytes where an additional layer of hydroxyapatite-like compound was gradually precipitating on top of Mg/MgO/Mg(OH)<sub>2</sub> layer [57]. What also can be concluded from the Bode plot ( $|Z|$ ) is that the resistance of the magnesium oxide, which is reflected in the middle frequency range is increasing along with the precipitation of the extra layer.

The absolute value of impedance at low frequency is typically used for rough comparison of the corrosion performance. To avoid the erroneous values at lower frequencies due to the non-stationary conditions attributed to the magnesium surface during EIS [58,59], the absolute value at frequency as low as 1 Hz (hereafter represented as  $|Z|_{1\text{ Hz}}$ ) has been taken to assess the corrosion rate of bare AZ21 qualitatively. As can be seen in Fig. 2a,  $|Z|_{1\text{ Hz}}$  gradually increases over the whole 4 days of exposure when AZ21 is exposed to the blank NaCl solution. Addition of DP in the electrolyte results in a slightly higher initial value of  $|Z|_{1\text{ Hz}}$  within the first 1 h. Further exposure to the electrolyte leads to a rapid enhancement of the  $|Z|_{1\text{ Hz}}$  within the first 3 h, followed by a slow decrease for the rest of the exposure period, indicating a gradual loss of corrosion resistance. However, even after 4 days of exposure,  $|Z|_{1\text{ Hz}}$  is still considerably higher as compared to the reference NaCl electrolyte.

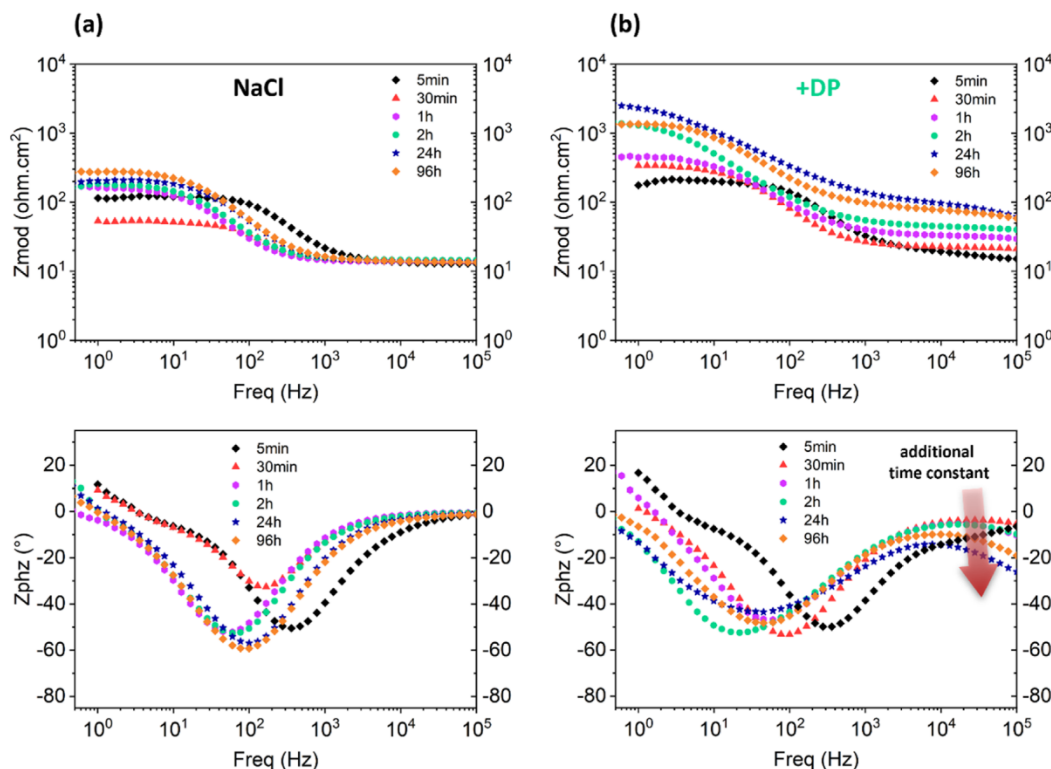
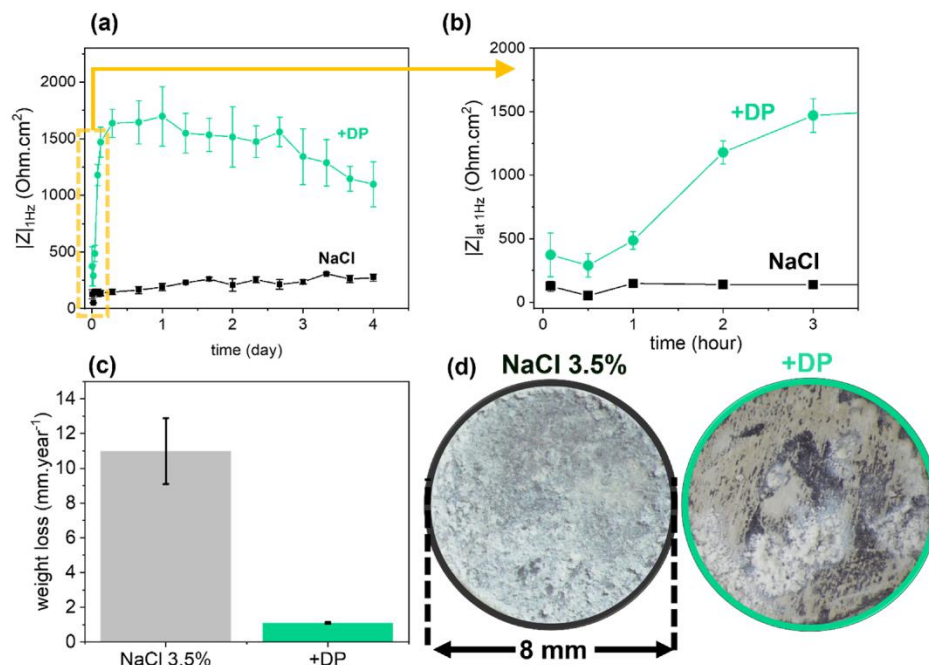


Fig. 1. Bode plots of EIS spectra obtained from the AZ21 samples exposed to NaCl 3.5 wt% electrolyte for 4 days (a) with and (b) without DP.



**Fig. 2.** (a), (b):  $|Z|$  value at 1 Hz obtained from the corresponding Bode plots in Fig. 1. (c): weight loss of AZ21 after 4 days of immersion in the NaCl solution with and without DP. (d): The visual appearance of the AZ21 surface after 4 days of immersion. The error bars present the standard deviation of three measurements away from the mean value.

The significant inhibition effect of DP is also evident from the weight loss measurement after 4 days, which reveals a 10-fold reduction (inhibition efficiency of 90% based on the calculation method in [23]) in the overall corrosion rate of AZ21 specimens (Fig. 2c). As can be seen from the appearance of the AZ21 samples after 4 days of exposure (Fig. 2d), the entire surface was covered with corrosion products in the case of blank NaCl electrolyte. However, when DP was added to the

electrolyte, only a portion of the sample's surface was covered with bulky corrosion products. The final pH of the solution was  $9.8 \pm 0.1$  and  $7.4 \pm 0.1$  for the solution without and with DP, respectively.

Fig. 3 illustrates SEM images of the surface of AZ21 substrate after exposure to the NaCl with and without DP. After just 5 min of exposure to the blank NaCl solution, signs of filiform corrosion appear on the surface with corrosion products on top, which are mainly  $\text{Mg}(\text{OH})_2$ .

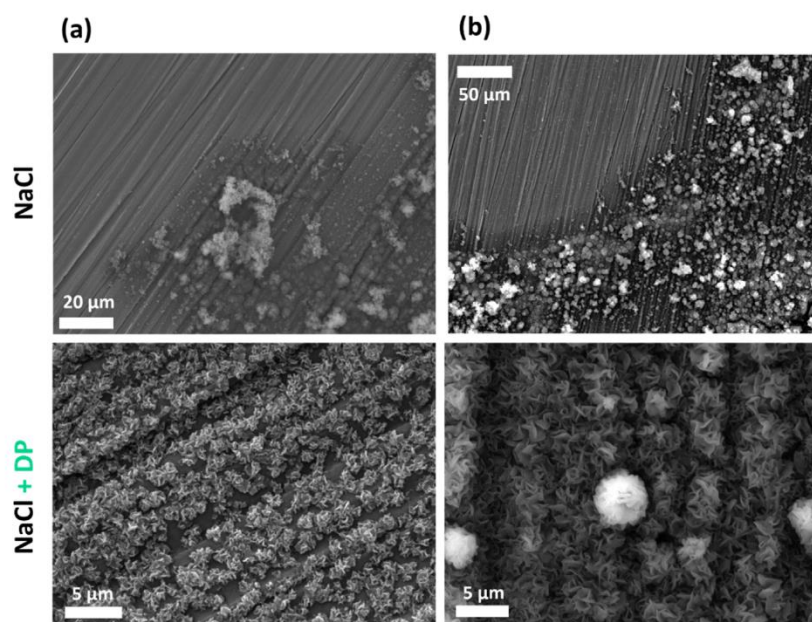


**Fig. 3.** surface morphology of bare AZ21 exposed to the NaCl with and without DP after (a) 5 min and (b) 1 h. (SEM images are taken in secondary electron mode).

Extending the exposure duration to one hour results in growth of the area covered with filiform corrosion and accumulation of  $\text{Mg}(\text{OH})_2$ .

When the NaCl solution contained DP, some precipitates formed and partially covered the Mg surface after just 5 min of immersion. The precipitates are homogeneously dispersed over the sample and no preferential nucleation/growth of these precipitates, for instance on the intermetallic second phases of AZ21, is observed. For the information on the intermetallic second phases see the supplementary materials in Fig. S1.

Prolonged exposure to the NaCl + DP solution for one hour results in the full surface coverage as illustrated in Fig. 3b. The deposits feature distorted flakes randomly grew on the surface, forming voids within each other. In some locations, brighter round-shaped precipitates with more dense flakes can be observed (e.g., in the center of the Fig. 3b). These are actually the precipitates with more vertical growth as can be seen in tilted images in supplementary material Fig. S3 as well as in a cross-sectional view in Fig. 4.

Fig. 4a illustrates the cross-sectional view of the AZ21 bare magnesium substrate after 1 h of exposure to the NaCl + DP solution. The EDS elemental maps of the cross-section are shown in Fig. 4b.

The precipitates cover the whole magnesium surface with a minimum thickness of about 3  $\mu\text{m}$ , although voids are often observed within the layer. The precipitates are rich in carbon, phosphorus, and magnesium, suggesting the formation of a compound consisting of DP and Mg. Moreover, the cross-sectional view reveals some regions, marked with red arrows, rich in oxygen but no evidence of phosphorus and carbon. These regions are mostly located below the straight dashed line in Fig. 4, representing the imaginary interface between the Mg substrate and the precipitates. These regions are expected to be made of  $\text{Mg}(\text{OH})_2$  as the primary corrosion product of Mg alloys.

Fig. 5 illustrates the XRD spectra obtained from the bare AZ21 surface after exposure to the NaCl electrolyte for 4 days, with and without DP. In a simple experiment of mixing DP-containing solution and  $\text{MgCl}_2$  we learned that DP forms an insoluble complex with Mg, which hereafter will be denoted as DP(Mg). The XRD pattern of the DP(Mg) powder is also included in Fig. 5 for the sake of comparison. The preparation procedure for the DP(Mg) powder is provided in supplementary material Section 4.

The XRD spectra of the reference sample exposed to the blank NaCl indicates that the corrosion products are mainly composed of  $\text{Mg}(\text{OH})_2$  phase. When DP is present in the electrolyte, additional diffraction peaks appear at  $2\theta$  of  $6.5^\circ$  and  $9.7^\circ$ , which are attributed to the DP(Mg) phase, as confirmed by the XRD spectra of its separately synthesized powder. The presence of diffraction peaks  $\text{Mg}(\text{OH})_2$  also reveals the co-existence of its phase with DP(Mg) phase. However, the significantly weaker intensity of  $\text{Mg}(\text{OH})_2$  suggests its minor existence in the formed corrosion products, which is consistent with the SEM images in Fig. 4.

AFM/SKPFM measurement provides insight into the changes occurring on the Mg surface after exposure to the electrolyte, from both

surface morphology and Volta potential perspective [60]. Fig. 6a presents the topography and Volta Potential Difference maps of the polished AZ21 surface after exposure to a drop of NaCl 3.5 wt% with and without DP for 60 s. Furthermore, an additional measurement with the same conditions was conducted for a drop of DI-W for comparison.

The topography of the specimen exposed to the DI-W drop reveals intermetallic phase (IMP) particles protruding from the surface marked by white arrows. The IMPs in the AZ21 alloy are mostly Al-Mn-based, as their characterizations are provided in the supplementary material Fig. S1. The brighter appearance of this intermetallic in the Volta potential map corresponds to its higher nobility as compared to the Mg matrix, indicating a maximum of  $\sim 130$  mV difference. Note that not all the bright points in the corresponding topography of the DI-W sample are associated to the IMPs. Some of these bright points do not show any difference in the VPD value as compared to that of the magnesium matrix. They are likely to be minuscule debris landed on the surface during the sample handling.

Similar to the specimen exposed to DI-W, the surface topography of specimen exposed to the NaCl solution shows several IMPs protruding from the magnesium surface. Comparing the VPD maps of the NaCl and DI-W samples, a relatively broader cathodic region on the IMPs can be observed for the latter. One speculation for this observation is that cathodic hydrogen evolution reaction (HER) and oxygen reduction reaction (ORR) mostly occur on the IMPs, resulting in galvanic corrosion with the Mg matrix [61]. In the case of DI-W, the mentioned cathodic reactions can also occur but considerably slower than in the NaCl solution due to the lack of corrosive  $\text{Cl}^-$  ions attacking the  $\text{MgO}$  protective layer. Due to the low conductivity of DI-W, slight galvanic corrosion is expected to happen confined to the periphery of IMPs, resulting in the cloud of cathodic potential around the IMPs. While in the NaCl solution, the presence of high concentration of  $\text{Cl}^-$  attacks the  $\text{MgO}$  all over the surface, which leads to the shift of VPD to more negative potential (more comprehensible comparison of VPDs in VPD histograms is provided below). Nevertheless, further investigation and local characterization of the IMPs and their surroundings are required to confirm this hypothesis.

In the case of exposure to the drop of NaCl + DP, micron-size deposits are rather homogeneously dispersed all over the surface, which are the initial precipitates of DP(Mg) (Fig. 6a). The corresponding VPD map depicts their higher Volta potential compared to that of matrix. The IMPs cannot be unambiguously pinpointed on the topography and VPD maps due to their considerably smaller size, which are likely concealed beneath the DP(Mg) deposits. As confirmation to the SEM figures in Fig. 3, it can be claimed that there is no preference in the location of initial DP(Mg) deposits, for example on IMPs.

The histograms of VPD values with respect to Ni reference sample are presented in Fig. 6b. The peaks of intensity in the histograms of samples exposed to DI-W and NaCl represent the VPD of the Mg matrix, and the more positive VPD of IMPs are barely visible in the histogram due to their negligible relative surface area. The overall VPD of the surface

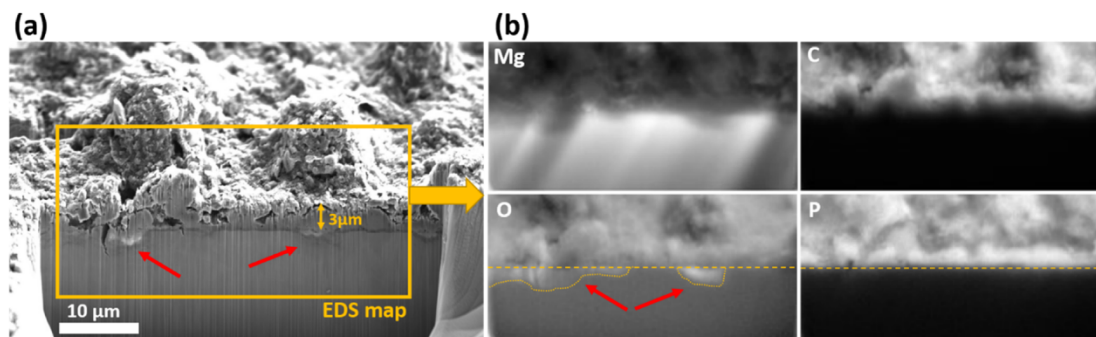


Fig. 4. (a) cross-sectional view of the bare AZ21 surface exposed to the NaCl + DP electrolyte after 1 h. (b) elemental mappings of the marked area in (a).

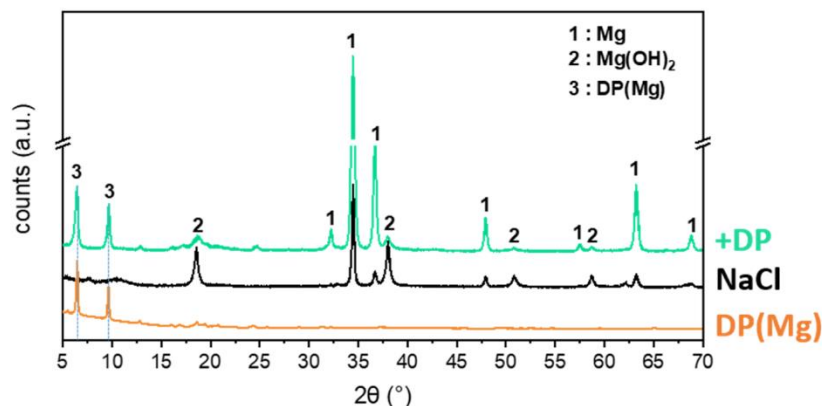


Fig. 5. XRD spectra of bare AZ21 magnesium exposed to NaCl 3.5 wt% solution with and without DP. The XRD pattern of the DP(Mg) powder is also presented for comparison.

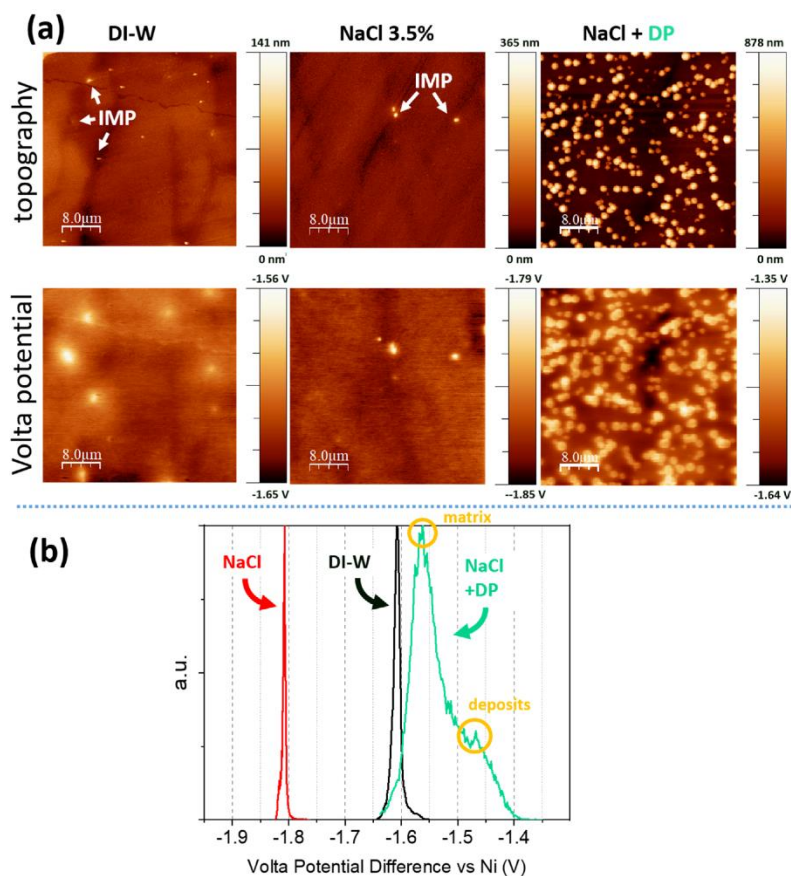


Fig. 6. (a) images of the topography (top) and VPD (bottom) maps of AZ21 surface exposed to a droplet of the NaCl solution with and without DP. (b) Histogram of VPD vs Ni from the maps in (a).

exposed to NaCl solution shows the most negative values with more than 200 mV potential difference to that of exposed to DI-W or NaCl+DP. The negative shift of Volta potential of Mg matrix after exposure to NaCl solution has been reported before, and has been attributed to the positively charged nature of Mg/MgO [53].

The corresponding VPD histogram of NaCl+DP reveals two peaks. The peak in higher VPD values is attributed to the DP(Mg) precipitates,

while the peak in lower VPD values belongs to the Mg matrix. The VPD of Mg matrix exposed to NaCl+DP has the most positive values as compared to the other samples, which means that the surface condition has been modified by the presence of DP in the solutions. Such surface modification can be due to the change in electronic properties of the MgO layer, the electric dipole of DP molecules on the surface, and their interaction with the substrate beneath [53]. The adsorption of

alkylphosphonic acids on different metal surfaces including Mg has been reported in several publications [62–65], with details on the bonding configuration between the phosphonic acid group and the metal surface. Several parameters related to the adsorbed molecules affecting VPD include the angle and magnitude of the DP dipole on the surface, whether or not they form a bilayer (as is commonly observed for surfactants [66]), the molecular structural relaxations, intermolecular charge rearrangement and depolarization [67–69]. Additionally, deposits themselves can provide an offset to VPD, if they consist of agglomerates or crystals with specific molecular orientations on the surface, resulting in effective dipole moments. Clearly, attributing VPD shifts to each of these factors requires a thorough examination of the parameters involved, which is beyond the scope of this work.

### 3.2. Effect of DP on PEO

The effect of DP on the PEO-coated AZ21 was investigated via direct exposure to the NaCl electrolyte with and without DP. The results of EIS measurement from the samples during the exposure are presented in Fig. 7. The Bode plots after 1 h of exposure to the NaCl electrolyte reveal two distinctive time constants at high and mid-frequency ranges. The high-frequency range ( $10^5$ – $10^2$  Hz) time constant is attributed to the capacitive properties of the PEO inner layer on the Mg surface. The middle-frequency range ( $<10^2$  Hz) time constant represents the MgO passive film on the Mg surface. For exposure times more than 1 h, the time constant corresponding to the MgO passive film becomes dominant in the frequency range between  $10^5$ – $10^{-1}$  Hz. The effect of charge transfer resistance coupled with the double layer capacitance is negligible at low frequency range below  $10^{-1}$  Hz for all recorded spectra. There is only a negligible change in the Bode spectra over the course of exposure till the third day, at which a considerable drop of impedance value at the low-frequency range was observed. For better visual

comprehension, the absolute values of the impedance at the low frequency of 0.01 Hz (denoted as  $|Z|_{0.01 \text{ Hz}}$ ), which are roughly indicating the corrosion resistance of the sample, are provided in Fig. 8a. The drop

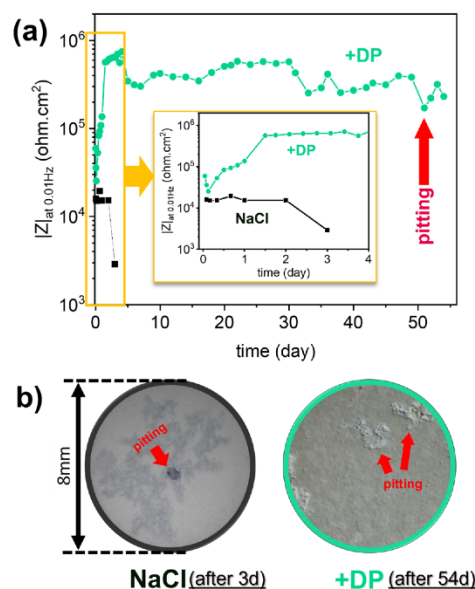


**Fig. 8.** (a) The corresponding  $|Z|_{0.01 \text{ Hz}}$  from Fig. 7. (b) The surface appearance of the PEO-coated AZ21 samples at the end of the exposure test (i.e., after 3 and 54 days for the sample exposed to the reference NaCl solution with and without DP, respectively).

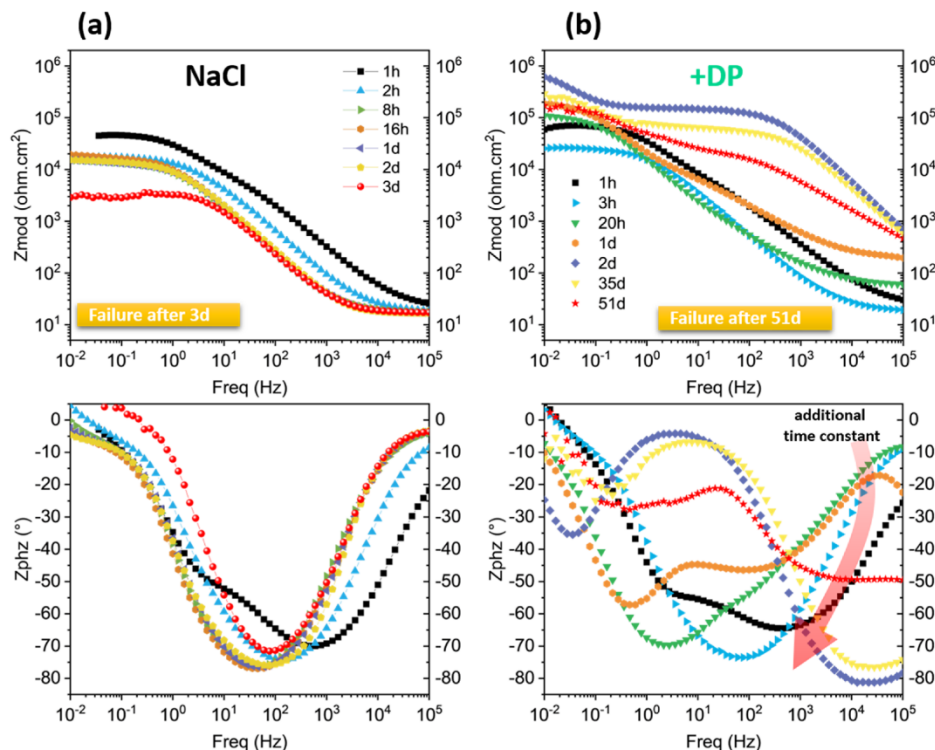


**Fig. 7.** Bode plots of the PEO-coated magnesium exposed to NaCl (a) without and (b) with DP. Failure is supported by visual observation of localized corrosion in Fig. 8.

in  $|Z|_{0.01 \text{ Hz}}$  after 3 days was accompanied by the occurrence of a pitting on the sample surface shown in Fig. 8b.

When DP is added to the electrolyte, the impedance spectra for the first 3 h of exposure are similar to those of samples exposed to the blank NaCl solution with two time constants. However, further exposure reveals the development of an additional time constant at high-frequency range of the Bode plot, which can be attributed to the formation of an extra protective layer on the surface. It is accompanied by an increased capacitance of the inner layer showing its dissolution as a result of a conversion process leading to formation of a new layer. Development of this high-frequency range time constant shifts the other time constants to lower frequencies, resulting in only two visible time constants over the tested frequency range. The shape of the Bode plots remains unchanged for the rest of the exposure, with slight fluctuations in the impedance values. At some points, instability of the Bode spectra, especially at low-frequency range, was observed (e.g., for “35 days” in Fig. 7b). After 51 days, the instability became more pronounced and the phase angle of the high-frequency time constant drifted further away from the  $-90^\circ$  for ideal capacitive behavior.  $|Z|_{0.01 \text{ Hz}}$  experiences an initial drop within the first 3 h, followed by an increase of one order of magnitude within the first 2 days (Fig. 8a). Then,  $|Z|_{0.01 \text{ Hz}}$  stays in a

limited range with slight variation for the rest of the exposure. Some pits were spotted after 51 days, accompanied by the generation of  $\text{H}_2$  bubbles from the pits' region, which indicates local degradation of the PEO coating and corrosion of the Mg substrate. This also coincides with a slight drop in impedance at 51 days, which is marked in Fig. 8a. However, further exposure to the electrolyte led to recovery of  $|Z|_{0.01 \text{ Hz}}$  to higher values as well as the formation of some precipitates on the severely corroded areas, as can be seen in the appearance of the pitted area the sample after 54 days (Fig. 8b).

Fig. 9 illustrates the surface of PEO coating before and after exposure to the NaCl solution with and without DP. The corresponding XRD analyses of the PEO layers are also presented in Fig. 9d. The pristine PEO layer has a smooth surface with pores and cracks present all over the sample. After exposure to the NaCl solution, the PEO layer surface becomes rough in some areas, suggesting degradation caused by the attack of NaCl electrolyte. The SEM image in Fig. 9b was taken after 1 day of exposure to the NaCl solution for the sake of visibility of the degradation. Nevertheless, it is plausible to infer that the degradation process starts from the beginning of the exposure. When DP is in the electrolyte, some precipitates, morphologically very similar to what is observed on the bare AZ21 Mg exposed to the DP-containing electrolyte (Fig. 3),

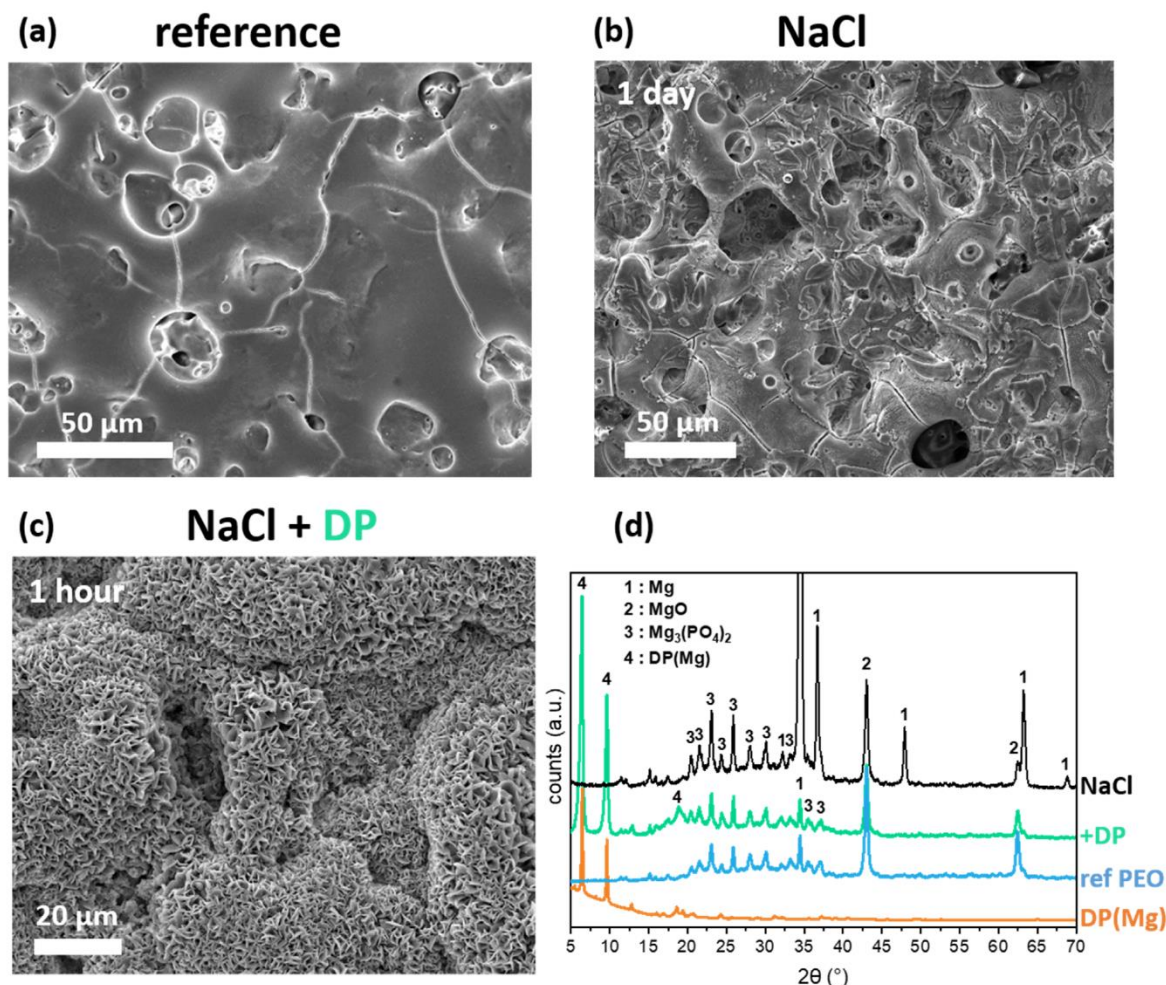


**Fig. 9.** SEM images from the surface of PEO coating: (a) Pristine PEO layer. (b), (c) after exposure to the NaCl solution with and without DP, respectively. The duration of exposure is indicated on top of each case. (d) XRD spectra of PEO-coated sample exposed to the NaCl solution with and without DP after 1 day. The XRD pattern of the DP(Mg) powder is also presented for comparison. The unlabeled small peaks between  $10^\circ$  and  $20^\circ$  can be associated to different magnesium hydrates [70].

cover the outer surface of PEO layer already after 1 h of exposure. XRD analysis of the pristine PEO-coated sample indicates  $\text{MgO}$  and  $\text{Mg}_3(\text{PO}_4)_2$  as the main phases of the PEO layer. The PEO layer exposed to NaCl reference solution reveals similar XRD spectra to the pristine PEO, but with higher ratio of Mg substrate peaks' intensity, suggesting the degradation of the PEO layer and easier penetration of X-Ray beam through this layer. The XRD analysis of PEO layer exposed to the DP-containing electrolyte reveals two extra peaks at  $2\theta$  of  $6.5^\circ$  and  $9.7^\circ$ , confirming that the precipitates on the PEO surface contain DP(Mg) complex.

Fig. 10 illustrates the cross-section of the PEO-coated AZ21 at the substrate/PEO interface after exposure to the NaCl solution with and without DP for 2 days. The duration of 2 days was selected since the obtained EIS spectra have already reached a stable phase without considerable change for some time. The corresponding PEO/substrate interface exposed to the reference NaCl solution reveals a corrosion

layer with the thickness of few micrometers, which features wide cracks so that the corrosive electrolyte can easily penetrate through. The EDS map of the corrosion layer reveals the presence of P, O, and Mg elements. The element C was homogeneously detected all over the corrosion products and the Mg substrate, but with very low signal intensity, indicating that it originates from the contamination deposited on the surface during the SEM/EDS analysis [71].

When DP was in the electrolyte, an additional dense layer was formed on the Mg substrate, which is outlined by dotted red lines in Fig. 10. The thickness of this layer is mostly below  $1\ \mu\text{m}$ . From the EDS map, this layer also contains elements O, Mg, and P. Similar to the case of NaCl reference electrolyte, there was no distinct distribution of element carbon in different regions of the cross-section. However, compared to the PEO layer, this compact layer contains less elemental P, indicating its different chemical composition. Additionally, there was an extra layer sandwiched between the PEO layer and the compact layer

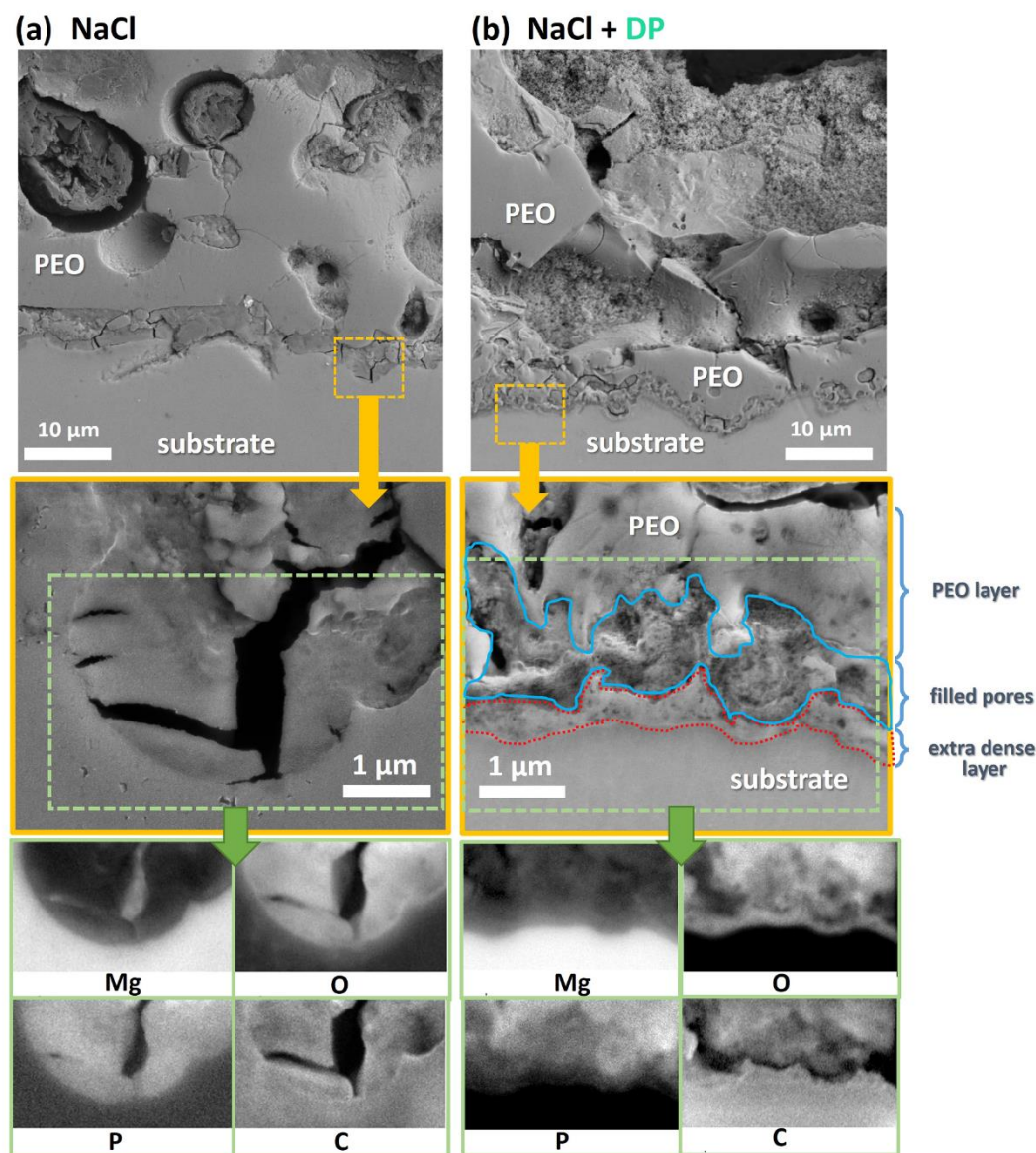


Fig. 10. Cross-sectional view of the interface between the PEO layer and the Mg substrate after exposure for 2 days to (a) NaCl solution and (b) NaCl + DP solution. The EDS maps of marked region are provided below each case.

(outlined by blue solid lines). This layer was the PEO porous region filled with some corrosion products, with smaller crack size and extension than those of the NaCl reference sample. Element Cl was also expected to be detected in the EDS analysis of both samples. However, likely due to the detection limit of EDS and a relatively high background noise, no distinctive contrast of Cl is observable across the cross-sections. Further details on the EDS analysis, including distribution of Cl elements, can be found in the supplementary material Section 4.

### 3.3. Incorporation of DP into PEO pores

So far, the interaction of DP molecules with both the PEO layer and Mg substrate has been studied, which is essential to develop an understanding of corrosion inhibition mechanism when DP is incorporated into PEO pores and cracks. In the following, the PEO-coated samples are incorporated with DP and their corrosion behavior, exposed to 3.5% NaCl solution, is studied.

The incorporation process was carried out via immersion of PEO-coated sample in high concentration (0.1 M) of DP solution, which was achieved by increasing the temperature to 60 °C. At this temperature, the solution is above the Krafft temperature ( $T_k$ ) of DP.  $T_k$  determines the minimum temperature at which micelles of a surfactant molecule can form (applicable to DP molecules), provided that the concentration of DP exceeds the critical micelle concentration (CMC). The phase diagram of the DP structures is depicted in Fig. 11b, which illustrates the relationship between the solubility of DP and solution temperature.

As the result of loading PEO pores with a high concentration of DP, the local depletion of DP, either via precipitation as DP(Mg) complex or

via dilution into the exposed electrolyte, will be delayed. A common approach to hinder the leaching of the incorporated inhibitors from the PEO pores into the corrosive medium is by applying a sealant on the PEO layer [1,10,11,72]. This approach, although effective in prolonging the inhibition effects of the inhibitor, adds more interacting components into the system, which leads to higher complexity of the system's behavior interpretation. Thus, the application of a sealant on such inhibitor-containing PEO coating will be presented in a separate report.

Fig. 11a illustrates the Bode representation of EIS spectra from the DP-loaded sample exposed to NaCl 3.5 wt%. The sample failed after 13 days (the drop of impedance value accompanied with the formation of a pit on the surface), which is a delay of 10 days as compared to the reference PEO-coated sample, Fig. 7a. The initial one-order-of-magnitude higher value of  $|Z|_{0.1 \text{ Hz}}$  at the commencement of exposure to the NaCl solution, visible in Fig. 11c, suggests that the inhibitor incorporation process itself has already improved the barrier properties of the PEO layer. This can be due to the formation of an additional protective layer, inferred from the high impedance modulus values at high-frequency ( $3 \cdot 10^3$  to  $7 \cdot 10^3 \text{ ohm} \cdot \text{cm}^2$ ) and initial negative high-frequency range phase angle, along with the corresponding high impedance modulus values (Fig. 11a). A gradual decrease in impedance value at all frequencies and fading (drifting toward zero) of the phase angle at the high-frequency range phase angle can be observed over the course of exposure. However, more careful observation of the commencement of exposure to the NaCl electrolyte reveals an initial opposing trend within the first 20 h, which are marked with orange circles in Fig. 11a, c. This is probably attributed to the incorporated DP molecules interacting according to the behavior observed in §4.2.

In order to gain more insight into the phase composition across the

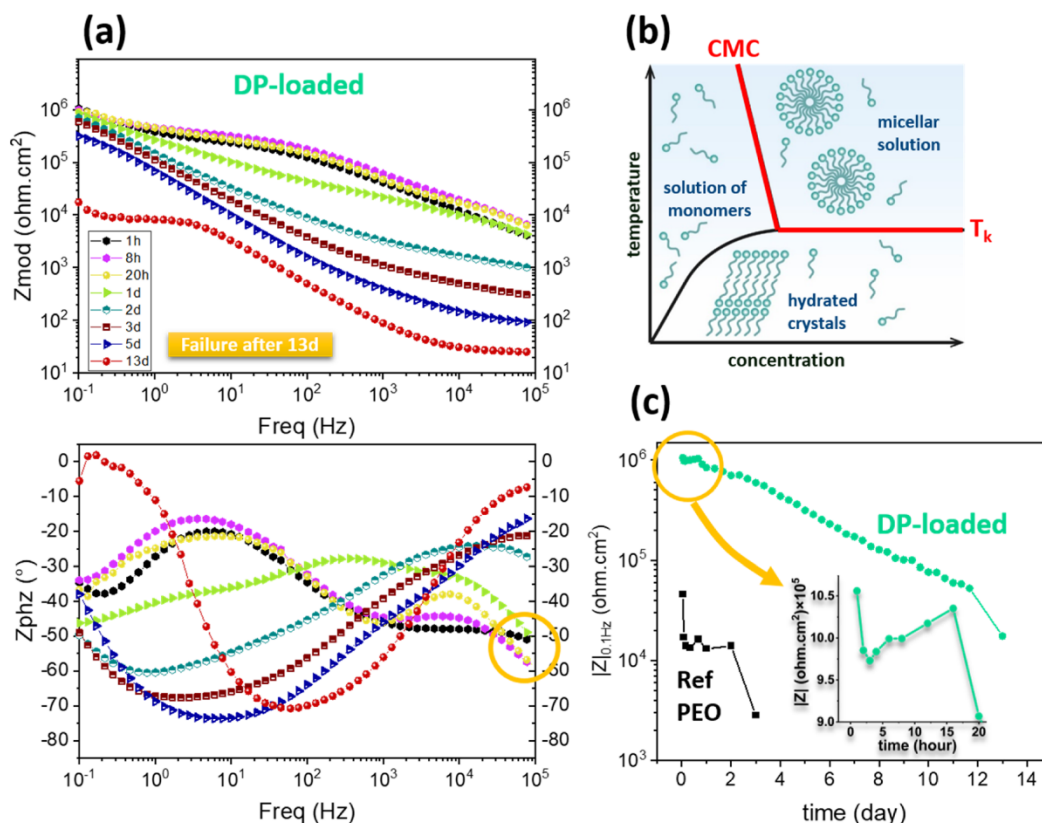


Fig. 11. (a) Bode plots of PEO-coated AZ21 impregnated with DP. (b) phase diagram of the DP structures (c) Absolute value of impedance at low frequency ( $|Z|_{0.1}$ ) from (a).

thickness of the PEO coating loaded with DP, two-dimensional scanning diffraction was carried out using a nano-focused X-ray beam. Fig. 12a illustrates a representative XRD spectra obtained from a single spot within the PEO layer to identify the phases in the samples loaded with DP before and after exposure to the NaCl solution for 3 days.

Diffraction peaks of main components of the PEO layer (i.e., MgO and  $\text{Mg}_3(\text{PO}_4)_2$ ) are identified and confirmed with the XRD analysis presented in Fig. 9d. For the sake of clarity only the highest intensity peaks of MgO and the region with population of  $\text{Mg}_3(\text{PO}_4)_2$  peaks between  $2\theta$  20–40° are marked in the figure.

The corresponding peaks of DP(Mg) complex are present on both samples, indicating that the incorporation process led to a reaction between the DP and Mg taken from PEO layer. The experimental set-up of the local diffractometry allows for acquiring diffraction even at  $2\theta$  as low as  $2^\circ$  with high precision and low background to noise ratio. As a result, an extra peak at  $2\theta$  of  $3.3^\circ$  was identified for DP(Mg) crystals with a considerably higher intensity as compared to the other associated peaks. Interestingly, the XRD spectra acquired from the DP-loaded sample before exposure to the NaCl solution revealed an additional peak at low  $2\theta$  of  $2.3^\circ$ , as well as some low intensity, shoulder-like peaks for each of DP(Mg) diffraction peaks, which can be attributed to unreacted incorporated DP crystals in the PEO pores. Bear in mind that the crystal structure of the unreacted DP depends on several parameters including DP concentration, electrolyte ionic strength, pH of the incorporation solution, and its cooling rate to the room temperature [73,74]. Since these parameters are unknown at the local conditions inside of the PEO pores, preparation of a reference DP powder as the “unreacted DP”

is not feasible.

Fig. 12b illustrates the 2D phase distribution over the sample cross-section based on the intensity of the corresponding peaks for the present phases. Peaks located at  $2\theta$  of  $34.5^\circ$ ,  $43.2^\circ$ ,  $3.3^\circ$ , and  $2.3^\circ$  are taken for the phases Mg, MgO, DP(Mg), and unreacted DP, respectively.

Using the 2D map of Mg and MgO (as one of the main phases of PEO), the borders of the PEO layer can be identified as marked with dash lines. The 2D maps show a rather homogenous distribution of MgO and  $\text{Mg}_3(\text{PO}_4)_2$  phases across the thickness of PEO layer of both samples. DP (Mg) can also be identified all over the PEO layer. However, the top half of the PEO layer is populated with slightly higher intensities of DP(Mg) indicating its higher intensity. The 2D map of unreacted DP also clearly indicates its higher intensity on the top half of the PEO. This inhomogeneity of the DP across the PEO layer is probably due to the usually larger pore area on the top of the PEO outer layer, which can accommodate more DP during the incorporation process. Moreover, the formation of DP(Mg) phases during the incorporation step leads to the blockage of the pathways for DP penetrations towards the substrate, resulting in fewer DP molecules reaching the bottom part of the PEO to either precipitate as DP(Mg) or remain unreacted.

The effect of DP incorporation into the PEO coating on the corrosion resistance of the samples was also evaluated through SST, and the appearances of the samples at different exposure times of the test are presented in Fig. 13. As can be seen in Fig. 13a, the surface of the reference sample is subjected to a gradual change of color to black during the SST. Similar color-change of PEO samples during SST has previously been reported for PEO coating with high content of

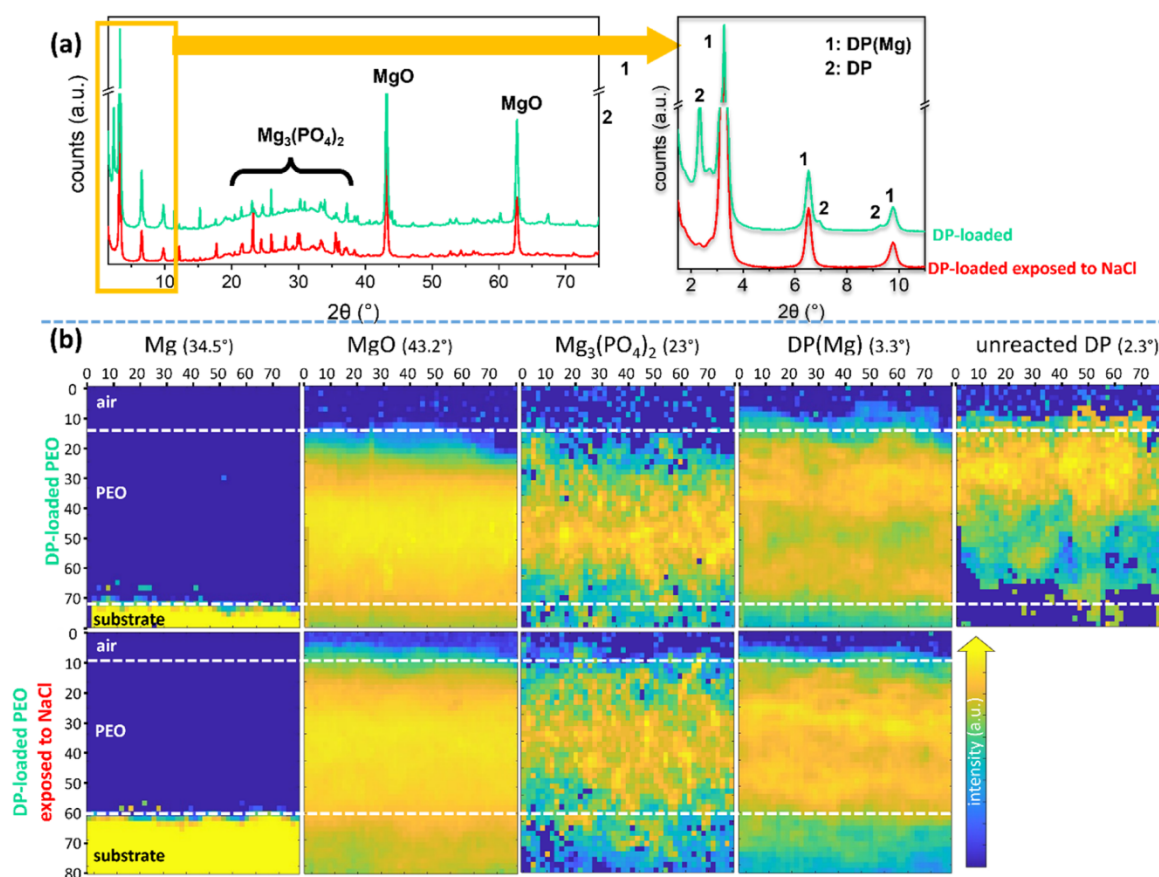


Fig. 12. (a) XRD patterns from two individual points selected from PEO coating regions of the DP-loaded sample before and after exposure to NaCl. (b) 2D maps of the phase distribution on cross-section of the PEO-coated AZ21 loaded with DP before and after exposure to the NaCl solution for 3 days. X and Y axes are in  $\mu\text{m}$ .

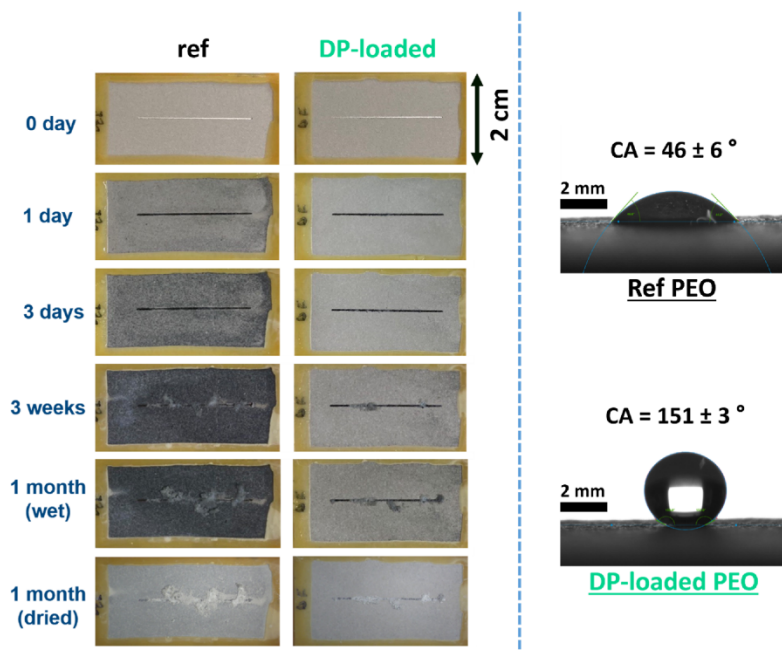


Fig. 13. (a) Macrographs of AZ21 sample coated with PEO with defect at different periods of SST; “ref” and “DP-loaded” denote the samples with and without the incorporation of DP. All the macrographs were taken immediately after taking out the sample from the SST chamber. The last row on the bottom shows the thoroughly dried sample after 1 month. (b) contact angle measurement of the reference PEO and DP-loaded PEO samples before SST.

phosphate-based phases [75], and has been attributed to the change in the refractive index of the PEO layer due to the increase in the size of PEO pores. The color-change of surface occurred at a significantly lower extent for the sample with the incorporated DP. On the other hand, when the sample is fully dried, the shade of black disappears, suggesting that the color is associated with the extend of wet substances on the sample. Fig. 13b confirms that the inhibitor incorporation process modifies the hydrophilic PEO surface toward a superhydrophobic surface, i.e., the increase in contact angle from  $46^\circ$  to  $151^\circ$ .

The corrosion creepage from scratch on the reference sample occurred more extensively than on the sample with the incorporated DP. Moreover, several spots away from the defect zone and covered with corrosion products were observed on the reference sample, indicating the local degradation of the PEO layer and pitting formation.

### 3.4. Discussion

#### 3.4.1. Effect of DP on bare Mg surface

The presence of DP in the NaCl solution was shown to yield high corrosion inhibition performance on bare AZ21 substrate. The formation of an insoluble complex between the DP molecule and  $Mg^{2+}$  ions, supplied via corrosion of the Mg substrate, results in the precipitation of a protective layer, as shown in the SEM images in Fig. 3. The barrier properties of this layer are reflected in the high-frequency range impedance in Fig. 1b. This is in contrast to weak or no barrier properties of  $Mg(OH)_2$  corrosion products in the reference NaCl electrolyte.

Many inhibitors with the precipitation mechanism tend to preferentially precipitate on the IMPs, which often act as cathodically active sites [10]. However, the AFM images of AZ21 after 1 min of exposure to DP-containing electrolyte revealed no preferential growth/nucleation of  $DP(Mg)$  precipitates. Similar behavior can be observed from the SEM images after 5 min of exposure. The seemingly high tendency of  $DP(Mg)$  complex to homogeneously nucleate on the Mg surface led to rapid coverage of Mg surface and, thus, rapid corrosion protection, which is evident from the rapid enhancement of  $|Z|_{0.1 \text{ Hz}}$  in Fig. 2a.

At the pH of the experiment ( $pH 7.0 \pm 0.1$ ), the phosphonic acid is in its monoanionic form and only one hydroxyl group is protonated ( $pK_{a1} = 3.98$  and  $pK_{a2} = 7.90$  [76]). Thus, DP shows a buffering effect against alkalinization caused by the cathodic HER and ORR on magnesium [77]. On the other hand, the formation of  $DP(Mg)$  complex leads to the acidification of the solution according to the reaction illustrated in Fig. 14. This slows down the pH increase and hinders the formation of poorly protective  $Mg(OH)_2$ , which is stabilized at an electrolyte pH of  $> 10.4$  [59]. The relatively low electrolyte pH increase (about 0.4 pH unit) after 4 days of exposure to NaCl–DP electrolyte is due to the above-mentioned acidification mechanisms as well as general corrosion inhibition.

However, as it was evidenced from the phase determination via XRD measurements (Fig. 5) and cross-sectional view (Fig. 4) of the sample exposed to the DP-containing electrolyte, there is still some  $Mg(OH)_2$  formed at the interface of Mg substrate covered with a  $DP(Mg)$  layer. The  $Mg(OH)_2$  is probably formed at locations with locally high cathodic activity on the Mg surface, which thermodynamically favors its formation. The formation of the  $DP(Mg)$  layer on the surface, besides providing a barrier against the corrosive medium, hinders DP molecules to pass through this layer and reach the Mg surface. As the result, the poorly protective  $Mg(OH)_2$  accumulates over time in between the Mg substrate and the  $DP(Mg)$  layer, which is reflected in the gradual decrease of  $|Z|_{0.1 \text{ Hz}}$  in Fig. 2a. If, at some point, the accumulation of the  $Mg(OH)_2$  causes the rupture of  $DP(Mg)$  protective layer, the instantaneous supply of local  $Mg^{2+}$  from the substrate and DP from the electrolyte locally triggers the formation of  $DP(Mg)$  complex. This is evident from the relatively large piles of corrosion products on the localized corrosion sites in Fig. 2d.

Investigations on the use of alkylphosphonic acids and their salts for



Fig. 14. Formation reaction of  $DP(Mg)$  salt.

the corrosion protection of Mg is scanty and limited to the study of self-assembled monolayers (SAM) with the aim of functionalizing the Mg surface via immersion in ethanolic solution of alkylphosphonic acids [64,65,78,79]. Here, the adsorption of DP molecules or initial deposition of DP(Mg) on the Mg surface also can be inferred from the positive shift of VPD detected on the Mg matrix exposed to the NaCl+DP solution. Nevertheless, as previously mentioned, the modification of the dielectric properties of the MgO layer also contributes to a change in the VPD, which is again due to the presence of DP molecules.

In addition to the adsorption and precipitation mechanisms of corrosion inhibitors, another proposed inhibition mechanism relies on the modification of the morphology of the  $\text{Mg}(\text{OH})_2$  corrosion products towards the formation of a dense layer on the Mg surface [25,53,80–82]. In recent investigations by Cui et al. [81,82], the anionic nature of a surfactant sodium dodecyl sulfate (SDS) is claimed to promote the nucleation kinetics of positively charged  $\text{Mg}(\text{OH})_2$  embryos, and thus, the formation of denser corrosion products layer. In this respect, DP molecule, with a negatively charged phosphonate group, may cause a densification of  $\text{Mg}(\text{OH})_2$  precipitates.

### 3.4.2. Effect of DP on PEO-coated Mg

The presence of DP in the NaCl electrolyte led to a significant enhancement in the corrosion resistance of PEO-coated sample. As a result, only temporary signs of pitting on the PEO coating were observed after 51 days, as opposed to the short 3-day failure time of the sample in the reference NaCl electrolyte.

DP(Mg) precipitates, similar to those observed on the bare Mg substrate, formed on the PEO layer (Fig. 9c,d). Even after 5 min of exposure to the DP-containing electrolyte, the surface of the PEO revealed extensive precipitation of DP(Mg) complex (SEM images are provided in the supplementary materials Fig. S4). However, such early and extensive corrosion of the coated Mg substrate is not expected to occur providing the required  $\text{Mg}^{2+}$  ions for the formation of DP(Mg). Instead, the  $\text{Mg}^{2+}$  ions are provided by the dissolution of the PEO layer (i.e., dissolution of MgO and  $\text{Mg}_3(\text{PO}_4)_2$  phases) in the NaCl electrolyte, as evident from the degraded morphology of the PEO outer layer illustrated in Fig. 9b. Apart from the aggressive nature of the NaCl solution towards the PEO layer, the formation of DP(Mg) itself and its resulting acidification (Fig. 14) initially promote the dissolution of PEO and growth of the protective layer as a result of a conversion process. Nevertheless, the barrier properties of DP(Mg) precipitates self-regulate their growth, in analogy to the formation of a conversion coating with passivating properties [83].

In addition to the protection of the PEO outer surface via the DP(Mg) layer formation, the precipitation of DP(Mg) in the PEO pores leads to their blockage, which in turn hinders the penetration of corrosive medium through the coating. The pores filled with relatively dense corrosion products marked in Fig. 10, confirming the sealing of the PEO pores. In addition to the DP(Mg), it is expected that the corrosion products also comprise a mixture of  $\text{Mg}(\text{OH})_2$  and  $\text{Mg}_3(\text{PO}_4)_2$ . The later phase originated from the re-precipitation of dissolved  $\text{Mg}_3(\text{PO}_4)_2$  from the PEO layer (most likely from its amorphous phase) [20,75,84]. The co-existence of  $\text{Mg}(\text{OH})_2$  and  $\text{Mg}_3(\text{PO}_4)_2$  has been thermodynamically illustrated to be possible at pH values higher than  $\sim 10$  [22].

Another layer with barrier properties was formed at the Mg/PEO interface, which features a dense morphology (Fig. 10b) and is evidenced in the EIS spectra by a time constant developed at high-frequency range. In addition to the barrier properties provided by this layer, its dense morphology means lower mechanical stress on the atop PEO layer, in contrast to the less dense corrosion products in the absence of DP. The local mechanical stress by the corrosion products in the substrate/PEO interface is believed to be one of the main accelerating factor for degradation of phosphate-based PEO coatings on Mg [22]. Characterization of this dense layer by EDS can only reveal that it is different from the PEO layer, corrosion products in the pores, and DP (Mg) complex. Moreover, although the contribution of DP molecules in

this layer could either be via co-precipitation as DP(Mg) or via adsorption on the corrosion product, the relatively low detected C signal can only be accounted for a minor existence of DP. From another point of view, as mentioned above, the presence of anionic surfactants can affect the morphology and crystallinity of  $\text{Mg}(\text{OH})_2$  precipitates via modification of  $\text{Mg}(\text{OH})_2$  nucleation/growth kinetics [85–88], which can lead to denser  $\text{Mg}(\text{OH})_2$ . The same effect is expected for the morphology alteration of re-precipitated  $\text{Mg}_3(\text{PO}_4)_2$  phase in the presence of DP molecules. Nevertheless, further characterization methods are required to obtain more information about the composition and crystallography of this layer.

### 3.4.3. DP as incorporated inhibitor

During the incorporation process, DP molecules are accommodated in the spacious PEO pores and interact with the PEO layer in a similar way as when they are present in the NaCl solution. Part of the PEO layer dissolves and DP(Mg) complex precipitates, forming a protective film on the PEO outer layer and blocking the PEO pores. The high concentration of DP in the incorporation solution, as well as the elevated temperature, accelerates the precipitation kinetics. Additionally, the absence of  $\text{Cl}^-$  in the impregnation solution mitigate the degradation of Mg substrate. Furthermore, the highly concentrated micellar solution of DP in the PEO pores crystallizes upon the cooling after the incorporation process, further contributing to the blockage of PEO pores.

When the sample is exposed to the NaCl solution, the loaded DP dissolves into the electrolyte and inhibits the degradation of the PEO-coated Mg and bare Mg in the defected areas, via the mechanisms explained for each case. This in turn enhances the barrier properties of the PEO coating.

The presence of DP molecules, either as adsorbed molecule on the surface or as compound in DP(Mg), functionalizes the surface with hydrophobicity, due to DP's hydrophobic alkane tail. Moreover, the micro-scale cavities between of the DP(Mg) flakes deposited on the surface forms an air cushion, significantly reducing the actual contact area between the corrosive medium and the surface [89–91]. This in turn effectively contributes to the high hydrophobicity of the surface, as observed from the high contact angle determined in Fig. 13.

Fig. 15 illustrates the schematic of the explained corrosion inhibition mechanism for PEO-coated Mg impregnated with DP in the presence of a

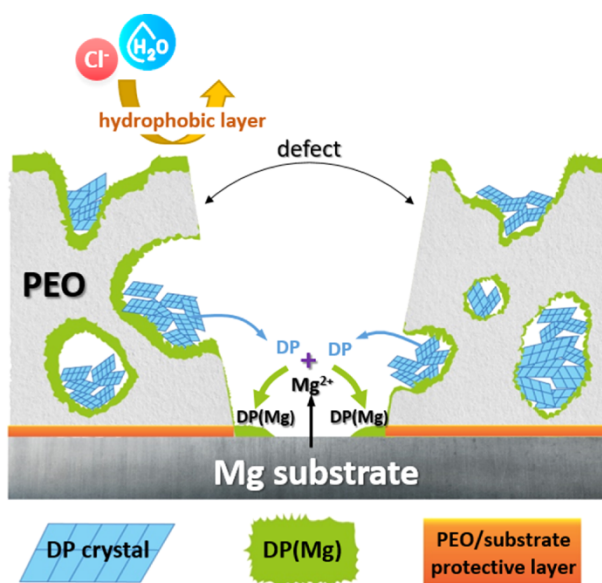


Fig. 15. schematic of mechanisms contributing to corrosion protection of PEO-coated Mg loaded with DP in the presence of a defect.

defect in the coating.

In the context of atmospheric corrosion, in which the SST test is relevant, the hydrophobicity of the surface prevents the electrolyte droplets from remaining on the surface, as evident from the less wetted surface in Fig. 13. From another perspective, the loaded DP molecules, when dissolved in the condensed electrolyte on the surface, also tend to stay in the air/liquid interface, which in turn can act as a hindrance for O<sub>2</sub> diffusion from air into the electrolyte [92–94]. As the result, ORR, which can play a decisive role in corrosion of the Mg [77,95], especially in atmospheric corrosion [96], is mitigated.

There have been several attempts to functionalize the surface of a PEO coating by immersion of the PEO-coated magnesium in ethanolic solutions of alkylphosphonic acids, such as octadecylphosphonic acid (ODP) in the work of Mingo et al. [97]. However, the functionalized surface via this approach leaves a thin layer of adsorbed ODP, which may provide only a short-term corrosion protection.

It is worth mentioning that from the literature on the use of alkylphosphonic acids for corrosion protection enhancement of different metals [39,65,98,99], a common conclusion can be drawn that the longer alkyl chain length results in higher hydrophobicity and higher corrosion protection. Therefore, octadecylphosphonic acid appears to be one of the most investigated alkylphosphonic acid [64,78,100,101]. However, this is mostly again from the perspective of adsorption inhibition mechanism. Nevertheless, increasing the alkyl chain length also decreases their solubility in aqueous environments, which means they may be less available to actively inhibit corrosion.

#### 4. Conclusion and outlook

In this work, the highly effective inhibition of decylphosphonate (DP) against both bare and PEO-coated AZ21 corrosion was demonstrated. The presence of DP in NaCl 3.5 wt% corrosive medium reduced the corrosion rate of bare AZ21 by about 10 times and delayed the occurrence of pitting on PEO-coated AZ21 from 3 days to 51 days.

The interaction of DP with both bare AZ21 and the PEO layer resulted in different corrosion inhibition mechanisms, including:

- DP forms insoluble complex with Mg<sup>2+</sup> + liberated as a result of Mg substrate activation. The precipitated DP(Mg) complex forms a protective layer on the Mg substrate against the corrosive species.
- Degradation of PEO layer, which is mainly composed of Mg<sub>3</sub>(PO<sub>4</sub>)<sub>2</sub> and MgO, also releases Mg<sup>2+</sup>. The resulting DP(Mg) complex protects the PEO layer from the corrosive medium.
- The formed DP(Mg) provides hydrophobic properties to the surface, inhibiting the access of aqueous corrosive medium to the substrate.
- The process of incorporation of DP into the PEO layer itself results in the sealing of the PEO pores, achieved through the formation of DP (Mg) protective layer and precipitation of DP crystals from the high concentration micellar solution.

The incorporation of a high concentration of DP into PEO layers via a simple immersion in a micellar solution of DP was found to be effective and merits more investigation.

These results are expected to stimulate further research on the use of surfactants as corrosion inhibitors in PEO coatings, paving the way for the development of cost-effective and environmentally friendly corrosion protection strategies for magnesium alloys.

#### CRedit authorship contribution statement

**Bahram Vaghefinazari:** Conceptualization, Investigation, Validation, Writing – original draft, Writing – review & editing. **Sviatlana V. Lamaka:** Conceptualization, Supervision, Writing – review & editing. **Eugen Gazenbiller:** Investigation, Writing – review & editing. **Kiryl Yasakau:** Investigation, Writing – review & editing. **Carsten Blawert:** Conceptualization, Supervision, Writing – review & editing. **Maria**

**Serdechnova:** Investigation, Writing – review & editing. **Nico Scharnagl:** Investigation, Writing – review & editing. **D.C.Florian Wieland:** Investigation, Writing – review & editing. **Mikhail L. Zheludkevich:** Conceptualization, Supervision, Writing – review & editing.

#### Declaration of Competing Interest

The authors of the manuscript entitled “corrosion inhibition of decylphosphonate on bare and PEO-coated Mg alloy” declare that they have no known competing financial interests or personal relationships that could have appeared to influence the work reported in this paper. The submitted abstract is provided at the end of this document.

#### Data Availability

The raw/processed data required to reproduce these findings cannot be shared at this time as the data also forms part of an ongoing study.

#### Acknowledgment

The authors would like to acknowledge the technical support from Mr. Ulrich Burmester, Mr. Volker Heitmann, Ms. Petra Fisher, and Mr. Gert Wiese. The author acknowledges Dr. Maryam Radjabian and Mr. Joachim Koll from the institute of Membrane Research at Helmholtz Zentrum Hereon for their support during contact angle measurements. The authors would like to thank Deutsches Elektronen Synchrotron (DESY, PETRA III, Hamburg, Germany) for accepting the proposal I\_20211343 (P.03 end-station) for carrying out the phase mapping of the coatings cross-sections. KY acknowledges the Portuguese Foundation for Science and Technology for the researcher grant (2021.00842. CEE-CIND). Part of this work was developed within the scope of the project CICECO-Aveiro Institute of Materials, UIDB/50011/2020, UIDP/50011/2020 & LA/P/0006/2020, financed by national funds through the FCT/MCTES (PIDDAC).

#### Appendix A. Supporting information

Supplementary data associated with this article can be found in the online version at doi:10.1016/j.corsci.2023.111651.

#### References

- [1] E. Wierzbicka, B. Vaghefinazari, M. Mohehdano, P. Visser, R. Posner, C. Blawert, M. Zheludkevich, S. Lamaka, E. Matykina, R. Arrabal, Chromate-free corrosion protection strategies for magnesium alloys-a review: part II-PEO and anodizing, *Materials* 15 (2022).
- [2] G. Barati Darband, M. Aliofkhaezai, P. Hamghalam, N. Valizade, Plasma electrolytic oxidation of magnesium and its alloys: mechanism, properties and applications, *J. Magnes. Alloy.* 5 (2017) 74–132.
- [3] X. Lu, M. Mohehdano, C. Blawert, E. Matykina, R. Arrabal, K.U. Kainer, M. L. Zheludkevich, Plasma electrolytic oxidation coatings with particle additions – a review, *Surf. Coat. Technol.* 307 (2016) 1165–1182.
- [4] A. Keyvani, M. Zamani, M. Bahamirian, E. Nikoomezari, A. Fattah-alhosseini, H. Sina, Role of incorporation of ZnO nanoparticles on corrosion behavior of ceramic coatings developed on AZ31 magnesium alloy by plasma electrolytic oxidation technique, *Surf. Interfaces* 22 (2021), 100728.
- [5] E. Wierzbicka, B. Vaghefinazari, S.V. Lamaka, M.L. Zheludkevich, M. Mohehdano, L. Moreno, P. Visser, A. Rodriguez, J. Velasco, R. Arrabal, E. Matykina, Flash-PEO as an alternative to chromate conversion coatings for corrosion protection of Mg alloy, *Corros. Sci.* 180 (2021), 109189.
- [6] T. Wu, C. Blawert, X. Lu, M. Serdechnova, M.L. Zheludkevich, Difference in formation of plasma electrolytic oxidation coatings on MgLi alloy in comparison with pure Mg, *J. Magnes. Alloy.* (2021).
- [7] K.V. Nadaraia, S.N. Suchkov, I.M. Imshinetskiy, D.V. Mashtalyar, S. L. Sinebrykhov, S.V. Gnedenkov, Some new aspects of the study of dependence of properties of PEO coatings on the parameters of current in potentiodynamic mode, *Surf. Coat. Technol.* 426 (2021), 127744.
- [8] R. Chaharmahali, A. Fattah-alhosseini, M. Nouri, K. Babaei, Improving surface characteristics of PEO coatings of Mg and its alloys with zirconia nanoparticles: a review, *Appl. Surf. Sci. Adv.* 6 (2021), 100131.
- [9] L. An, Y. Ma, L. Sun, Z. Wang, S. Wang, Investigation of mutual effects among additives in electrolyte for plasma electrolytic oxidation on magnesium alloys, *J. Magnes. Alloy.* 8 (2020) 523–536.

- [10] B. Vaghefinazari, E. Wierzbicka, P. Visser, R. Posner, R. Arrabal, E. Matykina, M. Mohedano, C. Blawert, M.L. Zheludkevich, S.V. Lamaka, Chromate-free corrosion protection strategies for magnesium alloys—a review: part III—corrosion inhibitors and combining them with other protection strategies, *Materials* 15 (2022).
- [11] S.V. Lamaka, G. Knörschild, D.V. Snihirova, M.G. Taryba, M.L. Zheludkevich, M. G.S. Ferreira, Complex anticorrosion coating for ZK30 magnesium alloy, *Electrochim. Acta* 55 (2009) 131–141.
- [12] M. Toorani, M. Aliofkhaizaei, M. Mahdavian, R. Naderi, Superior corrosion protection and adhesion strength of epoxy coating applied on AZ31 magnesium alloy pre-treated by PEO/Silane with inorganic and organic corrosion inhibitors, *Corros. Sci.* 178 (2021), 109065.
- [13] G. Zhang, E. Jiang, L. Wu, W. Ma, H. Yang, A. Tang, F. Pan, Corrosion protection properties of different inhibitors containing PEO/LDHs composite coating on magnesium alloy AZ31, *Sci. Rep.* 11 (2021) 2774.
- [14] D.K. Ivanov, K.A. Yasakau, S. Kallip, A.D. Lisenkov, M. Starykevich, S.V. Lamaka, M.G.S. Ferreira, M.L. Zheludkevich, Active corrosion protection coating for a ZE41 magnesium alloy created by combining PEO and sol-gel techniques, *RSC Adv.* 6 (2016) 12553–12560.
- [15] J. Yang, C. Blawert, S.V. Lamaka, D. Snihirova, X. Lu, S. Di, M.L. Zheludkevich, Corrosion protection properties of inhibitor containing hybrid PEO-epoxy coating on magnesium, *Corros. Sci.* 140 (2018) 99–110.
- [16] D. Liu, Y. Song, D. Shan, E.H. Han, Self-Healing Coatings Prepared by Loading Interphase Inhibitors into MAO Coating of AM60 Mg Alloy, *J. Electrochem. Soc.* 165 (2018) C412–C421.
- [17] Y. Chen, X. Lu, S.V. Lamaka, P. Ju, C. Blawert, T. Zhang, F. Wang, M. L. Zheludkevich, Active protection of Mg alloy by composite PEO coating loaded with corrosion inhibitors, *Appl. Surf. Sci.* 504 (2020), 144462.
- [18] G. Zhang, E. Jiang, L. Wu, A. Tang, A. Atrens, F. Pan, Active corrosion protection of phosphate loaded PEO/LDHs composite coatings: SIET study, *J. Magnes. Alloy.* 10 (2022) 1351–1357.
- [19] A.S. Gnedenkov, S.L. Sinebryukhov, V.S. Filonina, N.G. Plekhova, S. V. Gnedenkov, Smart composite antibacterial coatings with active corrosion protection of magnesium alloys, *J. Magnes. Alloy.* (2022).
- [20] B. Vaghefinazari, S.V. Lamaka, C. Blawert, M. Serdechnova, N. Scharnagl, P. Karlova, D.C.F. Wieland, M.L. Zheludkevich, Exploring the corrosion inhibition mechanism of 8-hydroxyquinoline for a PEO-coated magnesium alloy, *Corros. Sci.* 203 (2022), 110344.
- [21] L. Moreno, C. Wang, S.V. Lamaka, M.L. Zheludkevich, J. Rodríguez-Hernández, R. Arrabal, E. Matykina, Ciprofloxacin release and corrosion behaviour of a hybrid PEO/PCL coating on Mg3Zn0.4Ca alloy, *J. Funct. Biomater.* 14 (2023) 65.
- [22] B. Vaghefinazari, C. Wang, D. Mercier, D. Mei, A. Seyeux, P. Marcus, C. Blawert, S.V. Lamaka, M.L. Zheludkevich, Adverse effect of 2,5PDC corrosion inhibitor on PEO coated magnesium, *Corros. Sci.* (2021), 109830.
- [23] S.V. Lamaka, B. Vaghefinazari, D. Mei, R.P. Petruskas, D. Hoche, M. L. Zheludkevich, Comprehensive screening of Mg corrosion inhibitors, *Corros. Sci.* 128 (2017) 224–240.
- [24] J. Yang, C. Blawert, S.V. Lamaka, K.A. Yasakau, L. Wang, D. Laipple, M. Schieda, S. Di, M.L. Zheludkevich, Corrosion inhibition of pure Mg containing a high level of iron impurity in pH neutral NaCl solution, *Corros. Sci.* 142 (2018) 222–237.
- [25] A. Maltseva, S.V. Lamaka, K.A. Yasakau, D. Mei, D. Kurchavov, M. L. Zheludkevich, G. Lefevre, P. Volovitch, In situ surface film evolution during Mg aqueous corrosion in presence of selected carboxylates, *Corros. Sci.* 171 (2020), 108484.
- [26] A. Frignani, V. Grassi, F. Zanotto, F. Zucchi, Inhibition of AZ31 Mg alloy corrosion by anionic surfactants, *Corros. Sci.* 63 (2012) 29–39.
- [27] N. Dinodi, A.N. Shetty, Alkyl carboxylates as efficient and green inhibitors of magnesium alloy ZE41 corrosion in aqueous salt solution, *Corros. Sci.* 85 (2014) 411–427.
- [28] X. Lu, Y. Li, P. Ju, Y. Chen, J. Yang, K. Qian, T. Zhang, F. Wang, Unveiling the inhibition mechanism of an effective inhibitor for AZ91 Mg alloy, *Corros. Sci.* 148 (2019) 264–271.
- [29] J. Chen, J. He, L. Li, Spectroscopic insight into the role of SDBS on the interface evolution of Mg in NaCl corrosive medium, *Corros. Sci.* 182 (2021), 109215.
- [30] Y. Li, X. Lu, K. Wu, L. Yang, T. Zhang, F. Wang, Exploration the inhibition mechanism of sodium dodecyl sulfate on Mg alloy, *Corros. Sci.* 168 (2020), 108559.
- [31] T. Zhao, Z. Wang, Y. Feng, Q. Li, Synergistic corrosion inhibition of sodium phosphate and sodium dodecyl sulphate on magnesium alloy AZ91 in 3.5 wt% NaCl solution, *Mater. Today Commun.* 31 (2022), 103568.
- [32] D. Liu, Y.W. Song, D.Y. Shan, E.H. Han, Comparison of the inhibition effect of four inhibitors on the corrosion behaviour of AM60 magnesium alloy, *Int. J. Electrochem. Sci.* 13 (2018) 2219–2235.
- [33] Y. Chen, X. Wang, T. Lai, D. Liu, J. Pan, L. Lin, H. Guan, C. Luo, H. Song, Y. Xin, H. Yan, Z. Hu, Sodium dodecylbenzene sulfonate film absorbed on magnesium alloy surface: an electrochemical, SKPFM, and molecular dynamics study, *J. Mol. Liq.* 357 (2022), 119095.
- [34] H. Song, Z. Xu, L. Benabou, Z. Yin, H. Guan, H. Yan, L. Chao, Z. Hu, X. Wang, Sodium dodecyl sulfate (SDS) as an effective corrosion inhibitor for Mg-8Li-3Al alloy in aqueous NaCl: a combined experimental and theoretical investigation, *J. Magnes. Alloy.* (2021).
- [35] Y. Li, X. Lu, D. Mei, T. Zhang, F. Wang, Passivation of corrosion product layer on AM50 Mg by corrosion inhibitor, *J. Magnes. Alloy.* (2021).
- [36] A. Soltan, M.S. Dargusch, Z. Shi, D. Gerrard, A. Atrens, Influence of commercial corrosion-inhibiting compounds on the atmospheric corrosion of the magnesium alloys EV31A, WE43B, ZE41A and pure magnesium, *Mater. Corros.* 72 (2021) 672–693.
- [37] A. Soltan, M.S. Dargusch, Z. Shi, F. Jones, B. Wood, D. Gerrard, A. Atrens, Effect of corrosion inhibiting compounds on the corrosion behaviour of pure magnesium and the magnesium alloys EV31A, WE43B and ZE41A, *J. Magnes. Alloy.* 9 (2021) 432–455.
- [38] A. Chirkunov, A. Rakoch, E. Monakhova, A. Gladkova, Z. Khabibullina, V. Ogorodnikova, M. Serdechnova, C. Blawert, Y.I. Kuznetsov, M. Zheludkevich, Corrosion protection of magnesium alloy by PEO-coatings containing sodium oleate, *Int. J. Corros. Scale Inhib.* 8 (2019) 1170–1188.
- [39] I. Milošev, D. Zimerl, C. Carrière, S. Zanna, A. Seyeux, J. Iskra, S. Stavber, F. Chiter, M. Poberžnik, D. Costa, Editors' choice—the effect of anchor group and alkyl backbone chain on performance of organic compounds as corrosion inhibitors for aluminum investigated using an integrative experimental-modeling approach, *J. Electrochem. Soc.* 167 (2020), 061509.
- [40] A. Roberts, D. Engelberg, Y. Liu, G.E. Thompson, M.R. Alexander, Imaging XPS investigation of the lateral distribution of copper inclusions at the abraded surface of 2024T3 aluminium alloy and adsorption of decyl phosphonic acid, *Surface and Interface Analysis: An International Journal devoted to the development and application of techniques for the analysis of surfaces, interfaces and thin films*, 33 (2002) 697–703.
- [41] I. Milošev, A. Kokalj, M. Poberžnik, C. Carrière, D. Zimerl, J. Iskra, A. Nemes, D. Szabó, S. Zanna, A. Seyeux, The effects of perfluoroalkyl and alkyl backbone chains, spacers, and anchor groups on the performance of organic compounds as corrosion inhibitors for aluminum investigated using an integrative experimental-modeling approach, *J. Electrochem. Soc.* 168 (2021), 071506.
- [42] W. Zhao, T. Chang, C. Leygraf, C.M. Johnson, Corrosion inhibition of copper with octadecylphosphonic acid (ODPA) in a simulated indoor atmospheric environment, *Corros. Sci.* 192 (2021), 109777.
- [43] G. Fonder, I. Minet, C. Volcke, S. Devillers, J. Delhalle, Z. Mekhalif, Anchoring of alkylphosphonic derivatives molecules on copper oxide surfaces, *Appl. Surf. Sci.* 257 (2011) 6300–6307.
- [44] D.K. Kozlica, A. Kokalj, I. Milošev, Synergistic effect of 2-mercaptobenzimidazole and octylphosphonic acid as corrosion inhibitors for copper and aluminium – an electrochemical, XPS, FTIR and DFT study, *Corros. Sci.* 182 (2021), 109082.
- [45] F.X. Perrin, T.A. Phan, D.L. Nguyen, Preparation and characterization of polyaniline in reversed micelles of decylphosphonic acid for active corrosion protection coatings, *Eur. Polym. J.* 66 (2015) 253–265.
- [46] M. Alonso Frank, C. Meltzer, B. Braunschweig, W. Peukert, A.R. Boccaccini, S. Virtanen, Functionalization of steel surfaces with organic acids: influence on wetting and corrosion behavior, *Appl. Surf. Sci.* 404 (2017) 326–333.
- [47] C. Krywka, H. Neubauer, M. Priebe, T. Salditt, J. Keckes, A. Buffet, S.V. Roth, R. Doehrmann, M. Mueller, A two-dimensional waveguide beam for X-ray nanodiffraction, *J. Appl. Crystallogr.* 45 (2012) 85–92.
- [48] G. Ashiotis, A. Deschildre, Z. Nawaz, J.P. Wright, D. Karkoulis, F.E. Picca, J. Kieffer, The fast azimuthal integration Python library: pyFAI, *J. Appl. Crystallogr.* 48 (2015) 510–519.
- [49] T. Wu, C. Blawert, M. Serdechnova, P. Karlova, G. Dovzhenko, D.F. Wieland, M. L. Zheludkevich, PEO processing of AZ91Nd/Al2O3 MMC—the role of alumina fibers, *J. Magnes. Alloy.* 10 (2022) 423–439.
- [50] V. Guillaumin, P. Schmutz, G. Frankel, Characterization of corrosion interfaces by the scanning Kelvin probe force microscopy technique, *J. Electrochem. Soc.* 148 (2001) B163.
- [51] M. Hurley, C. Efav, P. Davis, J. Croteau, E. Graugnard, N. Birbilis, Volta potentials measured by scanning kelvin probe force microscopy as relevant to corrosion of magnesium alloys, *Corrosion* 71 (2015) 160–170.
- [52] M. Rohwerder, F. Turcu, High-resolution Kelvin probe microscopy in corrosion science: scanning Kelvin probe force microscopy (SKPFM) versus classical scanning Kelvin probe (SKP), *Electrochim. Acta* 53 (2007) 290–299.
- [53] K.A. Yasakau, A. Maltseva, S.V. Lamaka, D. Mei, H. Orvi, P. Volovitch, M.G. S. Ferreira, M.L. Zheludkevich, The effect of carboxylate compounds on Volta potential and corrosion inhibition of Mg containing different levels of iron, *Corros. Sci.* 194 (2022), 109937.
- [54] L. Wang, D. Snihirova, M. Deng, C. Wang, B. Vaghefinazari, G. Wiese, M. Langridge, D. Höche, S.V. Lamaka, M.L. Zheludkevich, Insight into physical interpretation of high frequency time constant in electrochemical impedance spectra of Mg, *Corros. Sci.* 187 (2021), 109501.
- [55] L. Wang, D. Snihirova, M. Deng, B. Vaghefinazari, D. Höche, S.V. Lamaka, M. L. Zheludkevich, Revealing physical interpretation of time constants in electrochemical impedance spectra of Mg via Tribo-EIS measurements, *Electrochim. Acta* (2021), 139582.
- [56] L. Wang, D. Snihirova, M.D. Havigh, M. Deng, S.V. Lamaka, H. Terryn, M. L. Zheludkevich, Non-stationarity in electrochemical impedance measurement of Mg-based materials in aqueous media, *Electrochim. Acta* 468 (2023), 143140.
- [57] D. Mei, S.V. Lamaka, J. Gonzalez, F. Feyerabend, R. Willumeit-Romer, M. L. Zheludkevich, The role of individual components of simulated body fluid on the corrosion behavior of commercially pure Mg, *Corros. Sci.* 147 (2019) 81–93.
- [58] V. Shkirskiy, A.D. King, O. Gharbi, P. Volovitch, J.R. Scully, K. Ogle, N. Birbilis, Revisiting the electrochemical impedance spectroscopy of magnesium with online inductively coupled plasma atomic emission spectroscopy, *ChemPhysChem* 16 (2015) 536–539.
- [59] B. Vaghefinazari, D. Snihirova, C. Wang, L. Wang, M. Deng, D. Höche, S. V. Lamaka, M.L. Zheludkevich, Exploring the effect of sodium salt of Ethylenediaminetetraacetic acid as an electrolyte additive on electrochemical behavior of a commercially pure Mg in primary Mg-air batteries, *J. Power Sources* 527 (2022), 231176.

- [60] K. Yasakau, Application of AFM-based techniques in studies of corrosion and corrosion inhibition of metallic alloys, *Corros. Mater. Degrad.* 1 (2020) 345–372.
- [61] K. Yasakau, M. Zheludkevich, M. Ferreira, Lanthanide salts as corrosion inhibitors for AA5083. Mechanism and efficiency of corrosion inhibition, *J. Electrochem. Soc.* 155 (2008) C169.
- [62] T. Ishizaki, M. Okido, Y. Masuda, N. Saito, M. Sakamoto, Corrosion resistant performances of alkanolic and phosphonic acids derived self-assembled monolayers on magnesium alloy AZ31 by vapor-phase method, *Langmuir* 27 (2011) 6009–6017.
- [63] Z. Grubač, M. Metikoš-Huković, R. Babić, I.Š. Rončević, M. Petravić, R. Peter, Functionalization of biodegradable magnesium alloy implants with alkylphosphonate self-assembled films, *Mater. Sci. Eng.: C* 33 (2013) 2152–2158.
- [64] V.K. Korrapati, N. Scharnagl, D. Letzig, M.L. Zheludkevich, Self-assembled layers for the temporary corrosion protection of magnesium-AZ31 alloy, *Corros. Sci.* 169 (2020), 108619.
- [65] S. Szillies, P. Thissen, D. Tabatabai, F. Feil, W. Fürbeth, N. Fink, G. Grundmeier, Formation and stability of organic acid monolayers on magnesium alloy AZ31: the role of alkyl chain length and head group chemistry, *Appl. Surf. Sci.* 283 (2013) 339–347.
- [66] Y. Zhu, M.L. Free, R. Woolam, W. Durnie, A review of surfactants as corrosion inhibitors and associated modeling, *Prog. Mater. Sci.* 90 (2017) 159–223.
- [67] A. Natan, Y. Zidon, Y. Shapira, L. Kronik, Cooperative effects and dipole formation at semiconductor and self-assembled-monolayer interfaces, *Phys. Rev. B* 73 (2006), 193310.
- [68] F. Andreatta, A. Turco, I. de Graeve, H. Terryn, J.H.W. de Wit, L. Fedrizzi, SKPFM and SEM study of the deposition mechanism of Zr/Ti based pre-treatment on AA6016 aluminum alloy, *Surf. Coat. Technol.* 201 (2007) 7668–7685.
- [69] J.F. Lübken, T. Baše, P. Rupper, T. Künniger, J. Macháček, S. Guimond, Tuning the surface potential of Ag surfaces by chemisorption of oppositely-oriented thiolated carborane dipoles, *J. Colloid Interface Sci.* 354 (2011) 168–174.
- [70] B. Lothenbach, B. Xu, F. Winnefeld, Thermodynamic data for magnesium (potassium) phosphates, *Appl. Geochem.* 111 (2019), 104450.
- [71] P. Hirsch, M. Kässens, M. Pittmann, Contamination in a scanning electron microscope and the influence of specimen cooling, *Scanning* 16 (1994) 101–110.
- [72] A.S. Gnedenkov, S.L. Sinebryukhov, V.S. Filonina, A.Y. Ustinov, S. V. Sukhoverkhov, S.V. Gnedenkov, New polycaprolactone-containing self-healing coating design for enhance corrosion resistance of the magnesium and its alloys, *Polymers* 15 (2023) 202.
- [73] H. Lu, I. Pezron, T. Gaudin, A. Drelich, Non-equilibrium micelles formed by sugar-based surfactants under their Krafft temperature, *Colloids Surf. A: Physicochem. Eng. Asp.* 540 (2018) 167–176.
- [74] R.J. Farn, *Chemistry and Technology of Surfactants*, Wiley, 2008.
- [75] Y. Mori, A. Koshi, J. Liao, H. Asoh, S. Ono, Characteristics and corrosion resistance of plasma electrolytic oxidation coatings on AZ31B Mg alloy formed in phosphate – silicate mixture electrolytes, *Corros. Sci.* 88 (2014) 254–262.
- [76] P.C. Schulz, M. Abrameto, J.E. Puig, F.A. Soltero-Martínez, A. Gonzalez-Alvarez, Phase behavior of the systems n-decanephosphonic acid/water and n-dodecanephosphonic acid/water, *Langmuir* 12 (1996) 3082–3088.
- [77] C. Wang, D. Mei, G. Wiese, L.Q. Wang, M. Deng, S.V. Lamaka, M.L. Zheludkevich, High rate oxygen reduction reaction during corrosion of ultra-high-purity magnesium, *npj Mater. Degrad.* 4 (2020) 42.
- [78] V.K. Korrapati, N. Scharnagl, D. Letzig, M.L. Zheludkevich, Bilayer coatings for temporary and long-term corrosion protection of magnesium–AZ31 alloy, *Prog. Org. Coat.* 163 (2022), 106608.
- [79] T. Ishizaki, K. Teshima, Y. Masuda, M. Sakamoto, Liquid phase formation of alkyl- and perfluoro-phosphonic acid derived monolayers on magnesium alloy AZ31 and their chemical properties, *J. Colloid Interface Sci.* 360 (2011) 280–288.
- [80] J.L. Wang, C. Ke, K. Pohl, N. Birbilis, X.B. Chen, The unexpected role of benzotriazole in mitigating magnesium alloy corrosion: a nucleating agent for crystalline nanostructured magnesium hydroxide film, *J. Electrochem. Soc.* 162 (2015) C403–C411.
- [81] Y. Cui, T. Zhang, F. Wang, New understanding on the mechanism of organic inhibitors for magnesium alloy, *Corros. Sci.* (2022), 110118.
- [82] Y. Cui, Z. Yang, T. Zhang, F. Wang, Inhibition mechanism of interaction effect between charged character of inhibitor and rare earth elements for Mg-Gd-Y alloy, *Corros. Sci.* 210 (2023), 110797.
- [83] B. Vaghefinazari, E. Wierzbicka, P. Visser, R. Posner, R. Arrabal, E. Matykina, M. Moledano, C. Blawert, M. Zheludkevich, S. Lamaka, Chromate-free corrosion protection strategies for magnesium alloys-a review: PART I-Pre-treatment and conversion coating, *Materials* 15 (2022).
- [84] G. Rapheal, S. Kumar, N. Scharnagl, C. Blawert, Effect of current density on the microstructure and corrosion properties of plasma electrolytic oxidation (PEO) coatings on AM50 Mg alloy produced in an electrolyte containing clay additives, *Surf. Coat. Technol.* 289 (2016) 150–164.
- [85] E. Piperopoulos, E. Mastronardo, M. Fazio, M. Lanza, S. Galvagno, C. Milone, Enhancing the volumetric heat storage capacity of Mg (OH) 2 by the addition of a cationic surfactant during its synthesis, *Appl. Energy* 215 (2018) 512–522.
- [86] Y.-F. Yang, X.-F. Wu, G.-S. Hu, B.-B. Wang, Effects of stearic acid on synthesis of magnesium hydroxide via direct precipitation, *J. Cryst. Growth* 310 (2008) 3557–3560.
- [87] Y. Gao, H. Wang, Y. Su, Q. Shen, D. Wang, Influence of magnesium source on the crystallization behaviors of magnesium hydroxide, *J. Cryst. Growth* 310 (2008) 3771–3778.
- [88] T.M. Bedair, Y. Heo, J. Ryu, H.M. Bedair, W. Park, D.K. Han, Biocompatible and functional inorganic magnesium ceramic particles for biomedical applications, *Biomater. Sci.* 9 (2021) 1903–1923.
- [89] J. Jia, J. Fan, B. Xu, H. Dong, Microstructure and properties of the super-hydrophobic films fabricated on magnesium alloys, *J. Alloy. Compd.* 554 (2013) 142–146.
- [90] Y. Zhang, S. Tang, J. Hu, T. Lin, Formation mechanism and corrosion resistance of the hydrophobic coating on anodized magnesium, *Corros. Sci.* 111 (2016) 334–343.
- [91] B. Yin, L. Fang, J. Hu, A.-Q. Tang, W.-H. Wei, J. He, Preparation and properties of super-hydrophobic coating on magnesium alloy, *Appl. Surf. Sci.* 257 (2010) 1666–1671.
- [92] M. Jamnongwong, K. Loubiere, N. Dietrich, G. Hébrard, Experimental study of oxygen diffusion coefficients in clean water containing salt, glucose or surfactant: consequences on the liquid-side mass transfer coefficients, *Chem. Eng. J.* 165 (2010) 758–768.
- [93] E. Mölder, T. Tenno, T. Tenno, Research of oxygen mass transfer through the air-water surface at low bulk concentrations of surfactants, *Proc. Est. Acad. Sci.* 58 (2009).
- [94] I. Ciani, D.P. Burt, S. Daniele, P.R. Unwin, Effect of surface pressure on oxygen transfer across molecular monolayers at the air/water interface: scanning electrochemical microscopy investigations using a mercury hemispherical microelectrode probe, *J. Phys. Chem. B* 108 (2004) 3801–3809.
- [95] E.L. Silva, S.V. Lamaka, D. Mei, M.L. Zheludkevich, The reduction of dissolved oxygen during magnesium corrosion, *ChemistryOpen* 7 (2018) 664–668.
- [96] M. Strebl, M. Bruns, S. Virtanen, Editors' choice—respirometric in situ methods for real-time monitoring of corrosion rates: part I. atmospheric corrosion, *J. Electrochem. Soc.* 167 (2020), 021510.
- [97] B. Mingo, R. Arrabal, M. Moledano, Y. Llamazares, E. Matykina, A. Yerokhin, A. Pardo, Influence of sealing post-treatments on the corrosion resistance of PEO coated AZ91 magnesium alloy, *Appl. Surf. Sci.* 433 (2018) 653–667.
- [98] E. Hoque, J. DeRose, P. Hoffmann, B. Bhushan, H. Mathieu, Alkylperfluorosilane self-assembled monolayers on aluminum: a comparison with alkylphosphonate self-assembled monolayers, *J. Phys. Chem. C* 111 (2007) 3956–3962.
- [99] N. Metoki, L. Liu, E. Beilis, N. Eliaz, D. Mandler, Preparation and characterization of alkylphosphonic acid self-assembled monolayers on titanium alloy by chemisorption and electrochemical deposition, *Langmuir* 30 (2014) 6791–6799.
- [100] P.A. Orrillo, S.B. Ribotta, L.M. Gassa, G. Benítez, R.C. Salvarezza, M.E. Vela, Phosphonic acid functionalization of nanostructured Ni-W coatings on steel, *Appl. Surf. Sci.* 433 (2018) 292–299.
- [101] D.K. Kozlica, I. Milošev, Corrosion inhibition of copper and aluminium by 2-mercaptobenzimidazole and octylphosphonic acid—surface pre-treatment and method of film preparation, *Electrochim. Acta* 431 (2022), 141154.

### 5.5.1 Supplementary material

#### S1. IMPs in AZ21 characterization

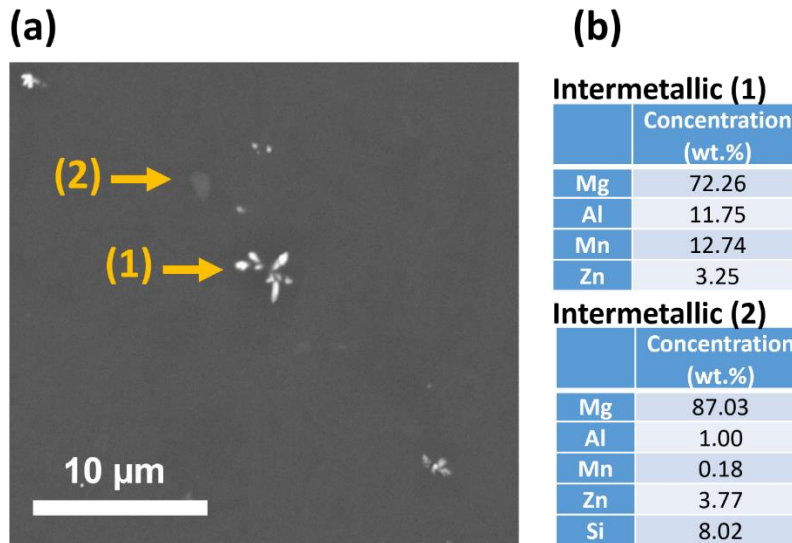


Fig. S1. (a): SEM (backscattered mode) image of intermetallic particles in AZ21 magnesium alloy. (b) EDS result obtained from the two types of intermetallic.

The Backscattered image in Fig. S1 revealed the presence of two different intermetallic particles. Intermetallic particle #1 which appears brighter in the backscattered images and exhibits a relatively high concentration of the alloying elements Al, Mn. Thus, they are likely Al-Mn-based intermetallic particles that have been frequently reported in magnesium alloys of AZ series [18, 176, 177]. The size of these Al-Mn IMPs is considerably smaller than what is typically reported in the literature for AZ31 alloys, which primarily stem from the lower alloying elements in AZ21. Additionally, their needle-like shape clustering at one location resembles the common morphology of reported  $\text{Al}_8\text{Mn}_5$  intermetallic [178]. Intermetallic #2 in Fig. S1, which appeared with lower contrast to the matrix as compared to the Al-Mn-rich intermetallic particles, are rich in Si. The Si-rich particles were found less frequently in the AZ21 surface as compared to the Al-Mn-rich particles.

S2. SEM from bare AZ21 exposed to NaCl solution with and without DP

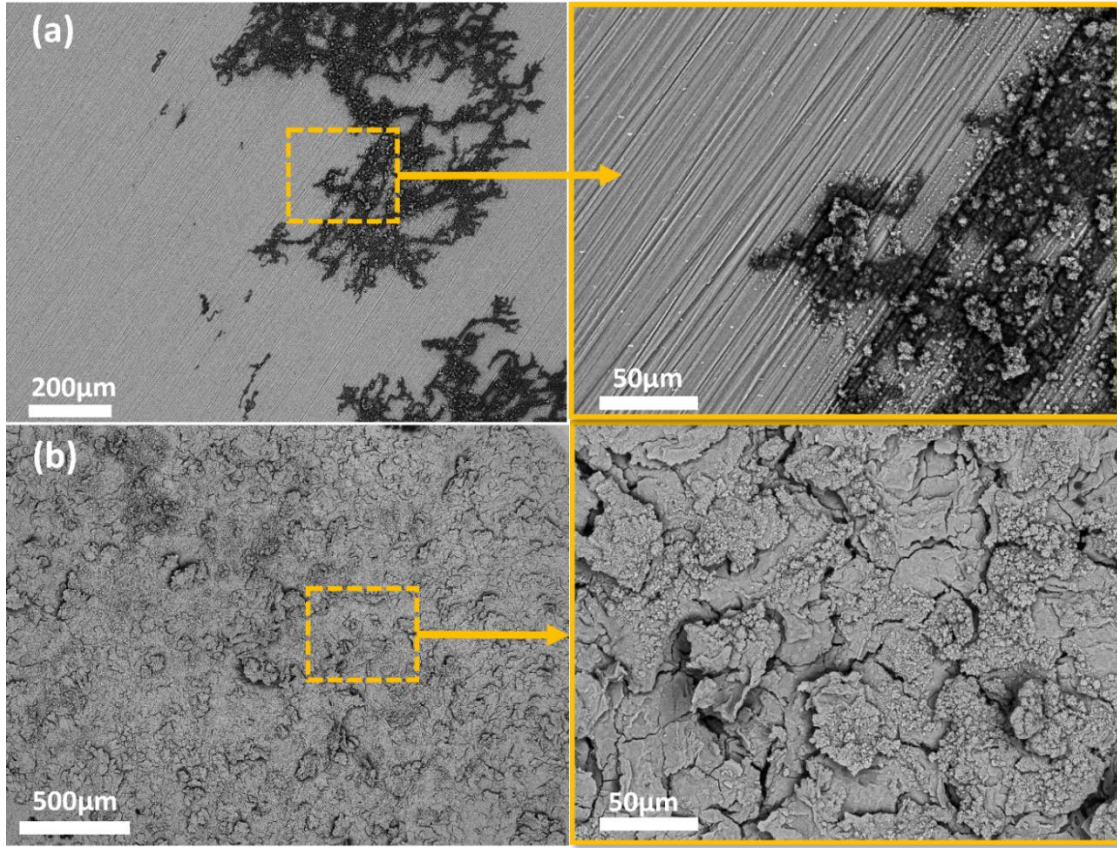


Fig. S2 Surface morphology of AZ21 exposed to NaCl solution after (a) 5 min and (b) 1 day [179].

Fig. S3 illustrates the SEM secondary electron mode images from the surface of AZ21 magnesium substrate after 1 hour of exposure to the NaCl + DP solution. Top and tilted views of the same region are presented to better understand the 3D morphology of the Mg(DP) precipitates. As can be seen, the Mg(DP) precipitates grow upward vertical to the surface of the magnesium substrate at random locations.

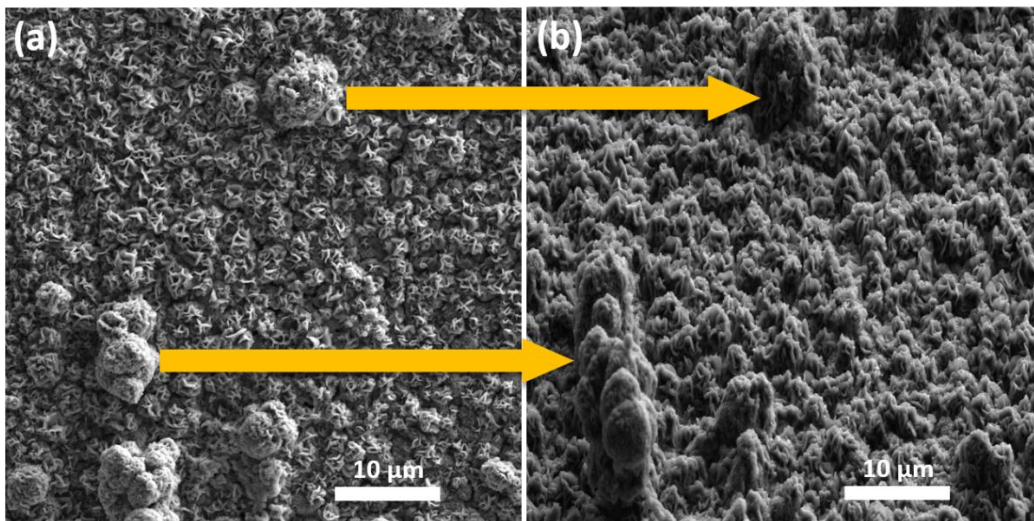


Fig. S3. SEM secondary electron mode images of the AZ21 surface after 1 hour of exposure to the NaCl + DP solution from (a) top view and (b) tilted view. These images are taken by TESCAN LYRA3.

S3. SEM from PEO-coated AZ21 exposed to NaCl + DP solution.

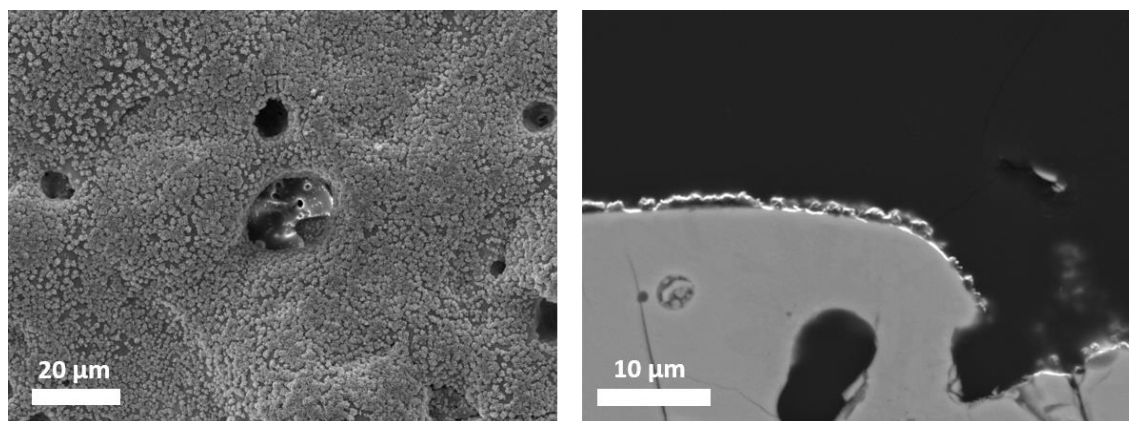


Fig. S4. Top-down (left) and cross-sectional (right) view of PEO coating after 5 min of exposure to the NaCl + DP electrolyte.

S4. Cross-sectional view of the interface between the PEO layer and the Mg

Fig. S5. is complementary to Fig. 9 in the manuscript with additional map of Cl element. As can be seen, the Cl signal appears throughout the maps, even on the Mg substrate, where it is not expected. This suggests that the main Cl signal likely arises from the EDS background noise.

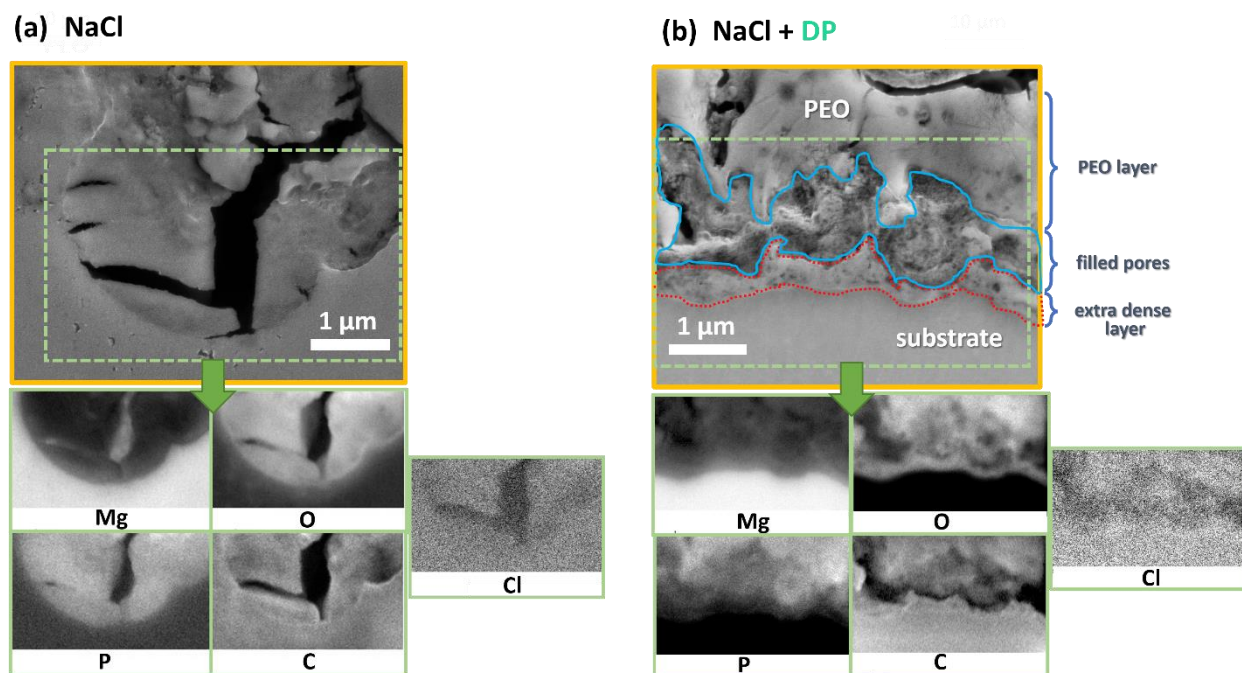


Fig. S5. cross-sectional view of the interface between the PEO layer and the Mg substrate after exposure for 2 days to (a) NaCl solution and (b) NaCl + DP solution. The EDS maps of marked region are provided below each case.

This is further supported when examining of individual EDS spectra of different regions on the maps, as provided in Fig. S6, which do not show any distinct peak around 2.621 KeV corresponds to  $K\alpha$  of Cl. Although there seem to be different contrasts in Cl intensity on the map, they are attributed again to the different background noise levels and different porosity across regions.

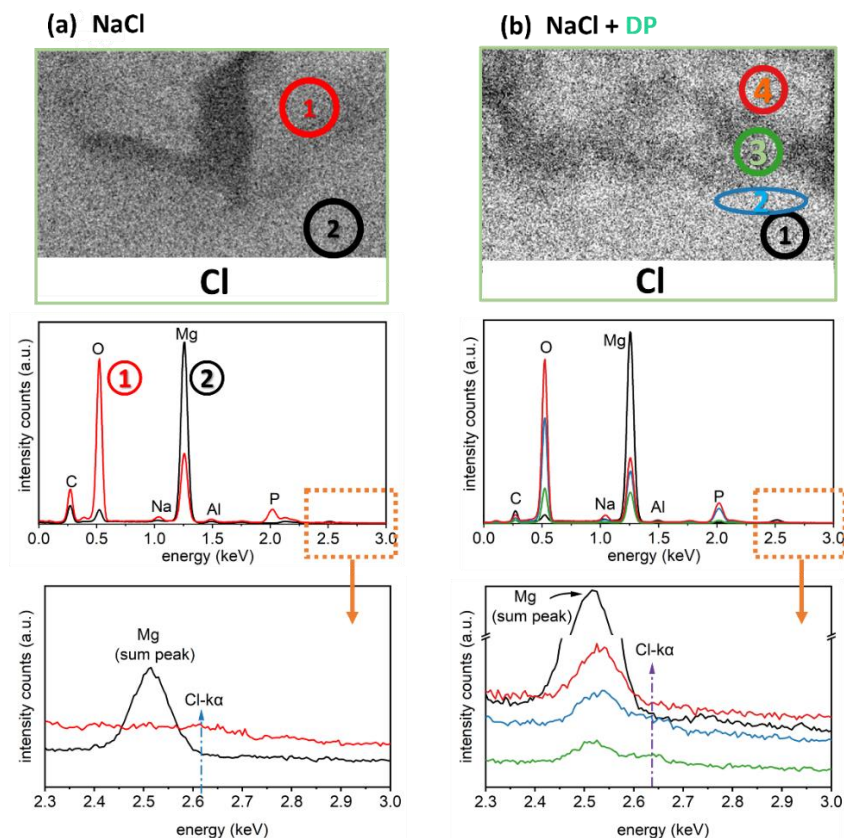


Fig. S6. EDS map of element Cl for the region marked in Fig. S6. Also, for each case (sample exposed to (a) NaCl and (b) NaCl+DP) EDS spectra of marked region are provided below them.

### S5. Preparation of DP(Mg) complex powder

Solution of DP was prepared by the addition of DPA, equivalent to 0.01M, in DI-W. pH of the solution was adjusted to  $7.0 \pm 0.1$  using NaOH solution. The total amount equivalent to 0.01 M of magnesium chloride hexahydrate was gradually added to the DP solution. As a result of complexation between the DP and  $Mg^{2+}$  ions, the insoluble DP(Mg) precipitates and one  $H^+$  is released from DP molecule. The pH of solution was concomitantly adjusted back to around 7 using NaOH solution. The final solution was passed through a filter paper (LLG-filter medium/fast). The remained precipitates were washed out 5 times by passing DI-W through the same filter. The filter paper containing the precipitates was dried out at 60 °C for 24 hours. The collected powder was analyzed by XRD.

### S6. XRD analysis of the corrosion products on bare AZ21

Fig. S7 illustrates the XRD patterns obtained from the surface of AZ21 after 4 days of exposure to the NaCl solution with and without DP. The intensity of the spectra is normalized to the most intense peak, which is the diffraction peak of Mg substrate at  $2\theta$  of  $34.5^\circ$ .

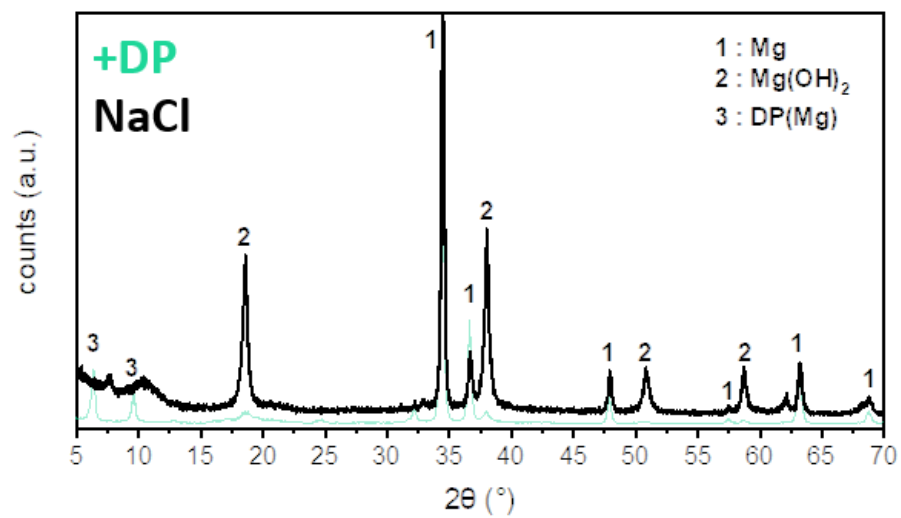


Fig. S7. XRD spectra from the surface of the AZ21 bare magnesium exposed to the NaCl with and without DP after 4 days. The spectra are normalized to the intensity of the Mg at  $2\theta$  of  $34.5^{\circ}$ .

## 6 Discussion

The comprehensive mechanistic investigation into the effects of three compounds on both bare and PEO-coated AZ21 substrates in [section 5](#), provides valuable insights into the development of criteria for effective corrosion inhibitors. The findings also help to distinguish inhibitors that enhance corrosion protection from those that may accelerate degradation.

Based on the results presented in [section 5.3](#), two primary mechanisms have been identified that contribute to the adverse effects of the 2,5PDC-Na inhibitor on the PEO coating on Mg alloys:

- 1- **Formation of soluble magnesium complexes:** The 2,5PDC-Na inhibitor forms soluble magnesium complexes, which degrade the PEO layer and compromise its protective properties.
- 2- **Mechanical stress on the PEO coating:** The formation of a protective layer on the Mg substrate induces mechanical stress on the PEO coating.

Given these interactions between 2,5PDC-Na and both the Mg substrate and the PEO layer, it is hypothesized that similar adverse effects might occur in other PEO systems on a Mg substrate. To test this hypothesis, a silicate-based PEO coating was applied to the AZ21 substrate, and the effect of 2,5PDC-Na on its corrosion protection was assessed using the same methodology as in the screening stage ([section 5.2](#)). Silicate-based PEO coatings primarily consist of MgO and Mg<sub>2</sub>SiO<sub>4</sub> [180-182]. In an aqueous environment, 2,5PDC-Na accelerates the hydration of MgO, as confirmed later in this section. The Mg<sub>2</sub>SiO<sub>4</sub> phase is also expected to lose stability in the presence of 2,5PDC-Na, much like Mg<sub>3</sub>(PO<sub>4</sub>)<sub>2</sub>, due to 2,5PDC-Na's tendency to form soluble complexes with Mg<sup>2+</sup> ions. Therefore, the first mechanism described above can explain the degradation of silicate-based PEO coating. The second mechanism also holds since the substrate remains the same AZ21.

**Figure 6.1** illustrates the visual appearance and EIS spectra of samples coated with the silicate-based PEO and exposed to a 3.5 wt.% NaCl solution, both with and without 0.05M 2,5PDC-Na. Notably, the high-frequency time constant associated with the barrier layer of the PEO coating dissipates more rapidly in the presence of 2,5PDC-Na, indicating a greater deterioration of the coating's barrier properties. Additionally, the lower impedance values observed at low frequencies when 2,5PDC-Na is present further confirms a reduction in the overall corrosion resistance of the coated samples. The visual appearance of the samples after the test also clearly reflects the deteriorative effect of 2,5PDC-Na on the AZ21 substrate coated with the silicate-based PEO coating.

It is noteworthy that both the silicate- and phosphate-based PEO layers investigated in this study contain the MgO phase, which is inherently unstable in aqueous environments. The kinetics of MgO hydration are influenced by the presence of carboxylates in solution [183]. To validate this effect specifically for 2,5PDC-Na, a straightforward experiment was conducted: 10 g of MgO was added to 200 ml of DI water, with and without 0.25M 2,5PDC-Na (initial pH = 7.0±0.1). The mixture was stirred for one hour, filtered through an LLG-filter (medium/fast), and the residual solid was dried in an oven at 80°C before characterization via XRD. The results, presented in **Figure 6.2**, show distinct diffraction peaks corresponding to the MgO phase when exposed only to DI water. However, the addition of 2,5PDC-Na resulted in the complete hydration of MgO to Mg(OH)<sub>2</sub>, confirming that 2,5PDC-Na facilitates this hydration process. It is important to note that 2,5PDC-Na exerts a negligible pH buffering effect within the neutral to alkaline range, with pK<sub>a</sub> values of pK<sub>a1</sub> = 3.0 and pK<sub>a2</sub> = 4.5.

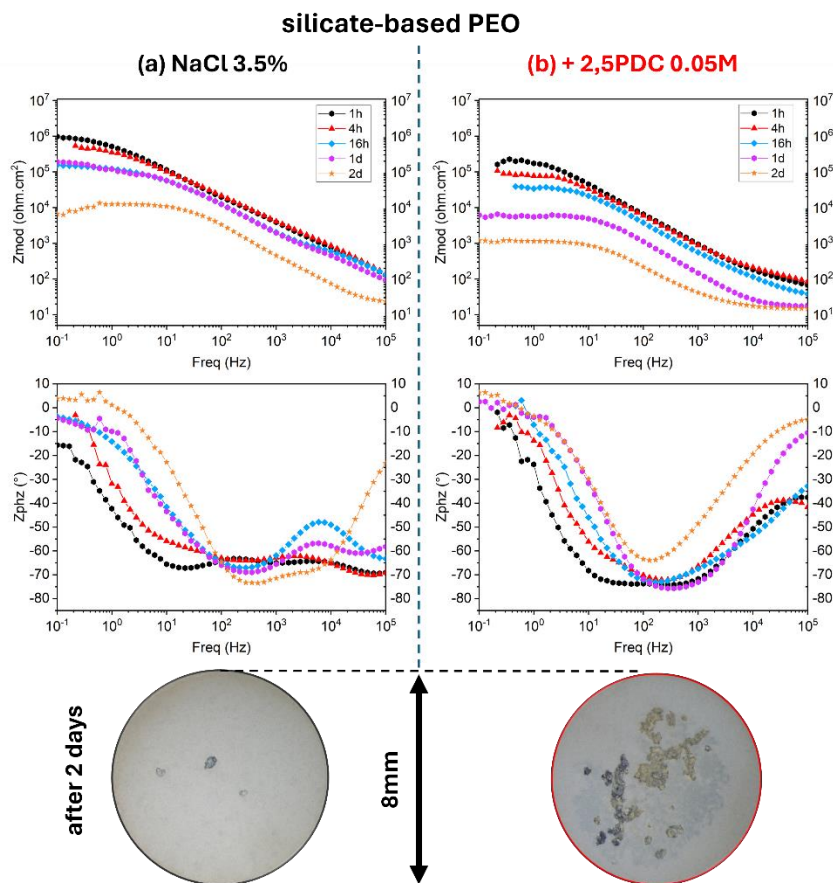


Figure 6.1 EIS spectra of silicate-based PEO-coated AZ21 substrate during exposure to NaCl 3.5 wt.% solution (a) without and (b) with 0.05M 2,5PDC-Na. The visual appearance of the samples at the end of EIS test is provided at the bottom of each case.

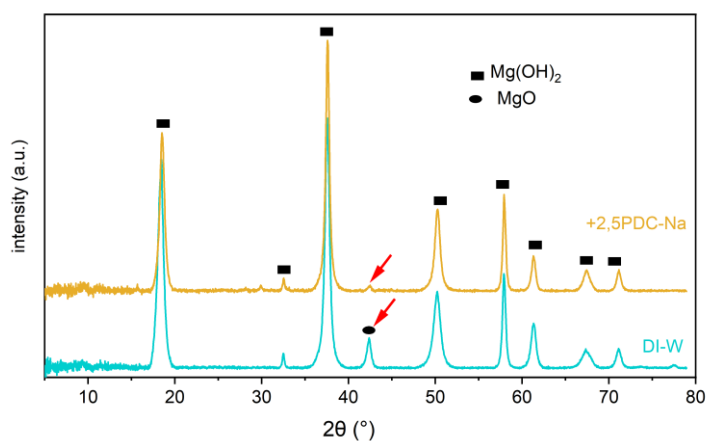


Figure 6.2 Normalized XRD spectra of MgO powder after exposure to DI-W with and without 0.25M 2,5PDC-Na for 1 h. The normalization is based on the highest peak intensity observed at  $2\theta$  value of  $37.6^\circ$ .

In line with the idea that forming soluble complexes with magnesium can result in its adverse effect, chelating complexing agents such as EDTA ( $\log K_{st}^{Mg^{2+}} = 8.6$  [184]) and DTPA ( $\log K_{st}^{Mg^{2+}} = 9$  [185]), which form highly soluble and stable complexes with  $Mg^{2+}$ , are expected to be detrimental to a PEO-coated Mg substrate. As a supporting example, Petrova et al. [186] reported strong etching behavior of DTPA against a PEO-coated AZ91, which consisted of MgO and  $MgAl_2O_4$  phases. Similarly, Chen et al. [187] observed dissolution of a PEO coating composed of MgO and  $Mg_2SiO_4$  on AM50 after exposure to a solution containing EDTA or SSA (5-sulfosalicylic acid,  $\log K_{st}^{Mg^{2+}} = 5.1$  [188]).

From the other hand, the other two effective inhibitors for the PEO-coated AZ21 alloys, 8HQ (section 5.4) and DP (section 5.5), were found to form insoluble complexes with magnesium ions. Additionally, from all the screened chemicals, presented in Figure 5.2 and Figure 5.3, all the top-performing chemicals for the PEO-coated AZ21 substrate - namely DP, 8HQ, NaF, Ca-Acetate, and ODP - exhibited precipitation on the PEO surface. Furthermore, the development of a high-frequency range time constant for these chemicals suggests the formation of an additional layer on the substrate. The insoluble complexes of  $Mg^{2+}$  with DP and 8HQ are discussed in section 5.4 and section 5.5. The fluoride ion ( $F^-$ ) in NaF forms the highly insoluble  $MgF_2$  salt. Although the acetate ion in Ca-acetate forms a soluble complex with  $Mg^{2+}$ , the  $Ca^{2+}$  interacts with the PEO layer, leading to the formation of insoluble hydroxyapatite ( $Ca_5(PO_4)_3OH$ ) and  $CaHPO_4$  [34]. ODP, which has a similar molecular structure to DP but with a longer alkane chain, also led to the formation of an additional layer on the PEO coating, likely resulting from the interaction between ODP and the released  $Mg^{2+}$ .

Given the observed correlation between the solubility of the Mg complex and its effect on the corrosion resistance of PEO-coated samples, an important question arises: Can the solubility of an Mg complex serve as a general criterion for predicting the impact of chemicals on the corrosion of PEO-coated magnesium? Specifically, is a soluble Mg complex consistently associated with adverse effects, and is an insoluble Mg complex sufficient to ensure positive outcomes? It is important to emphasize that we are focusing on measurable positive or negative effects, which are evaluated based on the exposure time required for the PEO coating to fail. As illustrated in Figure 5.2 and Figure 5.3, many of the tested chemicals did not exhibit any significant effects that could be quantified using our assessment approach. To address these questions, different scenarios regarding the solubility of Mg complexes are considered and discussed below.

8HQ is an example of a chemical that forms *highly* insoluble 8HQ(Mg) complex with  $K_{sp}$  reported in the range of  $4-6.8 \times 10^{-16}$  [189-191], which showed an inhibition effect. However, a chemical like oxalate, although known to form an insoluble compound with Mg, has a solubility of 0.38g/l [192] (equivalent to  $K_{sp} = 1.15 \times 10^{-5}$ ) which is orders of magnitude higher than that of 8HQ(Mg). This implies that Mg-oxalate is stable only within a narrower concentration range of its components, potentially offering less protection due to the limited coverage of the PEO and Mg surface. The slow kinetics of PEO degradation and  $Mg^{2+}$  ion diffusion at the PEO/electrolyte interface may result in continuous dissolution of PEO before a critical concentration of  $Mg^{2+}$  is reached for the precipitation of a sparingly soluble compound like Mg-oxalate. Consequently, it can be speculated that a lower  $K_{sp}$  of the formed complex with Mg correlates with more protective properties of the complexant. This might explain why, despite Mg-oxalate being sparingly soluble, oxalate-Na exhibited an adverse effect on the PEO-coated Mg (Figure 5.2 and Figure 5.3). The same reasoning can be applied to explain the adverse effect of tartrate-Na, which forms a sparingly soluble Mg-tartrate with  $K_{sp}$  of  $1.94 \times 10^{-3}$  (calculated based on solubility of 0.76g/100ml [193]).

Therefore, it can be speculated that a chemical that forms a Mg-complex with lower solubility is more likely to be an effective corrosion inhibitor for PEO-coated magnesium. Unfortunately, information on  $K_{sp}$ , as well as stability constants, is available in the literature for only a limited number of chemicals. Indeed, the recent advancements in prediction modeling could help predict the solubility of chemicals [194, 195]. Alternatively, the solubility of complexes can be roughly evaluated through laboratory experiments. This involves gradually adding  $MgCl_2$  to a neutralized solution of the inhibitor at the desired concentration. The pH of the solution should then be gradually adjusted to an alkaline condition, just below the typical pH for  $Mg(OH)_2$  formation (9.5-10.4 [196] in simple NaCl solution). The formation of insoluble complexes can be visually inspected during the experiment.

In conducting this experiment for the tested chemicals shown in **Figure 5.2** and **Figure 5.3**, we found that all chemicals with a positive inhibition effect on PEO-coated Mg formed insoluble complexes with Mg, except for fumarate-Na. Only at a high concentration of 0.5M did fumarate-Na show a slight improvement in the corrosion resistance of the PEO-coated AZ21, delaying PEO failure by just one day. This anomaly may be explained by examining its corrosion inhibition mechanisms more closely. Maltseva et al. [165] investigated the kinetics of  $\text{Mg}(\text{OH})_2$  formation on a Mg substrate using in-situ Raman spectroscopy during exposure to a NaCl solution with and without 2,5PDC-Na and fumarate-Na. Interestingly, they observed an induction period before 2,5PDC-Na slowed the formation of  $\text{Mg}(\text{OH})_2$  as a corrosion product. In contrast, fumarate-Na reduced the formation rate of  $\text{Mg}(\text{OH})_2$  on the Mg substrate from the beginning, with no detectable induction period. This suggests that the initial formation of a protective layer, which may contribute to PEO layer destruction, does not occur with fumarate-Na. Additionally, the corrosion product thickness on the CP-Mg surface was considerably lower in the presence of fumarate compared to 2,5PDC-Na, reducing mechanical stress on the PEO layer [165]. Furthermore, increasing the concentration of fumarate-Na from 0.005M to 0.5M led to higher corrosion resistance in a bare AZ21 sample, as indicated by higher low-frequency impedance values in EIS tests (**Figure 6.3**). In fact, fumarate-Na is one of the few inhibitors reported as a suitable corrosion inhibitor, capable of enhancing the corrosion resistance of PEO coating on Mg [197].

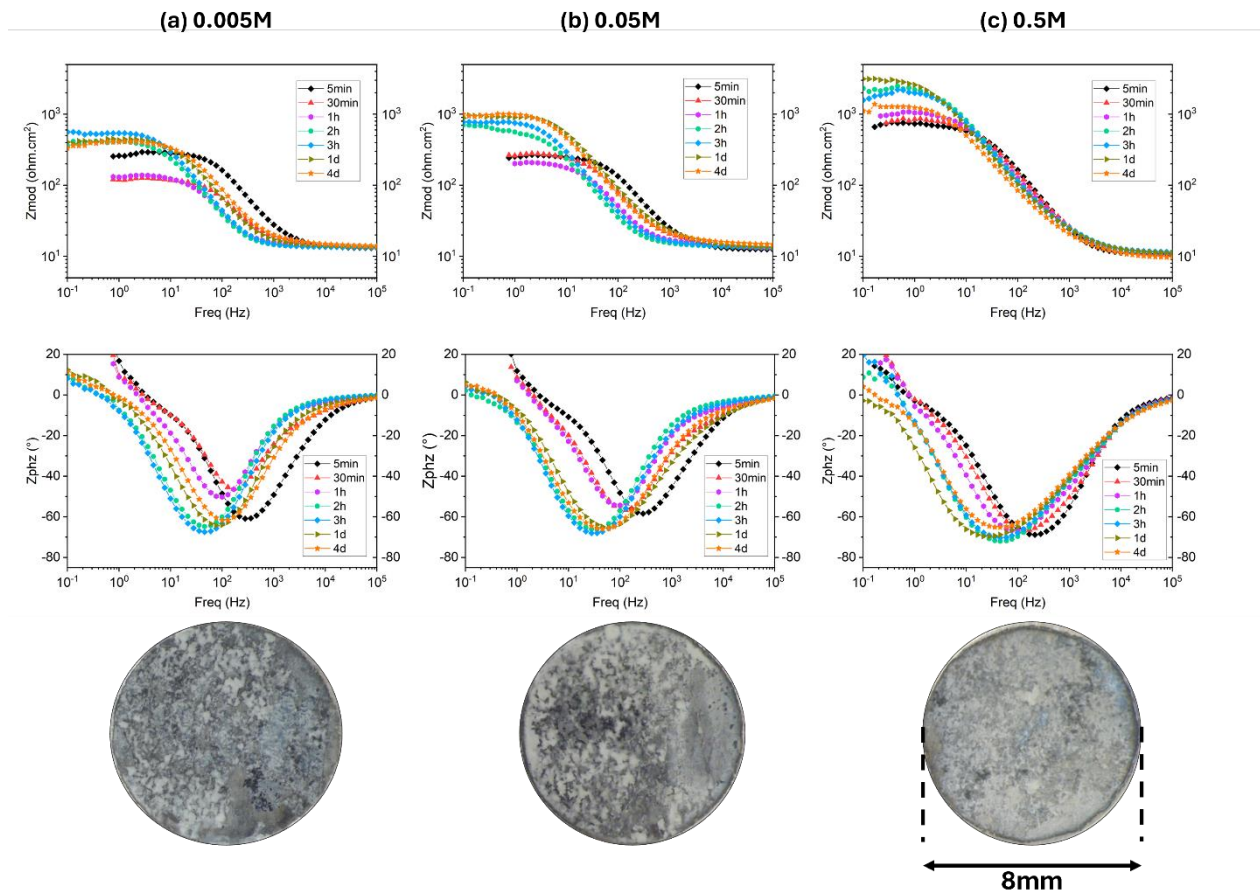


Figure 6.3 Bode plots of EIS spectra obtained from the AZ21 samples exposed to NaCl 3.5 wt.% electrolyte for 4 days. Concentration of fumarate-Na in the solutions: (a) 0.005M, (b) 0.05M, and 0.5M. The appearance of the substrate after 4 days is presented at the bottom of each case.

Another factor to consider is the concentration of inhibitors in the NaCl testing solution. Stearate-Na and SDBS, which form insoluble compounds with magnesium (as confirmed both in the lab and in the literature [173]), did not exhibit any positive effect on the PEO-coated magnesium. This lack of effectiveness could be due to their very low solubility in the 3.5 wt.% NaCl testing solution (<1mM).

Furthermore, in the case of SDBS, Frignani et al. [173] indicate that a relatively high concentration of 1M  $Mg^{2+}$  and an elevated pH of around 9.5 are required to initiate precipitation. While SDBS may adsorb onto the surface quickly, the precipitation process might be slower, as it depends on achieving the necessary magnesium ion concentration and pH level [173].

To conclude, the following key criteria have been identified from the discussion as guidelines for selecting an effective corrosion inhibitor for PEO-coated magnesium:

- Formation of an insoluble compound as the result of interaction between the inhibitor and  $Mg^{2+}$
- A higher degree of insolubility of the compound is preferable
- The inhibitor must have sufficient solubility in the testing medium

Indeed, as demonstrated by the case of fumarate-Na, which did not conform to these criteria, it is important to note that these guidelines apply primarily to chemicals with common inhibition mechanisms in this study. Exceptions to these criteria, involving different inhibition mechanisms, are possible.

### Comparison between 8HQ and DP

Both 8HQ and DP demonstrated the ability to enhance the corrosion resistance of PEO-coated AZ21. However, DP significantly outperformed 8HQ by delaying failure for over 50 days, compared to 11 days for 8HQ. The following analysis compares the characteristics and inhibition mechanisms of these two inhibitors to understand DP's superior performance:

1. The 8HQ(Mg) complex forms only when the pH exceeds 9.4 [190], whereas the DP(Mg) complex is insoluble even at neutral pH, as validated experimentally in the lab. This aligns with the previously defined criterion that greater insolubility of the formed complex is desirable.
2. DP(Mg) precipitates more uniformly on the surface of PEO and bare Mg, while 8HQ(Mg) precipitates are more prone to sporadic nucleation, leading to overgrown, flower-like structures. DP can adsorb onto the metal surface, which helps retard metal dissolution. This results in a lower concentration of metal ions at the PEO/substrate interface, favoring nucleation over crystal growth [198]. Additionally, DP's surfactant properties modify the electrolyte's surface tension, promoting better wetting and spreading on the metal surface, leading to a more uniform and complete substrate coverage [198, 199]. Adding surfactants to conversion coating baths is a common approach to achieve more homogeneous and compact coatings.

These factors mean that 8HQ is more efficient than DP to form a continuous protective layer. This is evident from the SEM images comparing the PEO surface exposed to inhibitor-containing solutions. For DP ([section 5, PART II, supplementary material, Figure S3](#)), the PEO surface is almost fully covered with DP(Mg) precipitates after only 5 minutes of exposure. In contrast, for 8HQ ([section 5, PART II, Figure 11a](#)), even after 1 hour of exposure, no continuous coverage of the PEO surface is achieved.

3. The DP(Mg) layer on the PEO coating exhibited superhydrophobicity, which is attributed to various mechanisms, including the hydrophobic nature of DP and the formation of an air cushion within the porous DP(Mg) morphology [200]. In contrast, 8HQ(Mg) lacks such hydrophobic molecular functionality. Additionally, the nucleation and growth of 8HQ(Mg) result in the formation of overgrown Mg-8HQ crystals, leading to inhomogeneity and reduced air cushion formation.

## 7 Conclusion and Outlook

PEO coatings have attracted significant attention due to their properties such as wear resistance, corrosion protection, thermal barrier capabilities, and ease of functionalization for specific applications. This interest has driven rapid advancements in optimizing PEO coatings for various applications, facilitating their commercialization. Despite the porous microstructure of PEO coatings often being highlighted as a promising feature for accommodating corrosion inhibitors—a concept introduced over 15 years ago [16]—there are still only a few reports demonstrating significant improvement in corrosion resistance through the impregnation of PEO with corrosion inhibitors [8].

The idea of this thesis was also initially launched based on observations that, despite the promise of several inhibitors for bare Mg alloys [8, 17], their effectiveness in enhancing the corrosion resistance of PEO-coated Mg was unsatisfactory. This research focused on understanding why an effective corrosion inhibitor for bare Mg substrate does not necessarily enhance the corrosion resistance of a PEO coating loaded with the inhibitor. Additionally, in-depth investigations into the interactions between effective inhibitors and the PEO/substrate interface led to findings that could guide the identification of more effective corrosion inhibitors and the design of optimized inhibitor-loaded systems. The key findings and conclusions from this thesis are as follows:

1. Over twenty potential chemicals were tested as corrosion inhibitors for both bare and PEO-coated AZ21. The results highlighted that a chemical's ability to inhibit corrosion on bare AZ21 does not necessarily translate to positive effects on PEO-coated AZ21 and may even deteriorate the protective properties of the PEO coating. For instance, while 2,5PDC-Na effectively inhibited corrosion of the AZ21 alloy at concentrations ranging from 0.005M to 0.25M, it significantly accelerated the degradation of the PEO coating.
2. An in-depth investigation into the interactions between 2,5PDC-Na and both bare AZ21 and the PEO coating provided insights into its unexpected adverse effects. Two main mechanisms were identified: firstly, the formation of soluble magnesium complexes by 2,5PDC<sup>2-</sup> accelerates the degradation of the PEO coating, which is primarily composed of MgO and Mg<sub>3</sub>(PO<sub>4</sub>)<sub>2</sub>. Secondly, the formation of a protective layer on the Mg substrate induces mechanical stress on the PEO coating. These detrimental interactions could be expected in other PEO systems on Mg substrates.
3. Among the tested chemicals, 8HQ and DP significantly improved the corrosion resistance of the PEO-coated AZ21, delaying the coating failure by 11 days and over 50 days, respectively. Both chemicals form insoluble compounds with Mg<sup>2+</sup> ions, which can be released due to either Mg substrate corrosion or PEO coating degradation. These precipitates cover the PEO coating and fill its pores, hindering the degradation of the coating and preventing the penetration of corrosive media towards the Mg substrate. For both inhibitors, an additional dense, capacitive layer formed at the substrate/PEO interface, protecting the Mg substrate from corrosion.
4. To design a protective system exposed to an inhibitor-free corrosive medium, a high-concentration micellar solution of DP (0.1M) was incorporated at an elevated temperature (60°C) for 2 hours. This process not only loaded the PEO pores with DP but also enhanced the initial protective properties of the PEO layer by filling its pores with DP(Mg) precipitates. In immersion corrosion tests, the treated sample delayed PEO failure by 10 days, tripling the protective lifespan of the coating. Additionally, a significant reduction in corrosion creep from a defect on the DP-loaded sample in a salt spray test, compared to the reference sample without the inhibitor, confirmed the effectiveness of loading the PEO with DP and demonstrated active corrosion protection.
5. Several factors contributed to DP's superior performance compared to 8HQ in inhibiting corrosion on PEO-coated AZ21, including the formation of a more uniform protective layer on the PEO coating.
6. Based on the findings of this study, key criteria have been identified for selecting effective corrosion inhibitors for PEO-coated magnesium:
  - Formation of an insoluble compound as a result of interaction between the inhibitor and Mg<sup>2+</sup>.
  - A higher degree of insolubility of the compound is preferable.
  - The inhibitor must have sufficient solubility in the testing medium.

- These guidelines primarily apply to chemicals with common inhibition mechanisms as investigated in this study. Exceptions, involving different inhibition mechanisms, are possible.

The established criteria for an effective corrosion inhibitor can help narrow down the list of potential organic chemicals. Many chemicals that form soluble or sparingly soluble compounds with Mg can be excluded from initial consideration, enabling a more efficient screening process in the search for effective corrosion inhibitors. In fact, a project has already been funded in 2024 by the DFG based on a proposal submitted by Hereon researchers supported by the findings of this work. This project will employ an automated, robotic testing system to evaluate the inhibition efficiency of a large number of organic compounds selected in light of this study's findings. In addition to identifying effective corrosion inhibitors and understanding their mechanisms, the compiled dataset will be used to train machine learning models to predict the inhibition efficiency of untested chemicals.

It is also worth noting that alkylphosphonates like DP, and surfactants in general, despite their potential for effective inhibition and their variety, have been relatively underexplored as corrosion inhibitors and merit further investigation

## 8 References

- [1] H. Hornberger, S. Virtanen, A.R. Boccaccini, Biomedical coatings on magnesium alloys – A review, *Acta Biomaterialia*, 8 (2012) 2442-2455. <https://doi.org/10.1016/j.actbio.2012.04.012>.
- [2] M. Yazdimamaghani, M. Razavi, D. Vashae, K. Moharamzadeh, A.R. Boccaccini, L. Tayebi, Porous magnesium-based scaffolds for tissue engineering, *Materials Science and Engineering: C*, 71 (2017) 1253-1266. <https://doi.org/10.1016/j.msec.2016.11.027>.
- [3] Z.-Z. Yin, W.-C. Qi, R.-C. Zeng, X.-B. Chen, C.-D. Gu, S.-K. Guan, Y.-F. Zheng, Advances in coatings on biodegradable magnesium alloys, *Journal of Magnesium and Alloys*, 8 (2020) 42-65. <https://doi.org/10.1016/j.jma.2019.09.008>.
- [4] H. Zhou, B. Liang, H. Jiang, Z. Deng, K. Yu, Magnesium-based biomaterials as emerging agents for bone repair and regeneration: from mechanism to application, *Journal of Magnesium and Alloys*, 9 (2021) 779-804. <https://doi.org/10.1016/j.jma.2021.03.004>.
- [5] D. Zhang, F. Peng, X. Liu, Protection of magnesium alloys: From physical barrier coating to smart self-healing coating, *Journal of Alloys and Compounds*, 853 (2021) 157010. <https://doi.org/10.1016/j.jallcom.2020.157010>.
- [6] B. Vaghefinazari, E. Wierzbicka, P. Visser, R. Posner, R. Arrabal, E. Matykina, M. Mohedano, C. Blawert, M. Zheludkevich, S. Lamaka, Chromate-free corrosion protection strategies for magnesium alloys—a review: PART I—pre-treatment and conversion coating, *Materials*, 15 (2022) 8676.
- [7] X. Chen, N. Birbilis, T. Abbott, Review of corrosion-resistant conversion coatings for magnesium and its alloys, *Corrosion*, 67 (2011) 035005-035001-035005-035016.
- [8] B. Vaghefinazari, E. Wierzbicka, P. Visser, R. Posner, R. Arrabal, E. Matykina, M. Mohedano, C. Blawert, M.L. Zheludkevich, S.V. Lamaka, Chromate-free corrosion protection strategies for magnesium alloys—a review: part III—corrosion inhibitors and combining them with other protection strategies, *Materials*, 15 (2022) 8489.
- [9] R.-G. Hu, S. Zhang, J.-F. Bu, C.-J. Lin, G.-L. Song, Recent progress in corrosion protection of magnesium alloys by organic coatings, *Progress in Organic Coatings*, 73 (2012) 129-141. <https://doi.org/10.1016/j.porgcoat.2011.10.011>.
- [10] S. Heise, S. Virtanen, A.R. Boccaccini, Tackling Mg alloy corrosion by natural polymer coatings—A review, *Journal of Biomedical Materials Research Part A*, 104 (2016) 2628-2641.
- [11] A. Bordbar-Khiabani, B. Yarmand, S. Sharifi-Asl, M. Mozafari, Improved corrosion performance of biodegradable magnesium in simulated inflammatory condition via drug-loaded plasma electrolytic oxidation coatings, *Materials Chemistry and Physics*, 239 (2020) 122003. <https://doi.org/10.1016/j.matchemphys.2019.122003>.
- [12] L. Moreno, C. Wang, S.V. Lamaka, M.L. Zheludkevich, J. Rodríguez-Hernández, R. Arrabal, E. Matykina, Ciprofloxacin release and corrosion behaviour of a hybrid PEO/PCL coating on Mg<sub>3</sub>Zn<sub>0.4</sub>Ca alloy, *Journal of Functional Biomaterials*, 14 (2023) 65.
- [13] K. Bai, Y. Zhang, Z. Fu, C. Zhang, X. Cui, E. Meng, S. Guan, J. Hu, Fabrication of chitosan/magnesium phosphate composite coating and the in vitro degradation properties of coated magnesium alloy, *Materials Letters*, 73 (2012) 59-61. <https://doi.org/10.1016/j.matlet.2011.12.102>.
- [14] J. Joo, D. Kim, H.-S. Moon, K. Kim, J. Lee, Durable anti-corrosive oil-impregnated porous surface of magnesium alloy by plasma electrolytic oxidation with hydrothermal treatment, *Applied Surface Science*, 509 (2020) 145361. <https://doi.org/10.1016/j.apsusc.2020.145361>.

- [15] Y. Shin, K. Bae, S. Lee, H. Kim, D. Shin, D. Kim, E. Choi, H.-S. Moon, J. Lee, Healable Anti-Corrosive and Wear-Resistant Silicone-Oil-Impregnated Porous Oxide Layer of Aluminum Alloy by Plasma Electrolytic Oxidation, *Nanomaterials*, 13 (2023) 2582.
- [16] S.V. Lamaka, G. Knörrschild, D.V. Snihirova, M.G. Taryba, M.L. Zheludkevich, M.G.S. Ferreira, Complex anticorrosion coating for ZK30 magnesium alloy, *Electrochimica Acta*, 55 (2009) 131-141. <https://doi.org/10.1016/j.electacta.2009.08.018>.
- [17] S.V. Lamaka, B. Vaghefinazari, D. Mei, R.P. Petrauskas, D. Höche, M.L. Zheludkevich, Comprehensive screening of Mg corrosion inhibitors, *Corrosion Science*, 128 (2017) 224-240. <https://doi.org/10.1016/j.corsci.2017.07.011>.
- [18] A.G. Rakoch, E.P. Monakhova, Z.V. Khabibullina, M. Serdechnova, C. Blawert, M.L. Zheludkevich, A.A. Gladkova, Plasma electrolytic oxidation of AZ31 and AZ91 magnesium alloys: Comparison of coatings formation mechanism, *Journal of Magnesium and Alloys*, 8 (2020) 587-600. <https://doi.org/10.1016/j.jma.2020.06.002>.
- [19] M. Mohedano, R. Arrabal, B. Mingo, A. Pardo, E. Matykina, Role of particle type and concentration on characteristics of PEO coatings on AM50 magnesium alloy, *Surface and Coatings Technology*, 334 (2018) 328-335. <https://doi.org/10.1016/j.surfcoat.2017.11.058>.
- [20] G.B. Darband, M. Aliofkhazraei, P. Hamghalam, N. Valizade, Plasma electrolytic oxidation of magnesium and its alloys: Mechanism, properties and applications, *Journal of Magnesium and Alloys*, 5 (2017) 74-132.
- [21] R.O. Hussein, X. Nie, D.O. Northwood, An investigation of ceramic coating growth mechanisms in plasma electrolytic oxidation (PEO) processing, *Electrochimica Acta*, 112 (2013) 111-119. <https://doi.org/10.1016/j.electacta.2013.08.137>.
- [22] S. Ikonopisov, Theory of electrical breakdown during formation of barrier anodic films, *Electrochimica Acta*, 22 (1977) 1077-1082. [https://doi.org/10.1016/0013-4686\(77\)80042-X](https://doi.org/10.1016/0013-4686(77)80042-X).
- [23] R. Hussein, X. Nie, D. Northwood, The application of plasma electrolytic oxidation (PEO) to the production of corrosion resistant coatings on magnesium alloys: a review, *Corrosion and Materials*, 38 (2013) 55-65.
- [24] M. Mohedano, X. Lu, E. Matykina, C. Blawert, R. Arrabal, M.L. Zheludkevich, Plasma Electrolytic Oxidation (PEO) of Metals and Alloys, in: K. Wandelt (Ed.) *Encyclopedia of Interfacial Chemistry*, Elsevier, Oxford, 2018, pp. 423-438.
- [25] A.L. Yerokhin, X. Nie, A. Leyland, A. Matthews, S.J. Dowey, Plasma electrolysis for surface engineering, *Surface and Coatings Technology*, 122 (1999) 73-93. [https://doi.org/10.1016/S0257-8972\(99\)00441-7](https://doi.org/10.1016/S0257-8972(99)00441-7).
- [26] G. Sundararajan, L.R. Krishna, Mechanisms underlying the formation of thick alumina coatings through the MAO coating technology, *Surface and Coatings Technology*, 167 (2003) 269-277.
- [27] L.O. Snizhko, A.L. Yerokhin, A. Pilkington, N.L. Gurevina, D.O. Misnyankin, A. Leyland, A. Matthews, Anodic processes in plasma electrolytic oxidation of aluminium in alkaline solutions, *Electrochimica Acta*, 49 (2004) 2085-2095. <https://doi.org/10.1016/j.electacta.2003.11.027>.
- [28] R. Hussein, X. Nie, D. Northwood, A. Yerokhin, A. Matthews, Spectroscopic study of electrolytic plasma and discharging behaviour during the plasma electrolytic oxidation (PEO) process, *Journal of Physics D: Applied Physics*, 43 (2010) 105203.
- [29] Y. Cheng, E. Matykina, P. Skeldon, G. Thompson, Characterization of plasma electrolytic oxidation coatings on Zircaloy-4 formed in different electrolytes with AC current regime, *Electrochimica Acta*, 56 (2011) 8467-8476. <https://doi.org/10.1016/j.electacta.2011.07.034>.
- [30] Y.-I. Cheng, Z.-g. Xue, Q. Wang, X.-Q. Wu, E. Matykina, P. Skeldon, G.E. Thompson, New findings on properties of plasma electrolytic oxidation coatings from study of an Al-Cu-Li alloy, *Electrochimica Acta*, 107 (2013) 358-378. <https://doi.org/10.1016/j.electacta.2013.06.022>.
- [31] X. Lu, C. Blawert, K.U. Kainer, M.L. Zheludkevich, Investigation of the formation mechanisms of plasma electrolytic oxidation coatings on Mg alloy AM50 using particles, *Electrochimica Acta*, 196 (2016) 680-691. <https://doi.org/10.1016/j.electacta.2016.03.042>.
- [32] L. Zhu, Z. Guo, Y. Zhang, Z. Li, M. Sui, A mechanism for the growth of a plasma electrolytic oxide coating on Al, *Electrochimica Acta*, 208 (2016) 296-303.
- [33] P. Zhang, X. Nie, D.O. Northwood, Influence of coating thickness on the galvanic corrosion properties of Mg oxide in an engine coolant, *Surface and Coatings Technology*, 203 (2009) 3271-3277. <https://doi.org/10.1016/j.surfcoat.2009.04.012>.
- [34] E. Wierzbicka, B. Vaghefinazari, M. Mohedano, P. Visser, R. Posner, C. Blawert, M. Zheludkevich, S. Lamaka, E. Matykina, R. Arrabal, Chromate-free corrosion protection strategies for magnesium alloys—a review: part II—PEO and anodizing, *Materials*, 15 (2022) 8515.

- [35] D. Veys-Renaux, E. Rocca, G. Henrion, Micro-arc oxidation of AZ91 Mg alloy: An in-situ electrochemical study, *Electrochemistry communications*, 31 (2013) 42-45.
- [36] A. Ghasemi, V.S. Raja, C. Blawert, W. Dietzel, K.U. Kainer, The role of anions in the formation and corrosion resistance of the plasma electrolytic oxidation coatings, *Surface and Coatings Technology*, 204 (2010) 1469-1478. <https://doi.org/10.1016/j.surfcoat.2009.09.069>.
- [37] X. Lu, S.P. Sah, N. Scharnagl, M. Störmer, M. Starykevich, M. Mohedano, C. Blawert, M.L. Zheludkevich, K.U. Kainer, Degradation behavior of PEO coating on AM50 magnesium alloy produced from electrolytes with clay particle addition, *Surface and Coatings Technology*, 269 (2015) 155-169. <https://doi.org/10.1016/j.surfcoat.2014.11.027>.
- [38] E. Wierzbicka, B. Vaghefinazari, S.V. Lamaka, M.L. Zheludkevich, M. Mohedano, L. Moreno, P. Visser, A. Rodriguez, J. Velasco, R. Arrabal, E. Matykina, Flash-PEO as an alternative to chromate conversion coatings for corrosion protection of Mg alloy, *Corrosion Science*, 180 (2021) 109189. <https://doi.org/10.1016/j.corsci.2020.109189>.
- [39] E. Wierzbicka, M. Mohedano, E. Matykina, R. Arrabal, Design and multidimensional screening of flash-PEO coatings for Mg in comparison to commercial chromium (VI) conversion coating, *Metals*, 11 (2021) 337.
- [40] E. Wierzbicka, B. Pillado, M. Mohedano, R. Arrabal, E. Matykina, Calcium doped flash-PEO coatings for corrosion protection of Mg alloy, *Metals*, 10 (2020) 916.
- [41] K. Dong, Y. Song, D. Shan, E.-H. Han, Corrosion behavior of a self-sealing pore micro-arc oxidation film on AM60 magnesium alloy, *Corrosion Science*, 100 (2015) 275-283. <https://doi.org/10.1016/j.corsci.2015.08.004>.
- [42] D. Shen, H. Ma, C. Guo, J. Cai, G. Li, D. He, Q. Yang, Effect of cerium and lanthanum additives on plasma electrolytic oxidation of AZ31 magnesium alloy, *Journal of Rare Earths*, 31 (2013) 1208-1213. [https://doi.org/10.1016/S1002-0721\(12\)60428-1](https://doi.org/10.1016/S1002-0721(12)60428-1).
- [43] Y. Song, K. Dong, D. Shan, E.-H. Han, Investigation of a novel self-sealing pore micro-arc oxidation film on AM60 magnesium alloy, *Journal of Magnesium and Alloys*, 1 (2013) 82-87. <https://doi.org/10.1016/j.jma.2013.02.009>.
- [44] M. Tang, Z. Feng, G. Li, Z. Zhang, R. Zhang, High-corrosion resistance of the microarc oxidation coatings on magnesium alloy obtained in potassium fluotitanate electrolytes, *Surface and Coatings Technology*, 264 (2015) 105-113. <https://doi.org/10.1016/j.surfcoat.2015.01.013>.
- [45] J. Liang, P.B. Srinivasan, C. Blawert, W. Dietzel, Comparison of electrochemical corrosion behaviour of MgO and ZrO<sub>2</sub> coatings on AM50 magnesium alloy formed by plasma electrolytic oxidation, *Corrosion Science*, 51 (2009) 2483-2492. <https://doi.org/10.1016/j.corsci.2009.06.034>.
- [46] X. Lu, M. Mohedano, C. Blawert, E. Matykina, R. Arrabal, K.U. Kainer, M.L. Zheludkevich, Plasma electrolytic oxidation coatings with particle additions—A review, *Surface and Coatings Technology*, 307 (2016) 1165-1182.
- [47] B. Han, Y. Yang, J. Li, H. Deng, C. Yang, Effects of the Graphene Additive on the Corrosion Resistance of the Plasma Electrolytic Oxidation (PEO) Coating on the AZ91 Magnesium Alloy, *International Journal of Electrochemical Science*, 13 (2018) 9166-9182. <https://doi.org/10.20964/2018.09.06>.
- [48] A.S.H. Makhlof, H. Soliman, Chapter 18 - Effect of Nano-Additives (Al<sub>2</sub>O<sub>3</sub> and NaF) on the Performance of Ceramic Coatings Formed by Microarc Oxidation on Magnesium Alloys, in: A.S.H. Makhlof, D. Scharnweber (Eds.) *Handbook of Nanoceramic and Nanocomposite Coatings and Materials*, Butterworth-Heinemann, 2015, pp. 389-401.
- [49] C. Blawert, S.P. Sah, J. Liang, Y. Huang, D. Höche, Role of sintering and clay particle additions on coating formation during PEO processing of AM50 magnesium alloy, *Surface and Coatings Technology*, 213 (2012) 48-58. <https://doi.org/10.1016/j.surfcoat.2012.10.013>.
- [50] Y. Chen, X. Lu, C. Blawert, M.L. Zheludkevich, T. Zhang, F. Wang, Formation of self-lubricating PEO coating via in-situ incorporation of PTFE particles, *Surface and Coatings Technology*, 337 (2018) 379-388. <https://doi.org/10.1016/j.surfcoat.2018.01.022>.
- [51] Y. Qin, D. Xiong, J. Li, Q. Jin, Y. He, R. Zhang, Y. Zou, Adaptive-lubricating PEO/Ag/MoS<sub>2</sub> multilayered coatings for Ti6Al4V alloy at elevated temperature, *Materials & Design*, 107 (2016) 311-321. <https://doi.org/10.1016/j.matdes.2016.06.053>.
- [52] A. Fattah-alhosseini, R. Chaharmahali, K. Babaei, Impressive strides in amelioration of corrosion and wear behaviors of Mg alloys using applied polymer coatings on PEO porous coatings: A review, *Journal of Magnesium and Alloys*, 10 (2022) 1171-1190. <https://doi.org/10.1016/j.jma.2022.01.015>.
- [53] X. Lu, C. Blawert, M. Mohedano, N. Scharnagl, M.L. Zheludkevich, K.U. Kainer, Influence of electrical parameters on particle uptake during plasma electrolytic oxidation processing of AM50 Mg alloy, *Surface and Coatings Technology*, 289 (2016) 179-185. <https://doi.org/10.1016/j.surfcoat.2016.02.006>.

- [54] M. Mohedano, R. Guzman, R. Arrabal, J.L. López Lacomba, E. Matykina, Bioactive plasma electrolytic oxidation coatings—the role of the composition, microstructure, and electrochemical stability, *Journal of Biomedical Materials Research Part B: Applied Biomaterials*, 101 (2013) 1524-1537.
- [55] Y. Bai, K.-A. Kim, I.S. Park, S.J. Lee, T.S. Bae, M.H. Lee, In situ composite coating of titania–hydroxyapatite on titanium substrate by micro-arc oxidation coupled with electrophoretic deposition processing, *Materials Science and Engineering: B*, 176 (2011) 1213-1221.
- [56] Y. Bai, I.S. Park, H.H. Park, T.S. Bae, M.H. Lee, Formation of bioceramic coatings containing hydroxyapatite on the titanium substrate by micro-arc oxidation coupled with electrophoretic deposition, *Journal of Biomedical Materials Research Part B: Applied Biomaterials*, 95 (2010) 365-373.
- [57] Q. Han, Y. Li, X. Lu, D. Mei, Q. Chen, T. Zhang, F. Wang, Fabrication of Ag containing antibacterial PEO coatings on pure Mg, *Materials Letters*, 293 (2021) 129731. <https://doi.org/10.1016/j.matlet.2021.129731>.
- [58] S. Ignjatović, Blawert, C., Serdechnova, M., Karpushenkov, S., Damjanović, M., Karlova, P., Wieland, D.C.F., Starykevich, M., Stojanović, S., Damjanović-Vasilić, L., Zheludkevich, M.L., Formation of multi-functional TiO<sub>2</sub> surfaces on AA2024 alloy using plasma electrolytic oxidation, *Applied Surface Science*, (2021) 148875. doi:10.1016/j.apsusc.2020.148875.
- [59] K. Yu, P. Li, Q. Han, Q. Wang, S.A. Karpushenkov, X. Lu, O.V. Ignatenko, Investigation of biodegradability, cytocompatibility and antibacterial property of plasma electrolytic oxidation coating on Mg, *Surfaces and Interfaces*, 30 (2022) 101840. <https://doi.org/10.1016/j.surf.2022.101840>.
- [60] R. Arrabal, E. Matykina, P. Skeldon, G.E. Thompson, Incorporation of zirconia particles into coatings formed on magnesium by plasma electrolytic oxidation, *Journal of Materials Science*, 43 (2008) 1532-1538. 10.1007/s10853-007-2360-9.
- [61] A. Seyfoori, S. Mirdamadi, Z.S. Seyedraoufi, A. Khavandi, M. Aliofkhaezai, Synthesis of biphasic calcium phosphate containing nanostructured films by micro arc oxidation on magnesium alloy, *Materials Chemistry and Physics*, 142 (2013) 87-94. <https://doi.org/10.1016/j.matchemphys.2013.06.045>.
- [62] K.M. Lee, K.R. Shin, S. Namgung, B. Yoo, D.H. Shin, Electrochemical response of ZrO<sub>2</sub>-incorporated oxide layer on AZ91 Mg alloy processed by plasma electrolytic oxidation, *Surface and Coatings Technology*, 205 (2011) 3779-3784. <https://doi.org/10.1016/j.surfcoat.2011.01.033>.
- [63] M. O'Hara, S.C. Troughton, R. Francis, T.W. Clyne, The incorporation of particles suspended in the electrolyte into plasma electrolytic oxidation coatings on Ti and Al substrates, *Surface and Coatings Technology*, 385 (2020) 125354. <https://doi.org/10.1016/j.surfcoat.2020.125354>.
- [64] S.C. Troughton, A. Nominé, A.V. Nominé, G. Henrion, T.W. Clyne, Synchronised electrical monitoring and high speed video of bubble growth associated with individual discharges during plasma electrolytic oxidation, *Applied Surface Science*, 359 (2015) 405-411. <https://doi.org/10.1016/j.apsusc.2015.10.124>.
- [65] A. Sobolev, M. Zinigrad, K. Borodianskiy, Ceramic coating on Ti-6Al-4V by plasma electrolytic oxidation in molten salt: Development and characterization, *Surface and Coatings Technology*, 408 (2021) 126847.
- [66] S. Sela, K. Borodianskiy, Synthesis of ceramic surface on Zr alloy using plasma electrolytic oxidation in molten salt, *Surfaces and Interfaces*, 36 (2023) 102533.
- [67] A. Sobolev, D. Bogachev, M. Zinigrad, K. Borodianskiy, Evolution of corrosion on microstructure of ceramic coating produced by plasma electrolytic oxidation in molten salt, *Ceramics International*, 48 (2022) 10990-10998. <https://doi.org/10.1016/j.ceramint.2021.12.318>.
- [68] Y. Yuferov, K. Borodianskiy, Ca/P in situ introduction for enhancing coating biocompatibility via plasma electrolytic oxidation in low-temperature molten salt, *Open Ceramics*, 18 (2024) 100602. <https://doi.org/10.1016/j.oceram.2024.100602>.
- [69] A. Sobolev, A. Kossenko, M. Zinigrad, K. Borodianskiy, An investigation of oxide coating synthesized on an aluminum alloy by plasma electrolytic oxidation in molten salt, *Applied Sciences*, 7 (2017) 889.
- [70] A. Sobolev, A. Kossenko, M. Zinigrad, K. Borodianskiy, Comparison of plasma electrolytic oxidation coatings on Al alloy created in aqueous solution and molten salt electrolytes, *Surface and Coatings Technology*, 344 (2018) 590-595. <https://doi.org/10.1016/j.surfcoat.2018.03.091>.
- [71] A. Sobolev, I. Wolicki, A. Kossenko, M. Zinigrad, K. Borodianskiy, Coating formation on Ti-6Al-4V alloy by micro arc oxidation in molten salt, *Materials*, 11 (2018) 1611.
- [72] A. Schwartz, A. Kossenko, M. Zinigrad, Y. Gofer, K. Borodianskiy, A. Sobolev, Hydroxyapatite coating on Ti-6Al-7Nb alloy by plasma electrolytic oxidation in salt-based electrolyte, *Materials*, 15 (2022) 7374.

- [73] A.B. Rogov, Y. Huang, D. Shore, A. Matthews, A. Yerokhin, Toward rational design of ceramic coatings generated on valve metals by plasma electrolytic oxidation: The role of cathodic polarisation, *Ceramics International*, 47 (2021) 34137-34158. <https://doi.org/10.1016/j.ceramint.2021.08.324>.
- [74] J.M. Runge, *The metallurgy of anodizing aluminum*, Cham: Springer International Publishing, (2018).
- [75] V. Malyshev, Coating formation by anodic-cathodic microarc oxidation, *Protection of metals*, 32 (1996) 607-611.
- [76] R. Arrabal, E. Matykina, T. Hashimoto, P. Skeldon, G.E. Thompson, Characterization of AC PEO coatings on magnesium alloys, *Surface and Coatings Technology*, 203 (2009) 2207-2220. <https://doi.org/10.1016/j.surfcoat.2009.02.011>.
- [77] R.O. Hussein, P. Zhang, X. Nie, Y. Xia, D.O. Northwood, The effect of current mode and discharge type on the corrosion resistance of plasma electrolytic oxidation (PEO) coated magnesium alloy AJ62, *Surface and Coatings Technology*, 206 (2011) 1990-1997. <https://doi.org/10.1016/j.surfcoat.2011.08.060>.
- [78] T.W. Clyne, S.C. Troughton, A review of recent work on discharge characteristics during plasma electrolytic oxidation of various metals, *International materials reviews*, 64 (2019) 127-162.
- [79] B. Zou, G.-h. Lü, G.-l. Zhang, Y.-y. Tian, Effect of current frequency on properties of coating formed by microarc oxidation on AZ91D magnesium alloy, *Transactions of Nonferrous Metals Society of China*, 25 (2015) 1500-1505. [https://doi.org/10.1016/S1003-6326\(15\)63751-7](https://doi.org/10.1016/S1003-6326(15)63751-7).
- [80] P. Su, X. Wu, Z. Jiang, Y. Guo, Effects of working frequency on the structure and corrosion resistance of plasma electrolytic oxidation coatings formed on a ZK60 Mg alloy, *International Journal of Applied Ceramic Technology*, 8 (2011) 112-119.
- [81] I.J. Hwang, D.Y. Hwang, Y.G. Ko, D.H. Shin, Correlation between current frequency and electrochemical properties of Mg alloy coated by micro arc oxidation, *Surface and Coatings Technology*, 206 (2012) 3360-3365. <https://doi.org/10.1016/j.surfcoat.2012.01.041>.
- [82] L. Magniez, C.D.S. Tusch, S. Fontana, S. Cahen, J. Martin, C. Hérold, G. Henrion, Plasma electrolytic oxidation of aluminium in electrolytes containing various concentrations of carbon black nanoparticles, *Surface and Coatings Technology*, 473 (2023) 129990. <https://doi.org/10.1016/j.surfcoat.2023.129990>.
- [83] A. Nominé, J. Martin, C. Noël, G. Henrion, T. Belmonte, I.V. Bardin, P. Lukeš, Surface charge at the oxide/electrolyte interface: toward optimization of electrolyte composition for treatment of aluminum and magnesium by plasma electrolytic oxidation, *Langmuir*, 32 (2016) 1405-1409.
- [84] A. Nominé, J. Martin, G. Henrion, T. Belmonte, Effect of cathodic micro-discharges on oxide growth during plasma electrolytic oxidation (PEO), *Surface and Coatings Technology*, 269 (2015) 131-137. <https://doi.org/10.1016/j.surfcoat.2015.01.076>.
- [85] J. Martin, A. Nominé, F. Brochard, J.L. Briançon, C. Noël, T. Belmonte, T. Czerwicz, G. Henrion, Delay in micro-discharges appearance during PEO of Al: Evidence of a mechanism of charge accumulation at the electrolyte/oxide interface, *Applied Surface Science*, 410 (2017) 29-41. <https://doi.org/10.1016/j.apsusc.2017.03.088>.
- [86] A. Buling, J. Zerrer, Increasing the application fields of magnesium by ultracera<sup>®</sup>: Corrosion and wear protection by plasma electrolytical oxidation (PEO) of Mg alloys, *Surface and Coatings Technology*, 369 (2019) 142-155. <https://doi.org/10.1016/j.surfcoat.2019.04.025>.
- [87] A.B. Rogov, Smart arbitrary waveform generator with digital feedback control for high-voltage electrochemistry, *Instruments*, 3 (2019) 13.
- [88] Y. Guo, A. Rogov, A. Hird, B. Mingo, A. Matthews, A. Yerokhin, Plasma electrolytic oxidation of magnesium by sawtooth pulse current, *Surface and Coatings Technology*, 429 (2022) 127938. <https://doi.org/10.1016/j.surfcoat.2021.127938>.
- [89] R.O. Hussein, D.O. Northwood, X. Nie, The influence of pulse timing and current mode on the microstructure and corrosion behaviour of a plasma electrolytic oxidation (PEO) coated AM60B magnesium alloy, *Journal of Alloys and Compounds*, 541 (2012) 41-48. <https://doi.org/10.1016/j.jallcom.2012.07.003>.
- [90] E. Matykina, R. Arrabal, M. Mohedano, B. Mingo, J. Gonzalez, A. Pardo, M.C. Merino, Recent advances in energy efficient PEO processing of aluminium alloys, *Transactions of Nonferrous Metals Society of China*, 27 (2017) 1439-1454. [https://doi.org/10.1016/S1003-6326\(17\)60166-3](https://doi.org/10.1016/S1003-6326(17)60166-3).
- [91] A.L. Yerokhin, A. Shatrov, V. Samsonov, P. Shashkov, A. Pilkington, A. Leyland, A. Matthews, Oxide ceramic coatings on aluminium alloys produced by a pulsed bipolar plasma electrolytic oxidation process, *Surface and Coatings Technology*, 199 (2005) 150-157. <https://doi.org/10.1016/j.surfcoat.2004.10.147>.

- [92] Q. Dou, W. Li, G. Zhang, X. Wan, Preparation and characterisation of black ceramic coating on AZ91D magnesium alloy by plasma electrolytic oxidation with reduced energy consumption, *Materials Research Innovations*, 19 (2015) S2-23-S22-27.
- [93] S. Ono, S. Moronuki, Y. Mori, A. Koshi, J. Liao, H. Asoh, Effect of Electrolyte Concentration on the Structure and Corrosion Resistance of Anodic Films Formed on Magnesium through Plasma Electrolytic Oxidation, *Electrochimica Acta*, 240 (2017) 415-423. <https://doi.org/10.1016/j.electacta.2017.04.110>.
- [94] H. Tian, Y. Zhang, X. Hao, H. Zhang, W. Wu, G. Han, Z. Dou, Y. Wei, Y. Zhang, F. Chen, Preparation and characterization of the low-energy plasma electrolysis oxide coatings on MgLi alloy, *Surface and Coatings Technology*, 440 (2022) 128445. <https://doi.org/10.1016/j.surfcoat.2022.128445>.
- [95] F. Jaspard-Mécuson, T. Czerwicz, G. Henrion, T. Belmonte, L. Dujardin, A. Viola, J. Beauvir, Tailored aluminium oxide layers by bipolar current adjustment in the Plasma Electrolytic Oxidation (PEO) process, *Surface and Coatings Technology*, 201 (2007) 8677-8682. <https://doi.org/10.1016/j.surfcoat.2006.09.005>.
- [96] A.B. Rogov, A. Yerokhin, A. Matthews, The role of cathodic current in plasma electrolytic oxidation of aluminum: Phenomenological concepts of the “soft sparking” mode, *Langmuir*, 33 (2017) 11059-11069.
- [97] E. Matykina, R. Arrabal, P. Skeldon, G. Thompson, P. Wang, P. Wood, Plasma electrolytic oxidation of a zirconium alloy under AC conditions, *Surface and Coatings Technology*, 204 (2010) 2142-2151.
- [98] P. Fernández-López, S.A. Alves, J.T. San-Jose, E. Gutierrez-Berasategui, R. Bayón, Plasma Electrolytic Oxidation (PEO) as a Promising Technology for the Development of High-Performance Coatings on Cast Al-Si Alloys: A Review, *Coatings*, 14 (2024) 217.
- [99] F. Tjiang, L.-W. Ye, Y.-J. Huang, C.-C. Chou, D.-S. Tsai, Effect of processing parameters on soft regime behavior of plasma electrolytic oxidation of magnesium, *Ceramics International*, 43 (2017) S567-S572. <https://doi.org/10.1016/j.ceramint.2017.05.179>.
- [100] R.O. Hussein, D.O. Northwood, J.F. Su, X. Nie, A study of the interactive effects of hybrid current modes on the tribological properties of a PEO (plasma electrolytic oxidation) coated AM60B Mg-alloy, *Surface and Coatings Technology*, 215 (2013) 421-430. <https://doi.org/10.1016/j.surfcoat.2012.08.082>.
- [101] D.-S. Tsai, C.-C. Chou, Review of the soft sparking issues in plasma electrolytic oxidation, *Metals*, 8 (2018) 105.
- [102] M. Mohedano, E. Lopez, B. Mingo, S. Moon, E. Matykina, R. Arrabal, Energy consumption, wear and corrosion of PEO coatings on preanodized Al alloy: the influence of current and frequency, *Journal of Materials Research and Technology*, 21 (2022) 2061-2075. <https://doi.org/10.1016/j.jmrt.2022.10.049>.
- [103] M.A. Iqbal, H. Asghar, V. Maurino, E. Matykina, R. Arrabal, M. Mohedano, Evaluating the energy consumption, structural, and corrosion resistance properties of photocatalytic TiO<sub>2</sub>-based PEO coatings on pre-anodized AA2024-Al, *Surfaces and Interfaces*, 44 (2024) 103659. <https://doi.org/10.1016/j.surfin.2023.103659>.
- [104] M.A. Iqbal, E. Matykina, R. Arrabal, M. Mohedano, Role of anodic precursor layer thickness on PEO coatings: Energy consumption and long-term corrosion performance, *Surface and Coatings Technology*, 476 (2024) 130186. <https://doi.org/10.1016/j.surfcoat.2023.130186>.
- [105] M. Mohedano, B. Mingo, H. Mora-Sánchez, E. Matykina, R. Arrabal, Effects of pre-anodizing and phosphates on energy consumption and corrosion performance of PEO coatings on AA6082, *Surface and Coatings Technology*, 409 (2021) 126892. <https://doi.org/10.1016/j.surfcoat.2021.126892>.
- [106] M. Kaseem, S. Fatimah, N. Nashrah, Y.G. Ko, Recent progress in surface modification of metals coated by plasma electrolytic oxidation: Principle, structure, and performance, *Progress in Materials Science*, 117 (2021) 100735. <https://doi.org/10.1016/j.pmatsci.2020.100735>.
- [107] J. Cai, F. Cao, L. Chang, J. Zheng, J. Zhang, C. Cao, The preparation and corrosion behaviors of MAO coating on AZ91D with rare earth conversion precursor film, *Applied Surface Science*, 257 (2011) 3804-3811. <https://doi.org/10.1016/j.apsusc.2010.11.153>.
- [108] J. Lu, X. He, H. Li, R. Song, Microstructure and corrosion resistance of PEO coatings formed on KBM10 Mg alloy pretreated with Nd (NO<sub>3</sub>)<sub>3</sub>, *Materials*, 11 (2018) 1062.
- [109] F. Wei, W. Zhang, T. Zhang, F. Wang, Microstructure and Corrosion Resistance Studies of PEO Coated Mg Alloys with a HF and US Pretreatment, *International Journal of Electrochemical Science*, 12 (2017) 155-165. <https://doi.org/10.20964/2017.01.62>.
- [110] L. Wang, J. Zhou, J. Liang, J. Chen, Corrosion mechanism of plasma electrolytic oxidation coated magnesium alloy with laser surface melting pretreatment, *Journal of The Electrochemical Society*, 161 (2013) C20.

- [111] C.Y. Tan, C. Wen, H.Q. Ang, Influence of laser parameters on the microstructures and surface properties in laser surface modification of biomedical magnesium alloys, *Journal of Magnesium and Alloys*, 12 (2024) 72-97. <https://doi.org/10.1016/j.jma.2023.12.008>.
- [112] A. Singh, S.P. Harimkar, Laser surface engineering of magnesium alloys: a review, *Jom*, 64 (2012) 716-733.
- [113] M. Karamimoghadam, M. Rezayat, M. Moradi, A. Mateo, G. Casalino, Laser Surface Transformation Hardening for Automotive Metals: Recent Progress, *Metals*, 14 (2024) 339.
- [114] J. Lou, Y. Sun, Y. Chen, R. Zan, H. Peng, S. Yang, X. Kang, Z. Peng, W. Wang, X. Zhang, Effects of MgF<sub>2</sub> coating on the biodegradation and biological properties of magnesium, *Surface and Coatings Technology*, 422 (2021) 127552.
- [115] D. Ivanou, K. Yasakau, S. Kallip, A. Lisenkov, M. Starykevich, S. Lamaka, M. Ferreira, M. Zheludkevich, Active corrosion protection coating for a ZE41 magnesium alloy created by combining PEO and sol-gel techniques, *RSC advances*, 6 (2016) 12553-12560.
- [116] Z. Li, X. Jing, Y. Yuan, M. Zhang, Composite coatings on a Mg-Li alloy prepared by combined plasma electrolytic oxidation and sol-gel techniques, *Corrosion Science*, 63 (2012) 358-366. <https://doi.org/10.1016/j.corsci.2012.06.018>.
- [117] Y. Chen, X. Lu, S.V. Lamaka, P. Ju, C. Blawert, T. Zhang, F. Wang, M.L. Zheludkevich, Active protection of Mg alloy by composite PEO coating loaded with corrosion inhibitors, *Applied Surface Science*, 504 (2020) 144462. <https://doi.org/10.1016/j.apsusc.2019.144462>.
- [118] W. Shang, B. Chen, X. Shi, Y. Chen, X. Xiao, Electrochemical corrosion behavior of composite MAO/sol-gel coatings on magnesium alloy AZ91D using combined micro-arc oxidation and sol-gel technique, *Journal of Alloys and Compounds*, 474 (2009) 541-545. <https://doi.org/10.1016/j.jallcom.2008.06.135>.
- [119] M. Ostapiuk, M.G. Taryba, L.M. Calado, J. Bieniaś, M.F. Montemor, A study on the galvanic corrosion of a sol-gel coated PEO Mg-CFRP couple, *Corrosion Science*, 186 (2021) 109470. <https://doi.org/10.1016/j.corsci.2021.109470>.
- [120] L. Pezzato, M. Rigon, A. Martucci, K. Brunelli, M. Dabalà, Plasma Electrolytic Oxidation (PEO) as pre-treatment for sol-gel coating on aluminum and magnesium alloys, *Surface and Coatings Technology*, 366 (2019) 114-123. <https://doi.org/10.1016/j.surfcoat.2019.03.023>.
- [121] J. Li, H. Bai, Z. Feng, Advances in the modification of Silane-Based Sol-Gel coating to improve the corrosion resistance of magnesium alloys, *Molecules*, 28 (2023) 2563.
- [122] J. Han, C. Blawert, S. Tang, J. Yang, J. Hu, M.L. Zheludkevich, Formation and corrosion behaviors of calcium phosphate coatings on plasma electrolytic oxidized Mg under changing chemical environment, *Surface and Coatings Technology*, 412 (2021) 127030. <https://doi.org/10.1016/j.surfcoat.2021.127030>.
- [123] M. Wu, Y. Guo, G. Xu, Y. Cui, Effects of Deposition Thickness on Electrochemical Behaviors of AZ31B Magnesium Alloy with Composite Coatings Prepared by Micro-arc Oxidation and Electrophoretic Deposition, *International Journal of Electrochemical Science*, 15 (2020) 1378-1390. <https://doi.org/10.20964/2020.02.08>.
- [124] C.-Y. Li, X.-L. Fan, L.-Y. Cui, R.-C. Zeng, Corrosion resistance and electrical conductivity of a nano ATO-doped MAO/methyltrimethoxysilane composite coating on magnesium alloy AZ31, *Corrosion Science*, 168 (2020) 108570. <https://doi.org/10.1016/j.corsci.2020.108570>.
- [125] S.V. Gnedenkov, S.L. Sinebryukhov, D.V. Mashtalyar, I.M. Imshinetskiy, Composite fluoropolymer coatings on Mg alloys formed by plasma electrolytic oxidation in combination with electrophoretic deposition, *Surface and Coatings Technology*, 283 (2015) 347-352. <https://doi.org/10.1016/j.surfcoat.2015.10.066>.
- [126] A. Zarei, C. Dehghanian, H. Farhangi, Z. Jafari, Improvement of Mg alloy corrosion resistance and apatite formation ability via PEO/Alginate/Akermanite hybrid coatings for biomedical purposes, *Ceramics International*, 50 (2024) 20994-21007. <https://doi.org/10.1016/j.ceramint.2024.03.198>.
- [127] M. Mohedano, P. Pérez, E. Matykina, B. Pillado, G. Garcés, R. Arrabal, PEO coating with Ce-sealing for corrosion protection of LPSO Mg-Y-Zn alloy, *Surface and Coatings Technology*, 383 (2020) 125253. <https://doi.org/10.1016/j.surfcoat.2019.125253>.
- [128] M. Mohedano, C. Blawert, M.L. Zheludkevich, Cerium-based sealing of PEO coated AM50 magnesium alloy, *Surface and Coatings Technology*, 269 (2015) 145-154. <https://doi.org/10.1016/j.surfcoat.2015.01.003>.
- [129] X. Lu, J. Ma, M. Mohedano, B. Pillado, R. Arrabal, K. Qian, Y. Li, T. Zhang, F. Wang, Ca-based sealing of plasma electrolytic oxidation coatings on AZ91 Mg alloy, *Surface and Coatings Technology*, 417 (2021) 127220. <https://doi.org/10.1016/j.surfcoat.2021.127220>.
- [130] D. Liu, Y. Song, D. Shan, E.H. Han, Self-Healing Coatings Prepared by Loading Interphase Inhibitors into MAO Coating of AM60 Mg Alloy, *Journal of The Electrochemical Society*, 165 (2018) C412. 10.1149/2.0011809jes.

- [131] J. Han, K. Fu, Z. Jiang, H. Zhang, H. San, H. Chen, X. Lu, C. Blawert, M.L. Zheludkevich, Smart gradient coating suitable for bone growth prepared on plasma-electrolytically oxidised Mg and its sequential degradation behaviour, *Journal of Magnesium and Alloys*, (2024). <https://doi.org/10.1016/j.jma.2024.05.026>.
- [132] L. Xu, X. Fu, H. Su, H. Sun, R. Li, Y. Wan, Corrosion and tribocorrosion protection of AZ31B Mg alloy by a hydrothermally treated PEO/chitosan composite coating, *Progress in Organic Coatings*, 170 (2022) 107002.
- [133] Y. Li, C. Guo, C. Qi, D. Zhang, H. Sun, S. Yang, Y. Wan, Y. Wang, Enhancement of the corrosion resistance of the PEO-coated 5052 aluminum alloy by the chitosan film: Effects of solvent acids, *Progress in Organic Coatings*, 192 (2024) 108495. <https://doi.org/10.1016/j.porgcoat.2024.108495>.
- [134] Y.-K. Kim, K.-B. Lee, S.-Y. Kim, Y.-S. Jang, J.H. Kim, M.-H. Lee, Improvement of osteogenesis by a uniform PCL coating on a magnesium screw for biodegradable applications, *Scientific Reports*, 8 (2018) 13264. 10.1038/s41598-018-31359-9.
- [135] M. Yazdimamaghani, M. Razavi, D. Vashaei, L. Tayebi, Surface modification of biodegradable porous Mg bone scaffold using polycaprolactone/bioactive glass composite, *Materials Science and Engineering: C*, 49 (2015) 436-444. <https://doi.org/10.1016/j.msec.2015.01.041>.
- [136] A. Alabbasi, A. Mehjabeen, M.B. Kannan, Q. Ye, C. Blawert, Biodegradable polymer for sealing porous PEO layer on pure magnesium: An in vitro degradation study, *Applied Surface Science*, 301 (2014) 463-467. <https://doi.org/10.1016/j.apsusc.2014.02.100>.
- [137] A. Azizi Amirabad, M. Johari, R. Parichehr, R. Mehdiavaz Aghdam, C. Dehghanian, S.R. Allahkaram, Improving corrosion, antibacterial and biocompatibility properties of MAO-coated AZ31 magnesium alloy by Cu(II)-chitosan/PVA nanofibers post-treatment, *Ceramics International*, 49 (2023) 17371-17382. <https://doi.org/10.1016/j.ceramint.2023.02.106>.
- [138] E. Parfenov, L. Parfenova, V. Mukaeva, R. Farrakhov, A. Stotskiy, A. Raab, K. Danilko, N. Rameshbabu, R. Valiev, Biofunctionalization of PEO coatings on titanium implants with inorganic and organic substances, *Surface and Coatings Technology*, 404 (2020) 126486. <https://doi.org/10.1016/j.surfcoat.2020.126486>.
- [139] E. Matykina, R. Arrabal, A. Pardo, M. Mohedano, B. Mingo, I. Rodríguez, J. González, Energy-efficient PEO process of aluminium alloys, *Materials Letters*, 127 (2014) 13-16. <https://doi.org/10.1016/j.matlet.2014.04.077>.
- [140] V. Dehnavi, W.J. Binns, J.J. Noël, D.W. Shoesmith, B.L. Luan, Growth behaviour of low-energy plasma electrolytic oxidation coatings on a magnesium alloy, *Journal of Magnesium and Alloys*, 6 (2018) 229-237. <https://doi.org/10.1016/j.jma.2018.05.008>.
- [141] A.s. technologies, <https://www.aalberts-st.com/processes/plasma-chemical-coatings/>, in, (accessed on 1 August 2024)
- [142] <https://www.keronite.com/>, <https://www.keronite.com/>, ((accessed on 1 September 2024)).
- [143] T.T.A. Group, <https://www.tagnite.com/tagnite-coating/>, ((accessed on 1 August 2024)).
- [144] E.L.H.Z. GmbH, <https://ceranod.de/en/treatments/plasma-ceramics/>, ((accessed on 1 August 2024)).
- [145] A. Santos-Coquillat, M. Esteban-Lucia, E. Martinez-Campos, M. Mohedano, R. Arrabal, C. Blawert, M.L. Zheludkevich, E. Matykina, PEO coatings design for Mg-Ca alloy for cardiovascular stent and bone regeneration applications, *Materials Science and Engineering: C*, 105 (2019) 110026. <https://doi.org/10.1016/j.msec.2019.110026>.
- [146] A. Fattah-alhosseini, R. Chaharmahali, K. Babaei, M. Nouri, M.K. Keshavarz, M. Kaseem, A review of effective strides in amelioration of the biocompatibility of PEO coatings on Mg alloys, *Journal of Magnesium and Alloys*, 10 (2022) 2354-2383. <https://doi.org/10.1016/j.jma.2022.09.002>.
- [147] H. Sampatirao, S. Radhakrishnapillai, S. Dondapati, E. Parfenov, R. Nagumothu, Developments in plasma electrolytic oxidation (PEO) coatings for biodegradable magnesium alloys, *Materials Today: Proceedings*, 46 (2021) 1407-1415. <https://doi.org/10.1016/j.matpr.2021.02.650>.
- [148] A. Kopp, H. Fischer, A.P. Soares, K. Schmidt-Bleek, C. Leber, H. Kreiker, G. Duda, N. Kröger, K. van Gaalen, H. Hanken, Long-term in vivo observations show biocompatibility and performance of ZX00 magnesium screws surface-modified by plasma-electrolytic oxidation in Göttingen miniature pigs, *Acta Biomaterialia*, 157 (2023) 720-733.
- [149] S. Stojadinović, N. Radić, R. Vasilčić, Photoluminescent and photocatalytic properties of Eu<sup>3+</sup>-doped MgAl oxide coatings formed by plasma electrolytic oxidation of AZ31 magnesium alloy, *Coatings*, 12 (2022) 1830.
- [150] E.V. Golyeva, I.E. Kolesnikov, E. Lähderanta, A.V. Kurochkin, M.D. Mikhailov, Effect of synthesis conditions on structural, morphological and luminescence properties of MgAl<sub>2</sub>O<sub>4</sub>:Eu<sup>3+</sup> nanopowders, *Journal of Luminescence*, 194 (2018) 387-393. <https://doi.org/10.1016/j.jlumin.2017.10.068>.

- [151] K. Ganesh Kumar, P. Balaji Bhargav, K. Aravinth, N. Ahmed, C. Balaji, Photoluminescence and electrochemical performance evaluation of Eu<sup>3+</sup> doped MgAl<sub>2</sub>O<sub>4</sub> phosphors for LED and energy storage applications, *Ceramics International*, 48 (2022) 36038-36045. <https://doi.org/10.1016/j.ceramint.2022.08.015>.
- [152] V.S. Rudnev, V.P. Morozova, I.V. Lukiyanichuk, I.A. Tkachenko, M.V. Adigamova, A.Y. Ustinov, P.V. Kharitonov, A.M. Frolov, S.A. Boev, Magnetic properties of plasma-electrolytic iron-containing oxide coatings on aluminum alloy, *Protection of Metals and Physical Chemistry of Surfaces*, 49 (2013) 309-318. 10.1134/S2070205113030143.
- [153] V.S. Rudnev, I.V. Lukiyanichuk, M.V. Adigamova, V.P. Morozova, I.A. Tkachenko, The effect of nanocrystallites in the pores of PEO coatings on their magnetic properties, *Surface and Coatings Technology*, 269 (2015) 23-29. <https://doi.org/10.1016/j.surfcoat.2015.01.073>.
- [154] C. Song, C. Wang, D. Mercier, B. Vaghefinazari, A. Seyeux, D. Snihirova, D.C.F. Wieland, P. Marcus, M.L. Zheludkevich, S.V. Lamaka, Corrosion inhibition mechanism of 2,6-pyridinedicarboxylate depending on magnesium surface treatment, *Corrosion Science*, 229 (2024) 111867. <https://doi.org/10.1016/j.corsci.2024.111867>.
- [155] D. Snihirova, L. Wang, S.V. Lamaka, C. Wang, M. Deng, B. Vaghefinazari, D. Höche, M.L. Zheludkevich, Synergistic Mixture of Electrolyte Additives: A Route to a High-Efficiency Mg–Air Battery, *The Journal of Physical Chemistry Letters*, 11 (2020) 8790-8798. 10.1021/acs.jpcclett.0c02174.
- [156] C. Krywka, H. Neubauer, M. Priebe, T. Salditt, J. Keckes, A. Buffet, S.V. Roth, R. Doebrmann, M. Mueller, A two-dimensional waveguide beam for X-ray nanodiffraction, *Journal of applied crystallography*, 45 (2012) 85-92.
- [157] G. Ashiotis, A. Deschildre, Z. Nawaz, J.P. Wright, D. Karkoulis, F.E. Picca, J. Kieffer, The fast azimuthal integration Python library: pyFAI, *Journal of applied crystallography*, 48 (2015) 510-519.
- [158] T. Wu, C. Blawert, M. Serdechnova, P. Karlova, G. Dovzhenko, D.C.F. Wieland, M.L. Zheludkevich, PEO processing of AZ91Nd/Al<sub>2</sub>O<sub>3</sub> MMC-the role of alumina fibers, *Journal of Magnesium and Alloys*, 10 (2022) 423-439. <https://doi.org/10.1016/j.jma.2021.09.017>.
- [159] H.R. Fleck, A. Ward, The determination of metals by means of 8-hydroxyquinoline. Part I. The effect of p H on the precipitation of magnesium, zinc, cobalt, nickel, copper and molybdenum from acetate solutions, *Analyst*, 58 (1933) 388-395.
- [160] V. Guillaumin, P. Schmutz, G. Frankel, Characterization of corrosion interfaces by the scanning Kelvin probe force microscopy technique, *Journal of the Electrochemical Society*, 148 (2001) B163.
- [161] M. Hurley, C. Efaw, P. Davis, J. Croteau, E. Graugnard, N. Biribilis, Volta potentials measured by scanning kelvin probe force microscopy as relevant to corrosion of magnesium alloys, *Corrosion*, 71 (2015) 160-170.
- [162] M. Rohwerder, F. Turcu, High-resolution Kelvin probe microscopy in corrosion science: Scanning Kelvin probe force microscopy (SKPFM) versus classical scanning Kelvin probe (SKP), *Electrochimica Acta*, 53 (2007) 290-299. <https://doi.org/10.1016/j.electacta.2007.03.016>.
- [163] K.A. Yasakau, A. Maltseva, S.V. Lamaka, D. Mei, H. Orvi, P. Volovitch, M.G.S. Ferreira, M.L. Zheludkevich, The effect of carboxylate compounds on Volta potential and corrosion inhibition of Mg containing different levels of iron, *Corrosion Science*, 194 (2022) 109937. <https://doi.org/10.1016/j.corsci.2021.109937>.
- [164] A. Seyeux, M. Liu, P. Schmutz, G. Song, A. Atrens, P. Marcus, ToF-SIMS depth profile of the surface film on pure magnesium formed by immersion in pure water and the identification of magnesium hydride, *Corrosion Science*, 51 (2009) 1883-1886. <https://doi.org/10.1016/j.corsci.2009.06.002>.
- [165] A. Maltseva, S. Lamaka, K. Yasakau, D. Mei, D. Kurchavov, M. Zheludkevich, G. Lefèvre, P. Volovitch, In situ surface film evolution during Mg aqueous corrosion in presence of selected carboxylates, *Corrosion Science*, 171 (2020) 108484.
- [166] J. Yang, C. Blawert, S.V. Lamaka, K.A. Yasakau, L. Wang, D. Laipple, M. Schieda, S. Di, M.L. Zheludkevich, Corrosion inhibition of pure Mg containing a high level of iron impurity in pH neutral NaCl solution, *Corrosion Science*, 142 (2018) 222-237.
- [167] L. Fockaert, T. Würger, R. Unbehau, B. Boelen, R.H. Meißner, S.V. Lamaka, M.L. Zheludkevich, H. Terryn, J. Mol, ATR-FTIR in Kretschmann configuration integrated with electrochemical cell as in situ interfacial sensitive tool to study corrosion inhibitors for magnesium substrates, *Electrochimica acta*, 345 (2020) 136166.
- [168] J. Yang, P. Jiang, Y. Qiu, C.-Y. Jao, C. Blawert, S. Lamaka, A. Bouali, X. Lu, M.L. Zheludkevich, W. Li, Experimental and quantum chemical studies of carboxylates as corrosion inhibitors for AM50 alloy in pH neutral NaCl solution, *Journal of Magnesium and Alloys*, 10 (2022) 555-568.
- [169] K. Qian, W. Li, X. Lu, X. Han, Y. Jin, T. Zhang, F. Wang, Effect of phosphate-based sealing treatment on the corrosion performance of a PEO coated AZ91D mg alloy, *Journal of Magnesium and Alloys*, 8 (2020) 1328-1340. <https://doi.org/10.1016/j.jma.2020.05.014>.

- [170] T. Würger, D. Mei, B. Vaghefinazari, D.A. Winkler, S.V. Lamaka, M.L. Zheludkevich, R.H. Meißner, C. Feiler, Exploring structure-property relationships in magnesium dissolution modulators, *npj Materials Degradation*, 5 (2021) 2. <https://doi.org/10.1038/s41529-020-00148-z>.
- [171] S.V. Lamaka, D. Höche, R.P. Petrauskas, C. Blawert, M.L. Zheludkevich, A new concept for corrosion inhibition of magnesium: Suppression of iron re-deposition, *Electrochemistry Communications*, 62 (2016) 5-8. <https://doi.org/10.1016/j.elecom.2015.10.023>.
- [172] Y. Chen, X. Wang, T. Lai, D. Liu, J. Pan, L. Lin, H. Guan, C. Luo, H. Song, Y. Xin, H. Yan, Z. Hu, Sodium dodecylbenzene sulfonate film absorbed on magnesium alloy surface: An electrochemical, SKPFM, and molecular dynamics study, *Journal of Molecular Liquids*, 357 (2022) 119095. <https://doi.org/10.1016/j.molliq.2022.119095>.
- [173] A. Frignani, V. Grassi, F. Zanotto, F. Zucchi, Inhibition of AZ31 Mg alloy corrosion by anionic surfactants, *Corrosion Science*, 63 (2012) 29-39. <https://doi.org/10.1016/j.corsci.2012.05.012>.
- [174] C. Verma, M.A. Quraishi, E.E. Ebenso, Quinoline and its derivatives as corrosion inhibitors: A review, *Surfaces and Interfaces*, 21 (2020) 100634. <https://doi.org/10.1016/j.surfin.2020.100634>.
- [175] C. Verma, K.Y. Rhee, M.A. Quraishi, E.E. Ebenso, Pyridine based N-heterocyclic compounds as aqueous phase corrosion inhibitors: A review, *Journal of the Taiwan Institute of Chemical Engineers*, 117 (2020) 265-277. <https://doi.org/10.1016/j.jtice.2020.12.011>.
- [176] E. Mena-Morcillo, L.P. Veleza, D.O. Wipf, Multi-scale monitoring the first stages of electrochemical behavior of AZ31B magnesium alloy in simulated body fluid, *Journal of the Electrochemical Society*, 165 (2018) C749.
- [177] A. Pardo, M. Merino, A. Coy, F. Viejo, R. Arrabal, S. Feliu Jr, Influence of microstructure and composition on the corrosion behaviour of Mg/Al alloys in chloride media, *Electrochimica Acta*, 53 (2008) 7890-7902.
- [178] S. Pawar, X. Zhou, G. Thompson, G. Scamans, Z. Fan, The role of intermetallics on the corrosion initiation of twin roll cast AZ31 Mg alloy, *Journal of The Electrochemical Society*, 162 (2015) C442.
- [179] B. Vaghefinazari, Lamaka, S.V., Blawert, C., Serdechnova, M., Scharnagl, N., Karlova, P., Wieland, D.C.F., Zheludkevich, M.L., Exploring the corrosion inhibition mechanism of 8-hydroxyquinoline for a PEO-coated magnesium alloy, *Corrosion Science*, (2022) 110344. doi:10.1016/j.corsci.2022.110344.
- [180] Y. Chen, Y. Yang, T. Zhang, W. Zhang, FuhuiWang, X. Lu, C. Blawert, M.L. Zheludkevich, Interaction effect between different constituents in silicate-containing electrolyte on PEO coatings on Mg alloy, *Surface and Coatings Technology*, 307 (2016) 825-836. <https://doi.org/10.1016/j.surfcoat.2016.09.031>.
- [181] R. Arrabal, A. Pardo, M.C. Merino, M. Mohedano, P. Casajús, E. Matykina, P. Skeldon, G.E. Thompson, Corrosion behaviour of a magnesium matrix composite with a silicate plasma electrolytic oxidation coating, *Corrosion Science*, 52 (2010) 3738-3749. <https://doi.org/10.1016/j.corsci.2010.07.024>.
- [182] A. Jangde, S. Kumar, C. Blawert, Role of glycerine on formation & corrosion characteristic of PEO layer formed over Mg alloy in a high-concentrated mixed silicate-phosphate-based electrolyte, *Surface and Coatings Technology*, 450 (2022) 128971. <https://doi.org/10.1016/j.surfcoat.2022.128971>.
- [183] M. Lintuluoto, H. Nakatsuji, M. Hada, H. Kanai, Theoretical study of the decomposition of HCOOH on an MgO(100) surface, *Surface Science*, 429 (1999) 133-142. [https://doi.org/10.1016/S0039-6028\(99\)00357-X](https://doi.org/10.1016/S0039-6028(99)00357-X).
- [184] B. Vaghefinazari, D. Snihirova, C. Wang, L. Wang, M. Deng, D. Höche, S.V. Lamaka, M.L. Zheludkevich, Exploring the effect of sodium salt of Ethylenediaminetetraacetic acid as an electrolyte additive on electrochemical behavior of a commercially pure Mg in primary Mg-air batteries, *Journal of Power Sources*, 527 (2022) 231176. <https://doi.org/10.1016/j.jpowsour.2022.231176>.
- [185] R.M.C. Dawson, D.C. Elliott, W.H. Elliott, K.M. Jones, Data for biochemical research, (1959).
- [186] E. Petrova, M. Serdechnova, T. Shulha, S.V. Lamaka, D.C.F. Wieland, P. Karlova, C. Blawert, M. Starykevich, M.L. Zheludkevich, Use of synergistic mixture of chelating agents for in situ LDH growth on the surface of PEO-treated AZ91, *Scientific Reports*, 10 (2020) 8645. 10.1038/s41598-020-65396-0.
- [187] Q. Chen, X. Lu, M. Serdechnova, T. Wu, D.C.F. Wieland, V. Kasneryk, T. Shulha, H. Liu, C. Blawert, M.L. Zheludkevich, F. Wang, Synergistic chelating agents for in-situ synthesis of Mg-Al LDH films on PEO treated Mg alloy, *Journal of Magnesium and Alloys*, (2024). <https://doi.org/10.1016/j.jma.2024.05.015>.
- [188] A. Martell, Critical Stability Constants: Volume 2: Amines, Springer Science & Business Media, 2012.
- [189] Q. Zong, L. Wang, W. Sun, G. Liu, Active deposition of bis (8-hydroxyquinoline) magnesium coating for enhanced corrosion resistance of AZ91D alloy, *Corrosion Science*, 89 (2014) 127-136. <https://doi.org/10.1016/j.corsci.2014.08.024>.
- [190] H.N. Soliman, Influence of 8-hydroxyquinoline addition on the corrosion behavior of commercial Al and Al-HO411 alloys in NaOH aqueous media, *Corrosion Science*, 53 (2011) 2994-3006. <https://doi.org/10.1016/j.corsci.2011.05.045>.

- [191] S.V. Lamaka, M.L. Zheludkevich, K.A. Yasakau, M.F. Montemor, M.G.S. Ferreira, High effective organic corrosion inhibitors for 2024 aluminium alloy, *Electrochimica Acta*, 52 (2007) 7231-7247. <https://doi.org/10.1016/j.electacta.2007.05.058>.
- [192] W.M. Haynes, CRC handbook of chemistry and physics, CRC press, 2016.
- [193] K. Chattejee, N. Dhar, Studies of sparingly soluble salts, *The Journal of Physical Chemistry*, 28 (2002) 1009-1028.
- [194] S. Boobier, D.R.J. Hose, A.J. Blacker, B.N. Nguyen, Machine learning with physicochemical relationships: solubility prediction in organic solvents and water, *Nature Communications*, 11 (2020) 5753. 10.1038/s41467-020-19594-z.
- [195] A. Schwaighofer, T. Schroeter, S. Mika, J. Laub, A. ter Laak, D. Sülzle, U. Ganzer, N. Heinrich, K.-R. Müller, Accurate Solubility Prediction with Error Bars for Electrolytes: A Machine Learning Approach, *Journal of Chemical Information and Modeling*, 47 (2007) 407-424. 10.1021/ci600205g.
- [196] C. Wang, C. Song, D. Mei, L. Wang, W. Wang, T. Wu, D. Snihirova, M.L. Zheludkevich, S.V. Lamaka, Low interfacial pH discloses the favorable biodegradability of several Mg alloys, *Corrosion Science*, 197 (2022) 110059. <https://doi.org/10.1016/j.corsci.2021.110059>.
- [197] A.S. Gnedenkov, S.L. Sinebryukhov, A.D. Nomerovskii, V.S. Marchenko, A.Y. Ustinov, S.V. Gnedenkov, Carboxylates as green corrosion inhibitors of magnesium alloy for biomedical application, *Journal of Magnesium and Alloys*, (2024). <https://doi.org/10.1016/j.jma.2024.07.004>.
- [198] B. Abd-El-Nabey, S. El-Housseiny, M. Abd-El-Fatah, Improved corrosion resistance of permanganate-phosphate conversion coat on steel surface by surfactants, *Scientific Reports*, 13 (2023) 15781.
- [199] T.S. Narayanan, The role of surfactants in phosphate conversion coatings, in: *Surfactants in Polymers, Coatings, Inks, and Adhesives*, Blackwell, 2020, pp. 271-302.
- [200] L.B. Boinovich, K.A. Emelyanenko, A.M. Emelyanenko, The mechanisms and advances in magnesium-based materials protection against corrosion by the superhydrophobic coatings, *Surface and Coatings Technology*, 481 (2024) 130607.

## Publications during candidacy

- 1- **B. Vaghefinazari**, C. Wang, D. Mercier, D. Mei, A. Seyeux, P. Marcus, C. Blawert, S.V. Lamaka, M.L. Zheludkevich, Adverse effect of 2,5PDC corrosion inhibitor on PEO coated magnesium, *Corrosion Science*, 192 (2021) 109830. doi:10.1016/j.corsci.2021.109830.
- 2- **B. Vaghefinazari**, Lamaka, S.V., Blawert, C., Serdechnova, M., Scharnagl, N., Karlova, P., Wieland, D.C.F., Zheludkevich, M.L., Exploring the corrosion inhibition mechanism of 8-hydroxyquinoline for a PEO-coated magnesium alloy, *Corrosion Science*, (2022) 110344. doi:10.1016/j.corsci.2022.110344.
- 3- **B. Vaghefinazari**, E. Wierzbicka, P. Visser, R. Posner, R. Arrabal, E. Matykina, M. Mohedano, C. Blawert, M. Zheludkevich, S. Lamaka, Chromate-free corrosion protection strategies for magnesium alloys—a review: PART I—pre-treatment and conversion coating, *Materials*, 15 (2022) 8676. doi:10.3390/ma15238676
- 4- E. Wierzbicka, **B. Vaghefinazari**, M. Mohedano, P. Visser, R. Posner, C. Blawert, M. Zheludkevich, S. Lamaka, E. Matykina, R. Arrabal, Chromate-free corrosion protection strategies for magnesium alloys—a review: part II—PEO and anodizing, *Materials*, 15 (2022) 8515. doi:10.3390/ma15238515.
- 5- **B. Vaghefinazari**, E. Wierzbicka, P. Visser, R. Posner, R. Arrabal, E. Matykina, M. Mohedano, C. Blawert, M.L. Zheludkevich, S.V. Lamaka, Chromate-free corrosion protection strategies for magnesium alloys—a review: PART III—corrosion inhibitors and combining them with other protection strategies, *Materials*, 15 (2022) 8489. doi:10.3390/ma15238489.
- 6- **B. Vaghefinazari**, S.V. Lamaka, E. Gazenbiller, K. Yasakau, C. Blawert, M. Serdechnova, N. Scharnagl, D.C.F. Wieland, M.L. Zheludkevich, Corrosion inhibition of decylphosphonate on bare and PEO-coated Mg alloy, *Corrosion Science*, 226 (2024) 111651. doi:10.1016/j.corsci.2023.111651.
- 7- S.V. Lamaka, **B. Vaghefinazari**, D. Mei, R.P. Petrauskas, D. Höche, M.L. Zheludkevich, Comprehensive screening of Mg corrosion inhibitors, *Corrosion Science*, 128 (2017) 224-240. doi:10.1016/j.corsci.2017.07.011.
- 8- D. Höche, S.V. Lamaka, **B. Vaghefinazari**, T. Braun, R.P. Petrauskas, M. Fichtner, M.L. Zheludkevich, Performance boost for primary magnesium cells using iron complexing agents as electrolyte additives, *Scientific Reports*, 8 (2018) 7578. <https://doi.org/10.1038/s41598-018-25789-8>.
- 9- M. Deng, D. Höche, D. Snihirova, L. Wang, **B. Vaghefinazari**, S. Lamaka, M. Zheludkevich, Magnesium Batteries: Research and Applications, *Bibliothèque Sainte Genevieve*, (2020) 275-308. <https://doi.org/10.1039/9781788016407>.
- 10- C. Feiler, D. Mei, **B. Vaghefinazari**, T. Würger, R.H. Meißner, B.J.C. Luthringer-Feyerabend, D.A. Winkler, M.L. Zheludkevich, S.V. Lamaka, In silico screening of modulators of magnesium dissolution, *Corrosion Science*, 163 (2020) 108245. <https://doi.org/10.1016/j.corsci.2019.108245>.
- 11- **B. Vaghefinazari**, D. Höche, S.V. Lamaka, D. Snihirova, M.L. Zheludkevich, Tailoring the Mg-air primary battery performance using strong complexing agents as electrolyte additives, *Journal of Power Sources*, 453 (2020) 227880. <https://doi.org/10.1016/j.jpowsour.2020.227880>.
- 12- L. Wang, D. Snihirova, M. Deng, **B. Vaghefinazari**, S.V. Lamaka, D. Höche, M.L. Zheludkevich, Tailoring electrolyte additives for controlled Mg-Ca anode activity in aqueous Mg-air batteries, *Journal of Power Sources*, 460 (2020) 228106. <https://doi.org/10.1016/j.jpowsour.2020.228106>.
- 13- D. Snihirova, L. Wang, S.V. Lamaka, C. Wang, M. Deng, **B. Vaghefinazari**, D. Höche, M.L. Zheludkevich, Synergistic mixture of electrolyte additives: A route to a high-efficiency Mg–Air battery, *The journal of physical chemistry letters*, 11 (2020) 8790-8798. <https://doi.org/10.1021/acs.jpcllett.0c02174>.
- 14- T. Würger, D. Mei, **B. Vaghefinazari**, D.A. Winkler, S.V. Lamaka, M.L. Zheludkevich, R.H. Meißner, C. Feiler, Exploring structure-property relationships in magnesium dissolution modulators, *npj Materials Degradation*, 5 (2021) 2. <https://doi.org/10.1038/s41529-020-00148-z>.
- 15- E. Wierzbicka, **B. Vaghefinazari**, S.V. Lamaka, M.L. Zheludkevich, M. Mohedano, L. Moreno, P. Visser, A. Rodriguez, J. Velasco, R. Arrabal, E. Matykina, Flash-PEO as an alternative to chromate conversion coatings

- for corrosion protection of Mg alloy, *Corrosion Science*, 180 (2021) 109189. <https://doi.org/10.1016/j.corsci.2020.109189>.
- 16- L. Wang, D. Snihirova, M. Deng, C. Wang, **B. Vaghefinazari**, G. Wiese, M. Langridge, D. Höche, S.V. Lamaka, M.L. Zheludkevich, Insight into physical interpretation of high frequency time constant in electrochemical impedance spectra of Mg, *Corrosion Science*, 187 (2021) 109501. <https://doi.org/10.1016/j.corsci.2021.109501>.
  - 17- M. Deng, L. Wang, **B. Vaghefinazari**, W. Xu, C. Feiler, S.V. Lamaka, D. Höche, M.L. Zheludkevich, D. Snihirova, High-energy and durable aqueous magnesium batteries: Recent advances and perspectives, *Energy Storage Materials*, 43 (2021) 238-247. <https://doi.org/10.1016/j.ensm.2021.09.008>.
  - 18- L. Wang, D. Snihirova, M. Deng, **B. Vaghefinazari**, D. Höche, S.V. Lamaka, M.L. Zheludkevich, Enhancement of discharge performance for aqueous Mg-air batteries in 2,6-dihydroxybenzoate-containing electrolyte, *Chemical Engineering Journal*, 429 (2022) 132369. <https://doi.org/10.1016/j.cej.2021.132369>.
  - 19- L. Wang, D. Snihirova, M. Deng, **B. Vaghefinazari**, D. Höche, S.V. Lamaka, M.L. Zheludkevich, Revealing physical interpretation of time constants in electrochemical impedance spectra of Mg via Tribo-EIS measurements, *Electrochimica Acta*, 404 (2022) 139582. <https://doi.org/10.1016/j.electacta.2021.139582>.
  - 20- **B. Vaghefinazari**, D. Snihirova, C. Wang, L. Wang, M. Deng, D. Höche, S.V. Lamaka, M.L. Zheludkevich, Exploring the effect of sodium salt of Ethylenediaminetetraacetic acid as an electrolyte additive on electrochemical behavior of a commercially pure Mg in primary Mg-air batteries, *Journal of Power Sources*, 527 (2022) 231176. <https://doi.org/10.1016/j.jpowsour.2022.231176>.
  - 21- L. Wang, D. Snihirova, M. Deng, **B. Vaghefinazari**, W. Xu, D. Höche, S.V. Lamaka, M.L. Zheludkevich, Sustainable aqueous metal-air batteries: An insight into electrolyte system, *Energy Storage Materials*, 52 (2022) 573-597. <https://doi.org/10.1016/j.ensm.2022.08.032>.
  - 22- E.J. Schiessler, T. Würger, **B. Vaghefinazari**, S.V. Lamaka, R.H. Meißner, C.J. Cyron, M.L. Zheludkevich, C. Feiler, R.C. Aydin, Searching the chemical space for effective magnesium dissolution modulators: a deep learning approach using sparse features, *npj Materials Degradation*, 7 (2023) 74. 10.1038/s41529-023-00391-0.

## Acknowledgement

The journey to completing this PhD has been a truly enriching experience, filled with challenges and invaluable support from many individuals. I am deeply grateful to everyone who helped me in countless ways, making this achievement possible.

First and foremost, I would like to express my sincere appreciation to my supervisor, Prof. Mikhail Zheludkevich. Thank you for giving me the opportunity to pursue this research under your guidance. Your unwavering positivity, support, and resilience in the face of any challenge have been a constant source of inspiration. I am truly grateful for your dedication and belief in my potential.

My deepest gratitude also goes to my daily supervisor, Dr. Sviatlana Lamaka, whose patient supervision and guidance shaped my journey from day one. I vividly remember our first meeting and how her encouragement motivated me to embrace not only the science but also various managerial responsibilities. She continuously challenged me to grow, and her unwavering support has been a fundamental part of my development.

I would also like to extend my heartfelt thanks to my colleagues in the MO institute for their kindness, assistance, and the sense of community they provided. I am especially grateful to Mr. Gert Wise, whom I considered as a wiser brother, and Ms. Petra Fischer, who was always kind to me like an older sister. I am also thankful for the support I received throughout my time at Hereon from Mr. Volker Heitmann, Mr. Ulrich Burmester, Mr. Daniel Strerath, Ms. Sabine Schrader, and Ms. Anja Franke.

I would also like to thank Dr. Daniel Höche, Dr. Christian Feiler, Dr. Carsten Blawert, Dr. Maria Serdechnova, and Dr. Nico Scharnagl for their insightful help and willingness to share their knowledge, which made a significant impact on my journey. The time you took to explain concepts and offer guidance not only deepened my understanding but also inspired me to approach challenges with curiosity and confidence.

The extended duration of my PhD gave me the unique opportunity to connect with a diverse group of wonderful people. I would like to acknowledge Anissa and Rosario, who were the first to offer help from my very first day at Hereon and whose courage and helpfulness left a lasting impression. Darya, a great friend with a creative mind, has been a consistent source of inspiration. I also owe thanks to Cheng Wang, with whom I shared many insightful discussions about science and life during our journeys home. Linqian and Min, a talented and supportive couple, were always there to help me when I needed it. I am grateful to all my friends and colleagues who brought me happiness throughout my PhD journey: Arash, Tatsiana, Evgeni, Eshwara, Serge, Ksenyia, Christos, Mathias, Di, Eugen, Lukas, Valeryia, Danilo, Natalia, Aravinth, Hyemin, Wendi, Ya-jing, Lisa, Tim, Ting, Yulong, Ci, Mengyao, Qianqian, Peng, and others.

Maman and Minoo, I am grateful for your constant love, encouragement, and support. You were my anchor in moments of doubt and always believed in my ability to persevere.

To Zizoo, always listening with an open heart and offering soul-soothing words during the toughest times. Your kindness and wisdom brought comfort and strength when I needed it most, helping me grow into a better person. I owe my peace throughout our journey to you, and for that, I will be **eternally** grateful.